THE UNIVERSITY
of EDINBURGH

The Quetrupillán Volcanic Complex, Chile:
Holocene volcanism, magmatic plumbing system, and future hazards

Isla Catherine Simmons

PhD Thesis

The University of Edinburgh

2021

I declare that the contents of this thesis result from my own work and that it has been composed by myself, except where stated otherwise. No part of this thesis has been previously submitted for any other degree or professional qualification.

Isla Catherine Simmons

August 2020

Quetrupillán

Abstract

The Quetrupillán Volcanic Complex in the Southern Andes of Chile (39°30’ S, 71°43’ W) is a composite volcanic system that has been active since the Pleistocene (>15 ky). It consists of a truncated and eroded stratocone plus sixteen well-preserved satellite vents on its lower flanks. In this work I combine the results of field observations, petrological and geochemical analyses of erupted products, and structural and tectonic considerations, to determine the volcanic activity that has occurred at Quetrupillán during the Holocene, the nature and geometry of the magmatic plumbing system below the volcanic edifice, and what hazards may be produced by Quetrupillán when it next erupts.

Intense scouring of the stratocone’s flanks by ice has removed much evidence of its Holocene eruptions, and thus the Holocene evolution of the stratocone cannot be determined. However, the sixteen flank vents lie outside the glacially scoured zone and so are well-preserved. They display a range of features, with some having constructed scoria cones, some having excavated craters, some having built tuff rings, and some having effused lava flows. The variation in vent morphology implies that a variety of eruption styles occurred from the flanks of Quetrupillán. Lava flows from flank vents range in size from less than 1×10^6 m^3 to over 60×10^6 m^3. The majority (~97%) of this lava is trachytic in composition, with only minor trachyandesite and basaltic andesite compositions erupted from the flanks of Quetrupillán. Trachyte, trachyandesite, basaltic andesite and basalt lavas have been erupted from the summit region of the stratocone.

The evolution of the magmatic plumbing system at Quetrupillán has been influenced by the structural control imposed by the surrounding Liquiñe-Ofqui Fault Zone. Basaltic melt is hindered on its ascent through the crust due to a compressional tectonic regime, causing it to stall and evolve through fractional crystallisation, resulting in a network of trachytic melt pockets within a transcrustal magmatic system. Extraction of melt from these pockets has generated the numerous trachytic eruptions which have occurred from the summit and flanks of Quetrupillán during the Holocene. Occasionally, some of the basaltic source melt has reached shallow levels within the plumbing system with minimal or no interaction with the trachytic melt, resulting in eruption of basalt, basaltic andesite and trachyandesite lavas.

Quetrupillán’s diverse volcanism poses issues for hazard mitigation, as the range of eruption styles means that a variety of hazards may be produced, including lava flows, tephra fall and pyroclastic density currents, though they are unlikely to reach large centres of population. As Quetrupillán is snow-covered for much of the year, any eruption is also likely to lead to the formation of lahars, which may affect the isolated settlements in the valleys on the flanks of the volcano.

Non-technical summary

Around the world, many people live close to active volcanoes. To protect their lives and livelihoods it is necessary to understand how future eruptions may impact them. Knowledge of how a volcano has erupted in the past, and of the magmatic plumbing system below the volcano, can improve our understanding of how it may erupt in the future. As every volcano is unique, detailed studies of individual volcanoes are essential to provide this crucial information.

Few previous studies have been conducted at the Quetrupillán Volcanic Complex in the Southern Andes of Chile. As it is located next to the most active volcano in South America, scientific attention is understandably diverted away from the currently dormant Quetrupillán, and so comparatively little is known about its volcanic system. This project aims to improve our knowledge of Quetrupillán, investigating its past volcanic activity, the nature of its magmatic plumbing system, and the volcanic hazards posed by future eruptions.

Eruptions have taken place at the summit of Quetrupillán, and also from sixteen vents on the lower flanks of the volcano. Field observations of these vents show they display a range of features, indicating that a variety of different eruption styles have occurred, from explosive excavation of craters to gentle effusion of lava flows. Eruptions happen when magma is extracted from the plumbing system below the volcano, which consists of multiple pockets of magma. Quetrupillán's diverse volcanism poses issues for hazard management, as the range of eruption styles means that a variety of hazards may be produced.

Acknowledgements

First and foremost, I want to thank my amazing supervisors, Eliza Calder, Joaquín (Caco) Cortés and Dave McGarvie for supporting me throughout the last four years. Eliza, I can't thank you enough for all the incredible opportunities that you have given me (and thanks to all the pots of money that you found to fund them!). You encouraged me to attend EGU back when I was a master's student. You sent me to do fieldwork at Calbuco, then took me to CoV and gave me my first oral conference presentation. Best of all, one day you passed me in the corridor, announced you were heading to Guatemala the following week, and casually asked if I wanted to come! Thank you for all these experiences, and for the good times over the years, both in Edinburgh and around the world.

Caco, thank you so much for all the fun we had up Quetrupillán! I have so many great memories of our trip: fighting our way through the jungle of colihue in the pouring rain, evenings spent chatting while sat around the stove, watching the sun turn Laguna Azul orange as it set down the valley, and our final expedition across the snow to conquer Quetrupillán and reach the summit. Thank you for being an awesome field assistant! And an extra special thank you for your endless support and encouragement and weekly skype chats during all these months of lockdown, and for reading so many drafts of this thesis.

Dave, thank you for your constant enthusiasm throughout my PhD. The day after I was accepted for the PhD you invited me to participate in the volcano-ice workshop in Lancaster, and ever since then you have always been full of energy for the project – discussions with you are always engaging and thought-provoking. And thank you for our time out in Chile, though not for providing the most stressful 18 hours of my PhD, or for the chance to help co-ordinate an international rescue!

The highlight of my PhD has surely been all the incredible fieldwork experiences. These adventures have given me plenty of stories to tell! Conducting fieldwork on Quetrupillán is no easy task, so I was fortunate to have the support of so many great people. Huge thanks to Christa at Rancho de Caballos for organising all the logistical aspects of getting up onto Quetrupillán, and to Armin for leading us, caring for the horses, and rescuing us from the storm. And also for saving me that time I took an unexpected gallop – sorry for all the chaos this caused! Thanks to the volunteers at the ranch who joined us on trips up or down the volcano: Feli, Vera, Anika, Inza and Martin, and special thanks to the wonderful Luisa for accompanying us on each trip – your skill with the horses was beautiful to watch. To Luna, Canela and Orión, thanks for carrying your burden of camping equipment, food and rocks without complaint. And most importantly, thank you Medianoche. We may not have got off to the best of starts, and I still wouldn't claim to be a fan of horses, but we worked it out in the end!

My first field trip was almost derailed when Dave was diagnosed with bronchitis ten days before we were due to fly to Chile. But it was saved by my dad, who is an absolute hero and stepped in to come as my field assistant. Thank you so much for accompanying me. Not only did you allow the trip to go ahead, but it was very reassuring to have you with me when clambering down cliff-faces and wading across glacial rivers, and it was wonderful to share such an adventure with you.

The second hero of the trip was Franco, who rode up the volcano to come to be my field assistant when my dad left. Thanks for keeping calm when I thought we were going to be struck by lightning, for that day of card games and sudokus huddled in the tent as we sheltered from the storm, and for helping me to progress from awkward conversations about "what do you like to do in your free time?" to in depth discussions about the political history of Chile – ¡muchas gracias!

This PhD project was conceived from the initial study and mapping done by Andrés Pavez. I'm grateful that your work has given me such incredible experiences, and I'm glad I had the chance to meet you at Rancho de Caballos to discuss the wonders of Quetrupillán. Finishing the last of my fieldwork alone, thank you to Cristian, Claudia, Fernando and Constanza for allowing me to camp at Reserva Huililco. Thank you for your hospitality and kindness to a complete stranger, for guiding me through your beautiful araucaria forest and for taking me to watch the eclipse with you.

Returning to Chile a year later for my second field trip, thanks to Luis Lara for facilitating my visit to SERNAGEOMIN in Santiago and for trying to date some of my Quetrupillán lava samples. Thanks also to Virginia Toloza for discussing your masters project with me, and to everyone else at SERNAGEOMIN who was so friendly. Huge thanks to Julia and Joaquín Cortés for having me to stay and welcoming me into the family, and especially for taking me to your book launch! And to Franco, thank you so much for inviting me to spend New Year's Eve with your family. Finally, thanks to Jack. I'm so glad you came out to Chile as your dad's field assistant – it was so much fun having you with us and you kept me constantly entertained with all your great stories.

This work would not have been possible without the technical support of the following people at the University of Edinburgh: Mike Hall, for preparing my thin sections; Nic Odling and Godfrey Fitton for conducting XRF analyses; Nicola Cayzer and John Craven for assisting with the SEM; and Chris Hayward for help with the electron microprobe; and also Valerie Olive at the Scottish Universities Environmental Research Centre for conducting REE analyses. Thank you all so much for your help. Thanks to Pablo at BGS for taking the time to run your VOLCANS model for Quetrupillán. A huge thank you to the PGR support staff: Stephanie, Sophie, Richard, Marc and Katy, and a big thank you to Ross and the rest of the IT team, for always being able to fix my computer problems.

Another highlight of my PhD was the opportunity to take a 3-month internship at INSIVUMEH in Guatemala. Thank you to Gustavo and Raúl for arranging the visit, and thank you so much to Dulce, Carla and Pancho for welcoming me into the volcanology team, and for inviting me along on such amazing field trips. I'll never forget the moment when we arrived at the summit of Pacaya, with molten clots of glowing lava being thrown out above us, or camping on the summit of Santa María, all squeezed into the leaking tent in the rain, in the fruitless hope that we might be able to look down upon an eruption of Santiaguito. Thanks also to Alfredo, Amílcar, Esteban and Roberto for being so friendly, and to Alan, for involving me in your outreach event in Xesuj. Running a volcano workshop in Spanish while helping a lot of very excitable children to conduct experiments was a challenge, but great fun! And to Rüdiger, thanks for letting me tag along with your fieldwork at Fuego, where I got to put into practice what I have been teaching the undergrads for the past four years about how to write a good rock description! Thank you to Carmen, Cesar, Marco and Carmen Aida for welcoming me into your home and family, and for all the frijoles y tortillas. To Juan Manuel and Rosa, thank you for your kindness. And finally, thanks to Alistair – it was so great to have a friendly face around!

Alongside the adventures of fieldwork, the best part of doing a PhD has been the friends I have made along the way. So thank you to everyone in the attic, past and present, for making the last four years so much fun. For endless coffee breaks in the museum, delicious baked goods on Cake Fridays, Raptor Runs around Blackford Hill, summer afternoon ice creams in the Zen Garden... And most of all, for all the laughter. You are all the reason I enjoyed my PhD so much.

A few people deserve a special shout-out: Rachel – what began as shared misery of freezing in the Crew Annex became a wonderful friendship full of carbonara. Amy and Hannah – thank you both so much for all the walks, dinners and general good times over the years. Ben and Amelia, my volcanology brother and sister – we've been through some things together, from the frustration of trying to teach Excel to first years, to all the fun and laughter in Portland. Eleri and Sally – please can we go back for another endless summer in Inch?! Paige – thanks for all the hugs! Sophie and Gillian – crafty discussions were always a welcome distraction from work. And last but not least, Kirsty – thanks for looking after everyone in the attic, and for the motivational oranges.

Thank you to my wonderful family for always supporting and encouraging me, and to all my friends who laughed when I said I was staying at university for another four years.

And most importantly of all, thank you Davide, for everything.

Contents

List of Figures

List of Tables

List of Equations

List of Abbreviations

AFC	assimilation and fractional crystallisation
An_x	anorthite content
b.d.l.	below detection limit
BSE	back scattered electron
c.f.u.	cations per formula unit
cpx	clinopyroxene
CSD	crystal size distribution
EMPA	electron microprobe analysis
En_x	enstatite content
Fs_x	ferrosilite content
Fo_x	forsterite content
HFSE	high field strength element
ICP-MS	inductively-coupled plasma mass spectrometry
LIA	Little Ice Age
LILE	large ion lithophile element
LOFZ	Liquiñe-Ofqui Fault Zone
LOI	loss on ignition
MEC	minor eruptive centre
Mg#	magnesium number
MORB	mid ocean ridge basalt
n.d.	not determined
N-MORB	normal mid ocean ridge basalt
N.O.	number of oxygens
opx	orthopyroxene
PDC	pyroclastic density current
ppm	parts per million
QAPF	quartz, alkali feldspar, plagioclase, feldspathoid
REE	rare earth element
SEM	scanning electron microscope
SVZ	Southern Volcanic Zone
TAS	total alkali silica
VEI	Volcanic Explosivity Index
Wo_x	wollastonite content
wt.%	weight percent
XRF	x-ray fluorescence
yr. BP	years before present

Chapter 1: Introduction

Morning reflections, Laguna Azul

1.1. Research context and rationale

Around the world, 58 million people live within a 10 km radius of a Holocene volcano, and over 11% of the world's population lives within a 100 km radius (Siebert et al., 2015). To protect the lives and livelihoods of those living close to active volcanoes, it is necessary to understand the workings of volcanic systems, as the nature of a volcano and the mechanisms of its eruptions will determine what impacts any future eruption may have on the area and the surrounding communities.

As every volcano is unique, detailed studies of individual volcanoes provide crucial information about the nature of that particular volcano. Research into specific volcanoes is not only essential for increasing understanding of individual volcanic systems and their activity, but also for increasing our understanding about volcanic systems in general. The knowledge gained from a specific volcano is transferrable, as scientific ideas and concepts developed from the studies of individual volcanoes can then be applied to other volcanic systems around the world.

Current thinking about volcanic plumbing systems has moved away from the idea of magma chambers as spherical or oblate bodies of liquid magma below volcanoes (Daly, 1911; Marsh, 1989; Gudmundsson, 2012) to transcrustal magmatic systems composed of transient, interconnected lenses of magma within a crystal mush (Cashman et al., 2017; Magee et al., 2018). The magmatic plumbing system below a volcano controls what products reach the surface to erupt, influencing the style of eruptions that occur, and hence determining the type of hazards that may be produced (Cassidy et al., 2018). As such, knowledge of the volcano's magmatic plumbing system is of fundamental importance, as is information about its past volcanic activity. Combining this data will improve our understanding of how the specific volcano may erupt in the future, and how future eruptions may impact surrounding communities.

The Quetrupillán Volcanic Complex (Complejo Volcánico Quetrupillán), henceforth shortened to Quetrupillán, is located in southern Chile at 39°30' S, 71°43' W, next to the persistently active Volcán Villarrica. For this reason, most scientific attention has been diverted away from Quetrupillán, to focus on the more immediate hazard from Villarrica. This is understandable, as it is one of the most active volcanoes in South America (Lara, 2004; Petit-Breuilh, 2004). There is an abundance of scientific literature focussed on Villarrica, covering a diverse range of topics including eruption dynamics (Lohmar et al., 2007; Castruccio and Contreras, 2016; Romero et al., 2018), geochemistry of volcanic products (Morgado et al., 2015; Pioli et al., 2015), gas emissions (Palma et al., 2008, 2011; Moussallam et al., 2016; Aiuppa et al., 2017), remote sensing (Delgado et al., 2017; Plank et al., 2018), volcano seismicity (Curilem et al., 2009; Richardson et al., 2014; Lehr et al., 2019), lahar generation (Naranjo and Moreno, 2004; Johnson and Palma, 2015), ice fluctuations (Brock et al.,

2007; Rivera et al., 2015) and the mental health of those involved in volcanic crises (Espinoza et al., 2019). In contrast, prior to the start of this project no papers specifically about Quetrupillán had been published in peer-reviewed journals, and to date published literature on Quetrupillán consists of three papers: Brahm et al. (2018), Simmons et al. (2020a) and Simmons et al. (2020b). As such, scientific understanding of Quetrupillán is limited compared to knowledge of the neighbouring volcanic system at Villarrica.

In this project I aim to investigate the volcanic system of Quetrupillán, improving our understanding of its Holocene activity, its magmatic plumbing system, and the hazards it poses to nearby communities.

1.2. Geological background

1.2.1. Regional geological setting

Subduction of the Nazca Plate below the South American Plate has resulted in the volcanic arc of the Andes along the western edge of South America (Stern, 2004; Stern et al., 2007). The rate and angle of convergence between these plates has varied through time, with alternating periods of rapid and slow convergence, at dextral oblique or orthogonal angles (Pardo-Casas and Molnar, 1987). Slow convergence from the Late Cretaceous to Early Eocene was followed by a period of rapid convergence during the Late Eocene, before a return to slow convergence (3.5 ± 2.5 cm/yr) during the Oligocene (Pardo-Casas and Molnar, 1987). The current period of fast convergence has been present since 26 Ma (just before the start of the Miocene) with rates of up to 11 cm/yr, and at 20 Ma convergence changed from orthogonal to dextral oblique (Pardo-Casas and Molnar, 1987; Cembrano et al., 2000).

The Southern Volcanic Zone (SVZ) of the Andes lies between 33° S and 46° S (López-Escobar et al., 1995), coinciding with the subduction of the Juan Fernandez Ridge into the Peru-Chile trench at the northern end and with the subduction of the Chile Rise at the southern end (Figure 1.1; Stern, 2004; Stern et al., 2007). Beneath the SVZ, the crustal thickness decreases steadily from 50 km at 33° S to 35 km at 46° S, with a corresponding decrease in elevation of the main cordillera, from 5000 m to less than 2000 m (Figure 1.1; Stern, 2004; Cembrano and Lara, 2009; Hickey-Vargas et al., 2016). The angle of the subducted Nazca Plate increases from ~20° at the northern end to >25° at the southern end (Figure 1.1; Stern, 2004).

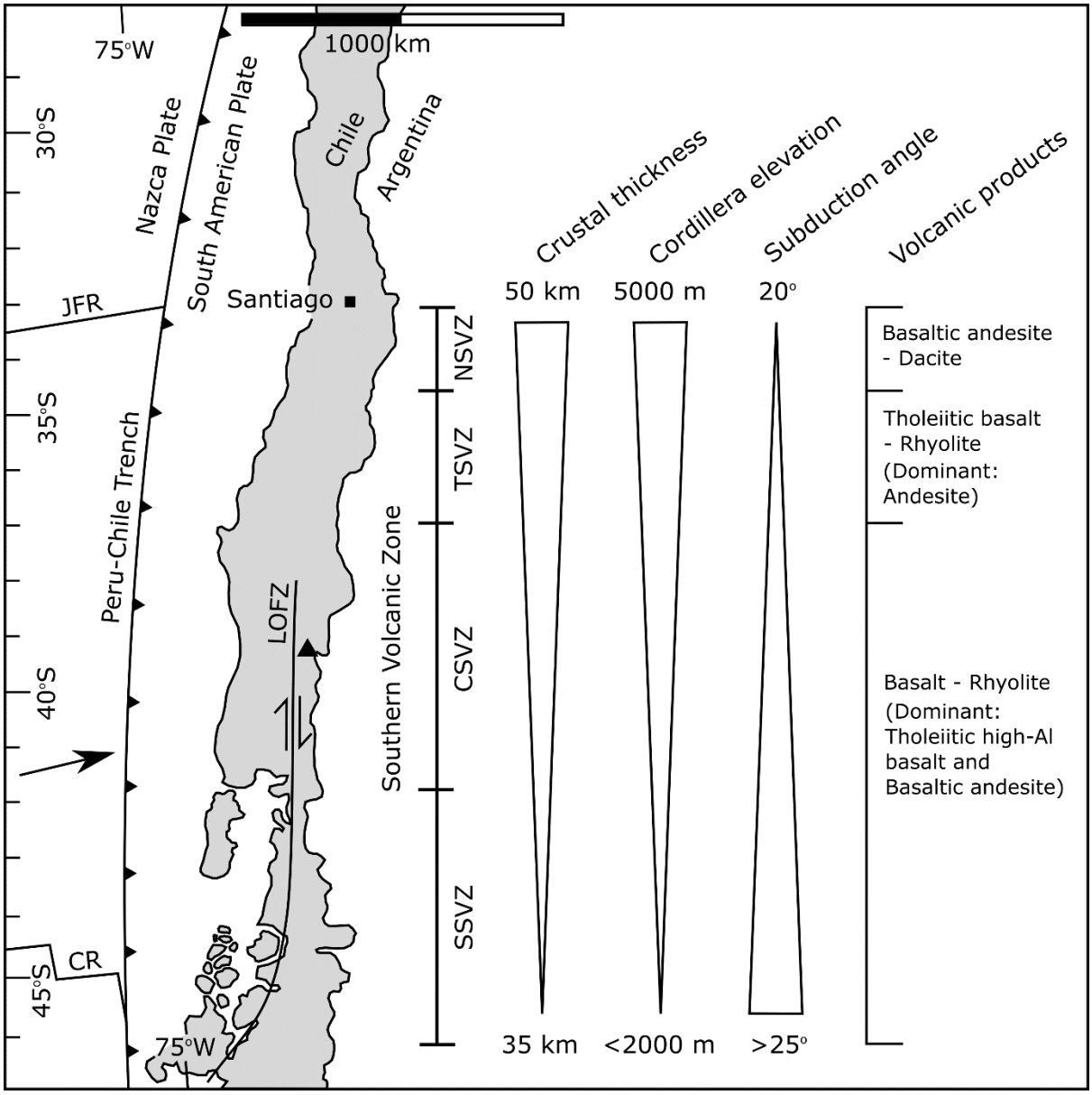

Figure 1.1: Subdivisions and features of the Southern Volcanic Zone. NSVZ – Northern Southern Volcanic Zone, TSVZ – Transitional Southern Volcanic Zone, CSVZ – Central Southern Volcanic Zone, SSVZ – Southern Southern Volcanic Zone, JFR – Juan Fernandez Ridge, CR – Chile Rise, LOFZ – Liquiñe-Ofqui Fault Zone. The arrow represents the direction of plate convergence, and Quetrupillán is denoted by the triangle. Data from Stern (2004) and Cembrano and Lara (2009).

The major tectonic feature in the SVZ is the Liquiñe-Ofqui Fault Zone (LOFZ; Figures 1.1 and 1.2), a ~1000 km long NNE-trending intra-arc fault system that dominates the tectonics of the region between 38° S and 47° S (Cembrano et al., 1996; Hernandez-Moreno et al., 2014). Transpression caused by the oblique convergence of the Nazca and South American Plates generated the LOFZ

(Hervé, 1994; Cembrano et al., 2000), which has acted as a dextral transpressive strike-slip structure for at least the last 6 Ma (Cembrano and Lara, 2009).

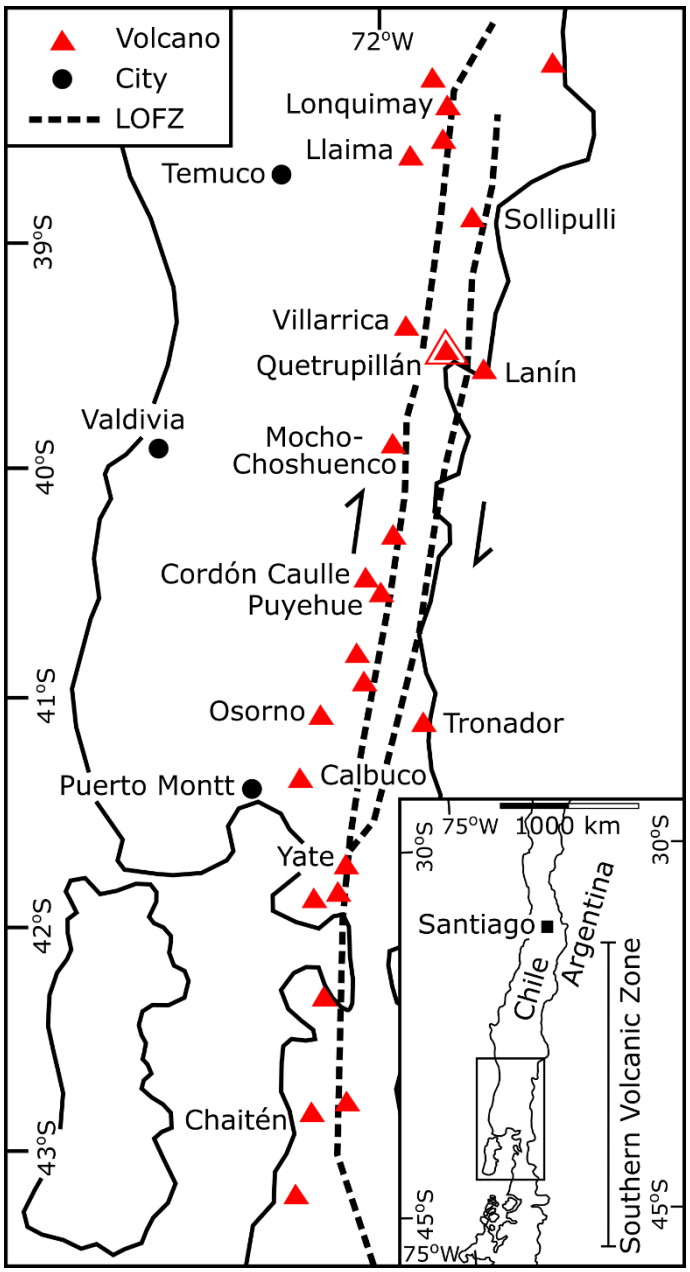

Figure 1.2: The LOFZ (dashed line) between 38° S and 43.5° S, modified from Cembrano and Lara (2009). Holocene stratovolcanoes are denoted by red triangles (Quetrupillán is highlighted) and major cities by black circles. The inset shows the location of this map within Chile.

Most Holocene volcanoes are located to the west of the LOFZ (e.g. Llaima, Villarrica, Mocho-Choshuenco and Calbuco). Between ~38.5° S and ~41.5° S the LOFZ splits into two parallel branches (Figure 1.2; Cembrano and Lara, 2009), and a few volcanoes are located to the east of the eastern

branch (e.g. Lanín and Tronador). Quetrupillán is unusual among the volcanoes of the SVZ as it is one of only two stratovolcanoes that lie between the two main branches of the LOFZ (the other being Sollipulli), though several stratovolcanoes appear to lie above or very close to the main trace of the LOFZ (e.g. Lonquimay and Yate; Figure 1.2).

The LOFZ consists of many interrelated faults. There appears to be a scarcity of field-based evidence for the location of these faults around Quetrupillán, with assumptions and interpretations made by different authors resulting in debate on their precise location. For example, Moreno & Lara (2008) map the LOFZ as passing immediately to the west of Quetrupillán, along the Palguín Valley, and the Reigolil-Pirihueico Fault to the east along the Trancura Valley, while Rosenau et al. (2006) map one fault of the LOFZ terminating to the south of Quetrupillán, another along the Trancura Valley to the east, and a sinstral strike-slip fault along the Rio Pucón Valley to the north (Figure 1.3). Hernandez-Moreno et al. (2014) map a splay of the LOFZ on either side of Quetrupillán, along the Trancura Valley to the east, and across the eastern flank of Villarrica to the west (Figure 1.3). Irrespective of the precise location of LOFZ faults in the area, tectonic stresses associated with the LOFZ are likely to have had a major influence on the development of volcanism at Quetrupillán. This will be explored further in Chapter 3.

Primary melts in the SVZ are generated by dehydration of the subducting Nazca Plate and consequent partial melting of the lithospheric mantle wedge (Stern, 2004; Cembrano and Lara, 2009). Along-arc variations in the isotopic compositions of SVZ volcanic rocks indicate varying degrees of contribution from different processes in the production of these arc magmas (Cembrano and Lara, 2009). The signature of SVZ magmas can be altered by crustal assimilation (Hildreth and Moorbath, 1988), interaction with the continental lithosphere (Hickey-Vargas et al., 2002), magma mixing, and contamination of the magma source region due to subduction erosion (Stern, 1991). The relative contribution of the different processes will depend on a number of factors such as the composition and rheology of the continental crust, the crustal thickness, local and regional tectonic regimes which will control magma ascent pathways, and the rate of subduction erosion (Cembrano and Lara, 2009).

Tholeiitic, high-Al basalts and basaltic andesites are the dominant products erupted from both stratovolcanoes and minor eruptive centres in the central and southern SVZ (south of 37° S, Figure 1.1; Hickey-Vargas et al., 1989; López-Escobar et al., 1995; Stern, 2004; Stern et al., 2007), while andesites, dacites and rhyolites are uncommon (Lara et al., 2006). The basalts of the central SVZ have lower than expected concentrations of MgO, Ni and Cr than basalts derived from primary mantle melts, which has been suggested to be due to deep fractional crystallisation (López-Escobar et al., 1995).

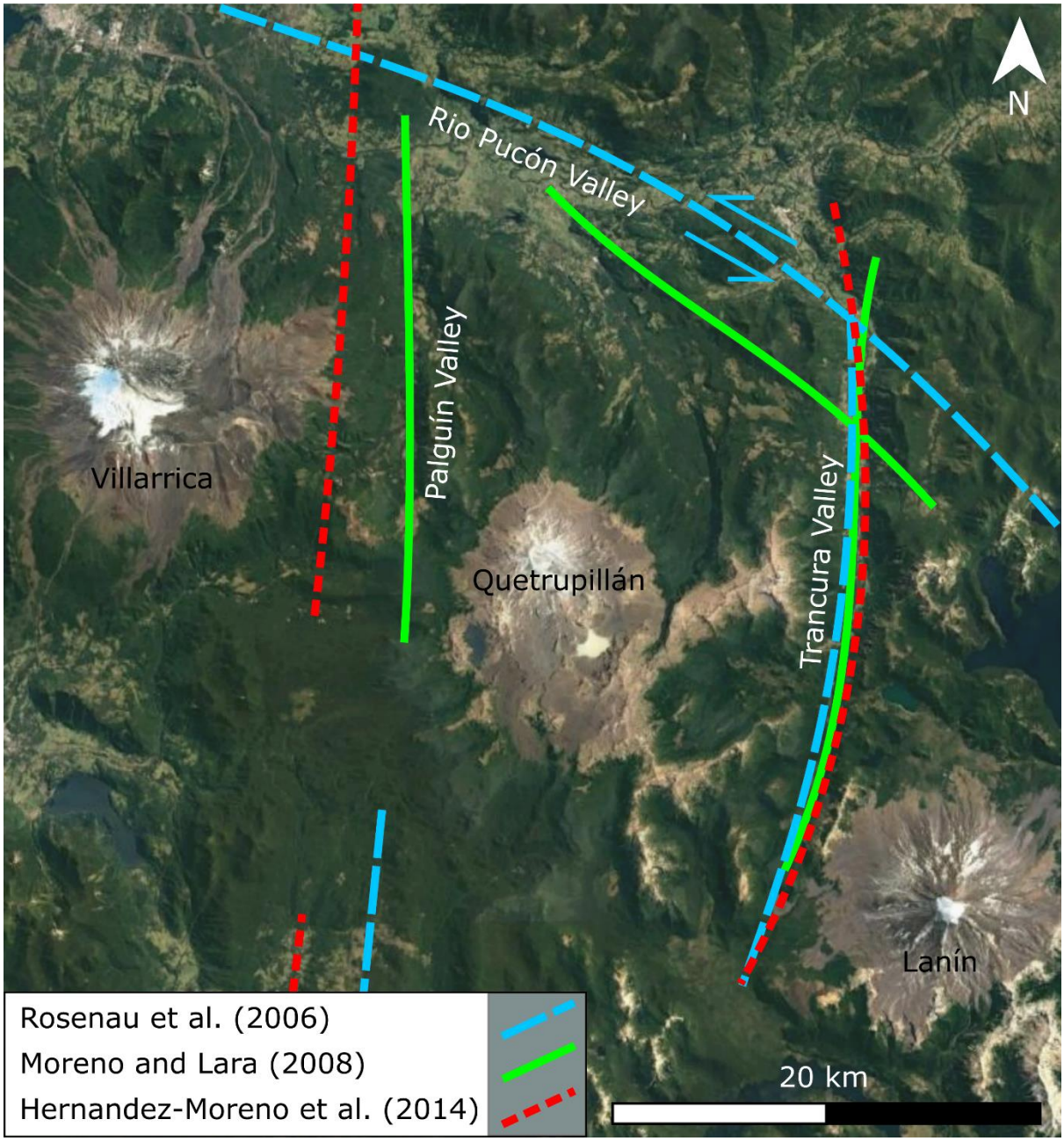

Figure 1.3: Location of faults of the LOFZ around Quetrupillán, as defined by Rosenau et al. (2006; blue long dashed line), Moreno and Lara (2008; green line) and Hernandez-Moreno et al. (2014; red short dashed line). Satellite image from Google Earth (downloaded 03/02/2020).

Regional tectonics control the alignment of volcanic chains in the SVZ, and the composition of erupted products. NE-striking alignments usually consist of basaltic and basaltic andesite stratovolcanoes and minor eruptive centres, while stratovolcanoes of a range of compositions are found in NW-striking alignments (López-Escobar et al., 1995; Lara et al., 2004; Cembrano and Lara, 2009). In general, NW-trending domains are more compressive, undergoing shortening and strike-

slip deformation, resulting in longer magma residence time within the crust and so allowing greater differentiation of eruptive products (López-Escobar et al., 1995; Cembrano and Lara, 2009).

1.2.2. Geological setting of Quetrupillán

Quetrupillán (elevation 2360 m) lies in the Southern Volcanic Zone of the Chilean Andes (Figures 1.1 and 1.4). It sits within the NW-SE oriented Villarrica-Quetrupillán-Lanín volcanic chain (Figures 1.4 and 1.5), a chain of three active volcanoes that lies oblique to the main volcanic arc of the Andes (Hickey-Vargas et al., 1989; Cembrano and Lara, 2009). Volcán Villarrica (39°25' S, 71°56' W; Figure 1.5B), the westernmost volcano, is one of the most active volcanoes in South America (Petit-Breuilh, 2004). It is an ice-capped, basaltic andesite stratocone with persistent open-vent degassing from the lava lake in its summit crater (Witter et al., 2004). Volcán Lanín (39°38' S, 71°30' W; Figure 1.5D) is the easternmost volcano. It is a basalt to dacite stratocone which has not had any recorded historic eruptions (Lara et al., 2004) and which has a small summit ice cap. Quetrupillán lies between Villarrica and Lanín, and its truncated stratocone contrasts strongly with the conical stratocones of Villarrica and Lanín (Figure 1.5).

Unlike its prominent neighbouring volcanoes, Quetrupillán is somewhat hidden from view, and this may explain why there is uncertainty over whether there have been any eruptions from it since the surrounding valleys were first settled by the Spanish in the mid-16th century (Petit-Breuilh, 2004). For example, Quetrupillán cannot be seen from the main settlements of either Villarrica or Pucón as it is hidden behind Volcán Villarrica. The last eruption from Quetrupillán is suspected to have occurred in 1872 AD (Petit-Breuilh, 2004), but the evidence for this is considered weak, as it lacks corroboration from multiple independent sources.

Quetrupillán has been constructed on a basement of Cretaceous and Miocene plutonic units and Triassic to Miocene volcano-sedimentary sequences of the Panguipulli, Curarrehue and Trapatrapa Formations (Moreno et al., 1994). It has been suggested that Quetrupillán overlies the eroded remnants of the unstudied and undated (possibly Pleistocene) stratovolcanoes of Quinquilil (also known as "Colmillo del Diablo"; Figure 1.4) and Cordillera El Mocho (Pavez, 1997).

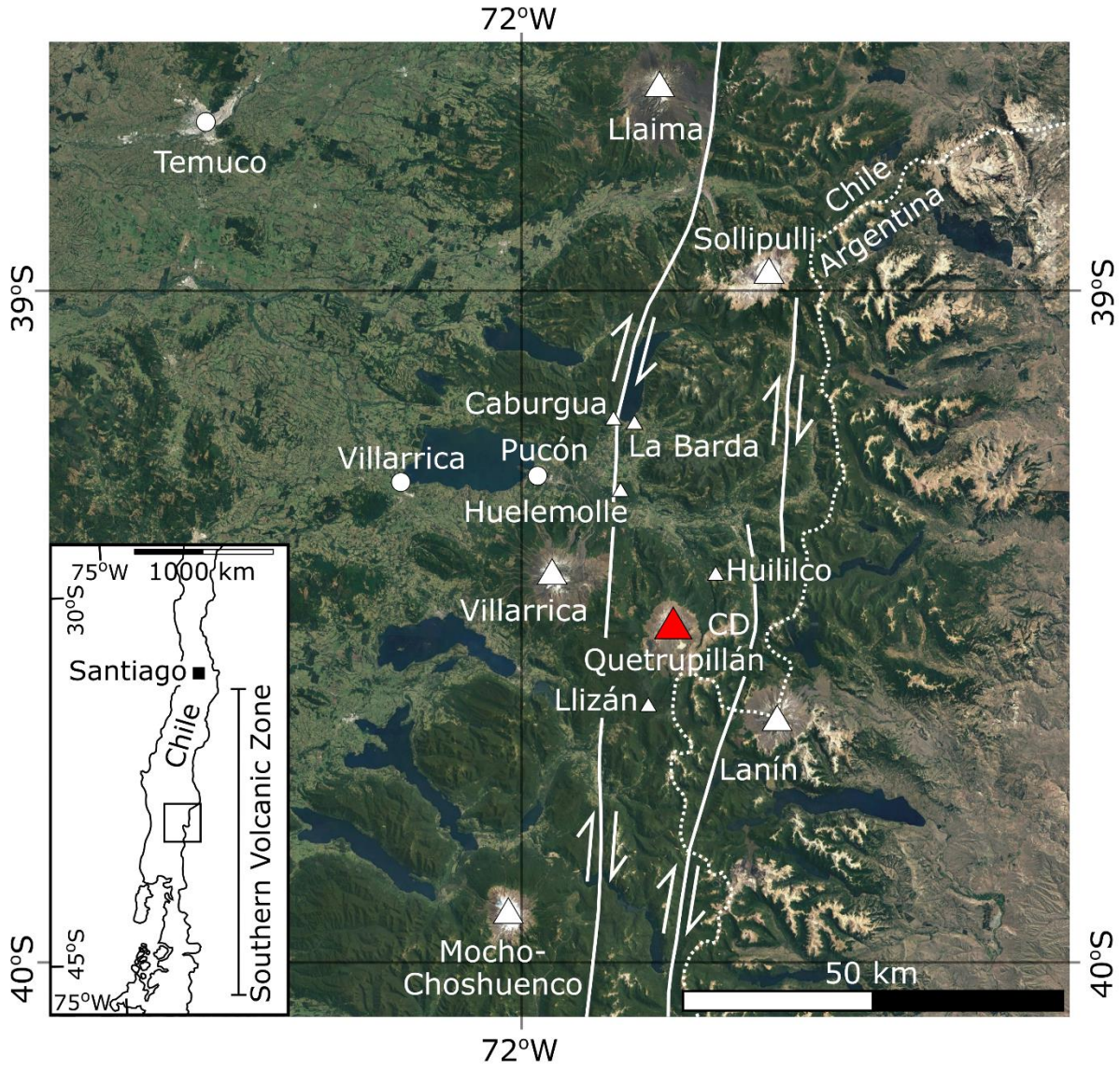

Figure 1.4: Satellite image of the area surrounding Quetrupillán showing the trace of the Liquiñe-Ofqui Fault Zone faults (solid lines), as defined by Hernandez-Moreno et al. (2014). Stratovolcanoes (large triangles; Quetrupillán highlighted in red), minor eruptive centres (small triangles; those mentioned in this thesis) and notable towns (circles) are indicated. Dotted line – international border between Chile and Argentina; CD – Colmillo del Diablo. The inset shows the location of this map within Chile. Satellite image from Google Earth (downloaded 03/02/2020).

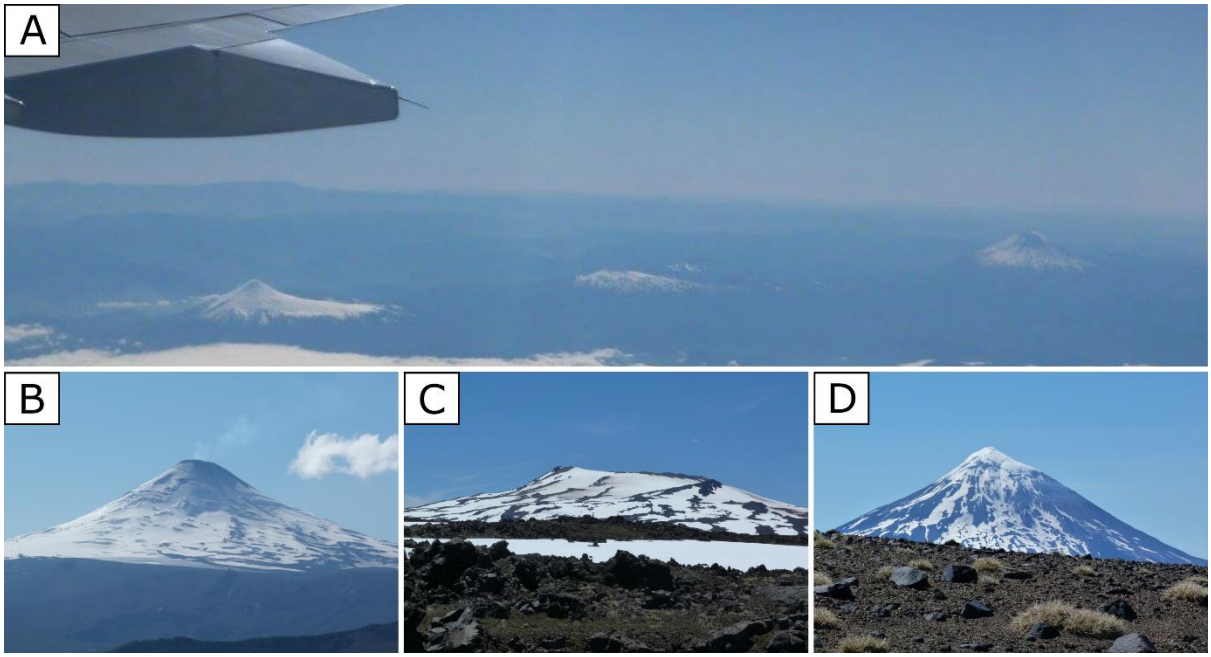

Figure 1.5: A) The Villarrica-Quetrupillán-Lanín volcanic chain (looking northeast) with Villarrica (B) to the left, Quetrupillán (C) in the middle and Lanín (D) to the right. The difference in morphology between the conical volcanoes of Villarrica and Lanín and the truncated stratocone of Quetrupillán is clearly visible. The distance between the summits of Villarrica and Lanín is ~45 km.

The volcanic complex of Quetrupillán consists of a truncated (headless) stratocone, and numerous satellite vents around the lower flanks of the stratocone, the features of which will be discussed in detail in Chapter 2. Two areas of distal volcanism have been speculated to be satellite vents of Quetrupillán: Huililco, a small basaltic to basaltic andesite scoria cone ~12 km to the northeast, and Llizán, a cluster of vegetated basaltic andesite to andesite scoria cones ~14 km to the SSW (Figure 1.4; Pavez, 1997; Sun, 2001; Valdivia Muñoz, 2016; Brahm et al., 2018). Given that their relationship to Quetrupillán is currently both uncertain and unproven, they are not considered further.

1.3. Previous studies at Quetrupillán

Past work on Quetrupillán has been sporadic, and a detailed geological map of the volcanic complex has not been published. Consequently, the stratigraphy of the volcano is unknown. Only reconnaissance-level mapping has been carried out as part of a dissertation at the Universidad de Chile. Results were presented at conferences (Pavez, 1997), but not in peer-reviewed journals. Quetrupillán appears across two official regional geological maps (southern flanks - Lara and Moreno, 2004; northern flanks - Moreno and Lara, 2008), where the mapped geological units of the

volcano are based on the reconnaissance mapping by Pavez (1997). A study of volcano-ice interactions at Quetrupillán during the late Pleistocene began in 2012 but has likewise only appeared in conference presentations (e.g. McGarvie et al., 2014). A dissertation at the Universidad de Concepción involved a study of tephra layers in the nearby Trancura Valley that have been attributed to explosive eruptions at Quetrupillán (Toloza, 2015). And most recently, Brahm et al. (2018) conducted a study that analysed a limited subset of Holocene trachytic lavas as part of a dissertation at the Universidad de Chile (Brahm, 2017). This project aims to improve scientific understanding of Quetrupillán and has resulted in the following publications: Simmons, I. C., McGarvie, D., Cortés, J. A., Calder, E. S., Pavez, A., 2020. Holocene volcanism at the Quetrupillán Volcanic Complex (39°30' S, 71°43' W), southern Chile, *Volcanica*, vol. 3, no. 1, p. 115-137; and Simmons, I. C., Cortés, J. A., McGarvie, D., Calder, E. S., 2020. Tectonic constraints on a magmatic plumbing system: the Quetrupillán Volcanic Complex (39°30' S, 71°43' W), Southern Andes, Chile, *Journal of Volcanology and Geothermal Research,* vol. 407. The published manuscripts are included at the end of this thesis.

1.4. Research aims

The aims of this research project are threefold and are considered by addressing the following questions:

Aim 1: To determine the volcanic activity and processes at Quetrupillán during the Holocene

- What style of activity/type of eruptions have occurred at Quetrupillán?
- What eruptive products and features have been produced by these eruptions?
- How many Holocene eruptions has Quetrupillán had?
- How was Quetrupillán impacted by Holocene glaciations?

Aim 2: To constrain the nature of the Holocene magmatic plumbing system below Quetrupillán

- How and where are Quetrupillán magmas produced?
- What is the nature of the plumbing system below Quetrupillán?
- How do geochemical and textural data of volcanic products reflect the plumbing system?
- How is magmatism at Quetrupillán influenced by the local tectonic regime?

Aim 3: To investigate future volcanic hazards from Quetrupillán

- What volcanic hazards have been produced by past eruptions?
- How would these hazards impact local communities in future eruptions?

These questions are explored and discussed in this thesis. The results of this work provide the first detailed study of Holocene volcanism and magmatism at Quetrupillán and provide new insights on the magmatic plumbing system and its interaction with the regional tectonics.

1.5. Thesis structure

Chapter 2: Holocene volcanism at the Quetrupillán Volcanic Complex

Chapter 2 investigates the Holocene activity that has occurred at Quetrupillán, both volcanic and glacial, and attempts to determine how many and what type of eruptions have occurred. This chapter is based on the published paper Simmons, I. C., McGarvie, D., Cortés, J. A., Calder, E. S., Pavez, A., 2020. Holocene volcanism at the Quetrupillán Volcanic Complex (39°30' S, 71°43' W), southern Chile. *Volcanica*, vol. 3, no. 1, p. 115-137.

Chapter 3: Holocene magmatism at the Quetrupillán Volcanic Complex

Chapter 3 investigates the geochemical and petrological aspects of Holocene volcanic products from Quetrupillán and combines this with investigation of the local tectonic setting. This chapter is based on the published paper Simmons, I. C., Cortés, J. A., McGarvie, D., Calder, E. S., 2020. Tectonic constraints on a magmatic plumbing system: the Quetrupillán Volcanic Complex (39°30' S, 71°43' W), Southern Andes, Chile. *Journal of Volcanology and Geothermal Research,* vol. 407.

Chapter 4: Volcanic hazards from the Quetrupillán Volcanic Complex

Chapter 4 considers the probability of a future eruption and combines the results of Chapters 2 and 3 to assess likely volcanic hazards that may occur from Quetrupillán when it next erupts. It also investigates volcanoes that are analogous to Quetrupillán, whose hazards may provide additional information about potential hazards from Quetrupillán.

Chapter 5: Discussions and conclusions

Chapter 5 is a discussion of all the aspects investigated in this thesis. The knowledge gained about Quetrupillán's Holocene volcanism and magmatism is combined with knowledge of the local tectonic setting to propose a conceptual model for the nature of the magmatic plumbing system below Quetrupillán. This chapter also considers where future work should be directed to continue to improve scientific understanding of the Quetrupillán Volcanic Complex.

Chapter 2: Holocene volcanism at the Quetrupillán Volcanic Complex

My trusty steed, Medianoche

This chapter is based on Simmons, I. C., McGarvie, D., Cortés, J. A., Calder, E. S., Pavez, A., 2020. Holocene volcanism at the Quetrupillán Volcanic Complex (39°30' S, 71°43' W), southern Chile. *Volcanica*, vol. 3, no. 1, p. 115-137. I performed fieldwork, subsequent laboratory work, overall analysis, and writing. Dr Dave McGarvie and Dr Joaquín Cortés assisted during the second field season of the project and contributed to discussions and manuscript drafts.

2.1. Introduction

In this chapter I examine the volcanic activity that has occurred from Quetrupillán during the Holocene, with a focus on observations of Quetrupillán's volcanic products and field features, to provide an understanding of Quetrupillán's past activity. As Quetrupillán has been active since the Pleistocene, when glaciations occurred in the region, the eruptive products have been stratigraphically organised based on their glacial interactions, allowing the categorisation of Holocene versus Pleistocene products. To understand the pattern of eruptive activity at Quetrupillán, I mapped features of Holocene volcanism and analysed lavas and pyroclastic deposits to determine the range of compositions erupted with time. I also examined pyroclastic deposits preserved in nearby valleys to establish the wider distribution and effects of explosive eruptions.

2.2. Methods

Two field seasons were conducted at Quetrupillán, in February 2017 and January 2018. Each trip involved ten nights spent camping on Quetrupillán at the southern tip of Laguna Azul, followed by a further two weeks working in the Palguín, Huililco and Trancura Valleys that surround the volcano (Figure 2.1; where official valley names were unknown, they have been named according to the principle river within the valley). The purpose of the fieldwork was to observe and map Holocene eruptive products and volcanic features, and to collect samples from lava flow deposits and pyroclastic sequences for subsequent analysis. Field mapping was supplemented with satellite imagery in order to identify and locate features across the volcano.

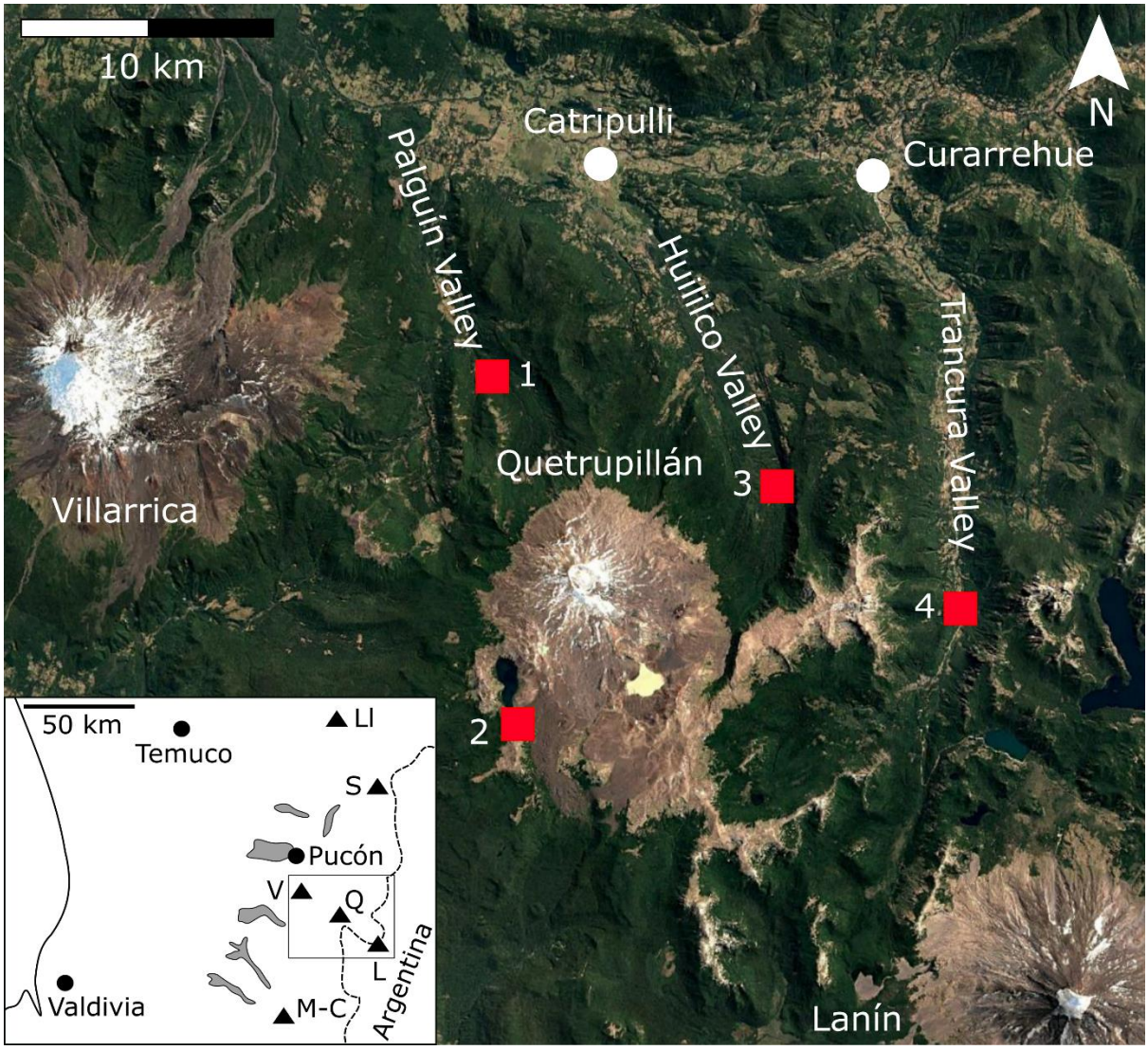

Figure 2.1: Locations of camps on and around Quetrupillán during field seasons, denoted by red squares: 1) Rancho de Caballos, Palguín Alto; 2) Laguna Azul, Quetrupillán; 3) Reserva Huililco, Huililco Valley; 4) Puesco camp, Trancura Valley. Inset shows the wider region, noting major towns (circles), lakes (grey areas), volcanoes (triangles; Ll – Llaima, S – Sollipulli, V – Villarrica, Q – Quetrupillán, L – Lanín, M-C – Mocho-Choshuenco) and the international border with Argentina (dashed line). Satellite image from Google Earth (downloaded 3/06/2020).

The camp at Rancho de Caballos (Figure 2.1) provided access to pyroclastic sections exposed in road cuttings in the Palguín Valley. A 6.5-hour horse ride led from Rancho de Caballos to the southern tip of Laguna Azul on the southwest flank of Quetrupillán, where a base camp was established on the volcano. From this camp, it was possible to walk across the western and southern flanks of Quetrupillán, and to reach the volcano's summit. The camp at Reserva Huililco provided foot access to the eastern and north-eastern flanks of Quetrupillán, and to lava flows from Quetrupillán that had

descended into the Huililco Valley. Access to the northwest flank was not achieved. Pyroclastic sections in road cuttings exposed along the Trancura Valley were accessed from the camp at Puesco.

During the two field seasons, 64 samples of lava were collected from the flanks of Quetrupillán, including at least one sample from each lava flow produced by flank vents, and a selection of lavas erupted from the summit of the stratocone. Where possible, the source vent of each sampled lava flow was determined. This was generally easy for lavas erupted from flank vents, as the lava flows could clearly be traced to their source. Lava flows that had no clear association with flank vents were assumed to have been erupted from the summit region of the stratocone.

In the Palguín Valley, three pyroclastic sections were logged, and 33 samples of pyroclastic deposits were collected. Nine samples of lava from Quetrupillán were collected that had flowed down the Huililco Valley. In the Trancura Valley three pyroclastic sections were logged and 16 samples of pyroclastic material collected, sampling every pyroclastic horizon that lay above the granitic basement. Pleistocene lavas analysed in Chapter 3 were collected by Dr Dave McGarvie during prior field trips.

A list of sample localities is provided in Appendix I for all samples upon which subsequent analysis was performed. Thirty lava samples and four pyroclastic samples were prepared as polished thin sections, and descriptions of these are in Appendix II.

2.3. The age of Quetrupillán's eruptive products

A volcanic stratigraphy corroborated by absolute age dating has not been established for Quetrupillán, and it was not possible to date lavas using potassium-argon dating as their young age prevented them from containing sufficient ^{40}Ar. Instead, the relative age of the different volcanic products was assessed using field relations and the degree of ice interaction. Specifically, physical characteristics of volcanic eruptive deposits were used to determine their age, categorising Holocene volcanic products as those that do not display features associated with eruption during periods of glaciation. Then, where possible, stratigraphic relationships between Holocene features were used to establish a Holocene stratigraphy.

The last glacial period in southern Chile, the Llanquihue event, has been dated between 29 400 and 14 550 yr. BP (Glasser et al., 2008), with the last glacial maximum occurring between 23 000 and 19 000 yr. BP, when ice covered the crest of the Andes for ~1800 km (Hulton et al., 2002). Ice cover at Quetrupillán would have been at least 500 m thick, and possibly as thick as 1300 m (Hulton et al., 2002). Deglaciation began ~17 500 – 17 150 yr. BP with abrupt and stepped warming leading to a

dramatic reduction of the ice mass covering the Andes in the area (Moreno et al., 1999; Hulton et al., 2002). Rapid glacial retreat resulted in glaciers receding to within 10 km of their current termini within ~2000 years of the initiation of warming (Lowell et al., 1995).

The known timings of glaciations in the region were used to assign ages to volcanic products from Quetrupillán. Any lava at Quetrupillán that clearly shows the combined evidence of ice confinement and of ice/meltwater-induced cooling fracture systems (characteristic of intermediate-silicic glaciovolcanic eruptions, e.g. McGarvie, 2009) is assumed to have erupted when significant ice covered the area, and is assigned a Pleistocene age (McGarvie et al., 2014). In comparison, lavas that display the typical subaerial characteristics of unconfined spreading across a landscape and have preservation of their delicate features such as loose, blocky carapaces, are assigned a Holocene age. Lavas and pyroclastic edifices with clear well-preserved subaerial features cannot have been erupted prior to the Llanquihue glaciation in the Pleistocene, as the thick ice mass that covered the region during the Llanquihue would have resulted in substantial erosion that removed these features (Denton et al., 1999; Hulton et al., 2002). As such, these lavas and volcanic features are assumed to be Holocene products.

Local ice masses increased during the Little Ice Age (~14^{th} – 19^{th} century; Matthews & Briffa, 2005), when ice cover at Quetrupillán would have increased. Any Holocene eruptions that occurred during this period are therefore likely to have encountered ice and so acquired the characteristics of glaciovolcanic eruptions. This means that using the simple characteristics-based classification to date lavas may result in an under-estimation of Holocene erupted volumes. Subglacial lavas erupted during periods of Holocene glaciation would display characteristics assumed to represent Pleistocene lavas and so would have been incorrectly assigned a Pleistocene age. This characteristics-based dating classification has been used at other Chilean volcanoes such as Nevados de Chillán, where lavas were dated depending on whether they displayed subglacial or subaerial characteristics (Dixon et al., 1999). No study appears to have addressed the issue of potential incorrect dating of features at Chilean volcanoes due to Holocene glaciations.

2.4. Holocene volcano-ice interactions at Quetrupillán

Currently, icefields of unknown thickness occur on the upper parts of the stratocone (Figure 2.2), with the main ice mass occupying the oval ~1.3 × 1 km summit crater and having an ice surface that dips gently to the southeast. The summit crater has walls of variable height, and at two low points ice has flowed out to form a small (~0.8 × 0.4 km) icefield to the northeast and another to the southeast (~1.4 × 0.7 km).

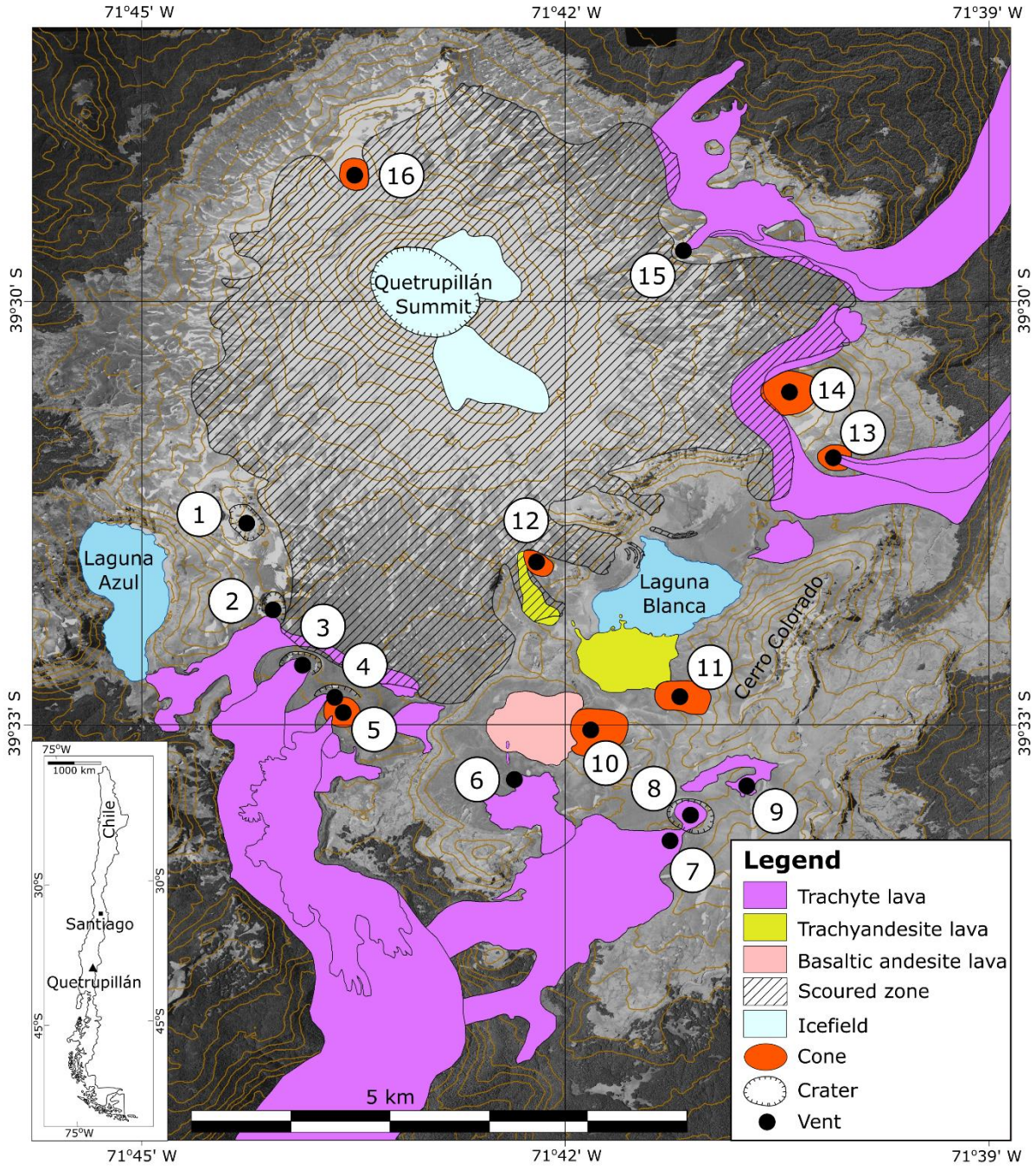

Figure 2.2: Map of the Holocene geology of Quetrupillán from the flank vents, produced using results from field mapping, observations of satellite images and geochemical analyses. Flank vents are labelled with the numbers that they are referred to in the text. The glacially scoured zone is indicated by the hatched area. The aerial photo background image is from the Servicio Aerofotogramétrico, Chile, and the 50 m interval contours were created from a digital elevation model downloaded from earthexplorer.usgs.gov (downloaded 21/10/2016). The inset shows the location of Quetrupillán in Chile.

A scoured zone (Figure 2.2) surrounds the stratocone and extends 2 – 5 km from the summit, within which all exposed lava surfaces are smooth and etched with parallel linear scratches and gouges (Figure 2.3A), and covered by an impersistent blanket of diamict (Figure 2.3B and C). Etching directions can be determined both on a micro scale from scratches on smooth lava surfaces (Figure 2.3A), and on a macro scale from satellite imagery in which irregular linear channels are eroded into the lava and diamict deposits (Figure 2.4A). All micro and macro direction indicators are oriented radially to the stratocone summit.

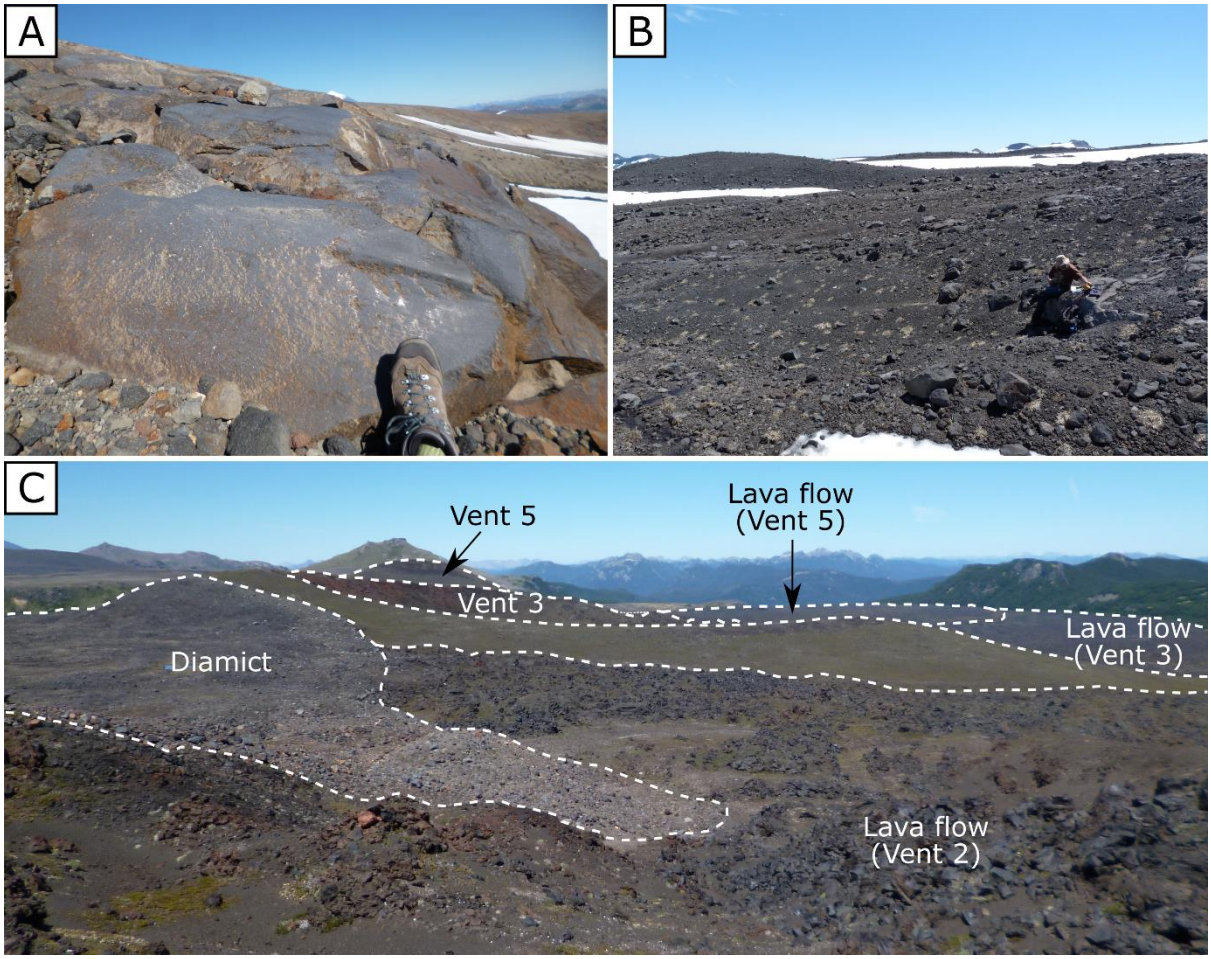

Figure 2.3: A) A scoured Holocene lava from the upper flanks. Striations are faintly visible above the boot, striking in a downhill (240°) direction (looking southeast); B) Diamict, composed of lava boulders of varying size and fine-grained silt, covers most of the upper flanks of Quetrupillán within the scoured zone, obscuring all underlying lava fields (looking west); C) Diamict covers the lava flow of Vent 2 and the tuff ring of Vent 3 (looking southeast from Vent 2). The field of view is ~200 m wide.

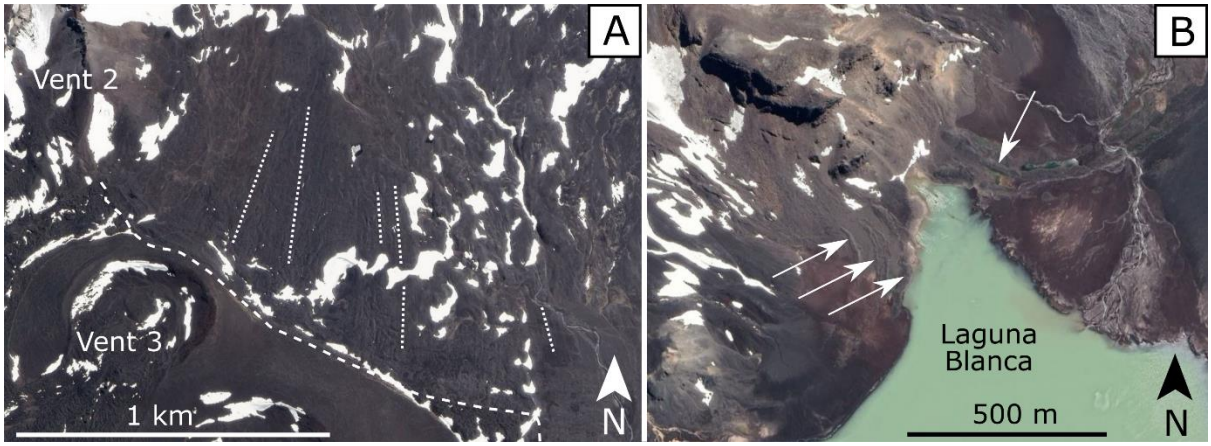

Figure 2.4: A) Linear channels are visible in the diamict in satellite images, oriented radially from the summit. The dotted lines highlight some that are visible to the north of Vent 3. The dashed line represents the edge of the scoured zone. Satellite image from Google Earth (downloaded 09/10/2019); B) Distinctive curving ridges of glacial deposits are visible in satellite images at the edge of the scoured zone on the shores of Laguna Blanca, highlighted by arrows. Satellite image from Google Earth (downloaded 07/10/2019).

The diamict blanket is a poorly sorted and unconsolidated deposit consisting of sub-rounded to sub-angular lava boulders of varying size, with a smaller sand-silt sized fraction (Figure 2.3B). The edge of the scoured zone is often marked by curved ridges of boulders that form distinct topographic highs (Figure 2.4B). These are typically ~2 m high but occasionally reach up to ~4 m in height. The proposed interpretation of these features is that the scoured zone is the product of glacial processes, with the scratches and gouges being glacial striations produced during ice advance, and the diamict representing glacial till deposition during ice retreat. The ridges of boulders around the edge are terminal moraines that represent the farthest extent of ice advance. The radial nature of striations and linear channels strongly suggests ice flow from the summit of the volcano to the lower flanks.

The scoured zone of Quetrupillán cannot have been formed during the Llanquihue glaciation, as during this period thick (>500 m) ice extended for many tens of kilometres on either side of the Andean chain (Hulton et al., 2002), whereas this scoured zone is a local feature, extending 2 – 5 km from the summit of Quetrupillán. Well-preserved lavas of Holocene age are also exposed below the terminus of the scoured zone and can be traced upslope into the scoured zone, where they have been smoothed by ice and/or covered in diamict. Examples of this include the lava flows of Vents 2 and 12 (Figure 2.2) which are both partly overlain by glacial till where they exist within the scoured zone (Figure 2.3C). As these lavas display pristine features outside the scoured zone, they are

assumed to be Holocene in age. And as they underlie the glacial till and are therefore stratigraphically older than the scoured zone, the scoured zone must be a Holocene feature.

An important implication of the scoured zone is that Holocene glacial erosion of the stratocone has occurred. This means that crucial evidence related to the growth and construction of the stratocone has been removed, such as the locations, numbers, and volumes of stratocone eruptions. Consequently, the total volume of well-preserved Holocene lava (~225 × 10^6 m^3; see section 2.5) that lies outside of the scoured zone is therefore a minimum estimation. It was also not possible to map the volcanic products erupted from the summit region, as most are covered by diamict.

No Holocene lava deposits with well-preserved blocky carapaces were found within the scoured zone. This suggests that the most recent volcanic products erupted from the stratocone have been eroded, and thus they must be older than the latest ice advance and retreat. In their study of Nevados de Chillán, Dixon et al. (1999) suggest that young small-scale moraines on Nevados de Chillán may have been formed during late Holocene re-advances such as the Little Ice Age (LIA), which ended in the late 19th century (Matthews and Briffa, 2005). From radiocarbon dates, dendrochronological data and pollen analyses, glacial advances throughout South America are known to have occurred between the 15th and 19th centuries (Clapperton & Sugden, 1988). Patagonian glaciers reached their maximum limits at various stages throughout the 17th, 18th and 19th centuries (Mercer, 1965), and glaciers in the Andes began to recede within the last two decades of the 19th century (Clapperton, 1983).

Given evidence of local ice advances across the Andes during the LIA, it is highly likely that glacial advances at Quetrupillán also occurred, with the last being towards the end of the 19th century. Scouring of the stratocone by ice is likely to have occurred during each period of glacial advance and retreat throughout the LIA. The presence of a clear terminal moraine at the outer limit of the scoured zone, and the lack of terminal moraines within the scoured zone, implies that the most recent glacial advance at Quetrupillán (in the late 19th century) was also the largest and most extensive. As the terminal moraine overlies the youngest erupted lavas on the lower flanks of the stratocone (Figure 2.3C), it is highly likely that there have been no effusive eruptions within the scoured zone since the major 19th century glacial advance. The most recent effusive activity from Quetrupillán is therefore older than this glacial advance.

The scoured zone of Quetrupillán appears to be an unusual feature, as study of satellite images suggests that there is no equivalent scoured zone at the nearby volcanoes of either Villarrica or Lanín. Villarrica currently has a much greater ice mass occupying its upper flanks than Quetrupillán, which would have been larger still during the LIA, but it does not appear to display a scoured zone.

Although Lanín currently has only a small summit ice cap, its summit lies at a much higher elevation (3747 m) than Quetrupillán (2360 m), and so during the LIA it is likely that the summit ice mass would have increased and spread substantially.

Temperature fluctuations in the LIA will have resulted in similar and multiple episodes of ice accumulation in summit regions, followed by ice advance to lower elevations at the ice-capped volcanoes of the Villarrica-Quetrupillán-Lanín chain. However, while Quetrupillán was extensively scoured by these LIA ice advances, the same process has not obviously occurred at either Villarrica or Lanín, even though their higher elevations would have led to accumulation of larger ice masses, with the potential to form extensive scoured zones on their stratocone flanks.

A possible explanation for this is that Quetrupillán lies only 21 km downwind (ESE) from Villarrica, one of Chile's most active volcanoes (Lara, 2004; Petit-Breuilh, 2004). Quetrupillán's downwind location relative to Villarrica means that it will receive frequent dustings of basaltic andesite tephra (mostly ash-sized) from explosive eruptions at Villarrica. This was experienced by Dr Dave McGarvie (*personal communication*) during fieldwork on Quetrupillán in 2015, following the 3rd March eruption of Villarrica (Figure 2.5).

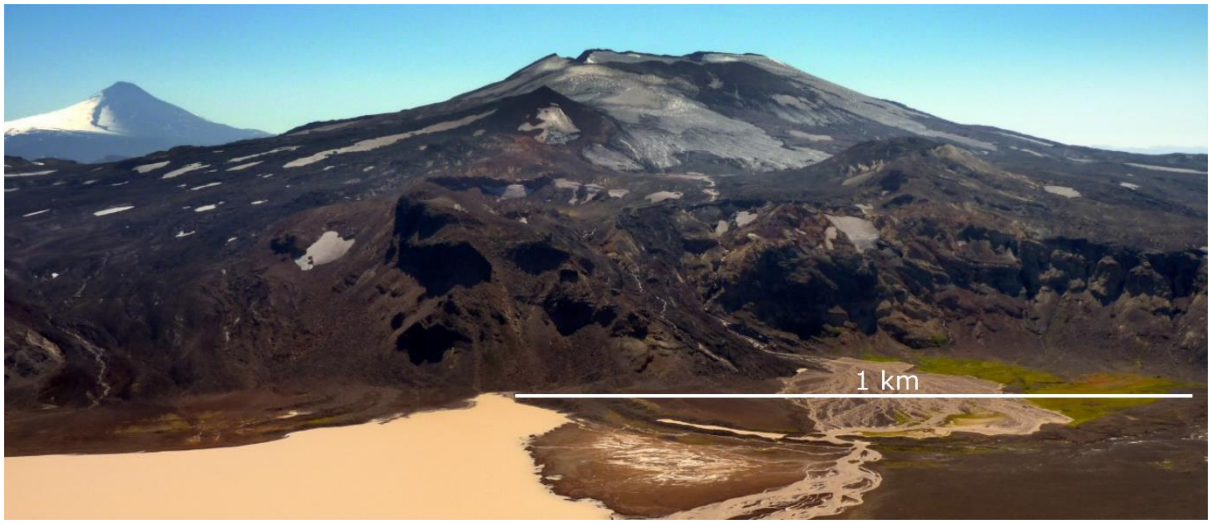

Figure 2.5: A photo of Quetrupillán (centre) and Villarrica (left) taken on 5th March 2015, two days after the eruption of Villarrica on 3rd March. A dusting of tephra covers Quetrupillán (the south-eastern icefield is visible in the centre of the photo) and the eastern slopes of Villarrica. The deposit of a mixed avalanche generated by the eruption is visible on Villarrica's glacier (Vera Rivadeneira, 2018) to the left of the tephra blanket (looking northwest from Cerro Colorado; photo by D. McGarvie).

Accumulation of tephra on a glacier will alter the glacier melting (ablation) rate, depending on the thickness of the deposit (Kirkbride and Dugmore, 2003; Nield et al., 2013; Möller et al., 2016; Barr et al., 2018). A thin tephra cover (less than a few centimetres thick; Kirkbride and Dugmore, 2003; Möller et al., 2016) will increase absorption of short wave radiation and so will increase surface melting, while thicker tephra deposits will insulate the ice and so decrease ablation (Kirkbride and Dugmore, 2003; Nield et al., 2013; Möller et al., 2016; Barr et al., 2018). At 21 km from Villarrica, the thickness of tephra cover deposited on Quetrupillán will almost always be below the threshold for insulating the ice, thus the deposition of each tephra blanket will result in increased melting of the ice surface. Following the 3rd March 2015 eruption of Villarrica, tephra cover at Quetrupillán was observed to consist of a thin and incomplete blanket of ash that had no measurable thickness (D. McGarvie, *personal communication*; Figure 2.5).

Increased glacial melting has been observed to occur at glaciers that lie downwind of volcanoes following tephra-producing eruptions, promoting glacier retreat (Barr et al., 2018). For example, the 1999 – 2001 eruption of Tungurahua in Ecuador deposited tephra on Chimborazo, resulting in increased melting and small-scale retreat of the glacier (Morueta-Holme et al., 2015; La Frenierre and Mark, 2017), and accelerated glacier retreat was observed at Seljavallajökull in Iceland, due to deposition of a thin tephra cover following the 1947 eruption of Hekla (Kirkbride and Dugmore, 2003).

Consequently, the prominent scoured zone at Quetrupillán may be a product of the frequent explosive eruptions of Villarrica. These have regularly covered the icefield on Quetrupillán's stratocone in thin tephra blankets, likely promoting surface ice melting and glacial retreat. If glacial retreat was followed by re-advance (with the truncated morphology and gentle slopes of Quetrupillán encouraging ice accumulation, in contrast to its steep, conical neighbours), then this subsequent re-advance of the glacier would result in scouring of the underlying lavas.

The high frequency of explosive eruptions at Villarrica means that this process has been repeated multiple times throughout the Holocene. While Villarrica, Quetrupillán and Lanín will all have experienced glacial advances and retreats during periods of Holocene glaciation, the erosion caused by the additional advances and retreats at Quetrupillán due to repeated tephra coverings may be responsible for developing the scoured zone at Quetrupillán. Tephra fall on Villarrica is likely to be relatively thick, resulting in insulation of its icefield following eruptions, and importantly, the tephra will only cover the downwind (eastern) flank, rather than the whole icefield (Figure 2.5). Tephra cover on Lanín, ~45 km from Villarrica, is likely to be negligible. Therefore, explosive eruptions at Villarrica will not have the same glacial impacts at Villarrica and Lanín as at Quetrupillán, possibly explaining why Quetrupillán has an extensive scoured zone but Villarrica and Lanín do not.

2.5. Geochemistry of Holocene volcanic products

The geochemistry, petrography and mineralogy of Holocene volcanic products erupted from Quetrupillán are discussed fully in Chapter 3, as well as the methodologies used to analyse them. Only a brief discussion is included here to provide context for this chapter.

Holocene eruptive products from the vents on the flanks of Quetrupillán range from basaltic andesite to trachyte (55 – 65 wt.% SiO_2, 3.2 – 5 wt.% Na_2O, 1.5 – 3.1 wt.% K_2O; Figure 2.6; Appendix III). Sampled Holocene lavas erupted from the stratocone summit range in composition from basalt to trachyte (52 – 64 wt.% SiO_2, 3.0 – 4.5 wt.% Na_2O, 1.0 – 3.2 wt.% K_2O). Most Holocene lavas are trachytic (62 – 65 wt.% SiO_2; 4.4 – 5.0 wt.% Na_2O, 2.7 – 3.2 wt.% K_2O), with twelve of the flank vents having produced trachytic products (Figure 2.2), representing ~96.7% of the volume of Holocene lava erupted from flank vents (Table 2.1). Two Holocene flank vents produced trachyandesite lava flows, representing ~1.8% of this volume, while one vent produced a basaltic andesite lava flow, accounting for the remaining ~1.5% of the volume (Table 2.1; Figure 2.2).

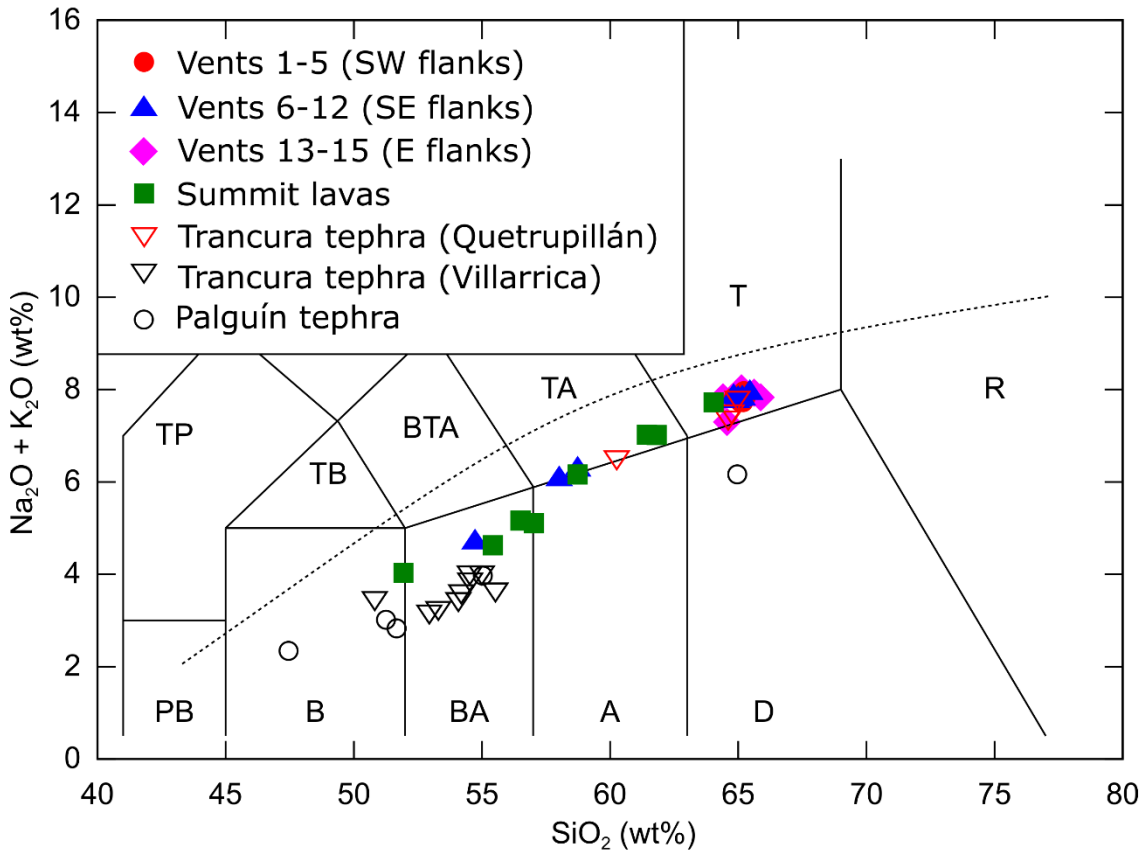

Figure 2.6: TAS plot of lava samples from Quetrupillán and tephra samples collected from the Trancura and Palguín Valleys. Samples are grouped according to their source vent: red circles – Vents 1 to 5 (obscured by the symbols of other trachyte samples); blue triangles – Vents 6 to 12; pink

diamonds – Vents 13 to 15; green squares – summit; open inverted red triangles – Trancura tephra from Quetrupillán; open inverted black triangles – Trancura tephra from Villarrica; open black circles – Palguín tephra.

The compositions of tephra deposits (ash and scoria) preserved in pyroclastic sequences in the Palguín and Trancura Valleys, to the northwest and east of Quetrupillán respectively (see Figure 2.1 for valley locations), were analysed to determine their provenance (see Chapter 3 and Appendix III for methodology and results). Whole-rock major element concentrations (Figure 2.6) and trace element abundances (Figure 2.7) in these tephra samples were measured. Trace element abundances were compared with the characteristic elemental abundances of volcanic products from Quetrupillán, Villarrica and Lanín (Figure 2.7; data from this work and other authors; see Appendix IV for references and data from other authors).

Table 2.1: Compositions, areas and volumes of lava flows produced by vents on the flanks of Quetrupillán. Vent numbers correspond to labels in Figure 2.2.

Vent	Location	Composition	Area (km^2)	Thickness (m)	Volume ($\times 10^6$ m^3)	Notes
1	39°31’40” S, 71°44’09” W	Trachyte	NA	NA	NA	No lava flow
2	39°32’12” S, 71°44’01” W	Trachyte	1.07	10	10.7	Includes assumed area below glacial till
3	39°32’35” S, 71°43’51” W	Trachyte	6.16	10	61.6	Includes assumed area below Vent 5 flow, may extend further south in the forested valley
4	39°32’49” S, 71°43’36” W	Trachyte	0.13	10	1.3	Only the exposed area, unknown area below Vent 3 and Vent 5 flows not included
5	39°32’54” S, 71°43’31” W	Trachyte	2.30	25	57.5	
6	39°33’24” S, 71°42’19” W	Trachyte	0.50	10	5	
7	39°33’49” S, 71°41’17” W	Trachyte	3.06	10	30.6	May extend below Vent 3 flow
8	39°33’37” S, 71°41’06” W	Trachyte	NA	NA	NA	No lava flow

Table 2.1 continued

Vent	Location	Composition	Area (km^2)	Thickness (m)	Volume ($\times 10^6$ m^3)	Notes
9	39°33’24” S, 71°40’43” W	Trachyte	0.23	5	1.2	
10	39°33’01” S, 71°41’45” W	Basaltic andesite	0.67	5	3.4	
11	39°32’48” S, 71°41’12” W	Trachyandesite	0.63	5	3.2	
12	39°31’50” S, 71°42’13” W	Trachyandesite	0.18	5	0.9	
13	39°31’06” S, 71°40’09” W	Trachyte	0.88	10	8.8	Not including any of the flow in the forested Huililco Valley
14	39°30’38” S, 71°40’25” W	Trachyte	1.98	10	19.8	Not including any of the flow in the forested Huililco Valley
15	39°29’40” S, 71°41’08” W	Trachyte	2.09	10	20.9	Not including any of the flow in the forested Huililco Valley
16	39°29’05” S, 71°43’30” W	Unknown	NA	NA	NA	No lava flow, vent not visited

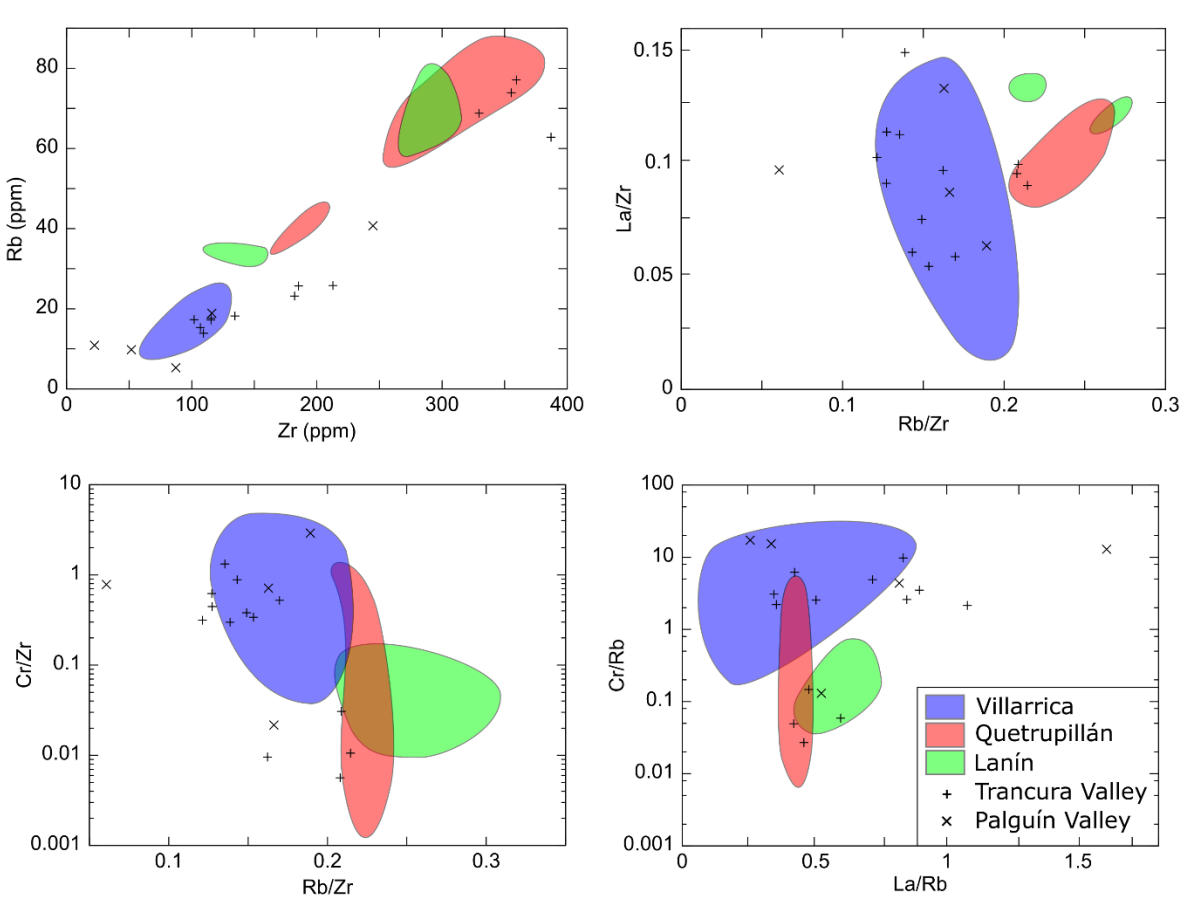

Figure 2.7: Trace element abundances of tephra samples from the Palguín Valley (x) and Trancura Valley (+), compared with the characteristic elemental abundances of Quetrupillán (red area), Villarrica (blue area) and Lanín (green area). Data for Quetrupillán, Villarrica and Lanín from other authors is available in Appendix IV.

Of the eleven tephra horizons analysed from the Trancura Valley, only three have trace element abundances that match those of Quetrupillán, suggesting that only three tephra horizons are likely to have been produced by Quetrupillán. The remaining eight tephra horizons have trace element abundances similar to eruptive products from Villarrica (Figure 2.7). This indicates that most of the tephra deposits preserved in pyroclastic sections in the Trancura Valley have likely been produced by Villarrica. Of the tephra horizons produced by Quetrupillán, two are trachytic with compositions matching those of the trachyte flank lavas, and one is trachyandesitic (Figure 2.6).

None of the analysed tephra deposits in the Palguín Valley match the trace element abundances of products from Quetrupillán. Four samples have abundances similar to those of Villarrica products. The horizon with dacitic composition (Figure 2.6) does not appear to be from Quetrupillán, Villarrica or Lanín. Literature investigation of eruptive products from volcanoes in the wider region suggests

that this horizon may be from Mocho-Choshuenco, 55 km to the southwest (Figure 2.1). The Neltume eruption of Mocho-Choshuenco (~10 000 yr. BP) was dacitic in composition and had a NNE dispersal axis, and the 50 cm isopach line is mapped along the Palguín Valley (Rawson et al., 2015).

2.6. Eruptive features on the flanks of Quetrupillán

The most evident and best-preserved products of Holocene volcanism at Quetrupillán are the sixteen exposed vents and their associated lavas that lie around the lower flanks of the stratocone (Figure 2.2). Twelve of these sixteen vents lie in a volcanic field that is located 3 – 7 km south of the main edifice summit. In this volcanic field, the volumetrically dominant erupted composition is trachyte (Table 2.1), with just one eruption of basaltic andesite and two eruptions of trachyandesite. The three vents on the eastern flanks of Quetrupillán (Vents 13, 14, and 15) have erupted trachyte lavas and have produced two sizeable scoria cones, along with a number of trachytic lavas that have flowed east until they met a ~250 m high suspected fault scarp and were channelled northwards along the Huililco Valley, against the lower edge of the scarp. Vent 16 can be clearly observed on aerial imagery but was not visited and sampled.

Most of the vents that lie within the volcanic field on the southern flank lie along two lineaments. Vents 1 to 5 (labelled in Figure 2.2) lie along a 2.7 km long lineament orientated at 157°, interpreted as a fissure. Samples collected from each of these five vents all have nearly identical trachyte compositions (Figure 2.6; Appendix III). This fissure is roughly parallel to a Pleistocene trachyte fissure that lies to the west of Laguna Azul (McGarvie et al., 2014), and is approximately perpendicular to the alignment of Vents 7, 8 and 9 (048°). Field evidence indicates that each vent within the volcanic field on the southern flank was only active for the duration of the related eruption, so may therefore be classified as monogenetic (Valentine and Gregg, 2008).

2.6.1. Features of Quetrupillán lava flows

Of the sixteen flank vents at Quetrupillán, thirteen have effused lava flows, which range in volume from ~0.9×10^6 m^3 to over 61×10^6 m^3 (Table 2.1). Some lava flows extend below the treeline of Quetrupillán, and it was not possible to measure the area of lava flows within forested valleys from satellite imagery. As such, the volumes of these lava flows are minimum estimates, only including the area on the exposed flanks of the volcano. Of the thirteen vents that effused lava flows, ten have produced trachyte lavas (over 200×10^6 m^3 in total), two have produced trachyandesite lavas (4.1×10^6 m^3) and one has produced a basaltic andesite lava flow (3.4×10^6 m^3; Table 2.1).

Trachyte lavas from Quetrupillán commonly contain patches of oxidised, red spatter fragments, which increase in abundance towards their source vents (Figure 2.8A). As such, they are interpreted as clastogenic lava flows, formed when accumulated spatter was sufficiently molten to coalesce and remobilise into a lava flow (Sumner, 1998; Andronico et al., 2008). The trachyte lavas form blocky lava flows with surfaces, flanks and termini consisting of black, glassy blocks that range in size from <30 cm to 1.5 m (Figure 2.8B). The blocks have a combination of rough, vesicular, irregular surfaces, and smooth, planar surfaces bounded by straight, sharp edges (Figures 2.8C and D), characteristic of typical blocky lava flows (Macdonald, 1953; Cigolini et al., 1984).

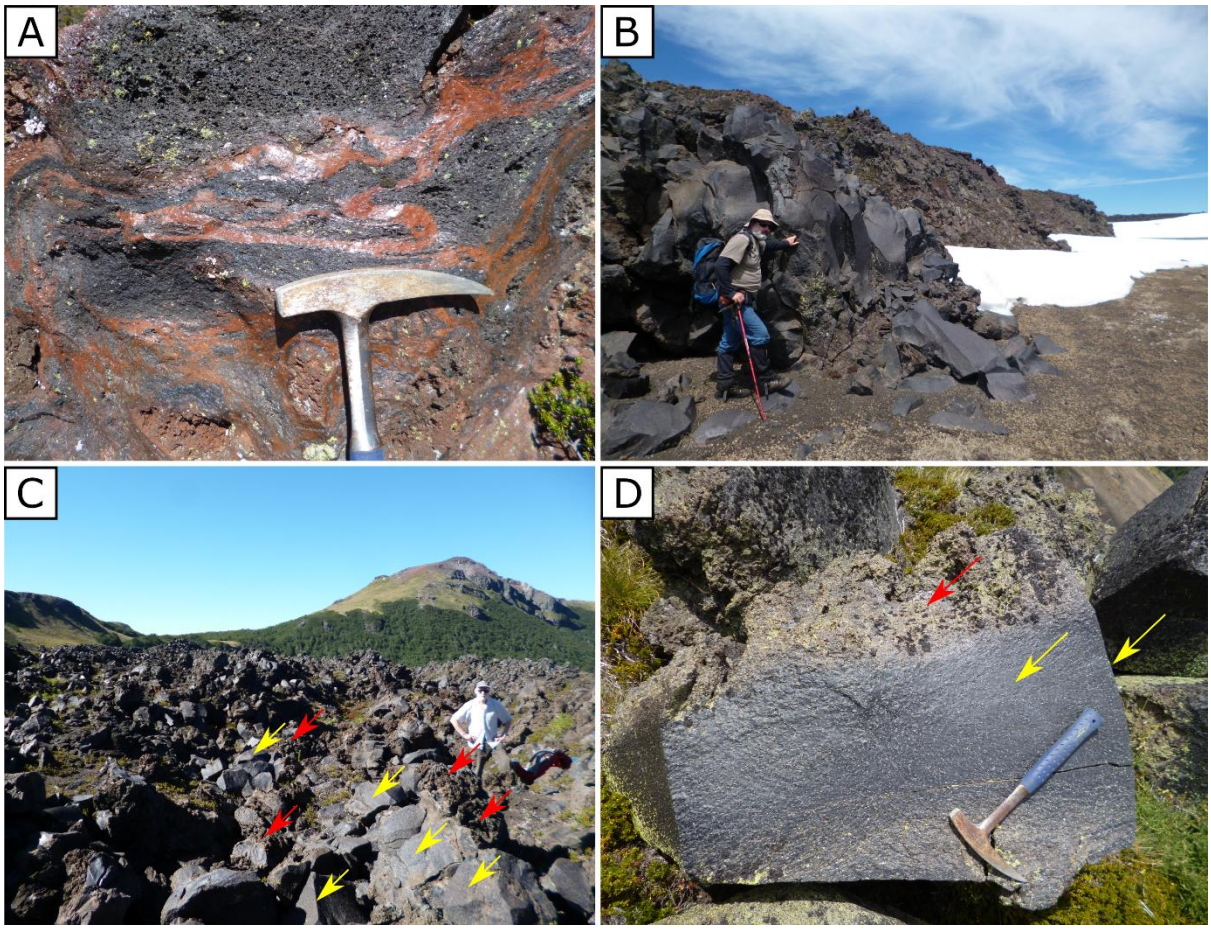

Figure 2.8: Trachytic blocky lavas. A) Trachyte lava from Vent 13 that contains red oxidised patches; B) The steep flow front of the lava flow from Vent 7 composed of polyhedral blocks of black, glassy trachyte (looking west); C) The lava flow from Vent 2 (looking east). Polyhedral blocks have a combination of smooth, planar surfaces with straight sharp edges (yellow arrows) and rough, vesicular, irregular surfaces (red arrows); D) A lava block from the lava flow of Vent 13, showing the contrasting smooth surfaces with sharp edges (yellow arrows) and vesicular, spinose edges (red arrow) to the polyhedral lava fragments.

Blocky lava flows are composed of polyhedral fragments of lava bounded by dihedral angles, with a mix of smooth and spinose surfaces, that were likely formed during auto-brecciation of the lava as the cooled crust fragmented (Macdonald, 1953; Cigolini et al., 1984). Rough vesicular surfaces are interpreted to represent the original upper surface of the active lava flow, while the smooth planar surfaces are interpreted to represent the fractured interior of the lava flow. The overall structure of a blocky lava flow is similar to that of an ‘a‘ā flow, with a massive central layer within the flow, overlain and underlain by brecciated lava fragments (Macdonald, 1953). This description fits well with observations of trachyte lavas at Quetrupillán, where lava flows on the flanks of the volcano have surfaces and termini composed of lava blocks (Figure 2.8B, C and D) while lavas located within the scoured zone have a massive texture with smooth surfaces (Figure 2.3A). These lavas from the summit of the stratocone were most likely to have been erupted as blocky lava flows, but glacial erosion has removed their upper blocky carapaces, exposing the massive interiors of the flows.

Many trachyte lava flows have ogives, arcuate ridges orthogonal to flow direction, on their surface, caused by folding and wrinkling of the lava flow crust during emplacement, and indicating rheological variations through the vertical thickness of the lava flow (Fink, 1980; Magnall et al., 2017). This feature is clearly observed in aerial images of the lava flow from Vent 5, where well-developed ogives are 40 – 80 m in wavelength and up to 15 m in amplitude (Figure 2.9A). Several lava flows have rubbly levees along their margins (Figure 2.9B), forming the edges of what was, during emplacement, the active flow channel (Sparks et al., 1976). The lava flow of Vent 5 is the thickest of all Holocene lava flows, with steep flow margins up to 25 m high defined by well-developed levees (Figure 2.9A). Numerous breakout lobes have also formed along the margins of this lava flow (Figures 2.9A and C). Breakout lobes form in cooling-limited lava flows when the cooled lava crust prevents advance of the flow. Pressure within the flow builds, until the crust is fractured and a breakout lobe forms (Magnall et al., 2017).

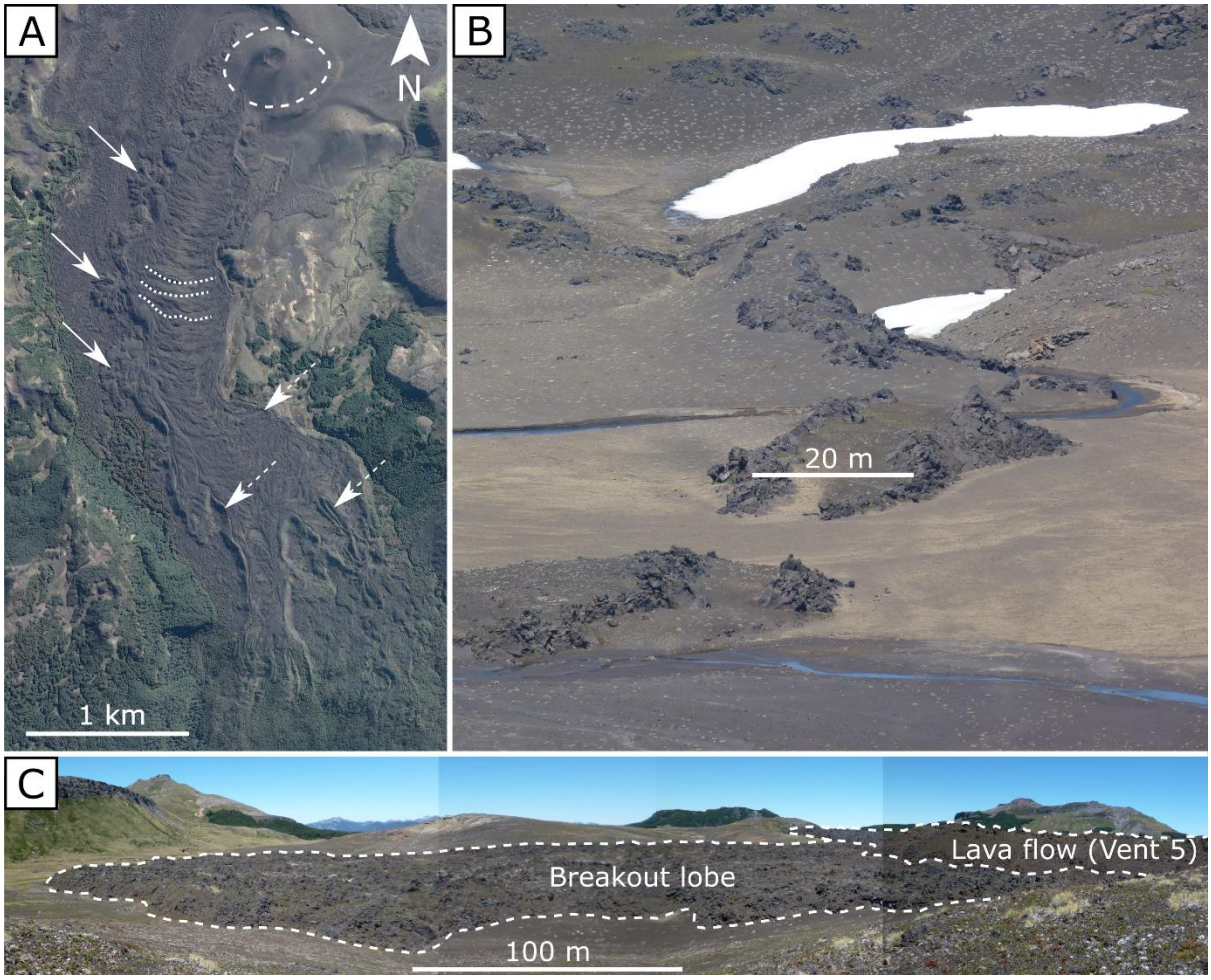

Figure 2.9: A) Satellite image of the lava flow from Vent 5 highlighting ogives in the flow interior (dotted lines), spidery breakout lobes (solid arrows) and levees along the flow margins (dashed arrows). The dashed circle outlines the scoria cone built around Vent 5. Satellite image from Google Earth (downloaded 03/12/2018); B) Rubbly levees along the edge of a lava flow from Vent 11, the lava channel is 20 m wide (looking south from Vent 12); C) A breakout lobe from the lava flow of Vent 5 (looking south).

Five channelized lava flows are visible in aerial images of the large (~30 × 10^6 m^3) trachyte lava flow field from Vent 7, highlighted by ogives on their surfaces and bounded by marginal shear zones (Figure 2.10A; Tuffen et al., 2013). During emplacement, separate channels were active at different times as the lava flowed downslope. In contrast, the emplacement of lava from Vent 6 across relatively flat topography may account for the fact that no features of channelization are visible. Instead, the lava flow has expanded laterally across the plain (Figure 2.10B).

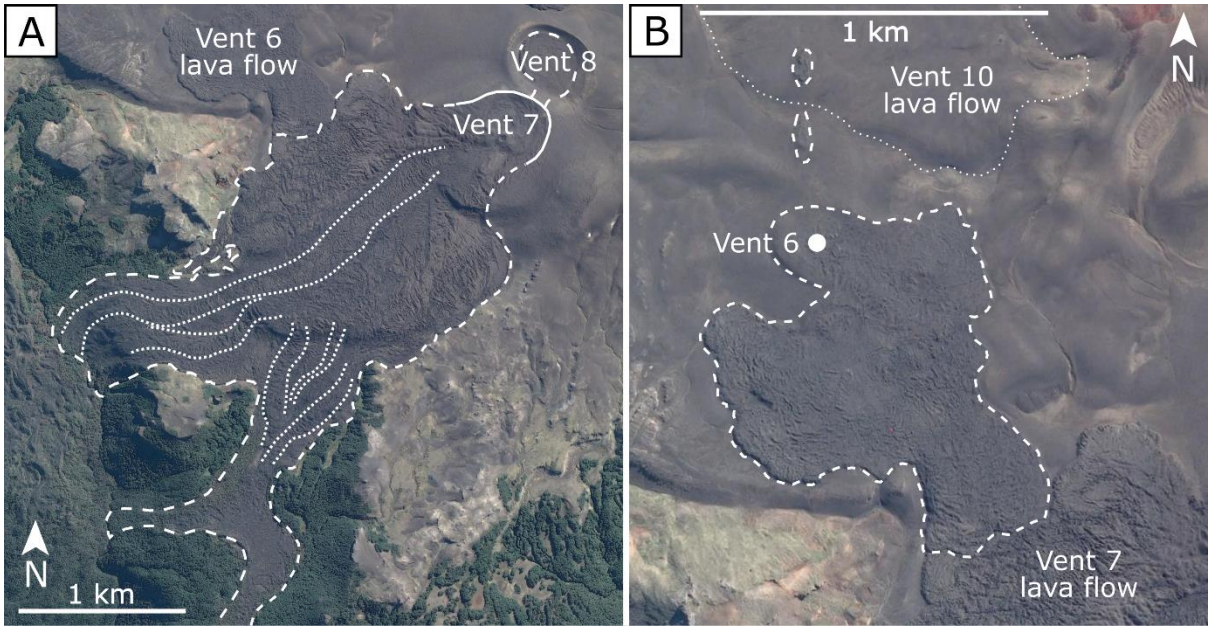

Figure 2.10: A) Satellite image of the lava flow field from Vent 7. Five channelized lava flows are highlighted with dotted lines; B) Satellite image of the lava flow from Vent 6 which expands across the relatively flat plateau. Satellite images from Google Earth (downloaded 03/12/2018).

2.6.2. Features of the flank vents

Seven of the vents on the flanks of Quetrupillán have constructed scoria cones (Figure 2.11A), of which three have a trachytic composition, two have a trachyandesitic composition and one has a basaltic andesitic composition (the composition of Vent 16 is unknown). All but one of the scoria cones on the flanks of Quetrupillán have produced accompanying lava flows. These scoria cones are interpreted to have been created by conventional Strombolian activity, with magma fragmentation producing tephra, scoria and bombs which followed ballistic trajectories to be deposited surrounding the vent (McGetchin et al., 1974; Valentine and Gregg, 2008; Valentine and Connor, 2015). The scoria cones range in height from 25 m to 120 m and have average basal diameters of ~290 m to 650 m, though all are asymmetric in shape due to a combination of the prevailing wind direction, the underlying palaeoslope, and likely, the conduit orientation (Tibaldi, 1995).

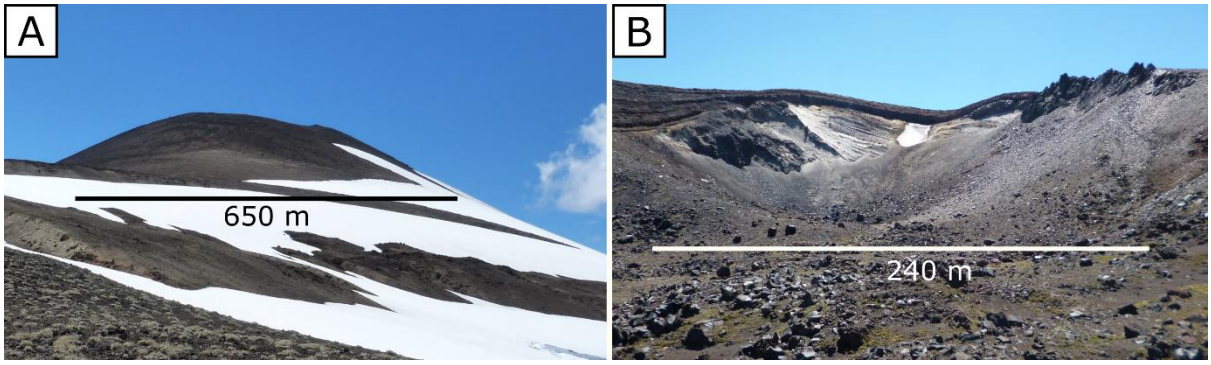

Figure 2.11: A) The scoria cone of Vent 14 which has a basal diameter of 650 m (looking north); B) Pleistocene lavas and pyroclastics exposed in the excavated crater of Vent 2 which has a width of 240 m (looking north).

There is evidence at some flank vents that groundwater played a role during eruptive activity. Vents 1 and 2 have excavated craters through pre-existing volcanic deposits (Figure 2.11B). Both craters have similar dimensions of ~270 m × ~400 m, with their long axes aligned with the strike of the associated fissure. A small amount of pyroclastic material (spatter) has accumulated on the eastern rim of Vent 1, but no lava flow has been produced at this vent. There is an absence of pyroclastic deposits on the crater rim of Vent 2, but lava flows have effused from the vent and flowed southwest and southeast (Figure 2.2). These field relations strongly suggest that explosive phreatic eruptions formed these craters when rising magma encountered groundwater within the bedrock. Once the groundwater supply was exhausted (i.e. the water:lava ratio had been greatly reduced; Valentine et al., 2011) magmatic activity ensued, with pyroclastic material erupted at Vent 1 and effusion of lava at Vent 2.

Three trachyte vents (3, 4 and 8) have produced shallow craters with diameters of ~400 m, surrounded by low-rimmed mounds of tephra with gently sloping sides (Figure 2.12A). The interior walls of the craters are composed of vesicular, welded spatter, while unconsolidated tephra (vesicular bombs, lapilli, and ash) drape the outer rims. These deposits are interpreted as tuff rings, formed during phreatomagmatic eruptions when interaction between magma and sufficient external water caused explosive fragmentation (Wohletz and Sheridan, 1983; Lorenz, 1986). As the influence of the groundwater waned, lava flows effused from Vents 3 and 4 and breached the tuff rings. Spines of lava aligned with the flow direction are interpreted as remnants of the breached tuff ring ramparts that have been transported by the lava flow (Figure 2.12B). Only three of the flank vents of Quetrupillán have produced tuff rings, suggesting that the presence of water was both transient and

local, as other neighbouring vents, active during the same fissure eruption, do not show any features indicating magma-water interactions.

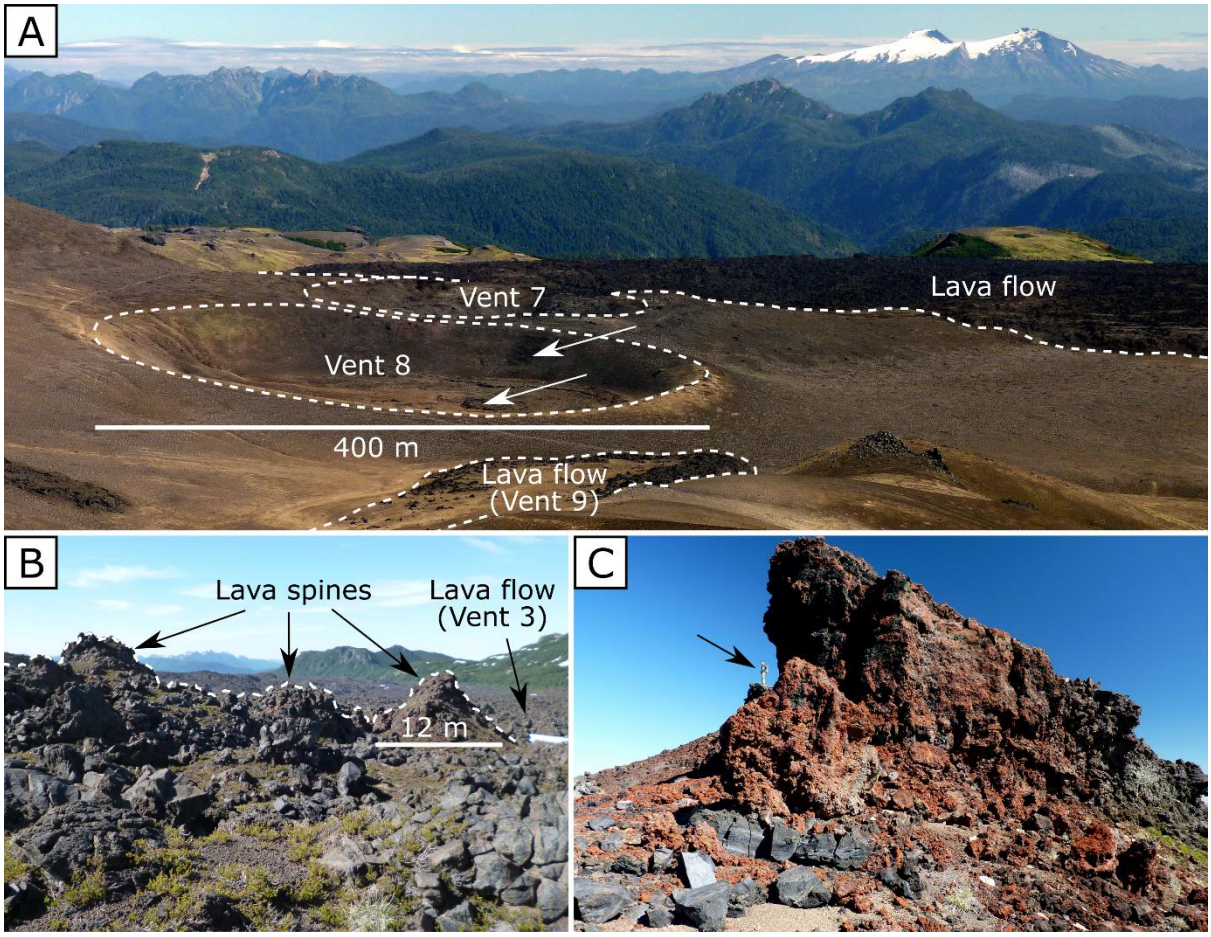

Figure 2.12: A) Vent 8 has produced a shallow ~400 m wide crater surrounded by a low-rimmed tuff ring. Arrows highlight where lava from Vent 7 has spilled into the crater. The lava flow of Vent 9 is visible in the foreground, and Volcán Mocho-Choshuenco is in the background (looking southwest; photo by D. McGarvie); B) Lava spines aligned with the flow direction of the lava flow of Vent 3 (looking south); C) A ~10 m thick drape of agglutinated spatter on the ridge of Cerro Colorado. Person for scale, highlighted by arrow (looking NNW; photo by D. McGarvie).

The vigour of explosive phases of Holocene eruptions is reflected in the extent and character of tephra blankets that occur generally to the east (i.e. downwind) of vents. For example, a particularly vigorous explosive phase is inferred to have occurred at Vent 11. A tephra blanket (consisting of agglutinated trachyandesite spatter with thickness of ~10 m) outcrops at a distance of 1 km from the vent (Figure 2.12C), covering the ridge of Cerro Colorado, southeast of Laguna Blanca (Figure 2.2).

2.7. Eruption stratigraphy of the flank eruptions

Stratigraphic relationships can be used to determine the relative ages of some of the lava flows from the vents on the flanks of Quetrupillán (Table 2.2). However, many of the lava flows are geographically isolated (Figure 2.2) and so it is not possible to determine their relative stratigraphy. Tephrostratigraphy was also not possible, as tephra deposits are poorly preserved on the exposed, unvegetated flanks of Quetrupillán and are only locally preserved. In addition, thick snow covers the area during winter months, so any tephra deposited on the snow has been removed or modified during melting in spring. For these reasons, the stratigraphy presented in Table 2.2 must be considered as tentative and incomplete. An attempt at estimation of the relative ages of the geographically isolated lava flows was made based on the degree of weathering, tephra cover and vegetation growth on the lava flows. However, this cannot be considered definitive as local climatic variations across the volcano may be responsible for differences in these characteristics.

In the volcanic field on the southern flank, the most recent eruption occurred from a fissure to the east of Laguna Azul, with activity from Vents 1 to 5 (termed Eruption A; Table 2.2). The lava flow of Vent 4 is overlain by the lava flow of Vent 3, which is in turn overlain by the lava flow of Vent 5, indicating that activity began at Vent 4. The younger Vent 5 has also constructed a scoria cone on the edge of the older tuff ring formed around Vent 4. The lava flow of Vent 2 diverges around and overlies the tuff rings of Vents 3 and 4 and so must be younger than them. This lava has the freshest appearance of all Holocene lavas, and so is interpreted as the youngest lava flow erupted from Quetrupillán. Vent 1 did not produce a lava flow, and so the relative timing of its activity within the fissure is unknown.

A second fissure eruption occurred on the southeast flanks of Quetrupillán, with activity from Vents 7 to 9 (Eruption B; Table 2.2). The creation of the Vent 8 tuff ring pre-dates the effusion of lava from Vent 7, as lava spills over the tuff ring into the Vent 8 crater (Figure 2.12A). The Vent 7 lava flow also spills into the valley containing the Vent 3 lava flow, which it underlies, indicating that Eruption B is older than Eruption A.

Vents 6 (Eruption C) and 10 (Eruption D) are located on a plateau of Pre-Holocene lava. The Vent 7 lava flow infills the lobate edge of the Vent 6 lava flow, suggesting that fissure Eruption B is younger than Eruption C. An eroded lava lobe from Vent 6 overlies the Vent 10 lava flow, implying Eruption D pre-dates Eruption C. The basaltic andesite lava flow from Vent 10 is completely infilled by tephra, with highly-weathered lava only occasionally exposed at the edges of the flow. The outline of the lava flow can be clearly traced in aerial images. This infilled and weathered appearance suggests that Eruption D is significantly older than the trachytic Eruptions A, B and C.

Table 2.2: Relative eruption stratigraphy of activity from the vents on the flanks of Quetrupillán, with eruption composition listed (Bas and. – basaltic andesite; Trachyand. – trachyandesite).

Eruption	Vents	Comp.	Stratigraphic evidence	Notes	Relative age
A	1,2,3,4,5	Trachyte	Vent 3 lava flow overlies Vent 7 lava flow, so this eruption is younger than Eruption B	This eruptive activity pre-dates the most recent ice advance as the glacial till partly covers the lava flow of Vent 2 and the tuff rings of Vents 3 and 4 (Figure 2.3C)	Youngest
B	7,8,9	Trachyte	Vent 7 lava flow underlies Vent 3 lava flow, so this eruption is older than Eruption A, and infills the lobate edge of Vent 6 lava flow, so this eruption is younger than Eruption C		
C	6	Trachyte	Vent 6 lava flow is infilled by Vent 7 lava flow, and so this eruption is older than Eruption B, and Vent 6 lava flow overlies Vent 10 lava flow, implying this eruption is younger than Eruption D		
D	10	Bas and.	An eroded lobe of Vent 6 lava overlies the Vent 10 lava flow, implying Eruption D pre-dates Eruption C	Lava flow is completely infilled and covered by tephra with only small patches of weathered lava exposed	Oldest
E	11	Trachyand.	None – isolated lava flow		Cannot be stratigra-phically related to eruptions A – D
F	12	Trachyand.	None – isolated lava flow		
G	13	Trachyte	Overlies the Vent 14 lava flow, so this eruption is younger than Eruption H	Lava flow is vegetated above treeline to elevation of ~1550 m	
H	14	Trachyte	Underlies the Vent 13 lava flow, so this eruption is older than Eruption G	Lava flow is vegetated above treeline to elevation of ~1550 m	
I	15	Trachyte	None – isolated lava flow		
J	16	Trachyte	None – isolated scoria cone	No lava flow	

The trachyandesite lava flows of Vents 11 and 12 are geographically isolated, and lack of contact with any other Holocene lava flows prevents determination of their relative stratigraphy. They have been termed Eruption E and F, respectively (Table 2.2). On the eastern flanks of Quetrupillán, the lava flow from Vent 13 (Eruption G) overlies the lava flow from Vent 14 (Eruption H), indicating that it is younger. The lava flow from Vent 15 (Eruption I) is geographically isolated, as is the cone of Vent 16 (Eruption J), and so the relative timing of these eruptions cannot be constrained.

2.8. Features of the stratocone

Section 2.4 highlights how the record of the Holocene volcanic activity that constructed the stratocone has been removed by repeated ice advances and retreats. Consequently, a major gap in our understanding of the Holocene eruptive activity of Quetrupillán will be the number, composition and volume of effusive eruptions that took place from the main edifice. This includes lavas effused from the summit crater and from any vents on the upper flanks of the stratocone within the scoured zone.

The remnants of columnar-jointed trachyte lava buttresses that are exposed within the scoured zone provide evidence that effusion of trachyte lavas from the stratocone took place during the last (Llanquihue) glacial period and/or earlier glacial periods (Figure 2.13A). Construction of the stratocone continued during the Holocene, as some of these subglacial lava buttresses have been partially buried by scoured Holocene lavas (Figure 2.13A).

The inner walls of the ice-filled summit crater are composed of beds of spatter, oxidised scoria and massive lava (Figure 2.13B). In some places around the crater rim all surfaces were covered by a yellow-white crusting, presumably sulphur precipitated by degassing of the summit crater, though no fumaroles were identified during fieldwork and no smell of sulphur was detected. The deposits forming the crater walls are assumed to represent the remnants of several undated eruptions from the summit.

Due to the removal of an unknown amount of lava from the stratocone by Holocene glacial erosion up until the end of the 19th century, it is not possible to state anything definitive about the Holocene construction of the main edifice by lava effusions from either the summit crater or from flank vents within the scoured zone. However, there are lavas present on the upper flanks that show no sign of ice-confinement or lava-ice interaction. As such, they are considered Holocene in age. Where these lavas outcrop through the glacial till, they are massive with smooth surfaces and striations striking in a downhill direction, caused by the glacial erosion (Figure 2.13C). These Holocene summit lavas range in composition from basalt to trachyte (Figure 2.6).

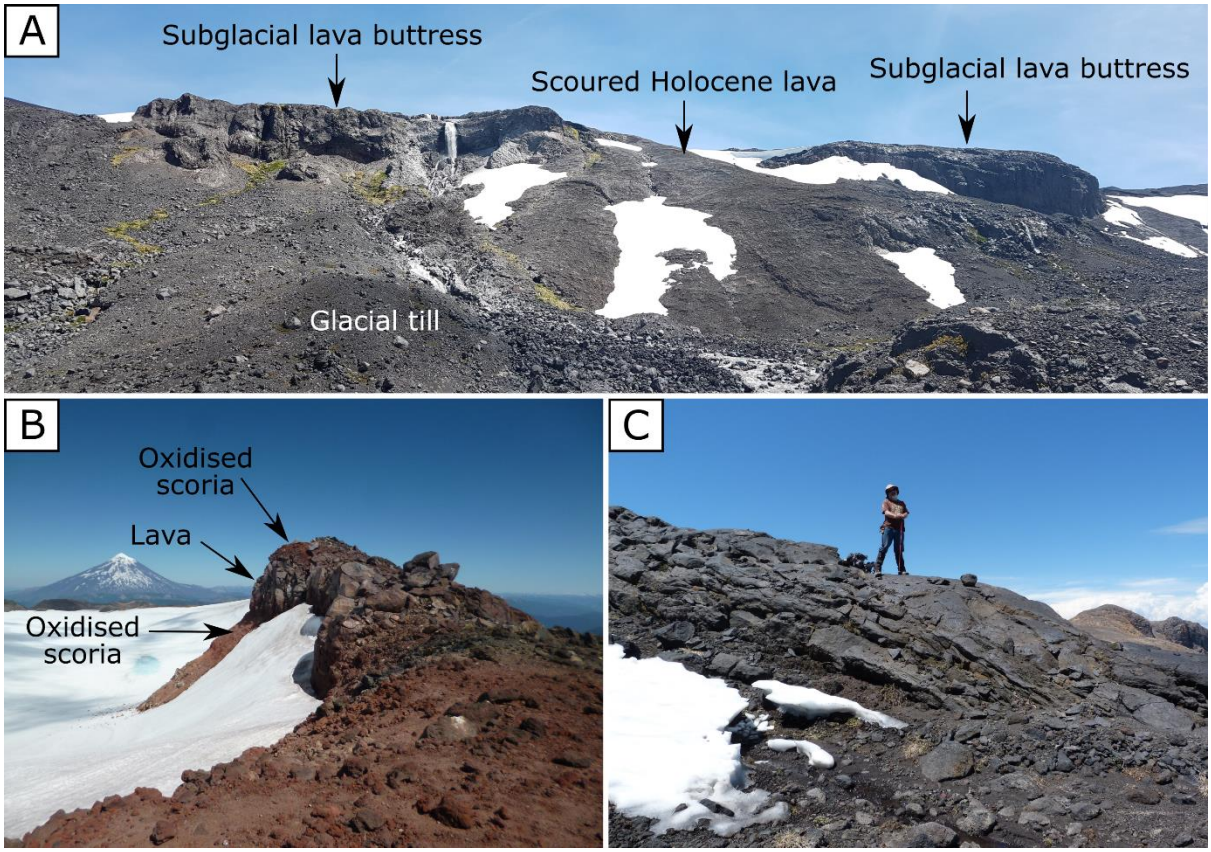

Figure 2.13: A) Subglacial lava buttresses within the scoured zone on the north-eastern flank of Quetrupillán, partially buried by Holocene lavas. The field of view is ~700 m wide, (looking east; photo by D. McGarvie); B) Beds of oxidised scoria and lava exposed in the inner walls of the summit crater, the labelled lava cliff is ~3 m high. The icefield filling the summit crater is visible to the left, and Lanín is in the background (looking southeast); C) Scoured lavas on the upper flanks, erupted from the summit region of the stratocone (looking northeast).

2.9. Tephra layers in surrounding valleys

Tephra layers are exposed in road cuttings in valleys surrounding Quetrupillán and two road cuttings were logged in the Trancura valley near Puesco, to the east (downwind) of Quetrupillán (Figure 2.14). An outcrop of Cretaceous granite basement rock is exposed at the base of section T1, presumably cleared of all overlying material during the last glacial period, strongly suggesting that the overlying pyroclastic sequence has all been deposited during the Holocene. Eleven tephra layers were identified within this section of which, according to analysis of trace element abundances (Figure 2.7), only three were produced by Quetrupillán. It was not possible to correlate these three tephra horizons with eruptive deposits on the flanks and summit of Quetrupillán. Villarrica is the most likely source of the remaining eight tephra layers.

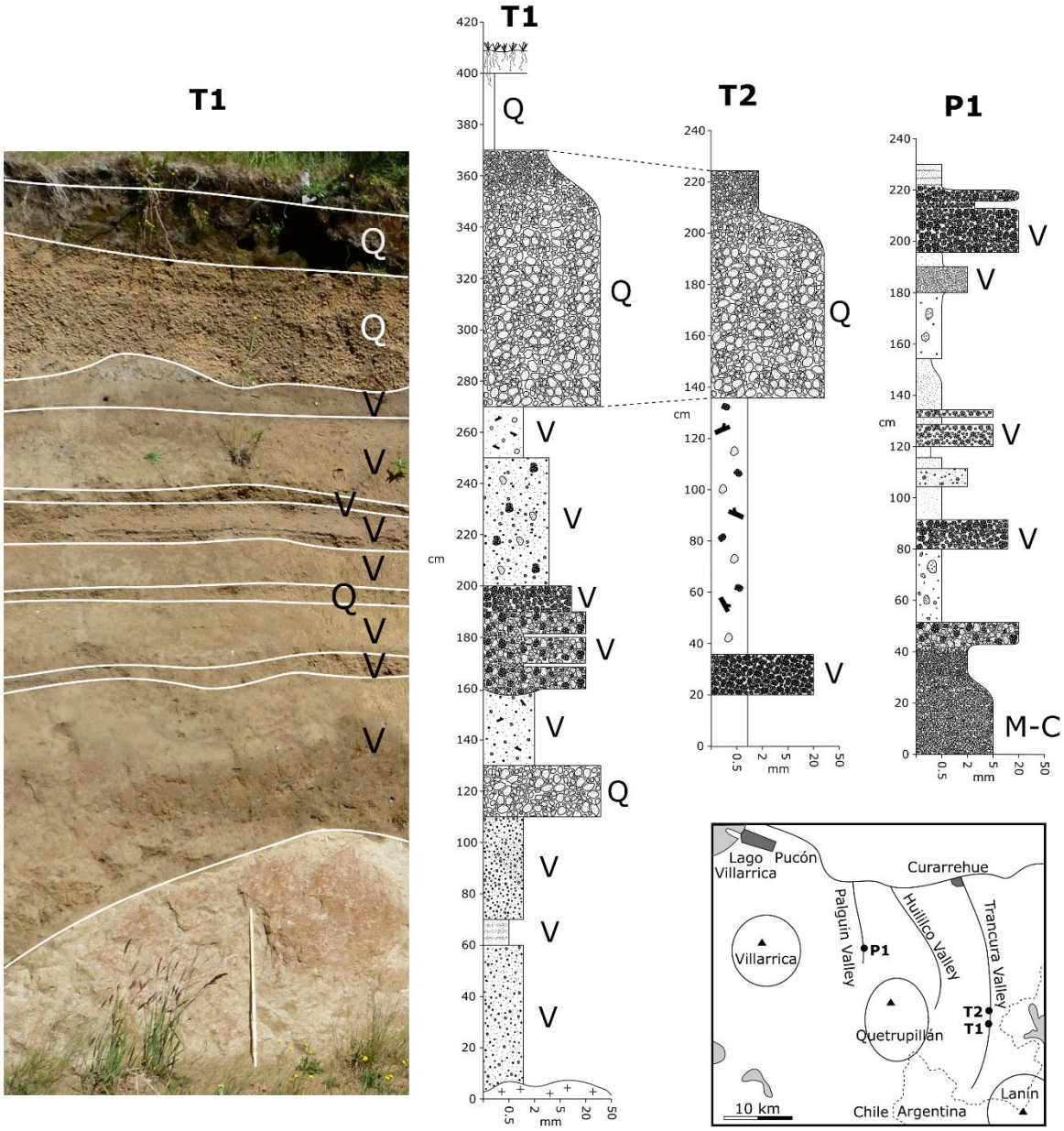

Figure 2.14: Logs of three pyroclastic sequences studied and sampled in the Trancura Valley (T1 and T2) and in the Palguín Valley (P1), and a labelled photo of the T1 section with a metre stick stood against the basement granite. Labels identify tephra layers from Quetrupillán (Q), Villarrica (V) and Mocho-Choshuenco (M-C). Inset shows a schematic map with the location of the logged sections in relation to Quetrupillán. T1: 39.52365° S, 71.55047° W; T2: 39.51823° S, 71.54813° W; P1: 39.42695° S, 71.76594° W.

Quetrupillán has produced the uppermost two tephra layers in the sequence (Figure 2.14). The top tephra layer is a 30 cm thick horizon of gritty, grey ash, with abundant modern organic material due

to the presence of root matter from the overlying vegetation. It has a trachytic composition (Figure 2.6). Below this is a 1 m thick tephra layer which consists of pale, poorly sorted subangular pumice that ranges from 2 – 40 mm and is interspersed with sparse obsidian lithics. This tephra layer, described elsewhere along the Trancura Valley by other authors, is an airfall deposit that has been named the Puesco Pumice by previous studies and dated at 1650 ± 70 yr. BP (Toloza, 2015) and 1850 – 1987 yr. BP (Fontijn et al., 2016). The Puesco Pumice has a trachytic composition that is very similar to the composition of Holocene trachyte lava flows on the flanks of Quetrupillán (Figure 2.6). The preservation of a 1 m thick airfall deposit containing pumice up to 40 mm at a distance of 15 km from the volcano suggests that the Puesco Pumice formed as the result of a large explosive eruption from Quetrupillán, most likely from the summit. Fontijn et al. (2016) estimated that the Puesco Pumice was produced by a VEI 4 eruption and calculated that it has a total volume of 0.3 km^3.

The third tephra layer produced by Quetrupillán is in the lower half of the sequence. It is a 15 cm thick horizon of moderately-sorted, orange-brown pumice ranging from 1 – 15 mm with an ashy matrix. This pumice is a trachyandesite (Figure 2.6).

The presence of three tephra horizons with trace element signatures matching those of effusive products from Quetrupillán suggests that three sizable explosive eruptions have occurred from Quetrupillán during the Holocene. At the studied localities in the Trancura Valley, all three of the Quetrupillán tephra layers had the characteristics of airfall deposits. There was no clear evidence of characteristics representing the lateral movement of clasts that typify pyroclastic density current deposits. An additional road cutting in the Palguín Valley was also logged during this work, but none of the analysed deposits from this horizon were produced by Quetrupillán (Figure 2.7). All the horizons studied in both the Trancura and Palguín Valleys appear to be airfall deposits.

2.10. The pattern of Holocene volcanism

The clearest expressions of Holocene volcanism at Quetrupillán are the flank vents and their lavas. Compositionally, these are trachytes, trachyandesites and basaltic andesites, with trachytes being volumetrically dominant (Table 2.1; Figure 2.6). Limited analyses of lavas from the eroded stratocone indicate eruptions of basalt to trachyte from the summit region. Consequently, there is no spatial-compositional pattern at Quetrupillán, as seen at some volcanic complexes. With the exception of one sampled basaltic lava, the same compositional range is erupted both at the stratocone and from the flank vents. In contrast, at Nevados de Chillán, the Cerro Blanco subcomplex erupts basaltic andesite and the Las Termas subcomplex erupts dacite to rhyolite (Dixon et al., 1999; Mee et al., 2009).

There is a noticeable “non-eruptive” arc of ~8 km in length around the western and northern margins of the scoured zone, in which there is only one vent (Vent 16; Figure 2.2) that appears to have produced only a small scoria cone. Elsewhere, gaps between vents are from a few hundred metres up to 2 km, with a concentration of twelve of the sixteen flank vents in a ~6 km long sector on the southern flank of the volcano, forming the volcanic field. This pattern may be related to a tendency for crustal rupturing to be focused in a zone south of the stratocone, associated with fault splays from the nearby Liquiñe-Ofqui Fault Zone (e.g. Cembrano & Lara, 2009; Schonwalder-Angel et al., 2018). It is notable that Vents 1 to 5 lie on a distinct fissure, as do Vents 7 to 9. Further evidence of crustal rupturing in this zone comes from two NNE-striking Pleistocene subglacial trachyte fissure eruptions that flank Laguna Azul (McGarvie et al., 2014). The interplay between the magmatic system at Quetrupillán and the local tectonic regime is discussed further in Chapter 3.

It is not possible to determine how many eruptions have occurred from the summit of the stratocone, as glacial scouring has removed evidence of the Holocene lava stratigraphy. However, as presented in Section 2.8, within the scoured zone are numerous eroded Holocene lava flows that have flowed around suspected Llanquihue-age lava buttresses and have partly buried them (Figure 2.13A). This field relationship strongly suggests that the stratocone grew during the Holocene as a result of substantial pre-LIA lava effusions that resurfaced its upper flanks. This effusion produced lava flows ranging in composition from basalt to trachyte, but the relative proportion of these compositions cannot be determined due to insufficient sampling of summit lavas. The lack of pristine lavas within the scoured zone implies there have been no lava effusions on the upper flanks of the stratocone since the end of the LIA in the late 19th century.

To evaluate the number of Holocene eruptions from the flank vents, two contrasting scenarios are considered: a simple scenario (i.e. fewest eruptions), and a complex scenario (i.e. the maximum reasonable number of eruptions). In the most complex scenario, each identified vent represents a separate eruptive episode. This would imply that sixteen eruptions have occurred on the lower flanks of Quetrupillán. An argument against this is that the orientation and physical nature of Vents 1 to 5 indicate that they lie along a fissure, and so they would have all been active during the same eruptive episode.

The simple scenario involves just three eruptions: one trachyte eruption, one trachyandesite eruption, and one basaltic andesite eruption. If all the trachyte vents were produced during just one eruption, then this eruption occurred along an arc of ~14 km in length, from Vent 1 in the west to Vent 15 in the northeast (possibly longer if Vent 16 is trachyte; Figure 2.2). This single trachyte eruption would define an arc that may be related either to a previous ring fracture, or to a more recent crustal weakness that could be activated during a future caldera-forming eruption. An

argument against this simplest scenario is the variation in composition within flank trachyte lavas and flank trachyandesite lavas.

An intermediate scenario between these extreme end members, whereby the sixteen vents represent ~10 different eruptive episodes, as presented in Table 2.2, seems more realistic. Vents 1 to 5 and Vents 7 to 9 represent fissure eruptions, with several vents active during a single eruptive episode, as discussed in section 2.7. The remaining vents are likely to represent individual eruptions.

Chapter 3: Holocene magmatism at the Quetrupillán Volcanic Complex

Camp, Laguna Azul

This chapter is based on Simmons, I. C., Cortés, J. A., McGarvie, D., Calder, E. S., 2020. Tectonic constraints on a magmatic plumbing system: the Quetrupillán Volcanic Complex (39°30' S, 71°43' W), Southern Andes, Chile. *Journal of Volcanology and Geothermal Research,* vol. 407. I performed fieldwork, subsequent laboratory work, overall analysis, and writing. Dr Joaquín Cortés and Dr Dave McGarvie assisted during the second field season of the project and contributed to discussions and manuscript drafts.

3.1. Introduction

In this chapter I examine the geochemical and textural characteristics of Holocene erupted products from Quetrupillán, in order to determine the processes that the magmas underwent before eruption at the surface. Petrological and geochemical studies allow volcanologists to unravel the evolution of magmatic systems (Burchardt and Galland, 2016), and the textures of volcanic rocks record their magmatic history (Hersum and Marsh, 2007), providing a first order understanding of the magmatic plumbing system below a volcano. The tectonic setting of Quetrupillán is also considered, in order to evaluate the influence of local tectonic stresses on Holocene magmatism at the volcano.

3.2. Methods

3.2.1. Geochemical analysis

Whole-rock compositions of 80 Holocene and Pleistocene lavas and pyroclastic samples (Appendix III) were analysed using a Panalytical PW2404 wavelength-dispersive sequential X-ray fluorescence (XRF) instrument, hosted at the University of Edinburgh (www.ed.ac.uk/geosciences/facilities/xrayfluorescence/xrf). Powdered samples were prepared as fused glass discs for major element analyses and pressed powder pellets for trace element analyses. Powders were heated at 1100 °C for 20 minutes and the loss on ignition (LOI) of volatiles was recorded, tephra samples having first been heated overnight at 450 °C to burn off any organic matter. Powders were then mixed with a borate flux and re-melted at 1100 °C, before casting on a hotplate.

Rare earth element (REE) concentrations were measured for 14 selected samples by inductively-coupled plasma mass spectrometry (ICP-MS). The analytical procedure is detailed in Olive et al. (2001), whereby dissolution of 0.1 g of sample powder was achieved by three-acid digestion (HF, HNO_3, HCl), followed by $HClO_4$ digestion to avoid the formation of insoluble fluorite and to ensure dissolution of spinel phases. Analyses were performed on the Agilent 7500ce ICP-MS instrument at

the Scottish Universities Environmental Research Centre (SUERC; www.gla.ac.uk/research/az/suerc /researchthemes/isotopegeoscience/icp-ms-oes/) using the USGS BCR2 standard (Wilson, 1997).

Polished thin sections of 30 samples of lavas were cut and were studied under a petrological microscope (Appendix II). A subset of eighteen thin sections were further analysed using the CAMECA SX100 electron microprobe at the University of Edinburgh (www.ed.ac.uk/geosciences/ facilities/electron/instrumentspec) to determine mineral chemistry and glass compositions (Appendix V). Mineral phases were analysed using the following beam conditions: pyroxene with 2 µm beam diameter, 4 nA beam current and 15 kV accelerating voltage; plagioclase and olivine with initial conditions of 2 µm beam diameter, 4 nA beam current and 15 kV accelerating voltage, followed by 2 µm beam diameter, 100 nA beam current and 15 kV accelerating voltage; groundmass glass and melt inclusions were analysed with initial conditions of 5 µm beam diameter, 1 nA beam current and 15 kV accelerating voltage followed by 5 µm beam diameter, 80 nA beam current and 15 kV accelerating voltage. If measured, Na was analysed first to minimise its diffusion.

Results of geochemical analyses were plotted graphically (see section 3.3.). Plots of whole-rock analyses were created using PINGU (Cortés and Palma, 2020) and plots of mineral analyses were created using CFU-PINGU (Cortés, 2020). Calculation of the cations per formula unit (c.f.u.) of mineral analyses was performed using CFU (Cortés, 2017). All three programmes are available through VHub (www.vhub.org), an online resource that contains freely available volcanology tools.

3.2.2. Crystal size distributions

Crystal size distributions (CSDs; Marsh, 1988, 1998; Higgins, 2006) of groundmass mineral phases were measured using high-resolution back scattered electron (BSE) images of 15 thin sections of representative samples of lavas erupted from Quetrupillán (Appendix VI). BSE images were taken on a Carl Zeiss SIGMA HD VP Field Emission scanning electron microscope (SEM) hosted at the University of Edinburgh (https://www.ed.ac.uk/geosciences/facilities/sem). These BSE images of lava groundmass were imported to Fiji (Schindelin et al., 2012), a popular distribution of the ImageJ open-source software (Schneider et al., 2012), where the greyscale profile of images was used to differentiate between the constituent components of the groundmass.

Micro-textural studies usually examine the CSDs of plagioclase microlites (e.g. Turner et al., 2003; Piochi et al., 2005; Melnik et al., 2011; Preece et al., 2013; Bain et al., 2019), however in most lava samples from Quetrupillán, plagioclase microlites could not be distinguished from groundmass glass due to their lack of a fully formed crystal shape and the similarity in greyscale intensity (see Appendix VI). Instead, pyroxene microlites were isolated from phenocryst-free, vesicle-free images

and the crystal sizes of a population of at least 200 crystals per lava sample (Mock and Jerram, 2005; Morgan and Jerram, 2006) were measured using Fiji's built-in best fit ellipse tool (see Appendix VI).

Mean crystal aspect ratios were determined using the CSDSlice methodology of Morgan and Jerram (2006) to estimate the 3D shape of the microlites. Fabric was considered massive (i.e. with no foliation) and measurements were corrected for crystal roundness assuming a value of 0.5. Resulting data were exported using the CSD output plugin (downloaded from http://www.uqac.ca/mhiggins/csdcorrections.html) into CSDCorrections 1.4 (Higgins, 2000, 2002, 2006) to calculate the crystal size distributions of the groundmass pyroxene microlites. The total imaged area and pyroxene phase abundance of the samples were determined using built-in features of Fiji (Appendix VI).

3.2.3. Geothermobarometry

Results from electron microprobe analysis (EMPA) of melt inclusions within clinopyroxene phenocryst hosts were used to estimate temperatures and pressures of crystallisation of Quetrupillán magmas (Appendix VII). Melt inclusions were analysed in the centre of the inclusion, and clinopyroxene hosts were analysed next to the inclusion.

Temperatures were calculated from the clinopyroxene-liquid geothermometer presented in Putirka (2008):

$$\frac{10^4}{T} = 7.53 - 0.14ln\left(\frac{X_{Jd}^{cpx} X_{CaO}^{liq} X_{Fm}^{liq}}{X_{DiHd}^{cpx} X_{NaO_{0.5}}^{liq} X_{AlO_{1.5}}^{liq}}\right) + 0.07\left(H_2O^{liq}\right) - 14.9\left(X_{CaO}^{liq} X_{SiO_2}^{liq}\right) - 0.08\ln\left(X_{TiO_2}^{liq}\right)$$
$$- 3.62\left(X_{NaO_{0.5}}^{liq} + X_{KO_{0.5}}^{liq}\right) - 1.1\left(Mg\#^{liq}\right) - 0.18\ln\left(X_{EnFs}^{cpx}\right) - 0.027P$$

(Eq. 3.1)

where T is the temperature in Kelvin and P is the pressure in kbar. X_y^z represents the component of *y* in either the clinopyroxene (*cpx*) or the melt (*liq*), calculated according to Putirka (2008). X_{Fm}^{liq} represents the components of Fe and Mg in the liquid phase, H_2O^{liq} is the wt.% of H_2O in the liquid phase and $Mg\#^{liq}$ is the magnesium number of the melt (see Appendix VII for all calculations).

This geothermometer requires the composition of the melt that is in equilibrium with the clinopyroxene (Putirka, 2008). The composition of the melt trapped within the melt inclusion is used as a proxy for this, as the melt inclusion is assumed to represent the melt from which the clinopyroxene host crystallised.

The concentrations of Al_2O_3 and Na_2O in some clinopyroxene phenocrysts from Quetrupillán are such that the jadeite component (X_{Jd}^{cpx}) yields negative values, preventing Equation 3.1 from being

suitable to estimate temperatures of crystallisation. For these clinopyroxene phenocrysts, Equation 3.2 (Putirka, 2008) was used instead, which generates the temperature at which a liquid is expected to become saturated in clinopyroxene at a given pressure:

$$\frac{10^4}{T} = 6.39 + 0.076\left(H_2O^{liq}\right) - 5.55\left(X_{CaO}^{liq} X_{SiO_2}^{liq}\right) - 0.386\ln\left(X_{MgO}^{liq}\right) - 0.046P + 2.2 \times 10^{-4}(P^2)$$

(Eq. 3.2)

where T is the temperature in Kelvin and P is the pressure in kbar. X_y^{liq} represents the component of *y* in the melt and H_2O^{liq} is the wt.% of H_2O in the liquid phase (see Appendix VII for all calculations). Both geothermometers (Equations 3.1 and 3.2) estimate temperatures with uncertainties of ± 45 °C (Putirka, 2008).

Pressures were calculated using the clinopyroxene geobarometer of Nimis (1999a), computed using the Nimis (1999b) clinopyroxene barometer which is implemented in the CpxBar Excel spreadsheet. This geobarometer is based on the crystal structure of clinopyroxene phenocrysts, dependent on the clinopyroxene composition, the nature of the co-existing melt (alkaline or subalkaline) and the temperature (Nimis, 1999a). Estimated pressures have uncertainties of 2 kbar, and for every 20 °C that the input temperature is underestimated by, the calculated pressure will increase by ~1 kbar (Nimis, 1999a).

As the geothermometer requires an input of pressure and the geobarometer requires an input of temperature, these equations were solved iteratively until convergence of the results. An initial pressure input for the geothermometer provided a temperature to enter into the geobarometer. The resultant pressure was re-entered into the geothermometer providing a new temperature to re-enter into the geobarometer. This process was repeated until the calculated pressure and temperature converged.

3.2.4. Structural analysis

To investigate the effect of tectonic stresses on magmatism and volcanism at Quetrupillán, the geometries of features and structures on the volcano were measured from satellite imagery, downloaded from Google Earth and imported into Fiji (Schindelin et al., 2012). Visible features that were used in analysis include fissures, dykes, possible fault scarps, and orientation of asymmetric cones, as well as lineaments defined by topography and geomorphology. Many of these features were identified only from satellite imagery based on their aerial appearance, and so lack robust field evidence to support their identification. Holocene fissures were mapped in the field during this

study, while possible Pleistocene fissures were identified from satellite imagery. Fault scarps were not examined in the field, and so field observations of features to confirm the identification of faults (e.g. slickensides, brecciation along fault planes etc.) are unavailable, as are data such as fault offsets and the direction of fault motion. The identification of possible faults is therefore an assumption.

The orientation of each identified lineament was measured and converted from a mathematical angle to a geological strike (from North at 000°) using the Fiji plugin Strike_Results.ijm (Cortés, 2019). Lineament orientations were imported into Stereonet (Allmendinger et al., 2013; Cardozo and Allmendinger, 2013) to generate rose diagrams.

3.3. Results

3.3.1. Geochemistry, petrography and mineral chemistry

Holocene lavas erupted from the summit of the stratocone range in composition from basalt to trachyte (52 – 64 wt.% SiO_2, 3.0 – 4.5 wt.% Na_2O, 1.0 – 3.2 wt.% K_2O), while Holocene lavas erupted from the flank vents range in composition from basaltic andesite to trachyte (55 – 65 wt.% SiO_2, 3.2 – 5.0 wt.% Na_2O, 1.5 – 3.1 wt.% K_2O; Figure 3.1; Table 3.1; Appendix III). This is a slightly narrower compositional range than the whole-rock compositions of the sampled Pleistocene lavas, which span from basalt to rhyolite (50 – 69 wt.% SiO_2, 2.9 – 5.6 wt.% Na_2O, 0.9 – 3.6 wt.% K_2O; Figure 3.1; Appendix III). Most Holocene lavas are trachytic in composition (62 – 65 wt.% SiO_2; 4.4 – 5.0 wt.% Na_2O, 2.7 – 3.2 wt.% K_2O; Figure 3.1). Twelve of the flank vents produced trachytic products, representing ~96.7% of the volume of Holocene lava erupted from satellite vents (see Chapter 2, section 2.5.).

The “T” field on the Total Alkali Silica (TAS) plot (Figure 3.1) includes both trachytes and trachydacites. Following the criteria in Le Maitre et al. (2002) for distinguishing between them, the Quetrupillán rocks in the “T” field are all trachytes. Trachytes and trachydacites are separated by the function $q = 100 \times Q / (Q + or + ab + an)$, representing the normative equivalent of Q in QAPF (Q – quartz; A – alkali feldspar; P – plagioclase; F – feldspathoid; or – orthoclase; ab – albite; an – anorthite). If $q < 20\%$ then the rock is trachyte, while if $q > 20\%$ then the rock is trachydacite (Le Maitre et al., 2002). The normative values of Quetrupillán rocks are such that $q < 20\%$ and the rocks are defined as trachytes. All analysed Quetrupillán samples, from both the Holocene and Pleistocene, plot within the subalkaline field of Irvine and Baragar (1971; Figure 3.1). Quetrupillán lavas display a calc-alkaline trend (Irvine and Baragar, 1971; Figure 3.2), with trachytes and trachyandesites plotting within the High-K Series defined by Rickwood (1989; Figure 3.3).

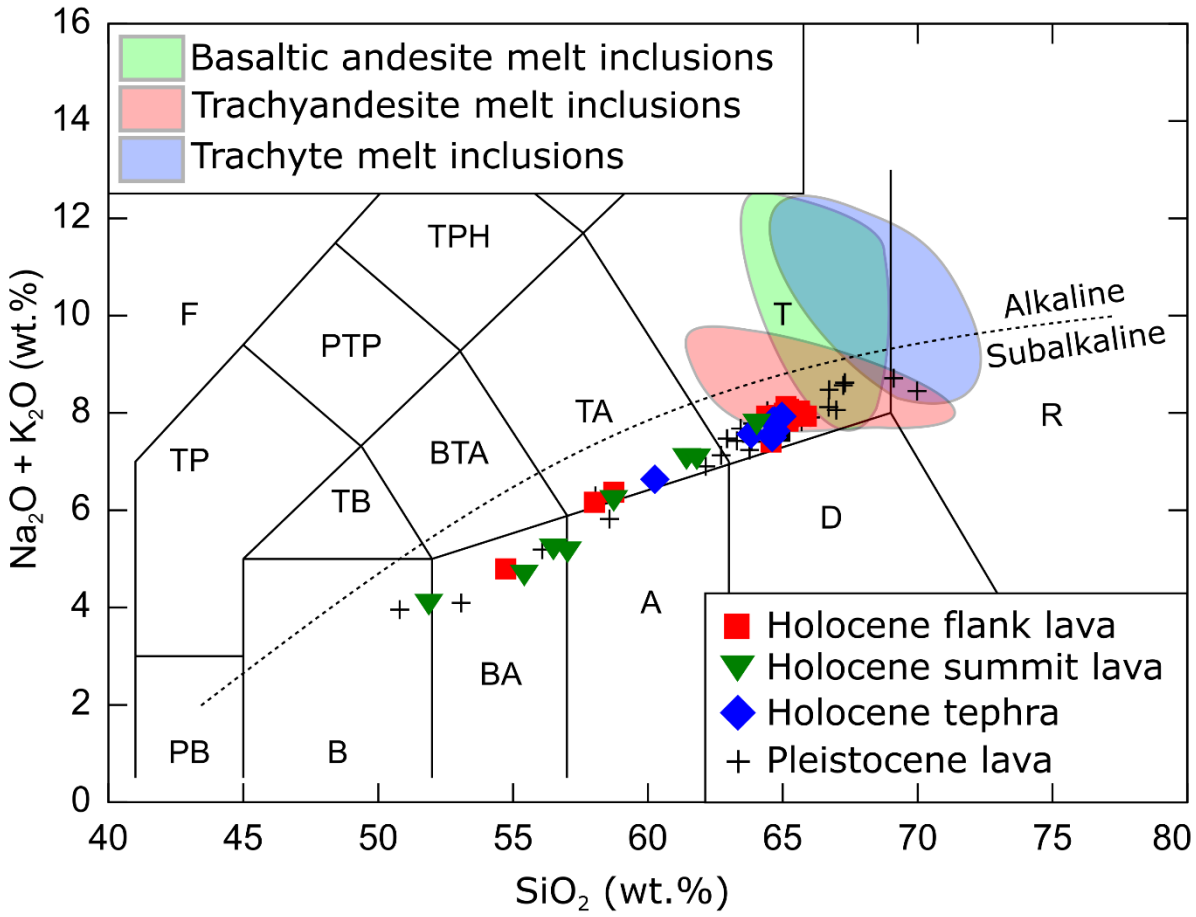

Figure 3.1: TAS plot with whole-rock compositions of Holocene flank lavas (red squares), Holocene summit lavas (green triangles), Holocene tephra deposits (blue diamonds) and Pleistocene lavas (black crosses). Shaded regions indicate the composition of melt inclusions in pyroxene hosts in lavas of different composition (green – basaltic andesite; red – trachyandesite; blue – trachyte). Classification is according to Le Maitre et al. (2002; B – basalt; BA – basaltic andesite; A – andesite; TA – trachyandesite; T – trachyte/trachydacite; R – rhyolite) and the dashed line represents the alkaline-subalkaline boundary proposed by Irvine and Baragar (1971).

Table 3.1: Whole-rock geochemical analyses of representative samples from Quetrupillán. Major element analyses are in wt.% and trace element analyses are in ppm. Some trace elements were not determined (n.d.) or below detection limit (b.d.l.). Samples marked * were analysed by ICP-MS for La, Ce, Pr, Nd, Sm, Eu, Gd, Tb, Dy, Ho, Er, Tm, Yb, Lu, Hf, Pb, Th and U. All other analyses were done by XRF. Results of all samples analysed during this study are available in Appendix III.

Sample	Q3*	Q8*	Q50*	Q62	Q60	Q63	Q67	Q44
Comp.	Trachyte	Trachy-andesite	Basaltic andesite	Trachyte	Trachy-andesite	Basaltic andesite	Basalt	Trachyte
Source /type	Vent 2 Flank	Vent 11 Flank	Vent 10 Flank	Summit	Summit	Summit	Summit	Tephra
SiO_2	64.96	58.66	54.84	63.56	58.25	55.37	51.93	62.27
TiO_2	1.11	1.36	1.04	1.24	1.17	1.06	1.06	1.13
Al_2O_3	15.36	16.17	16.23	14.97	16.08	16.03	17.87	15.55
$Fe_2O_3^T$	5.54	8.16	8.80	6.39	7.64	8.01	8.97	6.00
MnO	0.13	0.13	0.14	0.13	0.13	0.14	0.15	0.13
MgO	1.21	2.89	6.50	1.39	3.49	5.12	6.37	1.37
CaO	3.11	5.88	7.67	3.48	5.96	6.94	9.33	3.47
Na_2O	4.85	3.92	3.22	4.51	3.80	3.32	3.02	4.55
K_2O	3.05	2.34	1.48	3.16	2.31	1.74	1.01	2.73
P_2O_5	0.33	0.36	0.28	0.43	0.35	0.28	0.31	0.36
LOI	0.20	-0.02	-0.21	-0.06	-0.14	-0.04	-0.21	1.32
Total	99.84	99.84	100.00	99.19	99.04	97.96	99.80	98.87

Table 3.1 continued

Sample	Q3*	Q8*	Q50*	Q62	Q60	Q63	Q67	Q44
Comp.	Trachyte	Trachy-andesite	Basaltic andesite	Trachyte	Trachy-andesite	Basaltic andesite	Basalt	Trachyte
Source /type	Vent 2 Flank	Vent 11 Flank	Vent 10 Flank	Summit	Summit	Summit	Summit	Tephra
Sc	16.6	24.3	27.3	18.9	22.4	24.7	28.1	19.7
V	63.7	228.8	210.5	95.7	172.6	192.8	214.4	86.4
Cr	4.0	28.2	179.8	3.1	59.9	154.9	164.9	7.7
Ni	b.d.l.	18.6	78.3	1.3	27.8	66.2	66.4	3.3
Cu	14.5	59.9	56.7	21.0	46.3	44.1	63.2	24.4
Zn	71.2	76.1	74.4	75.9	69.9	68.7	65.7	81.1
Rb	77.8	60.3	36.2	82.1	60.4	43.9	22.0	68.6
Sr	284.3	371.8	429.4	276.9	389.5	403.5	568.1	307.4
Y	44.4	36.9	27.5	47.7	35.7	30.2	22.9	41.3
Zr	352.2	270.6	174.3	378.9	271.8	205.6	124.1	331.2
Nb	14.1	10.9	7.4	15.2	11.2	8.5	6.8	13.5
Ba	737.8	583.2	383.0	713.1	553.2	445.1	334.8	672.6
La	33.82	25.46	18.16	35.9	25.6	19.4	14.3	33.2
Ce	75.53	56.85	40.52	83.8	60.4	47.8	39.4	77.8
Pr	9.32	7.16	5.21	n.d.	n.d.	n.d.	n.d.	n.d.
Nd	37.31	29.12	21.59	42.0	32.3	24.5	20.3	38.5
Sm	7.73	6.20	4.70	n.d.	n.d.	n.d.	n.d.	n.d.
Eu	1.78	1.47	1.25	n.d.	n.d.	n.d.	n.d.	n.d.
Gd	7.43	5.95	4.51	n.d.	n.d.	n.d.	n.d.	n.d.
Tb	1.13	0.91	0.70	n.d.	n.d.	n.d.	n.d.	n.d.
Dy	6.84	5.44	4.16	n.d.	n.d.	n.d.	n.d.	n.d.
Ho	1.39	1.10	0.84	n.d.	n.d.	n.d.	n.d.	n.d.
Er	4.23	3.31	2.51	n.d.	n.d.	n.d.	n.d.	n.d.
Tm	0.69	0.52	0.39	n.d.	n.d.	n.d.	n.d.	n.d.
Yb	4.29	3.28	2.46	n.d.	n.d.	n.d.	n.d.	n.d.
Lu	0.67	0.51	0.37	n.d.	n.d.	n.d.	n.d.	n.d.
Hf	7.89	5.77	3.76	n.d.	n.d.	n.d.	n.d.	n.d.
Pb	24.74	17.54	11.19	n.d.	n.d.	n.d.	n.d.	n.d.
Th	9.88	7.13	4.31	n.d.	n.d.	n.d.	n.d.	n.d.
U	2.71	1.99	1.22	n.d.	n.d.	n.d.	n.d.	n.d.
Eu/Eu*	0.72	0.74	0.83	n.d.	n.d.	n.d.	n.d.	n.d.

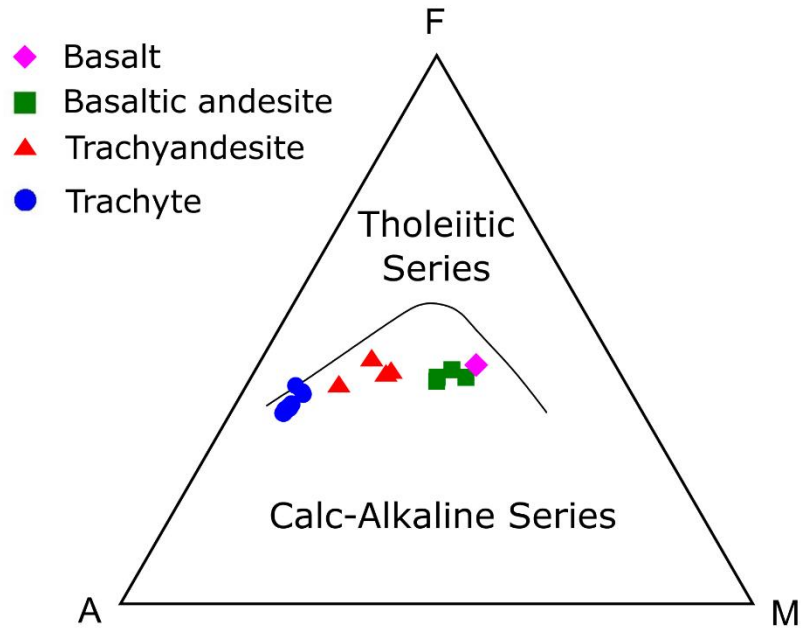

Figure 3.2: The AFM (A – $Na_2O + K_2O$; F – total iron as FeO; M – MgO; all in wt.%) diagram of Irvine and Baragar (1971) to distinguish between tholeiitic and calc-alkaline series. Quetrupillán Holocene lava samples are arranged by whole-rock composition (basalt – pink diamond; basaltic andesite – green squares; trachyandesite – red triangles; trachyte – blue circles).

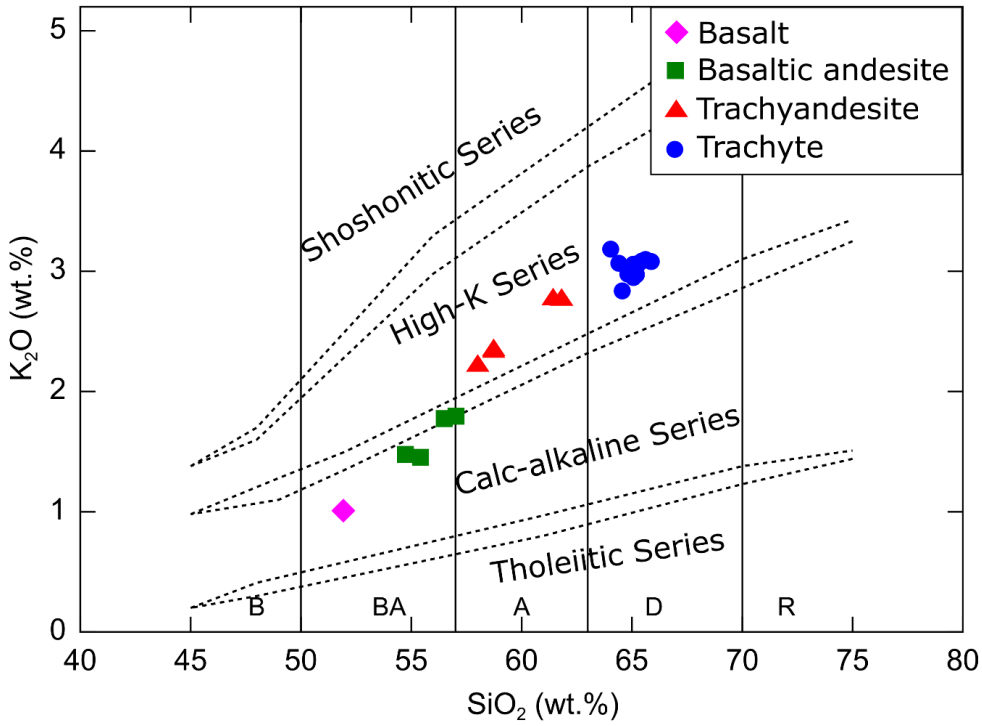

Figure 3.3: The K_2O vs SiO_2 diagram (fields according to Rickwood, 1986). Quetrupillán Holocene lava samples are arranged by whole-rock composition (basalt – pink diamond; basaltic andesite – green squares; trachyandesite – red triangles; trachyte – blue circles).

Trachyte lavas are porphyritic (Figures 3.4A and 3.4B), containing 5 – 15% phenocrysts and glomerocrysts, normalised to vesicle free. Vesicularity of lava varies greatly, even within individual blocks of lava. Vesicularity can be as high as >30% in the rough faces of lava blocks, while as low as <2% in the planar faces of lava blocks (see Chapter 2, section 2.6.1.). Plagioclase is the most abundant mineral phase, representing 50 – 70% of the phenocrysts, and has compositions from Andesine to Labradorite (An_{36-61}; Figure 3.5A; Table 3.2; Appendix V). One population of trachytic plagioclases have partially resorbed cores, surrounded by a zone of more calcic composition, before a return to the original composition at the phenocryst rim (Figures 3.6A and 3.6B).

Clino- and orthopyroxene phenocrysts comprise 15 – 40% of the phenocryst population in trachyte lavas (Augite: Mg# 68 – 77, $Wo_{40-43}En_{40-45}Fs_{13-18}$; Enstatite: Mg# 61 – 70, $Wo_{3-4}En_{61-68}Fs_{28-34}$; Figure 3.5B; Table 3.3). Trachyte lavas also contain Titanomagnetite and Ilmenite, which form a minor constituent (2 – 10%) of the phenocryst assemblage (Figure 3.5D).

Trachyte lavas have glassy groundmass with a composition of trachyte to rhyolite (63 – 72 wt.% SiO_2, 4.0 – 6.9 wt.% Na_2O, 1.8 – 5.7 wt.% K_2O), containing microlites of the same mineral phases plus Pigeonite (Mg# 55 – 59, $Wo_{8-12}En_{49-56}Fs_{36-39}$), and minor Apatite as an accessory phase. Melt inclusions within clino- and orthopyroxene hosts have similar compositions (66 – 72 wt.% SiO_2, 4.0 – 8.6 wt.% Na_2O, 3.0 – 5.9 wt.% K_2O) though some have anomalously high alkali contents (up to 12 wt.% $Na_2O + K_2O$; Figure 3.1).

Two Holocene flank vents produced trachyandesite lava flows, representing ~1.8% of the volume of Holocene lava erupted from flank vents (see Chapter 2, section 2.5.). Trachyandesite lavas are also porphyritic (Figures 3.4C and 3.4D) and have a higher abundance of phenocrysts and glomerocrysts than trachyte lavas (~30%). Plagioclase is the dominant phase (~60%), with compositions varying from Labradorite to Bytownite (An_{51-84}; Figure 3.5A). There are two distinct plagioclase populations, one of pristine phenocrysts (Figure 3.6C) and one showing sieve textures which are commonly zoned (Figure 3.6D). Clino- and orthopyroxene phenocrysts (~23%) are present as Augite to Diopside (Mg# 74 – 81, $Wo_{34-43}En_{44-51}Fs_{11-15}$) and rare Enstatite (Mg# ~73, $Wo_4En_{71}Fs_{25}$; Figure 3.5B). Trachyandesite lavas also contain ~15% olivine (Fo_{57-70}; Figure 3.5C), often with resorbed rims, and ~2% Titanomagnetite (Figure 3.5D). The groundmass of trachyandesite lavas is fully crystalline, composed of the same mineral phases, though plagioclase groundmass crystals are more sodic with a composition of Andesine (An_{39-42}; Figure 3.5A). Melt inclusions in pyroxene hosts have trachytic to rhyolitic glass compositions (62 – 70 wt.% SiO_2, 4.4 – 6.0 wt.% Na_2O, 2.2 – 5.4 wt.% K_2O; Figure 3.1).

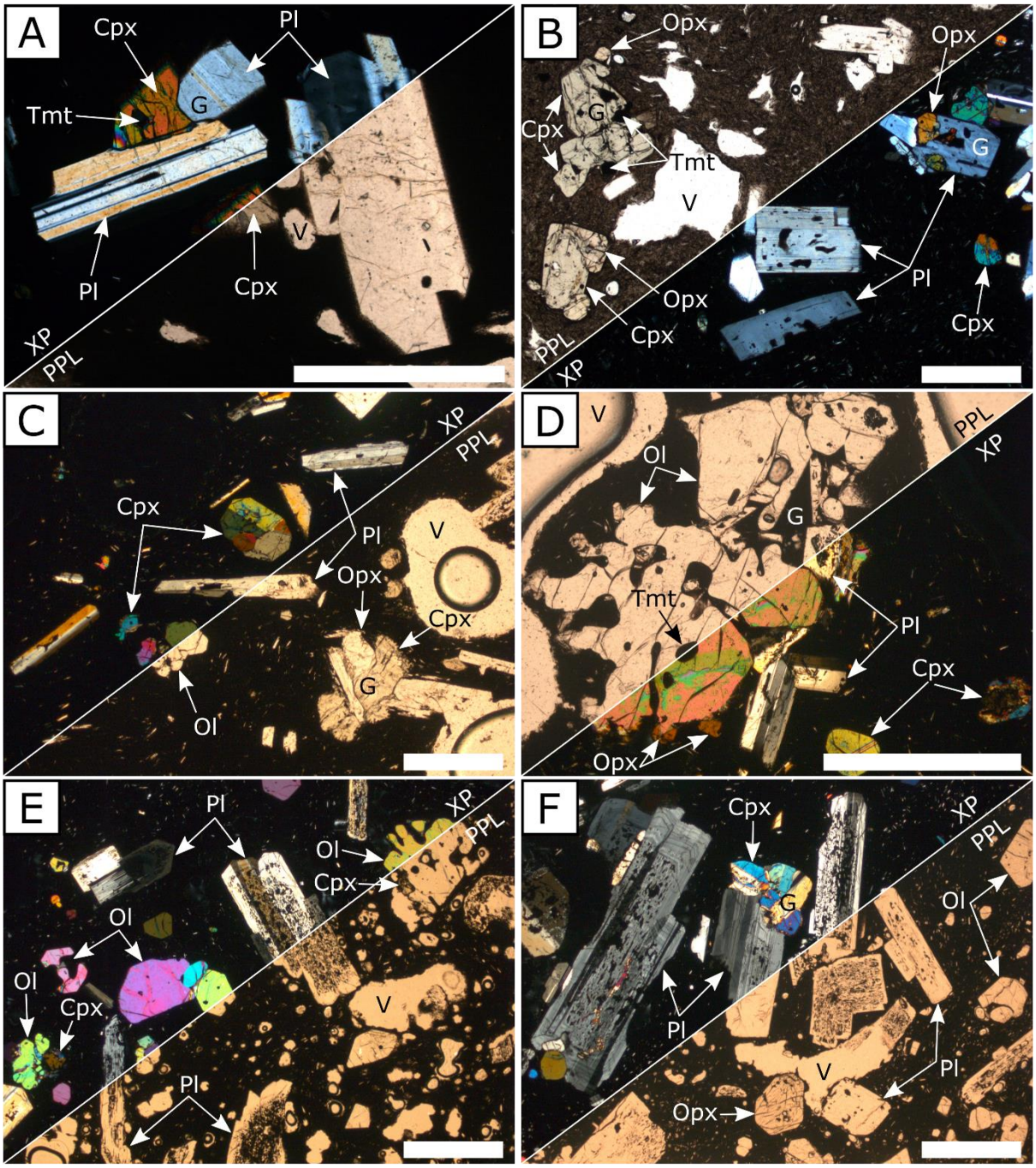

Figure 3.4: Thin section images of lavas from flank vents at Quetrupillán, of trachyte (A and B), trachyandesite (C and D) and basaltic andesite (E and F) composition. Pl – plagioclase, Cpx – clinopyroxene, Opx – orthopyroxene, Ol – olivine, Tmt – titanomagnetite, V – vesicle, G – glomerocryst. Scale bar in each image is 1 mm. Images show thin sections under plane polarised light (PPL) and under crossed polars (XP).

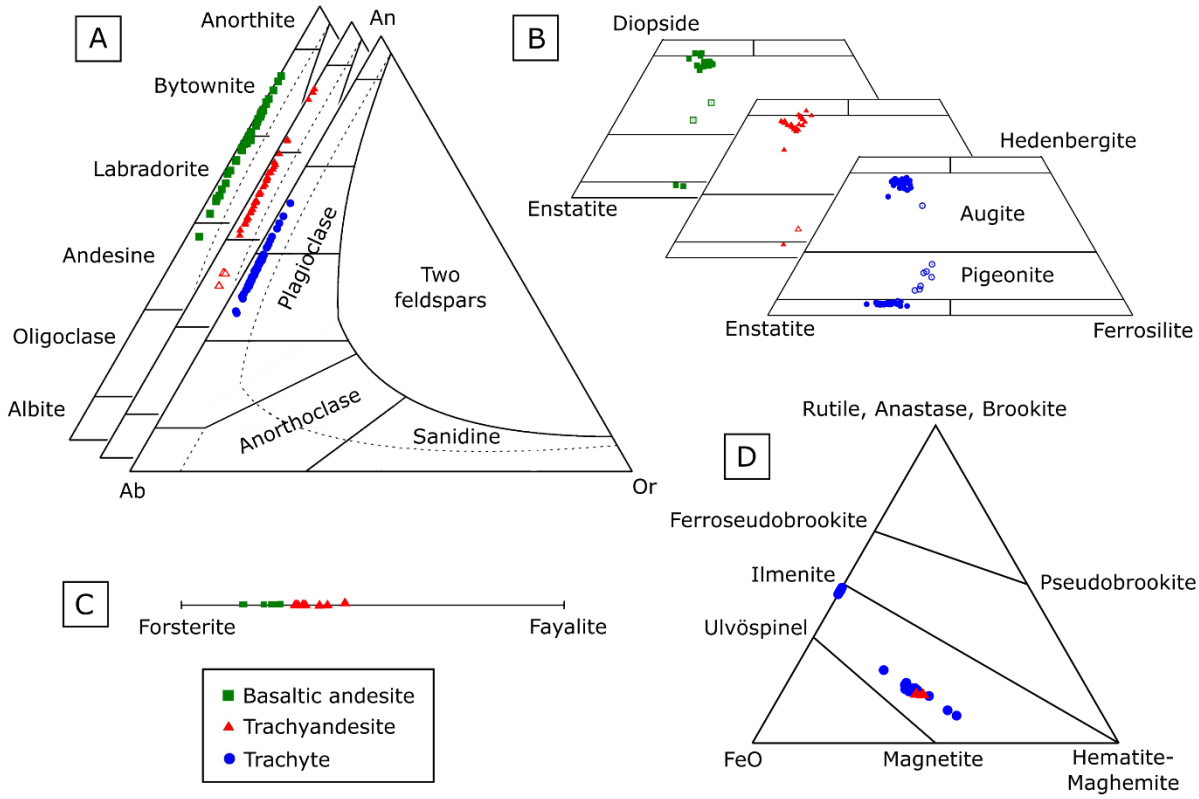

Figure 3.5: Mineral compositions of plagioclase (A), pyroxene (B), olivine (C) and oxide (D) phenocrysts, arranged by whole-rock composition: basaltic andesite – green squares, trachyandesite – red triangles, trachyte – blue circles. Open symbols represent groundmass microlites. Data are in Appendix V.

Table 3.2: Mineral analyses of representative plagioclases from samples of Quetrupillán lavas. Analyses (in wt.%) were made by EMPA. Cations per formula unit (c.f.u.) were calculated using the CFU programme (Cortés, 2017), based on the number of oxygen (N.O.). Some elements were below detection limit (b.d.l.). Results of all mineral analyses are available in Appendix V.

Texture	Sieve	Sieve	Pristine	Sieve	Microlite	Pristine	Pristine	Pristine
Analysis	Core	Core	Core	Core	Core	Core	Middle	Rim
Lava composition	Basaltic andesite	Basaltic andesite	Trachy-andesite	Trachy-andesite	Trachy-andesite	Trachyte	Trachyte	Trachyte
Sample	Q50	Q50	Q8	Q8	Q8	Q3	Q3	Q3
SiO_2	49.42	53.90	52.12	47.43	56.56	57.95	56.91	58.02
TiO_2	0.04	0.06	0.05	0.03	0.13	0.06	0.06	0.06
Al_2O_3	31.44	28.16	29.99	32.99	25.22	26.38	27.00	26.66
$Fe_2O_3^T$	0.67	0.65	0.73	0.71	1.16	0.53	0.54	0.50
SrO	0.13	0.13	0.14	0.12	0.16	0.12	0.13	0.14
MnO	b.d.l.	0.01	b.d.l.	b.d.l.	0.01	b.d.l.	0.01	b.d.l.
MgO	0.10	0.11	0.09	0.06	0.13	0.04	0.04	0.05
CaO	15.18	11.65	13.56	17.32	8.94	8.88	9.71	9.22
Na_2O	2.71	4.56	3.64	2.05	6.41	6.28	5.52	5.98
K_2O	0.13	0.26	0.20	0.07	0.61	0.41	0.35	0.37
Total	99.81	99.50	100.51	100.79	99.32	100.66	100.26	100.98
N.O.	8	8	8	8	8	8	8	8
Si	2.2691	2.4566	2.3645	2.1737	2.5805	2.5891	2.5547	2.5824
Ti	0.0014	0.0021	0.0017	0.0010	0.0045	0.0020	0.0020	0.0020
Al	1.7012	1.5125	1.6034	1.7818	1.3560	1.3890	1.4284	1.3984
Fe^{3+}	0.0231	0.0223	0.0249	0.0245	0.0397	0.0178	0.0182	0.0167
Sr	0.0035	0.0034	0.0037	0.0032	0.0042	0.0031	0.0034	0.0036
Mn	0.0000	0.0004	0.0000	0.0000	0.0004	0.0000	0.0004	0.0000
Mg	0.0068	0.0075	0.0061	0.0041	0.0088	0.0027	0.0027	0.0033
Ca	0.7467	0.5688	0.6591	0.8504	0.4370	0.4250	0.4670	0.4396
Na	0.2412	0.4029	0.3201	0.1821	0.5670	0.5440	0.4804	0.5160
K	0.0076	0.0151	0.0116	0.0041	0.0355	0.0234	0.0200	0.0210
Cation sum	5.00	4.99	5.00	5.03	5.04	5.00	4.98	4.98
%An	75	58	67	82	42	43	48	45

Table 3.3: Mineral analyses of representative pyroxenes from samples of Quetrupillán lavas. Analyses (in wt.%) were made by EMPA. Cations per formula unit (c.f.u.) were calculated using the CFU programme (Cortés, 2017), based on the number of oxygen (N.O.). Some elements were below detection limit (b.d.l.). Speciation of iron was estimated following Papike et al. (1974). Results of all mineral analyses are available in Appendix V.

Mineral	Augite	Augite	Augite	Augite	Augite	Augite	Enstatite	Pigeonite
Analysis	Core	Core	Core	Core	Core	Core	Core	Microlite
Lava composition	Basaltic andesite	Basaltic andesite	Trachy-andesite	Trachy-andesite	Trachyte	Trachyte	Trachyte	Trachyte
Sample	Q50	Q50	Q8	Q8	Q3	Q3	Q3	Q7
SiO_2	51.90	52.38	50.97	51.19	51.81	52.15	52.38	52.42
TiO_2	0.71	0.58	0.75	0.63	0.83	0.54	0.32	0.67
Al_2O_3	2.03	1.51	2.19	1.62	2.02	1.25	0.58	1.45
FeO^T	9.64	9.79	8.85	11.84	10.57	11.47	19.47	22.94
MnO	0.26	0.30	0.27	0.38	0.48	0.58	0.72	n.d.
MgO	14.17	13.77	15.65	17.31	14.73	13.79	23.73	18.62
NiO	0.02	0.03	0.02	b.d.l.	b.d.l.	0.01	b.d.l.	b.d.l.
CaO	20.38	20.38	20.53	16.21	20.17	19.58	1.80	3.91
Na_2O	0.32	0.32	0.32	0.32	0.37	0.34	0.03	n.d.
Total	99.42	99.05	99.53	99.48	100.98	99.70	99.03	100.01
N.O.	6	6	6	6	6	6	6	6
Si	1.9460	1.9711	1.9087	1.9201	1.9235	1.9644	1.9581	1.9714
Ti	0.0200	0.0164	0.0211	0.0176	0.0232	0.0154	0.0090	0.0190
Al	0.0897	0.0670	0.0966	0.0715	0.0884	0.0553	0.0256	0.0643
Fe^{3+}	0.0016	0.0000	0.0662	0.0758	0.0449	0.0098	0.0424	0.0000
Fe^{2+}	0.3007	0.3081	0.2109	0.2955	0.2833	0.3515	0.5663	0.7215
Mn	0.0083	0.0096	0.0085	0.0120	0.0151	0.0185	0.0228	0.0000
Mg	0.7921	0.7725	0.8736	0.9681	0.8153	0.7746	1.3225	1.0439
Ni	0.0006	0.0009	0.0005	0.0000	0.0000	0.0002	0.0000	0.0000
Ca	0.8186	0.8216	0.8236	0.6513	0.8022	0.7903	0.0721	0.1575
Na	0.0233	0.0233	0.0229	0.0229	0.0266	0.0248	0.0022	0.0000
Cation sum	4.00	3.99	4.03	4.03	4.02	4.00	4.02	3.98
Mg#	72	71	80	76	73	68	69	59
%Wo	43	43	43	34	42	41	4	8
%En	41	41	46	51	43	40	67	54
%Fs	16	16	11	15	15	18	29	38

Table 3.4: Mineral analyses of representative olivines from samples of Quetrupillán lavas. Analyses (in wt.%) were made by EMPA. Cations per formula unit (c.f.u.) were calculated using the CFU programme (Cortés, 2017), based on the number of oxygen (N.O.). Some elements were below detection limit (b.d.l.). Results of all mineral analyses are available in Appendix V.

Analysis	Core	Core	Core	Core	Core	Core
Lava composition	Basaltic andesite	Basaltic andesite	Basaltic andesite	Trachy-andesite	Trachy-andesite	Trachy-andesite
Sample	Q50	Q50	Q50	Q8	Q8	Q17
SiO_2	39.83	38.33	38.47	35.63	36.97	36.38
Al_2O_3	0.06	0.03	0.03	0.02	0.03	0.02
FeO	15.15	22.70	23.82	33.51	27.00	28.78
MnO	0.21	0.38	0.37	0.54	0.45	0.47
MgO	44.86	38.97	38.69	30.39	35.61	34.26
NiO	0.23	0.10	0.11	0.05	0.09	0.11
CaO	0.19	0.18	0.19	0.21	0.18	0.18
P_2O_5	0.04	0.05	0.07	0.05	b.d.l.	0.02
Total	100.58	100.74	101.75	100.40	100.34	100.22
N.O.	4	4	4	4	4	4
Si	0.9960	0.9924	0.9914	0.9798	0.9837	0.9788
Al	0.0018	0.0009	0.0010	0.0006	0.0009	0.0006
Fe^{2+}	0.3168	0.4915	0.5135	0.7707	0.6008	0.6477
Mn	0.0044	0.0083	0.0081	0.0126	0.0101	0.0108
Mg	1.6723	1.5042	1.4866	1.2459	1.4125	1.3745
Ni	0.0046	0.0021	0.0023	0.0011	0.0019	0.0024
Ca	0.0051	0.0050	0.0052	0.0062	0.0051	0.0052
P	0.0008	0.0011	0.0015	0.0012	0.0000	0.0005
Cation sum	3.00	3.01	3.01	3.02	3.02	3.02
%Fo	84	75	74	61	70	68

Table 3.5: Mineral analyses of representative oxides from samples of Quetrupillán lavas. Analyses (in wt.%) were made by SEM. Cations per formula unit (c.f.u.) were calculated using the CFU programme (Cortés, 2017), based on the number of oxygen (N.O.). Some elements were below detection limit (b.d.l.). Results of all mineral analyses are available in Appendix V.

Mineral	Cr-spinel	Cr-spinel	Ilmenite	Ilmenite	Magnetite	Magnetite
Analysis	Core	Core	Core	Core	Core	Core
Lava composition	Basaltic andesite	Basaltic andesite	Trachyte	Trachyte	Trachyte	Trachyte
Sample	Q50	Q50	Q12	Q69	Q53	Q61
TiO_2	0.76	6.24	49.21	47.76	17.55	17.24
Al_2O_3	22.65	10.22	0.36	0.46	2.89	2.77
Cr_2O_3	30.05	21.63	b.d.l.	b.d.l.	b.d.l.	b.d.l.
FeO^T	37.14	55.49	46.28	46.85	75.79	76.04
MnO	b.d.l.	b.d.l.	b.d.l.	0.77	0.60	0.72
MgO	9.88	6.69	3.23	3.97	2.58	3.20
Total	100.48	100.27	99.08	99.81	99.41	99.97
N.O.	8	8	3	3	4	4
Ti	0.0373	0.3430	0.9396	0.9102	0.5321	0.5198
Al	1.7417	0.8801	0.0108	0.0137	0.1373	0.1308
Cr	1.5501	1.2495	0.0000	0.0000	0.0000	0.0000
Fe^{2+}	2.0266	3.3909	0.9823	0.9925	2.5544	2.5486
Mn	0.0000	0.0000	0.0000	0.0165	0.0205	0.0244
Mg	0.9611	0.7288	0.1222	0.1499	0.1550	0.1912
Cation sum	6.32	6.59	2.05	2.08	3.40	3.41

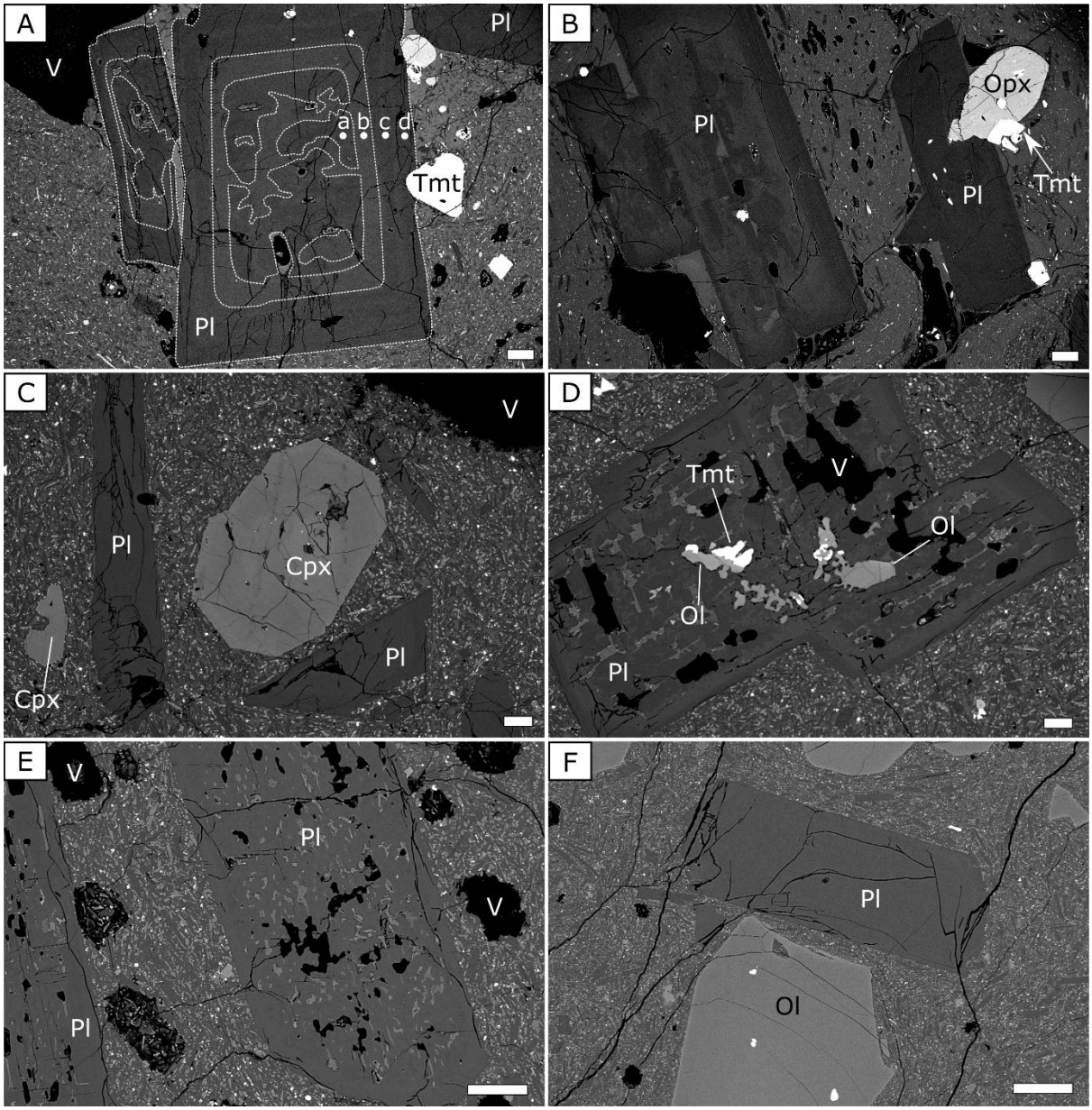

Figure 3.6: BSE images of different textures of plagioclase phenocrysts. A) A plagioclase phenocryst in trachyte lava with a partially resorbed core (a – An_{47}), surrounded by a more calcic zone (b – An_{54}), before a return to the original composition for the rim (c – An_{46}; d – An_{46}); B) plagioclase phenocrysts in trachyte lava, with partially resorbed core (left) and pristine texture (right); C) pristine plagioclase phenocrysts in trachyandesite lava; D) sieve-textured plagioclase phenocryst in trachyandesite lava; E) sieve-textured plagioclase phenocrysts in basaltic andesite; F) pristine plagioclase phenocryst in basaltic andesite. Pl – plagioclase, Cpx – clinopyroxene, Opx – orthopyroxene, Ol – olivine, Tmt – titanomagnetite, V – vesicle. Scale bar in each image is 100 µm.

Only one Holocene flank vent produced a basaltic andesite lava flow, accounting for ~1.5% of the volume of Holocene lava erupted from flank vents (see Chapter 2, section 2.5.). The basaltic andesite lava is also porphyritic, with ~37% phenocrysts and glomerocrysts (Figures 3.4E and 3.4F). Plagioclase is still the most abundant mineral phase, comprising ~40% of the phenocrysts, with compositions ranging from Andesine to Bytownite (An_{47-84}; Figure 3.5A). Phenocrysts are up to 2 mm and are commonly zoned (Figures 3.4E and 3.4F). Most plagioclases have highly sieve-textured interiors (Figures 3.4E, 3.4F and 3.6E) though some have pristine textures (Figure 3.6F). The secondary phenocryst phase in basaltic andesite lavas is olivine (Fo_{74-84}; Figure 3.5C) which accounts for ~35% of the phenocrysts. Some olivines have resorbed rims while others display pristine crystal morphologies (Figure 3.4E). Clino- and orthopyroxene phenocrysts comprise ~23% of phenocrysts in the basaltic andesite lava and consist of Augite to Diopside (Mg# 71 – 81, $Wo_{40-44}En_{41-46}Fs_{10-16}$) and rare Enstatite (Mg# 69 – 72, $Wo_4En_{67-69}Fs_{27-29}$; Figure 3.5B). There is also minor (~2%) Cr-spinel as an accessory phase. Melt inclusions in pyroxene hosts have compositions of trachyte (64 – 69 wt.% SiO_2, 3.8 – 6.5 wt.% Na_2O, 2.2 – 6.4 wt.% K_2O; Figure 3.1).

The sample of basalt lava (Q67; Table 3.1) erupted from the summit region of Quetrupillán was not analysed by EMPA or SEM, and so the composition of minerals within it are unknown.

The rare earth elements (REE) diagram (Figure 3.7), normalised to chondrite (Sun and McDonough, 1989), discriminates between the three different lava compositions erupted from the flanks of Quetrupillán. Trachyte lavas have the greatest values of rock/chondrite for each element, while the basaltic andesite lava has the lowest values. Lavas of all three composition have a gentle negative slope (La/Yb ~7 – 9) and display a small negative Eu anomaly (Eu/Eu* = 0.72 – 0.83). The spider diagrams (Figures 3.8 and 3.9), normalised to normal mid ocean ridge basalt (N-MORB) according to Sun and McDonough (1989), also distinguish between the three lava compositions. All lavas have a negative Nb anomaly, typical of arc magmas, a positive Pb anomaly (Figure 3.8), and are enriched in high field strength elements (HFSE) compared to N-MORB (Figure 3.9). Plotting Rb against Cr (Figure 3.10A) shows a steepening curve from basaltic andesite to trachyandesite to trachyte, and trace element ratio plots of La/Yb vs Nb/Zr (Figure 3.10B), La/Rb vs Cr/Rb (Figure 3.10C), Rb/Zr vs Cr/Zr (Figure 3.10D), Nb/Zr vs La/Yb (Figure 3.10E) and Nb/Zr vs Sm/Zr (Figure 3.10F) also distinguish between samples with different whole-rock composition.

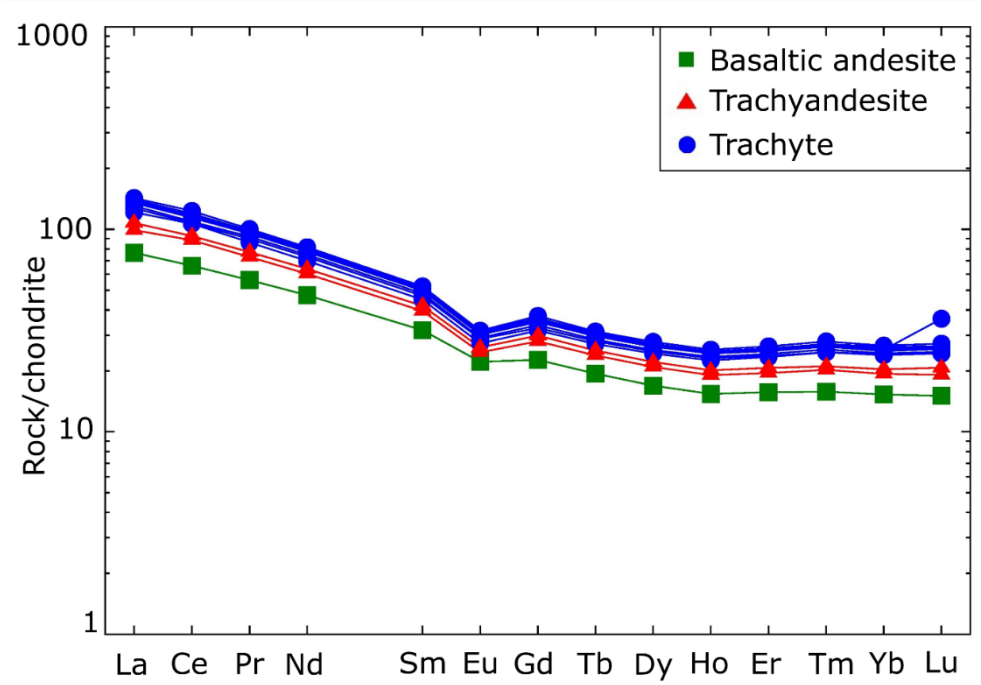

Figure 3.7: REE diagram, normalised to chondrite (Sun and McDonough, 1989). Samples are arranged by whole-rock composition: basaltic andesite – green squares, trachyandesite – red triangles, trachyte – blue circles.

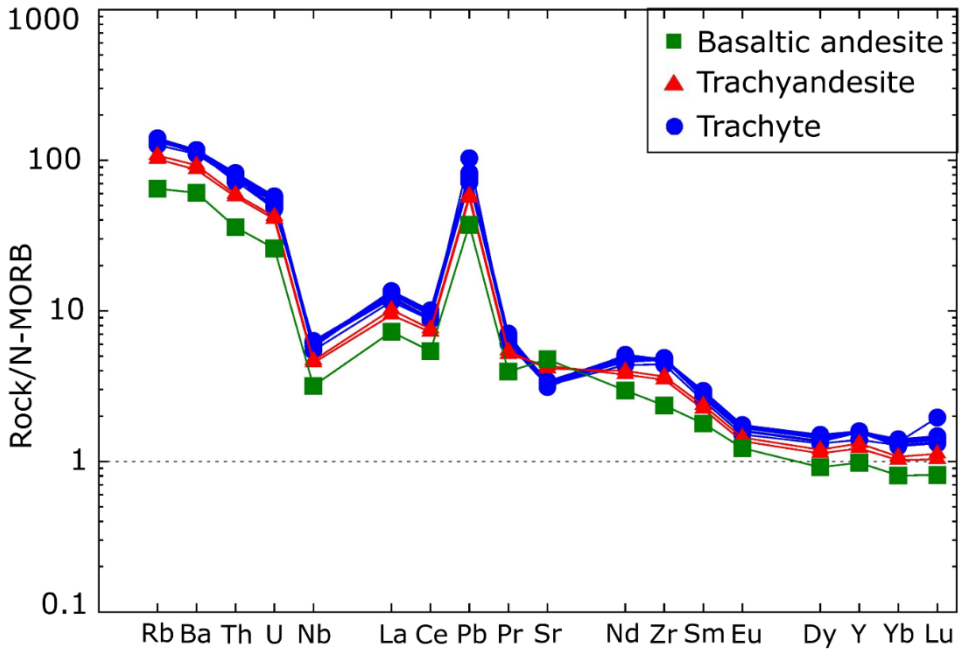

Figure 3.8: Spider diagram normalised to N-MORB (Sun and McDonough, 1989), with elements ordered by decreasing incompatibility. Samples are arranged by whole-rock composition: basaltic andesite – green squares, trachyandesite – red triangles, trachyte – blue circles.

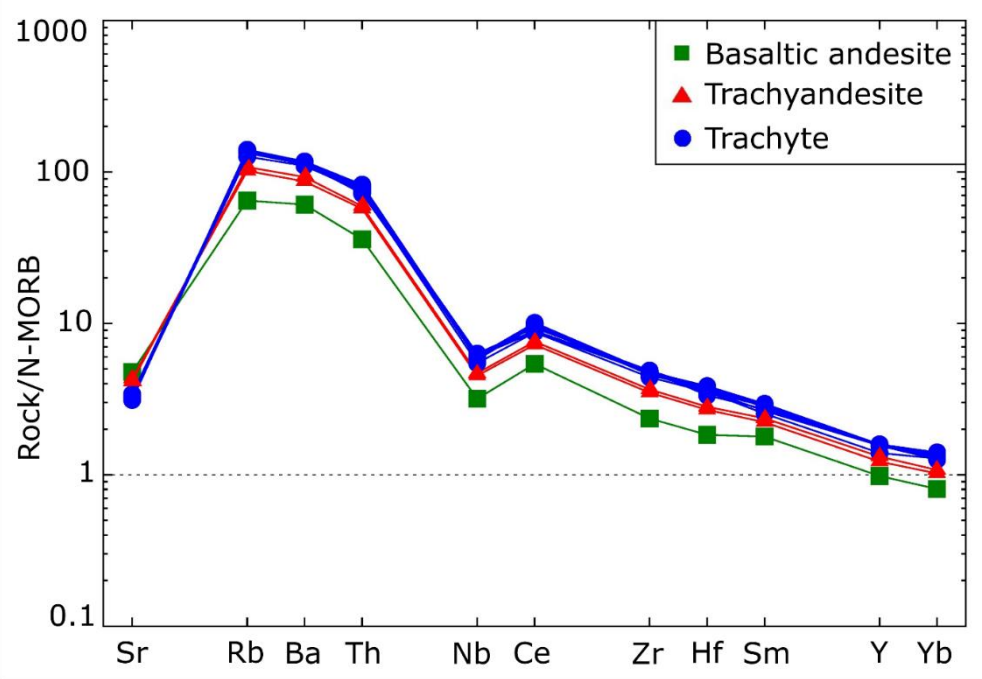

Figure 3.9: Spider diagram (Pearce, 1983), normalised to N-MORB (Sun and McDonough, 1989), with large ion lithophile elements (LILE) to the left and high field strength elements (HFSE) to the right. Samples are arranged by whole-rock composition: basaltic andesite – green squares, trachyandesite – red triangles, trachyte – blue circles.

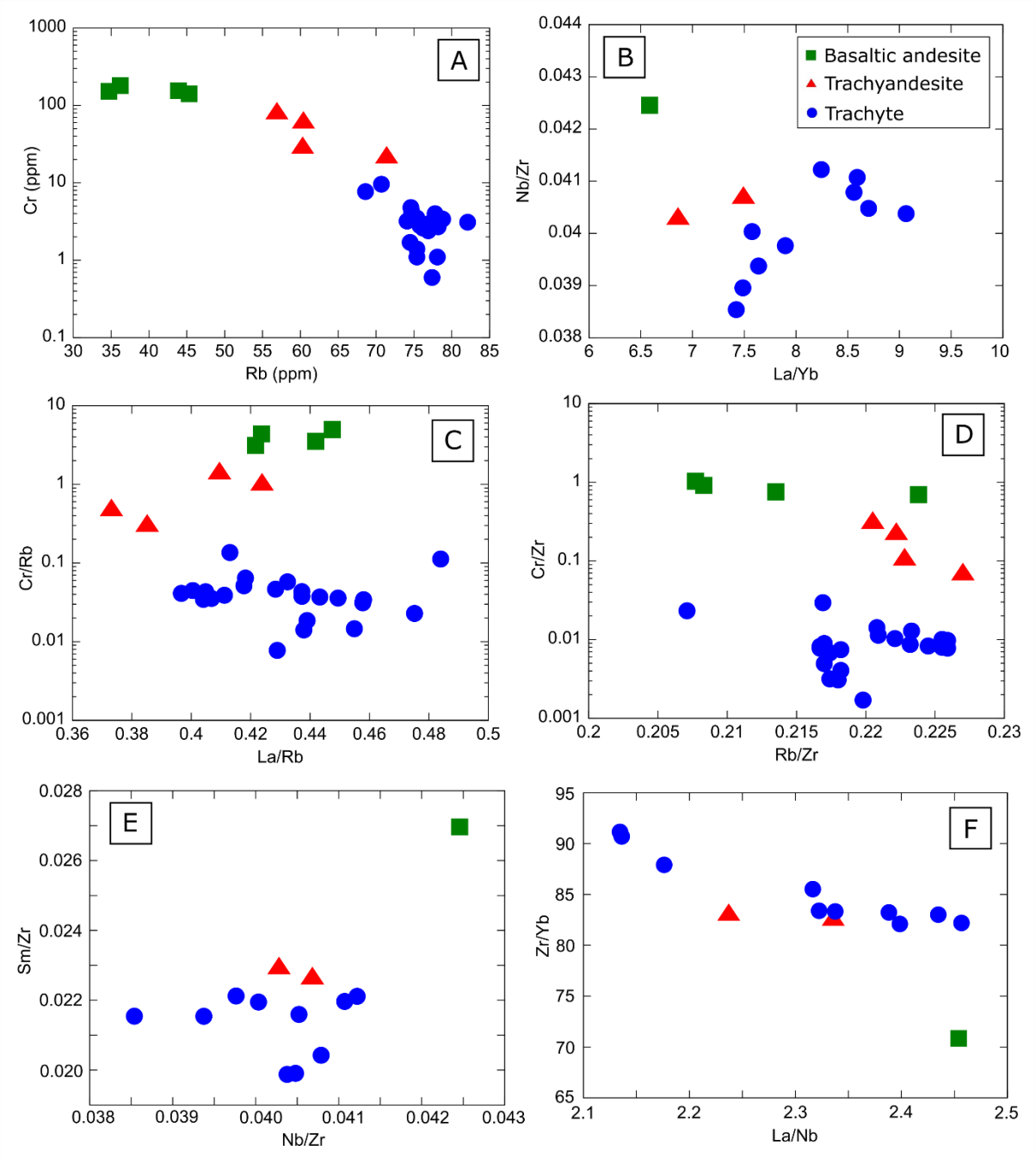

Figure 3.10: Trace element plots: A) Rb vs Cr; B) La/Yb vs Nb/Zr; C) La/Rb vs Cr/Rb; D) Rb/Zr vs Cr/Zr; E) Nb/Zr vs Sm/Zr; and F) La/Nb vs Zr/Yb. Samples are arranged by whole-rock composition: basaltic andesite – green squares, trachyandesite – red triangles, trachyte – blue circles.

3.3.2. Crystal size distributions (CSDs)

CSDs were measured for pyroxene microlites in the groundmass of basaltic andesite, trachyandesite and trachyte lava samples (Figure 3.11; Appendix VI). The large sizes of phenocrysts (some >2 mm) and the disparity between the sizes of phenocrysts and microlites (many <1 μm) meant that it was not possible to measure CSDs for phenocryst populations, only for the groundmass phase.

Most CSDs show concave-up curves (Figure 3.11), suggesting changes in activation energy and/or in the nucleation rate and conditions in the evolving system (Marsh, 1998; Higgins, 2006). The curved CSDs can be approximated by straight line segments, whose slope allows estimation of crystallisation times using the equation from Marsh (1988)

$$Slope = -1/G\tau \quad \text{(Eq. 3.3)}$$

where G is the crystal growth rate (assumed to be constant and independent of crystal size) and τ is the crystallisation time (assumed to be a proxy of magma residence time). Pyroxene growth rates of 8.4×10^{-8} mm/s to 1.68×10^{-8} (Lentz and McSween, 2000) were used (Tables 3.6 and 3.7).

The smallest crystal size bin was neglected in most cases as it contains fewer measured crystals than the second smallest size bin (Figure 3.11). This is an artefact of the measurement technique, as the size-limit resolution of the images results in an underestimation of the smallest measurable microlites (Higgins, 2006). The steepest part of the CSD profiles represents the smallest microlites, and calculated crystallisation times range from 5 to 146 hours for trachyte lavas, 8 to 149 hours for trachyandesite lavas, and 7 to 35 hours for basaltic andesite lava (Table 3.6). This implies that cooling and crystallisation of the groundmass took up to six days. The shallowest part of the CSD profile represents the largest microlites, with estimated crystallisation times of 9 to 209 hours for trachyte lavas (one outlier estimates 687 hours), 12 to 215 hours for trachyandesite lavas (one outlier estimates 521 hours) and 16 to 79 hours for basaltic andesite lava (Table 3.7). This suggests a crystallisation period of up to nine days (though up to 28 days when the outlier results are included).

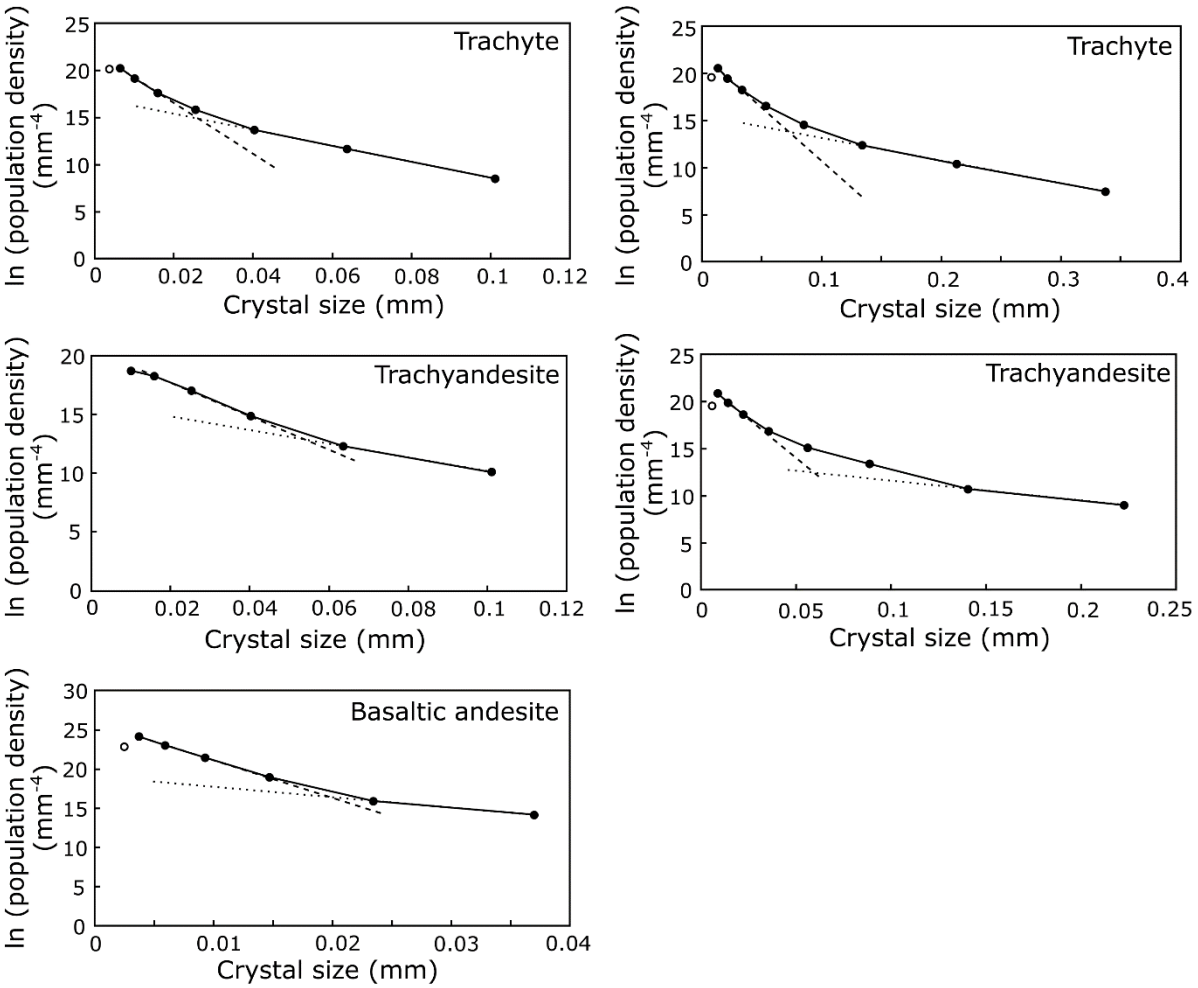

Figure 3.11: Representative CSD profiles of trachyte, trachyandesite and basaltic andesite lavas. Dashed lines represent the slope of the steepest section of the CSD profile, and dotted lines represent the slope of the shallowest section. Empty circles represent discounted bins that underrepresent the smallest groundmass crystals. CSD data are available in Appendix VI.

Table 3.6: Calculated crystallisation times (τ) of the smallest groundmass microlites in trachyte (^{T}), trachyandesite (^{TA}) and basaltic andesite (^{BA}) samples, based on the slope of the CSD profile (*Slope = -1/Gτ*) and assuming pyroxene growth rates (G) of 8.4×10^{-8} (min) and 1.68×10^{-8} (max).

Sample	Slope	Intercept	Gτ	τ_{min} (s)	τ_{min} (hr)	τ_{max} (s)	τ_{max} (hr)
Q3^{T}	-112.95	22.04	0.00885	105399	29	526993	146
Q7^{T}	-296.88	24.54	0.00337	40100	11	200498	56
Q10^{T}	-403.35	24.57	0.00248	29515	8	147574	41
Q12^{T}	-144.08	21.10	0.00694	82626	23	413130	115
Q36^{T}	-268.19	21.91	0.00373	44389	12	221946	62
Q39^{T}	-354.08	25.85	0.00282	33622	9	168108	47
Q40^{T}	-655.59	26.63	0.00153	18159	5	90794	25
Q41^{T}	-455.35	25.52	0.00220	26144	7	130721	36
Q53^{T}	-486.97	24.54	0.00205	24447	7	122233	34
Q66^{T}	-351.54	24.83	0.00284	33865	9	169323	47
Q69^{T}	-575.57	26.86	0.00174	20683	6	103417	29
Q8^{TA}	-110.95	19.88	0.00901	107298	30	536492	149
Q17^{TA}	-166.12	22.31	0.00602	71664	20	358318	100
Q20^{TA}	-438.72	25.71	0.00228	27135	8	135676	38
Q50^{BA}	-477.14	25.88	0.00210	24950	7	124751	35

Table 3.7: Calculated crystallisation times (τ) of the largest groundmass microlites in trachyte (^{T}), trachyandesite (^{TA}) and basaltic andesite (^{BA}) samples, based on the slope of the CSD profile (*Slope = -1/Gτ*) and assuming pyroxene growth rates (G) of 8.4×10^{-8} (min) and 1.68×10^{-8} (max).

Sample	Slope	Intercept	Gτ	τ_{min} (s)	τ_{min} (hr)	τ_{max} (s)	τ_{max} (hr)
Q3^{T}	-24.05	15.62	0.04158	494980	137	2474900	687
Q7^{T}	-260.81	23.58	0.00383	45645	13	228227	63
Q10^{T}	-210.32	21.16	0.00475	56603	16	283015	79
Q12^{T}	-78.98	18.65	0.01266	150729	42	753647	209
Q36^{T}	-85.03	17.11	0.01176	140008	39	700041	194
Q39^{T}	-170.05	22.10	0.00588	70007	19	350037	97
Q40^{T}	-133.70	20.69	0.00748	89041	25	445204	124
Q41^{T}	-230.03	22.60	0.00435	51753	14	258765	72
Q53^{T}	-133.96	19.05	0.00746	88868	25	444340	123
Q66^{T}	-100.27	19.16	0.00997	118727	33	593635	165
Q69^{T}	-358.26	24.97	0.00279	33229	9	166147	46
Q8^{TA}	-76.75	17.67	0.01303	155105	43	775524	215
Q17^{TA}	-31.73	15.84	0.03151	375178	104	1875888	521
Q 20TA	-280.22	23.21	0.00357	42484	12	212418	59
Q50^{BA}	-208.45	21.57	0.00480	57111	16	285554	79

3.3.3. Geothermobarometry

Sixteen pairs of melt inclusions within clinopyroxene hosts were used to estimate temperatures and pressures of crystallisation in trachyte, trachyandesite and basaltic andesite magmas (Figure 3.12; Table 3.8). Temperatures range from 871 – 988 ± 45 °C for trachyte lavas, 947 – 973 ± 45 °C for trachyandesite lavas, and 916 – 1018 ± 45 °C for basaltic andesite lavas (Figure 3.12A). Pressures range from 2.8 – 6.9 ± 2 kbar for trachyte lavas, 4.3 – 5.9 ± 2 kbar for trachyandesite lavas and 3.9 – 6.2 ± 2 kbar for basaltic andesite lavas (Figure 3.12B). Assuming a crustal density of 2800 kg/m^3 (Weidmann et al., 2013), these pressures correspond to depths of ~10 – 25 km for trachyte lavas, ~16 – 22 km for trachyandesite lavas and ~14 – 23 km for basaltic andesite lavas (Table 3.8).

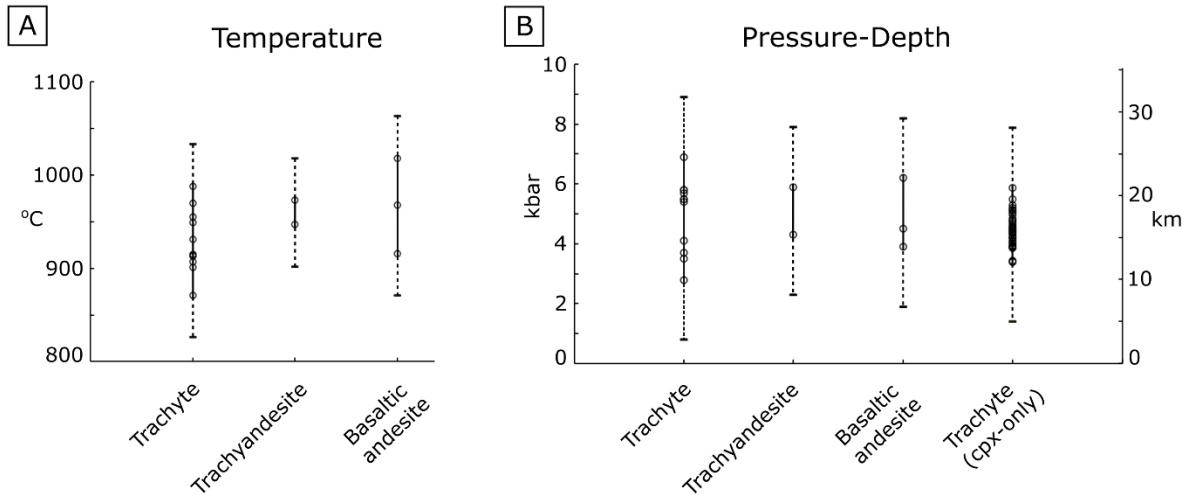

Figure 3.12: Estimated temperatures (A) and pressures (B) from clinopyroxene-melt pairs in trachyte, trachyandesite and basaltic andesite lavas. Depths (B) are calculated assuming a crustal density of 2800 kg/m^3 (Weidmann et al., 2013). The "Trachyte (cpx-only)" datapoints (in B) are pressures and depths estimated using clinopyroxenes in trachyte lavas that did not contain melt inclusions, assuming a temperature of 940 °C (the average temperature calculated from cpx-melt pairs). Solid lines connect estimated values (circles) and dashed lines represent the uncertainties of 2 kbar (Nimis, 1999a) and 45 °C (Putirka, 2008).

Table 3.8: Temperatures and pressures of clinopyroxene crystallisation, calculated iteratively from the geothermometer of Putirka (2008) and the geobarometer of Nimis (1999a,b), using the composition of clinopyroxene phenocrysts and their melt inclusions. The whole-rock composition (Comp.) of samples is listed (T – trachyte; TA – trachyandesite; BA – basaltic andesite), as is the number of the equation used to calculate the temperature (see section 3.2.3.). Depths are calculated from the pressure, assuming a crustal density of 2800 kg/m^3 (Weidmann et al., 2013).

	Comp.	T	T	T	T	T	T
	Sample	Q31_px3	Q36_px3	Q36_px7	Q40_px2	Q40_px3	Q41_px4
	P (kbar)	2.8	3.5	3.7	5.7	5.4	5.5
	T (°C)	970	949	955	914	931	913
	Depth (km)	10.2	12.8	13.5	20.8	19.7	20.0
	Equation	3.2	3.2	3.2	3.1	3.1	3.1
Clinopyroxene Composition	SiO_2	51.371	50.884	50.996	51.713	51.370	51.902
	TiO_2	0.613	0.539	0.622	0.703	0.815	0.559
	Al_2O_3	1.426	1.246	1.451	1.783	2.042	1.339
	Cr_2O_3	0.003	0.000	0.003	0.000	0.000	0.000
	FeO	10.497	10.587	10.197	9.965	10.052	11.739
	MnO	0.480	0.473	0.427	0.446	0.430	0.551
	MgO	14.797	14.740	15.001	14.659	14.597	14.559
	CaO	20.261	20.041	20.120	20.119	19.966	19.067
	Na_2O	0.344	0.343	0.338	0.361	0.380	0.350
	K_2O	0.000	0.000	0.000	0.009	0.003	0.003
Melt inclusion composition	SiO_2	67.910	68.888	67.102	71.654	70.183	70.705
	TiO_2	0.919	1.033	0.944	1.171	0.991	0.783
	Al_2O_3	15.153	14.980	15.487	13.087	16.449	15.159
	FeO	4.108	2.549	4.309	3.044	0.751	1.711
	MnO	0.106	0.106	0.123	0.068	0.056	0.075
	MgO	0.597	0.504	0.439	0.291	0.191	0.269
	CaO	2.186	1.736	1.613	0.713	1.323	1.498
	Na_2O	5.434	5.447	5.137	3.982	5.658	5.407
	K_2O	3.601	3.473	4.809	5.853	4.423	3.703

Table 3.8 continued

	Comp.	T	T	T	T	T
	Sample	Q46_px1	Q46_px1.2	Q61_px1.1	Q61_px1	Q61_px8
	P (kbar)	5.8	5.5	5.8	6.9	4.1
	T (°C)	907	915	901	871	988
	Depth (km)	21.1	20.0	21.1	25.1	14.9
	Equation	3.1	3.1	3.1	3.1	3.1
Clinopyroxene Composition	SiO_2	51.330	51.330	51.963	51.963	50.684
	TiO_2	0.726	0.726	0.536	0.536	1.010
	Al_2O_3	1.706	1.706	1.351	1.351	2.896
	Cr_2O_3	0.000	0.000	0.000	0.000	0.003
	FeO	11.151	11.151	10.501	10.501	11.207
	MnO	0.526	0.526	0.499	0.499	0.516
	MgO	14.214	14.214	14.761	14.761	13.788
	CaO	19.445	19.445	19.779	19.779	19.569
	Na_2O	0.382	0.382	0.349	0.349	0.416
	K_2O	0.003	0.003	0.009	0.009	0.003
Melt Inclusion Composition	SiO_2	71.180	70.561	70.934	69.994	69.615
	TiO_2	0.850	0.848	0.539	0.628	0.410
	Al_2O_3	14.223	14.896	15.261	15.889	15.692
	FeO	2.114	2.024	0.491	0.580	0.732
	MnO	0.063	0.056	0.062	0.053	0.085
	MgO	0.263	0.305	0.129	0.077	0.686
	CaO	1.258	1.278	1.133	1.176	2.070
	Na_2O	5.145	5.460	5.445	5.627	5.829
	K_2O	3.591	3.703	5.239	3.967	3.048

Table 3.8 continued

	Comp.	TA	TA	BA	BA	BA
	Sample	Q17_px2	Q17_px5	Q50_px13	Q50_px14	Q63_px3
	P (kbar)	4.3	5.9	3.9	6.2	4.5
	T (°C)	973	947	1018	968	916
	Depth (km)	15.7	21.5	14.2	22.6	16.4
	Equation	3.1	3.1	3.1	3.1	3.2
Clinopyroxene Composition	SiO_2	50.855	51.024	52.168	52.287	51.653
	TiO_2	0.760	0.667	0.620	0.613	0.766
	Al_2O_3	2.012	2.378	2.024	2.146	0.766
	Cr_2O_3	0.072	0.337	0.000	0.000	0.057
	FeO	10.541	8.417	9.778	8.931	10.267
	MnO	0.283	0.220	0.271	0.245	0.307
	MgO	15.083	15.974	13.566	14.198	14.673
	CaO	19.257	20.396	20.068	20.284	19.755
	Na_2O	0.329	0.292	0.347	0.290	0.349
	K_2O	0.002	0.004	0.000	0.004	0.000
Melt Inclusion Composition	SiO_2	64.915	67.273	64.546	69.177	68.766
	TiO_2	1.367	1.297	1.103	1.198	0.627
	Al_2O_3	15.402	15.973	14.475	17.019	16.331
	FeO	3.597	2.186	5.048	0.869	1.130
	MnO	0.094	0.057	0.136	0.043	0.028
	MgO	1.019	0.629	1.743	0.311	0.228
	CaO	3.081	2.303	3.993	1.873	1.063
	Na_2O	4.844	4.937	4.087	3.789	5.012
	K_2O	3.668	3.529	3.453	6.376	6.423

Unlike the clinopyroxene-liquid geothermometer of Putirka (2008), which depends upon the composition of the melt in equilibrium with the clinopyroxene, the geobarometer of Nimis (1999a) requires only the clinopyroxene composition and the nature of the melt, whether alkaline or subalkaline (subalkaline in the case of Quetrupillán; Figure 3.1), and the temperature to estimate pressures of crystallisation. As the equilibrium melt is not necessary for estimation of pressure, the geobarometer was also used to estimate the pressures of crystallisation for 40 clinopyroxene phenocrysts in trachyte lavas that do not contain melt inclusions (i.e. that do not have a proxy of the equilibrium melt), in order to increase the dataset (Table 3.9; Appendix VII). EMPA analyses were made in the core of clinopyroxene phenocrysts, and a temperature of 940 °C was used for all pressure calculations, as this is the average of temperatures calculated iteratively from clinopyroxene-melt pairs (Table 3.8). This generated pressure estimates of 3.4 – 5.9 kbar, corresponding to depths of ~12 – 21 km (Table 3.9; Appendix VII) within the range of pressures estimated from clinopyroxene-melt pairs.

Table 3.9: Representative pressures of clinopyroxene crystallisation in trachyte magmas, calculated from the geobarometer of Nimis (1999a,b), using the composition of clinopyroxene phenocrysts and the average temperature of 940 °C from Table 3.8. Depths are calculated from the pressure, assuming a density of 2800 kg/m^3 (Weidmann et al., 2013). Full results are in Appendix VII.

Sample	Q3_px16	Q12 _px3	Q34_ px4	Q36_ px7	Q40_px3	Q41_px4	Q61_px8
P (kbar)	3.4	3.9	4.6	4.3	5.1	4.5	5.9
T (°C)	940	940	940	940	940	940	940
Depth (km)	12.4	14.3	16.7	15.7	18.6	16.3	21.4
SiO_2	51.624	51.044	50.949	50.996	51.370	51.902	50.684
TiO_2	0.644	0.588	0.698	0.622	0.815	0.559	1.010
Al_2O_3	1.558	1.576	1.637	1.451	2.042	1.339	2.896
Cr_2O_3	0.000	0.002	0.000	0.003	0.000	0.000	0.003
FeO	10.311	11.319	10.877	10.197	10.052	11.739	11.207
MnO	0.464	0.515	0.502	0.427	0.430	0.551	0.516
MgO	13.653	14.745	14.864	15.001	14.597	14.559	13.788
CaO	20.546	20.224	19.732	20.120	19.966	19.067	19.569
Na_2O	0.333	0.340	0.356	0.338	0.380	0.350	0.416
K_2O	0.000	0.002	0.003	0.000	0.003	0.003	0.003

3.3.4. Structural analysis

Forty-four lineaments (e.g. fissures, dykes and possible fault scarps) were identified and measured from satellite imagery from Google Earth, and their orientations were plotted in rose diagrams (Figure 3.13). When considering the whole area around Quetrupillán, lineaments have a primary preferential orientation of NW-SE and a secondary orientation of NNE-SSW (Figure 3.13B). No lineaments are oriented W-E, and almost none are oriented N-S. Most lineaments are oriented tangentially to the summit, rather than radially to it (Figure 3.13A).

To enable comparison of lineaments across different zones of Quetrupillán, the volcano was divided into quadrants, centred on the southern rim of the summit crater (due to the asymmetric shape of the main edifice this is more central than the middle of the crater; Figure 3.13A). This division results in clear differences in lineament orientation across different flanks of the volcano. In the northeast and southwest quadrants, lineaments are mainly oriented NW-SE, while in the southeast quadrant, lineaments are mostly perpendicular to this orientation, aligned NE-SW (Figure 3.13C). In the northwest quadrant, lineaments mainly follow two preferred orientations at NW-SE and NNE-SSW. Differences in lineament orientation across flanks are also observed when the flanks are divided into northern, southern, eastern and western quadrants (Figure 3.13D). Lineaments in the western and southern quadrants are mainly oriented NW-SE. In the eastern quadrant lineaments have two

perpendicular orientations at NE-SW and NW-SE. Lineaments in the northern quadrant show no preferential orientation.

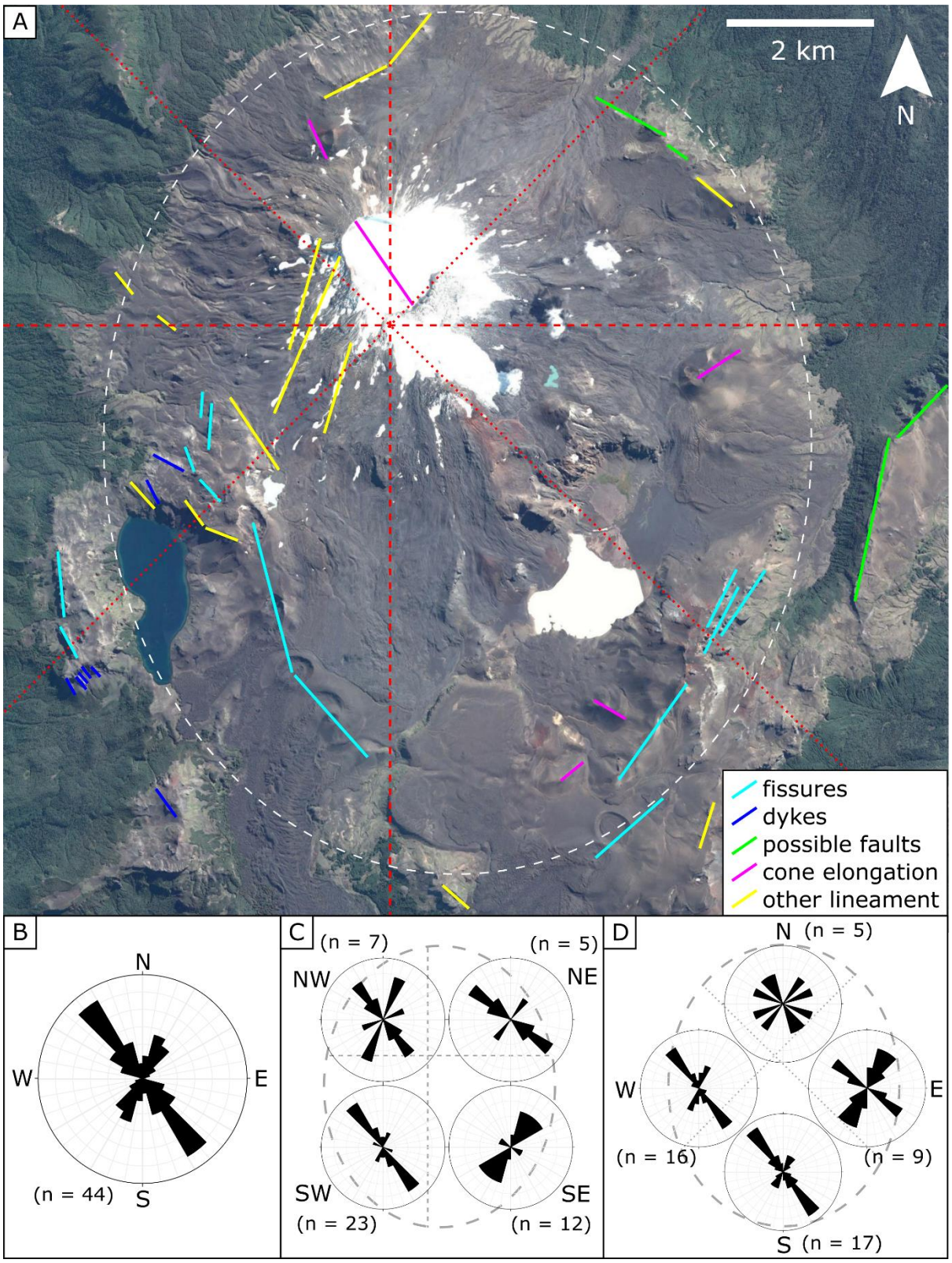

Figure 3.13: A) Identified structural lineaments on the flanks of Quetrupillán (light blue – Holocene and possible Pleistocene fissures; dark blue – dykes; green – possible faults; pink – cone elongation;

yellow – other lineaments defined by topography and geomorphology) with the flanks divided into segments (red dotted lines divide N-E-S-W quadrants; red dashed lines divide NW-NE-SE-SW quadrants; white dashed oval represents the volcano outline used in C and D); B) rose diagram of all 44 lineaments; C) rose diagrams of flanks divided into NW-NE-SE-SW quadrants; D) rose diagrams of flanks divided into N-E-S-W quadrants. The number of lineaments in each quadrant (n) is noted. Google Earth image downloaded 24/02/2020.

3.4. Discussion

3.4.1. Petrology and geochemistry

Clinopyroxene phenocrysts in basaltic andesite and trachyandesite lavas that erupted from the flanks and summit of Quetrupillán contain melt inclusions of trachytic composition (Figure 3.1). The composition of these melt inclusions strongly suggests that these clinopyroxene phenocrysts crystallised in a trachytic melt and therefore it is likely that they are xenocrysts in the basaltic andesite and trachyandesite lavas.

The basaltic andesite and trachyandesite lavas also contain rare phenocrysts of orthopyroxene co-existing alongside the abundant phenocrysts of olivine. As olivine cannot be in equilibrium with a melt that is in equilibrium with orthopyroxene (e.g. Carmichael et al., 1970), the presence of both phases strongly suggests that magma mixing has resulted in hybrid compositions. The high Forsterite content in olivine hosted in the basaltic andesite lava (Fo_{74-84}) indicates that they have crystallised from a relatively primitive basaltic melt. In contrast, the rare orthopyroxene phenocrysts (Enstatite; $Wo_4En_{67-69}Fs_{27-29}$) have crystallised in a more evolved melt. Like the clinopyroxenes with trachytic melt inclusions, the orthopyroxene phenocrysts are also likely to be xenocrysts in the basaltic andesite and trachyandesite lavas. Olivine phenocrysts in the trachyandesite lavas have lower Forsterite contents (Fo_{57-70}), which suggests that olivine continued to crystallise in the hybrid trachyandesite melt after the mixing event.

In contrast to the basaltic andesite and trachyandesite lavas, the mineral assemblage in the Holocene trachytes appears to be in equilibrium with the whole-rock composition. The trachyte lavas contain two pyroxene populations (clino- and orthopyroxene) and plagioclase with compositions of Andesine to Labradorite (An_{36-61}), within a trachytic to rhyolitic glass. This strongly suggests that the phenocryst assemblage in the trachyte lavas crystallised from melts with compositions close to that represented by the whole-rock composition. However, variations in the composition of melt inclusions, groundmass glass and the plagioclase phase suggest variations in the composition of the melts from which the trachyte lavas have been derived. Within individual

samples, melt inclusions in clino- and orthopyroxenes have similar compositions to groundmass glasses, suggesting that trachyte lavas crystallised in equilibrium with the melt in which they are found. This crystallisation is calculated to have occurred over a wide range of pressures, from 2.8 – 6.9 ± 2 kbar, suggesting that crystallisation of clinopyroxene phenocrysts happened across a range of depths (~10 – 25 km) below the volcano (Figure 3.12).

3.4.2. Trace and rare earth elements

Figures 3.10A to 3.10F show different plots with combinations of compatible-incompatible (e.g. Cr/Zr, Cr/Rb) and incompatible-incompatible (e.g. La/Yb, Rb/Zr) ratios to test for a common melt source and provide insights on the fractionation process. The relatively small variation in incompatible-incompatible ratios supports a common single source for these magmas, while the observed decreasing trends in compatible-incompatible ratios support a fractionation model as the main process for magma evolution.

The plot of Rb against Cr (Figure 3.10A) shows a steepening curve from basaltic andesite to trachyandesite to trachyte. This trend, with slight enrichment in Rb compared with the expected evolution of Rb in a fractionation-only model, is compatible with contamination, likely due to longer crustal residence time during fractionation. As Cr-spinel occurs in basaltic andesite lavas, the early fractionation of this phase might have played an important role in Cr behaviour. Additionally, although Cr is incompatible in olivine (crystallising in a basalt or basaltic andesite) it is compatible in pyroxene (Rollinson, 1993), suggesting a process with the initial fractionation of olivine in the basaltic andesite, followed by the fractionation of olivine + clinopyroxene.

The REE profiles of trachyte, trachyandesite and basaltic andesite lavas (Figure 3.7) all have a gentle negative slope (La/Yb ~7 – 9) and display a small negative Eu anomaly (Eu/Eu* = 0.72 – 0.83). A negative Eu anomaly is usually due to the fractionation of plagioclase (Rollinson, 1993), which is the dominant mineral phase in all Quetrupillán lavas. The relatively flat REE profile suggests there has been no fractionation of residual garnet in the melt source, as this would lead to a steeply negative REE profile (Rollinson, 1993; Hickey-Vargas et al., 2016a). The garnet-spinel transition depth is ~80 km (Robinson and Wood, 1998), above which garnet breaks down into spinel. The absence of garnet fractionation in the production of Quetrupillán melts suggests that primary melts were generated at depths of less than 80 km, in the lithospheric mantle, where spinel was the stable Al-bearing phase.

The spider diagrams (Figures 3.9 and 3.9) of Holocene lava samples from Quetrupillán show depletion of Nb in all lavas, typical of arc magmas, which may be associated with the fractionation of titanomagnetite from the onset of the evolution of the melts. Figure 3.9 also shows enrichment of

HFSEs compared to an uncontaminated melt derived from a N-MORB source. In comparison, the HFSEs in lavas erupted from Villarrica (Figure 3.14) do not show this enrichment compared to N-MORB (except in Ce) as values of Rock/N-MORB plot at around 1. The basaltic andesite lava sample at Quetrupillán, which has the lowest values of Rock/N-MORB among the Quetrupillán samples, still has higher HFSE concentrations than the basaltic andesite lavas produced by Villarrica. This enrichment is proposed to have been produced by crustal contamination, and the positive Pb anomaly observed in the full spider diagram (Figure 3.8) may also indicate crustal contamination, as Pb is only present in low concentrations in the mantle.

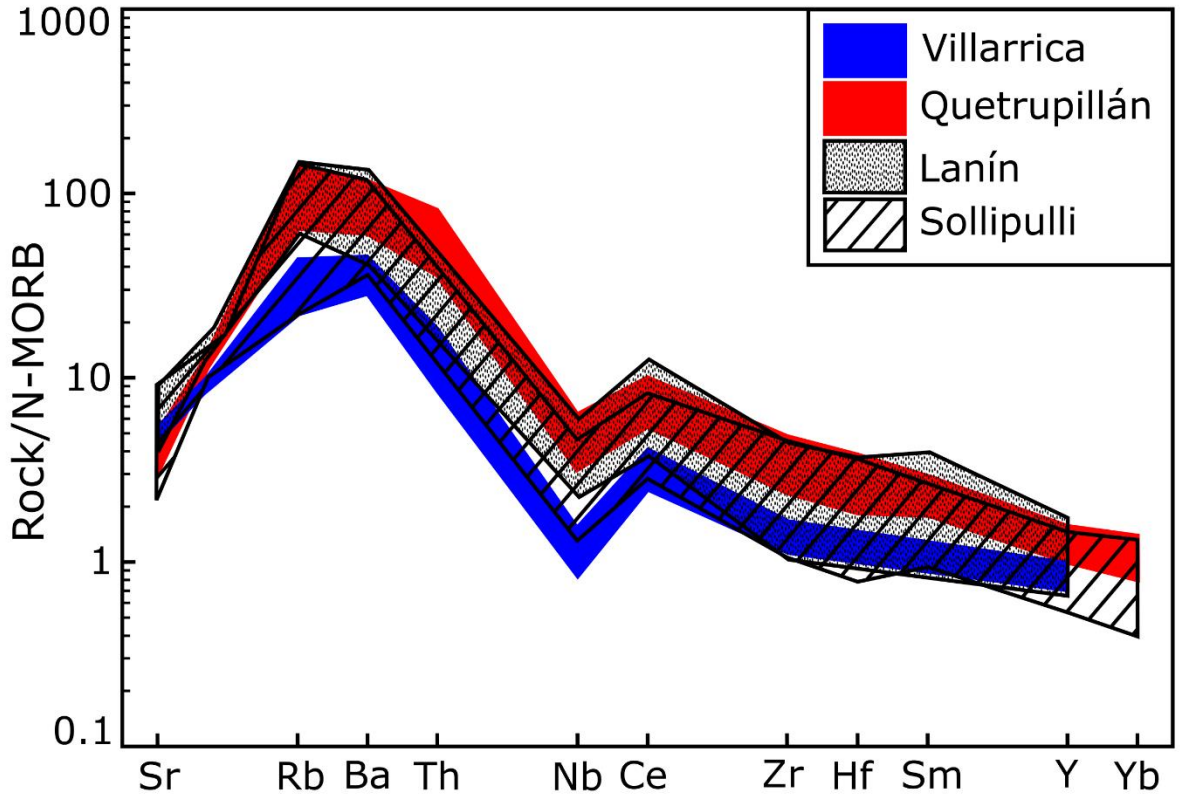

Figure 3.14: Spider diagram (Pearce, 1983), normalised to N-MORB (Sun and McDonough, 1989), with LILEs to the left and HFSEs to the right, of lavas from Quetrupillán (red field; this study, Holocene samples only), Villarrica (blue field), Lanín (dotted field) and Sollipulli (hatched field). See Appendix IV for other authors' data for Villarrica, Lanín and Sollipulli.

3.4.3. Magma generation at Quetrupillán

In the SVZ, basaltic melt is produced in the lithospheric mantle and evolves by fractionation to provide the source magmas that feed the volcanoes in the region (Hildreth and Moorbath, 1988; Hickey-Vargas et al., 2016b). Basalts are significant constituents of erupted products from Villarrica

and Lanín (Figure 3.15; Clavero and Moreno, 2004; Lara et al., 2004), and are minor products erupted by Quetrupillán (Figure 3.1). Basalts have also been erupted by eight minor eruptive centres (MECs) that are located 12 – 35 km north of Quetrupillán, including Huililco, Caburgua, La Barda, San Jorge and Huelemolle (Figure 1.4; Morgado et al., 2015; McGee et al., 2017). The abundance of basalt produced by surrounding volcanoes suggests that the composition of the original parental melt at Quetrupillán is likely to be basaltic.

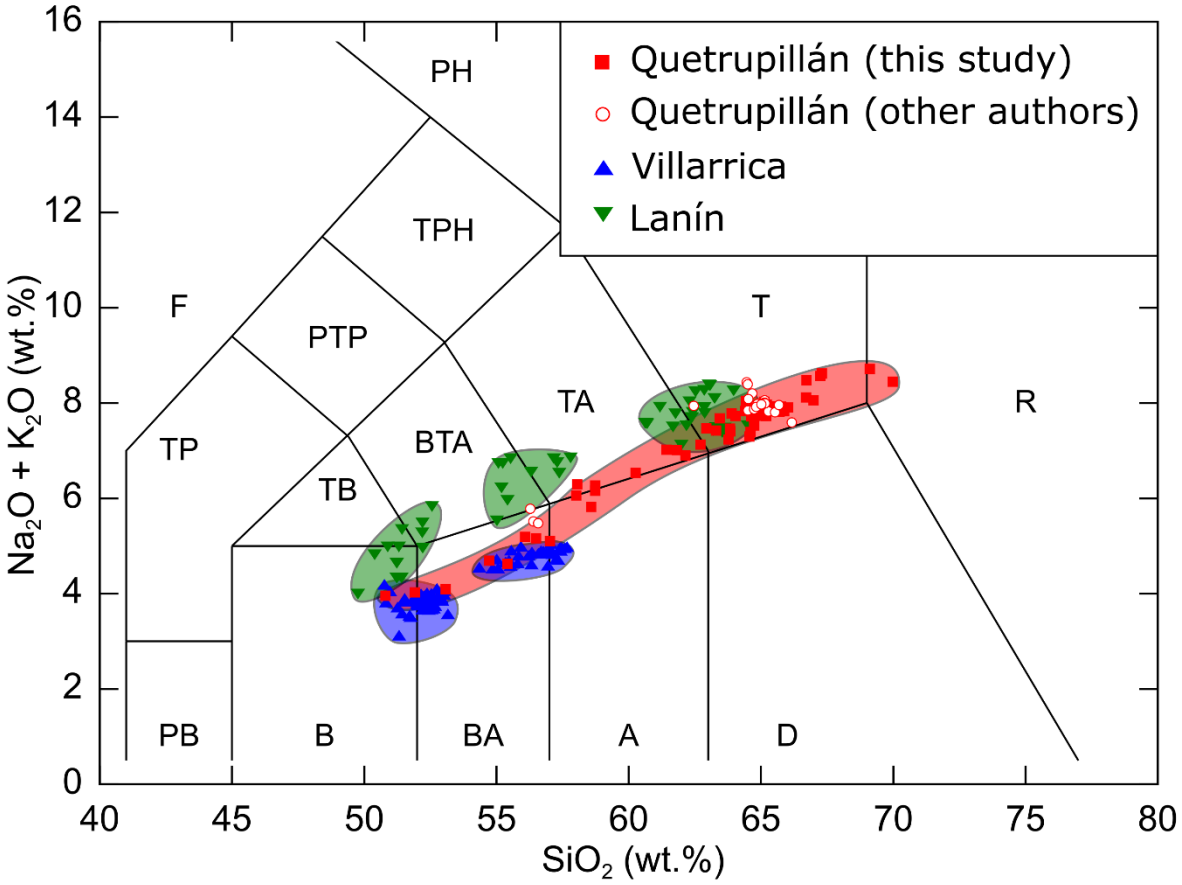

Figure 3.15: TAS plot of whole-rock analyses of samples from Villarrica (blue triangles), Quetrupillán (red squares – this study (Holocene and Pleistocene); red open circles – other authors) and Lanín (green inverted triangles). Data and data sources are listed in Appendix IV.

Previous authors (Pavez, 1997; Brahm et al., 2018) have suggested that the basaltic to basaltic andesite MEC of Huililco, which lies 12 km northeast of Quetrupillán's summit, represents the parental melt of Quetrupillán. As a result, Huililco basalt has been used in modelling calculations to determine the generation of Quetrupillán magmas (Brahm et al., 2018). During fieldwork for this project, a Holocene basaltic lava flow was identified on the flanks of Quetrupillán, assumed to have

erupted from the summit region. This provides a parental melt composition that is definitely present in the magmatic plumbing system below Quetrupillán, rather than a composition erupted from Huililco, a different volcano, 12 km away from Quetrupillán's main edifice.

This basalt from Quetrupillán's summit is porphyritic, with phenocrysts of plagioclase, olivine, clinopyroxene and an oxide phase in a coarsely crystalline groundmass of the same minerals (Appendix II). The total mineral proportions (including phenocrysts and groundmass), converted to weight percent, are 28% olivine, 20% clinopyroxene, 32% plagioclase and 20% oxide, though their compositions are unknown as this sample was only analysed by XRF.

Modelling fractional crystallisation of these mineral proportions (assuming the oxide phase is Magnetite) from the basaltic andesite composition can reproduce the REE concentrations observed in the trachyandesite and trachyte samples from Quetrupillán (Figure 3.16; Appendix VIII).

Both batch and Rayleigh fractionation were modelled, as the two end-members of fractional crystallisation models. During batch fractional crystallisation, crystals remain in equilibrium with the melt as they form and are later removed, while during Rayleigh fractionation each crystal is removed from the melt as it is formed. The true process of crystallisation is likely to be somewhere between these two extremes.

The equation to calculate the concentration of REEs during batch fractionation is

$$C_L/C_0 = 1/(D + F(1 - D)) \quad \text{(Eq. 3.4)}$$

and during Rayleigh fractionation is

$$C_L/C_0 = F^{(D-1)} \quad \text{(Eq. 3.5)}$$

where C_0 is the concentration of trace elements in the initial melt, C_L is the concentration of trace elements in the remaining melt, D is the bulk partition coefficient of the fractionating assemblage, and F is the fraction of melt remaining (Rollinson, 1993; see Appendix VIII for calculations).

During batch fractionation (Figure 3.16A) the trachyandesite REE pattern is reproduced when F = 0.6 and the trachyte REE pattern is reproduced when F = 0.3, while during Rayleigh fractionation (Figure 3.16B) the trachyandesite REE pattern is also reproduced when F = 0.6 and the trachyte REE pattern is reproduced when F = 0.4. In all cases, the concentrations of La and Ce are underestimated by the models. Fractionating the mineral assemblage equivalent to the basalt from the basaltic andesite can reproduce the trachyte and trachyandesite REE patterns, indicating that fractional crystallisation is a key process in producing the evolved magmas at Quetrupillán.

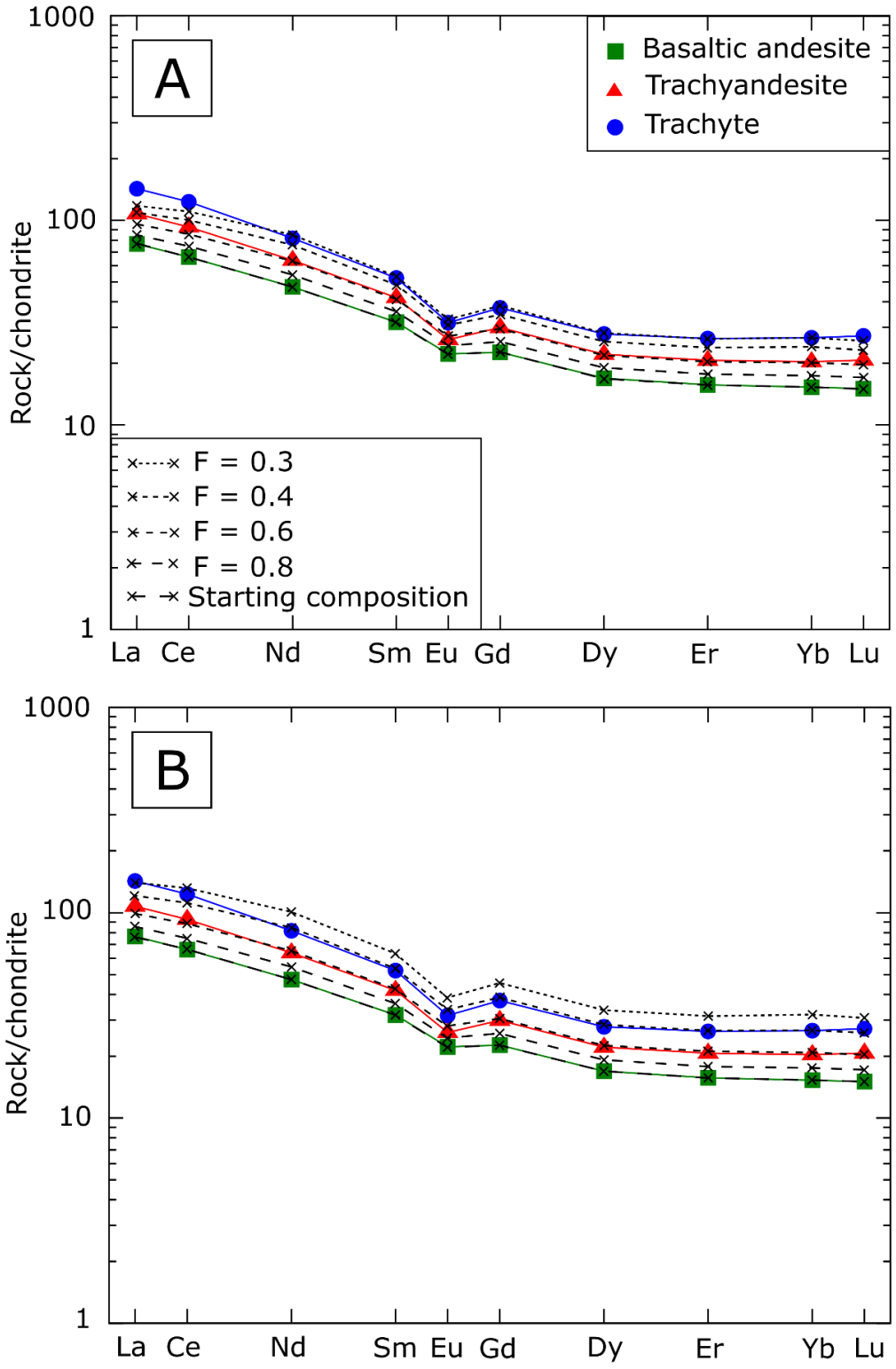

Figure 3.16: REE pattern of modelled compositions (black crosses) generated by A) batch and B) Rayleigh fractionation of 28% olivine, 20% clinopyroxene, 32% plagioclase and 20% magnetite from a basaltic andesite (green squares) lava from Quetrupillán. Different degrees of fractionation (F is the fraction of melt remaining) are denoted by different styles of dashed lines. The REE patterns of trachyte (blue circles) and trachyandesite (red triangles) lavas from Quetrupillán are also included.

Assimilation of crustal rock is also thought to play a role in magma genesis at Quetrupillán, resulting in the high alkali contents of the evolved lavas (Figure 3.1) and the enrichment of Pb (Figure 3.8) and HFSEs (Figure 3.9). Although no isotopic data were collected to test this, trace element concentrations of Quetrupillán lavas were used to model assimilation and fractional crystallisation (AFC; Appendix IX) with the following equation

$$C_L/C_0 = f' + \frac{r}{r-1+D} \times \frac{C_A}{C_0}(1 - f') \quad \text{(Eq. 3.6)}$$

where C_L is the concentration of a trace element in the melt, C_0 is the concentration in the initial melt, C_A is the concentration in the assimilating wall rock, D is the bulk partition coefficient of the element in the fractionating assemblage, r is the ratio between assimilation and fractional crystallisation, and f' is the modified value of F described by

$$f' = F^{-(r-1+D)/(r-1)} \quad \text{(Eq. 3.7)}$$

where F is the fraction of melt remaining after the solid phase removal (Rollinson, 1993; see Appendix IX for calculations).

As with modelling batch and Rayleigh fractionation, the composition of the basaltic andesite was used as the starting composition, and the mineral proportions in the basalt were fractionated from this, while also considering the effects of crustal assimilation. The composition of granite inclusions found within the ~3.6 ka Pucón ignimbrite from Villarrica (Lohmar, 2008) was used to represent the composition of the granitic crust below Quetrupillán.

Using partition coefficients from Rollinson (1993), an initial magma input (C_0) of Quetrupillán basaltic andesite and a basement composition (C_A) of granite inclusions from the Pucón ignimbrite, modelling of assimilation alongside fractional crystallisation was achieved (Figure 3.17; Appendix IX).

When the ratio of assimilation to fractional crystallisation is r = 0.05, the trace element concentrations of trachyandesite lavas are reproduced when F = 0.7 – 0.6 and the trace element concentrations of trachyte lavas are reproduced when F = 0.5 (Figure 3.17). This suggests that the trachyte magmas at Quetrupillán are produced by ~50% fractionation followed by ~5% assimilation of the basement granite.

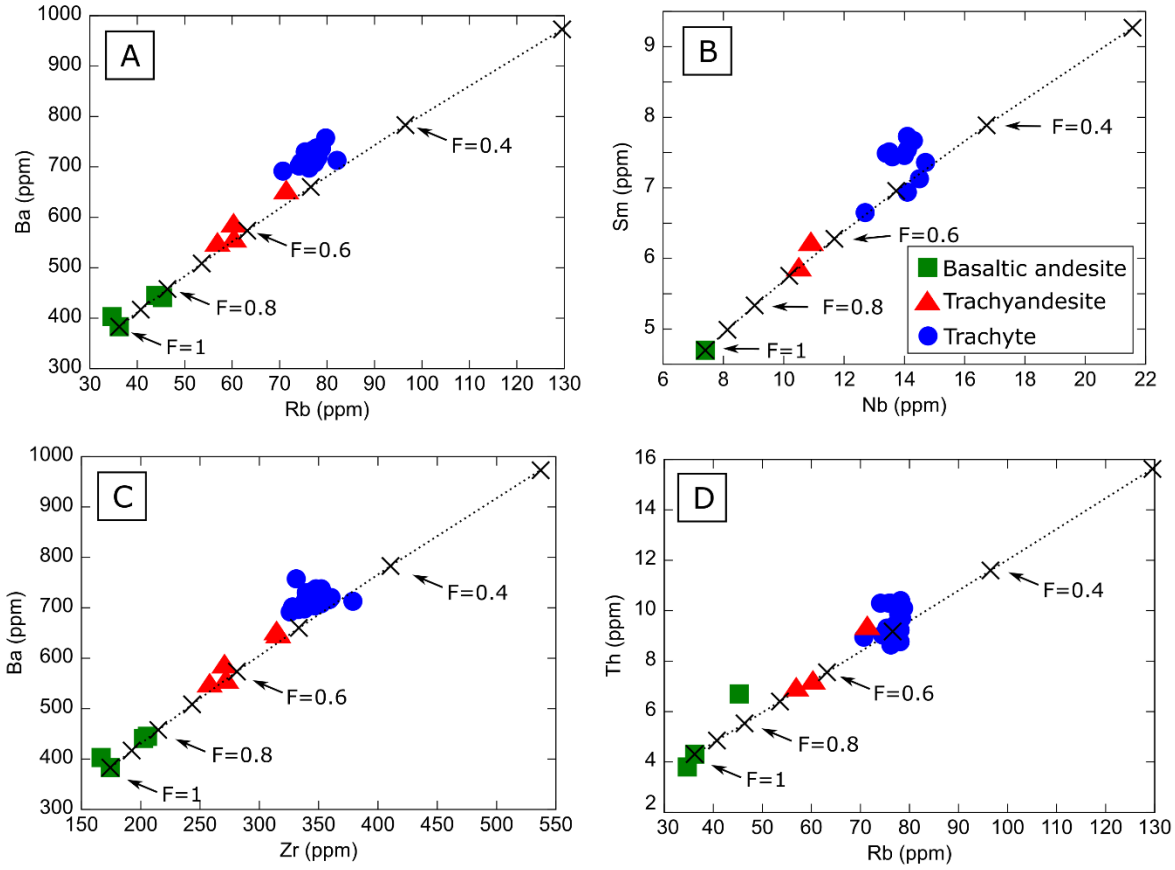

Figure 3.17: Trace element plots of AFC models (black crosses) when r = 0.05 with different values of F labelled. A) Rb vs Ba; B) Nb vs Sm; C) Zr vs Ba; and D) Rb vs Th. Samples are arranged by whole-rock composition: basaltic andesite – green squares, trachyandesite – red triangles, trachyte – blue circles.

Petrological evidence suggests that while fractional crystallisation is the primary process of magma evolution at Quetrupillán, a degree of magma mixing has also occurred to produce the basaltic andesite and trachyandesite hybrid compositions that contain rare orthopyroxene phenocrysts and clinopyroxene phenocrysts with trachytic melt inclusions.

Mixing of the Holocene basalt sample from Quetrupillán (Q67; Table 3.1) with a representative Holocene trachyte sample from Quetrupillán (Q3; Table 3.1) has been modelled using the online tool Olive 2.1.1 (Cortés, 2016). Modelled major element concentrations match the major element concentrations of erupted Holocene basaltic andesite and trachyandesite lava samples (Figure 3.18).

Mixing 77% basalt and 23% trachyte (samples Q67 and Q3 respectively; Table 3.1) produces a basaltic andesite very similar to the basaltic andesite erupted from the flanks of Quetrupillán, and mixing 71% basalt with 29% trachyte produces a composition similar to basaltic andesite erupted

from the summit of Quetrupillán. The two trachyandesite flank lava compositions are reproduced when mixing 56% and 48% basalt with 44% and 52% trachyte, respectively.

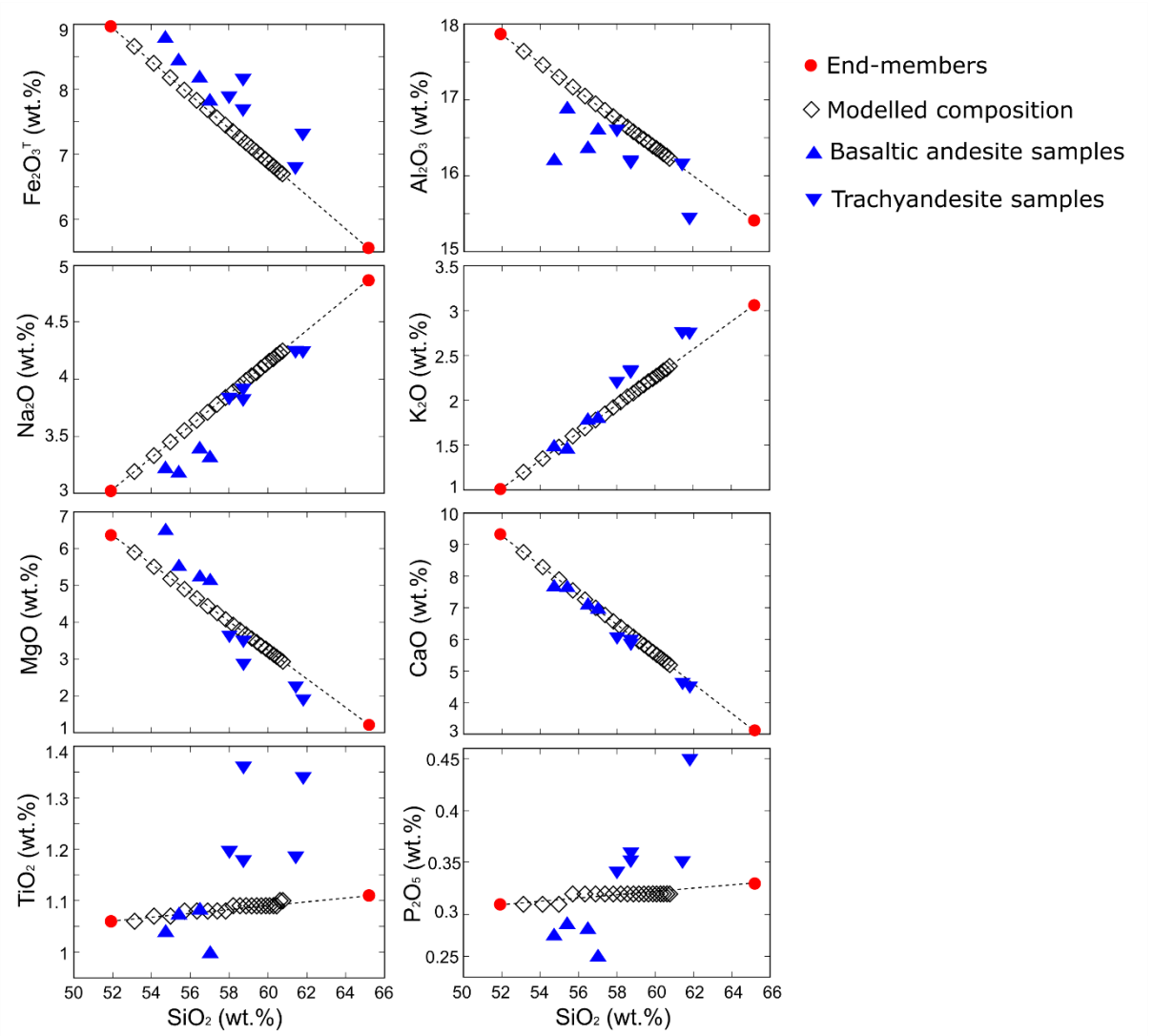

Figure 3.18: Harker diagrams showing modelled major element compositions (black diamonds) when mixing a basalt lava sample from Quetrupillán (Q67) with a trachyte lava sample (Q3; red circles). Basaltic andesite samples (blue triangles) and trachyandesite samples (inverted blue triangles) from Quetrupillán are also plotted.

The modelled compositions generated when mixing Quetrupillán basalt and trachyte lavas are a close fit in the concentration of CaO, Na_2O, K_2O and MgO when compared to the basaltic andesite and trachyandesite lavas erupted from the flanks and summit of Quetrupillán. The modelled compositions underestimate the concentration of $Fe_2O_3^T$ in the basaltic andesite and trachyandesite samples and overestimate the concentration of Al_2O_3. Neither TiO_2 nor P_2O_5 are well modelled, due

to their low concentrations in all Quetrupillán samples. TiO_2 is present in Ilmenite and Titanomagnetite, and P_2O_5 is present in Apatite, all accessory phases in Quetrupillán lavas.

The mixing of basalt and trachyte to produce the basaltic andesite and trachyandesite magmas is also supported by plotting major and trace element concentrations on an abacus diagram (Figure 3.19; following McGarvie et al., 1990). This illustrates whether a potential hybrid composition is likely to have been produced by mixing two selected end-member magmas. Concentrations of major and trace elements are plotted against the proportion of the end-members, and hybrid compositions generated by mixing the two selected end -member magmas will produce straight vertical lines (Figure 3.19; McGarvie et al., 1990).

The basaltic andesite and trachyandesite lavas from flank vents plot as near-vertical lines (Figure 3.19), indicating that they are very likely to be hybrid magmas formed by mixing the selected trachyte and basalt end-member magmas. Mixing of ~80% basalt with ~20% trachyte can produce the basaltic andesite lava and mixing of ~35 – 45% basalt with ~55 – 65% trachyte can produce the trachyandesite lavas, consistent with the proportions found using just major elements (Figure 3.18).

The mixing relationship is not perfect, as the basaltic andesite sample (Q50) is offset from a vertical line for Sr and Nb and the trachyandesite samples (Q8 and Q17) are slightly offset for SiO_2, CaO, Nd, and La. It should be noted that this diagram only produces vertical mixing lines when both end-member magmas and the resultant mixed hybrids occur in the same eruption. This does not occur at Quetrupillán, as magma mixing takes place at depth, and only the hybrid magma is erupted.

Consequently, the precise composition of the two end-member magmas is not known, although the abundance and restricted compositional range of Holocene trachyte lavas provides a good approximation of the likely trachyte end-member. The strong similarity in the range of compositions that have been erupted during both the Pleistocene and Holocene (Figure 3.1) suggests a continuity in the generation of magmas produced beneath Quetrupillán through time.

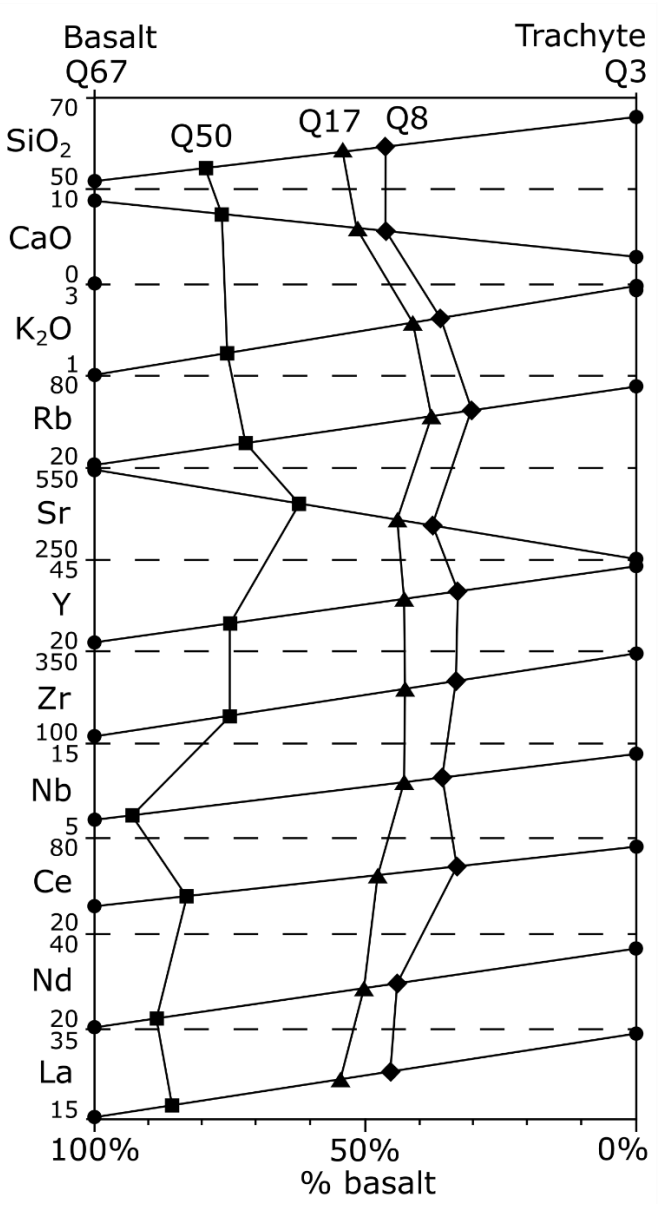

Figure 3.19: Abacus diagram illustrating mixing between a trachyte end-member (Q3) and a basalt end-member (Q67). The x-axis shows the proportion of the basalt end-member magma, and the y-axis gives major element (oxide wt.%) and trace element (ppm) concentrations. The compositions of the basaltic andesite (Q50 – squares) and trachyandesite (Q8 – diamonds; Q17 – triangles) flank vent lavas are plotted.

3.4.4. Textural implications

Sieve-textured plagioclases are uncommon in Quetrupillán's trachyte lavas, but abundant in trachyandesite and basaltic andesite lavas, where many plagioclase phenocrysts have well defined sieve textures (Figures 3.4 and 3.6). The mineral chemistries of plagioclase phenocrysts appear to be in chemical equilibrium with their whole-rock composition (An_{47-84} in the basaltic andesite, An_{51-84} in

the trachyandesite and An_{36-61} in the trachyte), suggesting that the sieve textures are not the result of magma mixing leading to chemical disequilibrium. If sieve texture is not the consequence of chemical disequilibrium, it can be produced by increasing temperature or decreasing pressure (Nelson and Montana, 1992). As a wide range of pressures have been estimated for the magmatic system, a rapid decompression during magma ascent is favoured for producing the observed sieve textures. The occurrence of zoned plagioclases, which are common in all three lava compositions, could be interpreted as crystal growth happening in a heterogeneous melt, in a melt of changing compositions, or as a result of mixing events.

The curved CSD profiles of pyroxene microlites suggest changes in conditions during magma ascent, which may reflect the associated changes in pressure and temperature. The size distributions of the smallest groundmass crystals indicate that cooling and crystallisation of the groundmass took up to six days, however some trachyte lava samples have a fully glassy groundmass containing no microlites. This may represent very rapid quenching of the lava, perhaps on interaction with snow or ice (see Chapter 2, section 2.4.).

Textural evidence that basalt melts have mixed with trachytic melts may be found in samples of pumice from the flanks of Quetrupillán (Q44; Table 3.1; Figure 3.20). The pumice has a whole-rock composition of trachyte (62 wt.% SiO_2, 4.6 wt.% Na_2O, 3.0 wt.% K_2O), however the pale brown pumice clasts contain irregular black bands through them, possibly indicating incomplete mixing between two different melt compositions.

Figure 3.20: Banded pumice with trachytic whole-rock composition, possibly showing evidence of incomplete mixing between two different melt compositions.

3.4.5. Tectonic constraints

It is known that in the SVZ, magmas migrating under crustal extension are significantly less evolved than those migrating under crustal compression, due to the latter having longer crustal residence times (Cembrano and Lara, 2009; Schonwalder-Angel et al., 2018). The western branch of the LOFZ passes immediately to the west of Quetrupillán, and the basaltic monogenetic cones of the Caburgua, La Barda and Huelemolle MECs all lie directly above this fault trace (Morgado et al., 2015; McGee et al., 2017), 23 – 34 km NNW of Quetrupillán (Figure 1.4). The presence of the fault directly below them has influenced their location and composition, providing ascent pathways for basaltic magma to reach the surface with minimum interruption and differentiation. It is speculated that major faults of the LOFZ connect the melting, assimilation, storage and homogenisation (MASH) zone (Hildreth and Moorbath, 1988) with the surface, and it is observed that the most primitive MECs are those located above these NNE-trending LOFZ master faults (Cembrano and Lara, 2009).

In contrast, most lavas erupted from Quetrupillán are much more evolved, suggesting longer crustal residence times due to local crustal compression (Cembrano and Lara, 2009). Tectonically, Quetrupillán has a unique position among the Holocene volcanoes of the SVZ as it is located between the two main branches of the LOFZ (Figure 1.2). According to Cembrano and Lara (2009), Quetrupillán and Sollipulli are the only stratovolcanoes that lie between the two branches of the LOFZ. Sollipulli, which lies 60 km north of Quetrupillán, is therefore analogous to Quetrupillán in that it is a volcanic complex in the same tectonic position, sitting between the branches of the LOFZ. However, no study that examines the tectonic and magmatic interplay at Sollipulli has been published to date, therefore no comparison between the systems is possible to determine whether similar structural controls influence their magmatism. The location of Quetrupillán within the LOFZ has resulted in tectonic stresses that appear to have influenced magmatism at the volcano.

Observed lineaments around the flanks of Quetrupillán (e.g. fissures, dykes and possible fault scarps) are predominantly oriented tangentially to the main edifice, with very few oriented radially to it (Figure 3.13). The load imposed by a volcanic edifice on the crust will cause stress perturbations that are expected to result in dykes and fissures with trajectories that are radial to the edifice summit, while beyond the influence of the volcanic edifice any lineaments are expected to be controlled by the regional stress regime (Roman and Jaupart, 2014). At Volcán Llaima, 90 km north of Quetrupillán, the influence of the tectonic regime is superimposed on the influence of the volcanic edifice, resulting in two sets of dykes, one oriented radially to the summit and one controlled by the stress regime generated by the relative location of the LOFZ (Schonwalder-Angel et al., 2018). At Quetrupillán, the absence of radially oriented lineaments strongly suggests that the regional stress

regime generated by the LOFZ overwhelms the local stress associated with the load of the volcanic edifice.

The secondary set of lineaments at Quetrupillán corresponds to the orientation of the LOFZ, while the primary set of lineaments seems to be a conjugate set to them (Figure 3.13). Unlike at Llaima (Schonwalder-Angel et al., 2018), there is no relation between the composition of products from vents on the flanks of Quetrupillán and the location of the vents (Figure 2.2), suggesting that compositional changes are a consequence of a more localised process.

The proposed model for the tectonic setting at Quetrupillán (Figure 3.21) is based on Quetrupillán's location in relation to the geometry of the LOFZ in the area, with the assumptions that all the structures are related and that they are associated with the LOFZ. This is dependent upon the assumptions and interpretations of other authors about the location and relative motion of the LOFZ (e.g. Rosenau et al., 2006; Moreno and Lara, 2008; Cembrano and Lara, 2009; Hernandez-Moreno et al., 2014). Dextral strike-slip movement along the branches of the LOFZ would result in a central block undergoing rotation, leading to zones of compression and tension within the block. It should be noted that the eastern branch of the LOFZ along the Trancura Valley appears to no longer be active. The dextral oblique convergence between the Nazca and South American Plates has resulted in a regional maximum compression axis (σ_1) that is subhorizontal and NE-trending in the SVZ, while the minimum compression axis (σ_3) is subhorizontal and NW-trending (Cembrano and Lara, 2009).

Assuming that Quetrupillán is located in the rotating block's southwest compressive quadrant, then the theoretical N-S strike-slip fault in the model matches the ~N-S aligned scarp that runs along the Huililco Valley. If so, Volcán Huililco (a basaltic scoria cone) would be located in the southeast extensional quadrant, on the other side of the Huililco Valley fault scarp. While the local compressional stress regime at Quetrupillán has hindered magma ascent, the location of Volcán Huililco in an extensional regime may account for its less evolved composition of basalt to basaltic andesite (Valdivia Muñoz, 2016). The theoretical W-E strike-slip fault in this model could be matched with the strike-slip fault running ~NW-SE along the Río Pucón Valley, north of Quetrupillán, defined by Rosenau et al. (2006; Figure 1.3).

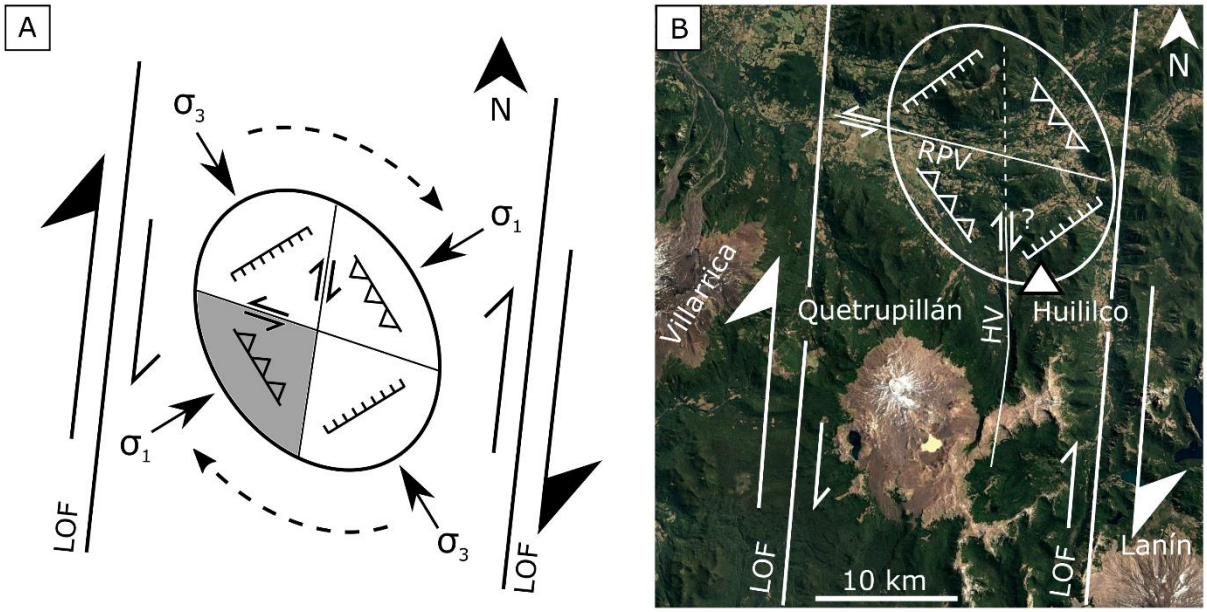

Figure 3.21: A) The proposed tectonic model for Quetrupillán, based on the ellipse of deformation from Rosenau et al. (2006). The grey region shows the proposed location of Quetrupillán, on a rotating block between the two NNE-trending dextral strike-slip Liquiñe-Ofqui faults (LOF). B) The proposed tectonic model superimposed over satellite imagery of the Villarrica-Lanín volcanic chain. A fault is suspected along the Huililco Valley (HV) due to the N-trending scarp to the east of Quetrupillán. Consistent with this model, a sinstral strike-slip fault is inferred in the Río Pucón Valley (RPV) to the north of Quetrupillán, and is outlined by Rosenau et al. (2006; Figure 1.3). Volcán Huililco is denoted by a triangle. Satellite image from Google Earth (downloaded 26/05/2020).

The ability of magma to ascend through the crust is controlled by the local stress regime. At Quetrupillán, this regime is imposed by the tectonic influence of the LOFZ, producing fault scarps aligned with and conjugate to the orientation of the LOFZ (Figure 3.13). Additionally, the tectonic influence results in compressional stresses that cause magma to stall and evolve within the crust, highlighting the importance of fractional crystallisation processes. The orientations of subsurface dykes that transport this magma to the surface are also controlled by this stress regime, resulting in fissures and exposed dykes that are tangential to the edifice summit.

Chapter 4: Volcanic hazards from the Quetrupillán Volcanic Complex

A landscape of lavas

In Section 4.6, the VOLCANS model used to identify volcanoes that are analogous to Quetrupillán was performed by Dr Pablo Tierz at the British Geological Survey, in consultation with myself.

4.1. Introduction

In this chapter I estimate the probability of a future eruption occurring from Quetrupillán and provide a qualitative discussion of the potential hazards that may be produced by such an eruption, and of how these hazards may impact the communities around Quetrupillán. I also investigate analogue volcanoes to Quetrupillán and consider the potential hazards at these volcanoes that may be relevant to Quetrupillán.

Volcanoes pose hazards to surrounding populations, which can impact lives and livelihoods. Since 1783 AD, over 220 000 people have died as a result of volcanic activity (Tanguy et al., 1998). Over 70% of these fatalities were the consequence of just five eruptions: the 1783 Laki eruption in Iceland led to ~10 000 deaths from famine; pyroclastic flows and ashfall during the 1815 Tambora eruption in Indonesia killed ~11 000, with an additional ~49 000 deaths from famine in the aftermath of the eruption; ~4600 were killed by pyroclastic flows during the 1883 eruption of Krakatau in Indonesia, and a further ~32 000 were killed by the resultant tsunami; ~29 000 were killed by pyroclastic flows in the 1902 eruption of Mt Pelée in Martinique; and ~23 000 were killed by lahars during the 1985 eruption of Nevado del Ruiz, Colombia (Tanguy et al., 1998).

4.2. Volcanic hazards

A wide range of hazards may be produced during volcanic eruptions, depending primarily on the style of eruption that occurs (Cassidy et al., 2018). Effusive eruptions produce lava flows (Andronico and Lodato, 2005; Del Negro et al., 2016) and may release copious quantities of gas and particulate matter resulting in reduced air quality (Whitty et al., 2020). Explosive eruptions can generate ballistics (Fitzgerald et al., 2017; Taddeucci et al., 2017), pyroclastic density currents (Jenkins et al., 2013; Castruccio et al., 2016) and tephra (Romero et al., 2016). Lahars may be initiated during a volcanic eruption if erupted products mix with snow, ice or water (Thouret et al., 2007; Castruccio et al., 2010), and may continue to happen for years after an eruption if unconsolidated volcanic sediments are mixed with rain (Jones et al., 2015; Cando-Jácome and Martínez-Graña, 2019). Volcanic hazards can also persist during times of quiescence, particularly the emission of toxic gases (Carapezza et al., 2012; Arellano et al., 2017).

The different hazards will impact different regions surrounding the volcano. While ballistics generally have a range of <5 km (Fitzgerald et al., 2017) and so only affect the immediate vicinity, lahars can have runout distances of >90 km (Naranjo et al., 1986) reaching communities far from the volcano, and gas and particulate matter that enters the upper atmosphere may be transported around the globe, leading to hemispheric or global changes in climate (Robock, 2000).

4.2.1. Lava flows

Fatalities caused by lava flows are rare as the speed at which lava moves is normally sufficiently slow to allow people to avoid them (Tanguy et al., 1998; Brown et al., 2017). One of the few examples of direct fatalities from lava flows occurred during the 2002 eruption of Nyiragongo, Democratic Republic of Congo, during which lavas reached speeds of over 20 km/hr, killing at least 200 people (Favalli et al., 2009; Arellano et al., 2017). Despite their usual slower speeds, lava flows still represent a significant hazard as they will bury anything in their path, leading to the destruction of property, agriculture and infrastructure (Macdonald, 1962; Branca et al., 2017).

Compositional variations among magmas (resulting in viscosity variations) produce lava flows with velocities that differ by orders of magnitude. Low viscosity basaltic lavas can travel at speeds in the order of metres per second (e.g. 1.55 m/s at Mauna Loa and 8.25 m/s at Kīlauea, Hawai'i; Lev et al., 2012), while high viscosity silicic lava flows will advance much more slowly, with velocities of 1 – 24 m/day (Latutrie et al., 2017). Examples include dacite lava flows at Santiaguito, Guatemala, advancing at 2 – 13 m/day (Harris et al., 2004) and rhyolite lava flows at Cordon Caulle, Chile, advancing at 1.5 – 3 m/day (Tuffen et al., 2013). During the 1988 – 1990 eruption of Lonquimay, Chile, the andesite lava flow advanced with an initial velocity of 0.04 m/s. This rate of advance decreased exponentially with distance from the source, and after almost nine months the flow had reached 9.7 km from the vent and was advancing at 5.6 m/day (Naranjo et al., 1992).

4.2.2. Pyroclastic density currents

Pyroclastic density currents (PDCs) are the deadliest hazard from volcanoes, accounting for over 50% of volcano-related fatalities in the 20th century (Tanguy et al., 1998). The high velocities of PDCs (e.g. 150 m/s at Mt St Helens, USA, 1980 (Esposti Ongaro et al., 2011); 100 m/s at Merapi, Indonesia, 2010 (Komorowski et al., 2013); 90 m/s at Soufrière Hills, Montserrat, 1997 (Sparks et al., 2002)) means that escape is unusually not possible. And if caught by a PDC, survival is unlikely. The intense heat (e.g. >350 °C at Mt St Helens, 1980 (Moore and Sisson, 1981); 200 – 300 °C at Merapi, 2010

(Komorowski et al., 2013); >300 °C at Soufrière Hills, 1997 (Sparks et al., 2002)) and dynamic pressure within a PDC cause thermal injury, asphyxiation and impact trauma (Baxter, 1990; Brown et al., 2017).

PDCs cover a spectrum of volcanically-derived gravity-driven currents consisting of pyroclasts and gas (Druitt, 1998; Dufek et al., 2015), from turbulent currents in which a low density of pyroclasts is carried in suspension, to concentrated granular avalanches (Druitt, 1998). They may be initiated by a variety of mechanisms, including collapse of a lava dome, collapse of an eruption column or directed blasts (e.g. Sparks et al., 1978; Esposti Ongaro et al., 2011; Nakada et al., 2019), and as such may be produced at a range of volcanoes during a variety of different eruption styles, from small-scale dome collapse events to very large caldera-forming eruptions (Dufek et al., 2015).

4.2.3. Tephra fall

Tephra can be transported for hundreds of kilometres by wind, making it the most widespread and disruptive volcanic hazard (Wilson et al., 2012; Blong et al., 2017). Most fatalities from tephra fall occur when a sufficient thickness of tephra accumulates to cause roof collapse (Spence et al., 2005). Even small eruptions that pose no threat to human life can cause significant disruption, as just a small thickness of tephra can have a significant impact (Wilson et al., 2012; Blong et al., 2017). Tephra can damage vegetation (Ayris and Delmelle, 2012) causing potentially serious consequences for agriculture and livestock (Craig et al., 2016), impact electricity generation and supply resulting in power outages which may affect other critical systems (Bebbington et al., 2008), interrupt transport networks (Magill et al., 2013), disrupt water supplies and wastewater treatment plants (Wilson et al., 2012), and pose a hazard for aviation (Alexander, 2013). Clean up costs following tephra deposition can total millions of pounds (Hayes et al., 2015). Tephra also poses hazards to human health, including respiratory problems and eye irritation (Horwell and Baxter, 2006).

4.2.4. Lahars

Primary lahars are most commonly generated when pyroclastic debris and hot gases flow or are blasted across the surface of snow or ice on a volcano, leading to thermal and mechanical erosion of the snow/ice and resulting in volcanic material becoming entrained in meltwater (Major and Newhall, 1989). The deposition of tephra on snow/ice will alter the ablation rate (Kirkbride and Dugmore, 2003; Nield et al., 2013) but generally will not result in sufficient meltwater to produce primary lahars (Major and Newhall, 1989). Secondary lahars occur when eruption deposits are

remobilised by rain water, and may continue to be initiated for years following an eruption (Jones et al., 2015; Cando-Jácome and Martínez-Graña, 2019).

Even minor eruptions at snow/ice-capped volcanoes have the potential to generate devastating lahars. The 1985 eruption of Nevado del Ruiz was not large (VEI 2; $10 – 20 \times 10^6$ m^3 pyroclastics produced; Thouret et al., 2007), but the lahars it triggered had a total deposit volume of $30 – 60 \times 10^6$ m^3 (Naranjo et al., 1986) and travelled at ~12 m/s (Lowe et al., 1986) for over 90 km from the volcano's summit (Naranjo et al., 1986), engulfing the town of Armero and killing ~23 000 people (Tanguy et al., 1998).

4.3. Eruption probability at Quetrupillán

Statistical analysis of eruption time series has been applied to many volcanoes around the world (Wickman, 1966; Klein, 1982; Ho, 1990; Bebbington, 2008; Dzierma and Wehrmann, 2010a), and the assumption that a volcano's past activity reflects its expected future behaviour allows the frequency of past eruptions to be used to assess the probability of future eruptions (Mendoza-Rosas and De la Cruz-Reyna, 2008; Dzierma and Wehrmann, 2010b).

As a first order approximation, the eruption time series of a volcano is usually modelled by a Poisson process (Ho, 1990; Mendoza-Rosas and De la Cruz-Reyna, 2008), with the assumption that eruptions occur as discrete random events (Meyer, 1970). The eruption time series may be modelled as a Poisson process if the occurrence of eruptions is:

1. rare (the probability of more than one eruption occurring in a small increment of time is negligible);
2. independent of other eruptions (the probability of an eruption in any given time interval is independent of any eruptions that happened before the start of that time interval); and
3. stationary with time (eruptions occur with constant probability and so there is no change in eruption frequency with time (Dzierma and Wehrmann, 2010a, 2010b; Wehrmann and Dzierma, 2011).

The repose time between eruptions is used to test for the independence and stationarity of the eruption series. Independence of eruptions is tested from the correlation between successive repose times (Mendoza-Rosas and De la Cruz-Reyna, 2008; Dzierma and Wehrmann, 2010a, 2010b) and stationarity is tested from a moving average of repose times (Mendoza-Rosas and De la Cruz-Reyna, 2008; Wehrmann and Dzierma, 2011). If the eruption frequency is constant, a linear increase in the

cumulative number of eruptions with time is expected (Dzierma and Wehrmann, 2010a; Wehrmann and Dzierma, 2011).

An assumption of independence for volcanic eruptions implies that when an eruption occurs, it will not influence the likelihood of another eruption occurring. Independence of eruptions is commonly assumed in petrology, with each eruption considered to result from a separate magma recharge event. However, if the occurrence of an eruption should "prime" the volcanic system and facilitate the occurrence of a successive eruption, it will result in an increased likelihood of a future eruption. And if an eruption is sufficiently large to empty the volcanic system, requiring significant re-accumulation of magma before a successive eruption can occur, it will result in a decreased likelihood of a future eruption.

The number of Holocene eruptions from Quetrupillán is unknown. It is proposed, based on stratigraphic and field evidence of flank vents, that ten eruptions have occurred from vents on the flanks of the volcano (see Chapter 2, section 2.7.), but the number of eruptions from the summit of Quetrupillán is not constrained. If the occurrence of eruptions is assumed to be stationary with time, then the eruption frequency of flank eruptions at Quetrupillán during the Holocene can be calculated as

$$\lambda = \left(\frac{events}{time}\right) = \frac{10\ eruptions}{11\,650\ yrs} = 8.6 \times 10^{-4}\ eruptions\ per\ year \qquad \text{(Eq. 4.1)}$$

However, there are no dates for these ten Holocene flank eruptions and as such, the repose times between eruptions cannot be determined. It is therefore not possible to statistically test whether flank eruptions at Quetrupillán are independent of each other and stationary with respect to time, which prevents testing of whether eruptions at Quetrupillán follow Poisson behaviour.

Studies of other volcanoes in the SVZ with dated eruption records show that many of them have eruptive activity that is consistent with Poisson behaviour (Dzierma and Wehrmann, 2010a). Twelve SVZ volcanoes have eruption records that were considered suitable for statistical analysis (at least seven VEI ≥ 2 eruptions in historical times), and of these, ten volcanoes had eruptive activity that could be approximated by a Poisson distribution with an assumption of independence and stationarity (Dzierma and Wehrmann, 2010a). For the purpose of this work, it is therefore assumed that past volcanic activity at Quetrupillán also follows Poisson behaviour, enabling the probability of future eruptions to be calculated using a Poisson process.

For a Poisson process, the probability of k events in an interval of time t is

$$P(X = k) = e^{-\lambda t}(\lambda t)^k/k! \qquad \text{(Eq. 4.2)}$$

where k is the number of eruptions, λ is the frequency of eruptions $\left(\frac{events}{time}\right)$, and t is the specified interval of time, in years (Meyer, 1970).

The probability of an eruption occurring $(k = 1)$ within the next year $(\mathrm{t} = 1)$ is therefore

$$P(X = 1) = e^{-8.6\times10^{-4}\times1}(8.6 \times 10^{-4} \times 1)^1/1! = 0.0008576 \quad \text{(Eq. 4.3)}$$

This means that there is a less than 0.1% probability of an eruption occurring from Quetrupillán within the next year. The probability of an eruption occurring from Quetrupillán within different future time intervals can also be calculated and is shown in Table 4.1. There is a 4.1% probability of an eruption in the next 50 years, a 7.9% probability of an eruption in the next 100 years, and a 36.4% probability of an eruption in the next 1000 years (Table 4.1).

Table 4.1: The probability of an eruption $(k = 1)$ occurring at Quetrupillán within different specified intervals of time (t), in years, assuming a Poisson process.

t	$P(X = 1)$
1	0.000858
50	0.041115
100	0.078776
1000	0.363822
2000	0.308414
3000	0.196083

These probabilities of future eruptions occurring at Quetrupillán are minimum estimates, as they have been calculated based only on the frequency of Holocene flank eruptions, and do not include the unknown frequency of Holocene eruptions from the summit of the stratocone. When considering both flank and summit eruptions, the eruption frequency will increase, as in total more than ten Holocene eruptions have occurred from Quetrupillán. This will therefore increase the calculated probabilities of a future eruption.

Three large explosive eruptions are interpreted to have occurred from Quetrupillán during the Holocene, based on the presence of three tephra horizons preserved in the Trancura Valley (see Chapter 2, section 2.9.). It is not known whether these tephra horizons were produced during explosive eruptions from the flanks of Quetrupillán, in which case they are included within the ten recognised Holocene eruptions, or whether they were produced during explosive eruptions from the summit, in which case their occurrence is not factored into the estimated eruption probability.

The Poisson process can also be applied to determine the time until the next eruption, i.e. the time interval in which no eruption will occur ($k = 0$). If $k = 0$, then the Poisson equation can be reduced to

$$P(X = 0) = e^{-\lambda t} \quad \text{(Eq. 4.4)}$$

and rearranged to

$$t = \ln(P) / -\lambda\,. \quad \text{(Eq. 4.5)}$$

The prediction of no eruption, with 95% confidence ($P = 0.95$), is therefore valid for the next 60 years, as

$$\ln(0.95) / -8.6 \times 10^{-4} = 60. \quad \text{(Eq. 4.6)}$$

4.4. Population around Quetrupillán

Quetrupillán is located in a reasonably sparsely populated area (Instituto Nacional de Estatísticas, 2017). The nearest major town is Pucón, 32 km northwest of the volcano (Figure 4.1). Pucón has a resident population of ~25 000, but this increases by an order of magnitude at the height of the summer season due to the influx of tourists who flock to the town (Johnson et al., 2018). Located at the foot of the persistently active Villarrica, inhabitants of Pucón are familiar with the presence of volcanic activity and eruptions from Villarrica sometimes necessitate evacuations of the surrounding population. Most recently, ~3700 residents of the Pucón region were evacuated during the 2015 eruption (Espinoza et al., 2019).

The town of Curarrehue (population ~2300; Instituto Nacional de Estatísticas, 2017) is situated 19 km northeast of Quetrupillán, and Coñaripe (population ~1400) is located 26 km WSW (Figure 4.1). There are numerous villages in the valleys surrounding the volcano, such as Huililco, Catripulli and Carén, as well as remote, isolated farms and small holdings. Rancho de Caballos (in Palguín Alto) and Reserva Huililco, in the Palguín and Huililco Valleys respectively, are both situated 8.4 km from the summit of Quetrupillán, and Paraiso Escondido is only 6.3 km WNW of the summit. These remote settlements have limited phone signal and no internet connection, which may prevent effective communication during an eruption.

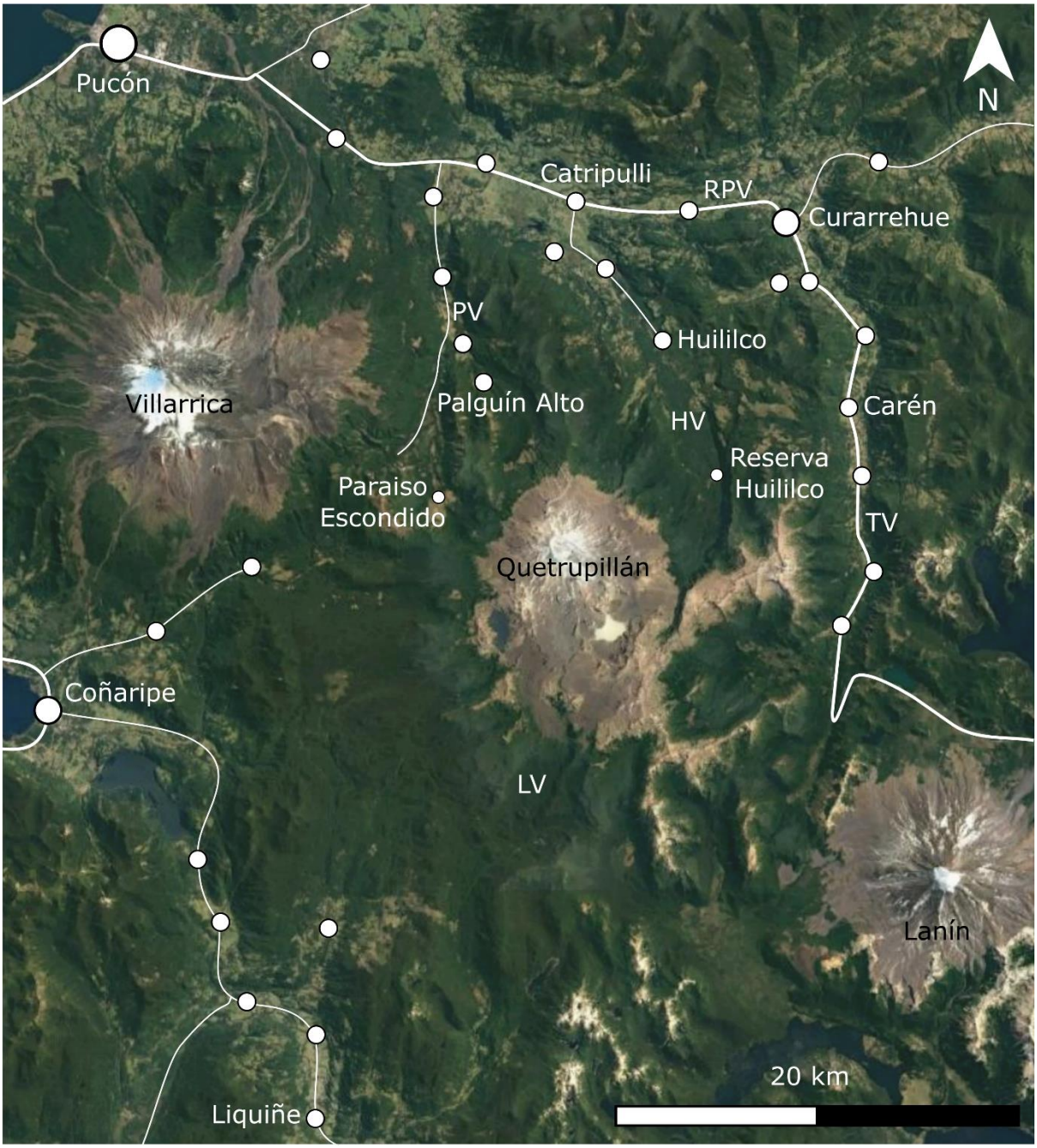

Figure 4.1: Centres of population (white circles) and principal roads (white lines) around Quetrupillán. The towns of Pucón, Curarrehue and Coñaripe are labelled, as are some of the villages and isolated settlements located in the valleys surrounding the volcano (PV – Palguín Valley; HV – Huililco Valley; TV – Trancura Valley; RPV – Río Pucón Valley; LV – Llizán Valley). Satellite image from Google Earth (downloaded 03/02/2020).

4.5. Potential volcanic hazards from Quetrupillán

Combining knowledge of past eruptions (Chapter 2) with knowledge of the volcano's magmatism (Chapter 3) can improve understanding of potential hazards that may occur during future eruptions at Quetrupillán. The prevalence of trachytic eruptions during the Holocene and the trachytic nature of magmatism at Quetrupillán suggests that any future eruption is also likely to also produce trachytic products. Less evolved compositions may also be erupted, as occurred to produce the basalt, basaltic andesite and trachyandesite lavas erupted from the summit and flanks of Quetrupillán during the Holocene, which will reflect the degree of fractionation of the magma and the amount of mixing with the resident trachyte melt.

Erosion of the stratocone means that the number of Holocene eruptions from the main edifice compared to flank vents is unknown, so it cannot be determined whether a future eruption is most likely from the summit or flanks. However, the most recent eruptions appear to be from vents on the southern flanks, and therefore the likelihood is that a future eruption will also take place from the flanks, rather than from the summit.

The monogenetic nature of vents on the flanks of Quetrupillán implies that future flank eruptions are most likely to take place from newly created vents, rather than with renewed activity at existing vents. The concentration of Holocene vents on the southern flank suggests that any formation of new vents will also most likely occur on the southern flank of the volcano. Of the sixteen Holocene flank vents, thirteen have produced lava flows, suggesting a high likelihood of lava effusion during future flank eruptions. The presence of three tuff rings (Figure 2.12A) on the southern flank indicates that should sufficient groundwater be present during future eruptions, they will have the potential to occur as explosive phreatomagmatic events.

4.5.1. Effusive eruptions from Quetrupillán

Six of the ten lava flows from vents on the southern flanks have small volumes of less than 5×10^6 m^3 (Table 2.1), with lengths of less than 1.5 km. These small volume lava flows are limited to the exposed flanks of the volcano (Figure 2.2). Larger volume Holocene lava flows (effused from the southern and eastern flanks, and from the stratocone) have travelled a maximum of ~15 km from their source (Figure 4.2). These lavas flowed off the flanks of the volcano when they entered the Huililco and Llizán Valleys, to the northeast and south respectively. Confined by the topography, they were channelled within the valleys to the north and south.

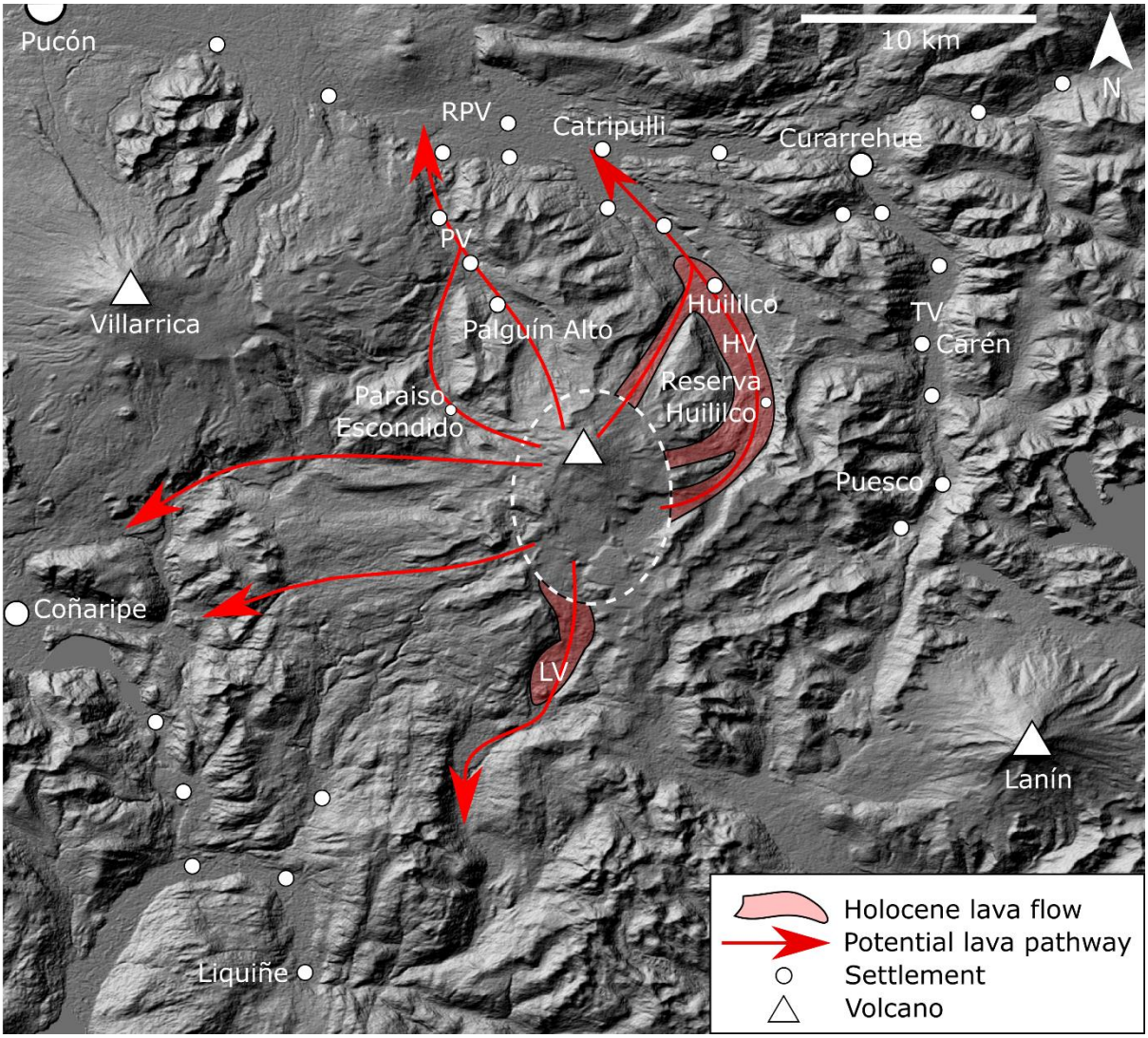

Figure 4.2: Large-volume Holocene lava flows (red shaded areas) and potential lava flow pathways (red arrows) down valleys leading off Quetrupillán (PV – Palguín Valley; HV – Huililco Valley; TV – Trancura Valley; RPV – Río Pucón Valley; LV – Llizán Valley). The dashed oval represents the outline of Quetrupillán's flanks, with the triangle denoting the summit. Settlements (white circles) in the surrounding area are mapped. The digital elevation model was downloaded from earthexplorer.usgs.gov (downloaded 21/10/2016).

The valleys that lead off Quetrupillán provide pathways for lava flows to potentially reach some of the settlements surrounding the volcano (Figure 4.2). The Huililco Valley provides a pathway of ~11 km to the village of Huililco and a pathway of ~20 km to Catripulli for lava flows from the eastern flanks of Quetrupillán. The western branch of the valley provides a pathway of ~18 km from the summit of Quetrupillán to Catripulli. Lavas from the summit of the stratocone that flow northwest would have an ~8.5 km pathway down the Palguín Valley to Palguín Alto, and an ~18 km pathway to

the Río Pucón Valley. The Llizán Valley provides a pathway to the south. Lava flows from vents on the southern flanks of the volcano have a pathway of ~27 km towards the village of Liquiñe (~30 km pathway from the summit). To the west there is a potential lava pathway of ~27 km from the summit towards Coñaripe, but there are no known Holocene lavas that have travelled in this direction.

Most Holocene lava flows are limited to the exposed flanks of the volcano. Provided future flank eruptions produce lava flows of similar volume there is little possibility of lavas causing damage to properties. However, the village of Huililco is built on one of the largest Holocene lava flows from Quetrupillán (Figure 4.2), indicating that lava flows from future eruptions have the potential to reach surrounding settlements. A lava flow with similar large volume, erupted from the summit or from a vent on the northern or eastern flanks, poses the greatest threat to the surrounding population as it would be capable of reaching the villages of Huililco or Palguín Alto if it descended the Huililco or Palguín Valleys.

However, even a large volume lava flow erupted from the southern flanks is unlikely to impact any settlements due to the distances required to reach centres of population to the south of Quetrupillán. As it is most likely that a future flank eruption will occur from the southern flanks, lava flows should not pose a significant threat to people or property. Should future lava flows be channelled off the flanks of the volcano, the expected relatively low velocities of trachytic lavas should allow ample time, assuming good communication, for evacuation of remote properties located in the higher valleys surrounding Quetrupillán. Effusive eruptions from Quetrupillán will also have the potential to generate lahars, and this will be discussed in section 4.5.3.

4.5.2. Explosive eruptions from Quetrupillán

During this study, pyroclastic sequences exposed in road cuttings were logged and sampled to evaluate the Holocene explosive eruptive activity from Quetrupillán (Figure 2.14). The prevailing wind is towards the east, so it was anticipated that sections in the Trancura Valley would provide the most comprehensive record of explosive volcanism from Quetrupillán. Pyroclastic sections in the Palguín Valley, to the northwest of the volcano, were expected to contain tephra only from the largest of Quetrupillán's explosive eruptions, as the valley is located orthogonal to the prevailing west-to-east dispersal axis of Quetrupillán's eruptive plumes (SERNAGEOMIN, 2013).

Trace element analyses of tephra layers in the Palguín Valley, conducted during this study, indicate that none of the sampled tephra layers were produced by Quetrupillán (Figure 2.7). Instead, one dacite layer is most likely from Mocho-Choshuenco (Rawson et al., 2015), and the rest are likely from Villarrica, which lies 15 km to the west (upwind) of the sampling locality (see Chapter 2, section 2.5.).

The absence of any tephra horizons from Quetrupillán in the Palguín Valley suggests that there have been no very large explosive eruptions from Quetrupillán during the Holocene. Irrespective of prevailing wind direction, a reasonable assumption is that a large (VEI ≥ 4) eruption would most likely have deposited tephra in this proximal valley, 8 km from the summit (Figure 4.3; (SERNAGEOMIN, 2013).

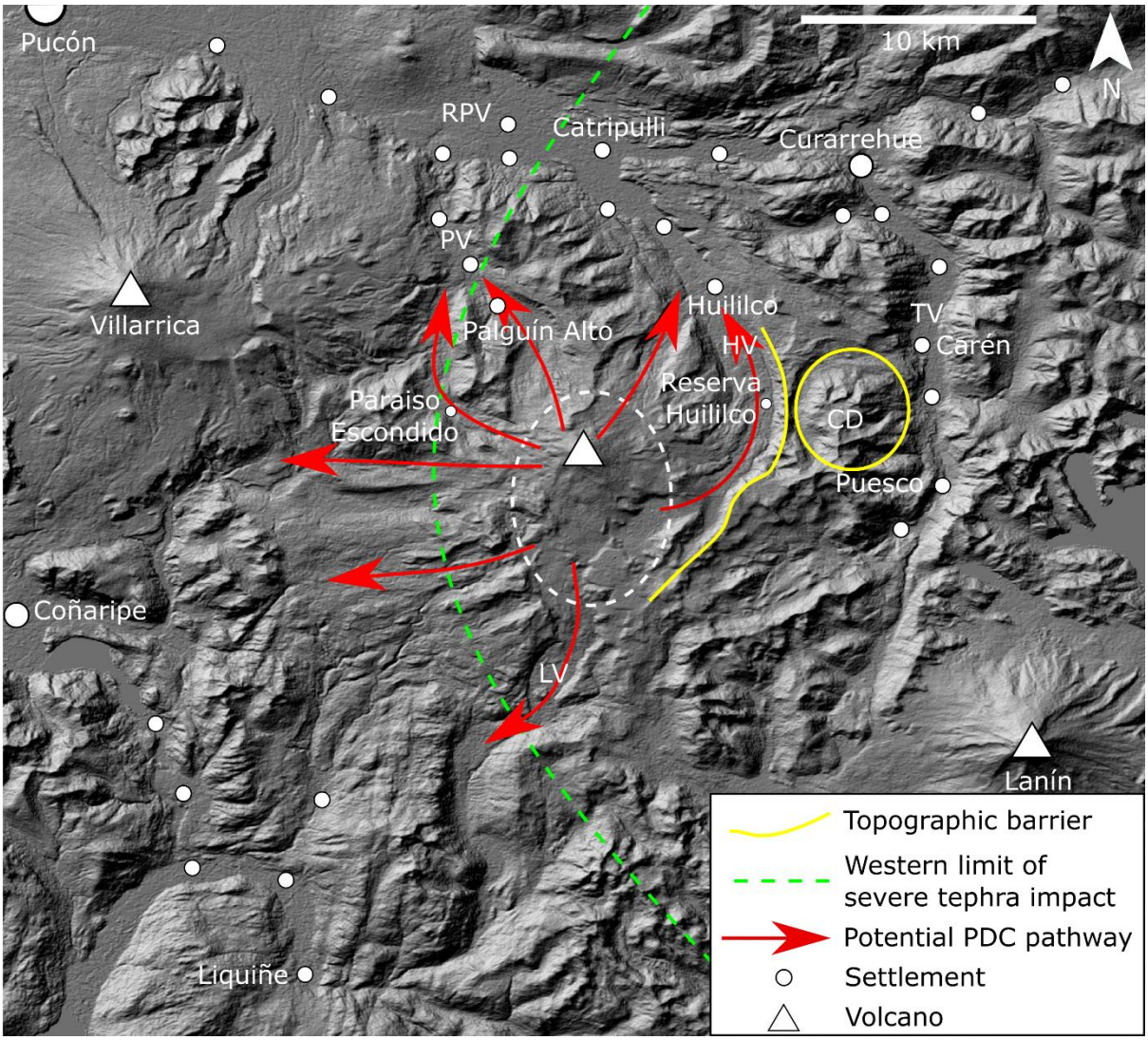

Figure 4.3: Potential PDC pathways (red arrows) down valleys leading off Quetrupillán (PV – Palguín Valley; HV – Huililco Valley; TV – Trancura Valley; RPV – Río Pucón Valley; LV – Llizán Valley). The topographic barriers of the eastern edge of the Huililco Valley and Colmillo del Diablo (CD) are highlighted in yellow. The green dashed line represents the expected western limit of severe impact from medium-coarse tephra fall during explosive eruptions, as noted by the official hazard map (SERNAGEOMIN, 2013). The dashed oval represents the outline of Quetrupillán's flanks, with the triangle denoting the summit. Settlements (white circles) in the surrounding area are mapped. The digital elevation model was downloaded from earthexplorer.usgs.gov (downloaded 21/10/2016).

In the Trancura Valley, the trace element analyses undertaken as part of this work identified three tephra layers from explosive eruptions at Quetrupillán (Figure 2.7), of which two are trachytic and one is trachyandesitic in composition (Figure 2.6). This pyroclastic section is notable as it spans the entire Holocene, with the lowermost tephra unit sitting directly on the plutonic basement (Figure 2.14).

According to information provided by SERNAGEOMIN (2019), based on Toloza (2015), nine explosive eruptions from Quetrupillán are preserved in the Trancura Valley. The results of this study disagree with that, as only three units are assigned with confidence to Quetrupillán. It should be noted that Toloza (2015) does not provide any geochemical evidence to support their claim of the nine Holocene explosive eruptions from Quetrupillán preserved in the Trancura Valley. Their underlying assumption seems to be that most pyroclastic layers in the Trancura Valley must have come from Quetrupillán, presumably due to its proximity. However, only by geochemically analysing each unit can the provenance of each horizon be established. The whole-rock major and trace element analyses from this study (Figures 2.6 and 2.7) strongly suggest that the majority of horizons preserved in the Trancura Valley were erupted from Villarrica, not from Quetrupillán, reducing by a factor of three the currently stated estimated hazard from explosive eruptions affecting areas to the east (e.g. the Trancura Valley; SERNAGEOMIN, 2019).

Fontijn et al. (2016) identified five possible units preserved in the Trancura Valley that may be products of explosive eruptions of Quetrupillán, based on the major element composition of groundmass glasses from tephra samples. They suggest, however, that the oldest three identified units may in fact be from Volcán Sollipulli, 60 km to the north, in which case only two horizons would be assigned to eruptions from Quetrupillán.

Toloza (2015) and the official hazard map (SERNAGEOMIN, 2013) also suggest that there is a substantial PDC hazard from Quetrupillán in the Trancura Valley. However, the observations made during fieldwork for this project suggest that all three pyroclastic layers in the Trancura Valley assigned to Quetrupillán are airfall deposits, with no evidence of sedimentary structures reflecting lateral transport, or the very poor sorting that characterises PDC deposits. It is notable though, that both Fontijn et al. (2014) and Rawson et al. (2015), who carried out detailed logging and sampling of tephra layers from numerous sites in this region of Chile, both comment on the variability in preservation of tephra even over short distances (i.e. 10s of metres). So, while no evidence of PDC deposits was found at the sites analysed for this study, they may be preserved elsewhere in the valley.

It is also important to note that the eroded remnants of the Colmillo del Diablo volcano lie to the east of Quetrupillán, as does the 200 – 380 m high near-vertical suspected fault scarp along the eastern edge of the Huililco Valley (highlighted in Figure 4.3). These form a major topographic barrier that would hinder, if not block, the passage of PDCs moving eastwards from Quetrupillán and into the Trancura Valley. It is more likely that PDCs would be channelled by this topographic barrier, flowing northwards down the Huililco Valley. PDCs could follow the same potential pathways as lava flows down the valleys off Quetrupillán (Figure 4.3). This could conceivably allow PDCs to reach the villages and isolated settlements located there, posing significant threats to the population which would require prompt evacuation to mitigate. As with effusive eruptions, explosive eruptions from Quetrupillán will also have the potential to generate lahars, which will be discussed in section 4.5.3.

Any eruption from Quetrupillán will produce tephra, as even effusive eruptions are likely to begin with an explosive phase. As Quetrupillán sits directly under the flight path for planes flying from Santiago to Balmaceda in Patagonia, this could pose a hazard for aviation. The prevailing wind will blow tephra east, where it will be deposited over villages in the Trancura Valley that lie below the dispersal axis, but beyond the international border, tephra will be carried into an unpopulated region of Argentina.

4.5.3. Lahar potential at Quetrupillán

No conclusive evidence of preserved lahar deposits was found during fieldwork on and around Quetrupillán. However, as Quetrupillán has an ice-filled summit crater and is snow-covered for much of the year, any eruption is likely to generate lahars. As valley-confined flows, these would follow the same possible pathways as the lava flows (Figure 4.4) but would have the potential to reach much greater distances from the volcano.

Lahars are the most recurrent phenomenon that occur during eruptions from the snow-clad volcanoes of the Southern Andes. For example, at neighbouring Villarrica, lahars have been generated by almost all eruptions, and are the primary volcanic hazard for populations living around the volcano (Naranjo and Moreno, 2004; Castruccio et al., 2010). The eruption in 1964 produced lahars that flowed south to the town of Coñaripe, where 22 people were killed (Naranjo and Moreno, 2004), and the most recent eruption in 2015 produced lahars that descended in multiple drainages (Johnson and Palma, 2015; Vera Rivadeneira, 2018). These lahars were generated when mixed avalanches produced by the paroxysmal eruption eroded the summit glacier and incorporated sufficient snow, ice and meltwater into the flow to become lahars (Vera Rivadeneira, 2018). In

contrast, an eruption in 1971 generated lahars when lava fountaining melted snow and ice, and the meltwater incorporated sediments as it flowed down the volcano (Castruccio et al., 2010).

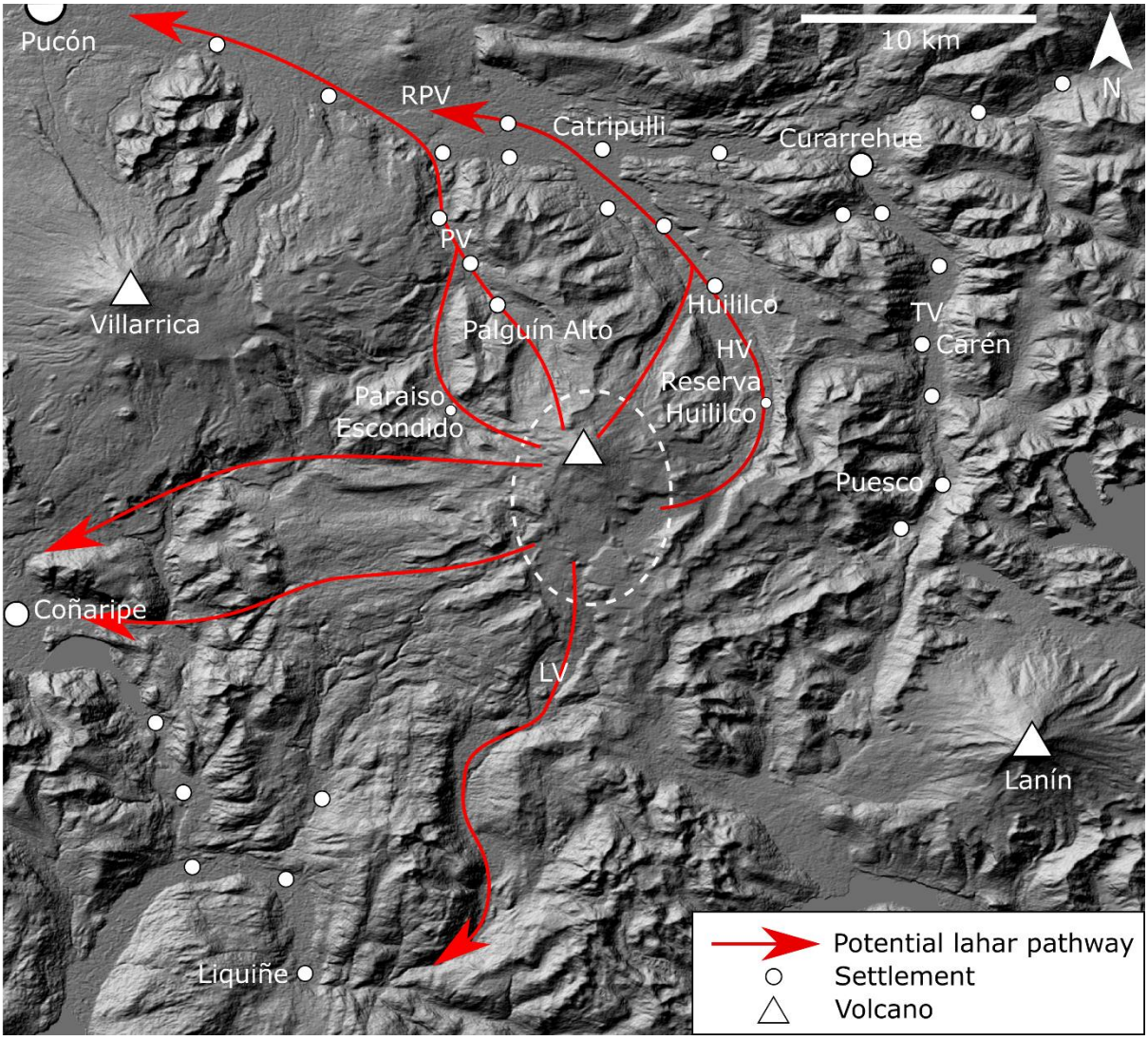

Figure 4.4: Potential lahar pathways (red arrows) down valleys leading off Quetrupillán (PV – Palguín Valley; HV – Huililco Valley; TV – Trancura Valley; RPV – Río Pucón Valley; LV – Llizán Valley). The dashed oval represents the outline of Quetrupillán's flanks, with the triangle denoting the summit. Settlements (white circles) in the surrounding area are mapped. The digital elevation model was downloaded from earthexplorer.usgs.gov (downloaded 21/10/2016).

An eruption below the icefields at the summit of Quetrupillán (Figures 2.2, 2.5 and 2.13B) may proceed as a subglacial eruption, depending on the thickness of ice and the volume of erupted material. If meltwater remained trapped within the summit crater or below the ice on the flanks,

then an eruption of this sort would not produce a major hazard. However, if this meltwater was released as a jökulhlaup, or if a subaerial eruption led to sufficient melting of snow or ice, then meltwater would descend the surrounding valleys, potentially incorporating unconsolidated volcanic deposits and sediment to form lahars, as in the 1971 eruption of Villarrica.

Lahars may continue to accumulate debris and water as they travel downstream from their source on a volcano's flanks, sustaining their momentum and giving them the ability to travel great distances (Fagents and Baloga, 2006). As such, lahars generated by future eruptions from Quetrupillán are likely to have the greatest reach of any flow hazard produced by the volcano. While the limited population to the south of Quetrupillán means that lahars initiated on the southern flanks are likely to have minimal impact, lahars initiated on the northern or eastern flanks will be channelled down the Palguín and Huililco Valleys, encountering the settlements located there. The town of Pucón is built on the deposits of lahars from Villarrica (Moreno, 2000; Castruccio and Clavero, 2015), and significantly large lahars from Quetrupillán may also have the potential to reach Pucón, as it is a 35 km pathway from the summit, down the Palguín Valley and along the Río Pucón Valley (Figure 4.4).

4.6. Analogue volcanoes

4.6.1. An objective method for finding analogue volcanoes

Lack of knowledge about the number and style of eruptions that have occurred from the summit of Quetrupillán is a limiting factor when considering future hazards posed by the volcano. The use of analogue volcanoes is a common method in hazard assessment when dealing with volcanoes that have insufficient data about their past activity. Analogue volcanoes are those that are considered to be similar in some way to the volcano of interest, sharing features such as volcano type, magma composition or eruption style (Newhall et al., 2017), and are therefore considered to represent potential activity from the target volcano.

Traditionally, analogue volcanoes are identified by categorising volcanoes into discrete and specific classifications, such as andesitic stratovolcanoes that produce dome-collapse PDCs, and the choice of potential analogues is limited by the knowledge of the individual researcher (Tierz et al., 2019). VOLCANS (VOLCano ANalogues Search; Tierz et al., 2019) is a method that provides an automated, objective approach to identifying analogue volcanoes, by quantitatively comparing the target volcano against all other volcanoes listed in global databases, to quantify their similarity. The criteria used to compare the volcanoes are tectonic setting (Ts), geochemistry (G), volcano morphology (M), eruption size (Sz) and eruption style (St).

Tectonic setting is described by the mantle melting mechanism (chemical driven versus decompression driven) and the ease of the melt's pathway to the surface. For Quetrupillán, the tectonic setting is a subduction zone with oceanic crust subducting below continental crust.

Geochemistry is described by the geochemical classifications from TAS and QAPF diagrams, as used in the Global Volcanism Program database (GVP, 2013). For Quetrupillán, the major geochemistry is trachyte, with minor basalt, basaltic andesite and rhyolite (see Chapter 3). However, a significant source of error in determining analogue volcanoes is the quality of geochemical data available in the GVP database, as the profile for Quetrupillán lists the major rock geochemistry as andesite, basaltic andesite and dacite, with minor basalt and rhyolite (GVP, 2013). Although the correct geochemistry for Quetrupillán was input into the VOLCANS model, it is unknown how accurate the listed geochemistry is for other volcanoes in the GVP database that Quetrupillán was compared with.

A volcano's morphology is usually described by classifying it within discrete categories (e.g. shield volcano, stratocone, caldera etc.), however the range in morphology covers a continuous spectrum of different volcano shapes (Tierz et al., 2019). In VOLCANS this spectrum is quantified, and volcano morphology is described by a variable (M) that considers the volcano's crater diameter (d), height (H), half-width (W^*) and truncation ($T = W_{summit}/W_{basal}$) using the equation

$$M = d + T - (H + H/W^*). \quad \text{(Eq. 4.7)}$$

Each of the four morphology components are ranked (smallest to largest) for every volcano listed in the databases compiled by Grosse et al. (2014; only includes positive-relief volcanoes) and Pike and Clow (1981; also includes calderas), and the percentile rank values are used to calculate M (Tierz et al., 2019). For Quetrupillán, the percentile rank values are d = 4, T = 7, H = 4 and H/W^* = 7, giving M = 0. To ensure that the morphology values of all volcanoes in the global databases lie between 0 and 1, they are normalised using the equation

$$M_{norm} = (M + x)/y \quad \text{(Eq. 4.8)}$$

where x = 19, equivalent to the most negative morphology value of all volcanoes in the database to ensure all M_{norm} values are positive (Volcán de Fuego, M = -19), and y = 38, the range in M values for all volcanoes. This gives a normalised morphology value for Quetrupillán of M_{norm} = 0.50.

Eruption size and eruption style are described according to classification in the GVP database (2013). Lack of knowledge about the number, size and style of eruptions from the summit of Quetrupillán precludes the use of these criteria when searching for analogues.

For each of the five criteria, a comparison is made between Quetrupillán and every other volcano in the databases, to find the single-criterion analogy (A), or degree of similarity, between Quetrupillán

and that volcano. An analogy of 1 implies that Quetrupillán is identical to the comparison volcano for that particular criterion. For example, if a volcano had A_{Ts} = 1 then it shares an identical tectonic setting with Quetrupillán, while if A_G = 1 then it has the same geochemistry as Quetrupillán. To calculate the total analogy of each volcano with Quetrupillán, each of the five single-criterion analogies is assigned a weighting depending upon its relative importance, with a higher weighting putting more emphasis on similarity of that aspect between the target volcano (Quetrupillán) and all other volcanoes, giving

$$A_{total} = (w_{Ts} \cdot A_{Ts}) + (w_G \cdot A_G) + (w_M \cdot A_M) + (w_{Sz} \cdot A_{Sz}) + (w_{St} \cdot A_{St}) \quad \text{(Eq. 4.9)}$$

where A_i is the single-criterion analogy (similarity) between Quetrupillán and the comparison volcano and w_i is the weighting applied for each criterion.

The following weightings were used to search for analogues for Quetrupillán: Ts = 0.35, G = 0.3, M = 0.35, Sz = 0 and St = 0. Equal weighting was given to tectonic setting (subduction under continental crust) and volcano morphology (M_{norm} = 0.50), and a slightly lower weighting was given to geochemistry (trachyte with minor basalt, basaltic andesite and rhyolite). Eruption size and eruption style were both set to zero as the number, size and style of eruptions from the summit is not constrained.

4.6.2. Analogue volcanoes of Quetrupillán

Table 4.2 and Figure 4.5 contain the top twenty analogue volcanoes for Quetrupillán, returned by the VOLCANS model (run by Dr Pablo Tierz at the British Geological Survey) when using the criteria and weightings outlined above. Study of hazards produced at these analogue volcanoes, which display similarities to Quetrupillán's tectonic setting, geochemistry and morphology, may help to constrain what potential hazards and hazard scenarios could be produced by Quetrupillán during future eruptions.

Table 4.2: Top twenty analogue volcanoes for Quetrupillán, returned by VOLCANS (Tierz et al., 2019). Single-criterion analogies are given for tectonic setting (A_{Ts}), geochemistry (A_G) and morphology (A_M) and the total analogy (A_{total}) is the weighted sum of these (where an analogy of 1 indicates a condition identical to Quetrupillán).

			Weight:	0.35	0.3	0.35
	Volcano	Country	A_{total}	A_{Ts}	A_G	A_M
1	Hudson	Chile	0.955	1.00	0.88	0.97
2	Westdahl	USA	0.949	1.00	0.92	0.92
3	Muria	Indonesia	0.946	1.00	0.88	0.95
4	Lamington	Papua New Guinea	0.946	1.00	0.85	0.97
5	Nevado de Toluca	Mexico	0.945	1.00	0.88	0.95
6	Santa Ana	El Salvador	0.944	1.00	0.87	0.95
7	Vulcano	Italy	0.942	1.00	0.93	0.89
8	Tambora	Indonesia	0.931	1.00	0.83	0.95
9	Rinjani	Indonesia	0.929	1.00	0.79	0.97
10	Copahue	Chile	0.927	1.00	0.91	0.87
11	Tangkubanparahu	Indonesia	0.926	1.00	0.75	1.00
12	Tutupaca	Peru	0.926	1.00	0.91	0.87
13	Tengger	Indonesia	0.926	1.00	0.87	0.89
14	Lipari	Italy	0.923	1.00	0.84	0.92
15	Vesuvius	Italy	0.922	1.00	0.74	1.00
16	Kirishimayama	Japan	0.922	1.00	0.74	1.00
17	Gorely	Russia	0.922	1.00	0.74	1.00
18	Ceboruco	Mexico	0.921	1.00	0.86	0.89
19	Los Atlixcos	Mexico	0.920	1.00	0.76	0.97
20	Zapatera	Nicaragua	0.920	1.00	0.76	0.97

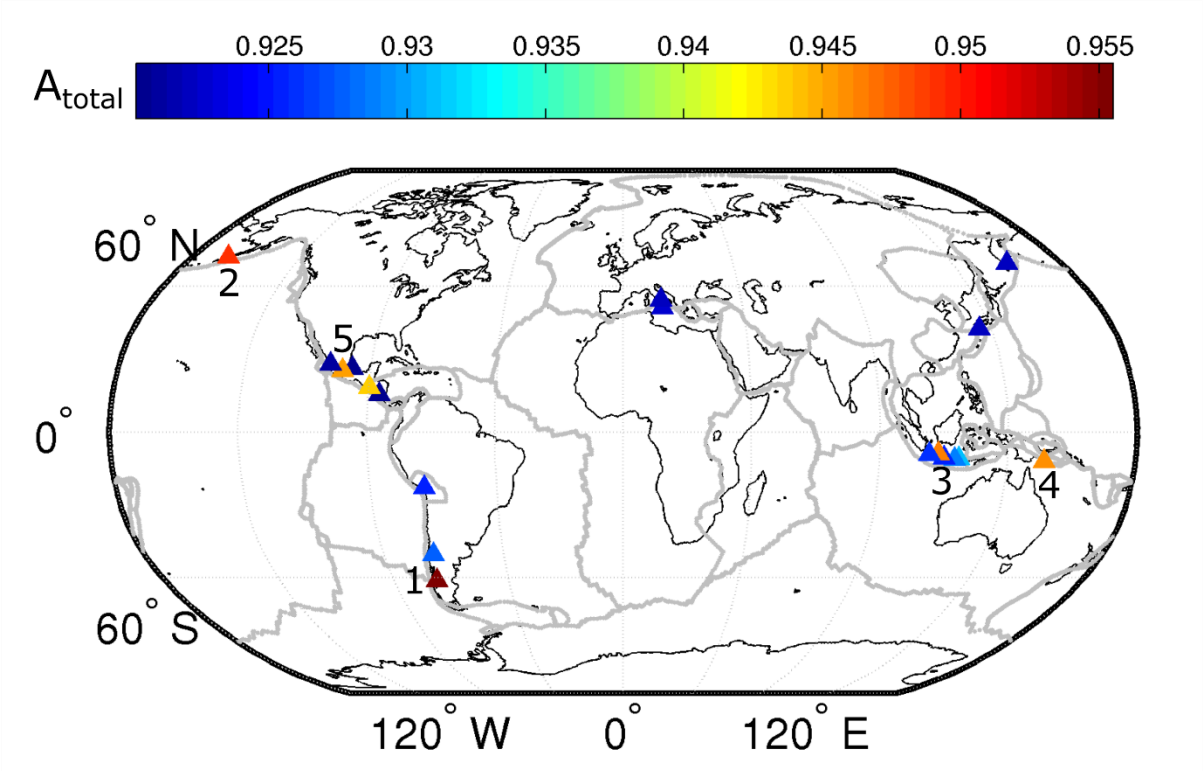

Figure 4.5: Top twenty analogue volcanoes for Quetrupillán, returned by VOLCANS (Tierz et al., 2019). Volcanoes are colour-coded according to their similarity with Quetrupillán, corresponding to the scale bar, where A_{total} = 1 indicates a volcano identical to Quetrupillán. The top five analogue volcanoes are labelled: 1 – Hudson, 2 – Westdahl, 3 – Muria, 4 – Lamington, 5 – Nevado de Toluca.

All of the top twenty analogue volcanoes to Quetrupillán have an identical tectonic setting (A_{Ts} = 1; Table 4.2), as all are located in subduction zones where oceanic crust is subducting below continental crust. The analogue volcanoes share strong similarities in morphology to Quetrupillán (A_M = 1 – 0.87; Table 4.2), with slightly less similarity in geochemistry (A_G = 0.93 – 0.74; Table 4.2). The top five analogous volcanoes are discussed below, with consideration of significant eruptions and hazards identified by previous studies, as these hazards may be applicable to Quetrupillán.

Hudson (A_{Total} = 0.955) is the southernmost active volcano of the SVZ (Figure 4.5) and shares a similar morphology to Quetrupillán (A_M = 0.97). Its eruption in 1991 was one of the largest explosive eruptions of the 20th century (Kratzmann et al., 2009), and produced an estimated total bulk volume of 7.6 km^3 of pyroclastic deposits (Scasso et al., 1994). The eruption began with a phreatomagmatic event that generated a 12 km high eruption column, 0.2 km^3 of tephra, and effusion of lava flows from a 4 km long fissure (Naranjo and Stern, 1998; Kratzmann et al., 2009). Resultant glacial melting led to jökulhlaups (Bitschene and Fernández, 1995). The subsequent Plinian eruption produced a

16 km high eruption column (Kratzmann et al., 2009) which was transported as an elongate plume, depositing over 7 km^3 of tephra (Naranjo and Stern, 1998) in a narrow band across Argentinian Patagonia and into the ocean (Scasso et al., 1994). The corresponding SO_2 plume (containing $>1.5 \times 10^9$ kg SO_2) fully encircled the Southern Ocean (Doiron et al., 1991). Studies of tephra deposits across Patagonia suggest that Hudson has had frequent large explosive eruptions throughout the Holocene, and may be the most active volcano of the SVZ, in terms of large explosive eruptions (Naranjo and Stern, 1998).

Westdahl (A_{Total} = 0.949) is a glacier-capped shield volcano in the Aleutian Islands (Figure 4.5; Lu et al., 2004) with both geochemistry and morphology similar to Quetrupillán (A_G = 0.92, A_M = 0.92). Eight eruptions have been recorded since the end of the 18th century (Miller et al., 1998), however due to its remote location is it suspected that additional, undetected eruptions have also occurred (Lu et al., 2004). These eruptions have covered a range of styles, from Vulcanian eruptions, which excavated craters through the ice cap and generated lahars, to phreatic eruptions, which produced 7 km high ash plumes, to Hawaiian eruptions, which occurred along fissures where lava fountaining fed lava flows (Lu et al., 2004).

Muria (A_{Total} = 0.946) is a stratovolcano on the northern coast of central Java (Figure 4.5) with a similar morphology to Quetrupillán (A_M = 0.95), which has had no historical activity (GVP, 2013). Deposits of lahars, debris flows and avalanches are found across the slopes of Muria, and it has numerous flank vents with associated lava flows, cinder cones and explosion craters (McBirney et al., 2003). A hazard assessment was conducted to determine what volcanic hazards may impact a proposed nuclear power plant due to be constructed at the base of Muria, 20 km from the summit, which identified tephra fall, pyroclastic flows, lahars, debris flows, slope failures and the opening of new vents as potential hazards (McBirney et al., 2003).

Lamington (A_{Total} = 0.946) is a stratovolcano in the east of Papua New Guinea (Figure 4.5), with a morphology similar to Quetrupillán (A_M = 0.97). Its devastating eruption in 1951 began with the intrusion of a cryptodome, accompanied by ash-rich Vulcanian explosions and landslides. The bugling cryptodome collapsed when it became unstable, resulting in a debris avalanche that triggered an explosive directed blast (Alexander et al., 2020). This blast generated PDCs that propagated radially from the volcano, at speeds of up to 94 m/s with temperatures of 200 °C, devastating an area of 230 km^2 (Taylor, 1983). Hummocky deposits surrounding the volcano indicate that previous sector collapses have occurred at Lamington, which generated debris avalanches and produced large explosive eruptions (Alexander et al., 2020).

Nevado de Toluca (A_{Total} = 0.945) in central Mexico (Figure 4.5) is a stratovolcano with a similar morphology to Quetrupillán (A_M = 0.95). Since the Pleistocene, it has undergone Vulcanian to Plinian activity (García-Palomo et al., 2002). Activity has included effusion of lava flows, block-and-ash flows generated by dome collapse, flank failure resulting in debris avalanches, PDCs produced by explosive eruptions, and rain-triggered secondary lahars (García-Palomo et al., 2002). A study of hazards from the volcano identified PDCs, lahars, ash fall and debris avalanches as the most significant potential hazards from Nevado de Toluca (Aceves-Quesada et al., 2006).

It has been observed that a variety of different eruptive styles have occurred from Quetrupillán (Chapter 2), and these analogue volcanoes also cover a wide range of activity, from Hawaiian to Plinian eruptions. Identified hazards at analogue volcanoes include lava flows, tephra fall, PDCs, debris avalanches, landslides, explosive opening of new vents, lahars, jökulhlaups and SO_2 emission. As the analogue volcanoes share similarities with Quetrupillán, all these hazards should be considered in relation to activity at Quetrupillán and investigated as to whether they may be potential hazards from future eruptions. For example, no evidence of jökulhlaup activity was found at Quetrupillán, however jökulhlaups occurred during the 1991 eruption of Volcán Hudson. Like Quetrupillán, Hudson has an ice-filled summit crater (though at Hudson this is a 10 km wide caldera; Naranjo and Stern, 1998) and is glaciated, and so conditions at Quetrupillán may also enable jökulhlaups to occur. In this way, evaluation of hazards produced at analogue volcanoes can increase understanding of potential future hazards from Quetrupillán.

Chapter 5: Discussion and conclusions

Conquering the volcano! At the summit of Quetrupillán

5.1. Introduction

Consideration of Holocene volcanism (Chapter 2), magmatism (Chapter 3) and the tectonic regime (Chapter 3) at Quetrupillán allows the development of a conceptual model for the magmatic plumbing system below the volcano. It also provides an insight into Quetrupillán's past activity, which, combined with scrutiny of glacial interactions, can be used to generate a tentative Holocene eruption stratigraphy for Quetrupillán (Chapter 2). Knowledge of Quetrupillán's Holocene volcanic activity can also be used to inform understanding of the possible hazards and impacts that any future eruptions may have (Chapter 4).

5.2. The conceptual model for Quetrupillán's magmatic plumbing system

Current understanding is that magmatic plumbing systems extend throughout the thickness of the crust, existing as transient, interconnected lenses of magma within a region of crystal mush (Cashman et al., 2017; Magee et al., 2018). Partial melting in the mantle supplies basaltic melt to the base of the crust, where it enters the transcrustal magmatic plumbing system, and then local and regional crustal tectonics influence whether this basaltic magma is able to reach the surface to erupt directly, or whether it will stall within the crust and evolve by fractional crystallisation and assimilation into more differentiated products (Cembrano and Lara, 2009).

This idea is consistent with the geochemical evidence and tectonic considerations presented in Chapters 2 and 3. A conceptual model is proposed for the magmatic plumbing system of Quetrupillán based upon this concept, in which it is a stable transcrustal magmatic system, composed of pockets of trachytic melt contained within a region of crystal mush (Figure 5.1). Partial melting in the lithospheric mantle feeds basaltic melt into the base of the crust (Hildreth and Moorbath, 1988; Hickey-Vargas et al., 2016b; Magee et al., 2018), which stalls on its ascent through the crust due to the local compressional tectonic regime in which Quetrupillán is located (Figure 3.21). In accordance with this model, these pockets of stalled melt evolve through fractional crystallisation (Hickey-Vargas et al., 1989; Brahm et al., 2018), and as liquid magma crystallises, the proportion of crystals suspended in the melt increases until they have formed a network of crystals containing interstitial melt, at which point they become crystal mush (Hildreth, 2004; Glazner et al., 2016). Crystallisation will result in an increased silica content in the remaining melt. It is proposed in Chapter 3 (section 3.4.3.) that a degree of crustal contamination will result in increased alkali and LILE concentrations, as well as enrichment in some of the HFSEs (Figure 3.9), producing the trachytic magmatic system present below Quetrupillán.

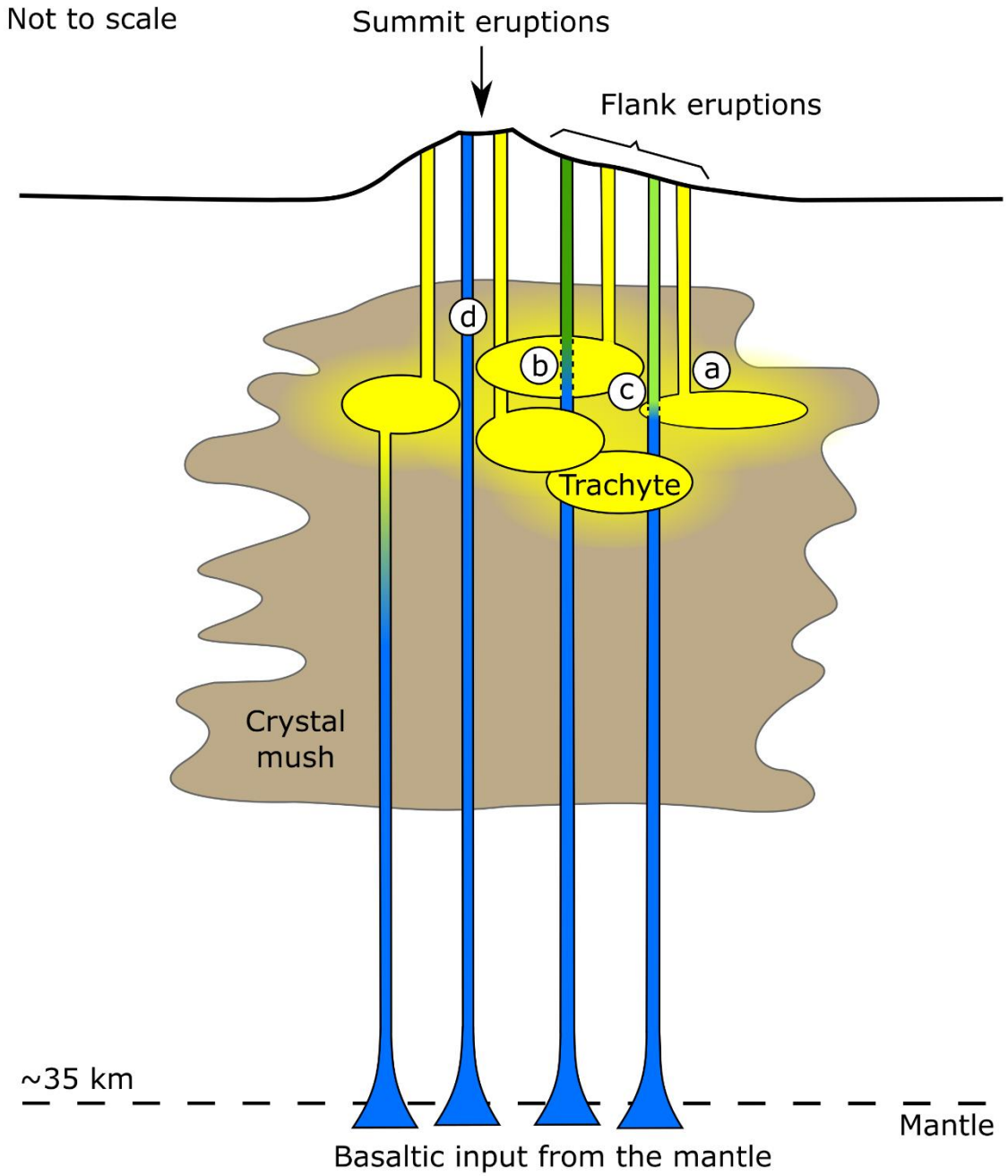

Figure 5.1: A conceptual model for the magmatic plumbing system below Quetrupillán, in which pockets of trachytic melt (yellow) are contained within a region of crystal mush (brown). Extraction of melt from these pockets produces trachytic eruptions (a). Basaltic melt (blue) is injected into the system at the base of the crust, and if it ascends close to the surface with minimal interaction with the resident trachyte melts and mush, then trachyandesite (b; blue-green), basaltic andesite (c; yellow-green) and basalt (d) melts will be produced and erupted, depending on the degree of interaction and mixing.

Most basaltic magma injected into the base of a magmatic plumbing system will either encounter a melt pocket, where it will mix with the established resident melts (Pansino and Taisne, 2019), or stall within the crystal mush, where it will form a new melt pocket and will evolve over time by fractional crystallisation. However, some injected basalt transported by deeply sourced feeder dykes will reach the surface with only minimal interaction with the resident melt (Pansino and Taisne, 2019).

As discussed in Chapter 3 (section 3.4.3.), the degree of interaction will control the extent of mixing, determining the composition of the resultant hybrid magma. If >~60% basalt is mixed with <~40% trachyte it will produce basaltic andesite magma, while if <~60% basalt is mixed with >~40% trachyte it will produce trachyandesite magma. If only a very small proportion of basalt mixes with the trachyte, then the resultant hybrid may retain a whole-rock trachyte composition, such as the magma mingling recorded by the trachytic banded pumice (Figure 3.20). The varying degrees of interaction and mixing may reflect whether ascending basalt intersects the thicker centre of a trachyte pocket (labelled “b” in Figure 5.1) or the thinner margin (labelled “c” in Figure 5.1), or whether ascending basalt intersects multiple stacked pockets. The eruption of basaltic lavas suggests that some rising basaltic magma had no interaction with trachytic melt pockets during its ascent (labelled “d” in Figure 5.1), retaining its basaltic composition when reaching the surface.

The Holocene basalt erupted from the summit region and used in the modelled magma mixing is a good approximation for the composition of the source basalt that was input into the base of the system (see Chapter 3, section 3.4.3.). The similarity in the range of erupted products through the Pleistocene and Holocene (Figure 3.1) suggests that there has been no significant change in magma production through time, implying that Quetrupillán’s magmatic plumbing system is a stable feature that was established by the Pleistocene.

5.2.1. Geochemical and petrological evidence

The majority of Holocene lavas erupted from Quetrupillán’s flank vents are trachytic in composition. Twelve of the fifteen analysed flank vents produced trachytic products, representing ~96.7% of the total volume of Holocene lava erupted from the flanks (see Chapter 2, section 2.5.). Only minor volumes of trachyandesite (~1.8%) and basaltic andesite (~1.5%) lavas were effused from Holocene flank vents. This strongly suggests a predominance of trachyte magma below the volcano, supporting the concept of a trachytic magmatic system. As trachyte magmas are also an important component in the generation of the erupted Holocene trachyandesite and basaltic andesite lavas (Chapter 3, section 3.4.3.), this reinforces the conclusion that trachytes are the dominant melt composition in the plumbing system.

Limited sampling of lavas effused from the summit region of the stratocone shows that a similar compositional range (trachyte, trachyandesite, basaltic andesite and basalt) has been erupted from the main edifice. The number of samples of summit lavas collected was insufficient to determine the relative proportions in which these compositions were erupted from the summit region. However, the same wide compositional range of products erupted from both the flanks and the summit (Figure 3.1) indicates that unlike at some other Chilean volcanic complexes (e.g. Nevados de Chillán; Dixon et al., 1999; Mee et al., 2009), there is no relationship between eruption location and magma composition at Quetrupillán.

As discussed in Chapter 3 (section 3.4.1.), basaltic andesite and trachyandesite lavas contain clinopyroxene phenocrysts with trachytic melt inclusions, and rare orthopyroxene phenocrysts co-existing with abundant olivine phenocrysts. These clinopyroxene phenocrysts with trachytic melt inclusions and orthopyroxene phenocrysts are considered to be xenocrysts in the basaltic andesite and trachyandesite lavas in which they are found. The trachytic nature of the melt inclusions suggests that the clinopyroxene hosts crystallised from a trachytic melt. Consistent with the proposed conceptual model (Figure 5.1), clino- and orthopyroxene phenocrysts crystallise within pockets of trachytic melt in the trachytic magmatic plumbing system. As injected basalt ascends to the surface and interacts with these trachytic melt pockets, mixing between the two compositions occurs. Phenocrysts of clino- and orthopyroxene from the trachyte melts are incorporated into the hybrid melts, and so are present in the hybrid basaltic andesite and trachyandesite lavas.

In Holocene trachyte lavas erupted from the summit and flanks of Quetrupillán, there are variations in the composition of groundmass glass, plagioclase phenocrysts and melt inclusions in clinopyroxene phenocrysts. These differences suggest that there are variations in the composition of the melts from which the trachyte lavas have been sourced. Each trachytic melt pocket in the magmatic system evolves with a slightly different composition, and extraction of melt from different pockets would result in the minor differences observed in trachytic erupted products. It is assumed that the restricted compositional range of Holocene trachyte lavas provides a good approximation of the likely trachyte end-member that mixed with ascending basalt to produce the hybrid basaltic andesite and trachyandesite lavas (see Chapter 3, section 3.4.3.). However, these variations indicate that different batches of hybrid melts have been produced from trachyte end-members with slight variations in their composition. This explains the range in the composition of melt inclusions found in clinopyroxene xenocrysts in the hybrid lavas (Figure 3.1).

The presence of a crystal mush in which the trachyte melt pockets reside is supported by the abundance of glomerocrysts in trachyte, trachyandesite and basaltic andesite lava samples (Figure 3.4). These glomerocrysts are composed of combinations of plagioclase, pyroxene and oxide (and

olivine in basaltic andesite and trachyandesite lavas) and are up to 5 mm in diameter (Appendix II). The glomerocrysts are interpreted as clots of crystals from the crystal mush that were incorporated into the melt (e.g. Brahm et al., 2018).

5.2.2. Tectonic constraints

Partial melting in the lithospheric mantle generates the basaltic melt that is injected into the base of the crust at all the magmatic plumbing systems in the SVZ (Hildreth and Moorbath, 1988). The input of basaltic melt into the base of the crust is considered to be incremental, with slow rates of melt generation and segregation in the mantle producing small volumes of melt at a steady rate (Annen, 2009; Cashman et al., 2017). The local tectonic regime at each volcano will then control how fast this basalt ascends through the crust. If the basaltic melt has an easy pathway to the surface, it is likely to ascend relatively fast with insufficient time to evolve (Cembrano and Lara, 2009). In regions of local extension the magma will be able to rapidly flux though the crust to erupt as basalt, while in regions of local compression the magma will stall within the crust and evolve to more differentiated compositions (Cembrano and Lara, 2009; Schonwalder-Angel et al., 2018).

To the north of Quetrupillán, the presence of the LOFZ has provided an easy pathway to allow basalt to ascend directly and rapidly from the base of the crust to the surface. This has resulted in the formation of the MECs of Caburgua, La Barda and Huelemolle, all of which lie directly above the main trace of the LOFZ (Figure 1.4) and have primitive basaltic compositions (Morgado et al., 2015; McGee et al., 2017; see Chapter 3, sections 3.4.3. and 3.4.5.). At Villarrica there is a continual flux of magma through the system. As one of the most active volcanoes in South America (Lara, 2004; Petit-Breuilh, 2004), the basaltic input is rapidly fluxed through the magmatic plumbing system and does not have the opportunity to evolve beyond a basaltic andesite composition (Witter et al., 2004). If an equivalent rate of basaltic injection is occurring beneath Quetrupillán as beneath Villarrica, then the tectonic setting at Quetrupillán is preventing it from fluxing through the system as rapidly. The local compressional regime in which Quetrupillán is located (Figure 3.21) prevents rapid ascent of the basalt magma through the crust, forcing it to stall below Quetrupillán, where it evolves through fractional crystallisation and assimilation into a trachytic composition.

The local tectonic stresses imposed on Quetrupillán by the LOFZ also influence the orientation of the subsurface dykes that transport the magma extracted from the trachytic melt pockets to the surface. Some of these are now exposed, oriented tangentially to the summit of the main edifice rather than radially to it (Figure 3.13). In turn, these dykes control the orientation of fissure eruptions on the flanks. Two Holocene flank eruptions are interpreted to have occurred as fissure eruptions (see

Chapter 2, section 2.6.), and at least one Pleistocene fissure has been identified (McGarvie et al., 2014), also oriented tangentially to the summit.

5.3. Past activity and future eruptions

As discussed in Chapter 2, Holocene eruptions have occurred both at the stratocone and from vents on its flanks. The number and type of eruptions from the summit region is unknown due to removal of lavas by ice during LIA glacial advances, resulting in the prominent scoured zone. However, subglacial buttresses on the flanks of the stratocone that are partially buried by scoured Holocene summit lavas indicate that some Holocene construction has taken place. It seems likely that effusive activity from the stratocone summit has been higher during the Holocene than its scoured appearance suggests.

The presence of three horizons of pyroclastic deposits, including a one-metre thick pumice horizon, preserved 15 km downwind in the Trancura Valley (Figure 2.14), suggests that three large explosive eruptions have occurred from Quetrupillán during the Holocene. It is unknown whether these deposits were produced during explosive eruptions at the summit of the stratocone or from flank vents, though large explosive eruptions seem more likely from the summit.

Sixteen vents were identified on the flanks of Quetrupillán, which are considered to represent ten Holocene eruptive episodes. Thirteen of these sixteen flank vents have effused lava flows, ranging in volume from $<1 \times 10^6$ m^3 to $>60 \times 10^6$ m^3 (Table 2.1). The smaller lava flows are limited to the exposed flanks of Quetrupillán, while larger flows have travelled down valleys for many kilometres (see Chapter 4, section 4.5.1.). Seven of the flank vents have constructed scoria cones, two have excavated craters into pre-existing deposits, and three have excavated shallow craters surrounded by low rimmed tuff rings. This suggests that the style of Holocene volcanic activity from the flanks of Quetrupillán has ranged from Strombolian to phreatomagmatic.

The range of volcanic activity that has occurred at Quetrupillán during the Holocene provides the likely range of future eruption styles. Future flank eruptions are expected to be located on the southern flanks of the volcano (see Chapter 4, section 4.5.) and may be Strombolian to phreatomagmatic in nature, depending on the availability of groundwater during the eruption (see Chapter 2, section 2.6.2.). The trachytic nature of Quetrupillán's magmas implies that any future eruptions, from flank or summit region, are most likely to be trachytic in composition, and the abundance of Holocene flank lava flows suggests that regardless of initial eruption style, subsequent lava effusion is likely to take place.

As discussed in Chapter 4 (section 4.3.), the probability of an eruption occurring from Quetrupillán within the next year is less than 0.1%, within the next 50 years is 4.1% and within the next 100 years is 7.9%. The prediction of no eruption, with 95% confidence, is valid for the next 60 years.

5.4. Directions for further investigation

5.4.1. Holocene activity from the stratocone

Holocene volcanic activity at Quetrupillán has occurred from both the flanks and summit region of the stratocone. However, determination of the eruption stratigraphy from the summit was prevented due to the scoured zone that covers the upper flanks (see Chapter 2, section 2.4.). Scouring by ice during past glaciations has removed eruption deposits, and the diamict deposited when glaciers receded covers all the remaining deposits within the scoured zone (Figure 2.3). As such, the number, volume and style of eruptions that took place in the summit region are all unknown, resulting in a gap in our understanding of Holocene volcanic activity at Quetrupillán.

To resolve this issue, a detailed investigation should be carried out within the scoured zone. Lava flows should be mapped in as much detail as possible where they are exposed through the diamict. Lavas erupted from the main edifice should also be sufficiently sampled to ensure representative coverage of Holocene activity from the summit. However, the remote and physical nature of conducting fieldwork on the upper flanks of Quetrupillán, and the limited exposure of summit lavas, means that mapping within the scoured zone will present a challenge.

If detailed investigation of summit region Holocene eruptive products can be achieved, it will allow a more comprehensive eruption stratigraphy to be developed and provide a more complete understanding of Quetrupillán's Holocene volcanic activity. This will help to address the questions that are still unanswered:

- Is the ratio of compositions erupted from the summit region the same as the ratio erupted from flank vents? (i.e. almost all trachytic with only minor less evolved compositions)
- What type of eruptions have occurred from the summit region?
- How many Holocene eruptions have occurred from the summit region of Quetrupillán?
- What is the probability of a future eruption from the summit of Quetrupillán?
- What is the probability of a future eruption from anywhere on Quetrupillán, when including both summit and flank Holocene eruptions in the calculation of eruption frequency?
- Is a future eruption more likely to occur from the summit or flanks?

5.4.2. Explosive eruptions from Quetrupillán

During this study, investigation of pyroclastic horizons identified three units that were produced by large explosive eruptions of Quetrupillán (two trachytic in composition and one trachyandesitic), based on the major and trace element whole-rock compositions of the pyroclastic samples (see Chapter 2, section 2.5.). All three horizons were interpreted as airfall deposits, composed of pumice and/or ash deposited from an eruption plume. These tephra horizons, preserved 15 km downwind in the Trancura Valley, led to the interpretation that three large explosive eruptions have occurred from Quetrupillán during the Holocene (see Chapter 2, section 2.9.).

At similar localities within the Trancura Valley, other studies have identified different numbers of pyroclastic horizons as being produced by Quetrupillán. Fontijn et al. (2016) identified five possible horizons from Quetrupillán, based on major element compositions of tephra groundmass glasses, though stated that three of these horizons may have been produced by Sollipulli. Toloza (2015) identified nine horizons from Quetrupillán, based on the apparent assumption that Quetrupillán is the closest volcano. Future detailed logging and sampling at multiple localities along the Trancura Valley may help to resolve the issue of how many pyroclastic horizons from Quetrupillán are preserved there, and therefore how many large explosive eruptions have occurred during the Holocene.

Toloza (2015) stated that most of the pyroclastic horizons preserved in the Trancura Valley are PDC deposits. Examination of these road cuttings during fieldwork did not reveal any unequivocal evidence of the lateral transport structures that are characteristic of PDCs, and so they were interpreted as airfall deposits. This interpretation suggests either that no substantial PDCs have been produced at Quetrupillán during the Holocene, or that the topographic barrier to the east has prevented them from reaching the Trancura Valley (see Chapter 4, section 4.5.2.). It should be emphasised that although the sections investigated during this study may not have contained PDC deposits, the variability of preservation potential in this region (Fontijn et al., 2014; Rawson et al., 2015) means that they may be preserved at other localities in the valley.

The suggested future detailed logging at multiple localities along the Trancura Valley could also help to resolve the issue of whether PDCs from Quetrupillán have entered the valley. If Holocene PDCs surmounted the topographic barriers of the Huililco Valley fault scarp and the remnants of Colmillo del Diablo (Figure 4.3), then their pathways should be established for hazard evaluation. The presence of PDC deposits should also be investigated in the Huililco Valley, as it seems more likely that the topography would channel them in this direction.

5.4.3. The formation of the scoured zone

The theory proposed for the formation of Quetrupillán's prominent scoured zone (Chapter 2, section 2.4.) is based on the repeated covering of Quetrupillán's glaciers by thin blankets of tephra from Villarrica. However, it is not known whether this is actually the process that produced the scoured zone. It is possible instead that some aspect of the glacier-volcano architecture of Quetrupillán resulted in a higher sensitivity to LIA conditions and more extensive ice advances and retreats than at Villarrica and Lanín. Further research into the Holocene glacial history of Quetrupillán may help to resolve why it has this well-defined scoured zone, while its neighbours lack such a feature.

5.4.4. Hazard modelling

This study has calculated the probability of a future eruption occurring at Quetrupillán and qualitatively considered the potential hazards that this may pose to the surrounding populations (see Chapter 4). To advance on this, numerical models should be run to quantitatively evaluate the risks generated by different hazards. Simulations should consider the variations in eruption style that are likely to occur during future eruptions, based on the eruptions that have occurred during the Holocene.

These numerical models include simulations of tephra fall, which should consider seasonal variations in prevailing wind direction, and flow hazards (lavas, PDCs and lahars), which should consider the range of possible source locations, as this will control which drainage the flow is likely to enter and therefore in which direction it will be channelled. Simulations of lahars should also consider the variation in snow cover throughout the year, as the timing of the eruption will influence the potential size of lahars that may be generated.

Consideration should also be given to the styles of eruption and resultant hazards that have been observed at volcanoes that are analogous to Quetrupillán. The top twenty analogue volcanoes are listed in Table 4.2, and evaluation of past activity at these volcanoes, and the hazards produced, can help to inform about potential hazards that may be posed by Quetrupillán.

5.5. Conclusions

In this study I have provided a detailed account of Holocene volcanism and magmatism at the Quetrupillán Volcanic Complex in the Southern Volcanic Zone of Chile, and considered the hazards posed by future eruptions.

Holocene activity has occurred from both the summit of the stratocone, and from vents on the flanks, though the number and style of eruptions from the summit region is unknown due to the removal of lavas by ice during Holocene glaciations, resulting in a prominent scoured zone. Sixteen identified flank vents are interpreted to represent ten eruptive episodes, with activity ranging from Strombolian to phreatomagmatic, resulting in construction of scoria cones, excavation of craters, and effusion of lava flows. The volumetrically dominant composition erupted from flank vents is trachyte, with minor trachyandesite and basaltic andesite. Limited sampling of stratocone lavas indicates that trachyte, trachyandesite, basaltic andesite and basalt lavas have erupted from the summit region.

The plumbing system of Quetrupillán has developed as a transcrustal magmatic system composed of pockets of trachytic melt within a crystal mush. Quetrupillán's location within the LOZF results in local compressive tectonic stresses that hinder magma ascent, and so promote stalling within the crust. This results in evolution of the basaltic melt injected into the system at the base of the crust, through fractional crystallisation and crustal assimilation. The tectonic stresses imposed by the LOFZ have a greater influence than the stresses imposed by the load of the volcanic edifice, resulting in lineaments that are tangential to the main edifice, rather than radial to it. Dyke formation enables evolved, trachytic melts to be extracted from the melt pockets of the magmatic plumbing system and ascend to the surface, forming the numerous trachytic eruptions that have occurred from Quetrupillán's summit and flanks during the Holocene. In some cases, basaltic melt is transported through the system with only minimal interaction with the established trachytic plumbing system. Varying degrees of mixing between basalt and trachyte result in the basalt, basaltic andesite and trachyandesite products that have also been erupted from Quetrupillán.

Future eruptions from Quetrupillán are therefore likely to be trachytic in composition. Future flank eruptions are most likely to occur on the southern flank of the volcano, which would result in any hazardous flows (lavas, PDCs and lahars) being directed away from settlements and channelled down the unpopulated valleys to the south of Quetrupillán. However, hazardous flows produced by eruptions from the main edifice or from the northern and eastern flanks would have the potential to follow pathways down the populated Palguín and Huililco Valleys to the north of Quetrupillán, potentially impacting the settlements located within these valleys.

The results of this work improve our knowledge of the Holocene activity, both volcanic and glacial, at Quetrupillán, provide new insights on the magmatic plumbing system and its interaction with the regional tectonics, and consider the possible hazards that might be posed by future eruptions, which serves to increase scientific understanding of this fascinating volcanic complex.

Appendices

Araucaria forest

Appendix I: Sample locations and descriptions

Locations and brief descriptions are provided for samples that subsequent analyses were performed upon. Samples are named according to whether they were collected from Quetrupillán (Q), in the Huililco Valley (H), in the Trancura Valley (T) or in the Palguín Valley (P). For Q and H samples, the source is listed according to whether the sample is from a flank vent (numbered in Figure 2.2) or from the summit of Quetrupillán; for T and P samples, the source is listed according to which volcano the deposit was most likely produced by (Mocho Ch. – Mocho Choshuenco).

Sample	Latitude	Longitude	Source	Description
Q3	-39.54597	-71.74645	Vent 2	Low vesicularity interior of lava flow
Q7	-39.54509	-71.73302	Vent 3	Lava from Vent 2
Q8	-39.54033	-71.69557	Vent 11	Highly vesicular lava
Q10	-39.54714	-71.72827	Vent 4	Younger black lava flow
Q12	-39.54916	-71.72717	Vent 5	Start of lava flow from Vent 3
Q16	-39.52805	-71.69707	Summit	Scoured lava in gully
Q17	-39.53790	-71.70322	Vent 12	Weathered exposed lava flow
Q20	-39.51233	-71.74663	Summit	West flank lava flow
Q23	-39.50102	-71.74318	Summit	West flank lava flow
Q25	-39.54671	-71.74754	?	Pumice in sequence by stream
Q26	-39.54671	-71.74754	?	Scoria in sequence by stream
Q29	-39.52407	-71.67397	Vent 14	Vesicular lava
Q31	-39.51704	-71.65781	Vent 13	Lava with distinct banding
Q34	-39.52016	-71.65932	Vent 13	Blocky lava from Vent 13
Q36	-39.52354	-71.66051	Vent 14	Blocky lava from Vent 14
Q39	-39.55730	-71.68585	Vent 9	Lava from edge of lava flow tongue
Q40	-39.56062	-71.68273	Vent 8	Vesicular lava/spatter from Vent 8 rim
Q41	-39.56308	-71.68713	Vent 7	Vesicular lava
Q43	-39.56081	-71.68620	Vent 7	Vesicular lava from banded flow
Q44	-39.55555	-71.68927	?	Brown pumice tephra
Q46	-39.56262	-71.70093	Vent 6	Lithic enclave in Vent 6 lava flow
Q48	-39.55626	-71.70560	Vent 6	Black glassy vesicular lava
Q50	-39.54955	-71.70946	Vent 10	Black low vesicular lava
Q53	-39.54588	-71.71910	Vent 2	Black non vesicular lava
Q54	-39.54867	-71.71621	Vent 4?	Low vesicularity lava
Q56	-39.55530	-71.72160	Vent 5	Black glassy lava

Sample	Latitude	Longitude	Source	Description
Q60	-39.52444	-71.70696	Summit	Scoured lava flow on upper flanks
Q61	-39.52699	-71.73449	Vent 1	Lava from rim of Vent 1 crater
Q62	-39.49862	-71.72275	Summit	Lava from caldera rim
Q63	-39.50037	-71.72420	Summit	Scoured lava near summit
Q65	-39.51431	-71.66669	Vent 14	Vesicular spatter
Q66	-39.52702	-71.67603	?	Lava from unknown flow
Q67	-39.50298	-71.65960	Summit	Mafic lava from cliff
Q69	-39.48869	-71.67398	Vent 15	Lava from Vent 15 flow
H24	-39.47298	-71.63585	Vent 14/15?	Lava surrounding the cold vent
H28	-39.43166	-71.66692	Summit	Non vesicular lava
T1	-39.51823	-71.54813	Quetrupillán	Pumice horizon
T2	-39.51823	-71.54813	Villarrica	Scoria from the scoria layer
T5	-39.52365	-71.55047	Quetrupillán	Pumice horizon
T6	-39.52365	-71.55047	Villarrica	Dark brown soil-like horizon
T7	-39.52365	-71.55047	Villarrica	Fine grained brown unit
T8	-39.52365	-71.55047	Villarrica	Black lithic rich layer
T9	-39.52365	-71.55047	Villarrica	Interbedded dark vesicular scoria/pumice
T10	-39.55344	-71.56437	Quetrupillán	Lower dark grey ashy horizon
T12	-39.52359	-71.55045	Villarrica	Fine grained brown unit
T13	-39.52359	-71.55045	Quetrupillán	Pumice horizon
T14	-39.52359	-71.55045	Villarrica	Orange ashy matrix supported horizon
T15	-39.52359	-71.55045	Villarrica	Dark grey interbedded ash
T16	-39.52359	-71.55045	Villarrica	Orange/brown sandy matrix
P13	-39.42695	-71.76594	Mocho-Ch.?	Pumice
P17	-39.42695	-71.76594	Villarrica	Reddish scoria
P21	-39.42695	-71.76594	Villarrica	Coarse tephra unit
P23	-39.42695	-71.76594	Villarrica	Pumice
P24	-39.42695	-71.76594	Villarrica	Orange scoria

Appendix II: Thin section descriptions

Thirty lava samples and four pyroclastic samples were prepared as polished thin sections (25 × 48 mm), and data, descriptions and photos of them are provided here. If the sample was analysed by XRF then the whole-rock composition is listed, if not then the assumed composition is denoted by (?). Where known, the source of the sample is listed, with vents numbered according to the labelled vents in Figure 2.2. The type of sample, whether lava or pyroclastic deposit, is also noted.

The proportion of phenocrysts, vesicles and groundmass was estimated by eye, as was the proportion of phenocryst phases. The proportion of groundmass phases was determined from the greyscale values of the different components in BSE images of the groundmass, using Fiji. For samples where BSE images were not acquired, the proportion of groundmass phases is not given, only a description of it.

Sample Q3

Whole-rock composition	Trachyte
Source	Vent 2
Type	Lava
Groundmass	94%
Phenocrysts	3%
Vesicles	3%

Phenocrysts

Plagioclase	55%
Clinopyroxene	20%
Orthopyroxene	15%
Oxide	10%

Groundmass

Glass	41%
Plagioclase	53%
Pyroxene	5%
Oxide	1%

Description: Porphyritic lava with sparse phenocrysts of euhedral pristine plagioclase (<1.5 mm), euhedral-subhedral pyroxene and subhedral oxide, and occasional glomerocrysts (<2.5 mm) of the same minerals, in a very dark brown microcrystalline groundmass.

Sample Q7

Whole-rock composition	Trachyte
Source	Vent 3
Type	Lava
Groundmass	85%
Phenocrysts	5%
Vesicles	10%

Phenocrysts

Plagioclase	55%
Clinopyroxene	20%
Orthopyroxene	20%
Oxide	5%

Groundmass

Glass	43%
Plagioclase	50%
Pyroxene	5%
Oxide	2%

Description: Porphyritic lava with phenocrysts of euhedral pristine plagioclase (<1 mm), rare sieve-textured plagioclase (2 mm), euhedral-subhedral pyroxene and subhedral oxide, in a dark brown microcrystalline groundmass. Phenocrysts are aligned with elongate vesicles.

Sample Q8

Whole-rock composition	Trachyandesite
Source	Vent 11
Type	Lava
Groundmass	45%
Phenocrysts	20%
Vesicles	35%

Phenocrysts

Plagioclase	60%
Clinopyroxene	20%
Orthopyroxene	3%
Olivine	15%
Oxide	2%

Groundmass

Glass	26%
Plagioclase	59%
Pyroxene	13%
Oxide	2%

Description: Porphyritic lava with phenocrysts of euhedral sieve-textured plagioclase (<2 mm), euhedral-subhedral pyroxene, subhedral olivine with resorbed rims and subhedral oxide, and glomerocrysts (<7 mm) of plagioclase and pyroxene, in a black glassy groundmass containing non-aligned plagioclase laths.

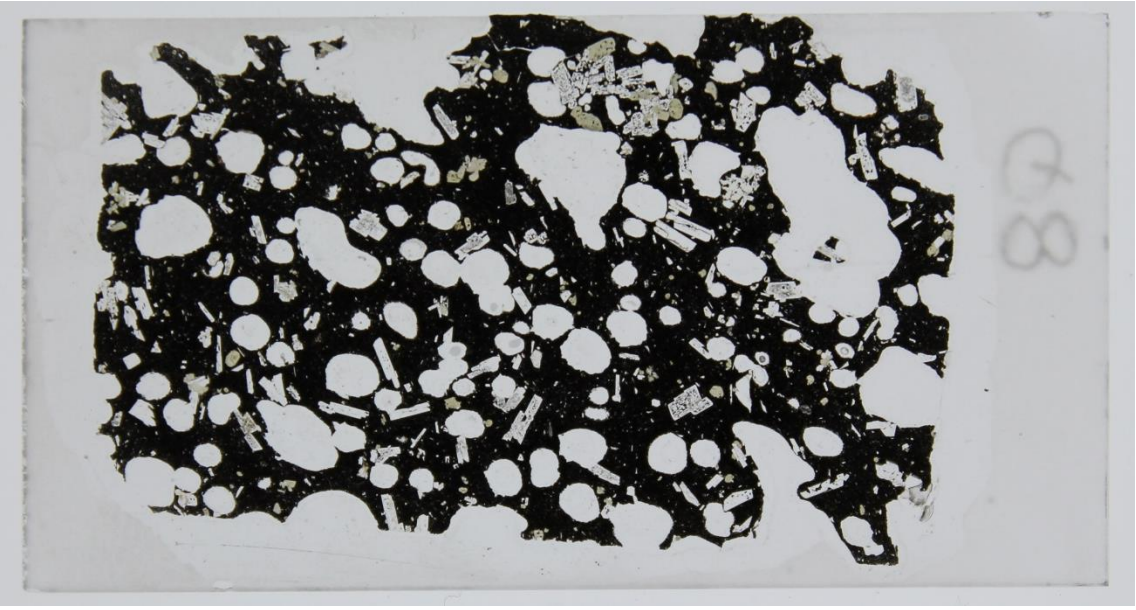

Sample Q10

Whole-rock composition	Trachyte
Source	Vent 4
Type	Lava
Groundmass	80%
Phenocrysts	5%
Vesicles	15%

Phenocrysts

Plagioclase	65%
Clinopyroxene	15%
Orthopyroxene	15%
Oxide	5%

Groundmass

Glass	41%
Plagioclase	50%
Pyroxene	7%
Oxide	2%

Description: Porphyritic lava with sparse phenocrysts of euhedral plagioclase (<1.5 mm), euhedral-subhedral pyroxene and euhedral oxide in a dark brown microcrystalline groundmass. Phenocrysts are aligned with elongate vesicles.

Sample Q12

Whole-rock composition	Trachyte
Source	Vent 5
Type	Lava
Groundmass	75%
Phenocrysts	7%
Vesicles	18%

Phenocrysts

Plagioclase	70%
Clinopyroxene	13%
Orthopyroxene	12%
Oxide	5%

Groundmass

Glass	46%
Plagioclase	47%
Pyroxene	4%
Oxide	3%

Description: Porphyritic lava with sparse phenocrysts of euhedral plagioclase, subhedral pyroxene and subhedral oxide, and glomerocrysts (<4 mm) of the same minerals, in a brown microcrystalline groundmass.

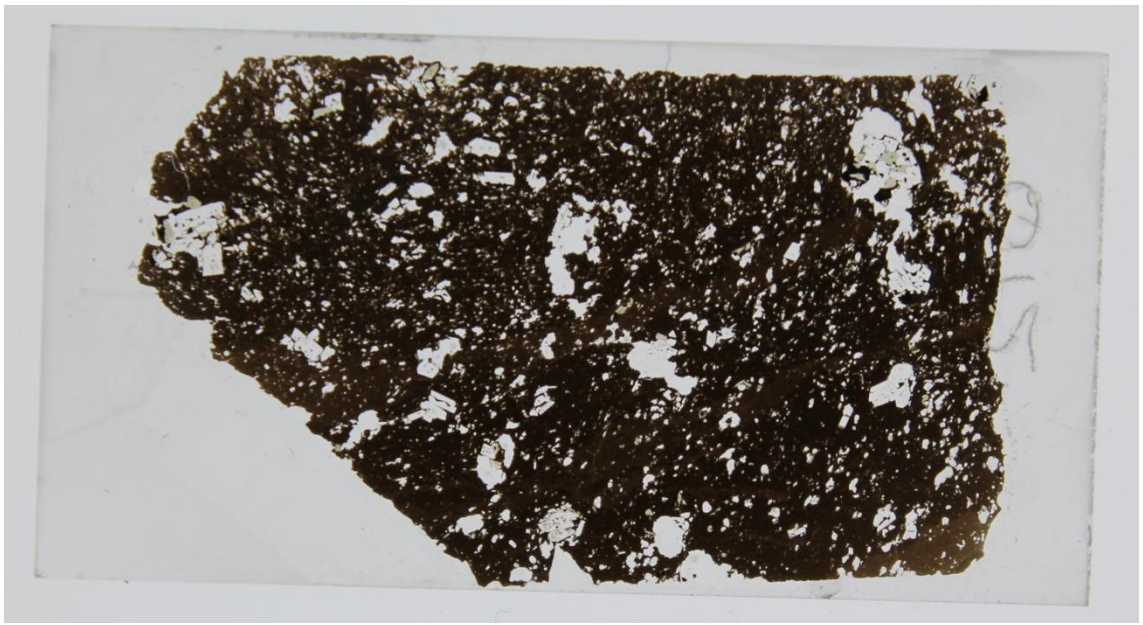

Sample Q16

Whole-rock composition	Basaltic andesite
Source	Summit
Type	Lava
Groundmass	80%
Phenocrysts	5%
Vesicles	15%

Phenocrysts

Plagioclase	70%
Clinopyroxene	15%
Orthopyroxene	3%
Olivine	10%
Oxide	2%

Groundmass	Fully crystalline groundmass composed predominantly of plagioclase laths (with no strong orientation), along with oxides and pyroxenes.
Description	Porphyritic lava with phenocrysts of pristine and sieve-textured euhedral plagioclase (<3 mm), euhedral-subhedral pyroxene, subhedral olivine (<2 mm) and subhedral oxide, and glomerocrysts (<4 mm) of sieve-textured plagioclase and pyroxene, in a crystalline groundmass of non-aligned plagioclase laths, oxides and pyroxenes.

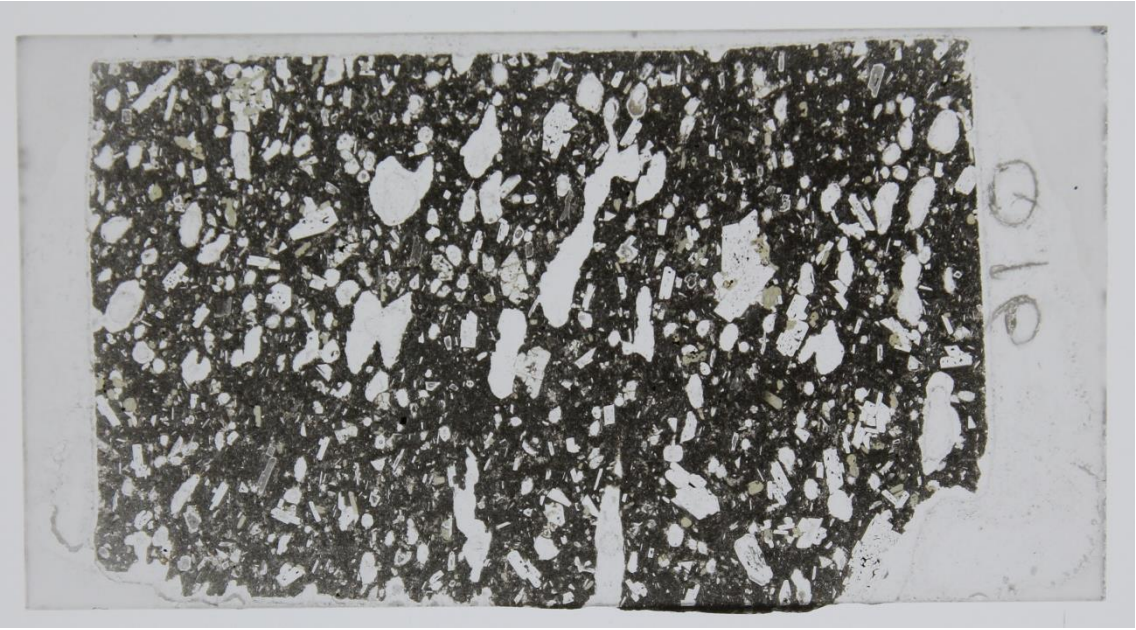

Sample Q17

Whole-rock composition	Trachyandesite
Source	Vent 12
Type	Lava
Groundmass	75%
Phenocrysts	10%
Vesicles	15%

Phenocrysts

Plagioclase	60%
Clinopyroxene	25%
Orthopyroxene	6%
Olivine	6%
Oxide	3%

Groundmass

Glass	53%
Plagioclase	36%
Pyroxene	7%
Oxide	4%

Description: Porphyritic lava with phenocrysts of euhedral sieve-textured plagioclase (<2.5 mm), euhedral-subhedral pyroxene (<2 mm), subhedral olivine and subhedral oxide, and glomerocrysts (<3 mm) of plagioclase and pyroxene, in a dark brown glassy groundmass containing plagioclase laths. Some large plagioclase phenocrysts have small pyroxenes growing around their edges.

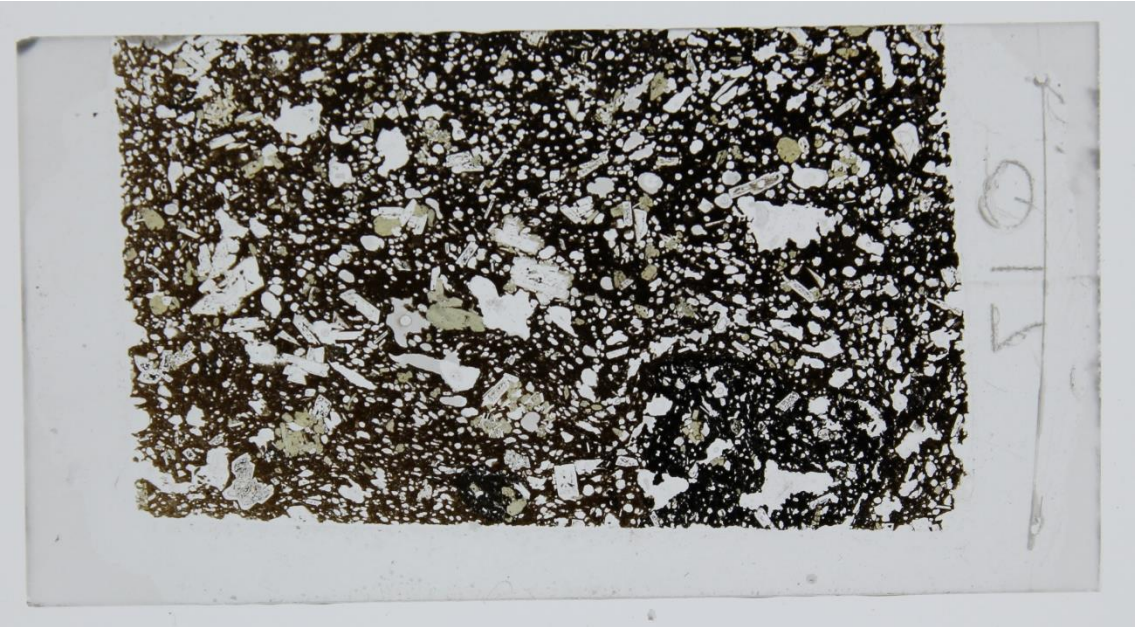

Sample Q20

Whole-rock composition	Trachyandesite
Source	Summit
Type	Lava
Groundmass	75%
Phenocrysts	5%
Vesicles	20%

Phenocrysts

Plagioclase	60%
Clinopyroxene	20%
Orthopyroxene	10%
Olivine	5%
Oxide	5%

Groundmass

Glass	56%
Plagioclase	36%
Pyroxene	6%
Oxide	2%

Description: Porphyritic lava with phenocrysts of pristine and sieve-textured euhedral plagioclase (<2 mm), euhedral-subhedral pyroxene, and subhedral olivine, and glomerocrysts (<2 mm) of plagioclase, pyroxene and oxide, in a dark brown microcrystalline groundmass.

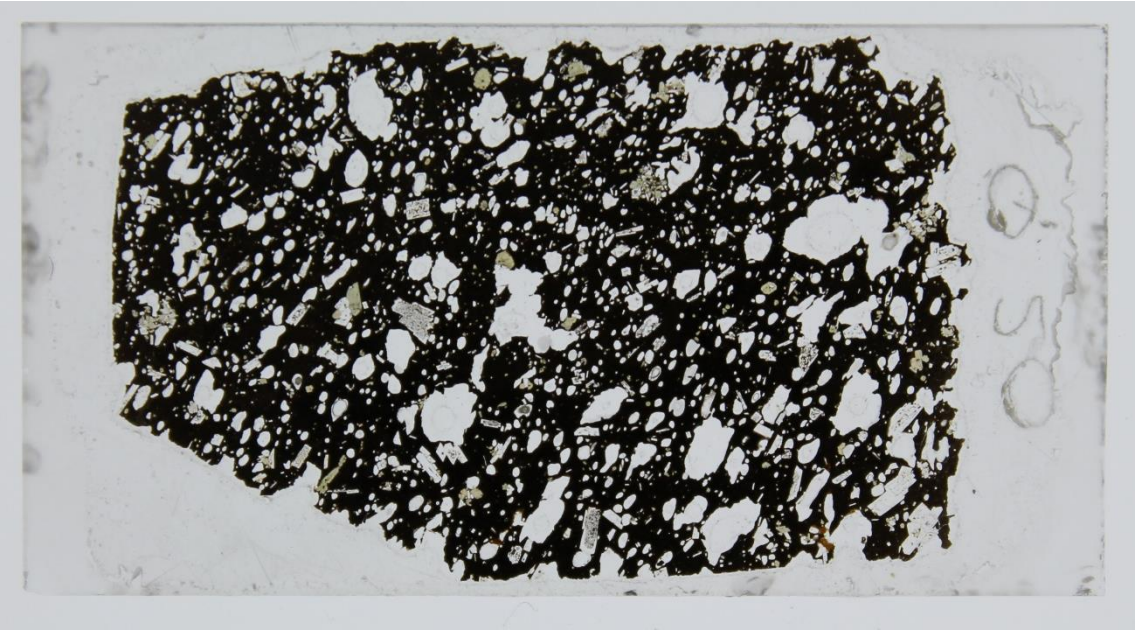

Sample Q23

Whole-rock composition	Basaltic andesite
Source	Summit
Type	Lava
Groundmass	75%
Phenocrysts	10%
Vesicles	15%

Phenocrysts

Plagioclase	50%
Clinopyroxene	25%
Orthopyroxene	10%
Olivine	10%
Oxide	5%

Groundmass	Black microcrystalline groundmass with occasional plagioclase laths and pyroxenes.
Description	Porphyritic lava with phenocrysts of pristine and sieve-textured euhedral plagioclase (<5 mm), euhedral-subhedral pyroxene, subhedral olivine and subhedral oxide, and glomerocrysts (<4 mm) of plagioclase and pyroxene, in a black microcrystalline groundmass.

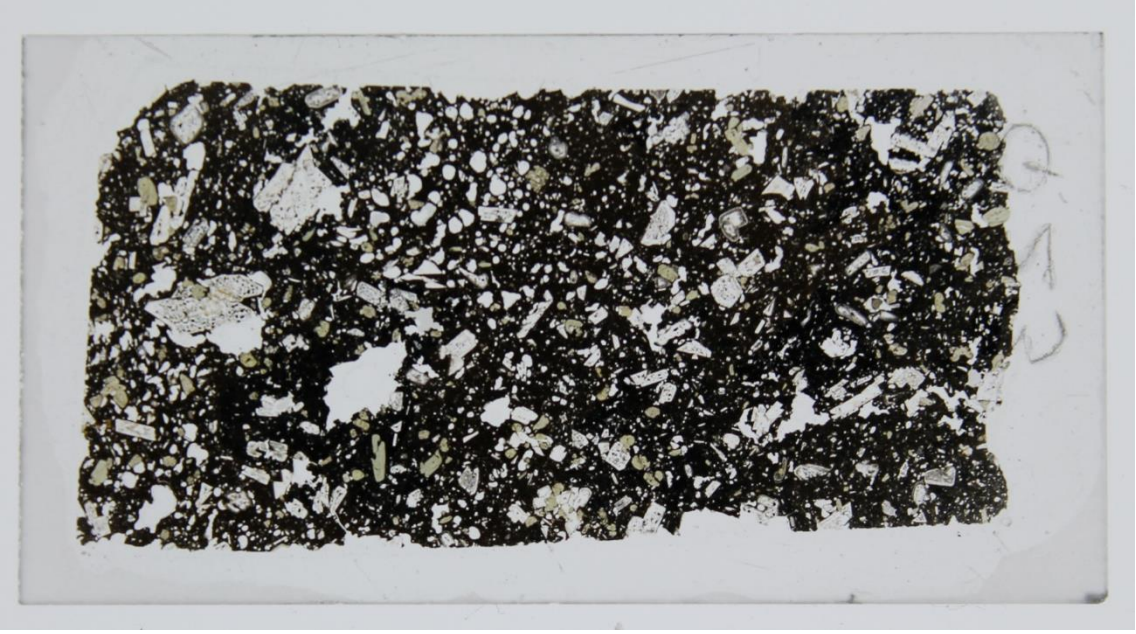

Sample Q25

Whole-rock composition	Trachyte
Source	Unknown
Type	Pumice
Groundmass	40%
Phenocrysts	2%
Vesicles	58%

Phenocrysts

Plagioclase	70%
Clinopyroxene	20%
Oxide	10%

Groundmass	Very pale brown glass filaments between vesicles
Description	Pumice composed of pale brown glass filaments between elongate vesicles, with very rare phenocrysts of euhedral pristine plagioclase, subhedral pyroxene and subhedral oxide.

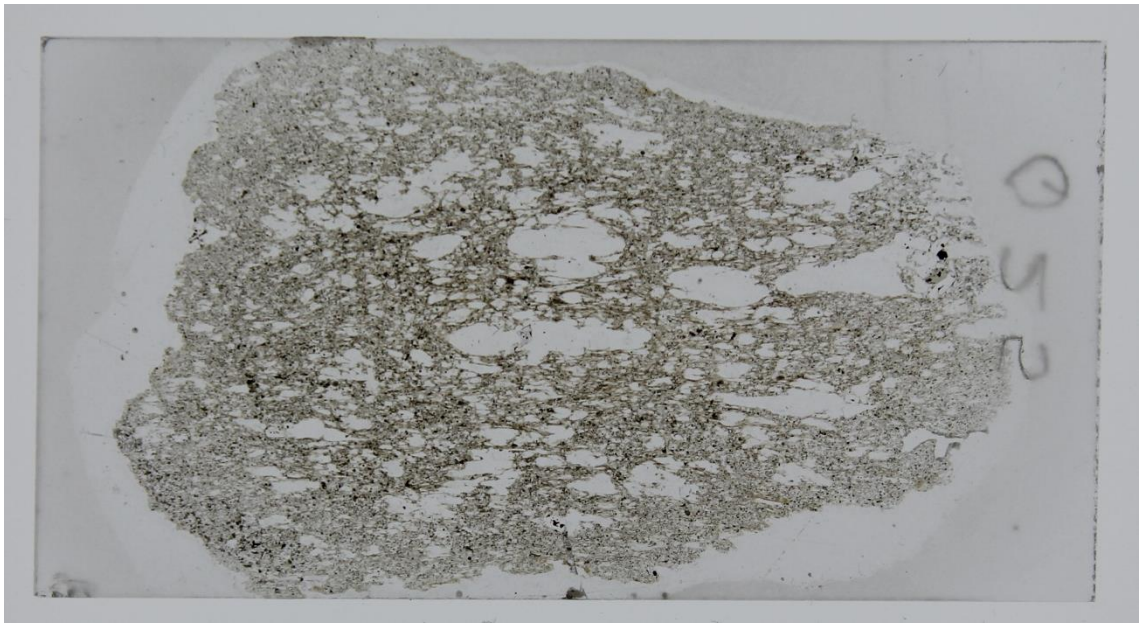

Sample Q26

Whole-rock composition	Trachyte
Source	Unknown
Type	Scoriaceous pumice
Groundmass	49%
Phenocrysts	1%
Vesicles	50%

Phenocrysts

Plagioclase	40%
Clinopyroxene	40%
Oxide	20%

Groundmass	Dark brown glass filaments between vesicles
Description	Scoriaceous pumice composed of dark brown glass filaments between elongate vesicles, with very rare phenocrysts of euhedral pristine plagioclase, subhedral pyroxene and euhedral oxide.

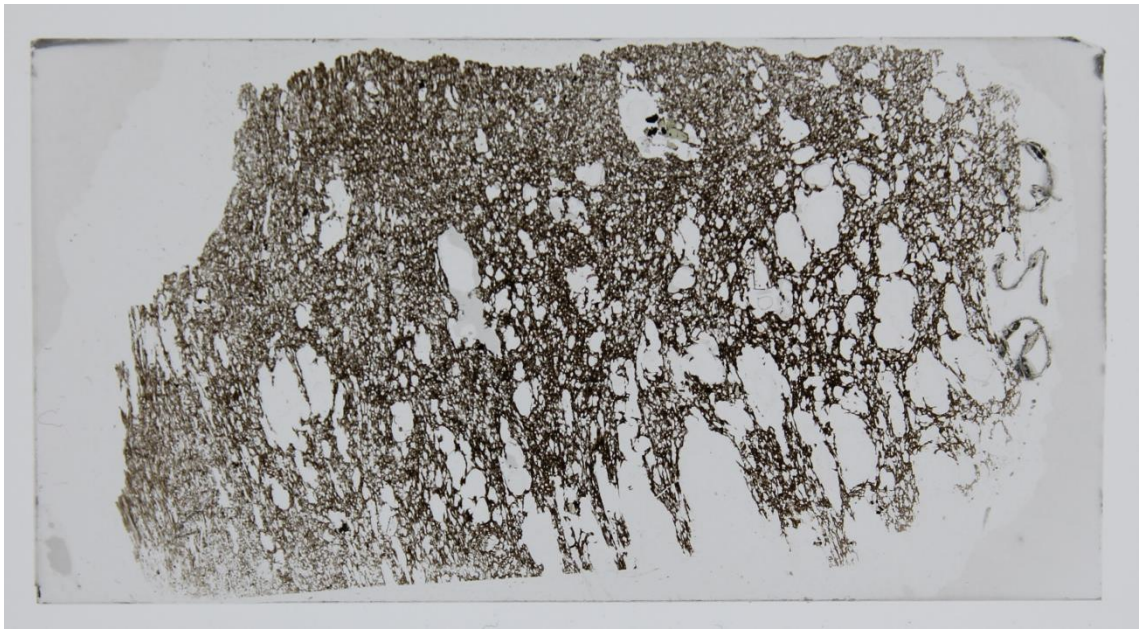

Sample Q27

Whole-rock composition	Trachyte (?)
Source	Unknown
Type	Scoriaceous pumice
Groundmass	49%
Phenocrysts	1%
Vesicles	50%

Phenocrysts

Plagioclase	50%
Clinopyroxene	30%
Oxide	20%

Groundmass	Dark brown glass filaments between vesicles
Description	Scoriaceous pumice composed of dark brown glass filaments between round-elongate vesicles, with very rare phenocrysts of sieve-textured and pristine euhedral plagioclase, subhedral pyroxene and subhedral oxide.

Sample Q29

Whole-rock composition	Trachyte
Source	Vent 14
Type	Lava
Groundmass	45%
Phenocrysts	10%
Vesicles	45%

Phenocrysts

Plagioclase	70%
Clinopyroxene	15%
Orthopyroxene	12%
Oxide	3%

Groundmass

Glass	98%
Plagioclase	1%
Oxide	1%

Description: Porphyritic lava with phenocrysts of euhedral pristine plagioclase (<1.5 mm), euhedral-subhedral pyroxene and euhedral oxide, and occasional glomerocrysts of the same minerals, in a fully glassy dark brown groundmass.

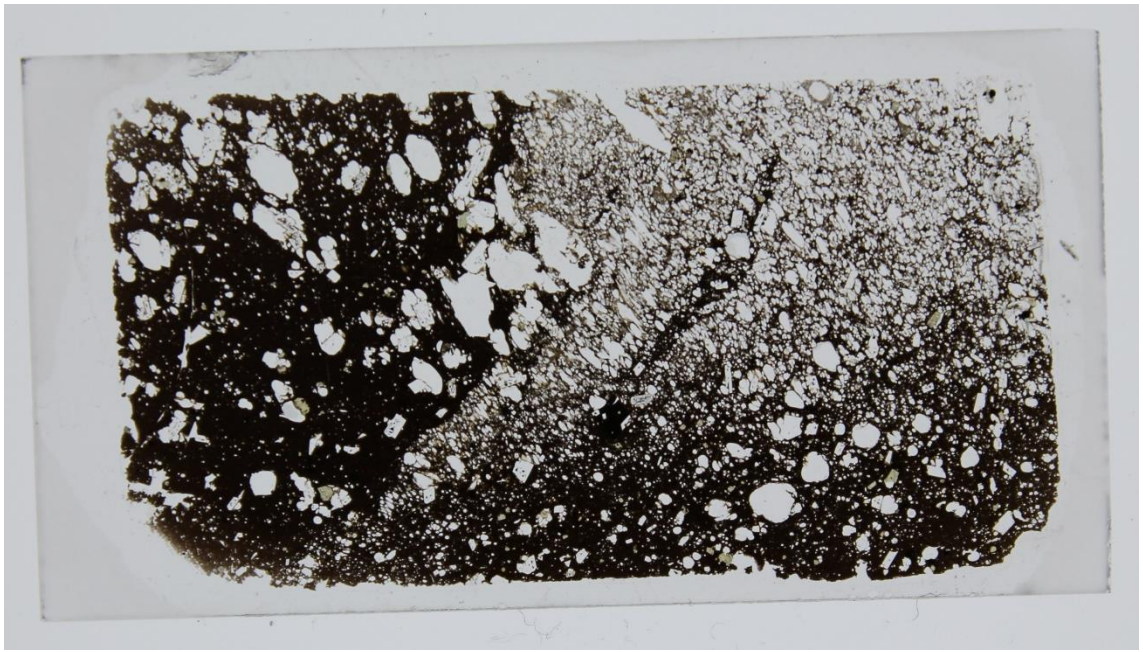

Sample Q31

Whole-rock composition	Trachyte
Source	Vent 13
Type	Lava
Groundmass	85%
Phenocrysts	5%
Vesicles	10%

Phenocrysts

Plagioclase	68%
Clinopyroxene	15%
Orthopyroxene	15%
Oxide	2%

Groundmass

Glass	76%
Plagioclase	18%
Pyroxene	4%
Oxide	2%

Description: Porphyritic lava with sparse phenocrysts of euhedral plagioclase (<2 mm), subhedral pyroxene and subhedral oxide, in a fully glassy black groundmass. Phenocrysts are aligned with elongate vesicles.

Sample Q34

Whole-rock composition	Trachyte
Source	Vent 13
Type	Lava
Groundmass	65%
Phenocrysts	15%
Vesicles	20%

Phenocrysts

Plagioclase	65%
Clinopyroxene	15%
Orthopyroxene	15%
Oxide	5%

Groundmass	Dark brown microcrystalline groundmass with bands of darker and lighter brown colour, some of which contain plagioclase laths aligned with the direction of banding.
Description	Porphyritic lava with phenocrysts of euhedral pristine plagioclase (<1.5 mm), subhedral pyroxene and subhedral oxide, and glomerocrysts (<2.5 mm) of the same minerals, in a dark brown microcrystalline groundmass. Phenocrysts and groundmass plagioclase laths are aligned with elongate vesicles.

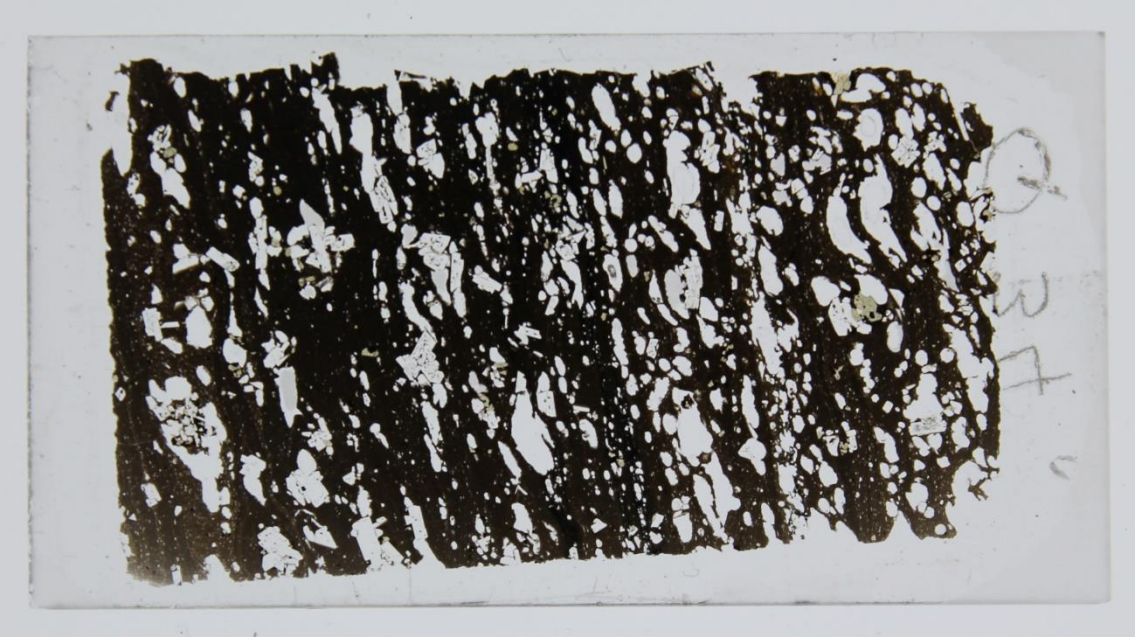

Sample Q36

Whole-rock composition	Trachyte
Source	Vent 14
Type	Lava
Groundmass	85%
Phenocrysts	10%
Vesicles	5%

Phenocrysts

Plagioclase	50%
Clinopyroxene	20%
Orthopyroxene	15%
Oxide	15%

Groundmass

Glass	54%
Plagioclase	40%
Pyroxene	5%
Oxide	1%

Description: Porphyritic lava with phenocrysts of pristine and occasional sieve-textured euhedral plagioclase, euhedral-subhedral pyroxene and subhedral oxide, and glomerocrysts (<4 mm) of the same minerals, in a crystalline groundmass of non-aligned plagioclase laths, pyroxene and oxide in brown glass.

Sample Q39

Whole-rock composition	Trachyte
Source	Vent 9
Type	Lava
Groundmass	70%
Phenocrysts	10%
Vesicles	20%

Phenocrysts

Plagioclase	65%
Clinopyroxene	15%
Orthopyroxene	10%
Oxide	10%

Groundmass

Glass	43%
Plagioclase	47%
Pyroxene	9%
Oxide	1%

Description: Porphyritic lava with phenocrysts of euhedral pristine plagioclase, euhedral-subhedral pyroxene and subhedral oxide, with glomerocrysts of the same minerals, in a dark brown microcrystalline groundmass containing aligned plagioclase laths.

Sample Q40

Whole-rock composition	Trachyte
Source	Vent 8
Type	Lava
Groundmass	50%
Phenocrysts	10%
Vesicles	40%

Phenocrysts

Plagioclase	50%
Clinopyroxene	20%
Orthopyroxene	20%
Oxide	10%

Groundmass

Glass	51%
Plagioclase	41%
Pyroxene	7%
Oxide	1%

Description: Porphyritic lava with phenocrysts of euhedral pristine plagioclase, subhedral pyroxene and subhedral oxide, and glomerocrysts (<2 mm) of the same minerals, in a groundmass composed of brown microcrystalline and black glass bands. Phenocrysts are aligned with elongate vesicles, and the lava is banded with bands of varying vesicularity.

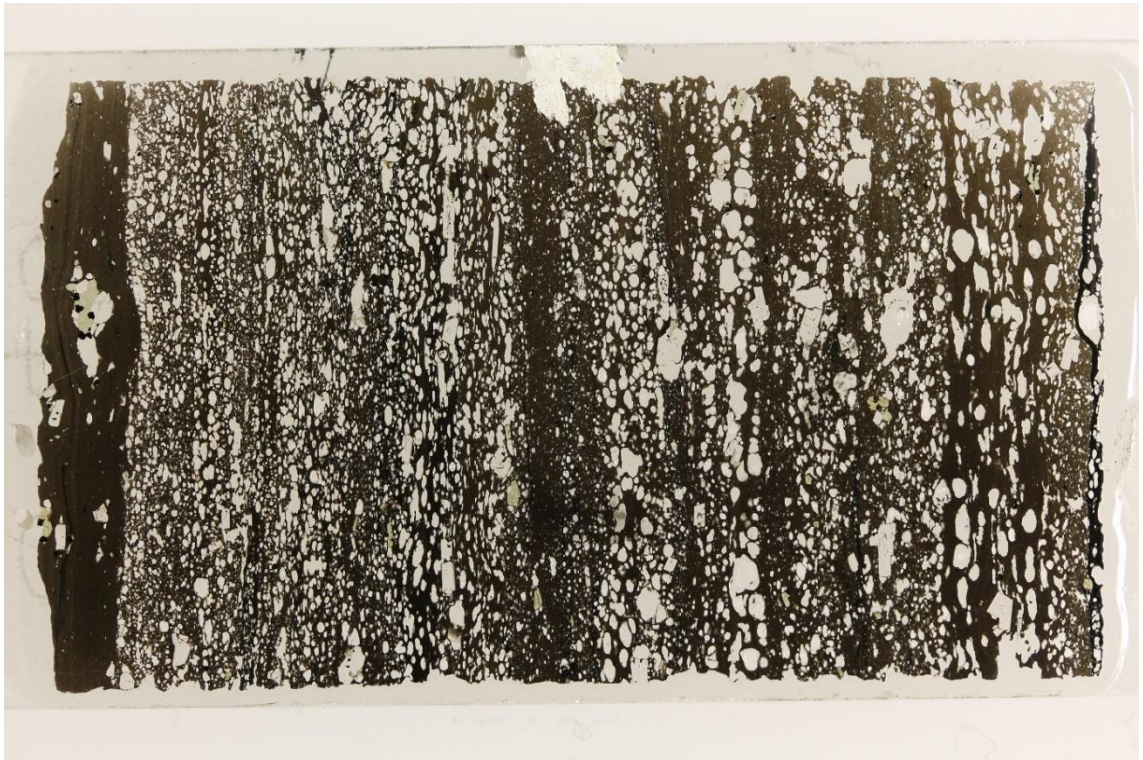

Sample Q41

Whole-rock composition	Trachyte
Source	Vent 7
Type	Lava
Groundmass	50%
Phenocrysts	10%
Vesicles	40%

Phenocrysts

Plagioclase	60%
Clinopyroxene	15%
Orthopyroxene	15%
Oxide	10%

Groundmass

Glass	40%
Plagioclase	52%
Pyroxene	7%
Oxide	1%

Description: Porphyritic lava with phenocrysts of euhedral pristine plagioclase, subhedral pyroxene and subhedral oxide, and glomerocrysts (<2mm) of the same minerals, in a brown microcrystalline groundmass.

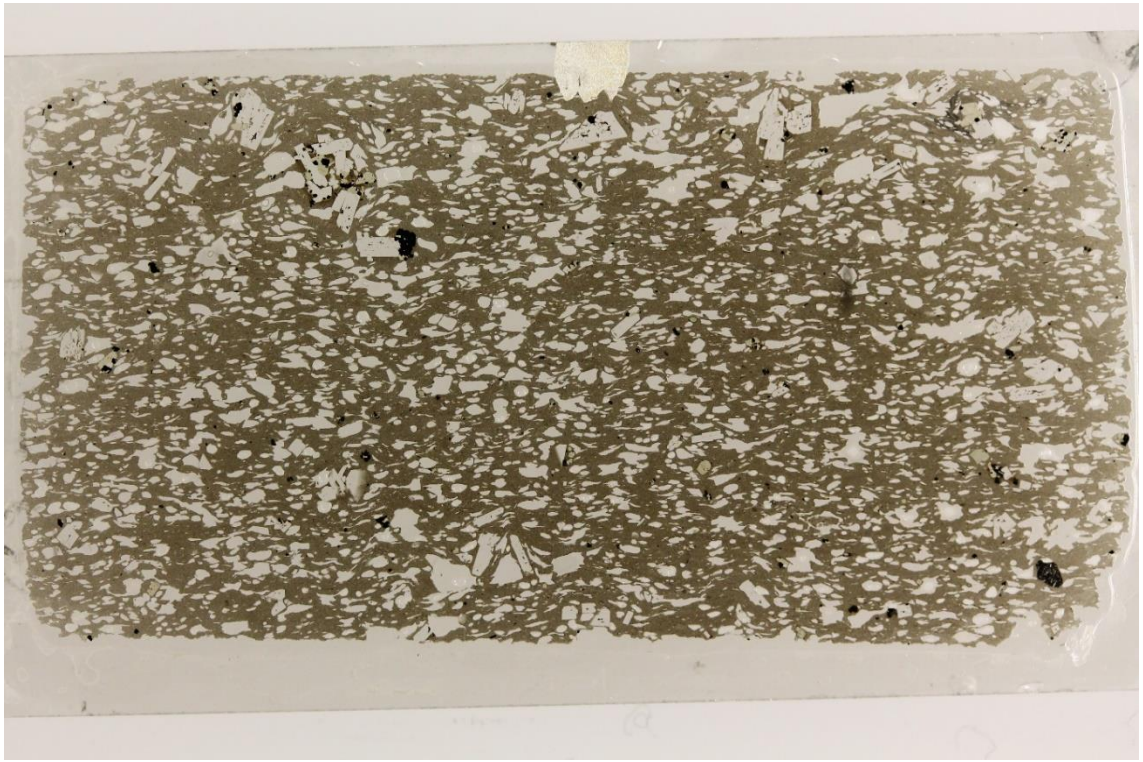

Sample Q46

Whole-rock composition	Trachyte (containing andesite enclave)
Source	Vent 6
Type	Lava
Groundmass	55%
Phenocrysts	10%
Vesicles	35%

Phenocrysts

Plagioclase	60%
Clinopyroxene	15%
Orthopyroxene	15%
Oxide	10%

Groundmass

Glass	49%
Plagioclase	44%
Pyroxene	6%
Oxide	1%

Description: Porphyritic lava with phenocrysts of pristine and sieve-textured plagioclase (<3 mm), euhedral-subhedral pyroxenes and subhedral oxides, with glomerocrysts (<3 mm) of the same minerals in dark brown microcrystalline groundmass. The andesite enclave is porphyritic, with phenocrysts of sieve-textured and pristine euhedral plagioclases, subhedral pyroxene, subhedral olivine and euhedral-subhedral oxide, and glomerocrysts (<2 mm) of the same minerals, in a fully crystalline groundmass of plagioclase laths, pyroxene and oxide.

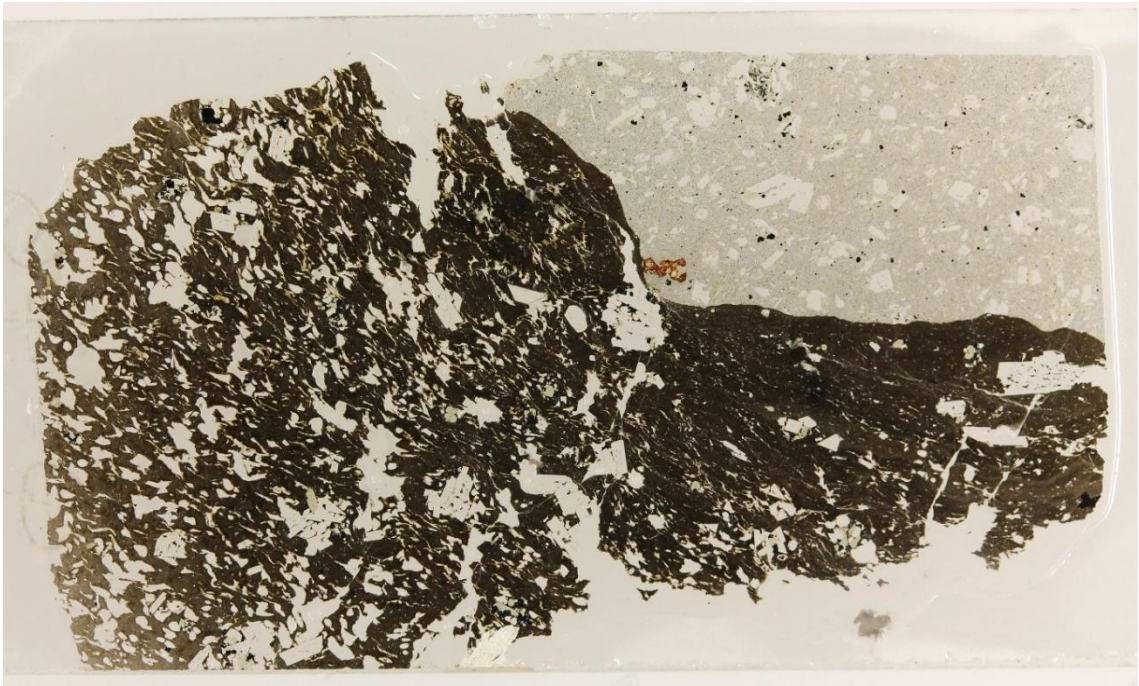

Sample Q50

Whole-rock composition	Basaltic andesite
Source	Vent 10
Type	Lava
Groundmass	50%
Phenocrysts	30%
Vesicles	20%

Phenocrysts

Plagioclase	40%
Clinopyroxene	19%
Orthopyroxene	5%
Olivine	35%
Oxide	1%

Groundmass

Glass	17%
Plagioclase	58%
Pyroxene	20%
Oxide	4%

Description: Porphyritic lava with phenocrysts of euhedral sieve-textured plagioclase (<3 mm), subhedral olivine and euhedral-subhedral pyroxene, in a crystalline black groundmass containing non-aligned plagioclase laths.

Sample Q53

Whole-rock composition	Trachyte
Source	Vent 2
Type	Lava
Groundmass	92%
Phenocrysts	8%
Vesicles	0%

Phenocrysts

Plagioclase	55%
Clinopyroxene	20%
Orthopyroxene	13%
Oxide	12%

Groundmass

Glass	55%
Plagioclase	38%
Pyroxene	6%
Oxide	1%

Description: Porphyritic lava with sparse phenocrysts of euhedral pristine plagioclase (<1.5 mm), subhedral pyroxene and euhedral-subhedral oxide, and glomerocrysts (<2.5 mm) of the same minerals, in a dark brown and black microcrystalline groundmass that is banded on a mm scale. Phenocrysts are aligned with the groundmass bands.

Sample Q54

Whole-rock composition	Trachyte
Source	Vent 4
Type	Lava
Groundmass	55%
Phenocrysts	10%
Vesicles	35%

Phenocrysts

Plagioclase	65%
Clinopyroxene	15%
Orthopyroxene	15%
Oxide	5%

Groundmass	Fully glassy groundmass of dark brown glass
Description	Porphyritic lava with sparse phenocrysts of euhedral pristine plagioclase, subhedral pyroxene and subhedral oxide, and occasional glomerocrysts (<2 mm) of the same minerals, in a fully glassy dark brown groundmass

Sample Q56

Whole-rock composition	Trachyte
Source	Vent 5
Type	Lava
Groundmass	80%
Phenocrysts	10%
Vesicles	10%

Phenocrysts

Plagioclase	65%
Clinopyroxene	15%
Orthopyroxene	15%
Oxide	5%

Groundmass	Dark brown microcrystalline groundmass
Description	Porphyritic lava with sparse phenocrysts of euhedral pristine plagioclase (<1.5 mm), euhedral-subhedral pyroxene and euhedral-subhedral oxide, and occasional glomerocrysts (<2.5 mm) of the same minerals, in a dark brown microcrystalline groundmass.

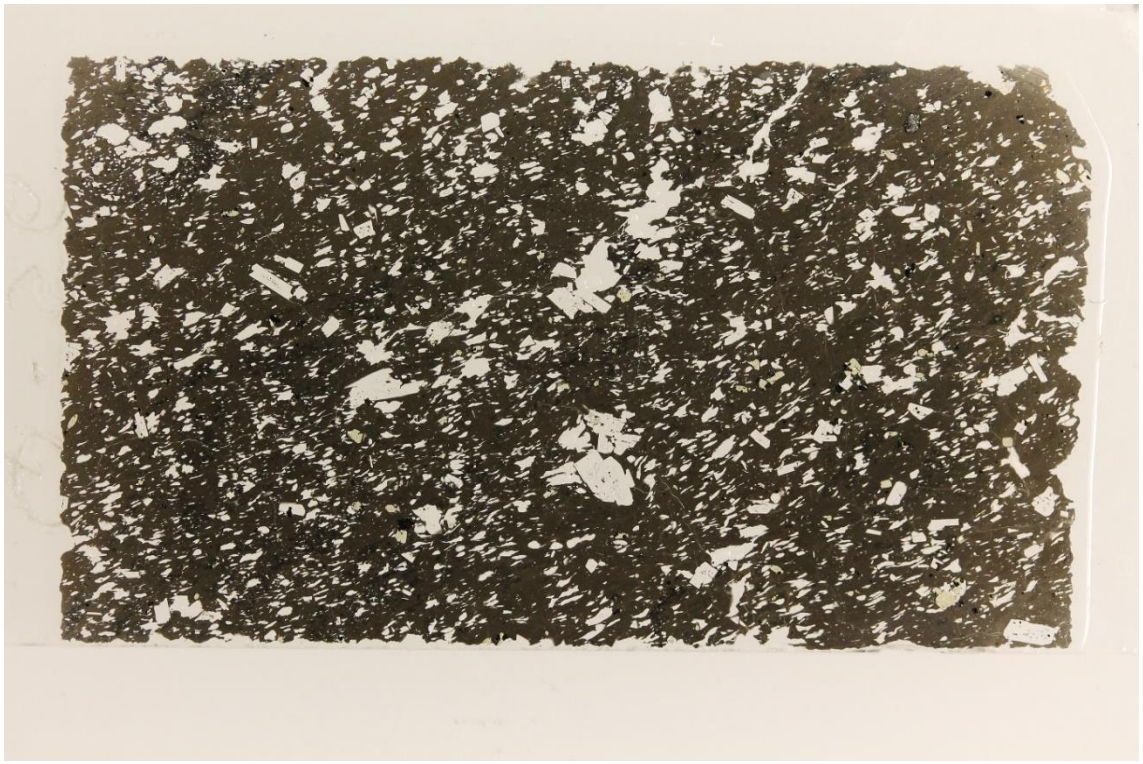

Sample Q61

Whole-rock composition	Trachyte
Source	Vent 1
Type	Lava
Groundmass	45%
Phenocrysts	5%
Vesicles	50%

Phenocrysts

Plagioclase	65%
Clinopyroxene	15%
Orthopyroxene	15%
Oxide	5%

Groundmass

Glass	83%
Plagioclase	1%
Pyroxene	15%
Oxide	1%

Description: Highly vesicular porphyritic lava with sparse phenocrysts of euhedral pristine plagioclase and euhedral-subhedral pyroxene, and glomerocrysts (<2 mm) of plagioclase, pyroxene and oxide, in a dark brown glassy groundmass.

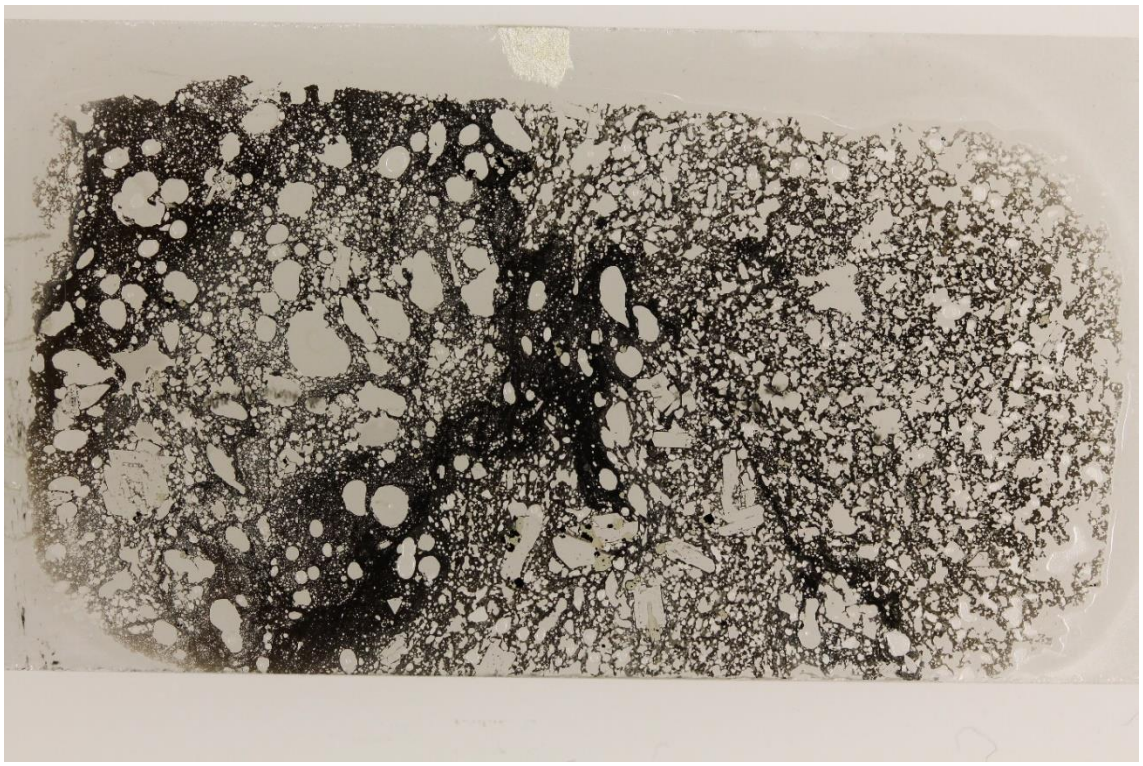

Sample Q62

Whole-rock composition	Trachyte
Source	Summit
Type	Lava
Groundmass	85%
Phenocrysts	5%
Vesicles	10%

Phenocrysts

Plagioclase	70%
Clinopyroxene	20%
Orthopyroxene	8%
Oxide	2%

Groundmass	Dark brown microcrystalline groundmass
Description	Porphyritic lava with phenocrysts of euhedral pristine plagioclase, euhedral-subhedral pyroxene and subhedral oxide, and occasional glomerocrysts (<4 mm) of plagioclase and pyroxene, in a dark brown microcrystalline groundmass. Phenocrysts are aligned with elongate vesicles and bands in the microcrystalline groundmass.

Sample Q63

Whole-rock composition	Basaltic andesite
Source	Summit
Type	Lava
Groundmass	75%
Phenocrysts	25%
Vesicles	0%

Phenocrysts

Plagioclase	50%
Clinopyroxene	25%
Orthopyroxene	5%
Olivine	15%
Oxide	5%

Groundmass	Fully crystalline groundmass, predominantly composed of non-aligned plagioclase laths, as well as pyroxenes and oxides
Description	Porphyritic lava with phenocrysts of pristine and sieve-textured euhedral plagioclase (<2 mm), euhedral-subhedral pyroxene, subhedral olivine and subhedral oxide, and glomerocrysts (<3.5 mm) of plagioclase, pyroxene and oxide, in a crystalline groundmass of non-aligned plagioclase laths.

Sample Q65

Whole-rock composition	Trachyte
Source	Vent 14
Type	Lava
Groundmass	45%
Phenocrysts	10%
Vesicles	45%

Phenocrysts

Plagioclase	75%
Clinopyroxene	10%
Orthopyroxene	10%
Oxide	5%

Groundmass

Glass	73%
Plagioclase	20%
Pyroxene	6%
Oxide	1%

Description: Highly vesicular porphyritic lava with phenocrysts of euhedral pristine plagioclase and subhedral pyroxene, and occasional glomerocrysts of plagioclase, pyroxene and oxide, in a brown glassy groundmass.

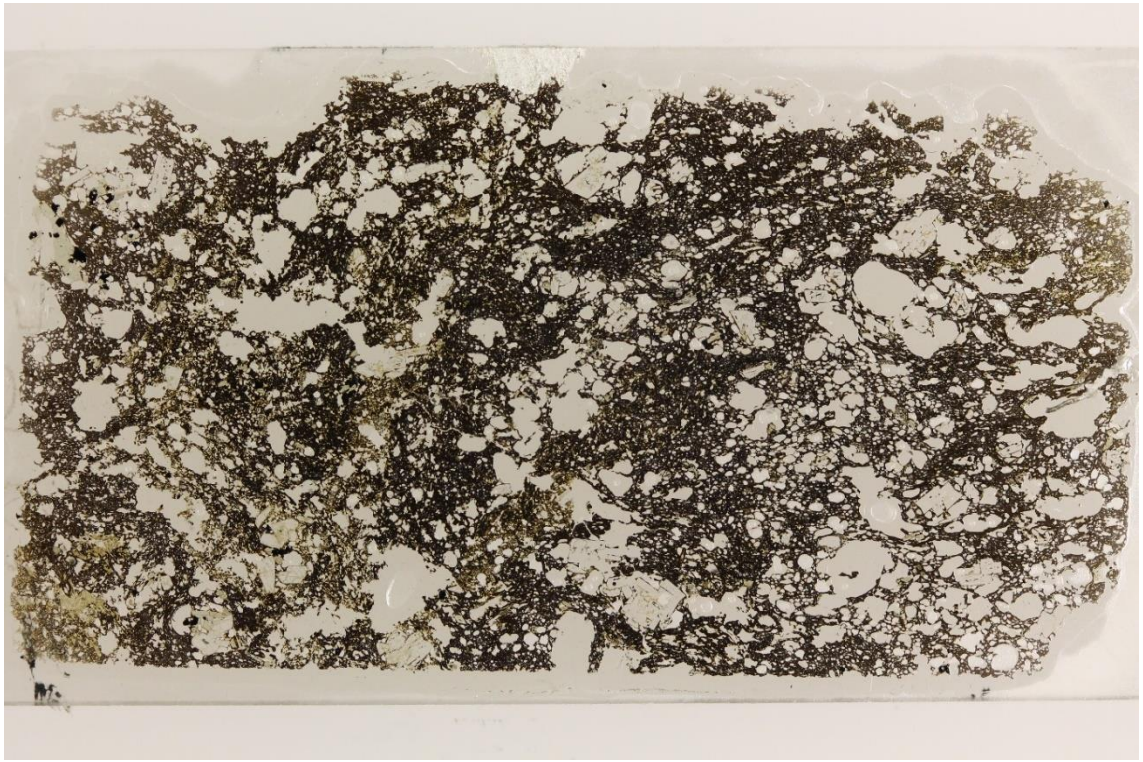

Sample Q66

Whole-rock composition	Trachyte
Source	Unknown
Type	Lava
Groundmass	55%
Phenocrysts	15%
Vesicles	30%

Phenocrysts

Plagioclase	50%
Clinopyroxene	20%
Orthopyroxene	15%
Oxide	15%

Groundmass	Microcrystalline brown groundmass
Description	Porphyritic lava with phenocrysts of euhedral pristine plagioclase, euhedral pyroxene and subhedral oxide, and glomerocrysts (<5 mm) of the same minerals, in a microcrystalline brown groundmass.

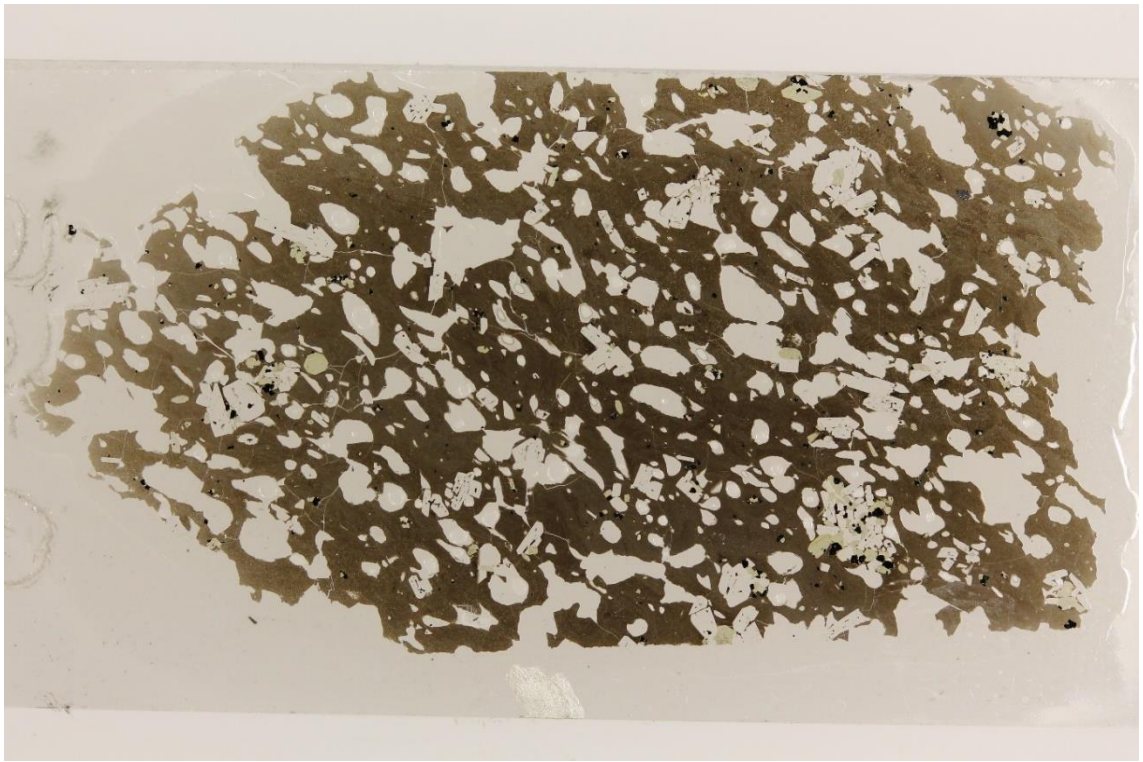

Sample Q67

Whole-rock composition	Basalt
Source	Summit
Type	Lava
Groundmass	80%
Phenocrysts	15%
Vesicles	5%

Phenocrysts

Plagioclase	40%
Clinopyroxene	25%
Olivine	30%
Oxide	5%

Groundmass

Plagioclase	40%
Pyroxene	20%
Olivine	25%
Oxide	15%

Description: Porphyritic lava with phenocrysts of euhedral sieve-textured plagioclase (<2 mm), euhedral-subhedral olivine and euhedral-subhedral pyroxene (<2.5 mm) in a coarsely crystalline groundmass composed of aligned plagioclase laths, olivine, pyroxene and oxides.

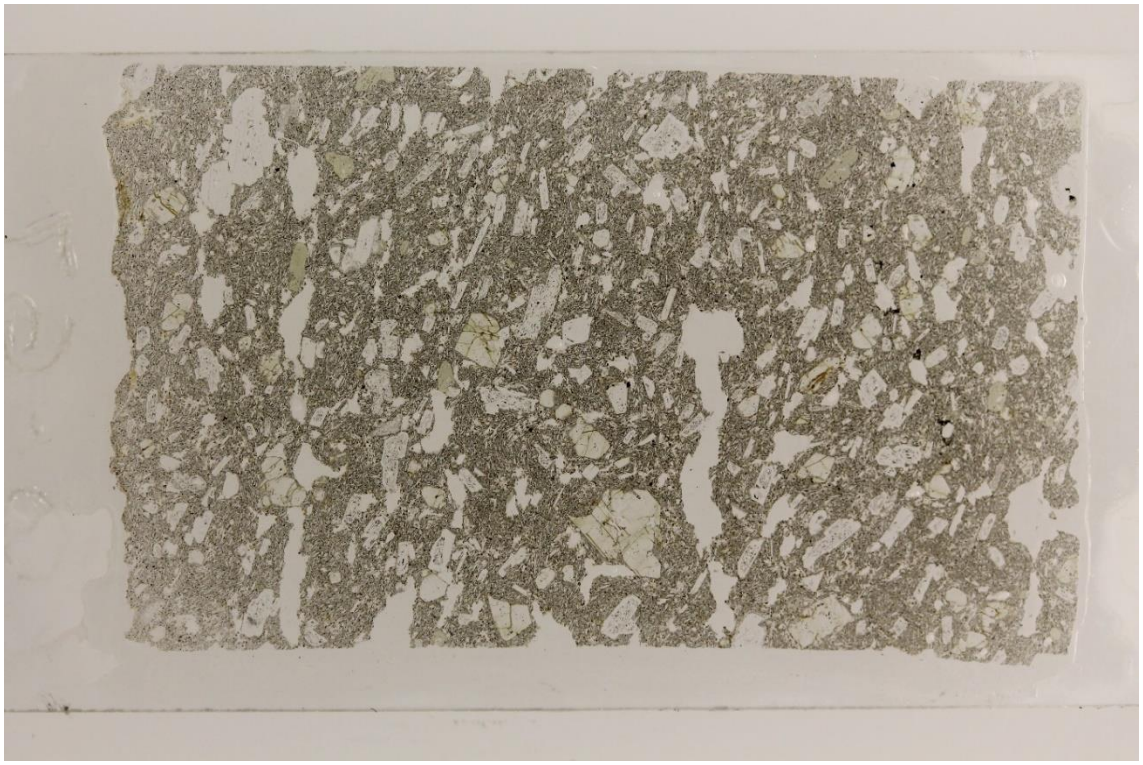

Sample Q69

Whole-rock composition	Trachyte
Source	Vent 15
Type	Lava
Groundmass	75%
Phenocrysts	10%
Vesicles	15%

Phenocrysts

Plagioclase	55%
Clinopyroxene	15%
Orthopyroxene	20%
Oxide	10%

Groundmass	Microcrystalline brown groundmass
Description	Porphyritic lava with phenocrysts of euhedral pristine plagioclase (<1.5 mm), euhedral-subhedral pyroxene and subhedral oxide in a brown microcrystalline groundmass.

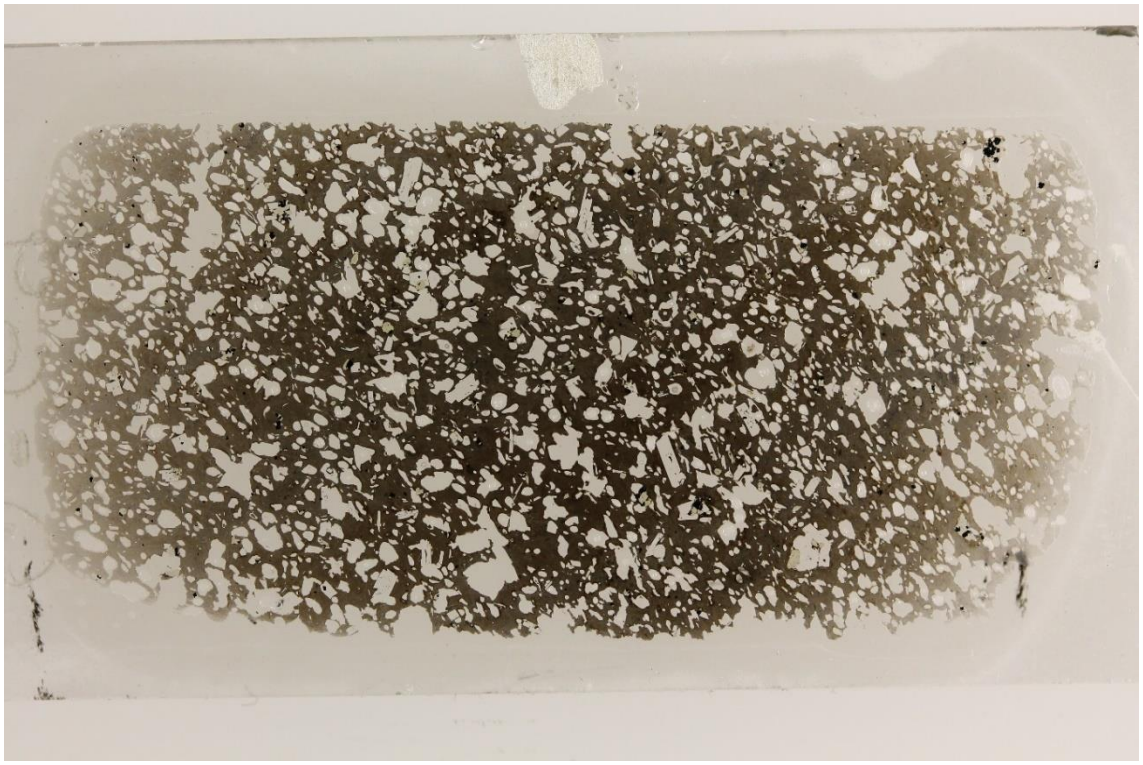

Sample H19

Whole-rock composition	Trachyte (?)
Source	Summit
Type	Lava
Groundmass	85%
Phenocrysts	5%
Vesicles	10%

Phenocrysts

Plagioclase	65%
Clinopyroxene	20%
Orthopyroxene	10%
Oxide	5%

Groundmass

Glass	50%
Plagioclase	39%
Pyroxene	8%
Oxide	3%

Description: Porphyritic lava with sparse phenocrysts of euhedral pristine plagioclase (<1.5 mm), subhedral pyroxene and subhedral oxide and glomerocrysts (<2 mm) of the same minerals, in a dark brown microcrystalline groundmass.

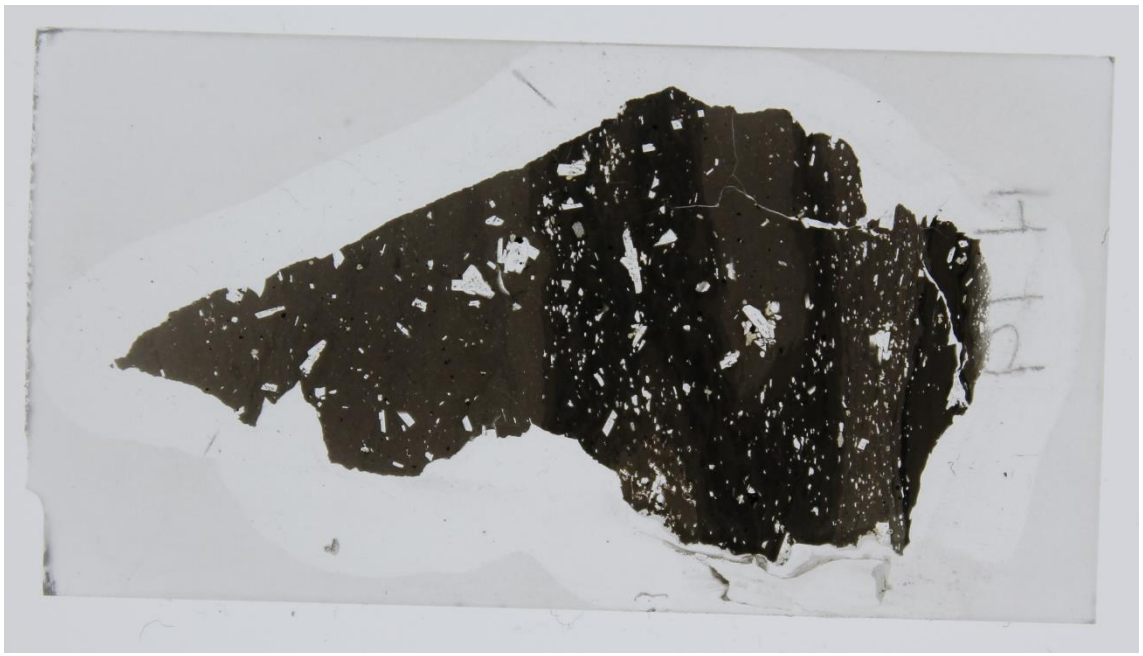

Sample H21

Whole-rock composition	Trachyte (?)
Source	Unknown
Type	Pumice
Groundmass	40%
Phenocrysts	1%
Vesicles	59%

Phenocrysts

Plagioclase	60%
Clinopyroxene	20%
Orthopyroxene	10%
Oxide	10%

Groundmass	Brown glass filaments between vesicles
Description	Pumice composed of brown glass filaments between vesicles, with rare phenocrysts of euhedral pristine plagioclase, subhedral pyroxene and subhedral oxide.

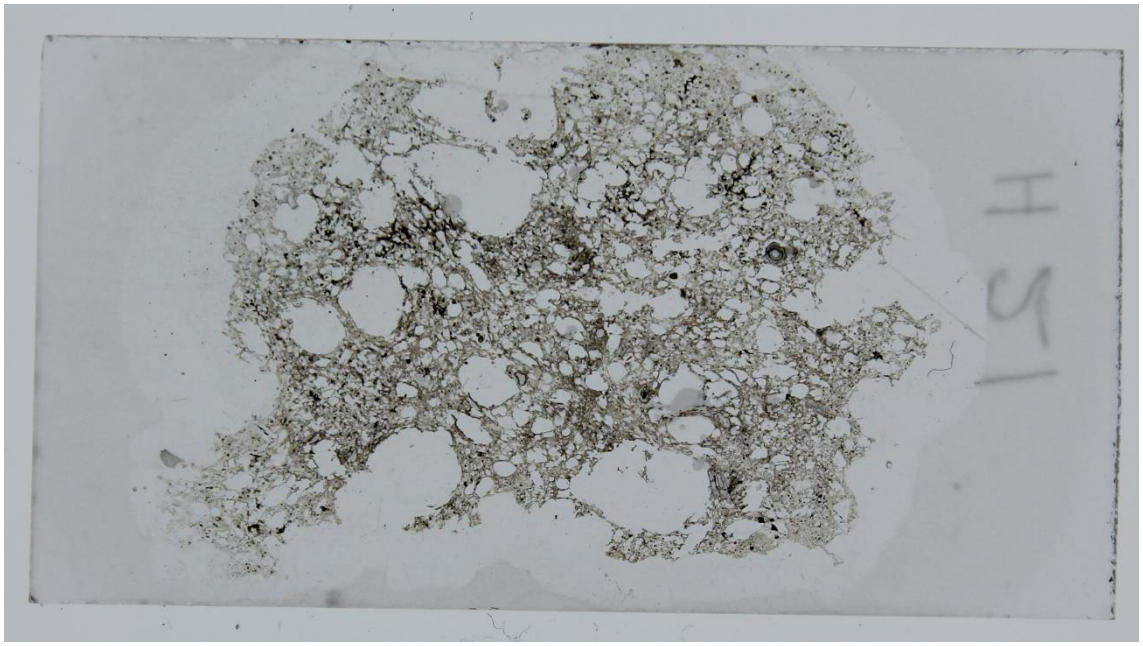

Sample H28

Whole-rock composition	Trachyandesite
Source	Summit
Type	Lava
Groundmass	80%
Phenocrysts	20%
Vesicles	0%

Phenocrysts

Plagioclase	60%
Clinopyroxene	20%
Orthopyroxene	5%
Olivine	10%
Oxide	5%

Groundmass	Black glassy groundmass with a thick band of microcrystalline grey groundmass.
Description	Porphyritic lava with phenocrysts of pristine and sieve-textured euhedral plagioclases (<3 mm), subhedral pyroxene, subhedral olivine and euhedral-subhedral oxide, and glomerocrysts (<4 mm) of the same minerals in a groundmass that varies between glassy black and microcrystalline grey.

Appendix III: Whole-rock geochemical analyses of lavas and pyroclastic samples

Major element analyses are in wt.% and trace element analyses are in ppm. Some trace elements were not determined (n.d.) or below detection limit (b.d.l.). Samples marked * were analysed by ICP-MS for La, Ce, Pr, Nd, Sm, Eu, Gd, Tb, Dy, Ho, Er, Tm, Yb, Lu, Hf, Pb, Th and U. All other analyses were done by XRF.

Samples labelled Q (collected from the flanks of Quetrupillán), H (from the Huililco Valley), T (from the Trancura Valley) and P (from the Palguín Valley) are Holocene products and were collected by me. Samples labelled D are Pleistocene lavas and were collected from the flanks of Quetrupillán by Dr Dave McGarvie during prior fieldwork and analysed by me.

The whole-rock composition (Comp.) of samples is listed (Trachyand. – trachyandesite; Bas and. – basaltic andesite), as is the type of sample: Holocene lava (Lava), Holocene tephra (Tephra) and Pleistocene lava (Pleist.). The sources of Holocene lavas are categorised as having erupted from the flanks (the number indicates the vent number, according to Figure 2.2) or summit of Quetrupillán, and the source of tephra samples are categorised according to the volcano they were erupted from (Quet. – Quetrupillán; Mocho-Ch. – Mocho Choshuenco).

Sample	Q3*	Q7*	Q8*	Q10	Q12*	Q17*	Q29*
Comp.	Trachyte	Trachyte	Trachyand.	Trachyte	Trachyte	Trachyand.	Trachyte
Source	Flank (2)	Flank (3)	Flank (11)	Flank (4)	Flank (5)	Flank (12)	Flank (14)
Type	Lava	Lava	Lava	Lava	Lava	Lava	Lava
SiO_2	64.96	65.03	58.66	64.89	64.74	57.64	63.06
TiO_2	1.11	1.12	1.36	1.11	1.15	1.19	1.12
Al_2O_3	15.36	15.35	16.17	15.50	15.48	16.51	15.46
$Fe_2O_3^T$	5.54	5.56	8.16	5.59	5.72	7.85	5.85
MnO	0.13	0.13	0.13	0.13	0.13	0.13	0.12
MgO	1.21	1.18	2.89	1.23	1.23	3.63	1.35
CaO	3.11	3.12	5.88	3.25	3.26	6.05	3.29
Na_2O	4.85	4.75	3.92	4.77	4.83	3.82	4.36
K_2O	3.05	3.05	2.34	2.94	2.99	2.20	2.77
P_2O_5	0.33	0.32	0.36	0.32	0.34	0.34	0.30
LOI	0.20	0.34	-0.02	0.03	0.11	0.28	1.93
Total	99.84	99.94	99.84	99.77	99.98	99.63	99.63
Sc	16.6	17.1	24.3	17.0	17.2	24.9	18.4
V	63.7	63.4	228.8	64.8	66.3	186.1	86.0
Cr	4.0	3.0	28.2	3.2	3.5	78.6	9.6
Ni	b.d.l.	b.d.l.	18.6	b.d.l.	b.d.l.	35.0	1.9
Cu	14.5	14.2	59.9	15.3	15.2	65.5	23.1
Zn	71.2	70.3	76.1	70.1	72.5	73.0	72.3
Rb	77.8	77.1	60.3	74.1	75.4	56.9	70.7
Sr	284.3	285.5	371.8	292.9	299.6	389.0	288.2
Y	44.4	43.9	36.9	43.2	43.8	34.2	39.0
Zr	352.2	345.4	270.6	328.0	339.5	258.1	326.0
Nb	14.1	13.6	10.9	12.9	13.5	10.5	12.7
Ba	737.8	733.8	583.2	701.8	730.0	545.1	691.8
La	33.82	32.48	25.46	32.4	32.87	23.49	28.77
Ce	75.53	71.60	56.85	81.2	71.90	54.21	65.39
Pr	9.32	8.98	7.16	n.d.	8.99	6.77	8.00
Nd	37.31	35.93	29.12	39.5	36.09	27.54	31.91
Sm	7.73	7.44	6.20	n.d.	7.51	5.84	6.65
Eu	1.78	1.73	1.47	n.d.	1.74	1.39	1.54
Gd	7.43	7.06	5.95	n.d.	7.12	5.57	6.30
Tb	1.13	1.09	0.91	n.d.	1.08	0.86	0.98
Dy	6.84	6.58	5.44	n.d.	6.55	5.15	5.99
Ho	1.39	1.35	1.10	n.d.	1.34	1.04	1.23
Er	4.23	4.08	3.31	n.d.	4.04	3.12	3.75
Tm	0.69	0.66	0.52	n.d.	0.66	0.50	0.61
Yb	4.29	4.15	3.28	n.d.	4.09	3.11	3.90
Lu	0.67	0.64	0.51	n.d.	0.89	0.47	0.61
Hf	7.89	7.64	5.77	n.d.	7.45	5.50	7.24
Pb	24.74	23.94	17.54	21.8	23.52	16.78	30.95
Th	9.88	9.44	7.13	10.3	9.31	6.86	8.95
U	2.71	2.62	1.99	3.2	2.58	1.91	2.47
Eu/Eu*	0.72	0.73	0.74	n.d.	0.73	0.75	0.73

Sample	Q31	Q34*	Q36	Q39*	Q40*	Q41*	Q43
Comp.	Trachyte	Trachyte	Trachyte	Trachyte	Trachyte	Trachyte	Trachyte
Source	Flank (13)	Flank (13)	Flank (14)	Flank (9)	Flank (8)	Flank (7)	Flank (7)
Type	Lava	Lava	Lava	Lava	Lava	Lava	Lava
SiO_2	64.52	64.89	64.05	65.13	64.49	64.38	64.91
TiO_2	1.09	1.08	1.08	1.08	1.11	1.10	1.11
Al_2O_3	15.43	15.53	15.16	15.34	15.42	15.43	15.46
$Fe_2O_3^T$	5.59	5.57	6.61	5.40	5.52	5.56	5.56
MnO	0.12	0.13	0.23	0.12	0.13	0.13	0.13
MgO	1.21	1.19	1.16	1.16	1.23	1.24	1.18
CaO	3.15	3.16	3.06	3.06	3.25	3.28	3.16
Na_2O	4.75	4.82	4.74	4.82	4.76	4.74	4.81
K_2O	3.02	3.05	3.05	3.07	2.97	2.95	2.97
P_2O_5	0.29	0.32	0.31	0.33	0.35	0.35	0.33
LOI	0.46	0.22	0.35	0.03	0.15	0.03	0.11
Total	99.64	99.95	99.80	99.54	99.37	99.19	99.71
Sc	16.4	16.8	16.0	15.9	16.5	17.3	17.8
V	70.3	67.3	67.4	60.6	65.6	67.6	62.6
Cr	2.7	3.5	3.4	b.d.l.	b.d.l.	1.4	2.7
Ni	b.d.l.	b.d.l.	b.d.l.	b.d.l.	b.d.l.	0.8	b.d.l.
Cu	18.0	18.7	13.4	14.1	15.1	16.5	13.7
Zn	68.7	68.3	66.9	70.5	72.2	71.7	68.1
Rb	78.2	78.4	78.8	78.1	75.4	75.4	76.2
Sr	287.3	286.2	280.2	286.0	303.2	306.5	294.1
Y	42.3	43.4	43.5	44.5	44.0	43.9	44.4
Zr	346.1	347.7	349.0	358.2	346.9	345.5	337.9
Nb	13.6	13.4	13.7	14.5	14.3	14.0	13.2
Ba	731.6	737.7	736.3	719.2	703.8	705.5	697.6
La	31.6	32.92	31.9	30.95	33.21	32.43	31.0
Ce	77.6	72.90	78.6	66.98	73.24	71.21	81.7
Pr	n.d.	8.99	n.d.	8.54	9.12	8.94	n.d.
Nd	36.3	35.00	38.3	34.23	36.65	35.94	39.7
Sm	n.d.	7.49	n.d.	7.13	7.67	7.46	n.d.
Eu	n.d.	1.72	n.d.	1.64	1.77	1.74	n.d.
Gd	n.d.	7.14	n.d.	6.69	7.23	7.07	n.d.
Tb	n.d.	1.09	n.d.	1.03	1.11	1.08	n.d.
Dy	n.d.	6.63	n.d.	6.24	6.69	6.53	n.d.
Ho	n.d.	1.36	n.d.	1.28	1.36	1.33	n.d.
Er	n.d.	4.14	n.d.	3.88	4.10	4.02	n.d.
Tm	n.d.	0.67	n.d.	0.63	0.66	0.65	n.d.
Yb	n.d.	4.23	n.d.	3.93	4.16	4.04	n.d.
Lu	n.d.	0.65	n.d.	0.61	0.65	0.63	n.d.
Hf	n.d.	7.79	n.d.	6.86	7.48	7.28	n.d.
Pb	23.3	23.89	21.4	21.41	22.30	21.78	21.2
Th	10.4	9.70	10.1	8.77	9.28	8.96	10.3
U	2.6	2.67	2.9	2.24	2.54	2.49	3.3
Eu/Eu*	n.d.	0.72	n.d.	0.73	0.73	0.73	n.d.

Sample	Q48*	Q50*	Q53	Q54	Q56	Q61*	Q65
Comp.	Trachyte	Bas and.	Trachyte	Trachyte	Trachyte	Trachyte	Trachyte
Source	Flank (6)	Flank (10)	Flank (2)	Flank (4)	Flank (5)	Flank (1)	Flank (14)
Type	Lava	Lava	Lava	Lava	Lava	Lava	Lava
SiO_2	64.24	54.84	64.97	64.92	64.78	63.92	64.59
TiO_2	1.11	1.04	1.10	1.08	1.11	1.07	1.05
Al_2O_3	15.37	16.23	15.63	15.37	15.36	15.25	15.01
$Fe_2O_3^T$	5.59	8.80	5.45	5.43	5.57	5.42	5.40
MnO	0.13	0.14	0.12	0.13	0.13	0.13	0.12
MgO	1.25	6.50	1.18	1.19	1.20	1.18	1.13
CaO	3.30	7.67	3.09	3.16	3.21	3.18	2.85
Na_2O	4.82	3.22	4.83	4.90	4.72	4.68	4.66
K_2O	2.95	1.48	2.96	3.03	2.96	2.96	3.02
P_2O_5	0.35	0.28	0.32	0.33	0.33	0.33	0.22
LOI	0.03	-0.21	0.19	-0.03	0.19	0.19	0.41
Total	99.13	100.00	99.84	99.50	99.55	98.31	98.45
Sc	18.1	27.3	16.0	16.2	17.5	15.5	15.5
V	70.4	210.5	63.3	64.2	63.0	63.7	64.9
Cr	1.7	179.8	2.8	2.4	3.3	2.6	3.2
Ni	b.d.l.	78.3	b.d.l.	b.d.l.	b.d.l.	2.5	b.d.l.
Cu	15.9	56.7	13.8	15.1	15.2	31.4	19.5
Zn	75.5	74.4	68.6	72.9	69.4	73.2	70.8
Rb	74.5	36.2	75.8	76.9	n.d.	76.2	77.9
Sr	306.2	429.4	294.3	293.4	296.4	299.5	275.6
Y	43.8	27.5	44.5	44.0	44.4	43.7	40.7
Zr	343.3	174.3	337.6	353.8	332.7	349.2	359.0
Nb	14.1	7.4	13.3	14.4	13.0	14.1	14.2
Ba	708.8	383.0	710.4	717.9	696.4	715.6	716.2
La	32.96	18.16	33.6	35.2	34.9	30.12	30.9
Ce	72.26	40.52	81.2	79.3	82.7	65.79	74.1
Pr	9.03	5.21	n.d.	n.d.	n.d.	8.32	n.d.
Nd	36.32	21.59	40.9	40.0	39.6	33.40	35.4
Sm	7.54	4.70	n.d.	n.d.	n.d.	6.94	n.d.
Eu	1.77	1.25	n.d.	n.d.	n.d.	1.62	n.d.
Gd	7.08	4.51	n.d.	n.d.	n.d.	6.48	n.d.
Tb	1.09	0.70	n.d.	n.d.	n.d.	1.01	n.d.
Dy	6.56	4.16	n.d.	n.d.	n.d.	6.14	n.d.
Ho	1.35	0.84	n.d.	n.d.	n.d.	1.26	n.d.
Er	4.06	2.51	n.d.	n.d.	n.d.	3.80	n.d.
Tm	0.65	0.39	n.d.	n.d.	n.d.	0.61	n.d.
Yb	4.12	2.46	n.d.	n.d.	n.d.	3.85	n.d.
Lu	0.63	0.37	n.d.	n.d.	n.d.	0.60	n.d.
Hf	7.24	3.76	n.d.	n.d.	n.d.	7.40	n.d.
Pb	21.74	11.19	21.5	n.d.	21.8	21.89	n.d.
Th	9.04	4.31	10.3	n.d.	10.3	8.64	n.d.
U	2.50	1.22	3.4	n.d.	3.1	2.37	n.d.
Eu/Eu*	0.74	0.83	n.d.	n.d.	n.d.	0.74	n.d.

Sample	Q66	Q69*	H24	Q16	Q20	Q23	Q60
Comp.	Trachyte	Trachyte	Trachyte	Bas and.	Trachyand.	Bas and.	Trachyand.
Source	Flank (?)	Flank (15)	Flank (15)	Summit	Summit	Summit	Summit
Type	Lava	Lava	Lava	Lava	Lava	Lava	Lava
SiO_2	64.25	65.02	64.64	55.32	61.06	57.20	58.25
TiO_2	1.07	1.08	1.08	1.07	1.18	1.00	1.17
Al_2O_3	15.34	15.22	15.35	16.85	16.07	16.65	16.08
$Fe_2O_3^T$	5.55	5.36	5.44	8.42	6.77	7.84	7.64
MnO	0.12	0.13	0.13	0.14	0.11	0.13	0.13
MgO	1.22	1.14	1.18	5.50	2.26	5.14	3.49
CaO	3.26	2.96	3.14	7.62	4.62	6.97	5.96
Na_2O	4.70	4.79	4.96	3.17	4.23	3.32	3.80
K_2O	3.00	3.07	3.01	1.45	2.75	1.80	2.31
P_2O_5	0.33	0.32	0.33	0.29	0.35	0.26	0.35
LOI	0.03	0.19	0.05	0.08	0.11	0.02	-0.14
Total	98.87	99.28	99.31	99.91	99.52	100.34	99.04
Sc	15.8	16.5	16.6	24.8	19.3	23.3	22.4
V	69.9	56.9	63.8	191.8	156.6	170.9	172.6
Cr	b.d.l.	2.8	2.1	152.2	21.2	141.2	59.9
Ni	b.d.l.	b.d.l.	1.0	62.5	12.8	49.5	27.8
Cu	16.1	15.0	15.3	51.8	39.8	46.5	46.3
Zn	68.4	70.0	72.4	70.5	68.6	64.2	69.9
Rb	77.4	78.1	79.7	34.7	71.4	45.3	60.4
Sr	297.7	280.7	309.4	471.2	324.6	410.2	389.5
Y	43.4	44.2	43.8	25.8	39.3	28.5	35.7
Zr	352.1	360.4	331.1	166.6	314.5	202.4	271.8
Nb	14.0	14.7	14.4	7.1	12.0	8.0	11.2
Ba	708.1	720.5	757.5	403.1	648.9	440.9	553.2
La	33.2	31.99	30.6	14.7	27.5	19.1	25.6
Ce	77.2	70.03	75.1	45.1	70.7	53.0	60.4
Pr	n.d.	8.84	n.d.	n.d.	n.d.	n.d.	n.d.
Nd	38.6	35.36	41.7	23.7	35.8	24.7	32.3
Sm	n.d.	7.36	n.d.	n.d.	n.d.	n.d.	n.d.
Eu	n.d.	1.70	n.d.	n.d.	n.d.	n.d.	n.d.
Gd	n.d.	6.94	n.d.	n.d.	n.d.	n.d.	n.d.
Tb	n.d.	1.07	n.d.	n.d.	n.d.	n.d.	n.d.
Dy	n.d.	6.47	n.d.	n.d.	n.d.	n.d.	n.d.
Ho	n.d.	1.33	n.d.	n.d.	n.d.	n.d.	n.d.
Er	n.d.	4.01	n.d.	n.d.	n.d.	n.d.	n.d.
Tm	n.d.	0.65	n.d.	n.d.	n.d.	n.d.	n.d.
Yb	n.d.	4.10	n.d.	n.d.	n.d.	n.d.	n.d.
Lu	n.d.	0.63	n.d.	n.d.	n.d.	n.d.	n.d.
Hf	n.d.	7.59	n.d.	n.d.	n.d.	n.d.	n.d.
Pb	n.d.	23.22	n.d.	10.0	20.9	12.9	n.d.
Th	n.d.	9.23	n.d.	3.8	9.3	6.7	n.d.
U	n.d.	2.29	n.d.	2.4	2.8	2.6	n.d.
Eu/Eu*	n.d.	0.73	n.d.	n.d.	n.d.	n.d.	n.d.

Sample	Q62	Q63	Q67	H28	Q25	Q26	Q44
Comp.	Trachyte	Bas and.	Basalt	Trachyand.	Trachyte	Trachyte	Trachyte
Source	Summit	Summit	Summit	Summit	Quet.	Quet.	Quet.
Type	Lava	Lava	Lava	Lava	Tephra	Tephra	Tephra
SiO_2	63.56	55.37	51.93	61.75	63.97	64.34	62.27
TiO_2	1.24	1.06	1.06	1.34	1.13	1.14	1.13
Al_2O_3	14.97	16.03	17.87	15.44	15.61	15.51	15.55
$Fe_2O_3^T$	6.39	8.01	8.97	7.32	5.69	5.71	6.00
MnO	0.13	0.14	0.15	0.14	0.13	0.13	0.13
MgO	1.39	5.12	6.37	1.92	1.23	1.26	1.37
CaO	3.48	6.94	9.33	4.53	3.23	3.33	3.47
Na_2O	4.51	3.32	3.02	4.25	4.71	4.74	4.55
K_2O	3.16	1.74	1.01	2.76	2.93	2.95	2.73
P_2O_5	0.43	0.28	0.31	0.45	0.36	0.35	0.36
LOI	-0.06	-0.04	-0.21	-0.07	0.83	0.30	1.32
Total	99.19	97.96	99.80	99.82	99.83	99.77	98.87
Sc	18.9	24.7	28.1	21.8	17.7	17.4	19.7
V	95.7	192.8	214.4	147.2	73.6	70.4	86.4
Cr	3.1	154.9	164.9	b.d.l.	4.8	4.3	7.7
Ni	1.3	66.2	66.4	b.d.l.	b.d.l.	b.d.l.	3.3
Cu	21.0	44.1	63.2	27.9	16.8	15.5	24.4
Zn	75.9	68.7	65.7	79.4	73.9	75.4	81.1
Rb	82.1	43.9	22.0	n.d.	74.6	74.7	68.6
Sr	276.9	403.5	568.1	325.8	292.8	301.7	307.4
Y	47.7	30.2	22.9	44.5	43.5	43.9	41.3
Zr	378.9	205.6	124.1	315.9	337.9	334.6	331.2
Nb	15.2	8.5	6.8	12.3	13.3	13.2	13.5
Ba	713.1	445.1	334.8	642.6	731.1	729.7	672.6
La	35.9	19.4	14.3	33.5	31.2	32.3	33.2
Ce	83.8	47.8	39.4	84.2	79.9	79.7	77.8
Nd	42.0	24.5	20.3	42.9	39.7	39.2	38.5
Pb	n.d.	n.d.	n.d.	20.6	21.4	21.3	n.d.
Th	n.d.	n.d.	n.d.	10.3	9.9	9.7	n.d.
U	n.d.	n.d.	n.d.	3.0	3.0	2.7	n.d.

Sample	T1	T2	T5	T6	T7	T8	T9
Comp.	Trachyte	Bas and.	Trachyte	Basalt	Bas and.	Bas and.	Bas and.
Source	Quet.	Villarrica	Quet.	Villarrica	Villarrica	Villarrica	Villarrica
Type	Tephra	Tephra	Tephra	Tephra	Tephra	Tephra	Tephra
SiO_2	64.10	53.14	64.42	50.32	52.09	53.85	53.40
TiO_2	1.08	1.27	1.13	1.24	1.34	1.20	1.31
Al_2O_3	15.70	17.76	16.01	19.16	20.37	18.17	18.75
$Fe_2O_3^T$	5.50	10.63	5.63	9.98	10.98	9.79	10.84
MnO	0.12	0.17	0.13	0.17	0.19	0.15	0.17
MgO	1.09	3.44	1.21	5.76	3.37	4.06	3.65
CaO	3.03	7.00	3.16	8.54	6.57	8.33	6.97
Na_2O	4.70	3.06	4.47	2.57	2.47	2.86	2.69
K_2O	3.02	0.73	3.02	0.88	0.67	0.75	0.73
P_2O_5	0.32	0.23	0.33	0.40	0.33	0.22	0.23
LOI	1.22	2.43	0.40	0.60	1.37	0.22	1.09
Total	99.88	99.86	99.91	99.62	99.75	99.60	99.83
Sc	16.8	37.8	16.6	36.5	38.2	34.8	37.7
V	69.3	332.9	78.1	265	297.3	312.7	334.7
Cr	3.8	39.2	2.0	177.7	68	53.3	43.9
Ni	b.d.l.	15.2	1.4	65.1	24.6	29.9	28
Cu	16.7	108.1	18.3	70	97.2	105.7	120.7
Zn	69.9	99.0	68.5	76.9	96.5	97	111
Rb	77.1	17.7	73.9	18.2	13.9	17.3	17.2
Sr	271.1	362.6	274.5	496.4	326	413.1	353.6
Y	44.8	27.5	44.9	23.7	25.8	25.9	28.8
Zr	359.4	115.4	355.3	134.5	109.4	101.9	115.4
Nb	13.9	2.9	13.5	7.1	3.6	2.4	2.6
Ba	728.1	237.6	721.8	304.9	262.6	247.7	301.2
La	32.5	6.3	34.0	15.2	10	6	8.7
Ce	81.1	24.8	83.9	44.9	34.2	24.6	26.1
Nd	40.3	17.4	41.9	22.7	19.8	17.1	17.5
Pb	22.5	9.8	22.7	8.1	9.3	8.2	9.4
Th	10.8	2.4	10.7	2.5	2.2	2.1	1
U	2.8	0.3	3.8	1.6	1.2	1.9	1.6

Sample	T10	T12	T13	T14	T15	T16	P13
Comp.	Trachyte	Bas and.	Trachyand.	Bas and.	Bas and.	Bas and.	Dacite
Source	Quet.	Villarrica	Quet.	Villarrica	Villarrica	Villarrica	Mocho-Ch.?
Type	Tephra	Tephra	Tephra	Tephra	Tephra	Tephra	Tephra
SiO_2	64.31	53.38	59.30	53.39	52.46	52.62	61.76
TiO_2	1.14	1.37	1.51	1.42	1.19	1.34	0.71
Al_2O_3	15.84	19.58	17.46	19.46	18.20	20.32	18.75
$Fe_2O_3^T$	5.72	10.20	7.97	10.38	10.43	10.40	4.33
MnO	0.13	0.18	0.13	0.15	0.17	0.21	0.13
MgO	1.53	2.72	1.56	2.74	4.74	2.72	0.80
CaO	3.20	5.44	3.60	4.79	7.82	4.74	2.57
Na_2O	4.50	2.72	3.80	2.35	2.54	2.82	4.19
K_2O	2.86	1.20	2.63	1.18	0.68	1.08	1.67
P_2O_5	0.31	0.28	0.45	0.29	0.20	0.26	0.17
LOI	0.31	2.64	1.38	3.54	1.26	3.46	4.76
Total	99.86	99.71	99.79	99.71	99.69	99.96	99.85
Sc	18.4	36.5	24.6	36.6	40.8	37.3	19.1
V	70.8	259.3	154.3	283.4	312.7	234.5	44.1
Cr	10.1	55.3	3.7	67	94.6	81.2	5.3
Ni	3.4	16.4	4.0	22.6	41	27.2	5.3
Cu	12.6	114.3	33.7	82	93.7	127.9	10.3
Zn	72.8	92.4	76.0	94.5	94.6	92.4	89.5
Rb	68.8	25.7	62.8	25.8	15.3	23.2	40.7
Sr	304.2	410.2	259.2	286.5	345.7	310.3	372.0
Y	42.4	43.5	47.2	37.1	26.2	40.5	46.1
Zr	329.6	185.4	387.1	212.8	106.9	182.2	244.8
Nb	12.8	7	14.8	7.3	2.4	6.2	7.0
Ba	695.0	447.4	640.6	423.7	223.5	346.2	735.0
La	32.9	27.7	37.6	21.9	6.5	20.8	21.4
Ce	75.3	55	85.9	57.5	25.7	54.5	60.2
Nd	39.0	37.1	46.3	31.6	17.1	33.6	34.0
Pb	22.8	15.8	28.0	19.7	8.6	15.4	18.9
Th	9.8	7.5	12.3	7.6	0.7	5.8	6.1
U	3.6	2.6	3.4	2.2	1.5	1.6	2.3

Sample	P17	P21	P23	P24	D1	D2	D3
Comp.	Basalt	Basalt	Bas and.	Basalt	Trachyte	Trachyte	Trachyand.
Source	Villarrica	Villarrica	Villarrica	Villarrica	Quet.	Quet.	Quet.
Type	Tephra	Tephra	Tephra	Tephra	Pleist.	Pleist.	Pleist.
SiO_2	49.91	50.51	51.95	43.79	66.72	63.02	57.82
TiO_2	0.97	0.94	1.06	1.86	0.81	1.25	1.28
Al_2O_3	19.77	19.43	20.86	22.32	15.33	14.92	16.06
$Fe_2O_3^T$	9.70	8.84	8.04	13.68	4.09	6.52	8.57
MnO	0.13	0.14	0.17	0.15	0.12	0.16	0.16
MgO	4.81	5.88	3.16	2.66	0.92	1.66	2.85
CaO	8.28	9.68	5.21	5.31	2.40	3.73	6.21
Na_2O	2.29	2.43	2.93	1.89	5.56	5.10	4.40
K_2O	0.44	0.54	0.82	0.27	2.99	2.53	1.87
P_2O_5	0.29	0.16	0.20	0.35	0.20	0.44	0.38
LOI	3.07	1.07	5.60	7.58	0.41	0.54	-0.17
Total	99.66	99.63	99.98	99.85	99.55	99.88	99.41
Sc	50.2	41.2	37.8	64.6	14.5	10.6	29.7
V	281.1	291.7	201.7	467.8	26.3	24.2	222.9
Cr	150.7	188.3	82.7	68.5	n.d.	n.d.	7.2
Ni	53.4	81.3	38.4	35.3	b.d.l.	n.d.	5.8
Cu	94.2	117.3	101.4	146.8	11.4	17.2	37.8
Zn	66.1	70.1	77.8	63.9	68.6	47.8	87.4
Rb	9.8	10.9	18.9	5.3	69.3	88.3	44.0
Sr	410.4	586.2	381.5	411.9	249.6	181.1	464.5
Y	21.0	18.1	36.8	34.5	44.1	39.0	33.9
Zr	51.8	22.3	116.1	87.3	330.1	360.9	208.2
Nb	2.3	1.7	5.0	3.4	12.8	12.3	7.9
Ba	206.6	226.8	354.1	209.6	737.7	755.5	501.8
La	3.3	2.8	15.5	8.5	36.5	33.8	25.9
Ce	22.3	21.6	46.7	38.0	80.8	76.2	59.7
Nd	13.8	13.6	27.6	26.7	39.3	32.0	30.8
Pb	7.7	9.5	17.4	12.2	23.0	23.4	17.2
Th	0.4	3.0	5.1	3.0	9.4	11.8	7.2
U	1.3	1.9	2.0	1.4	2.7	3.0	1.2

Sample	D6	D10	D18a	D18b	D19	D20	D21
Comp.	Trachyte	Trachyte	Trachyte	Trachyand.	Trachyte	Trachyte	Trachyte
Source	Quet.	Quet.	Quet.	Quet.	Quet.	Quet.	Quet.
Type	Pleist.	Pleist.	Pleist.	Pleist.	Pleist.	Pleist.	Pleist.
SiO_2	66.95	66.21	66.38	61.22	64.78	63.18	63.01
TiO_2	0.83	0.84	0.81	0.93	0.98	1.21	1.23
Al_2O_3	14.96	15.08	15.21	16.02	15.68	15.43	15.72
$Fe_2O_3^T$	4.55	4.65	4.07	6.26	5.37	6.23	6.36
MnO	0.11	0.11	0.12	0.13	0.13	0.17	0.17
MgO	1.00	1.08	0.95	2.00	1.34	1.53	1.69
CaO	2.43	2.64	2.40	4.88	3.29	3.48	3.56
Na_2O	5.25	5.23	5.53	4.70	5.07	4.89	4.96
K_2O	3.28	3.18	2.97	2.10	2.77	2.44	2.43
P_2O_5	0.21	0.22	0.20	0.27	0.29	0.41	0.41
LOI	0.38	0.34	1.19	1.19	-0.11	0.48	0.25
Total	99.96	99.58	99.84	99.70	99.57	99.45	99.79
Sc	14.2	14.6	19.7	19.7	22.5	20.1	20.7
V	34.7	38.6	109.2	78.1	57.6	53.6	54.6
Cr	1.7	2.4	5.5	1.6	9.5	2.1	3.1
Ni	1.3	2.8	3.6	3.4	5.3	b.d.l.	2.0
Cu	19.2	21.5	31.9	21.7	11.9	6.9	12.1
Zn	64.4	66.7	73.8	80.8	89.9	91.5	91.7
Rb	81.9	79.3	51.1	51.4	58.8	55.1	55.1
Sr	220.7	237.9	342.2	396.5	321.2	355.9	352.3
Y	43.3	42.6	34.2	47.3	46.9	45.9	46.1
Zr	346.3	335.1	214.8	265.6	286.9	281.4	283.7
Nb	12.6	12.3	6.3	9.9	10.7	11.1	11.1
Ba	770.4	760.9	519.2	645.6	659.8	667.4	666.1
La	37.0	35.6	21.4	39.2	34.3	30.9	31.0
Ce	80.7	79.3	52.9	81.3	76.9	73.0	75.9
Nd	37.5	37.1	26.9	46.4	40.1	40.9	41.7
Pb	23.3	22.2	15.3	18.8	20.0	21.2	23.0
Th	11.9	11.0	6.4	9.3	8.6	8.6	8.6
U	2.9	2.7	1.6	1.9	2.2	3.0	3.1

Sample	D22	D23	D24	D25	D29	D30	D31
Comp.	Trachyand.	Trachyte	Trachyte	Basalt	Trachyte	Trachyand.	Rhyolite
Source	Quet.	Quet.	Quet.	Quet.	Quet.	Quet.	Quet.
Type	Pleist.	Pleist.	Pleist.	Pleist.	Pleist.	Pleist.	Pleist.
SiO_2	62.63	66.74	64.39	50.30	65.03	62.97	67.72
TiO_2	1.42	0.86	1.02	1.02	0.74	1.00	0.57
Al_2O_3	15.33	14.99	15.68	18.24	15.77	15.49	14.80
$Fe_2O_3^T$	6.94	5.26	5.56	9.07	4.80	5.81	3.42
MnO	0.17	0.13	0.14	0.14	0.11	0.14	0.08
MgO	1.76	0.91	1.38	5.79	1.40	1.54	0.74
CaO	3.99	2.49	3.39	10.28	3.43	3.63	1.98
Na_2O	4.76	4.82	5.35	2.94	5.02	5.06	5.14
K_2O	2.36	3.21	2.69	0.98	2.80	2.61	3.40
P_2O_5	0.50	0.23	0.34	0.26	0.19	0.31	0.13
LOI	-0.10	0.12	0.36	0.88	0.33	0.99	1.67
Total	99.75	99.78	100.29	99.90	99.63	99.56	99.65
Sc	21.7	16.2	16.7	35.1	13.4	19.7	18.2
V	64.6	25.4	60.0	274.1	65.8	69.3	46.2
Cr	2.9	5.2	n.d.	69.3	3.3	2.7	n.d.
Ni	1.0	b.d.l.	1.3	33.3	1.7	2.4	1.2
Cu	24.0	11.3	19.9	70.7	20.9	24.8	16.5
Zn	92.3	81.1	76.4	69.6	55.6	80.6	76.5
Rb	53.4	77.3	61.8	19.6	69.7	61.4	68.1
Sr	362.0	232.4	324.4	701.2	296.8	329.8	301.6
Y	46.4	47.2	42.0	19.0	36.1	41.5	42.2
Zr	270.1	348.1	284.4	90.4	300.4	274.2	292.8
Nb	10.2	11.5	11.1	4.7	10.4	10.9	11.2
Ba	631.9	736.7	693.8	363.1	652.7	687.1	688.7
La	28.7	33.8	34.5	17.3	31.5	33.6	35.0
Ce	71.6	77.7	75.7	37.2	66.0	75.5	75.3
Nd	39.9	38.3	37.7	19.3	29.6	37.0	37.8
Pb	21.6	23.5	20.1	10.2	20.8	18.4	19.9
Th	8.6	10.9	9.3	6.4	9.7	8.5	9.7
U	3.0	4.1	2.1	1.3	2.4	1.7	2.6

Sample	D44	D47	D51	D59	D60	D61	D62
Comp.	Andesite	Trachyte	Rhyolite	Trachyte	Bas and.	Trachyand.	Trachyte
Source	Quet.	Quet.	Quet.	Quet.	Quet.	Quet.	Quet.
Type	Pleist.	Pleist.	Pleist.	Pleist.	Pleist.	Pleist.	Pleist.
SiO_2	56.33	64.87	68.74	63.27	55.53	58.11	65.07
TiO_2	1.27	1.10	0.54	1.04	1.21	0.82	0.93
Al_2O_3	15.18	15.05	14.93	15.91	16.75	13.80	15.51
$Fe_2O_3^T$	8.81	5.45	3.24	6.04	8.63	4.37	5.01
MnO	0.16	0.15	0.09	0.16	0.15	0.11	0.13
MgO	2.67	1.13	0.51	1.59	3.85	1.02	1.25
CaO	5.78	2.93	1.76	3.72	7.40	6.98	2.97
Na_2O	3.89	5.05	4.74	4.80	3.65	4.39	4.94
K_2O	1.71	2.67	3.56	2.38	1.49	2.51	2.90
P_2O_5	0.37	0.33	0.12	0.30	0.36	0.23	0.25
LOI	-0.16	0.09	1.54	0.15	-0.05	0.48	0.10
Total	96.01	98.82	99.76	99.35	98.97	92.83	99.06
Sc	27.9	18.4	8.6	18.9	30.2	15.7	15.3
V	210.9	29.7	25.5	60.1	214.9	42.6	45.6
Cr	8.6	2.4	3.3	14.1	58.7	4.7	9.6
Ni	5.6	b.d.l.	b.d.l.	4.0	19.7	b.d.l.	3.3
Cu	56.6	5.3	13.6	15.8	58.9	15.8	14.4
Zn	95.1	86.7	51.1	77.6	81.7	72.9	73.9
Rb	42.1	63.6	91.6	56.3	34.8	71.7	73.9
Sr	418.9	326.6	188.3	393.7	470.5	295.2	303.1
Y	36.6	46.0	38.7	39.6	30.8	41.8	41.9
Zr	202.7	293.0	349.0	256.2	182.7	304.1	299.7
Nb	8.1	12.8	13.2	10.3	7.7	12.9	12.8
Ba	496.3	722.5	798.0	697.3	452.9	754.4	747.4
La	27.9	18.4	8.6	18.9	30.2	15.7	15.3
Ce	51.7	71.6	70.9	63.3	44.7	71.6	69.7
Nd	29.7	42.7	35.2	35.6	27.0	39.4	40.4

Sample	D63	D65	D181
Comp.	Trachyte	Bas and.	Trachyte
Source	Quet.	Quet.	Quet.
Type	Pleist.	Pleist.	Pleist.
SiO_2	64.21	52.97	66.12
TiO_2	0.95	1.17	0.91
Al_2O_3	15.63	17.67	15.43
$Fe_2O_3^T$	4.83	9.77	4.84
MnO	0.13	0.16	0.12
MgO	0.95	4.36	0.89
CaO	2.60	9.33	2.50
Na_2O	4.84	3.20	5.00
K_2O	2.85	0.89	3.05
P_2O_5	0.26	0.27	0.27
LOI	1.66	-0.18	0.18
Total	98.90	99.60	99.31
Sc	15.2	31.2	14.0
V	38.0	266.2	39.9
Cr	2.7	44.6	5.4
Ni	b.d.l.	18.1	b.d.l.
Cu	18.8	89.7	19.2
Zn	75.6	72.8	68.1
Rb	71.0	19.0	75.6
Sr	281.2	566.4	279.4
Y	42.3	25.0	43.2
Zr	313.5	123.4	317.9
Nb	13.3	4.4	13.4
Ba	765.5	331.0	803.6
La	15.2	31.2	14.0
Ce	74.8	31.3	73.6
Nd	42.2	19.9	41.7

Appendix IV: Whole-rock data from other authors for Quetrupillán and other volcanoes

Data from other authors are listed according to volcano (Q – Quetrupillán, V – Villarrica, L – Lanín and S – Sollipulli) and data sources are numbered according to the references listed below. Some data were not determined (n.d.).

1. Hickey-Vargas, R., Moreno Roa, H., Lopez-Escobar, L., Frey, F. A., 1989. Geochemical variations in Andean basaltic and silicic lavas from the Villarrica-Lanín volcanic chain (39.5°S): an evaluation of source heterogeneity, fractional crystallization and crustal assimilation. *Contributions to Mineralogy and Petrology*, 103(3), 361–386. DOI: 10.1007/BF00402922.
2. Brahm, R. (2017) Lavas traquíticas del Complejo Volcánico Quetrupillán, Chile (39°30'S): Ejemplos de rejuvenecimiento de un reservorio tipo mush cristalino. *Thesis*, Univsersidad de Chile.
3. Wehrmann, H., Hoernle, K., Jacques, G., Garbe-Schönberg, D., Schumann, K., Mahlke, J., Lara, L. E., 2014. Volatile (sulphur and chlorine), major, and trace element geochemistry of mafic to intermediate tephras from the Chilean Southern Volcanic Zone (33–43°S). *International Journal of Earth Sciences*, 103(7), 1945–1962. DOI: 10.1007/s00531-014-1006-9.
4. Morgado, E., Parada, M. A., Contreras, C., Castruccio, A., Gutiérrez, F., McGee, L. E., 2015. Contrasting records from mantle to surface of Holocene lavas of two nearby arc volcanic complexes: Caburgua-Huelemolle Small Eruptive Centers and Villarrica Volcano, Southern Chile. *Journal of Volcanology and Geothermal Research*, 306, 1–16. DOI: 10.1016/j.jvolgeores.2015.09.023.
5. Witter, J. B., Kress, V. C., Delmelle, P., Stix, J., 2004. Volatile degassing, petrology, and magma dynamics of the Villarrica Lava Lake, Southern Chile. *Journal of Volcanology and Geothermal Research*, 134(4), 303–337. DOI: 10.1016/j.jvolgeores.2004.03.002.
6. Lohmar, S., Parada, M., Gutiérrez, F., Robin, C., Gerbe, M. C., 2012. Mineralogical and numerical approaches to establish the pre-eruptive conditions of the mafic Licán Ignimbrite, Villarrica Volcano (Chilean Southern Andes). *Journal of Volcanology and Geothermal Research,* 235, 55–69. DOI: 10.1016/j.jvolgeores.2012.05.006.
7. Cortés, J. A., Unpublished data
8. Lara, L. E., Naranjo, J. A. and Moreno, H., 2004. Lanín volcano (39.5°S), Southern Andes: geology and morphostructural evolution. *Revista Geológica de Chile*, 31(2), 1–14. DOI: 10.4067/S0716-02082004000200004.

9. Murphy, M. D., 1996. Magmatic evolution at Volcán Sollipulli, southern Andes of Chile. *Thesis*, University of Bristol.

Ref.	1	1	1	1	1	1	1	2	2
Volcano	Q	Q	Q	Q	Q	Q	Q	Q	Q
SiO_2	56.41	56.44	56.69	62.22	64.57	64.33	64.32	64.32	63.73
TiO_2	1.41	1.45	1.4	1.3	1.08	1.09	1.12	1.13	1.13
Al_2O_3	16.07	16.7	16.62	15.16	15.6	15.38	15.41	15.51	15.33
$Fe_2O_3^T$	10.36	9.4	9.38	6.78	5.43	5.56	5.49	1.08	1.14
FeO	n.d.	n.d.	n.d.	n.d.	n.d.	n.d.	n.d.	4.3	4
MnO	0.17	0.16	0.15	0.14	0.12	0.14	0.14	0.13	0.13
MgO	3.07	3.17	3.08	1.65	1.22	1.25	1.23	1.23	1.23
CaO	6.61	6.77	7	4	3.31	3.27	3.3	3.38	3.33
Na_2O	4	4.33	4.12	5.02	5.2	5.46	5.41	4.88	4.89
K_2O	1.52	1.47	1.37	2.89	2.99	2.96	2.96	2.99	2.96
P_2O_5	0.41	0.4	0.4	0.46	0.33	0.36	0.35	0.36	0.34
LOI	n.d.	n.d.	n.d.	n.d.	n.d.	n.d.	n.d.	-0.13	-0.16
Sc	n.d.	n.d.	n.d.	n.d.	n.d.	n.d.	n.d.	15	15
V	n.d.	n.d.	n.d.	n.d.	n.d.	n.d.	n.d.	74	74
Rb	n.d.	n.d.	n.d.	n.d.	n.d.	n.d.	n.d.	80	81
Sr	n.d.	n.d.	n.d.	n.d.	n.d.	n.d.	n.d.	297	303
Y	29.6	29.6	31.2	42.2	40.9	40.8	41.1	38	37
Zr	163	n.d.	n.d.	366	369	360	373	330	326
Nb	5.1	n.d.	n.d.	13	13.6	12.3	13	13	13
Ba	n.d.	n.d.	n.d.	n.d.	n.d.	n.d.	n.d.	768	762
La	n.d.	n.d.	n.d.	n.d.	n.d.	n.d.	n.d.	36.4	35.8
Ce	n.d.	n.d.	n.d.	n.d.	n.d.	n.d.	n.d.	75.1	74.7
Nd	n.d.	n.d.	n.d.	n.d.	n.d.	n.d.	n.d.	36.9	37.7
Pb	n.d.	n.d.	n.d.	n.d.	n.d.	n.d.	n.d.	20	20
Th	n.d.	n.d.	n.d.	n.d.	n.d.	n.d.	n.d.	9.9	9.7
U	n.d.	n.d.	n.d.	n.d.	n.d.	n.d.	n.d.	2.9	2.9

Ref.	2	2	2	2	2	2	2	2	2
Volcano	Q	Q	Q	Q	Q	Q	Q	Q	Q
SiO_2	64.41	64.35	64.09	65.06	63.38	64.18	65.51	64.64	63.89
TiO_2	1.14	1.11	1.12	1.13	1.12	1.13	1.12	1.14	1.18
Al_2O_3	15.45	15.12	15.01	15.22	15.4	14.89	14.64	15.04	15.37
$Fe_2O_3^T$	0.51	1.01	0.98	1.12	1.21	0.97	0.7	0.83	1.52
FeO	4.8	4.3	4.2	4.1	4	4.2	4.5	4.4	3.8
MnO	0.13	0.13	0.13	0.13	0.13	0.13	0.13	0.13	0.13
MgO	1.27	1.25	1.24	1.32	1.3	1.31	1.27	1.31	1.39
CaO	3.38	3.35	3.33	3.46	3.41	3.44	3.28	3.43	3.61
Na_2O	4.93	4.91	4.93	4.99	4.96	4.82	4.7	4.97	4.91
K_2O	2.99	2.98	3	3.01	2.98	2.87	2.82	2.96	2.86
P_2O_5	0.36	0.34	0.36	0.35	0.34	0.37	0.34	0.36	0.39
LOI	-0.18	-0.11	-0.21	-0.18	-0.09	-0.22	-0.28	-0.18	-0.04
Sc	15	15	15	16	16	16	16	16	16
V	77	75	73	79	76	78	77	78	82
Rb	78	79	77	84	73	82	73	83	80
Sr	306	291	299	306	307	304	300	303	322
Y	38	38	39	38	39	38	36	39	37
Zr	332	333	331	330	294	320	278	331	316
Nb	15	14	15	12	12	12	10	13	12
Ba	773	768	772	780	770	749	731	771	750
La	36.3	36.4	36.7	36.3	34.5	35.2	35.2	36.3	34.7
Ce	75.6	75.7	76.2	76.1	71.7	74.1	72.5	75.6	72.6
Nd	37.3	38	37.9	37.6	37.1	37.9	37.7	37.6	36
Pb	21	20	20	21	20	20	20	21	20
Th	9.9	10.1	10.2	9.8	9.5	9.5	9.6	9.8	9.2
U	2.9	2.9	3	2.9	2.8	2.8	2.8	2.9	2.7

Ref.	2	2	2	2	2	2	1	1	1
Volcano	Q	Q	Q	Q	Q	Q	V	V	V
SiO_2	64.14	65.73	64.46	63.71	64.75	63.87	56.69	55.56	52.49
TiO_2	1.14	1.08	1.05	1.09	1.11	1.09	1.29	1.02	1.23
Al_2O_3	15.34	15.1	14.66	15.09	15.46	15.08	15.79	16.88	16.55
$Fe_2O_3^T$	0.66	2.03	0.52	1.59	1.57	1.46	10.03	8.42	10.25
FeO	4.6	3.4	4.6	3.8	3.8	3.8	n.d.	n.d.	n.d.
MnO	0.13	0.12	0.12	0.13	0.13	0.12	0.18	0.17	0.16
MgO	1.36	1.28	1.25	1.26	1.3	1.26	3.56	4.53	6.4
CaO	3.53	3.45	3.38	3.39	3.52	3.39	7.2	8.32	9
Na_2O	4.9	4.85	4.83	4.86	4.91	4.85	3.51	3.98	3.08
K_2O	2.9	2.98	2.98	2.98	3	2.98	1.03	0.9	0.71
P_2O_5	0.37	0.29	0.29	0.32	0.34	0.34	0.27	0.22	0.24
LOI	-0.22	0.02	-0.19	-0.13	-0.15	-0.1	n.d.	n.d.	n.d.
Sc	16	15	15	15	16	15	n.d.	n.d.	n.d.
V	82	83	80	83	83	81	n.d.	n.d.	n.d.
Rb	80	85	85	84	85	86	n.d.	n.d.	n.d.
Sr	318	303	295	299	309	302	n.d.	n.d.	n.d.
Y	38	39	38	38	37	37	27.6	23.1	24.4
Zr	327	336	331	330	337	333	124	118	106
Nb	13	12	12	12	12	12	3.2	3.6	2.3
Ba	760	763	759	763	770	760	n.d.	n.d.	n.d.
La	35.6	34.8	35.6	34.6	34.8	35.5	n.d.	n.d.	n.d.
Ce	74.3	72.9	74.6	72.3	72.6	73.8	n.d.	n.d.	n.d.
Nd	37.6	36.1	37.2	35.9	36.4	37.1	n.d.	n.d.	n.d.
Pb	20	18	20	20	20	20	n.d.	n.d.	n.d.
Th	9.3	9.8	9.9	9.8	9.6	9.8	n.d.	n.d.	n.d.
U	2.8	2.8	3	2.9	2.9	2.9	n.d.	n.d.	n.d.

Ref.	1	1	1	1	1	1	1	1	1
Volcano	V	V	V	V	V	V	V	V	V
SiO_2	52.87	51.79	55	51.97	55.38	52.4	52.68	51.47	52.74
TiO_2	1.11	1.14	1.37	0.98	1.32	1.11	1.05	0.86	1.03
Al_2O_3	17.37	16.89	16.11	16.9	16.04	17.97	18.74	17.58	18.2
$Fe_2O_3^T$	9.28	10.03	10.06	9.51	10.68	9.3	8.92	9.12	9.13
MnO	0.15	0.16	0.16	0.16	0.17	0.15	0.15	0.15	0.15
MgO	5.08	6.63	4.2	7.4	3.67	5.01	4.47	7.04	5.07
CaO	9.86	9.77	8.1	9.81	7.65	10.31	10.25	10.84	10.22
Na_2O	2.88	2.91	3.83	2.92	3.75	3	3.06	2.67	3.08
K_2O	0.64	0.61	0.86	0.58	0.91	0.66	0.61	0.43	0.58
P_2O_5	0.2	0.21	0.29	0.19	0.26	0.23	0.19	0.13	0.19
Y	21.7	21.9	25.2	19.5	27.1	22.6	20.7	17	19.9
Zr	95	92	114	84	118	97	89	62	84
Nb	2.6	2.4	2.8	1.9	3.1	2.4	2.5	1.3	2.9

Ref.	1	1	1	1	1	1	1	1	1
Volcano	V	V	V	V	V	V	V	V	V
SiO_2	52.71	52.04	52.21	52.43	52.19	52.37	52.6	52.23	52.16
TiO_2	1.23	1.14	1.32	1.17	1.14	1.15	1.15	1.16	1.13
Al_2O_3	18.25	17.59	16.62	18.13	16.82	16.85	16.79	16.86	17.44
$Fe_2O_3^T$	8.81	9.71	10.46	9.36	9.73	9.76	9.76	9.98	9.54
MnO	0.17	0.15	0.17	0.15	0.16	0.16	0.16	0.16	0.16
MgO	4.48	5.74	5.33	4.9	6.12	6.11	6.05	5.85	5.46
CaO	9.91	9.74	9.59	9.95	9.61	9.58	9.62	9.44	10.06
Na_2O	3.38	3.2	3.13	3.23	3.18	3.21	3.12	3.17	3.06
K_2O	0.69	0.64	0.78	0.68	0.63	0.65	0.65	0.66	0.68
P_2O_5	0.29	0.22	0.28	0.24	0.24	0.22	0.22	0.24	0.24
Y	22.5	22.3	26.4	23.5	23.1	23.3	23.2	23	22.7
Zr	110	94	119	100	100	99	102	103	103
Nb	2.7	2.1	3.4	2.1	2.7	2	2.6	3.1	2.8

Ref.	1	1	3	3	3	3	4	4	4
Volcano	V	V	V	V	V	V	V	V	V
SiO_2	55.84	53.15	53.01	52.44	52.14	51.44	52.85	51.92	52.47
TiO_2	1.13	1.08	1	0.95	1.32	1.18	1.11	1.12	1.11
Al_2O_3	16.28	18.68	18.85	18.08	16.07	15.88	16.76	16.68	16.71
$Fe_2O_3^T$	10.24	8.74	9.07	9.29	11.04	10.83	3.05	3.17	3.31
FeO	n.d.	n.d.	n.d.	n.d.	n.d.	n.d.	7.2	6.6	6.7
MnO	0.17	0.15	0.15	0.17	0.17	0.16	0.16	0.15	0.15
MgO	3.58	4.32	4.02	5.05	5.98	7.36	6.39	5.95	6.1
CaO	7.74	10.26	9.75	10.22	9.03	9.37	9.76	9.57	9.61
Na_2O	3.86	3.2	3.32	3.08	3.19	2.92	3.06	3.01	3.06
K_2O	0.91	0.66	0.63	0.55	0.77	0.64	0.64	0.64	0.65
P_2O_5	0.25	0.21	0.19	0.17	0.28	0.23	0.21	0.23	0.23
LOI	n.d.	n.d.	n.d.	n.d.	n.d.	n.d.	-0.61	-0.47	-0.51
Sc	n.d.	n.d.	n.d.	n.d.	n.d.	n.d.	414	420	420
Rb	n.d.	n.d.	n.d.	n.d.	n.d.	n.d.	14	14	15
Y	26.4	21.1	n.d.	n.d.	n.d.	n.d.	22	22	22
Zr	118	96	n.d.	n.d.	n.d.	n.d.	85	86	87
Nb	2.8	2.5	n.d.	n.d.	n.d.	n.d.	1	1	1
Ba	n.d.	n.d.	n.d.	n.d.	n.d.	n.d.	201	199	200
La	n.d.	n.d.	n.d.	n.d.	n.d.	n.d.	6.9	7.2	7.3
Ce	n.d.	n.d.	n.d.	n.d.	n.d.	n.d.	17.5	17.8	17.8
Pb	n.d.	n.d.	n.d.	n.d.	n.d.	n.d.	6	7	7
Th	n.d.	n.d.	n.d.	n.d.	n.d.	n.d.	1.2	1.2	1.2
U	n.d.	n.d.	n.d.	n.d.	n.d.	n.d.	0.4	0.4	0.4

Ref.	4	4	5	5	5	5	5	5	6
Volcano	V	V	V	V	V	V	V	V	V
SiO_2	52.93	51.76	52.53	52.64	52.79	52.52	52.89	52.76	57.4
TiO_2	1.13	1.13	1.23	1.24	1.23	1.23	1.19	1.17	1.16
Al_2O_3	16.77	16.59	17.19	17.07	17.15	17.11	16.9	17.03	16.3
$Fe_2O_3^T$	2.83	4.55	8.97	9.06	9.08	9.07	9.07	9.07	9.87
FeO	7.1	5.5	n.d.	n.d.	n.d.	n.d.	n.d.	n.d.	n.d.
MnO	0.15	0.15	0.16	0.16	0.16	0.16	0.16	0.16	0.17
MgO	6.02	6.1	5.77	5.9	5.74	5.64	6.05	5.91	3.14
CaO	9.63	9.55	9.52	9.46	9.49	9.47	9.58	9.54	6.82
Na_2O	3.08	2.98	3.22	3.2	3.18	3.16	3.16	3.2	3.96
K_2O	0.65	0.63	0.68	0.68	0.68	0.67	0.66	0.67	0.91
P_2O_5	0.18	0.2	0.25	0.25	0.25	0.25	0.24	0.24	0.22
LOI	-0.55	-0.41	n.d.	n.d.	n.d.	n.d.	n.d.	n.d.	n.d.
Sc	428	417	35	38	35	28	29	33	n.d.
V	n.d.	n.d.	267	293	292	287	286	279	n.d.
Cu	n.d.	n.d.	137	141	132	116	133	n.d.	n.d.
Zn	n.d.	n.d.	82	85	89	83	85	95	n.d.
Rb	15	14	16	15	15	16	15	15	n.d.
Sr	n.d.	n.d.	460	453	458	456	448	473	n.d.
Y	22	21	26	26	25	26	25	23	n.d.
Zr	87	85	93	95	94	96	91	103	n.d.
Nb	2	1	3.3	3.5	3	3.2	3.1	3.1	n.d.
Ba	198	197	199	209	200	215	201	202	n.d.
La	8	7	12	5	5	5	7	8	n.d.
Ce	19.7	17.3	25	31	25	25	40	22	n.d.
Pb	8	6	8	6	7	7	5	n.d.	n.d.
Th	1.3	1.2	2	1	2	n.d.	2	1	n.d.
U	0.5	0.4	n.d.	n.d.	n.d.	n.d.	n.d.	n.d.	n.d.

Ref.	6	6	6	6	6	6	6	6	6
Volcano	V	V	V	V	V	V	V	V	V
SiO_2	57.2	57.7	57.1	54.5	54.3	55.5	54.7	57.3	56.6
TiO_2	1.17	1.17	1.18	1.23	1.23	1.21	1.24	1.16	1.18
Al_2O_3	16.48	16.3	16.4	17.24	17.25	16.85	16.9	16.16	16.3
$Fe_2O_3^T$	9.93	9.95	9.95	10.38	10.2	10.2	10.4	9.86	9.95
MnO	0.17	0.17	0.17	0.18	0.18	0.17	0.18	0.17	0.18
MgO	3.18	3.17	3.19	3.26	3.23	3.25	3.28	3.12	3.14
CaO	6.97	6.88	6.85	6.9	6.72	6.62	6.58	6.77	6.74
Na_2O	3.92	4.04	4.08	3.86	3.74	3.89	3.75	4	3.95
K_2O	0.89	0.92	0.94	0.7	0.71	0.82	0.77	0.92	0.87
P_2O_5	0.23	0.22	0.22	0.22	0.22	0.22	0.23	0.24	0.23

Ref.	6	6	6	6	6	6	6	6	6
Volcano	V	V	V	V	V	V	V	V	V
SiO_2	56	56.4	57	57	57.5	57.8	56.9	56.8	56.5
TiO_2	1.19	1.18	1.18	1.18	1.15	1.17	1.16	1.18	1.18
Al_2O_3	16.9	16.55	16.45	16.28	16	16.15	16.25	16.3	16.45
$Fe_2O_3^T$	10	10	9.8	9.8	9.85	9.95	9.9	10	10
MnO	0.17	0.17	0.17	0.17	0.17	0.17	0.17	0.17	0.17
MgO	3.21	3.17	3.27	3.19	3.18	3.16	3.2	3.23	3.2
CaO	7.2	6.97	7.05	7.02	6.7	6.8	6.8	7.3	6.8
Na_2O	3.81	4	3.97	3.82	4.03	4.04	3.8	3.98	3.9
K_2O	0.75	0.84	0.87	0.86	0.91	0.91	0.85	0.88	0.88
P_2O_5	0.2	0.22	0.23	0.22	0.22	0.22	0.22	0.22	0.23

Ref.	6	6	6	7	7	7	7	7	7
Volcano	V	V	V	V	V	V	V	V	V
SiO_2	56.2	55.8	53	52.51	52.42	52.45	52.57	52.42	52.52
TiO_2	1.2	1.47	1.2	1.28	1.21	1.2	1.2	1.19	1.16
Al_2O_3	16.5	15.9	16.55	16.52	17.24	17.35	17.36	17.08	17.29
$Fe_2O_3^T$	10.14	11.05	10.25	10.36	9.85	9.78	9.86	9.99	10.07
MnO	0.19	0.18	0.16	0.17	0.16	0.16	0.16	0.16	0.16
MgO	3.22	3.35	5.68	5.75	5.63	5.56	5.66	5.94	6.3
CaO	6.86	6.8	8.88	9.12	9.41	9.41	9.43	9.42	9.42
Na_2O	3.93	4.05	3.32	3.26	3.29	3.3	3.28	3.2	3.19
K_2O	0.85	0.9	0.71	0.71	0.68	0.69	0.67	0.67	0.64
P_2O_5	0.23	0.28	0.22	0.26	0.25	0.25	0.24	0.24	0.24
LOI	n.d.	n.d.	n.d.	-0.09	-0.02	0	-0.45	-0.56	-0.47
Sc	n.d.	n.d.	n.d.	31	34	34	34	39	n.d.
V	n.d.	n.d.	n.d.	328	311	313	296	310	267
Cr	n.d.	n.d.	n.d.	136	137	135	139	156	114
Ni	n.d.	n.d.	n.d.	50	59	61	60	64	50
Cu	n.d.	n.d.	n.d.	117	123	132	71	129	119
Zn	n.d.	n.d.	n.d.	87	90	90	88	91	86
Rb	n.d.	n.d.	n.d.	17	16	16	15	16	15
Sr	n.d.	n.d.	n.d.	450	473	465	471	456	460
Y	n.d.	n.d.	n.d.	27	26	24	25	24	26
Zr	n.d.	n.d.	n.d.	107	100	101	102	98	89
Nb	n.d.	n.d.	n.d.	3	3	2	3	3	5
Ba	n.d.	n.d.	n.d.	199	204	198	192	200	185
La	n.d.	n.d.	n.d.	n.d.	n.d.	n.d.	n.d.	n.d.	7
Ce	n.d.	n.d.	n.d.	n.d.	n.d.	n.d.	n.d.	n.d.	19
Nd	n.d.	n.d.	n.d.	n.d.	n.d.	n.d.	n.d.	n.d.	22
Pb	n.d.	n.d.	n.d.	8	8	6	7	7	6
Th	n.d.	n.d.	n.d.	4	1	n.d.	n.d.	n.d.	n.d.
U	n.d.	n.d.	n.d.	2	n.d.	n.d.	n.d.	3	n.d.

Ref.	7	7	7	7	7	7	7	7	7
Volcano	V	V	V	V	V	V	V	V	V
SiO_2	52.45	50.76	51.94	52.6	52.73	52.76	52.2	51.68	51.43
TiO_2	1.19	1.18	1.19	1.2	1.21	1.14	1.18	1.2	1.11
Al_2O_3	17.27	16.3	16.6	16.45	16.66	17.18	16.52	16.86	16.58
$Fe_2O_3^T$	10.1	10.83	10.19	10.26	10.26	9.88	10.09	10.24	10.16
MnO	0.16	0.17	0.15	0.16	0.16	0.16	0.16	0.16	0.15
MgO	6.28	6.25	6.2	6.02	6.22	5.84	6.46	6.49	6.52
CaO	9.43	10.09	9.62	9.36	9.41	9.7	9.39	9.55	9.92
Na_2O	3.2	3.46	3.24	3	3.2	3.19	3.14	3.21	3.14
K_2O	0.65	0.7	0.65	0.66	0.68	0.66	0.66	0.67	0.66
P_2O_5	0.25	0.25	0.24	0.25	0.25	0.23	0.24	0.24	0.23
LOI	-0.41	-0.54	-0.42	-0.46	-0.3	-0.53	-0.35	-0.27	-0.34
Sc	n.d.	n.d.	n.d.	n.d.	33	37	n.d.	n.d.	n.d.
V	257	244	259	257	290	298	254	253	223
Cr	118	116	124	153	165	270	148	142	164
Ni	52	50	48	51	59	62	50	52	54
Cu	137	122	118	103	134	128	128	112	121
Zn	86	88	85	86	88	86	84	79	83
Rb	15	15	14	18	16	17	16	16	15
Sr	463	460	449	454	455	425	444	447	415
Y	26	26	25	26	26	25	25	27	26
Zr	93	90	91	93	100	97	91	91	89
Nb	5	5	3	7	3	3	5	6	4
Ba	184	175	176	198	188	192	189	198	186
La	4	12	5	6	n.d.	n.d.	6	2	10
Ce	7	n.d.	2	2	n.d.	n.d.	3	n.d.	1
Nd	7	5	5	10	n.d.	n.d.	18	11	13
Pb	5	5	11	11	7	9	9	6	5
Th	n.d.	n.d.	n.d.	4	1	1	n.d.	n.d.	n.d.
U	n.d.	n.d.	n.d.	n.d.	2	2	n.d.	n.d.	n.d.

Ref.	7	7	7	7	7	7	7	7	7
Volcano	V	V	V	V	V	V	V	V	V
SiO_2	52.02	51.84	50.91	50.71	51.19	n.d.	51.49	51.6	52.78
TiO_2	1.09	1.1	1.18	1.13	1.12	n.d.	1.21	1.19	1.17
Al_2O_3	16.64	16.73	15.99	16.25	16.49	n.d.	16.85	16.92	17.3
$Fe_2O_3^T$	10	9.95	10.73	10.53	10.36	n.d.	9.99	10.15	9.86
MnO	0.15	0.15	0.16	0.16	0.16	n.d.	0.16	0.16	0.15
MgO	6.5	6.24	6.58	6.85	6.85	n.d.	5.66	6.25	6.13
CaO	9.61	9.72	10.07	10.13	9.76	n.d.	8.82	9.16	9.37
Na_2O	3.08	3.09	3.32	3.13	3.04	n.d.	3.17	3.16	3.18
K_2O	0.64	0.65	0.7	0.65	0.64	n.d.	0.71	0.67	0.65
P_2O_5	0.24	0.23	0.24	0.23	0.24	n.d.	0.27	0.27	0.24
LOI	-0.34	-0.18	-0.33	-0.36	-0.25	n.d.	1.37	0.52	-0.43
Sc	n.d.	n.d.	n.d.	n.d.	n.d.	33	34	n.d.	n.d.
V	238	227	224	220	226	257	313	262	260
Cr	165	157	147	195	213	94	149	142	120
Ni	56	52	53	63	64	45	64	53	49
Cu	120	116	125	116	128	98	127	115	117
Zn	84	81	85	82	83	82	95	91	85
Rb	16	16	19	16	15	13	18	18	16
Sr	414	415	447	413	412	468	430	430	456
Y	25	28	28	26	26	20	25	25	24
Zr	89	91	90	85	89	80	108	94	90
Nb	4	4	5	4	5	3	3	5	4
Ba	167	169	168	155	158	184	213	194	185
La	4	5	2	2	13	n.d.	n.d.	8	5
Ce	n.d.	3	n.d.	n.d.	n.d.	n.d.	n.d.	5	7
Nd	1	18	7	11	18	n.d.	n.d.	10	8
Pb	9	6	10	14	9	5	7	7	5
Th	2	n.d.	5	2	1	1	2	1	n.d.
U	n.d.	n.d.	n.d.	n.d.	n.d.	2	1	n.d.	n.d.

Ref.	7	7	7	7	7	7	7	7	7
Volcano	V	V	V	V	V	V	V	V	V
SiO_2	55.17	56.02	54.81	54.61	n.d.	n.d.	n.d.	n.d.	n.d.
TiO_2	1.18	1.2	1.18	1.19	n.d.	n.d.	n.d.	n.d.	n.d.
Al_2O_3	16.9	16.52	16.57	16.97	n.d.	n.d.	n.d.	n.d.	n.d.
$Fe_2O_3^T$	9.86	10	9.96	10.11	n.d.	n.d.	n.d.	n.d.	n.d.
MnO	0.17	0.17	0.16	0.16	n.d.	n.d.	n.d.	n.d.	n.d.
MgO	3.96	3.54	4.22	4.43	n.d.	n.d.	n.d.	n.d.	n.d.
CaO	8.23	6.95	8.29	8.25	n.d.	n.d.	n.d.	n.d.	n.d.
Na_2O	3.69	3.94	3.71	3.74	n.d.	n.d.	n.d.	n.d.	n.d.
K_2O	0.82	0.87	0.79	0.8	n.d.	n.d.	n.d.	n.d.	n.d.
P_2O_5	0.22	0.22	0.21	0.22	n.d.	n.d.	n.d.	n.d.	n.d.
LOI	-0.31	0.1	-0.33	-0.36	n.d.	n.d.	n.d.	n.d.	n.d.
Sc	35	n.d.	n.d.	n.d.	31.3	32.9	30.9	31.9	32.6
V	313	272	265	273	223	266	192	222	246
Cr	40	4	34	33	333	20	86	228	134
Ni	15	10	15	16	102	19	21	81	42
Cu	43	61	108	103	n.d.	n.d.	n.d.	n.d.	n.d.
Zn	97	99	91	95	80	108	81	80	89
Rb	20	20	21	18	12.9	24.7	19.4	17.8	15.1
Sr	421	396	415	413	439	402	463	437	437
Y	25	29	28	29	19.5	27.6	23.1	24.4	21.7
Zr	108	106	99	99	84	124	118	106	95
Nb	3	4	4	5	1.9	3.2	3.6	2.3	2.6
Ba	228	309	217	227	182	285	287	229	200
La	n.d.	4	n.d.	2	7.3	10.6	10.6	7.96	7.74
Ce	n.d.	n.d.	8	n.d.	18.7	27.8	25.9	22.3	19.5
Nd	n.d.	4	22	4	11.9	17	15.5	15.1	13.2
Pb	8	10	10	6	n.d.	n.d.	n.d.	n.d.	n.d.
Th	3	2	1	1	1.3	2.2	1.8	1.3	1.7
U	1	n.d.	n.d.	n.d.	n.d.	n.d.	n.d.	n.d.	n.d.

Ref.	7	7	7	7	7	7	7	7	7
Volcano	V	V	V	V	V	V	V	V	V
Sc	33.3	32.4	32.2	33.4	31.3	35.3	33.5	40	31.8
V	246	312	300	254	239	217	246	233	256
Cr	248	35	17	126	147	225	108	105	219
Ni	85	22	12	40	36	70	42	28	64
Zn	87	101	104	88	90	73	85	79	87
Rb	14.6	20.4	21.4	15.5	14	9.7	12.2	14.7	14.9
Sr	429	428	428	453	482	410	474	493	465
Y	21.9	25.2	27.1	22.6	20.7	17	19.9	22.5	22.3
Zr	92	114	118	97	89	62	84	110	94
Nb	2.4	2.8	3.1	2.4	2.5	1.3	2.9	2.7	2.1
Ba	191	255	256	200	196	138	181	217	193
La	7.8	10.1	9.76	8.15	6.8	4.21	6.68	10.2	8.07
Ce	19.8	25.8	26.3	21.5	19	12.9	18.2	25.3	21
Nd	12.2	16.3	16.6	13.6	12.1	8.9	12	15.4	13.4
Th	1.5	1.7	2	1.5	1.3	0.6	1	1.4	1.2

Ref.	7	7	7	7	7	7	7	7	7
Volcano	V	V	V	V	V	V	V	V	V
Sc	35.2	31	34.8	33.6	33.7	33	33.7	32.1	31.4
V	282	257	263	268	269	279	260	288	239
Cr	104	129	180	185	183	161	133	17	88
Ni	47	52	74	73	74	67	54	21	35
Zn	99	85	100	95	101	95	91	105	84
Rb	18.7	15.6	15.5	15.5	15.7	15.3	15.1	20.6	14.8
Sr	426	469	429	432	433	473	457	428	470
Y	26.4	23.5	23.1	23.3	23.2	23	22.7	26.4	21.1
Zr	119	100	100	99	102	103	103	118	96
Nb	3.4	2.1	2.7	2	2.6	3.1	2.8	2.8	2.5
Ba	238	209	198	193	206	202	210	258	211
La	10.5	8.18	7.91	8.04	8.02	7.77	8.31	9.8	7.74
Ce	27	22.2	22.3	22	22.2	22.4	21.9	26.6	21.2
Nd	16.7	14.3	14.1	14.2	13.2	13.9	13.7	16	12.8
Th	2	1.3	1.5	1.2	1.1	1.1	1.4	1.8	1.2

Ref.	7	7	7	1	1	1	1	1	1
Volcano	V	V	V	L	L	L	L	L	L
SiO_2	n.d.	52.3	52.61	51.23	51.39	60.56	62.74	61.9	62.93
TiO_2	n.d.	1.19	1.16	1.3	1.31	1.27	1.14	0.92	0.92
Al_2O_3	n.d.	17.22	16.6	18.11	18.02	15.3	15.2	15.84	16.01
$Fe_2O_3^T$	n.d.	9.92	10.06	10.87	11	8.73	7.76	7.42	6.25
MnO	n.d.	0.16	0.15	0.19	0.18	0.23	0.22	0.21	0.18
MgO	n.d.	5.86	6.05	4.94	4.69	1.68	1.2	1.33	1.25
CaO	n.d.	9.28	9.23	8.63	8.63	3.96	3.2	3.57	3.5
Na_2O	n.d.	3.25	3.17	3.19	3.44	5.2	5.2	4.99	5.63
K_2O	n.d.	0.67	0.66	1.17	1.25	2.41	2.73	2.68	2.77
P_2O_5	n.d.	0.25	0.25	0.36	0.4	0.57	0.43	0.37	0.39
LOI	n.d.	-0.08	-0.41	n.d.	n.d.	n.d.	n.d.	n.d.	n.d.
Sc	30	n.d.	n.d.	n.d.	n.d.	n.d.	n.d.	n.d.	n.d.
V	307	n.d.	n.d.	n.d.	n.d.	n.d.	n.d.	n.d.	n.d.
Cr	148	n.d.	n.d.	n.d.	n.d.	n.d.	n.d.	n.d.	n.d.
Ni	68	n.d.	n.d.	n.d.	n.d.	n.d.	n.d.	n.d.	n.d.
Cu	164	n.d.	n.d.	n.d.	n.d.	n.d.	n.d.	n.d.	n.d.
Rb	17	n.d.	n.d.	n.d.	n.d.	n.d.	n.d.	n.d.	n.d.
Sr	458	n.d.	n.d.	n.d.	n.d.	n.d.	n.d.	n.d.	n.d.
Y	n.d.	n.d.	n.d.	27.3	27.4	43.1	45.5	40.9	42.3
Zr	94	n.d.	n.d.	154	157	270	311	285	302
Nb	n.d.	n.d.	n.d.	6.3	6.6	11.3	13.3	11.1	10.8
Ba	232	n.d.	n.d.	n.d.	n.d.	n.d.	n.d.	n.d.	n.d.
La	8.9	n.d.	n.d.	n.d.	n.d.	n.d.	n.d.	n.d.	n.d.
Ce	24.7	n.d.	n.d.	n.d.	n.d.	n.d.	n.d.	n.d.	n.d.
Th	1.55	n.d.	n.d.	n.d.	n.d.	n.d.	n.d.	n.d.	n.d.
U	0.48	n.d.	n.d.	n.d.	n.d.	n.d.	n.d.	n.d.	n.d.

Ref.	8	8	8	8	8	8	8	8	8
Volcano	L	L	L	L	L	L	L	L	L
SiO_2	63.09	63.28	63.37	55.2	55.02	54.85	51.2	55.32	57.06
TiO_2	0.87	0.89	0.86	1.12	1.31	1.26	1.18	1.29	1.32
Al_2O_3	16.25	16.31	16.13	17.63	17.35	16.79	20.33	16.95	16.6
$Fe_2O_3^T$	5.89	5.83	5.76	8.6	8.31	8.86	8.46	8.37	9.06
MnO	0.15	0.15	0.15	0.18	0.21	0.19	0.15	0.19	0.17
MgO	1.66	1.54	1.59	2.79	2.51	2.64	3.61	2.5	2.59
CaO	3.93	3.87	3.94	7.78	7.74	7.84	10.07	7.77	5.47
Na_2O	5.05	5.01	5.03	4.55	4.7	4.67	3.39	4.83	4.83
K_2O	2.45	2.38	2.45	1.42	2.04	2.07	0.96	2.01	1.93
P_2O_5	0.34	0.34	0.33	0.34	0.42	0.42	0.24	0.38	0.56
Sc	13	13	13	n.d.	n.d.	n.d.	n.d.	n.d.	20
V	63	64	61	n.d.	n.d.	n.d.	n.d.	n.d.	86
Cr	5	5	5	n.d.	n.d.	n.d.	n.d.	n.d.	5
Ni	5	5	5	n.d.	n.d.	n.d.	n.d.	n.d.	5
Cu	8	8	5	n.d.	n.d.	n.d.	n.d.	n.d.	14
Zn	77	76	79	n.d.	n.d.	n.d.	n.d.	n.d.	93
Sr	440	460	454	n.d.	n.d.	n.d.	n.d.	n.d.	550
Y	33.9	33.3	34.5	n.d.	n.d.	n.d.	n.d.	n.d.	38.8
Zr	216	221	226	n.d.	n.d.	n.d.	n.d.	n.d.	167
Ba	710	710	690	n.d.	n.d.	n.d.	n.d.	n.d.	570
La	32	31	32	n.d.	n.d.	n.d.	n.d.	n.d.	31
Ce	72	70	71	n.d.	n.d.	n.d.	n.d.	n.d.	69
Nd	37	34	37	n.d.	n.d.	n.d.	n.d.	n.d.	38
Sm	7.2	7.22	6.98	n.d.	n.d.	n.d.	n.d.	n.d.	7.5
Eu	1.9	1.87	1.85	n.d.	n.d.	n.d.	n.d.	n.d.	2.15
Gd	5.75	6	5.9	n.d.	n.d.	n.d.	n.d.	n.d.	7.3
Hf	6.2	5.1	5.8	n.d.	n.d.	n.d.	n.d.	n.d.	4.9

Ref.	8	8	8	8	8	8	8	8	8
Volcano	L	L	L	L	L	L	L	L	L
SiO_2	56.93	54.79	51.99	62.99	51.11	52.35	57.57	57.15	54.98
TiO_2	1.3	1.38	1.44	0.88	1.2	1.35	0.83	0.98	0.94
Al_2O_3	16.41	17.15	16.77	16.01	18.64	17.87	17.49	17.6	18.26
$Fe_2O_3^T$	9.33	10.28	12.02	6.53	10.55	9.59	6.7	8.25	7.91
MnO	0.18	0.17	0.15	0.16	0.15	0.18	0.18	0.16	0.17
MgO	2.61	3.26	4.02	1.35	4.3	3.51	2.09	2.52	2.5
CaO	5.44	6.61	7.88	3.24	8.39	8.56	7.35	5.91	8.05
Na_2O	4.9	4.09	3.85	5.12	3.8	4.36	4.93	4.95	4.6
K_2O	1.94	1.45	1.12	2.98	1.2	1.48	1.93	1.59	1.63
P_2O_5	0.54	0.4	0.34	0.34	0.27	0.35	0.53	0.5	0.58
Sc	22	25	26	16	27	n.d.	n.d.	11	n.d.
V	88	162	260	21	250	n.d.	n.d.	86	n.d.
Cr	5	5	5	5	n.d.	n.d.	n.d.	5	n.d.
Ni	587	5	5	5	5	n.d.	n.d.	5	n.d.
Cu	n.d.	29	45	8	44	n.d.	n.d.	14	n.d.
Zn	n.d.	81	86	90	76	n.d.	n.d.	77	n.d.
Sr	556	610	608	385	650	n.d.	n.d.	730	n.d.
Y	40.2	31.7	29.9	46.3	n.d.	n.d.	n.d.	27.2	n.d.
Zr	177	145	108	274	119	n.d.	n.d.	43	n.d.
Ba	576	476	363	742	387	n.d.	n.d.	510	n.d.
La	28	23	20	35	19	n.d.	n.d.	26	n.d.
Ce	65	54	48	80	42	n.d.	n.d.	59	n.d.
Nd	36	30	25	41	24	n.d.	n.d.	31	n.d.
Sm	7.8	6.27	6	9.12	4.6	n.d.	n.d.	6.05	n.d.
Eu	2.13	1.94	1.7	2.18	1.23	n.d.	n.d.	1.75	n.d.
Gd	6.17	5.68	5.02	7.41	4.31	n.d.	n.d.	5.39	n.d.
Hf	5.1	4.1	3.3	7.2	3.5	n.d.	n.d.	3.9	n.d.

Ref.	8	8	8	8	8	8	8	8	8
Volcano	L	L	L	L	L	L	L	L	L
SiO_2	56.09	51.22	61.42	62.05	60.45	62.39	51.03	51.03	50.18
TiO_2	0.9	1.49	0.98	0.97	1.16	0.98	1.29	1.3	1.17
Al_2O_3	17.77	18.35	16.39	16.75	16.12	16.3	18.04	17.89	19.45
$Fe_2O_3^T$	7.36	10.77	7.14	6.36	7.16	5.88	10.83	10.92	9.82
MnO	0.18	0.15	0.17	0.16	0.18	0.15	0.19	0.18	0.21
MgO	2.4	3.8	1.54	1.34	2.08	1.29	4.92	4.66	5.05
CaO	7.88	8.02	4.07	3.49	4.44	3.63	8.6	8.57	8.5
Na_2O	4.79	4.01	4.92	5.25	5.13	5.42	3.18	3.42	3.68
K_2O	1.77	1.35	2.58	2.78	2.44	2.82	1.17	1.24	1.15
P_2O_5	0.47	0.43	0.38	0.45	0.44	0.4	0.36	0.4	0.36
Sc	11	n.d.	18	n.d.	n.d.	n.d.	29.3	28	n.d.
V	63	n.d.	37	n.d.	n.d.	n.d.	216	219	n.d.
Cr	6	n.d.	5	n.d.	n.d.	n.d.	19	23	n.d.
Ni	2	n.d.	12	n.d.	n.d.	n.d.	27	24	n.d.
Cu	n.d.	n.d.	9	n.d.	n.d.	n.d.	n.d.	n.d.	n.d.
Zn	n.d.	n.d.	6	n.d.	n.d.	n.d.	93	97	n.d.
Rb	35	n.d.	n.d.	n.d.	n.d.	n.d.	32.1	34.2	n.d.
Sr	691	n.d.	451	n.d.	n.d.	n.d.	621	626	n.d.
Y	26	n.d.	48.9	n.d.	n.d.	n.d.	27.3	27.4	n.d.
Zr	114	n.d.	243	n.d.	n.d.	n.d.	154	157	n.d.
Nb	7	n.d.	n.d.	n.d.	n.d.	n.d.	6.3	6.6	n.d.
Ba	n.d.	n.d.	746	n.d.	n.d.	n.d.	375	384	n.d.
La	26	n.d.	37	n.d.	n.d.	n.d.	20.8	21.6	19.9
Ce	55	n.d.	83	n.d.	n.d.	n.d.	48.5	51.3	57
Nd	33	n.d.	44	n.d.	n.d.	n.d.	24	25.9	26
Sm	n.d.	n.d.	10.1	n.d.	n.d.	n.d.	5.65	5.75	5.19
Eu	n.d.	n.d.	2.37	n.d.	n.d.	n.d.	1.67	1.63	1.45
Gd	n.d.	n.d.	9.19	n.d.	n.d.	n.d.	n.d.	n.d.	n.d.
Hf	n.d.	n.d.	7.5	n.d.	n.d.	n.d.	3.7	3.7	n.d.

Ref.	8	8	8	8	8	8	8	8	8
Volcano	L	L	L	L	L	L	L	L	L
SiO_2	51.98	60.42	62.6	62.13	62.79	62.83	60.94	62.28	62.18
TiO_2	1.18	1.27	1.14	0.92	0.92	0.8	1.26	0.97	1.13
Al_2O_3	19.81	15.19	15.17	15.9	15.97	16.71	15.29	16.09	15.65
$Fe_2O_3^T$	8.64	8.71	7.74	7.45	6.24	5.96	7.81	6.37	7.17
MnO	0.14	0.23	0.22	0.21	0.18	0.14	0.2	0.16	0.18
MgO	3.72	1.67	1.2	1.33	1.25	1.01	1.81	1.51	1.47
CaO	8.49	3.95	3.19	3.58	3.49	3.48	3.83	3.62	3.57
Na_2O	3.99	5.18	5.19	5.01	5.62	5.54	5.45	5.45	5.3
K_2O	1.3	2.4	2.72	2.69	2.76	2.83	2.47	2.79	2.51
P_2O_5	0.34	0.57	0.43	0.37	0.39	0.31	0.54	0.37	0.45
Sc	n.d.	19.9	17.9	15.7	17.2	n.d.	n.d.	n.d.	18
V	n.d.	32	17	19	15	n.d.	n.d.	n.d.	32
Cr	n.d.	8	6	8	3	10	n.d.	n.d.	5
Ni	n.d.	10	9	10	10	n.d.	n.d.	n.d.	5
Cu	n.d.	n.d.	n.d.	n.d.	n.d.	n.d.	n.d.	n.d.	8
Zn	n.d.	110	100	93	87	n.d.	n.d.	n.d.	98
Rb	n.d.	59.4	66.9	77.1	77.8	n.d.	n.d.	n.d.	n.d.
Sr	n.d.	410	334	414	392	n.d.	n.d.	n.d.	394
Y	n.d.	43.1	45.5	40.9	42.3	n.d.	n.d.	n.d.	49
Zr	n.d.	270	311	285	302	n.d.	n.d.	n.d.	218
Nb	n.d.	11.3	13.3	11.1	10.8	n.d.	n.d.	n.d.	n.d.
Ba	n.d.	708	802	730	747	n.d.	n.d.	n.d.	700
La	n.d.	37.1	40.7	34.4	35.1	33	37	37	36
Ce	n.d.	87.6	89.1	78.9	78.6	71	82	80	83
Nd	n.d.	45.3	45.3	38.6	40.2	39	48	45	44
Sm	n.d.	9.92	9.45	8.21	8.49	6.68	7.9	7.74	9.43
Eu	n.d.	2.57	2.49	2.2	2.3	2.17	2.55	2.32	2.5
Gd	n.d.	n.d.	n.d.	n.d.	n.d.	6.64	8.79	8.1	8.1
Hf	n.d.	6.3	6.7	6.4	7.2	n.d.	n.d.	n.d.	7.5

Ref.	8	8	8	8	8	8	8	8	8
Volcano	L	L	L	L	L	L	L	L	L
SiO_2	62.62	61.73	61.53	63.7	63.52	62.95	61.94	64.25	50.69
TiO_2	0.97	1.04	0.67	0.64	0.92	0.98	0.99	0.94	1.4
Al_2O_3	15.83	18.22	17.95	16.45	15.75	15.68	17.27	15.22	17.67
$Fe_2O_3^T$	6.74	5.95	6.71	5.69	6.06	6.29	6.91	6.13	11.14
MnO	0.17	0.16	0.17	0.17	0.52	0.15	0.17	0.15	0.17
MgO	1.56	1.54	1.22	1.24	1.52	1.67	1.28	1.42	4.78
CaO	3.55	3.42	3.2	3.14	3.6	4.06	3.1	3.59	8.33
Na_2O	5	4.44	4.99	5.3	4.55	4.55	4.78	4.58	3.62
K_2O	2.79	2.68	2.79	2.96	2.83	2.88	2.75	2.95	1.38
P_2O_5	0.37	0.41	0.38	0.29	0.35	0.39	0.42	0.38	0.43
Sc	17	n.d.	17	n.d.	15	15	15	16	29
V	30	n.d.	24	n.d.	49	53	24	47	235
Cr	5	n.d.	6	n.d.	5	5	5	5	13
Ni	5	n.d.	2	n.d.	5	5	5	5	17
Cu	12	n.d.	n.d.	n.d.	11	16	11	10	56
Zn	92	n.d.	93	n.d.	75	75	92	79	85
Rb	n.d.	n.d.	80	n.d.	n.d.	n.d.	n.d.	n.d.	n.d.
Sr	340	n.d.	345	n.d.	381	370	340	362	613
Y	48.4	n.d.	43	n.d.	39.5	38.2	49.5	42.6	33.4
Zr	236	n.d.	291	n.d.	245	179	277	236	156
Nb	n.d.	n.d.	10	n.d.	n.d.	n.d.	n.d.	n.d.	n.d.
Ba	670	n.d.	707	n.d.	702	677	680	680	392
La	35	n.d.	37	n.d.	31	32	37	33	25
Ce	82	n.d.	84	n.d.	72	73	85	78	58
Nd	42	n.d.	42	n.d.	36	36	47	41	33
Sm	9.23	n.d.	n.d.	n.d.	7.56	7.36	9.72	8.36	6.96
Eu	2.32	n.d.	n.d.	n.d.	1.91	1.83	2.26	1.97	1.75
Gd	8.1	n.d.	n.d.	n.d.	6.67	6.98	8.66	7.35	5.76
Hf	7.5	n.d.	n.d.	n.d.	7.3	7.4	7.9	7.2	5.2

Ref.	8	8	9	9	9	9	9	9	9	9
Volcano	L	L	S	S	S	S	S	S	S	S
SiO_2	51.98	49.56	50.19	53.81	57.04	66.06	67.01	61.07	51.75	53.87
TiO_2	1.42	1.11	n.d.	n.d.	n.d.	n.d.	n.d.	n.d.	n.d.	n.d.
Al_2O_3	18.72	21.91	n.d.	n.d.	n.d.	n.d.	n.d.	n.d.	n.d.	n.d.
$Fe_2O_3^T$	10.81	9.6	n.d.	n.d.	n.d.	n.d.	n.d.	n.d.	n.d.	n.d.
MnO	0.17	0.14	n.d.	n.d.	n.d.	n.d.	n.d.	n.d.	n.d.	n.d.
MgO	3.3	3.28	n.d.	n.d.	n.d.	n.d.	n.d.	n.d.	n.d.	n.d.
CaO	7.25	9.8	n.d.	n.d.	n.d.	n.d.	n.d.	n.d.	n.d.	n.d.
Na_2O	4.2	3.32	n.d.	n.d.	n.d.	n.d.	n.d.	n.d.	n.d.	n.d.
K_2O	1.3	0.69	n.d.	n.d.	n.d.	n.d.	n.d.	n.d.	n.d.	n.d.
P_2O_5	0.43	0.19	n.d.	n.d.	n.d.	n.d.	n.d.	n.d.	n.d.	n.d.
Sc	25	23	n.d.	n.d.	n.d.	n.d.	n.d.	n.d.	n.d.	n.d.
V	190	n.d.	n.d.	n.d.	n.d.	n.d.	n.d.	n.d.	n.d.	n.d.
Cr	9	7	n.d.	n.d.	n.d.	n.d.	n.d.	n.d.	n.d.	n.d.
Ni	9	2	n.d.	n.d.	n.d.	n.d.	n.d.	n.d.	n.d.	n.d.
Cu	34	n.d.	n.d.	n.d.	n.d.	n.d.	n.d.	n.d.	n.d.	n.d.
Zn	90	68	n.d.	n.d.	n.d.	n.d.	n.d.	n.d.	n.d.	n.d.
Rb	n.d.	n.d.	13	23	37	69	72	44	14	21
Sr	641	753	632	683	446	228	209	345	835	665
Y	30	18	15	18	23	35	36	38	22	23
Zr	136	75	78	111	174	309	332	214	128	130
Nb	n.d.	5	3	3	7	10	10	9	6	4
Ba	370	246	232	335	431	676	753	573	384	347
La	21	12	n.d.	n.d.	n.d.	n.d.	n.d.	n.d.	n.d.	n.d.
Ce	47	27	21.4	31.1	36.5	56.6	60	56.1	44.3	46.2
Nd	29	20	n.d.	n.d.	n.d.	n.d.	n.d.	n.d.	n.d.	n.d.
Sm	5.8	n.d.	2.49	3.79	3.91	5.78	5.4	6.68	4.75	5.82
Eu	1.8	n.d.	n.d.	n.d.	n.d.	n.d.	n.d.	n.d.	n.d.	n.d.
Gd	5.2	n.d.	n.d.	n.d.	n.d.	n.d.	n.d.	n.d.	n.d.	n.d.
Yb	n.d.	n.d.	1.2	1.63	2.39	3.53	3.04	3.48	1.69	2.55
Hf	3.5	n.d.	1.61	2.45	3.45	6.87	6.73	4.46	2.84	n.d.

Ref.	9	9	9
Volcano	S	S	S
SiO_2	67.83	53.31	52.55
Rb	82	13	12
Sr	200	583	584
Y	41	15	18
Zr	337	81	82
Nb	11	4	3
Ba	708	243	229
Ce	62.1	23.3	24.1
Sm	7.06	3.21	3.06
Yb	4.02	1.44	1.43
Hf	7.39	1.85	n.d.

Appendix V: Mineral analyses

Analyses of minerals from samples of Quetrupillán lavas. Analyses of plagioclase (Plag), pyroxene, olivine and glass were made by EMPA and analyses of oxides were made by SEM. Samples (Q – lavas from Quetrupillán; H – lavas from the Huililco Valley) and whole-rock lava composition (Bas and. – basaltic andesite; Tr.and. – trachyandesite) are listed. The analysis label includes the mineral (pl – plagioclase; px – pyroxene; ol – olivine; ox – oxide; Gr.mass – groundmass glass; mi – melt inclusion), mineral number and location of analysis within the crystal (core, zone or rim). All analyses are in wt.%. Cations per formula unit (c.f.u.) were calculated using the CFU programme (Cortés, 2017), based on the number of oxygen (N.O.), with speciation of iron estimated following Papike et al. (1974). Some elements were below detection limit (b.d.l.).

Mineral	Plag	Plag	Plag	Plag	Plag	Plag	Plag
Lava comp.	Bas and.	Bas and.	Bas and.	Bas and.	Bas and.	Bas and.	Bas and.
Sample	Q50	Q50	Q50	Q50	Q50	Q50	Q50
Analysis	pl1_core	pl2_core	pl3_zone1	pl3_rim	pl4_core	pl4_zone1	pl4_zone2
SiO_2	50.85	54.54	52.10	51.55	50.53	51.84	50.68
TiO_2	0.05	0.07	0.05	0.06	0.05	0.04	0.05
Al_2O_3	30.83	28.58	29.20	29.76	30.17	29.75	30.02
$Fe_2O_3^T$	0.62	0.66	0.63	0.69	0.60	0.59	0.60
SrO	0.09	0.10	0.11	0.11	0.12	0.12	0.12
MnO	0.01	b.d.l.	b.d.l.	b.d.l.	0.01	b.d.l.	b.d.l.
MgO	0.16	0.11	0.11	0.13	0.12	0.12	0.12
CaO	14.20	11.65	13.14	13.81	14.26	13.81	13.80
Na_2O	3.58	4.97	3.91	3.69	3.46	3.63	3.69
K_2O	0.14	0.28	0.19	0.20	0.17	0.15	0.15
Total	100.54	100.95	99.46	100.00	99.48	100.03	99.23
N.O.	8	8	8	8	8	8	8
Si	2.3130	2.4520	2.3826	2.3510	2.3206	2.3606	2.3309
Ti	0.0016	0.0023	0.0019	0.0019	0.0017	0.0014	0.0017
Al	1.6528	1.5140	1.5739	1.5995	1.6327	1.5964	1.6274
Fe^{3+}	0.0236	0.0249	0.0240	0.0262	0.0231	0.0224	0.0232
Sr	0.0023	0.0026	0.0030	0.0030	0.0033	0.0031	0.0031
Mn	0.0004	0.0000	0.0000	0.0000	0.0002	0.0000	0.0000
Mg	0.0110	0.0072	0.0075	0.0086	0.0083	0.0078	0.0081
Ca	0.6922	0.5609	0.6440	0.6745	0.7014	0.6738	0.6799
Na	0.3159	0.4331	0.3470	0.3266	0.3077	0.3201	0.3292
K	0.0083	0.0162	0.0000	0.0000	0.0000	0.0000	0.0000
Cation sum	5.02	5.01	4.99	5.00	5.01	4.99	5.01
%An	68	56	65	67	70	68	67

Mineral	Plag	Plag	Plag	Plag	Plag	Plag	Plag
Lava comp.	Bas and.	Bas and.	Bas and.	Bas and.	Bas and.	Bas and.	Bas and.
Sample	Q50	Q50	Q50	Q50	Q50	Q50	Q50
Analysis	pl4_rim	pl5_core	pl5_zone1	pl6_core	pl6_zone1	pl6_zone2	pl6_zone3
SiO_2	48.90	49.42	50.40	48.22	49.06	47.35	47.93
TiO_2	0.04	0.04	0.04	0.03	0.03	0.03	0.03
Al_2O_3	31.70	31.44	30.43	32.35	32.31	33.14	33.15
$Fe_2O_3^T$	0.67	0.67	0.65	0.63	0.58	0.59	0.59
SrO	0.12	0.13	0.12	0.13	0.11	0.11	0.10
MnO	b.d.l.	b.d.l.	b.d.l.	b.d.l.	0.01	b.d.l.	b.d.l.
MgO	0.11	0.10	0.11	0.09	0.11	0.10	0.10
CaO	15.51	15.18	14.76	16.52	16.29	17.30	17.05
Na_2O	2.65	2.71	3.26	2.16	2.40	1.81	1.95
K_2O	0.10	0.13	0.15	0.08	0.09	0.06	0.07
Total	99.78	99.80	99.90	100.20	100.99	100.47	100.96
N.O.	8	8	8	8	8	8	8
Si	2.2474	2.2667	2.3079	2.2124	2.2306	2.1714	2.1851
Ti	0.0012	0.0012	0.0013	0.0010	0.0010	0.0010	0.0009
Al	1.7167	1.6997	1.6422	1.7490	1.7311	1.7913	1.7807
Fe^{3+}	0.0257	0.0256	0.0249	0.0240	0.0220	0.0226	0.0226
Sr	0.0031	0.0033	0.0032	0.0034	0.0030	0.0028	0.0027
Mn	0.0000	0.0000	0.0000	0.0000	0.0002	0.0000	0.0000
Mg	0.0072	0.0070	0.0076	0.0063	0.0073	0.0066	0.0065
Ca	0.7636	0.7461	0.7240	0.8121	0.7933	0.8499	0.8326
Na	0.2357	0.2407	0.2894	0.1924	0.2119	0.1609	0.1721
K	0.0000	0.0000	0.0000	0.0000	0.0000	0.0000	0.0000
Cation sum	5.00	5.00	5.01	5.00	5.00	5.01	5.01
%An	76	76	71	81	79	84	83

Mineral	Plag	Plag	Plag	Plag	Plag	Plag	Plag
Lava comp.	Bas and.	Bas and.	Bas and.	Bas and.	Bas and.	Bas and.	Bas and.
Sample	Q50	Q50	Q50	Q50	Q50	Q50	Q50
Analysis	pl6_rim	pl7_core	pl7_zone1	pl7_rim	pl8_core	pl8_zone1	pl9_zone1
SiO_2	51.90	53.90	54.92	51.76	50.91	50.72	50.12
TiO_2	0.05	0.06	0.07	0.05	0.04	0.05	0.03
Al_2O_3	30.23	28.16	27.89	29.97	30.16	30.74	31.18
$Fe_2O_3^T$	0.72	0.65	0.67	0.65	0.63	0.65	0.70
SrO	0.12	0.13	0.11	0.11	0.11	0.11	0.11
MnO	b.d.l.	0.01	b.d.l.	0.01	b.d.l.	b.d.l.	b.d.l.
MgO	0.10	0.11	0.10	0.11	0.11	0.11	0.10
CaO	14.04	11.65	11.37	14.07	14.48	14.36	14.79
Na_2O	3.32	4.56	4.69	3.47	3.30	3.32	3.01
K_2O	0.17	0.26	0.31	0.22	0.16	0.16	0.18
Total	100.64	99.50	100.12	100.43	99.91	100.21	100.22
N.O.	8	8	8	8	8	8	8
Si	2.3491	2.4510	2.4768	2.3490	2.3271	2.3112	2.2867
Ti	0.0017	0.0021	0.0023	0.0018	0.0015	0.0016	0.0009
Al	1.6127	1.5093	1.4821	1.6030	1.6249	1.6507	1.6766
Fe^{3+}	0.0272	0.0248	0.0252	0.0247	0.0242	0.0248	0.0268
Sr	0.0032	0.0035	0.0030	0.0029	0.0029	0.0030	0.0028
Mn	0.0000	0.0003	0.0000	0.0005	0.0000	0.0000	0.0000
Mg	0.0065	0.0073	0.0069	0.0076	0.0072	0.0076	0.0069
Ca	0.6807	0.5677	0.5491	0.6843	0.7093	0.7008	0.7229
Na	0.2911	0.4022	0.4097	0.3052	0.2925	0.2933	0.2667
K	0.0000	0.0000	0.0000	0.0000	0.0000	0.0000	0.0000
Cation sum	4.98	4.98	4.97	4.99	5.00	5.00	5.00
%An	70	59	57	69	71	70	73

Mineral	Plag	Plag	Plag	Plag	Plag	Plag	Plag
Lava comp.	Bas and.	Bas and.	Bas and.	Bas and.	Bas and.	Bas and.	Bas and.
Sample	Q50	Q50	Q50	Q50	Q50	Q50	Q50
Analysis	pl9_zone2	pl9_rim	pl10_core	pl10_zone1	pl10_zone2	pl10_rim	pl11_core
SiO_2	50.74	49.45	52.51	53.15	53.18	51.06	50.13
TiO_2	0.02	0.04	0.04	0.03	0.04	0.04	0.04
Al_2O_3	30.32	31.81	29.05	28.29	29.47	30.14	31.49
$Fe_2O_3^T$	0.65	0.63	0.59	0.59	0.58	0.60	0.67
SrO	0.12	0.11	0.12	0.11	0.12	0.13	0.12
MnO	b.d.l.	0.01	b.d.l.	b.d.l.	0.01	b.d.l.	0.02
MgO	0.10	0.09	0.12	0.11	0.12	0.11	0.12
CaO	14.32	15.43	13.12	12.35	13.10	14.24	15.25
Na_2O	3.30	2.64	3.89	4.23	3.92	3.33	2.80
K_2O	0.15	0.13	0.19	0.16	0.19	0.15	0.15
Total	99.72	100.32	99.63	99.01	100.74	99.77	100.77
N.O.	8	8	8	8	8	8	8
Si	2.3231	2.2569	2.3949	2.4334	2.3968	2.3343	2.2764
Ti	0.0008	0.0013	0.0013	0.0012	0.0014	0.0015	0.0013
Al	1.6360	1.7109	1.5618	1.5262	1.5651	1.6238	1.6852
Fe^{3+}	0.0249	0.0240	0.0226	0.0227	0.0219	0.0228	0.0253
Sr	0.0031	0.0028	0.0031	0.0029	0.0032	0.0034	0.0032
Mn	0.0000	0.0002	0.0000	0.0000	0.0003	0.0000	0.0006
Mg	0.0070	0.0059	0.0079	0.0073	0.0083	0.0075	0.0079
Ca	0.7025	0.7544	0.6413	0.6059	0.6325	0.6973	0.7419
Na	0.2927	0.2336	0.3442	0.3752	0.3422	0.2947	0.2463
K	0.0000	0.0000	0.0000	0.0000	0.0000	0.0000	0.0000
Cation sum	5.00	5.00	4.98	4.98	4.98	4.99	4.99
%An	71	76	65	62	65	70	75

Mineral	Plag	Plag	Plag	Plag	Plag	Plag	Plag
Lava comp.	Bas and.	Bas and.	Bas and.	Bas and.	Bas and.	Bas and.	Tr.and.
Sample	Q50	Q50	Q50	Q63	Q63	Q63	Q8
Analysis	pl11_zone1	pl11_rim	pl12_core	pl1_core	pl3_core	pl4_core	Microlite
SiO_2	49.22	49.70	53.72	53.81	56.16	54.52	56.56
TiO_2	0.05	0.04	0.07	0.06	0.06	0.06	0.13
Al_2O_3	30.83	30.95	28.41	28.35	26.98	28.00	25.22
$Fe_2O_3^T$	0.64	0.63	0.64	0.61	0.61	0.66	1.16
SrO	0.10	0.11	0.12	0.10	0.09	0.09	0.16
MnO	b.d.l.	b.d.l.	b.d.l.	b.d.l.	0.01	b.d.l.	0.01
MgO	0.12	0.12	0.09	0.07	0.07	0.09	0.13
CaO	15.54	15.33	12.12	11.78	9.88	10.91	8.94
Na_2O	2.79	2.99	4.46	5.14	5.93	5.33	6.41
K_2O	0.12	0.16	0.29	0.33	0.44	0.36	0.61
Total	99.42	100.04	99.92	100.25	100.24	100.02	99.32
N.O.	8	8	8	8	8	8	8
Si	2.2707	2.2771	2.4357	2.4415	2.5325	2.4719	2.5806
Ti	0.0018	0.0015	0.0023	0.0021	0.0021	0.0022	0.0045
Al	1.6763	1.6711	1.5184	1.5161	1.4337	1.4959	1.3561
Fe^{3+}	0.0248	0.0240	0.0244	0.0231	0.0231	0.0252	0.0442
Sr	0.0027	0.0029	0.0032	0.0026	0.0025	0.0024	0.0042
Mn	0.0000	0.0000	0.0000	0.0000	0.0002	0.0000	0.0003
Mg	0.0083	0.0085	0.0062	0.0046	0.0049	0.0060	0.0085
Ca	0.7679	0.7525	0.5890	0.5727	0.4772	0.5301	0.4371
Na	0.2495	0.2658	0.3919	0.4522	0.5189	0.4683	0.5669
K	0.0000	0.0000	0.0000	0.0188	0.0256	0.0208	0.0357
Cation sum	5.01	5.01	4.98	5.03	5.02	5.02	5.04
%An	75	74	60	55	47	52	42

Mineral	Plag	Plag	Plag	Plag	Plag	Plag	Plag
Lava comp.	Tr.and.	Tr.and.	Tr.and.	Tr.and.	Tr.and.	Tr.and.	Tr.and.
Sample	Q8	Q8	Q8	Q8	Q8	Q8	Q8
Analysis	pl2_core	pl11_core	pl11_zone1	pl11_rim	pl12_rim	pl13_core	pl13_rim
SiO_2	51.72	51.83	51.91	52.00	55.68	53.83	52.92
TiO_2	0.06	0.04	0.05	0.05	0.06	0.06	0.06
Al_2O_3	29.40	30.63	30.03	30.24	27.99	28.47	28.90
$Fe_2O_3^T$	0.69	0.58	0.64	0.69	0.67	0.68	0.70
SrO	0.12	0.12	0.11	0.12	0.13	0.13	0.13
MnO	b.d.l.	b.d.l.	b.d.l.	0.01	b.d.l.	b.d.l.	b.d.l.
MgO	0.10	0.11	0.10	0.10	0.09	0.10	0.09
CaO	12.79	14.20	14.02	13.46	10.89	12.11	12.36
Na_2O	4.48	3.34	3.62	3.88	4.87	4.54	4.27
K_2O	0.23	0.14	0.15	0.15	0.33	0.28	0.26
Total	99.61	100.98	100.63	100.70	100.70	100.19	99.69
N.O.	8	8	8	8	8	8	8
Si	2.3710	2.3383	2.3521	2.3526	2.4917	2.4351	2.4091
Ti	0.0022	0.0015	0.0016	0.0016	0.0022	0.0019	0.0022
Al	1.5884	1.6284	1.6034	1.6123	1.4758	1.5182	1.5502
Fe^{3+}	0.0266	0.0218	0.0242	0.0261	0.0250	0.0259	0.0265
Sr	0.0031	0.0030	0.0029	0.0032	0.0034	0.0034	0.0035
Mn	0.0000	0.0000	0.0000	0.0004	0.0000	0.0000	0.0000
Mg	0.0071	0.0075	0.0064	0.0065	0.0059	0.0065	0.0064
Ca	0.6282	0.6863	0.6807	0.6522	0.5220	0.5870	0.6026
Na	0.3981	0.2922	0.3179	0.3407	0.4221	0.3978	0.3771
K	0.0136	0.0000	0.0000	0.0000	0.0000	0.0000	0.0000
Cation sum	5.04	4.98	5.00	5.00	4.96	4.99	4.99
%An	60	70	68	66	55	60	62

Mineral	Plag	Plag	Plag	Plag	Plag	Plag	Plag
Lava comp.	Tr.and.	Tr.and.	Tr.and.	Tr.and.	Tr.and.	Tr.and.	Tr.and.
Sample	Q8	Q8	Q8	Q8	Q8	Q8	Q8
Analysis	pl14_core	pl14_zone1	pl14_rim	pl15_core	pl15_zone1	pl15_zone2	pl15_rim
SiO_2	55.13	55.70	55.36	52.78	54.55	53.40	53.15
TiO_2	0.07	0.07	0.07	0.06	0.06	0.07	0.06
Al_2O_3	28.14	28.04	27.20	29.06	28.13	28.18	29.08
$Fe_2O_3^T$	0.60	0.61	0.62	0.66	0.69	0.69	0.72
SrO	0.11	0.13	0.12	0.12	0.11	0.13	0.11
MnO	b.d.l.	b.d.l.	0.01	b.d.l.	b.d.l.	b.d.l.	b.d.l.
MgO	0.08	0.08	0.08	0.09	0.09	0.09	0.09
CaO	10.98	10.92	10.72	12.40	11.64	12.06	12.76
Na_2O	4.81	4.77	4.95	4.36	4.70	4.49	4.06
K_2O	0.33	0.33	0.36	0.25	0.30	0.27	0.25
Total	100.25	100.65	99.50	99.79	100.27	99.38	100.29
N.O.	8	8	8	8	8	8	8
Si	2.4789	2.4923	2.5067	2.4013	2.4607	2.4365	2.4059
Ti	0.0024	0.0022	0.0024	0.0022	0.0020	0.0023	0.0022
Al	1.4911	1.4788	1.4515	1.5583	1.4952	1.5151	1.5513
Fe^{3+}	0.0224	0.0228	0.0236	0.0251	0.0260	0.0262	0.0274
Sr	0.0030	0.0034	0.0032	0.0032	0.0028	0.0035	0.0029
Mn	0.0000	0.0000	0.0002	0.0000	0.0000	0.0000	0.0000
Mg	0.0051	0.0051	0.0057	0.0064	0.0064	0.0061	0.0063
Ca	0.5291	0.5233	0.5198	0.6043	0.5627	0.5893	0.6186
Na	0.4194	0.4137	0.4348	0.3848	0.4107	0.3971	0.3566
K	0.0000	0.0000	0.0000	0.0000	0.0000	0.0000	0.0000
Cation sum	4.96	4.95	4.96	5.00	4.98	4.99	4.98
%An	56	56	54	61	58	60	63

Mineral	Plag	Plag	Plag	Plag	Plag	Plag	Plag
Lava comp.	Tr.and.	Tr.and.	Tr.and.	Tr.and.	Tr.and.	Tr.and.	Tr.and.
Sample	Q8	Q8	Q8	Q8	Q8	Q8	Q8
Analysis	pl16_core	pl16_zone1	pl16_rim	pl17_core	pl17_rim	pl18_core	pl18_zone1
SiO_2	52.12	51.52	52.60	55.42	52.21	47.43	46.86
TiO_2	0.05	0.06	0.06	0.07	0.05	0.03	0.03
Al_2O_3	29.99	30.14	28.49	27.27	29.28	32.99	33.26
$Fe_2O_3^T$	0.73	0.71	0.74	0.70	0.75	0.71	0.71
SrO	0.14	0.11	0.13	0.13	0.11	0.12	0.11
MnO	b.d.l.	b.d.l.	b.d.l.	0.01	0.01	b.d.l.	b.d.l.
MgO	0.09	0.08	0.09	0.10	0.10	0.06	0.07
CaO	13.56	13.60	12.68	10.73	13.10	17.32	17.31
Na_2O	3.64	3.56	4.16	4.95	3.92	2.05	1.82
K_2O	0.20	0.20	0.25	0.35	0.21	0.07	0.08
Total	100.52	99.98	99.19	99.74	99.75	100.79	100.25
N.O.	8	8	8	8	8	8	8
Si	2.3604	2.3468	2.4097	2.5047	2.3816	2.1724	2.1568
Ti	0.0016	0.0019	0.0022	0.0024	0.0019	0.0010	0.0010
Al	1.6009	1.6179	1.5384	1.4525	1.5741	1.7808	1.8042
Fe^{3+}	0.0276	0.0269	0.0283	0.0266	0.0287	0.0272	0.0275
Sr	0.0036	0.0029	0.0034	0.0034	0.0028	0.0032	0.0029
Mn	0.0000	0.0000	0.0000	0.0003	0.0003	0.0000	0.0000
Mg	0.0062	0.0056	0.0063	0.0067	0.0067	0.0044	0.0047
Ca	0.6580	0.6636	0.6223	0.5197	0.6402	0.8497	0.8537
Na	0.3194	0.3143	0.3691	0.4340	0.3466	0.1824	0.1620
K	0.0000	0.0000	0.0000	0.0000	0.0000	0.0000	0.0000
Cation sum	4.99	4.99	4.99	4.96	4.99	5.02	5.02
%An	67	68	63	54	65	82	84

Mineral	Plag	Plag	Plag	Plag	Plag	Plag	Plag
Lava comp.	Tr.and.	Tr.and.	Tr.and.	Tr.and.	Tr.and.	Tr.and.	Tr.and.
Sample	Q8	Q8	Q8	Q8	Q8	Q8	Q8
Analysis	pl18_zone2	pl18_zone3	pl18_rim	pl19_zone1	pl19_zone2	pl19_rim	pl20_core
SiO_2	47.06	52.12	53.10	49.90	49.75	54.35	54.83
TiO_2	0.02	0.06	0.06	0.05	0.04	0.07	0.06
Al_2O_3	32.76	29.20	28.90	30.87	31.17	27.81	27.79
$Fe_2O_3^T$	0.64	0.71	0.75	0.72	0.67	0.71	0.69
SrO	0.11	0.12	0.12	0.12	0.12	0.12	0.12
MnO	b.d.l.	0.01	0.01	b.d.l.	0.02	0.02	b.d.l.
MgO	0.06	0.10	0.10	0.08	0.08	0.09	0.12
CaO	17.50	13.36	12.69	14.87	14.94	11.33	11.54
Na_2O	1.74	3.80	4.07	3.02	3.00	4.74	4.66
K_2O	0.06	0.21	0.24	0.15	0.14	0.31	0.32
Total	99.95	99.70	100.03	99.78	99.94	99.55	100.14
N.O.	8	8	8	8	8	8	8
Si	2.1723	2.3797	2.4097	2.2887	2.2791	2.4682	2.4745
Ti	0.0008	0.0020	0.0019	0.0016	0.0014	0.0023	0.0022
Al	1.7820	1.5714	1.5459	1.6688	1.6824	1.4883	1.4779
Fe^{3+}	0.0249	0.0273	0.0284	0.0276	0.0256	0.0270	0.0261
Sr	0.0028	0.0033	0.0031	0.0032	0.0032	0.0032	0.0032
Mn	0.0000	0.0003	0.0003	0.0000	0.0007	0.0007	0.0000
Mg	0.0041	0.0068	0.0065	0.0058	0.0057	0.0064	0.0078
Ca	0.8652	0.6535	0.6172	0.7305	0.7333	0.5512	0.5580
Na	0.1558	0.3363	0.3584	0.2683	0.2663	0.4170	0.4081
K	0.0000	0.0000	0.0000	0.0000	0.0000	0.0000	0.0000
Cation sum	5.01	4.99	4.98	5.00	5.00	4.98	4.97
%An	85	66	63	73	73	57	58

Mineral	Plag	Plag	Plag	Plag	Plag	Plag	Plag
Lava comp.	Tr.and.	Tr.and.	Tr.and.	Tr.and.	Tr.and.	Tr.and.	Tr.and.
Sample	Q8	Q8	Q8	Q8	Q8	Q8	Q8
Analysis	pl20_zone1	pl20_zone2	pl20_zone3	pl20_zone4	pl20_rim	pl21_rim	pl22_core
SiO_2	54.89	54.36	53.88	51.74	53.77	54.09	54.25
TiO_2	0.07	0.07	0.07	0.06	0.06	0.07	0.06
Al_2O_3	27.66	27.98	28.40	29.60	28.66	28.72	28.19
$Fe_2O_3^T$	0.65	0.66	0.66	0.69	0.75	0.72	0.69
SrO	0.11	0.10	0.11	0.10	0.12	0.12	0.13
MnO	0.01	b.d.l.	0.01	0.01	b.d.l.	b.d.l.	b.d.l.
MgO	0.10	0.10	0.10	0.09	0.09	0.09	0.09
CaO	11.11	11.60	11.68	13.61	12.03	11.96	11.97
Na_2O	4.84	4.80	4.57	3.72	4.24	4.56	4.52
K_2O	0.32	0.31	0.30	0.22	0.25	0.28	0.30
Total	99.74	99.99	99.78	99.84	99.98	100.61	100.19
N.O.	8	8	8	8	8	8	8
Si	2.4836	2.4600	2.4433	2.3607	2.4348	2.4354	2.4514
Ti	0.0023	0.0023	0.0023	0.0021	0.0022	0.0023	0.0021
Al	1.4749	1.4919	1.5180	1.5917	1.5296	1.5238	1.5011
Fe^{3+}	0.0245	0.0251	0.0251	0.0262	0.0283	0.0270	0.0261
Sr	0.0030	0.0026	0.0030	0.0027	0.0031	0.0032	0.0034
Mn	0.0002	0.0000	0.0003	0.0002	0.0000	0.0000	0.0000
Mg	0.0067	0.0065	0.0065	0.0064	0.0064	0.0063	0.0062
Ca	0.5384	0.5625	0.5676	0.6652	0.5835	0.5769	0.5793
Na	0.4248	0.4212	0.4021	0.3295	0.3721	0.3978	0.3957
K	0.0000	0.0000	0.0000	0.0000	0.0000	0.0000	0.0000
Cation sum	4.97	4.98	4.98	4.99	4.97	4.98	4.98
%An	56	57	59	67	61	59	59

Mineral	Plag	Plag	Plag	Plag	Plag	Plag	Plag
Lava comp.	Tr.and.	Tr.and.	Tr.and.	Trachyte	Trachyte	Trachyte	Trachyte
Sample	Q8	Q8	Q17	Q3	Q3	Q3	Q3
Analysis	pl22_zone1	pl22_rim	pl5_core	pl7_zone1	pl8_zone1	pl8_zone2	pl8_zone3
SiO_2	52.13	53.04	53.88	55.79	56.52	57.40	56.56
TiO_2	0.05	0.06	0.07	0.06	0.06	0.06	0.06
Al_2O_3	29.51	29.04	27.91	27.96	26.49	26.73	26.80
$Fe_2O_3^T$	0.68	0.73	0.65	0.55	0.55	0.56	0.56
SrO	0.12	0.13	0.12	0.13	0.14	0.14	0.14
MnO	0.01	0.01	b.d.l.	b.d.l.	b.d.l.	b.d.l.	b.d.l.
MgO	0.09	0.09	0.10	0.07	0.07	0.07	0.06
CaO	13.51	12.86	11.54	10.46	9.68	9.55	9.76
Na_2O	3.72	3.96	5.04	5.67	5.53	6.00	5.92
K_2O	0.20	0.24	0.31	0.30	0.34	0.37	0.36
Total	100.02	100.16	99.61	100.99	99.38	100.87	100.22
N.O.	8	8	8	8	8	8	8
Si	2.3723	2.4048	2.4574	2.4925	2.5537	2.5567	2.5394
Ti	0.0017	0.0020	0.0024	0.0021	0.0021	0.0022	0.0022
Al	1.5826	1.5515	1.5004	1.4720	1.4105	1.4029	1.4179
Fe^{3+}	0.0260	0.0279	0.0246	0.0207	0.0209	0.0209	0.0209
Sr	0.0032	0.0035	0.0033	0.0033	0.0037	0.0037	0.0036
Mn	0.0003	0.0003	0.0000	0.0000	0.0000	0.0000	0.0000
Mg	0.0059	0.0062	0.0065	0.0043	0.0049	0.0043	0.0041
Ca	0.6588	0.6247	0.5638	0.5009	0.4687	0.4559	0.4694
Na	0.3280	0.3480	0.4453	0.4910	0.4845	0.5178	0.5154
K	0.0000	0.0000	0.0181	0.0000	0.0000	0.0000	0.0000
Cation sum	4.99	4.98	5.02	5.00	4.96	4.98	4.99
%An	67	64	55	50	49	47	48

Mineral	Plag	Plag	Plag	Plag	Plag	Plag	Plag
Lava comp.	Trachyte	Trachyte	Trachyte	Trachyte	Trachyte	Trachyte	Trachyte
Sample	Q3	Q3	Q3	Q3	Q3	Q3	Q3
Analysis	pl8_rim	pl9_zone2	pl9_zone3	pl9_zone4	pl9_rim	pl10_core	pl10_zone2
SiO_2	57.30	59.28	58.35	57.36	58.39	57.24	57.76
TiO_2	0.07	0.05	0.06	0.05	0.06	0.05	0.06
Al_2O_3	26.48	25.12	25.37	26.55	26.21	26.82	26.40
$Fe_2O_3^T$	0.59	0.54	0.55	0.52	0.55	0.51	0.54
SrO	0.15	0.15	0.15	0.14	0.14	0.13	0.15
MnO	b.d.l.	b.d.l.	b.d.l.	b.d.l.	b.d.l.	b.d.l.	b.d.l.
MgO	0.06	0.06	0.06	0.05	0.05	0.05	0.06
CaO	9.66	7.47	8.06	9.51	8.85	9.39	9.17
Na_2O	5.73	6.85	6.54	6.01	6.23	5.95	5.94
K_2O	0.34	0.47	0.46	0.35	0.40	0.37	0.39
Total	100.39	99.99	99.58	100.55	100.87	100.51	100.46
N.O.	8	8	8	8	8	8	8
Si	2.5635	2.6450	2.6194	2.5622	2.5926	2.5561	2.5771
Ti	0.0025	0.0016	0.0020	0.0018	0.0019	0.0017	0.0021
Al	1.3960	1.3210	1.3422	1.3979	1.3713	1.4112	1.3881
Fe^{3+}	0.0219	0.0200	0.0208	0.0193	0.0204	0.0191	0.0202
Sr	0.0040	0.0038	0.0038	0.0037	0.0035	0.0033	0.0038
Mn	0.0000	0.0000	0.0000	0.0000	0.0000	0.0000	0.0000
Mg	0.0043	0.0038	0.0038	0.0036	0.0036	0.0035	0.0038
Ca	0.4630	0.3568	0.3877	0.4550	0.4208	0.4492	0.4385
Na	0.4969	0.5928	0.5689	0.5202	0.5361	0.5147	0.5136
K	0.0000	0.0000	0.0000	0.0000	0.0000	0.0000	0.0000
Cation sum	4.97	4.96	4.97	4.98	4.97	4.97	4.96
%An	48	38	41	47	44	47	46

Mineral	Plag	Plag	Plag	Plag	Plag	Plag	Plag
Lava comp.	Trachyte	Trachyte	Trachyte	Trachyte	Trachyte	Trachyte	Trachyte
Sample	Q3	Q3	Q3	Q3	Q3	Q3	Q3
Analysis	pl10_rim	pl11_core	pl11_zone1	pl11_rim	pl12_zone1	pl12_zone2	pl12_rim
SiO_2	57.56	57.95	56.91	58.02	57.89	56.27	56.73
TiO_2	0.05	0.06	0.06	0.06	0.06	0.06	0.06
Al_2O_3	26.01	26.38	27.00	26.66	26.13	27.00	26.40
$Fe_2O_3^T$	0.55	0.53	0.54	0.50	0.57	0.58	0.59
SrO	0.14	0.12	0.13	0.14	0.14	0.14	0.13
MnO	0.01	b.d.l.	0.01	b.d.l.	b.d.l.	b.d.l.	b.d.l.
MgO	0.05	0.04	0.04	0.05	0.06	0.06	0.06
CaO	9.01	8.88	9.71	9.22	8.90	10.00	9.04
Na_2O	5.87	6.28	5.52	5.98	6.07	5.68	6.09
K_2O	0.39	0.41	0.35	0.37	0.40	0.36	0.39
Total	99.64	100.66	100.26	100.97	100.21	100.16	99.49
N.O.	8	8	8	8	8	8	8
Si	2.5875	2.5803	2.5474	2.5748	2.5877	2.5290	2.5601
Ti	0.0016	0.0021	0.0020	0.0018	0.0021	0.0022	0.0019
Al	1.3782	1.3843	1.4242	1.3943	1.3767	1.4302	1.4041
Fe^{3+}	0.0206	0.0196	0.0202	0.0185	0.0214	0.0217	0.0224
Sr	0.0038	0.0032	0.0034	0.0035	0.0036	0.0037	0.0035
Mn	0.0004	0.0000	0.0004	0.0000	0.0000	0.0000	0.0000
Mg	0.0036	0.0029	0.0028	0.0031	0.0039	0.0038	0.0038
Ca	0.4337	0.4234	0.4655	0.4381	0.4262	0.4816	0.4369
Na	0.5117	0.5422	0.4792	0.5142	0.5260	0.4945	0.5328
K	0.0000	0.0000	0.0000	0.0000	0.0000	0.0000	0.0000
Cation sum	4.96	4.97	4.96	4.96	4.96	4.98	4.98
%An	46	44	49	46	45	49	45

Mineral	Plag	Plag	Plag	Plag	Plag	Plag	Plag
Lava comp.	Trachyte	Trachyte	Trachyte	Trachyte	Trachyte	Trachyte	Trachyte
Sample	Q3	Q3	Q3	Q3	Q3	Q3	Q3
Analysis	pl13_rim	pl14_core	pl14_zone1	pl14_zone2	pl14_rim	pl15_core	pl15_rim
SiO_2	56.76	53.39	53.34	54.12	56.95	57.71	58.50
TiO_2	0.06	0.06	0.06	0.06	0.06	0.06	0.06
Al_2O_3	27.06	29.37	29.02	28.53	26.63	26.12	25.64
$Fe_2O_3^T$	0.59	0.55	0.55	0.59	0.57	0.55	0.54
SrO	0.13	0.15	0.13	0.14	0.15	0.14	0.14
MnO	0.01	b.d.l.	b.d.l.	0.01	0.01	b.d.l.	b.d.l.
MgO	0.06	0.05	0.05	0.06	0.06	0.05	0.05
CaO	9.95	12.55	11.97	11.46	9.77	8.72	8.68
Na_2O	5.54	4.22	4.55	4.89	5.87	6.08	6.24
K_2O	0.33	0.20	0.22	0.25	0.34	0.40	0.43
Total	100.49	100.53	99.90	100.11	100.40	99.83	100.28
N.O.	8	8	8	8	8	8	8
Si	2.5391	2.4083	2.4191	2.4461	2.5510	2.5880	2.6104
Ti	0.0019	0.0019	0.0019	0.0022	0.0019	0.0022	0.0019
Al	1.4263	1.5611	1.5511	1.5200	1.4057	1.3806	1.3486
Fe^{3+}	0.0219	0.0206	0.0210	0.0225	0.0214	0.0205	0.0202
Sr	0.0034	0.0040	0.0035	0.0036	0.0039	0.0036	0.0037
Mn	0.0004	0.0000	0.0000	0.0003	0.0003	0.0000	0.0000
Mg	0.0041	0.0037	0.0036	0.0040	0.0039	0.0037	0.0036
Ca	0.4769	0.6063	0.5817	0.5548	0.4691	0.4187	0.4147
Na	0.4801	0.3688	0.4005	0.4285	0.5093	0.5290	0.5395
K	0.0000	0.0000	0.0000	0.0000	0.0000	0.0000	0.0000
Cation sum	4.97	4.98	4.99	4.99	4.98	4.96	4.96
%An	50	62	59	56	48	44	43

Mineral	Plag	Plag	Plag	Plag	Plag	Plag	Plag
Lava comp.	Trachyte	Trachyte	Trachyte	Trachyte	Trachyte	Trachyte	Trachyte
Sample	Q3	Q3	Q7	Q10	Q12	Q12	Q31
Analysis	pl16_core	pl16_rim	pl2_core	pl2_core	Microlite	pl3_core	pl1_core
SiO_2	58.79	57.24	55.66	56.93	61.26	55.36	54.36
TiO_2	0.06	0.06	0.06	0.07	0.32	0.06	0.06
Al_2O_3	25.97	26.83	26.32	26.60	22.69	26.88	27.84
$Fe_2O_3^T$	0.49	0.56	0.64	0.60	1.14	0.57	0.59
SrO	0.15	0.15	0.15	0.12	0.08	0.13	0.15
MnO	b.d.l.	b.d.l.	b.d.l.	0.01	0.02	0.01	b.d.l.
MgO	0.05	0.06	0.06	0.06	0.17	0.06	0.06
CaO	8.02	9.42	9.74	9.33	5.54	10.00	10.66
Na_2O	6.42	5.79	6.16	6.27	7.64	5.74	5.44
K_2O	0.38	0.37	0.32	0.38	1.09	0.32	0.27
Total	100.32	100.47	99.10	100.37	99.94	99.13	99.43
N.O.	8	8	8	8	8	8	8
Si	2.6164	2.5565	2.5408	2.5590	2.7470	2.5239	2.4772
Ti	0.0019	0.0019	0.0019	0.0025	0.0109	0.0021	0.0021
Al	1.3619	1.4122	1.4158	1.4091	1.1990	1.4444	1.4949
Fe^{3+}	0.0184	0.0209	0.0245	0.0227	0.0426	0.0217	0.0226
Sr	0.0038	0.0038	0.0039	0.0031	0.0020	0.0034	0.0039
Mn	0.0000	0.0000	0.0000	0.0002	0.0007	0.0004	0.0000
Mg	0.0035	0.0037	0.0041	0.0040	0.0112	0.0042	0.0040
Ca	0.3823	0.4507	0.4763	0.4494	0.2660	0.4887	0.5202
Na	0.5536	0.5016	0.5450	0.5464	0.6642	0.5074	0.4807
K	0.0000	0.0000	0.0188	0.0218	0.0622	0.0184	0.0156
Cation sum	4.96	4.97	5.03	5.02	5.01	5.01	5.02
%An	41	47	46	44	27	48	51

Mineral	Plag	Plag	Plag	Plag	Plag	Plag	Plag
Lava comp.	Trachyte	Trachyte	Trachyte	Trachyte	Trachyte	Trachyte	Trachyte
Sample	Q31	Q31	Q31	Q31	Q34	Q34	Q36
Analysis	pl2_core	pl3_core	pl4_core	pl5_core	pl3_core	pl4_core	pl3_core
SiO_2	46.60	56.69	53.07	55.35	56.43	54.52	55.98
TiO_2	0.04	0.11	0.05	0.07	0.06	0.06	0.07
Al_2O_3	32.56	26.36	28.78	27.18	26.53	27.84	26.71
$Fe_2O_3^T$	0.61	0.66	0.53	0.53	0.55	0.69	0.57
SrO	0.13	0.13	0.15	0.14	0.15	0.15	0.14
MnO	b.d.l.	0.01	0.01	b.d.l.	b.d.l.	b.d.l.	b.d.l.
MgO	0.05	0.06	0.06	0.05	0.06	0.06	0.06
CaO	17.00	9.24	11.97	10.28	9.20	10.74	9.96
Na_2O	1.97	6.19	4.87	5.73	6.26	5.43	5.98
K_2O	0.06	0.37	0.22	0.31	0.37	0.28	0.34
Total	99.00	99.81	99.70	99.63	99.60	99.76	99.80
N.O.	8	8	8	8	8	8	8
Si	2.1722	2.5624	2.4206	2.5129	2.5557	2.4778	2.5358
Ti	0.0012	0.0039	0.0016	0.0022	0.0020	0.0019	0.0023
Al	1.7887	1.4040	1.5470	1.4544	1.4160	1.4909	1.4260
Fe^{3+}	0.0238	0.0250	0.0201	0.0200	0.0210	0.0264	0.0216
Sr	0.0034	0.0034	0.0039	0.0036	0.0040	0.0038	0.0036
Mn	0.0000	0.0003	0.0002	0.0000	0.0000	0.0000	0.0000
Mg	0.0032	0.0037	0.0038	0.0034	0.0038	0.0038	0.0042
Ca	0.8489	0.4473	0.5851	0.4999	0.4463	0.5227	0.4832
Na	0.1776	0.5424	0.4310	0.5044	0.5498	0.4785	0.5249
K	0.0037	0.0212	0.0131	0.0181	0.0213	0.0161	0.0194
Cation sum	5.02	5.01	5.03	5.02	5.02	5.02	5.02
%An	82	44	57	49	44	51	47

Mineral	Plag	Plag	Plag	Plag	Plag	Plag	Plag
Lava comp.	Trachyte	Trachyte	Trachyte	Trachyte	Trachyte	Trachyte	Trachyte
Sample	Q36	Q36	Q39	Q40	Q41	Q41	Q61
Analysis	pl4_core	pl5_core	pl1_core	pl1_core	pl1_core	pl2_core	pl2_core
SiO_2	54.84	54.00	57.15	56.19	57.59	57.31	55.55
TiO_2	0.06	0.06	0.06	0.07	0.07	0.07	0.06
Al_2O_3	27.32	27.78	26.47	26.64	26.17	26.28	27.16
$Fe_2O_3^T$	0.64	0.53	0.52	0.57	0.51	0.51	0.51
SrO	0.14	0.15	0.12	0.11	0.10	0.11	0.11
MnO	b.d.l.	0.01	0.02	0.01	0.01	0.01	b.d.l.
MgO	0.08	0.05	0.06	0.06	0.06	0.05	0.06
CaO	10.84	11.23	8.89	9.86	8.79	8.53	10.05
Na_2O	5.34	5.18	6.41	6.07	6.58	6.64	5.90
K_2O	0.27	0.24	0.38	0.33	0.41	0.41	0.32
Total	99.53	99.24	100.08	99.91	100.29	99.91	99.73
N.O.	8	8	8	8	8	8	8
Si	2.4962	2.4683	2.5717	2.5414	2.5856	2.5817	2.5182
Ti	0.0021	0.0021	0.0020	0.0022	0.0023	0.0023	0.0020
Al	1.4655	1.4966	1.4039	1.4201	1.3849	1.3950	1.4511
Fe^{3+}	0.0243	0.0202	0.0197	0.0217	0.0192	0.0193	0.0195
Sr	0.0036	0.0039	0.0032	0.0029	0.0027	0.0030	0.0029
Mn	0.0000	0.0003	0.0007	0.0002	0.0002	0.0002	0.0000
Mg	0.0051	0.0035	0.0041	0.0043	0.0039	0.0035	0.0039
Ca	0.5284	0.5500	0.4285	0.4780	0.4229	0.4118	0.4882
Na	0.4711	0.4592	0.5590	0.5322	0.5724	0.5798	0.5184
K	0.0158	0.0140	0.0220	0.0190	0.0235	0.0234	0.0184
Cation sum	5.01	5.02	5.01	5.02	5.02	5.02	5.02
%An	52	54	42	46	42	41	48

Mineral	Plag	Plag	Plag	Plag
Lava comp.	Trachyte	Trachyte	Trachyte	Trachyte
Sample	Q61	H19	H19	H19
Analysis	pl3_core	pl1_core	pl3_core	pl4_core
SiO_2	56.34	55.32	56.47	54.83
TiO_2	0.06	0.07	0.05	0.06
Al_2O_3	26.36	26.72	26.54	27.70
$Fe_2O_3^T$	0.81	0.57	0.52	0.54
SrO	0.13	0.13	0.15	0.13
MnO	0.01	b.d.l.	b.d.l.	b.d.l.
MgO	0.06	0.07	0.05	0.06
CaO	9.45	9.98	8.98	10.07
Na_2O	6.30	5.84	6.20	5.75
K_2O	0.36	0.32	0.38	0.30
Total	99.88	99.02	99.35	99.43
N.O.	8	8	8	8
Si	2.5511	2.5261	2.5609	2.4939
Ti	0.0020	0.0022	0.0019	0.0022
Al	1.4065	1.4378	1.4183	1.4847
Fe^{3+}	0.0307	0.0219	0.0198	0.0204
Sr	0.0033	0.0036	0.0040	0.0035
Mn	0.0002	0.0000	0.0000	0.0000
Mg	0.0040	0.0047	0.0036	0.0041
Ca	0.4586	0.4885	0.4362	0.4906
Na	0.5532	0.5172	0.5448	0.5068
K	0.0207	0.0184	0.0220	0.0172
Cation sum	5.03	5.02	5.01	5.02
%An	44	48	43	48

Mineral	Augite	Augite	Augite	Augite	Augite	Augite	Augite
Lava comp.	Bas. and.	Bas. and.	Bas. and.	Bas. and.	Bas. and.	Bas. and.	Bas. and.
Sample	Q50	Q50	Q50	Q63	Q63	Q63	Q63
Analysis	px8_core	px14_core	px15_core	px1_core	px2_core	px3_core	px6_core
SiO_2	51.897	52.287	52.380	51.540	51.016	51.653	51.901
TiO_2	0.705	0.613	0.575	0.469	0.712	0.766	0.694
Al_2O_3	2.035	2.146	1.510	2.406	1.677	2.165	1.718
FeO^T	9.644	8.931	9.793	7.692	10.388	10.267	10.357
MnO	0.256	0.245	0.296	0.208	0.371	0.307	0.347
MgO	14.173	14.198	13.770	15.707	15.197	14.673	15.156
NiO	0.015	0.014	0.028	0.022	0.001	0.005	0.009
CaO	20.380	20.284	20.380	21.063	19.874	19.755	19.804
Na_2O	0.316	0.290	0.316	0.280	0.343	0.349	0.343
Total	99.42	99.01	99.05	99.81	99.58	100.00	100.33
N.O.	6	6	6	6	6	6	6
Si	1.9459	1.9588	1.9713	1.9157	1.9208	1.9300	1.9343
Ti	0.0199	0.0173	0.0163	0.0131	0.0202	0.0215	0.0195
Al	0.0899	0.0947	0.0670	0.1054	0.0744	0.0953	0.0754
Fe^{3+}	0.0015	0.0000	0.0000	0.0446	0.0685	0.0253	0.0417
Fe^{2+}	0.3009	0.2798	0.3082	0.1945	0.2586	0.2955	0.2811
Mn	0.0081	0.0078	0.0094	0.0066	0.0118	0.0097	0.0109
Mg	0.7923	0.7929	0.7726	0.8704	0.8530	0.8173	0.8421
Ni	0.0005	0.0004	0.0008	0.0007	0.0000	0.0001	0.0003
Ca	0.8186	0.8141	0.8217	0.8387	0.8017	0.7908	0.7907
Na	0.0230	0.0211	0.0230	0.0201	0.0250	0.0253	0.0247
Cation sum	4.00	3.99	3.99	4.01	4.03	4.01	4.02
Mg#	72	73	71	81	76	73	74
%Wo	43	43	43	44	42	42	41
%En	41	42	41	46	45	43	44
%Fs	16	15	16	10	14	16	15

Mineral	Augite	Enstatite	Enstatite	Augite	Augite	Augite	Augite
Lava comp.	Bas. and.	Bas. and.	Bas. and.	Tr.and.	Tr.and.	Tr.and.	Tr.and.
Sample	Q63	Q63	Q63	Q17	Q17	Q8	Q8
Analysis	px7_core	px5_core	px8_core	px2_core	px5_core	px1_core	px2_core
SiO_2	52.138	54.037	54.138	50.855	51.024	50.969	50.529
TiO_2	0.688	0.333	0.290	0.760	0.667	0.749	0.719
Al_2O_3	1.845	0.906	0.773	2.012	2.378	2.189	2.175
FeO^T	10.237	17.493	18.704	10.541	8.417	8.849	9.529
MnO	0.339	0.447	0.471	0.283	0.220	0.269	0.258
MgO	15.468	25.053	24.362	15.083	15.974	15.649	15.766
NiO	0.008	0.027	0.022	0.032	0.016	0.017	0.028
CaO	19.462	1.971	1.853	19.257	20.396	20.528	20.112
Na_2O	0.296	0.037	0.031	0.329	0.292	0.315	0.309
Total	100.54	100.37	100.67	99.15	99.38	99.53	99.43
N.O.	6	6	6	6	6	6	6
Si	1.9346	1.9676	1.9745	1.9189	1.9034	1.9087	1.8993
Ti	0.0192	0.0091	0.0080	0.0216	0.0187	0.0211	0.0203
Al	0.0807	0.0389	0.0332	0.0895	0.1045	0.0966	0.0963
Fe^{3+}	0.0306	0.0084	0.0030	0.0515	0.0625	0.0662	0.0849
Fe^{2+}	0.2871	0.5243	0.5675	0.2811	0.2001	0.2109	0.2146
Mn	0.0107	0.0138	0.0145	0.0090	0.0069	0.0085	0.0082
Mg	0.8557	1.3600	1.3247	0.8485	0.8884	0.8736	0.8835
Ni	0.0002	0.0008	0.0006	0.0010	0.0005	0.0005	0.0009
Ca	0.7736	0.0769	0.0724	0.7785	0.8151	0.8236	0.8099
Na	0.0213	0.0026	0.0022	0.0241	0.0211	0.0229	0.0225
Cation sum	4.01	4.00	4.00	4.02	4.02	4.03	4.04
Mg#	74	72	69	75	81	80	80
%Wo	40	4	4	41	43	43	42
%En	45	69	67	44	47	46	46
%Fs	15	27	29	15	11	11	11

Mineral	Augite	Augite	Augite	Augite	Enstatite	Pigeonite	Augite
Lava comp.	Tr.and.	Tr.and.	Tr.and.	Tr.and.	Tr.and.	Tr.and.	Trachyte
Sample	Q8	Q8	Q8	Q8	Q17	Q8	Q3
Analysis	px4_core	px6_core	px8_core	Microlite	px4_core	Microlite	px1_core
SiO_2	51.083	50.250	51.188	49.622	52.595	51.617	51.090
TiO_2	0.752	0.760	0.625	1.045	0.413	0.692	0.699
Al_2O_3	1.619	1.968	1.618	2.921	1.160	0.912	1.513
FeO^T	10.876	9.734	11.838	10.583	17.879	20.412	10.402
MnO	0.339	0.302	0.379	0.309	0.440	0.561	0.476
MgO	14.932	15.531	17.313	15.003	25.346	20.481	15.017
NiO	0.012	0.011	b.d.l.	0.020	0.034	0.006	b.d.l.
CaO	19.447	20.365	16.208	19.479	1.741	4.304	20.120
Na_2O	0.325	0.320	0.315	0.285	0.032	0.106	0.349
Total	99.38	99.24	99.48	99.27	99.64	99.09	99.67
N.O.	6	6	6	6	6	6	6
Si	1.9280	1.8985	1.9201	1.8768	1.9372	1.9507	1.9244
Ti	0.0214	0.0216	0.0176	0.0297	0.0114	0.0197	0.0198
Al	0.0720	0.0876	0.0715	0.1302	0.0503	0.0406	0.0672
Fe^{3+}	0.0529	0.0956	0.0758	0.0776	0.0546	0.0248	0.0700
Fe^{2+}	0.2904	0.2120	0.2955	0.2572	0.4961	0.6203	0.2577
Mn	0.0108	0.0097	0.0120	0.0099	0.0137	0.0179	0.0152
Mg	0.8402	0.8747	0.9681	0.8460	1.3917	1.1539	0.8433
Ni	0.0004	0.0003	0.0000	0.0006	0.0010	0.0002	0.0000
Ca	0.7863	0.8243	0.6513	0.7893	0.0687	0.1743	0.8119
Na	0.0237	0.0235	0.0229	0.0209	0.0023	0.0078	0.0255
Cation sum	4.03	4.05	4.03	4.04	4.03	4.01	4.03
Mg#	74	80	76	76	73	64	76
%Wo	41	43	34	42	4	9	42
%En	44	46	51	45	71	59	44
%Fs	15	11	15	14	25	32	13

Mineral	Augite	Augite	Augite	Augite	Augite	Augite	Augite
Lava comp.	Trachyte	Trachyte	Trachyte	Trachyte	Trachyte	Trachyte	Trachyte
Sample	Q3	Q3	Q3	Q3	Q3	Q3	Q3
Analysis	px2_core	px6_core	px9_core	px11_core	px12_core	px13_core	px14_core
SiO_2	51.257	50.943	51.810	51.336	52.737	51.963	52.105
TiO_2	0.611	0.608	0.826	0.879	0.643	0.593	0.568
Al_2O_3	1.425	1.523	2.025	2.161	1.593	1.348	1.238
FeO^T	10.318	10.453	10.572	10.785	10.005	10.052	11.237
MnO	0.506	0.470	0.477	0.495	0.447	0.457	0.481
MgO	14.877	14.858	14.734	14.167	14.513	14.726	13.928
NiO	b.d.l.	b.d.l.	b.d.l.	b.d.l.	b.d.l.	b.d.l.	b.d.l.
CaO	19.794	20.184	20.165	19.671	20.415	20.116	19.955
Na_2O	0.337	0.350	0.374	0.368	0.349	0.326	0.329
Total	99.13	99.39	100.99	99.86	100.70	99.58	99.84
N.O.	6	6	6	6	6	6	6
Si	1.9376	1.9254	1.9233	1.9274	1.9551	1.9509	1.9598
Ti	0.0174	0.0173	0.0231	0.0248	0.0179	0.0167	0.0161
Al	0.0635	0.0678	0.0886	0.0956	0.0696	0.0597	0.0549
Fe^{3+}	0.0513	0.0723	0.0456	0.0266	0.0094	0.0288	0.0173
Fe^{2+}	0.2749	0.2581	0.2827	0.3121	0.3008	0.2868	0.3362
Mn	0.0162	0.0150	0.0150	0.0157	0.0140	0.0145	0.0153
Mg	0.8384	0.8372	0.8154	0.7930	0.8021	0.8242	0.7810
Ni	0.0000	0.0000	0.0000	0.0000	0.0000	0.0000	0.0000
Ca	0.8016	0.8173	0.8020	0.7912	0.8108	0.8091	0.8041
Na	0.0247	0.0256	0.0269	0.0268	0.0251	0.0237	0.0240
Cation sum	4.03	4.04	4.02	4.01	4.00	4.01	4.01
Mg#	74	75	73	71	72	73	69
%Wo	42	43	42	42	42	42	42
%En	44	44	43	42	42	43	41
%Fs	14	13	15	16	16	15	17

Mineral	Augite	Augite	Augite	Augite	Augite	Augite	Augite
Lava comp.	Trachyte	Trachyte	Trachyte	Trachyte	Trachyte	Trachyte	Trachyte
Sample	Q3	Q3	Q3	Q10	Q12	Q31	Q34
Analysis	px15_core	px16_core	px18_core	px4_core	px3_core	px3_core	px2_core
SiO_2	52.145	51.624	52.311	52.060	51.044	51.371	51.153
TiO_2	0.543	0.644	0.689	0.649	0.588	0.613	0.627
Al_2O_3	1.246	1.558	1.823	1.417	1.576	1.426	1.459
FeO^T	11.468	10.311	10.557	10.866	11.319	10.497	10.104
MnO	0.580	0.464	0.455	0.483	0.515	0.480	0.420
MgO	13.792	13.653	13.653	14.668	14.745	14.797	15.115
NiO	0.006	b.d.l.	b.d.l.	b.d.l.	b.d.l.	b.d.l.	b.d.l.
CaO	19.582	20.546	20.091	19.573	20.224	20.261	20.220
Na_2O	0.339	0.333	0.349	0.339	0.340	0.344	0.341
Total	99.70	99.13	99.92	100.05	100.35	99.79	99.44
N.O.	6	6	6	6	6	6	6
Si	1.9644	1.9521	1.9580	1.9492	1.9184	1.9328	1.9283
Ti	0.0154	0.0183	0.0194	0.0183	0.0166	0.0174	0.0178
Al	0.0553	0.0694	0.0804	0.0625	0.0698	0.0632	0.0648
Fe^{3+}	0.0098	0.0142	0.0000	0.0274	0.0848	0.0615	0.0678
Fe^{2+}	0.3515	0.3118	0.3305	0.3129	0.2710	0.2688	0.2507
Mn	0.0185	0.0149	0.0144	0.0153	0.0164	0.0153	0.0134
Mg	0.7746	0.7696	0.7619	0.8187	0.8262	0.8300	0.8495
Ni	0.0002	0.0000	0.0000	0.0000	0.0000	0.0000	0.0000
Ca	0.7903	0.8323	0.8056	0.7851	0.8143	0.8167	0.8166
Na	0.0248	0.0244	0.0253	0.0246	0.0247	0.0251	0.0249
Cation sum	4.00	4.01	4.00	4.01	4.04	4.03	4.03
Mg#	68	70	69	71	74	75	76
%Wo	41	43	42	41	43	43	43
%En	40	40	40	43	43	43	44
%Fs	18	16	17	16	14	14	13

Mineral	Augite	Augite	Augite	Augite	Augite	Augite	Augite
Lava comp.	Trachyte	Trachyte	Trachyte	Trachyte	Trachyte	Trachyte	Trachyte
Sample	Q34	Q34	Q36	Q36	Q36	Q39	Q40
Analysis	px4_core	px5_core	px2_core	px5_core	px7_core	px3_core	px1_core
SiO_2	50.949	50.785	51.060	51.297	50.996	51.833	51.900
TiO_2	0.698	0.763	0.670	0.590	0.622	0.607	0.576
Al_2O_3	1.637	1.820	1.781	1.368	1.451	1.332	1.292
FeO^T	10.877	11.624	9.805	10.996	10.197	10.362	10.264
MnO	0.502	0.546	0.358	0.481	0.427	0.527	0.486
MgO	14.864	13.930	15.315	14.535	15.001	14.620	14.992
NiO	b.d.l.	b.d.l.	b.d.l.	0.007	b.d.l.	b.d.l.	b.d.l.
CaO	19.732	19.604	20.009	19.510	20.120	19.956	20.078
Na_2O	0.356	0.374	0.342	0.347	0.338	0.359	0.339
Total	99.62	99.45	99.34	99.13	99.15	99.60	99.86
N.O.	6	6	6	6	6	6	6
Si	1.9225	1.9254	1.9222	1.9428	1.9288	1.9490	1.9453
Ti	0.0198	0.0218	0.0190	0.0168	0.0177	0.0172	0.0163
Al	0.0728	0.0813	0.0790	0.0611	0.0647	0.0590	0.0571
Fe^{3+}	0.0688	0.0517	0.0636	0.0451	0.0670	0.0349	0.0443
Fe^{2+}	0.2745	0.3169	0.2450	0.3032	0.2556	0.2909	0.2774
Mn	0.0161	0.0175	0.0114	0.0154	0.0137	0.0168	0.0154
Mg	0.8362	0.7874	0.8595	0.8207	0.8459	0.8195	0.8377
Ni	0.0000	0.0000	0.0000	0.0002	0.0000	0.0000	0.0000
Ca	0.7977	0.7963	0.8070	0.7916	0.8153	0.8039	0.8062
Na	0.0261	0.0275	0.0250	0.0255	0.0248	0.0262	0.0246
Cation sum	4.03	4.03	4.03	4.02	4.03	4.02	4.02
Mg#	74	70	77	72	76	73	74
%Wo	42	42	42	41	43	42	42
%En	44	41	45	43	44	43	44
%Fs	14	17	13	16	13	15	14

Mineral	Augite	Augite	Augite	Augite	Augite	Augite	Augite
Lava comp.	Trachyte	Trachyte	Trachyte	Trachyte	Trachyte	Trachyte	Trachyte
Sample	Q40	Q40	Q41	Q41	Q46	Q61	Q61
Analysis	px2_core	px3_core	px4_core	px5_core	px1_core	px1_core	px2_core
SiO_2	51.713	51.370	51.902	51.802	51.330	51.963	51.957
TiO_2	0.703	0.815	0.559	0.522	0.726	0.536	0.628
Al_2O_3	1.783	2.042	1.339	1.168	1.706	1.351	1.516
FeO^T	9.965	10.052	11.739	11.317	11.151	10.501	10.267
MnO	0.446	0.430	0.551	0.556	0.526	0.499	0.468
MgO	14.659	14.597	14.559	14.233	14.214	14.761	15.026
NiO	b.d.l.	b.d.l.	b.d.l.	b.d.l.	b.d.l.	b.d.l.	b.d.l.
CaO	20.119	19.966	19.067	19.838	19.445	19.779	20.001
Na_2O	0.361	0.380	0.350	0.351	0.382	0.349	0.351
Total	99.72	99.65	100.06	99.79	99.47	99.74	100.21
N.O.	6	6	6	6	6	6	6
Si	1.9383	1.9280	1.9492	1.9523	1.9379	1.9504	1.9400
Ti	0.0198	0.0230	0.0158	0.0148	0.0206	0.0151	0.0176
Al	0.0787	0.0903	0.0593	0.0519	0.0759	0.0598	0.0667
Fe^{3+}	0.0314	0.0353	0.0363	0.0395	0.0352	0.0346	0.0434
Fe^{2+}	0.2809	0.2802	0.3324	0.3171	0.3169	0.2950	0.2772
Mn	0.0142	0.0137	0.0175	0.0177	0.0168	0.0158	0.0148
Mg	0.8191	0.8167	0.8151	0.7997	0.8000	0.8260	0.8364
Ni	0.0000	0.0000	0.0000	0.0000	0.0000	0.0000	0.0000
Ca	0.8079	0.8028	0.7672	0.8010	0.7865	0.7953	0.8001
Na	0.0262	0.0276	0.0255	0.0257	0.0280	0.0254	0.0254
Cation sum	4.02	4.02	4.02	4.02	4.02	4.02	4.02
Mg#	74	74	70	70	71	73	74
%Wo	42	42	40	42	41	42	42
%En	43	43	43	42	42	43	44
%Fs	15	15	17	17	17	15	14

Mineral	Augite	Augite	Augite	Augite	Enstatite	Enstatite	Enstatite
Lava comp.	Trachyte	Trachyte	Trachyte	Trachyte	Trachyte	Trachyte	Trachyte
Sample	Q61	Q61	H19	H19	Q3	Q3	Q3
Analysis	px5_core	px8_core	px2_core	px5_core	px3_core	px7_core	px17_core
SiO_2	51.074	50.684	50.964	51.468	52.383	51.890	52.939
TiO_2	0.844	1.010	0.634	0.558	0.322	0.416	0.455
Al_2O_3	2.131	2.896	1.471	1.216	0.582	0.846	1.181
FeO^T	10.752	11.207	10.462	10.802	19.465	20.035	20.899
MnO	0.510	0.516	0.482	0.514	0.723	0.786	0.793
MgO	14.591	13.788	14.797	14.752	23.726	23.492	20.998
NiO	b.d.l.	b.d.l.	b.d.l.	b.d.l.	b.d.l.	b.d.l.	b.d.l.
CaO	19.302	19.569	20.399	19.886	1.799	1.770	2.064
Na_2O	0.376	0.416	0.350	0.353	0.030	0.030	0.038
Total	99.58	100.09	99.56	99.55	99.03	99.26	99.36
N.O.	6	6	6	6	6	6	6
Si	1.9224	1.9037	1.9244	1.9417	1.9582	1.9425	1.9809
Ti	0.0239	0.0285	0.0180	0.0158	0.0090	0.0117	0.0128
Al	0.0945	0.1282	0.0654	0.0540	0.0256	0.0373	0.0521
Fe^{3+}	0.0403	0.0375	0.0753	0.0565	0.0420	0.0563	0.0000
Fe^{2+}	0.2982	0.3146	0.2551	0.2843	0.5665	0.5709	0.6540
Mn	0.0163	0.0164	0.0154	0.0164	0.0229	0.0249	0.0251
Mg	0.8188	0.7721	0.8330	0.8297	1.3223	1.3110	1.1713
Ni	0.0000	0.0000	0.0000	0.0000	0.0000	0.0000	0.0000
Ca	0.7783	0.7874	0.8252	0.8038	0.0720	0.0710	0.0827
Na	0.0275	0.0303	0.0256	0.0258	0.0022	0.0022	0.0027
Cation sum	4.02	4.02	4.04	4.03	4.02	4.03	3.98
Mg#	72	70	75	73	69	69	63
%Wo	41	42	43	42	4	4	4
%En	43	41	44	43	67	67	61
%Fs	16	17	13	15	29	29	34

Mineral	Enstatite	Enstatite	Pigeonite	Enstatite	Enstatite	Enstatite	Enstatite
Lava comp.	Trachyte	Trachyte	Trachyte	Trachyte	Trachyte	Trachyte	Trachyte
Sample	Q7	Q7	Q7	Q10	Q10	Q12	Q12
Analysis	px1_core	px2_core	Microlite	px2_core	px3_core	px2_core	Microlite
SiO_2	53.053	52.613	52.42	52.957	53.354	52.018	53.29
TiO_2	0.326	0.313	0.67	0.297	0.342	0.307	0.58
Al_2O_3	0.886	0.731	1.45	0.563	0.826	0.694	0.83
FeO^T	19.366	19.384	22.94	19.975	19.376	20.007	21.29
MnO	0.708	0.706	b.d.l.	0.846	0.752	0.810	b.d.l.
MgO	23.525	24.179	18.62	23.525	23.815	23.705	22.25
NiO	b.d.l.	b.d.l.	b.d.l.	0.013	b.d.l.	b.d.l.	b.d.l.
CaO	1.764	1.665	3.91	1.647	1.713	1.629	2.19
Na_2O	0.030	0.028	b.d.l.	0.032	0.034	0.030	b.d.l.
Total	99.66	99.62	100.01	99.86	100.21	99.20	100.43
N.O.	6	6	6	6	6	6	6
Si	1.9654	1.9527	1.9714	1.9655	1.9652	1.9475	1.9708
Ti	0.0091	0.0087	0.0190	0.0083	0.0095	0.0087	0.0161
Al	0.0387	0.0320	0.0643	0.0246	0.0358	0.0306	0.0362
Fe^{3+}	0.0144	0.0470	0.0000	0.0300	0.0172	0.0592	0.0000
Fe^{2+}	0.5856	0.5547	0.7215	0.5900	0.5797	0.5672	0.6585
Mn	0.0222	0.0222	0.0000	0.0266	0.0235	0.0257	0.0000
Mg	1.2993	1.3378	1.0439	1.3017	1.3077	1.3231	1.2267
Ni	0.0000	0.0000	0.0000	0.0004	0.0000	0.0000	0.0000
Ca	0.0700	0.0662	0.1575	0.0655	0.0676	0.0653	0.0868
Na	0.0022	0.0020	0.0000	0.0023	0.0024	0.0022	0.0000
Cation sum	4.01	4.02	3.98	4.01	4.01	4.03	4.00
Mg#	68	70	59	68	68	69	65
%Wo	4	3	8	3	3	3	4
%En	66	68	54	67	67	68	62
%Fs	30	28	38	30	30	29	33

Mineral	Enstatite	Enstatite	Enstatite	Enstatite	Enstatite	Enstatite	Enstatite
Lava comp.	Trachyte	Trachyte	Trachyte	Trachyte	Trachyte	Trachyte	Trachyte
Sample	Q31	Q31	Q34	Q36	Q36	Q36	Q36
Analysis	px2_core	px4_core	px1_core	px1_core	px4_core	px6_core	Microlite
SiO_2	52.334	52.816	52.378	52.641	52.418	52.883	52.234
TiO_2	0.393	0.288	0.409	0.362	0.283	0.319	0.399
Al_2O_3	0.829	0.549	0.908	0.761	0.478	0.628	0.762
FeO^T	19.430	20.558	19.899	20.154	19.157	19.812	21.280
MnO	0.740	0.825	0.719	0.828	0.764	0.747	0.893
MgO	23.875	23.007	24.015	23.413	24.113	23.748	22.041
NiO	0.006	b.d.l.	b.d.l.	0.015	0.008	b.d.l.	b.d.l.
CaO	1.880	1.716	1.806	1.744	1.958	1.763	2.029
Na_2O	0.026	0.030	0.035	0.032	0.032	0.031	0.034
Total	99.51	99.79	100.17	99.95	99.21	99.93	99.67
N.O.	6	6	6	6	6	6	6
Si	1.9474	1.9670	1.9399	1.9552	1.9551	1.9601	1.9582
Ti	0.0110	0.0081	0.0114	0.0101	0.0079	0.0089	0.0113
Al	0.0364	0.0241	0.0396	0.0333	0.0210	0.0274	0.0337
Fe^{3+}	0.0487	0.0277	0.0602	0.0384	0.0550	0.0369	0.0299
Fe^{2+}	0.5560	0.6127	0.5562	0.5876	0.5425	0.5773	0.6373
Mn	0.0233	0.0260	0.0225	0.0261	0.0241	0.0235	0.0283
Mg	1.3245	1.2774	1.3260	1.2964	1.3408	1.3122	1.2318
Ni	0.0002	0.0000	0.0000	0.0005	0.0002	0.0000	0.0000
Ca	0.0750	0.0685	0.0717	0.0694	0.0782	0.0700	0.0815
Na	0.0019	0.0022	0.0025	0.0023	0.0023	0.0022	0.0024
Cation sum	4.02	4.01	4.03	4.02	4.03	4.02	4.01
Mg#	70	67	70	68	70	69	65
%Wo	4	3	4	4	4	4	4
%En	68	65	68	66	68	67	63
%Fs	28	31	28	30	28	29	33

Mineral	Enstatite	Enstatite	Enstatite	Enstatite	Enstatite	Enstatite	Pigeonite
Lava comp.	Trachyte	Trachyte	Trachyte	Trachyte	Trachyte	Trachyte	Trachyte
Sample	Q39	Q39	Q39	Q41	Q41	Q41	Q41
Analysis	px1_core	px2_core	px4_core	px1_core	px3_core	px6_core	Microlite
SiO_2	53.127	52.618	53.076	53.337	53.246	53.201	52.97
TiO_2	0.377	0.324	0.409	0.366	0.326	0.442	b.d.l.
Al_2O_3	0.765	0.892	0.744	0.730	0.602	1.219	1.05
FeO^T	19.065	19.712	19.832	20.035	19.612	19.335	21.84
MnO	0.731	0.724	0.848	0.793	0.825	0.748	1.01
MgO	23.533	23.078	22.895	23.389	23.550	23.091	18.77
NiO	b.d.l.	b.d.l.	b.d.l.	b.d.l.	b.d.l.	b.d.l.	b.d.l.
CaO	1.786	1.759	1.942	1.763	1.705	1.925	3.69
Na_2O	0.033	0.043	0.030	0.031	0.031	0.036	b.d.l.
Total	99.42	99.14	99.77	100.44	99.89	100.01	99.33
N.O.	6	6	6	6	6	6	6
Si	1.9705	1.9643	1.9704	1.9666	1.9708	1.9637	2.0007
Ti	0.0105	0.0091	0.0114	0.0102	0.0091	0.0123	0.0000
Al	0.0334	0.0392	0.0326	0.0317	0.0262	0.0530	0.0467
Fe^{3+}	0.0069	0.0171	0.0060	0.0171	0.0163	0.0000	0.0000
Fe^{2+}	0.5845	0.5983	0.6097	0.6007	0.5908	0.5968	0.6899
Mn	0.0230	0.0229	0.0267	0.0248	0.0259	0.0234	0.0323
Mg	1.3013	1.2844	1.2671	1.2857	1.2995	1.2707	1.0569
Ni	0.0000	0.0000	0.0000	0.0000	0.0000	0.0000	0.0000
Ca	0.0710	0.0703	0.0772	0.0696	0.0676	0.0761	0.1493
Na	0.0024	0.0031	0.0021	0.0022	0.0022	0.0026	0.0000
Cation sum	4.00	4.01	4.00	4.01	4.01	4.00	3.98
Mg#	68	67	67	67	68	67	59
%Wo	4	4	4	4	3	4	8
%En	67	66	65	66	66	65	56
%Fs	30	31	31	31	30	31	36

Mineral	Pigeonite	Enstatite	Enstatite	Enstatite	Enstatite	Enstatite	Enstatite
Lava comp.	Trachyte	Trachyte	Trachyte	Trachyte	Trachyte	Trachyte	Trachyte
Sample	Q41	Q61	Q61	Q61	Q61	H19	H19
Analysis	Microlite	px3_core	px4_core	px6_core	px7_core	px3_core	px4_core
SiO_2	52.62	52.842	52.991	53.383	53.357	53.312	52.182
TiO_2	b.d.l.	0.400	0.419	0.298	0.411	0.348	0.364
Al_2O_3	1.77	0.769	0.748	0.611	1.011	0.646	0.859
FeO^T	22.85	20.471	19.820	20.311	19.591	19.866	20.197
MnO	0.87	0.780	0.803	0.863	0.734	0.828	0.774
MgO	16.18	22.793	23.336	23.060	23.745	23.616	23.555
NiO	b.d.l.	b.d.l.	b.d.l.	b.d.l.	0.005	0.009	b.d.l.
CaO	5.53	1.793	1.803	1.671	1.782	1.740	1.834
Na_2O	b.d.l.	0.039	0.034	0.036	0.031	0.030	0.033
Total	99.82	99.90	99.94	100.22	100.67	100.39	99.80
N.O.	6	6	6	6	6	6	6
Si	1.9949	1.9647	1.9634	1.9747	1.9584	1.9659	1.9436
Ti	0.0000	0.0112	0.0117	0.0083	0.0113	0.0096	0.0102
Al	0.0791	0.0337	0.0327	0.0266	0.0437	0.0281	0.0377
Fe^{3+}	0.0000	0.0172	0.0197	0.0103	0.0189	0.0231	0.0571
Fe^{2+}	0.7245	0.6193	0.5944	0.6181	0.5824	0.5896	0.5721
Mn	0.0279	0.0245	0.0252	0.0270	0.0228	0.0259	0.0244
Mg	0.9145	1.2634	1.2890	1.2717	1.2993	1.2983	1.3079
Ni	0.0000	0.0000	0.0000	0.0000	0.0002	0.0003	0.0000
Ca	0.2246	0.0714	0.0716	0.0662	0.0701	0.0687	0.0732
Na	0.0000	0.0028	0.0024	0.0026	0.0022	0.0022	0.0024
Cation sum	3.97	4.01	4.01	4.01	4.01	4.01	4.03
Mg#	55	66	68	66	68	68	69
%Wo	12	4	4	3	4	4	4
%En	49	65	66	65	67	66	67
%Fs	39	32	30	32	30	30	29

Mineral	Enstatite
Lava comp.	Trachyte
Sample	H19
Analysis	px6_core
SiO_2	52.694
TiO_2	0.338
Al_2O_3	0.592
FeO^T	19.857
MnO	0.842
MgO	23.475
NiO	b.d.l.
CaO	1.725
Na_2O	0.034
Total	99.56
N.O.	6
Si	1.9621
Ti	0.0095
Al	0.0260
Fe^{3+}	0.0334
Fe^{2+}	0.5849
Mn	0.0265
Mg	1.3031
Ni	0.0000
Ca	0.0688
Na	0.0024
Cation sum	4.02
Mg#	68
%Wo	4
%En	67
%Fs	30

Mineral	Olivine	Olivine	Olivine	Olivine	Olivine	Olivine	Olivine
Lava comp.	Bas and.	Bas and.	Bas and.	Bas and.	Bas and.	Bas and.	Bas and.
Sample	Q50	Q50	Q50	Q50	Q50	Q50	Q50
Analysis	ol1_core	ol2_core	ol3_core	ol4_core	ol5_core	ol6_core	ol8_core
SiO_2	39.05	39.83	38.33	38.47	38.78	38.47	38.89
Al_2O_3	0.03	0.06	0.03	0.03	0.02	0.03	0.03
FeO^T	22.54	15.15	22.70	23.82	21.88	23.19	22.12
MnO	0.35	0.21	0.38	0.37	0.34	0.35	0.36
MgO	39.48	44.86	38.97	38.69	39.73	38.99	39.33
NiO	0.11	0.23	0.10	0.11	0.11	0.11	0.11
CaO	0.18	0.19	0.18	0.19	0.19	0.18	0.19
P_2O_5	0.02	0.04	0.05	0.07	0.06	0.02	0.01
Total	101.77	100.58	100.74	101.75	101.12	101.35	101.04
N.O.	4	4	4	4	4	4	4
Si	0.9984	0.9965	0.9932	0.9914	0.9962	0.9921	1.0000
Al	0.0008	0.0017	0.0009	0.0010	0.0007	0.0008	0.0009
Fe^{2+}	0.4820	0.3170	0.4918	0.5135	0.4700	0.5002	0.4756
Mn	0.0076	0.0045	0.0083	0.0081	0.0073	0.0077	0.0079
Mg	1.5050	1.6733	1.5051	1.4866	1.5217	1.4992	1.5078
Ni	0.0023	0.0046	0.0020	0.0023	0.0022	0.0024	0.0023
Ca	0.0050	0.0050	0.0050	0.0052	0.0053	0.0050	0.0051
P	0.0004	0.0008	0.0011	0.0015	0.0013	0.0004	0.0002
Cation sum	3.00	3.00	3.01	3.01	3.00	3.01	3.00
%Fo	75	84	75	74	76	75	76

Mineral	Olivine	Olivine	Olivine	Olivine	Olivine	Olivine
Lava comp.	Bas and.	Tr.and.	Tr.and.	Tr.and.	Tr.and.	Tr.and.
Sample	Q50	Q17	Q17	Q8	Q8	Q8
Analysis	ol9_core	ol2_core	ol3_core	ol1_core	ol2_core	ol3_core
SiO_2	38.45	36.38	36.65	35.08	35.63	36.23
Al_2O_3	0.02	0.02	0.03	0.03	0.02	0.02
FeO^T	23.23	28.78	28.84	36.50	33.51	31.92
MnO	0.37	0.47	0.48	0.62	0.54	0.51
MgO	39.02	34.26	34.09	27.52	30.39	31.65
NiO	0.11	0.11	0.11	0.04	0.05	0.06
CaO	0.19	0.18	0.18	0.38	0.21	0.19
P_2O_5	0.01	0.02	0.07	0.08	0.05	0.04
Total	101.40	100.22	100.46	100.25	100.40	100.62
N.O.	4	4	4	4	4	4
Si	0.9914	0.9788	0.9829	0.9819	0.9798	0.9848
Al	0.0007	0.0006	0.0010	0.0010	0.0006	0.0008
Fe^{2+}	0.5009	0.6477	0.6469	0.8545	0.7705	0.7257
Mn	0.0081	0.0108	0.0110	0.0147	0.0126	0.0117
Mg	1.4997	1.3745	1.3632	1.1486	1.2460	1.2825
Ni	0.0023	0.0024	0.0024	0.0008	0.0012	0.0013
Ca	0.0051	0.0052	0.0053	0.0115	0.0062	0.0056
P	0.0002	0.0005	0.0016	0.0019	0.0012	0.0009
Cation sum	3.01	3.02	3.01	3.01	3.02	3.01
%Fo	75	68	67	57	61	63

Mineral	Olivine	Olivine
Lava comp.	Tr.and.	Tr.and.
Sample	Q8	Q8
Analysis	ol4_core	ol5_core
SiO_2	36.97	37.47
Al_2O_3	0.03	0.07
FeO^T	27.00	29.31
MnO	0.45	0.42
MgO	35.61	34.20
NiO	0.09	0.08
CaO	0.18	0.19
P_2O_5	0.00	0.03
Total	100.34	101.78
N.O.	4	4
Si	0.9836	0.9914
Al	0.0009	0.0021
Fe^{2+}	0.6007	0.6485
Mn	0.0102	0.0095
Mg	1.4125	1.3490
Ni	0.0019	0.0017
Ca	0.0052	0.0053
P	0.0000	0.0007
Cation sum	3.02	3.01
%Fo	70	67

Mineral	Cr spinel	Cr spinel	Cr spinel	Ilmenite	Ilmenite	Ilmenite	Ilmenite
Lava comp	Bas and.	Bas and.	Bas and.	Trachyte	Trachyte	Trachyte	Trachyte
Sample	Q50	Q50	Q50	Q3	Q10	Q10	Q12
Analysis	ox1_core	ox2_core	ox3_core	ox1_core	ox1_core	ox2_core	ox1_core
TiO_2	0.76	1.07	6.24	48.50	49.02	49.81	49.21
Al_2O_3	22.65	20.87	10.22	b.d.l.	0.40	b.d.l.	0.36
Cr_2O_3	30.05	30.13	21.63	b.d.l.	b.d.l.	b.d.l.	b.d.l.
FeO^T	37.14	40.22	55.49	49.50	47.56	48.15	46.28
MnO	b.d.l.	b.d.l.	b.d.l.	b.d.l.	b.d.l.	b.d.l.	b.d.l.
MgO	9.88	9.16	6.69	2.66	3.22	3.38	3.23
Total	100.48	101.45	100.27	100.66	100.20	101.34	99.08
N.O.	8	8	8	3	3	3	3
Ti	0.0373	0.0530	0.3430	0.9250	0.9294	0.9349	0.9396
Al	1.7417	1.6191	0.8801	0.0000	0.0119	0.0000	0.0108
Cr	1.5501	1.5681	1.2495	0.0000	0.0000	0.0000	0.0000
Fe^{2+}	2.0266	2.2143	3.3909	1.0495	1.0024	1.0046	0.9823
Mn	0.0000	0.0000	0.0000	0.0000	0.0000	0.0000	0.0000
Mg	0.9611	0.8990	0.7288	0.1005	0.1210	0.1257	0.1222
Cation sum	6.32	6.35	6.59	2.07	2.06	2.07	2.05

Mineral	Ilmenite	Ilmenite	Ilmenite	Ilmenite	Ilmenite	Magnetite	Magnetite
Lava comp	Trachyte	Trachyte	Trachyte	Trachyte	Trachyte	Trachyte	Trachyte
Sample	Q39	Q46	Q69	Q69	H19	Q53	Q53
Analysis	ox1_core	ox1_core	ox1_core	ox2_core	ox1_core	ox1_core	ox2_core
TiO_2	47.26	47.18	47.76	47.98	48.47	16.76	16.90
Al_2O_3	0.49	b.d.l.	0.46	b.d.l.	0.35	3.06	2.95
Cr_2O_3	b.d.l.	b.d.l.	b.d.l.	b.d.l.	b.d.l.	b.d.l.	b.d.l.
FeO^T	46.65	47.19	46.85	46.27	46.87	75.92	75.38
MnO	0.74	0.90	0.77	1.06	b.d.l.	0.83	0.77
MgO	4.00	4.00	3.97	4.18	4.47	3.19	3.27
Total	99.14	99.27	99.81	99.49	100.16	99.76	99.27
N.O.	3	3	3	3	3	4	4
Ti	0.9072	0.9087	0.9102	0.9176	0.9161	0.5065	0.5126
Al	0.0147	0.0000	0.0137	0.0000	0.0104	0.1449	0.1402
Cr	0.0000	0.0000	0.0000	0.0000	0.0000	0.0000	0.0000
Fe^{2+}	0.9954	1.0104	0.9925	0.9836	0.9848	2.5505	2.5417
Mn	0.0160	0.0195	0.0165	0.0228	0.0000	0.0282	0.0263
Mg	0.1522	0.1527	0.1499	0.1584	0.1674	0.1910	0.1966
Cation sum	2.09	2.09	2.08	2.08	2.08	3.42	3.42

Mineral	Magnetite	Magnetite	Magnetite	Magnetite	Magnetite	Magnetite	Magnetite
Lava comp	Trachyte	Trachyte	Trachyte	Trachyte	Trachyte	Trachyte	Trachyte
Sample	Q53	Q53	Q53	Q53	Q53	Q53	Q53
Analysis	ox3_core	ox4_core	ox5_core	ox6_core	ox7_core	ox8_core	ox9_core
TiO_2	17.00	17.10	17.17	17.28	17.32	17.55	18.01
Al_2O_3	2.94	2.84	2.92	2.88	2.86	2.89	2.86
Cr_2O_3	b.d.l.	b.d.l.	b.d.l.	b.d.l.	b.d.l.	b.d.l.	b.d.l.
FeO^T	76.03	75.73	76.32	76.41	76.59	75.79	75.75
MnO	0.60	0.70	0.61	b.d.l.	0.71	0.60	0.82
MgO	3.16	2.78	2.39	2.49	2.82	2.58	2.89
Total	99.73	99.15	99.41	99.06	100.30	99.41	100.33
N.O.	4	4	4	4	4	4	4
Ti	0.5137	0.5207	0.5224	0.5268	0.5213	0.5321	0.5392
Al	0.1392	0.1355	0.1392	0.1375	0.1349	0.1373	0.1341
Cr	0.0000	0.0000	0.0000	0.0000	0.0000	0.0000	0.0000
Fe^{2+}	2.5541	2.5636	2.5814	2.5896	2.5628	2.5544	2.5212
Mn	0.0204	0.0240	0.0209	0.0000	0.0241	0.0205	0.0276
Mg	0.1892	0.1678	0.1441	0.1504	0.1682	0.1550	0.1715
Cation sum	3.42	3.41	3.41	3.40	3.41	3.40	3.39

Mineral	Magnetite	Magnetite	Magnetite	Magnetite	Magnetite
Lava comp	Trachyte	Trachyte	Trachyte	Trachyte	Trachyte
Sample	Q53	Q61	Q61	Q61	Q61
Analysis	ox10_core	ox1_core	ox2_core	ox3_core	ox4_core
TiO_2	18.73	17.05	17.15	17.23	17.24
Al_2O_3	2.84	3.03	2.91	2.99	2.77
Cr_2O_3	b.d.l.	b.d.l.	b.d.l.	b.d.l.	b.d.l.
FeO^T	74.92	75.36	76.33	75.09	76.04
MnO	0.78	0.66	0.59	0.55	0.72
MgO	2.61	3.40	3.36	3.30	3.20
Total	99.88	99.50	100.34	99.16	99.97
N.O.	4	4	4	4	4
Ti	0.5613	0.5148	0.5146	0.5217	0.5198
Al	0.1333	0.1433	0.1368	0.1418	0.1308
Cr	0.0000	0.0000	0.0000	0.0000	0.0000
Fe^{2+}	2.4960	2.5295	2.5460	2.5272	2.5486
Mn	0.0263	0.0224	0.0199	0.0187	0.0244
Mg	0.1550	0.2034	0.1998	0.1980	0.1912
Cation sum	3.37	3.41	3.42	3.41	3.41

Mineral	Glass	Glass	Glass	Glass	Glass	Glass	Glass
Lava comp.	Bas and.	Bas and.	Bas and.	Bas and.	Bas and.	Bas and.	Bas and.
Sample	Q50	Q50	Q50	Q50	Q63	Q63	Q63
Analysis	Gr.mass	px1_mi	px4_mi	px5_mi	px3_mi	px4_mi	px5_mi
SiO_2	65.732	66.544	65.410	67.388	68.766	64.415	69.009
TiO_2	2.535	1.282	1.188	1.489	0.627	1.157	0.536
Al_2O_3	15.923	17.852	18.338	17.455	16.331	19.028	16.891
Cr_2O_3	b.d.l.	0.006	0.006	0.005	0.014	b.d.l.	0.004
FeO^T	2.377	1.303	1.470	1.191	1.130	1.095	1.738
MnO	0.054	0.067	0.075	0.058	0.028	0.021	0.046
MgO	0.648	0.558	0.723	0.488	0.228	0.127	0.141
CaO	1.280	2.951	3.215	2.675	1.063	1.782	1.771
Na_2O	4.846	5.567	5.498	5.542	5.012	6.462	5.806
K_2O	6.279	2.427	3.098	2.228	6.423	5.939	3.862
P_2O	0.718	0.430	0.402	0.462	0.451	0.303	0.555
Total	100.86	99.20	99.63	99.21	100.56	100.44	100.63
N.O.	1	1	1	1	1	1	1
Si	0.3693	0.3706	0.3654	0.3738	0.3826	0.3620	0.3801
Ti	0.0107	0.0054	0.0050	0.0062	0.0026	0.0049	0.0022
Al	0.1054	0.1172	0.1207	0.1141	0.1071	0.1260	0.1096
Cr	0.0000	0.0000	0.0000	0.0000	0.0001	0.0000	0.0000
Fe^{2+}	0.0112	0.0061	0.0069	0.0055	0.0053	0.0051	0.0080
Mn	0.0003	0.0003	0.0004	0.0003	0.0001	0.0001	0.0002
Mg	0.0054	0.0046	0.0060	0.0040	0.0019	0.0011	0.0012
Ca	0.0077	0.0176	0.0192	0.0159	0.0063	0.0107	0.0105
Na	0.0528	0.0601	0.0595	0.0596	0.0541	0.0704	0.0620
K	0.0450	0.0172	0.0221	0.0158	0.0456	0.0426	0.0271
P	0.0034	0.0020	0.0019	0.0022	0.0021	0.0014	0.0026
Cation sum	0.61	0.60	0.61	0.60	0.61	0.62	0.60

Mineral	Glass	Glass	Glass	Glass	Glass	Glass	Glass
Lava comp.	Tr.and.	Tr.and.	Tr.and.	Tr.and.	Trachyte	Trachyte	Trachyte
Sample	Q8	Q8	Q8	Q17	Q3	Q3	Q7
Analysis	px13_mi	px14_mi	px17_mi	px5_mi	px12_mi	px8_mi	Gr.mass
SiO_2	62.452	69.243	67.365	67.273	68.416	66.978	70.795
TiO_2	1.291	1.107	1.124	1.297	0.946	0.822	0.916
Al_2O_3	18.375	16.584	17.321	15.973	15.813	15.719	13.346
Cr_2O_3	b.d.l.	b.d.l.	b.d.l.	0.008	b.d.l.	0.001	b.d.l.
FeO^T	5.477	1.603	1.977	2.186	3.220	3.217	3.413
MnO	0.094	0.068	0.086	0.057	0.093	0.094	0.058
MgO	0.222	0.204	0.272	0.629	0.152	0.125	0.182
CaO	2.375	1.790	2.416	2.303	0.485	0.922	1.127
Na_2O	4.408	5.010	5.566	4.937	7.314	5.552	5.080
K_2O	5.365	3.944	3.386	3.529	3.904	5.694	4.305
P_2O	0.490	0.443	0.455	0.506	0.291	0.272	0.138
Total	100.55	99.99	99.97	98.70	100.63	99.40	99.36
N.O.	1	1	1	1	1	1	1
Si	0.3422	0.3717	0.3655	0.3776	0.3697	0.3794	0.3957
Ti	0.0053	0.0045	0.0046	0.0055	0.0038	0.0035	0.0039
Al	0.1187	0.1049	0.1107	0.1057	0.1007	0.1049	0.0879
Cr	0.0000	0.0000	0.0000	0.0000	0.0000	0.0000	0.0000
Fe^{2+}	0.0251	0.0072	0.0090	0.0103	0.0145	0.0152	0.0160
Mn	0.0004	0.0003	0.0004	0.0003	0.0004	0.0005	0.0003
Mg	0.0018	0.0016	0.0022	0.0053	0.0012	0.0011	0.0015
Ca	0.0139	0.0103	0.0140	0.0139	0.0028	0.0056	0.0067
Na	0.0468	0.0521	0.0585	0.0537	0.0766	0.0610	0.0551
K	0.0000	0.0000	0.0000	0.0253	0.0000	0.0412	0.0307
P	0.0249	0.0179	0.0156	0.0024	0.0179	0.0013	0.0007
Cation sum	0.58	0.57	0.58	0.60	0.59	0.61	0.60

Mineral	Glass	Glass	Glass	Glass	Glass	Glass	Glass
Lava comp.	Trachyte	Trachyte	Trachyte	Trachyte	Trachyte	Trachyte	Trachyte
Sample	Q7	Q7	Q10	Q31	Q31	Q31	Q31
Analysis	Gr.mass	px1_mi	px2_mi	Gr.mass	Gr.mass	Gr.mass	px3_mi
SiO_2	66.407	69.348	67.897	68.871	67.363	68.577	67.910
TiO_2	0.533	0.669	0.986	0.763	0.950	0.889	0.919
Al_2O_3	18.077	15.406	15.468	14.561	15.130	15.025	15.153
Cr_2O_3	b.d.l.	0.002	0.006	0.001	0.004	0.003	0.003
FeO^T	1.793	2.700	3.347	3.847	3.912	3.504	4.108
MnO	0.031	0.074	0.096	0.078	0.111	0.103	0.106
MgO	0.107	0.120	0.175	0.590	0.861	0.656	0.597
CaO	3.320	1.708	2.086	1.736	2.492	1.936	2.186
Na_2O	6.865	5.758	5.632	5.335	5.113	5.480	5.434
K_2O	2.338	3.606	3.732	3.562	3.627	3.674	3.601
P_2O	0.084	0.260	0.490	0.163	0.211	0.162	0.211
Total	99.56	99.65	99.98	99.51	99.77	100.01	100.23
N.O.	1	1	1	1	1	1	1
Si	0.3707	0.3859	0.3796	0.3859	0.3786	0.3828	0.3799
Ti	0.0022	0.0028	0.0041	0.0032	0.0040	0.0037	0.0039
Al	0.1189	0.1010	0.1019	0.0962	0.1002	0.0989	0.0999
Cr	0.0000	0.0000	0.0000	0.0000	0.0000	0.0000	0.0000
Fe^{2+}	0.0084	0.0126	0.0156	0.0180	0.0184	0.0164	0.0192
Mn	0.0001	0.0003	0.0005	0.0004	0.0005	0.0005	0.0005
Mg	0.0009	0.0010	0.0015	0.0049	0.0072	0.0055	0.0050
Ca	0.0199	0.0102	0.0125	0.0104	0.0150	0.0116	0.0131
Na	0.0743	0.0621	0.0610	0.0580	0.0557	0.0593	0.0589
K	0.0167	0.0256	0.0266	0.0255	0.0260	0.0262	0.0257
P	0.0004	0.0012	0.0023	0.0008	0.0010	0.0008	0.0010
Cation sum	0.61	0.60	0.61	0.60	0.61	0.61	0.61

Mineral	Glass	Glass	Glass	Glass	Glass	Glass	Glass
Lava comp.	Trachyte	Trachyte	Trachyte	Trachyte	Trachyte	Trachyte	Trachyte
Sample	Q34	Q36	Q36	Q36	Q36	Q39	Q39
Analysis	Gr.mass	Gr.mass	Gr.mass	px3_mi	px7_mi	Gr.mass	Gr.mass
SiO_2	70.849	71.643	71.423	68.888	67.102	67.230	66.836
TiO_2	0.874	0.891	0.899	1.033	0.944	0.790	0.790
Al_2O_3	13.424	12.650	12.669	14.980	15.487	15.915	14.875
Cr_2O_3	b.d.l.	b.d.l.	b.d.l.	0.005	0.003	0.010	0.011
FeO^T	2.927	3.532	3.284	2.549	4.309	3.070	4.845
MnO	0.079	0.089	0.083	0.106	0.123	0.037	0.146
MgO	0.203	0.266	0.304	0.504	0.439	0.130	0.799
CaO	1.312	1.062	1.051	1.736	1.613	2.491	2.140
Na_2O	4.797	4.176	4.654	5.447	5.137	5.651	6.850
K_2O	4.510	4.677	4.633	3.473	4.809	3.393	2.632
P_2O	0.249	0.133	0.128	0.207	0.233	0.226	0.213
Total	99.22	99.12	99.13	98.93	100.20	99.08	100.38
N.O.	1	1	1	1	1	1	1
Si	0.3958	0.4005	0.3996	0.3858	0.3777	0.3790	0.3763
Ti	0.0037	0.0037	0.0038	0.0044	0.0040	0.0034	0.0033
Al	0.0884	0.0834	0.0835	0.0989	0.1027	0.1057	0.0987
Cr	0.0000	0.0000	0.0000	0.0000	0.0000	0.0000	0.0001
Fe^{2+}	0.0137	0.0165	0.0154	0.0119	0.0203	0.0145	0.0228
Mn	0.0004	0.0004	0.0004	0.0005	0.0006	0.0002	0.0007
Mg	0.0017	0.0022	0.0025	0.0042	0.0037	0.0011	0.0067
Ca	0.0078	0.0064	0.0063	0.0104	0.0097	0.0150	0.0129
Na	0.0519	0.0453	0.0505	0.0591	0.0561	0.0618	0.0748
K	0.0321	0.0334	0.0331	0.0248	0.0345	0.0244	0.0189
P	0.0012	0.0006	0.0006	0.0010	0.0011	0.0011	0.0010
Cation sum	0.60	0.59	0.60	0.60	0.61	0.61	0.62

Mineral	Glass	Glass	Glass	Glass	Glass	Glass	Glass
Lava comp.	Trachyte	Trachyte	Trachyte	Trachyte	Trachyte	Trachyte	Trachyte
Sample	Q39	Q39	Q39	Q40	Q40	Q40	Q41
Analysis	Gr.mass	px1_mi	px4_mi	Gr.mass	px2_mi	px3_mi	Gr.mass
SiO_2	71.015	70.387	70.796	70.558	71.654	70.183	66.884
TiO_2	1.049	0.764	0.696	1.228	1.171	0.991	1.137
Al_2O_3	14.352	15.512	15.274	13.016	13.087	16.449	13.563
Cr_2O_3	0.007	0.001	b.d.l.	0.001	b.d.l.	0.006	b.d.l.
FeO^T	2.734	1.463	1.236	3.553	3.044	0.751	4.923
MnO	0.064	0.051	0.065	0.107	0.068	0.056	0.153
MgO	0.104	0.159	0.205	0.472	0.291	0.191	0.778
CaO	1.178	1.538	1.422	1.150	0.713	1.323	1.755
Na_2O	5.569	5.850	5.626	3.987	3.982	5.658	4.821
K_2O	4.454	3.558	3.877	5.683	5.853	4.423	4.714
P_2O	0.230	0.249	0.230	0.274	0.201	0.288	0.260
Total	100.92	99.63	99.68	100.37	100.35	100.55	99.22
N.O.	1	1	1	1	1	1	1
Si	0.3913	0.3889	0.3912	0.3941	0.3981	0.3851	0.3823
Ti	0.0043	0.0032	0.0029	0.0052	0.0049	0.0041	0.0049
Al	0.0932	0.1010	0.0995	0.0857	0.0857	0.1064	0.0914
Cr	0.0000	0.0000	0.0000	0.0000	0.0000	0.0000	0.0000
Fe^{2+}	0.0126	0.0068	0.0057	0.0166	0.0141	0.0034	0.0235
Mn	0.0003	0.0002	0.0003	0.0005	0.0003	0.0003	0.0007
Mg	0.0009	0.0013	0.0017	0.0039	0.0024	0.0016	0.0066
Ca	0.0070	0.0091	0.0084	0.0069	0.0042	0.0078	0.0107
Na	0.0595	0.0627	0.0603	0.0432	0.0429	0.0602	0.0534
K	0.0313	0.0251	0.0273	0.0405	0.0415	0.0310	0.0344
P	0.0011	0.0012	0.0011	0.0013	0.0009	0.0013	0.0013
Cation sum	0.60	0.60	0.60	0.60	0.60	0.60	0.61

Mineral	Glass	Glass	Glass	Glass	Glass	Glass	Glass
Lava comp.	Trachyte	Trachyte	Trachyte	Trachyte	Trachyte	Trachyte	Trachyte
Sample	Q41	Q41	Q41	Q46	Q46	Q61	Q62
Analysis	Gr.mass	Gr.mass	px4_mi	Gr.mass	px1_mi	px2_mi	Gr.mass
SiO_2	70.999	67.823	70.705	70.477	71.180	66.265	66.208
TiO_2	0.922	1.065	0.783	1.271	0.850	0.939	1.524
Al_2O_3	12.907	15.837	15.159	12.975	14.223	14.675	12.726
Cr_2O_3	b.d.l.	b.d.l.	0.014	0.001	b.d.l.	b.d.l.	b.d.l.
FeO^T	2.973	3.560	1.711	4.422	2.114	3.420	6.143
MnO	0.078	0.083	0.075	0.109	0.063	0.097	0.135
MgO	0.264	0.284	0.269	0.366	0.263	1.691	0.690
CaO	1.462	2.298	1.498	1.375	1.258	3.124	2.126
Na_2O	4.995	5.686	5.407	4.899	5.145	5.340	5.123
K_2O	4.533	3.620	3.703	4.293	3.591	4.649	3.897
P_2O	0.238	0.256	0.192	0.360	0.186	0.206	0.417
Total	99.61	100.73	99.61	100.80	99.09	100.62	99.24
N.O.	1	1	1	1	1	1	1
Si	0.3968	0.3778	0.3908	0.3918	0.3954	0.3738	0.3803
Ti	0.0039	0.0045	0.0033	0.0053	0.0036	0.0040	0.0066
Al	0.0850	0.1040	0.0987	0.0850	0.0931	0.0976	0.0861
Cr	0.0000	0.0000	0.0001	0.0000	0.0000	0.0000	0.0000
Fe^{2+}	0.0139	0.0166	0.0079	0.0206	0.0098	0.0161	0.0295
Mn	0.0004	0.0004	0.0004	0.0005	0.0003	0.0005	0.0007
Mg	0.0022	0.0024	0.0022	0.0030	0.0022	0.0142	0.0059
Ca	0.0088	0.0137	0.0089	0.0082	0.0075	0.0189	0.0131
Na	0.0541	0.0614	0.0579	0.0528	0.0554	0.0584	0.0570
K	0.0323	0.0257	0.0261	0.0304	0.0254	0.0335	0.0286
P	0.0011	0.0012	0.0009	0.0017	0.0009	0.0010	0.0020
Cation sum	0.60	0.61	0.60	0.60	0.59	0.62	0.61

Mineral	Glass	Glass
Lava comp.	Trachyte	Trachyte
Sample	H19	H19
Analysis	Gr.mass	px4_mi
SiO_2	68.109	71.702
TiO_2	0.401	0.636
Al_2O_3	18.195	14.836
Cr_2O_3	0.006	0.002
FeO^T	1.383	1.660
MnO	0.023	0.053
MgO	0.075	0.149
CaO	2.747	1.281
Na_2O	6.455	5.522
K_2O	2.948	3.809
P_2O	0.075	0.229
Total	100.42	99.88
N.O.	1	1
Si	0.3752	0.3942
Ti	0.0017	0.0026
Al	0.1181	0.0961
Cr	0.0000	0.0000
Fe^{2+}	0.0064	0.0076
Mn	0.0001	0.0002
Mg	0.0006	0.0012
Ca	0.0162	0.0075
Na	0.0689	0.0589
K	0.0207	0.0267
P	0.0004	0.0011
Cation sum	0.61	0.60

Appendix VI: Crystal size distributions (CSDs)

This expands sections 3.2.2. and 3.3.2. in Chapter 3. CSDs of pyroxene microlites were measured using BSE images (Figure VI.1A) of 15 thin sections of Quetrupillán lavas. The number of images used per sample and the total image area are recorded in Table VI.1.

Plagioclase microlites could not be distinguished from the lava groundmass glass due to their lack of a fully formed crystal shape and the similarity in greyscale intensity between plagioclase and glass. The darkest grey areas in Figure VI.1A represent plagioclase microlites but they cannot be isolated from the surrounding dark grey groundmass. Instead, pyroxene microlites were isolated in Fiji (Figure VI.1B) as their greyscale intensity contrasts strongly with the groundmass and they display well-formed crystal shapes (Figure VI.1A).

The image area (%) covered by pyroxene and the number of pyroxene microlites measured per sample is recorded in Table VI.1. Microlite dimensions were measured using Fiji's best fit ellipse tool (Figure VI.1C and Table VI.2) and the mean crystal aspect ratios were used to estimate the 3D shape of microlites in CSDSlice (Table VI.1; Morgan and Jerram, 2006). Ellipse data were exported using the CSD output plugin into CSDCorrections 1.4 to calculate the crystal size distributions of the groundmass pyroxene phase (Tables VI.3, VI.4 and VI.5). CSD profiles are plotted in Figure 3.9 (Chapter 3).

Table VI.1: Data of the BSE images and pyroxene microlites used to calculate CSDs of trachyte (^{T}), trachyandesite (^{TA}) and basaltic andesite (^{BA}) samples.

Sample	No. of images	Total image area (mm^2)	No. of crystals	Area of pyroxene (%)	3D shape estimate
Q3 ^{T}	4	0.032	491	6	acicular
Q7 ^{T}	4	0.008	244	5	rectangular prism
Q10 ^{T}	4	0.0192	283	7	rectangular prism
Q12 ^{T}	4	0.072	271	5	acicular
Q36 ^{T}	4	0.1824	307	4	acicular
Q39 ^{T}	4	0.0016	233	7	acicular
Q40 ^{T}	5	0.02	233	8	rectangular prism
Q41 ^{T}	5	0.003	203	7	acicular
Q53 ^{T}	4	0.0252	279	7	rectangular prism
Q66 ^{T}	4	0.008	227	6	rectangular prism
Q69 ^{T}	4	0.0024	262	8	acicular
Q8 ^{TA}	4	0.128	255	12	rectangular prism
Q17 ^{TA}	4	0.0252	241	11	acicular
Q 20 ^{TA}	4	0.008	350	8	rectangular prism
Q50 ^{BA}	2	0.0126	499	21	rectangular prism

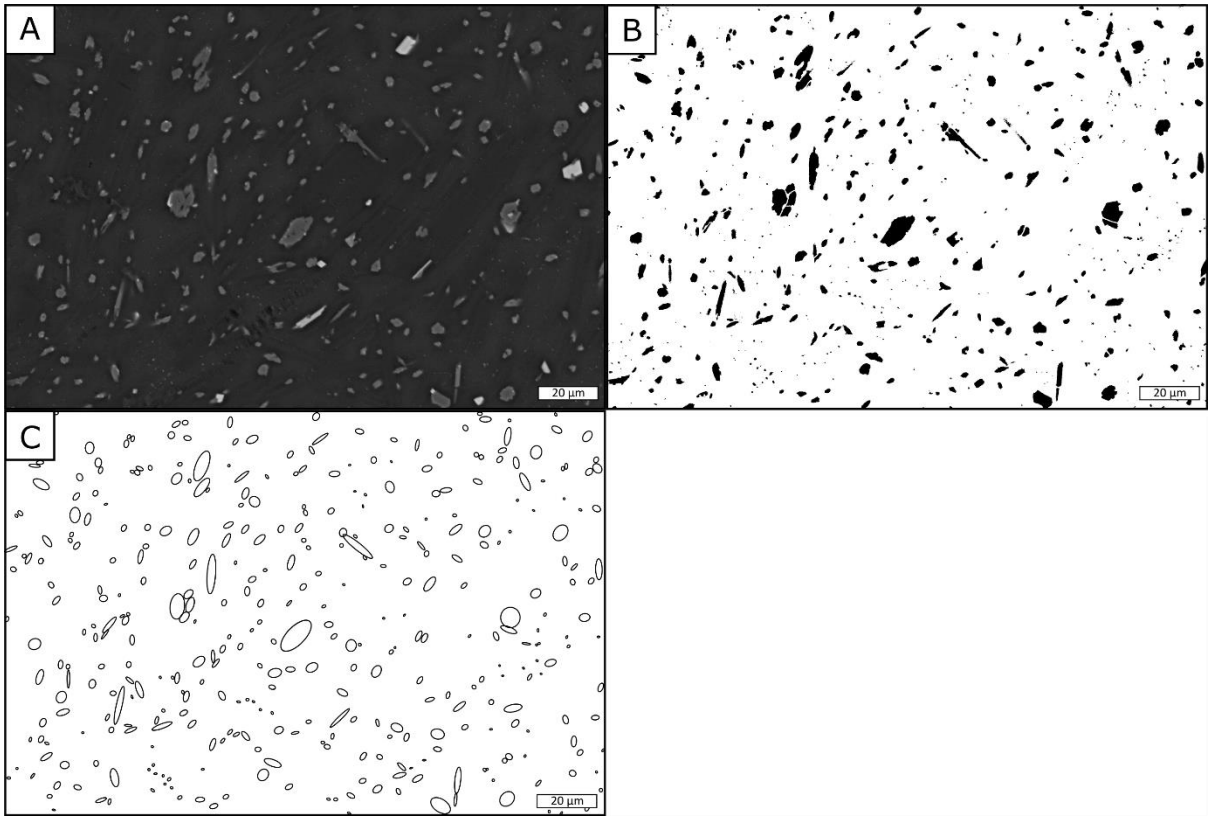

Figure VI.1: A) A BSE image of the groundmass of a trachyte lava. The greyscale intensity relates to the mineral density (white – oxide; light grey – pyroxene; dark grey – plagioclase and glass); B) Pyroxene microlites isolated using Fiji; C) Ellipses describing the pyroxene microlites using Fiji's best fit ellipse tool. The scale bar is 20 µm in each image.

Table VI.2: Dimensions of major and minor axes (mm) of a small sample of ellipses of pyroxene microlites in a trachyte lava.

Major	Minor	Major	Minor	Major	Minor
0.0025	0.0016	0.0017	0.0009	0.0015	0.0010
0.0069	0.0013	0.0031	0.0021	0.0019	0.0008
0.0273	0.0022	0.0294	0.0058	0.0034	0.0023
0.0036	0.0013	0.0255	0.0028	0.0331	0.0028
0.0303	0.0040	0.0071	0.0024	0.0027	0.0017
0.0019	0.0018	0.0079	0.0057	0.0308	0.0024
0.0024	0.0011	0.0034	0.0014	0.0029	0.0014
0.0035	0.0021	0.0035	0.0015	0.0027	0.0023
0.0020	0.0012	0.0060	0.0020	0.0026	0.0010
0.0432	0.0042	0.0069	0.0029	0.0040	0.0024
0.0021	0.0011	0.0018	0.0008	0.0102	0.0016
0.0071	0.0018	0.0018	0.0014	0.0019	0.0010

Table VI.3: CSDs of trachyte lavas. For each sample, the size (mm) of the bin and natural logarithm of the population density (ln(PD)) within the bin are listed. Results in brackets represent an underestimation of microlite population in the smallest size bin.

Q3	Size	ln(PD)
	0.3371	7.53
	0.2127	10.46
	0.1342	12.42
	0.0847	14.63
	0.0534	16.63
	0.0337	18.28
	0.0213	19.51
	0.0134	20.6
	(0.0085	19.58)

Q36	Size	ln(PD)
	0.1603	6.52
	0.1011	8.51
	0.0638	11.68
	0.0403	13.68
	0.0254	15.85
	0.016	17.63
	0.0101	19.18
	0.0064	20.21
	(0.004	20.13)

Q39	Size	ln(PD)
	0.0386	15.46
	0.0243	18.16
	0.0154	19.36
	0.0097	21.56
	0.0061	23.27
	0.0039	24.53
	0.0024	24.84
	0.0015	25.42
	(0.001	25.01)

Q7	Size	ln(PD)
	0.0403	13.09
	0.0254	16.9
	0.016	19.44
	0.0101	21.52
	0.0064	22.69
	0.004	23.32
	(0.0025	18.02)

Q10	Size	ln(PD)
	0.0403	12.92
	0.0254	15.2
	0.016	18.17
	0.0101	20.51
	0.0064	21.94
	0.004	22.98
	(0.0025	20.07)

Q12	Size	ln(PD)
	0.1025	10.6
	0.0647	13.42
	0.0408	15.5
	0.0258	17.36
	0.0163	18.81
	0.0103	19.58
	(0.0065	18.98)

Q40	Size	ln(PD)
	0.0524	13.9
	0.0331	15.69
	0.0209	18.24
	0.0132	19.99
	0.0083	21.74
	0.0052	23.22
	0.0033	24.48
	0.0021	25.25
	0.0013	25.05
	(0.0008	24.05)

Q69	Size	ln(PD)
	0.0536	13.68
	0.0338	13.61
	0.0213	17.38
	0.0135	20.02
	0.0085	21.99
	0.0054	23.68
	0.0034	24.94
	(0.0021	19.88)

Q53	Size	ln(PD)
	0.0524	12.29
	0.0331	13.95
	0.0209	16.66
	0.0132	18.56
	0.0083	20.51
	0.0052	21.99
	0.0033	22.95

Q66	Size	ln(PD)
	0.0638	13.09
	0.0403	14.27
	0.0254	17.13
	0.016	19.37
	0.0101	21.23
	0.0064	22.69
	0.004	23.35

Q41	Size	ln(PD)
	0.0325	15.14
	0.0205	17.83
	0.0129	19.66
	0.0082	21.82
	0.0052	23.07
	0.0033	24.07

Table VI.4: CSDs of trachyandesite lavas. For each sample, the size (mm) of the bin and natural logarithm of the population density (ln(PD)) within the bin are listed. Results in brackets represent an underestimation of microlite population in the smallest size bin.

Q8 Size	ln(PD)
0.1011	10.1
0.0638	12.27
0.0403	14.88
0.0254	17
0.016	18.27
0.0101	18.66

Q17 Size	ln(PD)
0.2225	9.02
0.1404	10.76
0.0886	13.41
0.0559	15.15
0.0353	16.93
0.0222	18.66
0.014	19.9
0.0089	20.89
(0.0056	19.62)

Q20 Size	ln(PD)
0.0325	14.17
0.0205	17.3
0.0129	19.7
0.0082	22.06
0.0052	23.56
0.0033	24.18

Table VI.5: CSD of basaltic andesite lava. The size (mm) of the bin and natural logarithm of the population density (ln(PD)) within the bin are listed. Results in brackets represent an underestimation of microlite population in the smallest size bin.

Q50 Size	ln(PD)
0.0587	11.18
0.037	14.16
0.0234	15.91
0.0147	18.98
0.0093	21.46
0.0059	23.03
0.0037	24.14
(0.0023	22.86)

Appendix VII: Geothermobarometry

This expands sections 3.2.3. and 3.3.3. in Chapter 3. Temperatures and pressures of crystallisation were estimated by iteratively solving the clinopyroxene-liquid geothermometer of Putirka (2008) and the clinopyroxene geobarometer of Nimis (1999a,b) using EMPA results of melt inclusions hosted within clinopyroxene phenocrysts (Table VII.1).

Table VII.1: EMPA results of clinopyroxene phenocrysts (Px) containing melt inclusions (M.I.) used for calculating temperatures and pressures of crystallisation.

Sample		SiO_2	TiO_2	Al_2O_3	Cr_2O_3	FeO	MnO	MgO	CaO	Na_2O	K_2O
Q31	Px3	51.371	0.613	1.426	0.003	10.497	0.480	14.797	20.261	0.344	0.000
Q31	M.I.	67.910	0.919	15.153	0.000	4.108	0.106	0.597	2.186	5.434	3.601
Q36	Px3	50.884	0.539	1.246	0.000	10.587	0.473	14.740	20.041	0.343	0.000
Q36	M.I.	68.888	1.033	14.980	0.000	2.549	0.106	0.504	1.736	5.447	3.473
Q36	Px7	50.996	0.622	1.451	0.003	10.197	0.427	15.001	20.120	0.338	0.000
Q36	M.I.	67.102	0.944	15.487	0.000	4.309	0.123	0.439	1.613	5.137	4.809
Q40	Px2	51.713	0.703	1.783	0.000	9.965	0.446	14.659	20.119	0.361	0.009
Q40	M.I.	71.654	1.171	13.087	0.000	3.044	0.068	0.291	0.713	3.982	5.853
Q40	Px3.2	51.370	0.815	2.042	0.000	10.052	0.430	14.597	19.966	0.380	0.003
Q40	M.I.	70.183	0.991	16.449	0.000	0.751	0.056	0.191	1.323	5.658	4.423
Q41	Px4	51.902	0.559	1.339	0.000	11.739	0.551	14.559	19.067	0.350	0.003
Q41	M.I.	70.705	0.783	15.159	0.000	1.711	0.075	0.269	1.498	5.407	3.703
Q46	Px1.1	51.330	0.726	1.706	0.000	11.151	0.526	14.214	19.445	0.382	0.003
Q46	M.I.	71.180	0.850	14.223	0.000	2.114	0.063	0.263	1.258	5.145	3.591
Q46	Px1.2	51.330	0.726	1.706	0.000	11.151	0.526	14.214	19.445	0.382	0.003
Q46	M.I.	70.561	0.848	14.896	0.000	2.024	0.056	0.305	1.278	5.460	3.703
Q61	Px1.1	51.963	0.536	1.351	0.000	10.501	0.499	14.761	19.779	0.349	0.009
Q61	M.I.	70.934	0.539	15.261	0.000	0.491	0.062	0.129	1.133	5.445	5.239
Q61	Px1.2	51.963	0.536	1.351	0.000	10.501	0.499	14.761	19.779	0.349	0.009
Q61	M.I.	69.994	0.628	15.889	0.000	0.580	0.053	0.077	1.176	5.627	3.967
Q61	Px8	50.684	1.010	2.896	0.003	11.207	0.516	13.788	19.569	0.416	0.003
Q61	M.I.	69.615	0.410	15.692	0.000	0.732	0.085	0.686	2.070	5.829	3.048
Q17	Px2	50.855	0.760	2.012	0.072	10.541	0.283	15.083	19.257	0.329	0.002
Q17	M.I.	64.915	1.367	15.402	0.000	3.597	0.094	1.019	3.081	4.844	3.668
Q17	Px5	51.024	0.667	2.378	0.337	8.417	0.220	15.974	20.396	0.292	0.004
Q17	M.I.	67.273	1.297	15.973	0.000	2.186	0.057	0.629	2.303	4.937	3.529
Q50	Px13	52.168	0.620	2.024	0.000	9.778	0.271	13.566	20.068	0.347	0.000
Q50	M.I.	64.546	1.103	14.475	0.000	5.048	0.136	1.743	3.993	4.087	3.453
Q50	Px14	52.287	0.613	2.146	0.000	8.931	0.245	14.198	20.284	0.290	0.004
Q50	M.I.	69.177	1.198	17.019	0.000	0.869	0.043	0.311	1.873	3.789	6.376
Q63	Px3	51.653	0.766	0.766	0.057	10.267	0.307	14.673	19.755	0.349	0.000
Q63	M.I.	68.766	0.627	16.331	0.000	1.130	0.028	0.228	1.063	5.012	6.423

Temperatures were calculated from Equation 33 in Putirka (2008):

$$\frac{10^4}{T} = 7.53 - 0.14ln\left(\frac{X_{Jd}^{cpx} X_{CaO}^{liq} X_{Fm}^{liq}}{X_{DiHd}^{cpx} X_{NaO_{0.5}}^{liq} X_{AlO_{1.5}}^{liq}}\right) + 0.07\left(H_2O^{liq}\right) - 14.9\left(X_{CaO}^{liq} X_{SiO_2}^{liq}\right) - 0.08\ln\left(X_{TiO_2}^{liq}\right)$$
$$- 3.62\left(X_{NaO_{0.5}}^{liq} + X_{KO_{0.5}}^{liq}\right) - 1.1\left(Mg\#^{liq}\right) - 0.18\ln\left(X_{EnFs}^{cpx}\right) - 0.027P$$

where T is the temperature in Kelvin, P is the pressure in kbar and X_y^z represents the component of *y* in either the clinopyroxene (*cpx*; Table VII.2) or the melt (*liq*; Table VII.3). X_{Fm}^{liq} represents the components of Fe and Mg in the liquid phase, H_2O^{liq} is the wt.% of H_2O in the liquid phase and $Mg\#^{liq}$ is the magnesium number of the melt.

For clinopyroxenes in which the concentrations of Al_2O_3 and Na_2O are such that the jadeite component (X_{Jd}^{cpx}) yields a negative value, Equation 34 of Putirka (2008) was used instead:

$$\frac{10^4}{T} = 6.39 + 0.076\left(H_2O^{liq}\right) - 5.55\left(X_{CaO}^{liq} X_{SiO_2}^{liq}\right) - 0.386\ln\left(X_{MgO}^{liq}\right) - 0.046P + 2.2 \times 10^{-4}(P^2)$$

where T is the temperature in Kelvin, P is the pressure in kbar, X_y^{liq} represents the component of *y* in the melt and H_2O^{liq} is the wt.% of H_2O in the liquid phase (Table VII.3). Both geothermometers estimate temperatures with uncertainties of ± 45 °C (Putirka, 2008).

Table VII.2: Calculation of clinopyroxene components (Pyroxene 2, Q40; Table VII.1). The instructions for the calculations are in the text following the table.

		SiO_2	TiO_2	Al_2O_3	FeO	MnO	MgO	CaO	Na_2O	K_2O	Cr_2O_3
1	Cpx wt.%	51.713	0.703	1.783	9.965	0.446	14.659	20.119	0.361	0.009	0.000
2	Mol wt.	60.08	79.88	101.96	71.85	70.94	40.30	56.08	61.98	94.20	152.00
3	Mol prop	0.861	0.009	0.017	0.139	0.006	0.364	0.359	0.006	0.000	0.000
4	Anions	2	2	3	1	1	1	1	1	1	3
5	Cations	1	1	2	1	1	1	1	2	2	2
6	N.O.	1.721	0.018	0.052	0.139	0.006	0.364	0.359	0.006	0.000	0.000
7	N.O. sum	2.665									
8	ORF	2.252									
		Cations on the basis of 6 oxygens									
		X_{Si}^{cpx}	X_{Ti}^{cpx}	X_{Al}^{cpx}	X_{Fe}^{cpx}	X_{Mn}^{cpx}	X_{Mg}^{cpx}	X_{Ca}^{cpx}	X_{Na}^{cpx}	X_{K}^{cpx}	X_{Cr}^{cpx}
9	Cat/6 ox	1.938	0.020	0.079	0.312	0.014	0.819	0.808	0.026	0.000	0.000
10	Cat sum	4.016									

				Clinopyroxene components					
	$X_{Al(IV)}^{cpx}$	$X_{Al(VI)}^{cpx}$	$X_{Fe(3+)}^{cpx}$	X_{Jd}^{cpx}	X_{CaTs}^{cpx}	X_{CaTi}^{cpx}	X_{CrCaTs}^{cpx}	X_{DiHd}^{cpx}	X_{EnFs}^{cpx}
11	0.062	0.017	0.052	0.017	0.000	0.031	0.000	0.777	0.177
12			Total	1.002					

The following method for calculating the values in Table VII.2 is from Table 3 of Putirka (2008). Row 1 is the composition of the clinopyroxene (in wt.%) measured by EMPA. The mole proportion (Row 3) is obtained by dividing the cpx wt.% (Row 1) by the molecular weight (Row 2) for each oxide. The number of anions (oxygen atoms; Row 4) and the number of cations (Row 5) in each oxide is recorded. The number of oxygens (N.O.; Row 6) is calculated by multiplying the mole proportion (Row 3) by the number of anions (oxygen atoms) per formula unit (Row 4). Row 7 contains the sum of Row 6. The Oxygen Renormalisation Factor (ORF; Row 8) is calculated as the number of oxygens per clinopyroxene formula unit (six) divided by the N.O. sum (Row 7).

To calculate the number of cations on the basis of six oxygens in a clinopyroxene (Row 9), each mole proportion (Row 3) is multiplied by the ORF (Row 8) and the number of cations in the formula unit (Row 5). Row 10 contains the sum of cations per six oxygens. For a "good" pyroxene analysis, this should be close to 4 (Putirka, 2008). The clinopyroxene components in Row 11 are calculated from the cations per six oxygens (Row 9) using the following equations (Putirka, 2008):

$X^{cpx}_{Al(IV)}$ = 2 – X^{cpx}_{Si};

$X^{cpx}_{Al(VI)}$ = X^{cpx}_{Al} – $X^{cpx}_{Al(IV)}$;

$X^{cpx}_{Fe(3+)}$ = X^{cpx}_{Na} + $X^{cpx}_{Al(IV)}$ – $X^{cpx}_{Al(VI)}$ – 2 X^{cpx}_{Ti} – X^{cpx}_{Cr};

X^{cpx}_{Jd} = $X^{cpx}_{Al(VI)}$ or X^{cpx}_{Na}, whichever is smallest;

X^{cpx}_{CaTs} = $X^{cpx}_{Al(VI)}$ – X^{cpx}_{Jd}, if excess $X^{cpx}_{Al(VI)}$ remains after forming X^{cpx}_{Jd};

X^{cpx}_{CaTi} = ($X^{cpx}_{Al(IV)}$ – X^{cpx}_{CaTs})/2, if $X^{cpx}_{Al(IV)}$ > X^{cpx}_{CaTs};

X^{cpx}_{CrCaTs} = X^{cpx}_{Cr}/2;

X^{cpx}_{DiHd} = X^{cpx}_{Ca} – X^{cpx}_{CaTi} – X^{cpx}_{CaTs} – X^{cpx}_{CrCaTs};

X^{cpx}_{EnFs} = (X^{cpx}_{Fe} + X^{cpx}_{Mg} – X^{cpx}_{DiHd})/2

The sum of clinopyroxene components (Row 12) should be close to 1 (Putirka, 2008).

Table VII.3: Calculation of liquid components (melt inclusion within Pyroxene 2, Q40; Table VII.1). The instructions for the calculations are in the text following the table.

		SiO_2	TiO_2	Al_2O_3	FeO	MnO	MgO	CaO	Na_2O	K_2O
1	Liq wt.%	71.654	1.171	13.087	3.044	0.068	0.291	0.713	3.982	5.853
2	Mol wt.	60.08	79.88	101.96	71.85	70.94	40.30	56.08	61.98	94.20
3	Mol prop	1.193	0.015	0.128	0.042	0.001	0.007	0.013	0.064	0.062
4	Total	1.525								
5	Mol frac	0.782	0.010	0.084	0.028	0.001	0.005	0.008	0.042	0.041
6	Cations	1	1	2	1	1	1	1	2	2
		SiO_2	TiO_2	$AlO_{1.5}$	FeO	MnO	MgO	CaO	$NaO_{0.5}$	$KO_{0.5}$
7	Mol wt.	60.08	79.88	50.98	71.85	70.94	40.30	56.08	30.99	47.10
8	Cat prop	1.193	0.015	0.257	0.042	0.001	0.007	0.013	0.128	0.124
9	Total	1.780								
		$X^{liq}_{SiO_2}$	$X^{liq}_{TiO_2}$	$X^{liq}_{AlO_{1.5}}$	X^{liq}_{FeO}	X^{liq}_{MnO}	X^{liq}_{MgO}	X^{liq}_{CaO}	$X^{liq}_{NaO_{0.5}}$	$X^{liq}_{KO_{0.5}}$
10	Cat frac	0.670	0.008	0.144	0.024	0.001	0.004	0.007	0.072	0.070

The following method for calculating the values in Table VII.3 is from Table 1 of Putirka (2008). Row 1 is the composition of the melt inclusion (in wt.%) measured by EMPA. The mole proportion (Row 3) is obtained by dividing the liquid wt.% (Row 1) by the molecular weight (Row 2) for each oxide. Row 4 contains the sum of Row 3. Mole fractions (Row 5) are obtained by dividing the mole proportions (Row 3) by the mole proportion sum (Row 4).

The molecular weight per cation (Row 7) is obtained by dividing the molecular weight (Row 2) by the number of cations in each oxide (Row 6). Cation proportions (Row 8) are calculated by dividing the liquid wt.% (Row 1) by the molecular weight per cation (Row 7). Row 9 contains the sum of Row 8. Cation fractions (Row 10) are calculated by dividing the cation proportions (Row 8) by the cation proportion sum (Row 9).

The geothermometer (Equation 33; Putirka, 2008) also requires the components X_{Fm}^{liq}, where Fm = Fe + Mg (in the liquid phase), H_2O^{liq}, which is the wt.% of H_2O in the liquid phase (calculated as 100 – the sum of Row 1), and the magnesium number (Mg#) of the melt, calculated by

$$Mg\#^{liq} = \frac{MgO^{liq}/40.3}{MgO^{liq}/40.3 + FeO^{liq}/71.85}$$

where MgO^{liq} and FeO^{liq} are the wt.% of MgO and FeO, respectively, in the liquid phase (Putirka, 2008). For the melt inclusion within Pyroxene 2 of lava sample Q40 (Table VII.3) this gives X_{Fm}^{liq} = 0.028, H_2O^{liq} = 0.14 and $Mg\#^{liq}$ = 0.146.

The results of iteratively solving the geothermometer of Putirka (2008) and the geobarometer of Nimis (1999a,b) using the composition of clinopyroxene phenocrysts and their melt inclusions are presented in Table 3.5 in Chapter 3 (section 3.3.3.). Clinopyroxene phenocrysts without melt inclusions were used to estimate additional pressures of crystallisation using the geobarometer of Nimis (1999a,b), based on the average calculated temperature of 940 °C (Table VII.4).

Table VII.4: Pressures of clinopyroxene crystallisation in trachyte magmas, calculated from the barometer of Nimis (1999a,b), using the composition of clinopyroxene phenocrysts and the average temperature of 940 °C from Table 3.5. Depths are calculated from the pressure, based on a density of 2800 kg/m^3 (Weidmann et al., 2013).

Sample	Q3_px1	Q3_px2	Q3_px6	Q3_px9	Q3_px10	Q3_px11	Q3_px12
P (kbar)	4.3	4.4	4.2	4.6	4.8	5.1	4.7
T (°C)	940	940	940	940	940	940	940
Depth (km)	15.8	16.1	15.3	16.9	17.4	18.7	17.1
SiO_2	51.090	51.257	50.943	51.810	52.943	51.336	52.737
TiO_2	0.699	0.611	0.608	0.826	0.655	0.879	0.643
Al_2O_3	1.513	1.425	1.523	2.025	1.545	2.161	1.593
Cr_2O_3	0.000	0.000	0.003	0.000	0.000	0.000	0.000
FeO	10.402	10.318	10.453	10.572	10.396	10.785	10.005
MnO	0.476	0.506	0.470	0.477	0.463	0.495	0.447
MgO	15.017	14.877	14.858	14.734	14.898	14.167	14.513
CaO	20.120	19.794	20.184	20.165	20.167	19.671	20.415
Na_2O	0.349	0.337	0.350	0.374	0.340	0.368	0.349
K_2O	0.003	0.005	0.000	0.002	0.000	0.000	0.000

Sample	Q3_px13	Q3_px14	Q3_px15	Q3_px16	Q3_px18	Q3_px19	Q10_px4
P (kbar)	4.1	3.4	3.9	3.4	5.2	5.0	4.5
T (°C)	940	940	940	940	940	940	940
Depth (km)	15.0	12.4	14.1	12.4	19.0	18.1	16.4
SiO_2	51.963	52.105	52.145	51.624	52.311	51.439	52.060
TiO_2	0.593	0.568	0.543	0.644	0.689	0.657	0.649
Al_2O_3	1.348	1.238	1.246	1.558	1.823	1.596	1.417
Cr_2O_3	0.000	0.000	0.000	0.000	0.000	0.000	0.000
FeO	10.052	11.237	11.468	10.311	10.557	11.490	10.866
MnO	0.457	0.481	0.580	0.464	0.455	0.572	0.483
MgO	14.726	13.928	13.792	13.653	13.653	13.704	14.668
CaO	20.116	19.955	19.582	20.546	20.091	18.892	19.573
Na_2O	0.326	0.329	0.339	0.333	0.349	0.323	0.339
K_2O	0.000	0.000	0.001	0.000	0.000	0.000	0.000

Table VII.4 continued

Sample	Q12_px3	Q31_px3	Q34_px2	Q34_px3	Q34_px4	Q34_px5	Q36_px2
P (kbar)	3.9	4.0	4.4	4.4	4.6	3.9	5.0
T (°C)	940	940	940	940	940	940	940
Depth (km)	14.3	14.4	15.9	16.1	16.7	14.3	18.4
SiO_2	51.044	51.371	51.153	50.624	50.949	50.785	51.060
TiO_2	0.588	0.613	0.627	0.641	0.698	0.763	0.670
Al_2O_3	1.576	1.426	1.459	1.630	1.637	1.820	1.781
Cr_2O_3	0.002	0.003	0.003	0.001	0.000	0.002	0.000
FeO	11.319	10.497	10.104	10.421	10.877	11.624	9.805
MnO	0.515	0.480	0.420	0.516	0.502	0.546	0.358
MgO	14.745	14.797	15.115	14.788	14.864	13.930	15.315
CaO	20.224	20.261	20.220	19.903	19.732	19.604	20.009
Na_2O	0.340	0.344	0.341	0.343	0.356	0.374	0.342
K_2O	0.002	0.000	0.002	0.000	0.003	0.000	0.000

Sample	Q36_px3	Q36_px5	Q36_px7	Q39_px3	Q40_px1	Q40_px2	Q40_px3.1
P (kbar)	3.9	4.2	4.3	4.1	4.2	4.8	5.1
T (°C)	940	940	940	940	940	940	940
Depth (km)	14.2	15.3	15.7	14.8	15.4	17.4	18.6
SiO_2	50.884	51.297	50.996	51.833	51.900	51.713	51.370
TiO_2	0.539	0.590	0.622	0.607	0.576	0.703	0.815
Al_2O_3	1.246	1.368	1.451	1.332	1.292	1.783	2.042
Cr_2O_3	0.000	0.000	0.003	0.000	0.006	0.000	0.000
FeO	10.587	10.996	10.197	10.362	10.264	9.965	10.052
MnO	0.473	0.481	0.427	0.527	0.486	0.446	0.430
MgO	14.740	14.535	15.001	14.620	14.992	14.659	14.597
CaO	20.041	19.510	20.120	19.956	20.078	20.119	19.966
Na_2O	0.343	0.347	0.338	0.359	0.339	0.361	0.380
K_2O	0.000	0.001	0.000	0.005	0.003	0.009	0.003

Table VII.4 continued

Sample	Q40_px3.2	Q40_px4	Q41_px4	Q41_px5	Q46_px1	Q61_px1
P (kbar)	4.5	4.8	4.5	3.4	4.5	4.4
T (°C)	940	940	940	940	940	940
Depth (km)	16.5	17.7	16.3	12.5	16.5	15.9
SiO_2	51.716	52.051	51.902	51.802	51.330	51.963
TiO_2	0.630	0.641	0.559	0.522	0.726	0.536
Al_2O_3	1.528	1.356	1.339	1.168	1.706	1.351
Cr_2O_3	0.001	0.000	0.000	0.000	0.000	0.000
FeO	9.647	10.918	11.739	11.317	11.151	10.501
MnO	0.463	0.461	0.551	0.556	0.526	0.499
MgO	14.918	15.036	14.559	14.233	14.214	14.761
CaO	20.151	19.240	19.067	19.838	19.445	19.779
Na_2O	0.356	0.337	0.350	0.351	0.382	0.349
K_2O	0.003	0.001	0.003	0.002	0.003	0.009

Sample	Q61_px2	Q61_px5	Q61_px8	H19_px1	H19_px2	H19_px5
P (kbar)	4.6	5.5	5.9	5.3	3.9	4.0
T (°C)	940	940	940	940	940	940
Depth (km)	16.6	20.0	21.4	19.3	14.2	14.6
SiO_2	51.957	51.074	50.684	50.659	50.964	51.468
TiO_2	0.628	0.844	1.010	0.731	0.634	0.558
Al_2O_3	1.516	2.131	2.896	1.695	1.471	1.216
Cr_2O_3	0.000	0.000	0.003	0.003	0.003	0.004
FeO	10.267	10.752	11.207	10.525	10.462	10.802
MnO	0.468	0.510	0.516	0.493	0.482	0.514
MgO	15.026	14.591	13.788	15.192	14.797	14.752
CaO	20.001	19.302	19.569	19.287	20.399	19.886
Na_2O	0.351	0.376	0.416	0.347	0.350	0.353
K_2O	0.002	0.003	0.003	0.000	0.007	0.001

Appendix VIII: Batch and Rayleigh fractional crystallisation models

This appendix contains the calculations used in the batch and Rayleigh fractional crytsalisation models presented in section 3.4.3. in Chapter 3, used to determine the expected REE concentrations in magmas following different degrees of fractionation.

The equation to calculate the concentration of REEs during batch fractionation is

$$C_L/C_0 = 1/(D + F(1 - D))$$

and during Rayleigh fractionation is

$$C_L/C_0 = F^{(D-1)}$$

where C_0 is the concentration of trace elements in the initial melt (represented by the basaltic andesite sample Q50; Table VIII.1), C_L is the concentration of trace elements in the remaining melt, D is the bulk partition coefficient of the fractionating assemblage (Table VIII.2), and F is the fraction of melt remaining (Rollinson, 1993). Modelled fractionation results were compared with the REE concentrations in the trachyandesite sample (Q8) and trachyte sample (Q3), with values first normalised to chondrite (Table VIII.1).

Table VIII.1: REE concentrations of Quetrupillán lavas of different composition (Bas and. – basaltic andesite; Tr.and. – trachyandesite) and normalised to chondrite.

Sample	Q50	Q8	Q3	Chondrite	Bas and.	Tr.and.	Trachyte
Comp.	Bas and.	Tr.and.	Trachyte		Chondrite	Chondrite	Chondrite
La	18.16	25.46	33.82	0.237	76.624	107.426	142.700
Ce	40.52	56.85	75.53	0.612	66.209	92.892	123.415
Nd	21.59	29.12	37.31	0.467	46.231	62.355	79.893
Sm	4.70	6.20	7.73	0.153	30.719	40.523	50.523
Eu	1.25	1.47	1.78	0.058	21.552	25.345	30.690
Gd	4.51	5.95	7.43	0.206	21.946	28.954	36.156
Dy	4.16	5.44	6.84	0.254	16.378	21.417	26.929
Er	2.51	3.31	4.23	0.166	15.166	20.000	25.559
Yb	2.46	3.28	4.29	0.170	14.471	19.294	25.235
Lu	0.37	0.51	0.67	0.025	14.567	20.079	26.378

Table VIII.2: Bulk partition coefficients (D values) of the extract, calculated from the partition coefficients of REEs in basalts and basaltic andesites (Table VIII.3) and on the mineral percentages in the fractionating assemblage (Table VIII.4).

	Extract D values
La	0.503857
Ce	0.428572
Nd	0.368201
Sm	0.428572
Eu	0.542577
Gd	0.421026
Dy	0.432953
Er	0.423392
Yb	0.391395
Lu	0.409496

Table VIII.3: Partition coefficients for basalts and basaltic andesites (Rollinson, 1993).

	D (partition coefficients)			
	Olivine	Clinopyroxene	Plagioclase	Magnetite
La	0.0670	0.056	0.190	1.5
Ce	0.0069	0.150	0.111	1.3
Nd	0.0066	0.310	0.090	1.0
Sm	0.0066	0.500	0.072	1.1
Eu	0.0068	0.510	1.126	0.6
Gd	0.0077	0.610	0.071	1.0
Dy	0.0096	0.680	0.063	1.0
Er	0.0011	0.650	0.057	1.0
Yb	0.0100	0.620	0.056	0.9
Lu	0.0160	0.560	0.053	1.0

Table VIII.4: Mineral percentages in the fractionating assemblage (mineral proportions in the Quetrupillán basalt sample Q67).

	Olivine	Clinopyroxene	Plagioclase	Magnetite	Sum
Mineral Mode %	28	20	32	20	100
Mineral density	3.6	3.4	2.7	5.1	
Mass	100.8	68	86.4	102	357.2
wt.%	28.22	19.04	24.19	28.56	100

Table VIII.5: Batch fractionation calculated using the equation $C_L/C_0 = 1/(D + F(1 - D))$ where C_0 is the concentration of trace elements in the initial melt (Q50; Table VIII.1), C_L is the concentration of trace elements in the remaining melt, D is the bulk partition coefficient of the fractionating assemblage (Table VIII.2), and F is the fraction of melt remaining.

F	0.1	0.2	0.3	0.4	0.5	0.6	0.7	0.8	0.9
La	1.807	1.658	1.532	1.424	1.330	1.248	1.175	1.110	1.052
Ce	2.059	1.842	1.667	1.522	1.400	1.296	1.207	1.129	1.061
Nd	2.318	2.022	1.793	1.611	1.462	1.338	1.234	1.145	1.067
Sm	2.059	1.842	1.667	1.522	1.400	1.296	1.207	1.129	1.061
Eu	1.700	1.577	1.471	1.378	1.297	1.224	1.159	1.101	1.048
Gd	2.088	1.863	1.681	1.532	1.407	1.301	1.210	1.131	1.061
Dy	2.042	1.830	1.658	1.516	1.396	1.293	1.205	1.128	1.060
Er	2.079	1.856	1.677	1.529	1.405	1.300	1.209	1.130	1.061
Yb	2.211	1.949	1.742	1.575	1.437	1.322	1.223	1.139	1.065
Lu	2.134	1.895	1.705	1.549	1.419	1.309	1.215	1.134	1.063

Table VIII.6: REE concentrations of the remaining melt (C_L) during batch fractionation at different values of F.

F	0.1	0.2	0.3	0.4	0.5	0.6	0.7	0.8	0.9	1
La	32.811	30.112	27.823	25.857	24.151	22.656	21.336	20.160	19.108	18.16
Ce	83.423	74.642	67.533	61.661	56.728	52.526	48.903	45.748	42.976	40.52
Nd	50.049	43.655	38.710	34.771	31.560	28.891	26.639	24.713	23.046	21.59
Sm	9.676	8.658	7.833	7.152	6.580	6.093	5.672	5.306	4.985	4.70
Eu	2.125	1.971	1.839	1.723	1.621	1.530	1.449	1.376	1.310	1.25
Gd	9.417	8.401	7.583	6.911	6.348	5.869	5.458	5.101	4.787	4.51
Dy	8.496	7.614	6.898	6.305	5.806	5.380	5.013	4.692	4.410	4.16
Er	5.218	4.659	4.209	3.838	3.527	3.262	3.035	2.837	2.664	2.51
Yb	5.439	4.794	4.286	3.875	3.536	3.252	3.009	2.801	2.619	2.46
Lu	0.790	0.701	0.631	0.573	0.525	0.484	0.450	0.420	0.393	0.37

Table VIII.7: REE concentrations of the remaining melt (C_L) during batch fractionation at different values of F, normalised to chondrite.

F	0.1	0.2	0.3	0.4	0.5	0.6	0.7	0.8	0.9	1
La	138.444	127.054	117.396	109.103	101.904	95.596	90.024	85.065	80.625	76.624
Ce	136.313	121.964	110.349	100.753	92.693	85.827	79.908	74.752	70.222	66.209
Nd	107.170	93.479	82.890	74.456	67.580	61.866	57.043	52.918	49.349	46.231
Sm	63.245	56.587	51.198	46.746	43.007	39.821	37.075	34.683	32.581	30.719
Eu	36.633	33.990	31.703	29.704	27.942	26.378	24.980	23.722	22.585	21.552
Gd	45.825	40.882	36.902	33.628	30.888	28.561	26.560	24.821	23.295	21.946
Dy	33.448	29.976	27.158	24.824	22.859	21.183	19.735	18.473	17.362	16.378
Er	31.527	28.153	25.431	23.189	21.310	19.713	18.338	17.143	16.094	15.166
Yb	31.996	28.201	25.211	22.794	20.800	19.127	17.703	16.476	15.408	14.471
Lu	31.090	27.610	24.831	22.560	20.670	19.072	17.703	16.518	15.481	14.567

Table VIII.8: Rayleigh fractionation calculated from the equation $C_L/C_0 = F^{(D-1)}$ where C_0 is the concentration of trace elements in the initial melt (Q50; Table VIII.1), C_L is the concentration of trace elements in the remaining melt, D is the bulk partition coefficient of the fractionating assemblage (Table VIII.2), and F is the fraction of melt remaining.

F	0.1	0.2	0.3	0.4	0.5	0.6	0.7	0.8	0.9
La	3.134	2.222	1.817	1.576	1.410	1.288	1.194	1.117	1.054
Ce	3.728	2.508	1.990	1.688	1.486	1.339	1.226	1.136	1.062
Nd	4.284	2.764	2.140	1.784	1.549	1.381	1.253	1.151	1.069
Sm	3.728	2.508	1.990	1.688	1.486	1.339	1.226	1.136	1.062
Eu	2.867	2.088	1.735	1.521	1.373	1.263	1.177	1.107	1.049
Gd	3.793	2.539	2.008	1.700	1.494	1.344	1.229	1.138	1.063
Dy	3.690	2.491	1.979	1.681	1.481	1.336	1.224	1.135	1.062
Er	3.772	2.529	2.002	1.696	1.491	1.343	1.228	1.137	1.063
Yb	4.061	2.663	2.081	1.747	1.525	1.365	1.242	1.145	1.066
Lu	3.895	2.587	2.036	1.718	1.506	1.352	1.234	1.141	1.064

Table VIII.9: REE concentrations of the remaining melt (C_L) during Rayleigh fractionation at different values of F.

F	0.1	0.2	0.3	0.4	0.5	0.6	0.7	0.8	0.9	1
La	56.919	40.356	33.002	28.612	25.614	23.398	21.676	20.286	19.135	18.16
Ce	151.042	101.644	80.623	68.401	60.212	54.255	49.680	46.031	43.034	40.52
Nd	92.481	59.684	46.196	38.519	33.454	29.814	27.047	24.859	23.076	21.59
Sm	17.520	11.790	9.352	7.934	6.984	6.293	5.763	5.339	4.992	4.70
Eu	3.584	2.610	2.168	1.901	1.716	1.579	1.472	1.384	1.312	1.25
Gd	17.106	11.451	9.055	7.666	6.737	6.062	5.544	5.132	4.794	4.51
Dy	15.351	10.362	8.234	6.994	6.163	5.558	5.092	4.721	4.416	4.16
Er	9.469	6.349	5.025	4.257	3.743	3.370	3.083	2.855	2.667	2.51
Yb	9.989	6.551	5.119	4.297	3.751	3.357	3.056	2.818	2.623	2.46
Lu	1.441	0.957	0.753	0.636	0.557	0.500	0.457	0.422	0.394	0.37

Table VIII.10: REE concentrations of the remaining melt (C_L) during Rayleigh fractionation at different values of F, normalised to chondrite.

F	0.1	0.2	0.3	0.4	0.5	0.6	0.7	0.8	0.9	1
La	240.166	170.277	139.248	120.727	108.074	98.727	91.458	85.595	80.736	76.624
Ce	246.800	166.084	131.736	111.767	98.386	88.652	81.177	75.213	70.318	66.209
Nd	198.032	127.804	98.921	82.481	71.635	63.841	57.917	53.231	49.413	46.231
Sm	114.508	77.058	61.121	51.856	45.648	41.132	37.664	34.897	32.625	30.719
Eu	61.788	44.999	37.382	32.772	29.592	27.225	25.371	23.868	22.616	21.552
Gd	83.241	55.725	44.065	37.305	32.783	29.499	26.980	24.973	23.327	21.946
Dy	60.437	40.795	32.416	27.537	24.264	21.881	20.049	18.587	17.386	16.378
Er	57.212	38.363	30.365	25.724	22.618	20.361	18.629	17.249	16.116	15.166
Yb	58.761	38.537	30.110	25.274	22.065	19.747	17.979	16.575	15.429	14.471
Lu	56.738	37.680	29.657	25.024	21.934	19.696	17.982	16.619	15.502	14.567

Appendix IX: Assimilation and fractional crystallisation model

This appendix contains the calculations used in the assimilation and fractional crystallisation (AFC) model presented in section 3.4.3. in Chapter 3, used to determine the expected trace element concentrations in magmas following different degrees of fractionation and assimilation of basement rock.

The equation for AFC is

$$C_L/C_0 = f' + \frac{r}{r-1+D} \times \frac{C_A}{C_0}(1 - f')$$

where C_L is the concentration of a trace element in the melt, C_0 is the concentration in the initial melt (represented by the basaltic andesite sample Q50; Table IX.1), C_A is the concentration in the assimilating wall rock (represented by the granite sample VR57-4M from the Pucón ignimbrite; Lohmar 2008; Table IX.1), D is the bulk partition coefficient of the element in the fractionating assemblage (Table IX.2), r is the ratio between assimilation and fractional crystallisation, and f' is the modified value of F described by

$$f' = F^{-(r-1+D)/(r-1)}$$

where F is the fraction of melt remaining (Rollinson, 1993).

Table IX.1: Input values for AFC modelling.

Sample number	Q50	VR57-4M
Composition	Bas. and.	Granite
Equation value	C_0	C_A
Rb	36.2	106
Sr	429.4	193
Ba	383	675
Y	27.5	10.9
Zr	174.3	4
Nb	7.4	3.5
Th	4.31	11.8
U	1.22	n.d.
Sm	4.7	1.7
Yb	2.46	0.98

Table IX.2: Bulk partition coefficients (D values) of the extract, calculated from the partition coefficients of trace elements in basalts and basaltic andesites (Table IX.3) and on the mineral percentages in the fractionating assemblage (Table IX.4).

	Extract D Values
Rb	0.025841
Sr	0.458016
Ba	0.271394
Y	0.238522
Zr	0.062589
Nb	0.120414
Th	0.010034
U	0.010598
Sm	0.427363
Yb	0.395185

Table IX.3: Partition coefficients for basalts and basaltic andesites (Rollinson, 1993)

	D (partition coefficients)			
	Olivine	Clinopyroxene	Plagioclase	Magnetite
Rb	0.0098	0.031	0.071	0
Sr	0.014	0.06	1.83	0
Ba	0.0099	0.026	1.09	0
Y	0.01	0.9	0.03	0.2
Zr	0.012	0.1	0.048	0.1
Nb	0.01	0.005	0.01	0.4
Th	0	0.04	0.01	0
U	0.002	0.04	0.01	0
Sm	0.0066	0.5	0.067	1.1
Yb	0.014	0.62	0.067	0.9

Table IX.4: Mineral percentages in the fractionating assemblage (mineral proportions in the Quetrupillán basalt sample Q67).

	Olivine	Clinopyroxene	Plagioclase	Magnetite	Sum
Mineral Mode %	28	20	32	20	100
Mineral density	3.6	3.4	2.7	5.1	
Mass	100.8	68	86.4	102	357.2
wt.%	28.22	19.04	24.19	28.56	100

The resulting modelled trace element values were compared with the trace element concentrations in the trachyandesite sample (Q8) and trachyte sample (Q3; Table IX.5) for different values of r (Tables IX.6-IX.11).

Table IX.5: Trace element concentrations of Quetrupillán lavas representing trachyte (Q3) and trachyandesite (Q8) compositions.

Sample	Q3	Q8
Comp.	Trachyte	Tr.and.
Rb	77.8	60.3
Sr	284.3	371.8
Ba	737.8	583.2
Y	44.4	36.9
Zr	352.2	270.6
Nb	14.1	10.9
Th	9.88	7.13
U	2.71	1.99
Sm	7.73	6.2
Yb	4.29	3.28

Table IX.6: f' values following the equation $f' = F^{-(r-1+D)/(r-1)}$ where F is the fraction of melt remaining, r is the ratio of assimilation to fractional crystallisation, and D is the bulk partition coefficient of the fractionating assemblage for r = 0.05.

F	0.1	0.2	0.3	0.4	0.5	0.6	0.7	0.8	0.9
Rb	9.393	4.786	3.226	2.438	1.963	1.644	1.415	1.242	1.108
Sr	3.295	2.301	1.865	1.607	1.432	1.303	1.203	1.123	1.056
Ba	5.180	3.157	2.363	1.924	1.641	1.440	1.290	1.173	1.078
Y	5.610	3.338	2.464	1.986	1.681	1.466	1.306	1.182	1.082
Zr	8.592	4.497	3.079	2.354	1.911	1.612	1.395	1.232	1.103
Nb	7.469	4.077	2.862	2.226	1.832	1.562	1.365	1.215	1.096
Th	9.760	4.916	3.291	2.476	1.985	1.658	1.423	1.247	1.110
U	9.746	4.911	3.289	2.475	1.985	1.657	1.423	1.247	1.110
Sm	3.549	2.424	1.939	1.655	1.464	1.324	1.217	1.131	1.060
Yb	3.837	2.560	2.020	1.708	1.499	1.348	1.232	1.139	1.063

Table IX.7: Values of C_L/C_0 assuming fractional crystallisation and an assimilation ratio of r = 0.05 following the equation $C_L/C_0 = f' + \frac{r}{r-1+D} \times \frac{C_A}{C_0}(1 - f')$, where r is the ratio of assimilation to fractional crystallisation, D is the bulk partition coefficient of the fractionating assemblage and C_A is the composition of the assimilating basement rock.

F	0.1	0.2	0.3	0.4	0.5	0.6	0.7	0.8	0.9
Rb	10.723	5.386	3.579	2.666	2.115	1.746	1.480	1.281	1.125
Sr	3.400	2.361	1.905	1.635	1.452	1.317	1.212	1.128	1.059
Ba	5.723	3.437	2.540	2.044	1.724	1.498	1.328	1.195	1.088
Y	5.738	3.403	2.505	2.014	1.699	1.479	1.315	1.187	1.084
Zr	8.602	4.501	3.082	2.355	1.912	1.612	1.396	1.232	1.104
Nb	7.653	4.165	2.915	2.261	1.855	1.578	1.376	1.221	1.099
Th	11.035	5.486	3.625	2.691	2.129	1.753	1.485	1.283	1.126
U	9.746	4.911	3.289	2.475	1.985	1.657	1.423	1.247	1.110
Sm	3.638	2.473	1.972	1.678	1.480	1.336	1.224	1.135	1.062
Yb	3.939	2.616	2.057	1.733	1.517	1.360	1.240	1.144	1.066

Table IX.8: Concentration of trace elements in the melt (C_L) after extraction and an assimilation ratio of r = 0.05.

F	0.1	0.2	0.3	0.4	0.5	0.6	0.7	0.8	0.9
Rb	388.156	194.959	129.545	96.522	76.568	63.192	53.594	46.367	40.726
Sr	1459.966	1013.722	818.007	702.066	623.306	565.379	520.494	484.406	454.581
Ba	2191.790	1316.456	972.911	782.947	660.258	573.559	508.570	457.778	416.825
Y	157.792	93.584	68.874	55.376	46.736	40.673	36.155	32.641	29.821
Zr	1499.374	784.609	537.163	410.528	333.244	281.024	243.306	214.748	192.350
Nb	56.633	30.821	21.568	16.730	13.731	11.679	10.181	9.037	8.133
Th	47.563	23.645	15.623	11.598	9.176	7.558	6.400	5.530	4.853
U	11.891	5.991	4.012	3.019	2.421	2.022	1.736	1.521	1.354
Sm	17.096	11.624	9.268	7.887	6.957	6.278	5.754	5.335	4.990
Yb	9.690	6.435	5.059	4.263	3.732	3.346	3.050	2.815	2.622

Table IX.9: f' values following the equation $f' = F^{-(r-1+D)/(r-1)}$ where F is the fraction of melt remaining, r is the ratio of assimilation to fractional crystallisation, and D is the bulk partition coefficient of the fractionating assemblage for r = 0.1.

F	0.1	0.2	0.3	0.4	0.5	0.6	0.7	0.8	0.9
Rb	9.360	4.774	3.220	2.435	1.961	1.642	1.414	1.242	1.108
Sr	3.098	2.204	1.806	1.568	1.406	1.285	1.191	1.116	1.053
Ba	4.994	3.077	2.318	1.896	1.623	1.429	1.283	1.169	1.076
Y	5.432	3.264	2.423	1.961	1.664	1.456	1.300	1.178	1.081
Zr	8.520	4.471	3.066	2.346	1.906	1.608	1.394	1.231	1.103
Nb	7.349	4.031	2.837	2.212	1.823	1.557	1.362	1.213	1.096
Th	9.747	4.911	3.289	2.475	1.985	1.657	1.423	1.247	1.110
U	9.733	4.906	3.286	2.473	1.984	1.657	1.423	1.247	1.110
Sm	3.351	2.328	1.882	1.618	1.439	1.308	1.206	1.124	1.057
Yb	3.638	2.466	1.965	1.672	1.475	1.332	1.221	1.133	1.061

Table IX.10: Values of C_L/C_0 assuming fractional crystallisation and an assimilation ratio of r = 0.1 following the equation $C_L/C_0 = f' + \frac{r}{r-1+D} \times \frac{C_A}{C_0}(1 - f')$, where r is the ratio of assimilation to fractional crystallisation, D is the bulk partition coefficient of the fractionating assemblage and C_A is the composition of the assimilating basement rock.

F	0.1	0.2	0.3	0.4	0.5	0.6	0.7	0.8	0.9
Rb	12.161	6.038	3.964	2.916	2.282	1.858	1.553	1.323	1.144
Sr	3.311	2.327	1.888	1.626	1.447	1.314	1.211	1.128	1.059
Ba	6.114	3.660	2.688	2.148	1.797	1.549	1.362	1.216	1.098
Y	5.698	3.399	2.508	2.019	1.704	1.483	1.318	1.189	1.085
Zr	8.541	4.480	3.071	2.349	1.908	1.610	1.395	1.231	1.103
Nb	7.734	4.215	2.949	2.285	1.873	1.590	1.384	1.226	1.101
Th	12.437	6.114	3.993	2.928	2.288	1.859	1.553	1.323	1.144
U	9.733	4.906	3.286	2.473	1.984	1.657	1.423	1.247	1.110
Sm	3.531	2.430	1.949	1.665	1.473	1.331	1.222	1.134	1.061
Yb	3.847	2.582	2.041	1.725	1.513	1.358	1.239	1.144	1.066

Table IX.11: Concentration of trace elements in the melt (C_L) after extraction and an assimilation ratio of r = 0.1.

F	0.1	0.2	0.3	0.4	0.5	0.6	0.7	0.8	0.9
Rb	440.218	218.592	143.487	105.552	82.621	67.245	56.208	47.896	41.407
Sr	1421.935	999.088	810.819	698.238	621.233	564.288	519.963	484.188	454.522
Ba	2341.594	1401.760	1029.562	822.602	688.390	593.241	521.727	465.706	420.448
Y	156.689	93.485	68.969	55.511	46.865	40.781	36.236	32.695	29.847
Zr	1488.686	780.875	535.321	409.492	332.627	280.652	243.088	214.630	192.302
Nb	57.230	31.193	21.822	16.909	13.859	11.768	10.241	9.074	8.150
Th	53.605	26.352	17.210	12.621	9.859	8.014	6.693	5.701	4.929
U	11.874	5.985	4.009	3.017	2.420	2.021	1.736	1.521	1.354
Sm	16.594	11.422	9.162	7.827	6.922	6.257	5.742	5.329	4.988
Yb	9.463	6.352	5.020	4.243	3.721	3.341	3.048	2.814	2.622

References

Summer at Quetrupillán

Aceves-Quesada, F., López-Blanco, J., del Pozzo, A.L.M., 2006. Determinación de peligros volcánicos aplicando técnicas de evaluación multicriterio y SIG en el área del Nevado de Toluca, centro de México. *Revista Mexicana de Ciencias Geológicas*, 23(2), 113–124.

Aiuppa, A., Bitetto, M., Francofonte, V., Velasquez, G., Moussallam, Y., Peters, N., Tamburello, G., Valderrama, O.A., 2017. A CO_2-gas precursor to the March 2015 Villarrica volcano eruption. *Geochemistry, Geophysics and Geosystems,* 18, 2120–2132. DOI: 10.1002/ 2017GC006892

Alexander, B., Marina, B., Richard, H., Herman, P., 2020. The 1951 eruption of Mount Lamington, Papua New Guinea: Devastating directed blast triggered by small-scale edifice failure. *Journal of Volcanology and Geothermal Research,* 401, 106947. DOI: 10.1016/j.jvolgeores. 106947

Alexander, D., 2013. Volcanic ash in the atmosphere and risks for civil aviation: A study in European crisis management. *International Journal of Disaster Risk Science,* 4, 9–19. DOI: 10.1007/s13753-013-0003-0

Allmendinger, R.W., Cardozo, N.C., Fisher, D., 2013. Structural Geology Algorithms: Vectors & Tensors. Cambridge University Press.

Andronico, D., Cristaldi, A., Scollo, S., 2008. The 4 – 5 September 2007 lava fountain at South-East Crater of Mt Etna, Italy. *Journal of Volcanology and Geothermal Research,* 173, 325–328. DOI: 10.1016/j.jvolgeores.2008.02.004

Andronico, D., Lodato, L., 2005. Effusive activity at Mount Etna volcano (Italy) during the 20th century: A contribution to volcanic hazard assessment. *Natural Hazards,* 36, 407–443. DOI: 10.1007/s11069-005-1938-2

Annen, C., 2009. From plutons to magma chambers: Thermal constraints on the accumulation of eruptible silicic magma in the upper crust. *Earth and Planetary Science Letters,* 284, 409–416. DOI: 10.1016/j.epsl.2009.05.006

Arellano, S., Yalire, M., Galle, B., Bobrowski, N., Dingwell, A., Johansson, M., Norman, P., 2017. Long-term monitoring of SO_2 quiescent degassing from Nyiragongo's lava lake. *Journal of African Earth Sciences,* 134, 866–873. DOI: 10.1016/j.jafrearsci.2016.07.002

Ayris, P.M., Delmelle, P., 2012. The immediate environmental effects of tephra emission. *Bulletin of Volcanology,* 74, 1905–1936. DOI: 10.1007/s00445-012-0654-5

Bain, A.A., Calder, E.S., Cortés, J.A., Cortés, G.P., Loughlin, S.C., 2019. Textural and geochemical constraints on andesitic plug emplacement prior to the 2004–2010 vulcanian explosions at Galeras volcano, Colombia. *Bulletin of Volcanology,* 81, 1–25. DOI: 10.1007/s00445-018-1260-y

Barr, I.D., Lynch, C.M., Mullan, D., De Siena, L., Spagnolo, M., 2018. Volcanic impacts on modern glaciers: A global synthesis. *Earth-Science Reviews,* 182, 186–203. DOI: 10.1016/ j.earscirev.2018.04.008

Baxter, P.J., 1990. Medical effects of volcanic eruptions. *Bulletin of Volcanology,* 52, 532–544. DOI: 10.1007/bf00301534

Bebbington, M., 2008. Incorporating the eruptive history in a stochastic model for volcanic eruptions. *Journal of Volcanology and Geothermal Research,* 175, 325–333. DOI: 10.1016/j. volgeores.2008. 03.013.

Bebbington, M., Cronin, S.J., Chapman, I., Turner, M.B., 2008. Quantifying volcanic ash fall hazard to electricity infrastructure. *Journal of Volcanology and Geothermal Research,* 177, 1055–1062. DOI: 10.1016/j.jvolgeores.2008.07.023

Bitschene, P.R., Fernández, M.I., 1995. Volcanology and petrology of fallout ashes from the August 1991 eruption of the Hudson Volcano (Patagonian Andes), in: Bitschene, P.R., Mendia, J. (Eds.),

The August 1991 Eruption of the Hudson Volcano (Patagonian Andes); a Thousand Days After. 27–54.

Blong, R.J., Grasso, P., Jenkins, S.F., Magill, C.R., Wilson, T.M., McMullan, K., Kandlbauer, J., 2017. Estimating building vulnerability to volcanic ash fall for insurance and other purposes. *Journal of Applied Volcanology,* 6. DOI: 10.1186/s13617-017-0054-9

Brahm, R., 2017. Lavas traquíticas del Complejo Volcánico Quetrupillán, Chile (39°30'S): Ejemplos de rejuvenecimiento de un reservorio tipo mush cristalino. *Thesis*, Univsersidad de Chile.

Brahm, R., Parada, M.A., Morgado, E., Contreras, C., McGee, L.E., 2018. Origin of Holocene trachyte lavas of the Quetrupillán volcanic complex, Chile: Examples of residual melts in a rejuvenated crystalline mush reservoir. *Journal of Volcanology and Geothermal Research,* 357, 163–176. DOI: 10.1016/j.jvolgeores.2018.04.020

Branca, S., De Beni, E., Chester, D., Duncan, A., Lotteri, A., 2017. The 1928 eruption of Mount Etna (Italy): Reconstructing lava flow evolution and the destruction and recovery of the town of Mascali. *Journal of Volcanology and Geothermal Research,* 335, 54–70. DOI: 10.1016 /j.jvolgeores.2017.02.002

Brock, B., Rivera, A., Casassa, G., Bown, F., Acuña, C., 2007. The surface energy balance of an active ice-covered volcano: Villarrica Volcano, southern Chile. *Annals of Glaciology,* 45, 104–114.

Brown, S.K., Jenkins, S.F., Sparks, R.S.J., Odbert, H., Auker, M.R., 2017. Volcanic fatalities database: analysis of volcanic threat with distance and victim classification. *Journal of Applied Volcanology,* 6. DOI: 10.1186/s13617-017-0067-4

Burchardt, S., Galland, O., 2016. Studying volcanic plumbing systems - multidisciplinary approaches to a multifaceted problem, in: Nemeth, K. (Ed.), Updates in Volcanology - from Volcano Modelling to Volcano Geology. IntechOpen, 23–53. DOI: 10.5772/63959

Cando-Jácome, M., Martínez-Graña, A., 2019. Determination of primary and secondary lahar flow paths of the Fuego Volcano (Guatemala) using morphometric parameters. *Remote Sensing,* 11, 727. DOI: 10.3390/rs11060727

Carapezza, M.L., Barberi, F., Ranaldi, M., Ricci, T., Tarchini, L., Barrancos, J., Fischer, C., Granieri, D., Lucchetti, C., Melian, G., Perez, N., Tuccimei, P., Vogel, A., Weber, K., 2012. Hazardous gas emissions from the flanks of the quiescent Colli Albani volcano (Rome, Italy). *Applied Geochemistry,* 27, 1767–1782. DOI: 10.1016/j.apgeochem.2012.02.012

Cardozo, N.C., Allmendinger, R.W., 2013. Spherical projections with OSXStereonet. *Computers and Geosciences*, 51, 193–205. DOI: 10.1016/j.cageo.2012.07.021

Carmichael, I.S.E., Nicholls, J., Smith, A.L., 1970. Silica Activity in Igneous Rocks. *The American Mineralogist,* 55, 246–263.

Cashman, K. V., Sparks, R.S.J., Blundy, J.D., 2017. Vertically extensive and unstable magmatic systems: A unified view of igneous processes. *Science*, 355. DOI: 10.1126/ science.aag3055

Cassidy, M., Manga, M., Cashman, K., Bachmann, O., 2018. Controls on explosive-effusive volcanic eruption styles. *Nature Communications,* 9. DOI: 10.1038/s41467-018-05293-3

Castruccio, A., Clavero, J., 2015. Lahar simulation at active volcanoes of the Southern Andes: implications for hazard assessment. *Natural Hazards,* 77, 693–716. DOI: 10.1007 /s11069-015-1617-x

Castruccio, A., Clavero, J., Rivera, A., 2010. Comparative study of lahars generated by the 1961 and 1971 eruptions of Calbuco and Villarrica volcanoes, Southern Andes of Chile. *Journal of Volcanology and Geothermal Research,* 190, 297–311. DOI: 10.1016/j.jvolgeores. 2009.12.005

Castruccio, A., Clavero, J., Segura, A., Samaniego, P., Roche, O., Le Pennec, J.L., Droguett, B., 2016. Eruptive parameters and dynamics of the April 2015 sub-Plinian eruptions of Calbuco volcano (southern Chile). *Bulletin of Volcanology,* 78. DOI: 10.1007/s00445-016-1058-8

Castruccio, A., Contreras, M.A., 2016. The influence of effusion rate and rheology on lava flow dynamics and morphology: A case study from the 1971 and 1988–1990 eruptions at Villarrica and Lonquimay volcanoes, Southern Andes of Chile. *Journal of Volcanology and Geothermal Research,* 327, 469–483. DOI: 10.1016/j.jvolgeores.2016.09.015

Cembrano, J., Hervé, F., Lavenu, A., 1996. The Liquiñe-Ofqui Fault Zone: a long-lived intra-arc fault system in southern Chile. *Tectonophysics,* 259, 55–66. DOI: 10.1016/0040-1951(95)00066-6

Cembrano, J., Lara, L., 2009. The link between volcanism and tectonics in the southern volcanic zone of the Chilean Andes: A review. *Tectonophysics,* 471, 96–113. DOI: 10.1016/j.tecto. 2009.02.038

Cembrano, J., Schermer, E., Lavenu, A., Sanhueza, A., 2000. Contrasting nature of deformation along an intra-arc shear zone, the Liquiñe-Ofqui fault zone, southern Chilean Andes. *Tectonophysics,* 319, 129–149. DOI: 10.1016/S0040-1951(99)00321-2

Cigolini, C., Borgia, A., Casertano, L., 1984. Intra-crater activity, aa-block lava, viscosity and flow dynamics: Arenal Volcano, Costa Rica. *Journal of Volcanology and Geothermal Research,* 20, 155–176. DOI: 10.1016/0377-0273(84)90072-6

Clapperton, C., Sugden, D.E., 1988. Holocene glacier fluctuations in South America and Antarctica. *Quaternary Science Reviews*, 7, 185–198. DOI: 10.1016/0277-3791(88)90005-4

Clapperton, C.M., 1983. The glaciation of the Andes. *Quaternary Science Reviews,* 2, 83–155. DOI: 10.1016/0277-3791(83)90005-7

Clavero, J., Moreno, H., 2004. Evolution of Villarrica Volcano, in: Lara, L., Clavero, J. (Eds.), Villarrica Volcano (39.5°S), Southern Andes, Chile. Servicio Nacional de Geología y Minería, 17–27.

Cortés, J.A., 2016. Olive. Available through VHub: https://vhub.org/resources/olive

Cortés, J.A., 2017. CFU. Available through VHub: https://vhub.org/resources/cfu

Cortés, J.A., 2019. Strike converter 1.0 for ImageJ. Fiji plugin Strikes_Results.ijm. Available through VHub: https://vhub.org/resources/4540

Cortés, J.A., 2020. CFU-Pingu. Available through VHub: https://vhub.org/resources/cfupingu

Cortés, J.A., Palma, J.L., 2020. Petrological Input Graphical oUput (PINGU): an online tool for plotting geochemical diagrams. Available through VHub: https://vhub.org/resources/pingu

Craig, H., Wilson, T., Stewart, C., Villarosa, G., Outes, V., Cronin, S., Jenkins, S., 2016. Agricultural impact assessment and management after three widespread tephra falls in Patagonia, South America, *Natural Hazards*, 82, 1167-1229, DOI: 10.1007/s11069-016-2240-1

Curilem, G., Vergara, J., Fuentealba, G., Acuña, G., Chacón, M., 2009. Classification of seismic signals at Villarrica volcano (Chile) using neural networks and genetic algorithms. *Journal of Volcanology and Geothermal Research,* 180, 1–8. DOI: 10.1016/j.jvolgeores.2008. 12.002

Daly, R.A., 1911. The Nature of Volcanic Action. *Proceedings of the American Academy of Arts and Sciences*, 47(3), 47–122.

Del Negro, C., Cappello, A., Ganci, G., 2016. Quantifying lava flow hazards in response to effusive eruption. *Bulletin of the Geological Society of America,* 128, 1–13. DOI: 10.1130 /B31364.1

Delgado, F., Pritchard, M.E., Ebmeier, S., González, P., Lara, L., 2017. Recent unrest (2002–2015) imaged by space geodesy at the highest risk Chilean volcanoes: Villarrica, Llaima, and Calbuco

(Southern Andes). *Journal of Volcanology and Geothermal Research,* 344, 270–288. DOI: 10.1016/j.jvolgeores.2017.05.020

Denton, G.H., Heusser, C.J., Lowell, T. V., Moreno, P.I., Andersen, B.G., Heusser, L.E., Schlüchter, C., Marchant, D.R., 1999. Interhemispheric linkage of paleoclimate during the last glaciation. *Geografiska Annaler (Physical Geography),* 81, 107–153. DOI: 10.1111/j.0435-3676.1999.00055.x

Dixon, H.J., Murphy, M.D., Sparks, S.J., Chávez, R., Naranjo, J.A., Dunkley, P.N., Young, S.R., Gilbert, J.S., Pringle, M.R., 1999. The Geology of Nevados De Chillán. *Revista Geológica de Chile,* 26, 227–253. DOI: 10.4067/S0716-02081999000200006

Doiron, S.D., Bluth, G.J.S., Schnetzler, C.C., Krueger, A.J., Walter, L.S., 1991. Transport of Cerro Hudson SO_2 clouds. *EOS*, 72, 489–490. DOI: 10.1029/90EO00354

Druitt, T.H., 1998. Pyroclastic density currents, in: Gilbert, J.S., Sparks, R.S.J. (Eds.), The Physics of Explosive Volcanic Eruptions. Geological Society of London, Special Publication, 145–182. DOI: 10.1144/GSL.SP.1996.145.01.08

Dufek, J., Esposti Ongaro, T., Roche, O., 2015. Pyroclastic Density Currents, in: Sigurdsson, H., Houghton, B., McNutt, S.R., Rymer, H., Stix, J. (Eds), The Encyclopedia of Volcanoes, 2nd Edition, Elsevier Inc. 617-629, DOI: 10.1016/B978-0-12-385938-9.00035-3

Dzierma, Y., Wehrmann, H., 2010a. Statistical eruption forecast for the Chilean Southern Volcanic Zone: Typical probabilities of volcanic eruptions as baseline for possibly enhanced activity following the large 2010 Concepción earthquake. *Natural Hazards and Earth System Sciences,* 10, 2093–2108. DOI: 10.5194/nhess-10-2093-2010

Dzierma, Y., Wehrmann, H., 2010b. Eruption time series statistically examined: Probabilities of future eruptions at Villarrica and Llaima Volcanoes, Southern Volcanic Zone, Chile. *Journal of Volcanology and Geothermal Research,* 193, 82–92. DOI: 10.1016/j.jvolgeores. 2010.03.009

Espinoza, A.E., Osorio-Parraguez, P., Posada Quiroga, E., 2019. Preventing mental health risks in volunteers in disaster contexts: The case of the Villarrica Volcano eruption, Chile. *International Journal of Disaster Risk Reduction,* 34, 154–164. DOI: 10.1016/j.ijdrr.2018.11.013

Esposti Ongaro, T., Widiwijayanti, C., Clarke, A.B., Voight, B., Neri, A., 2011. Multiphase-flow numerical modeling of the 18 May 1980 lateral blast at Mount St. Helens, USA. *Geology,* 39, 535–538. DOI: 10.1130/G31865.1

Fagents, S.A., Baloga, S.M., 2006. Toward a model for the bulking and debulking of lahars. *Journal of Geophysical Research: Solid Earth,* 111, 1–21. DOI: 10.1029/2005JB003986

Favalli, M., Chirico, G.D., Papale, P., Pareschi, M.T., Boschi, E., 2009. Lava flow hazard at Nyiragongo volcano, D.R.C. 1. Model calibration and hazard mapping. *Bulletin of Volcanology*, 71, 363–374. DOI: 10.1007/s00445-008-0233-y

Fink, J., 1980. Surface folding and viscosity of rhyolite flows. *Geology,* 8, 250–254. DOI: 10.1130 /0091-7613(1980)

Fitzgerald, R.H., Kennedy, B.M., Wilson, T.M., Leonard, G.S., Tsunematsu, K., Keys, H., 2017. The communication and risk management of volcanic ballistic hazards, in: Fearnley, C.J., Bird, D.K., Haynes, K., McGuire, W.J., Jolly, G. (Eds.), Observing the Volcano World. Advances in Volcanology. IAVCEI.

Fontijn, K., Lachowycz, S.M., Rawson, H., Pyle, D.M., Mather, T.A., Naranjo, J.A., Moreno-Roa, H., 2014. Late Quaternary tephrostratigraphy of southern Chile and Argentina. *Quaternary Science Reviews,* 89, 70–84. DOI: 10.1016/j.quascirev.2014.02.007

Fontijn, K., Rawson, H., Van Daele, M., Moernaut, J., Abarzúa, A.M., Heirman, K., Bertrand, S., Pyle, D.M., Mather, T.A., De Batist, M., Naranjo, J.A., Moreno, H., 2016. Synchronisation of sedimentary records using tephra: A postglacial tephrochronological model for the Chilean Lake District. *Quaternary Science Reviews,* 137, 234–254. DOI: 10.1016/j.quascirev. 2016.02.015

García-Palomo, A., Macías, J.L., Arce, J.L., Capra, L., Garduño, V.H., Espíndola, J.M., 2002. Geology of Nevado de Toluca Volcano and surrounding areas, central Mexico. *Geological Society of America Map and Chart Series*

Glasser, N.F., Jansson, K.N., Harrison, S., Kleman, J., 2008. The glacial geomorphology and Pleistocene history of South America between 38°S and 56°S. *Quaternary Science Reviews,* 27, 365–390. DOI: 10.1016/j.quascirev.2007.11.011

Glazner, A., Bartley, J., Coleman, D., 2016. We Need a New Definition for "Magma." *EOS*, 97, 1–7. DOI: 10.1029/2016eo059741

Grosse, P., Euillades, P.A., Euillades, L.D., van Wyk de Vries, B., 2014. A global database of composite volcano morphometry. *Bulletin of Volcanology,* 76, 1–16. DOI: 10.1007/s00445-013-0784-4

Gudmundsson, A., 2012. Magma chambers: Formation, local stresses, excess pressures, and compartments. *Journal of Volcanology and Geothermal Research,* 237–238, 19–41. DOI: 10.1016/j.jvolgeores.2012.05.015

GVP, 2013. Global Volcanism Program, Volcanoes of the World, https://volcano.si.edu/ gvp_votw.cfm

Harris, A.J.L., Flynn, L.P., Matias, O., Rose, W.I., Cornejo, J., 2004. The evolution of an active silicic lava flow field: An ETM+ perspective. *Journal of Volcanology and Geothermal Research,* 135, 147–168. DOI: 10.1016/j.jvolgeores.2003.12.011

Hayes, J.L., Wilson, T.M., Magill, C., 2015. Tephra fall clean-up in urban environments. *Journal of Volcanology and Geothermal Research,* 304, 359–377. DOI: 10.1016/j.jvolgeores .2015.09.014

Hernandez-Moreno, C., Speranza, F., Di Chiara, A., 2014. Understanding kinematics of intra-arc transcurrent deformation: Paleomagnetic evidence from the Liquiñe-Ofqui fault zone (Chile, 38–41°S). *Tectonics,* 33, 1964–1988. DOI: 10.1002/2014TC003622

Hersum, T.G., Marsh, B.D., 2007. Igneous textures: On the kinetics behind the words. *Elements*, 3, 247–252. DOI: 10.2113/gselements.3.4.247

Hervé, F., 1994. The Southern Andes between 39° and 44°S latitude: The geological signature of a transpressive tectonic regime related to a magmatic arc, in: Reutter, K.J., Scheuber, E., Wigger, P.J. (Eds.), Tectonics of the Southern Central Andes. Springer, Berlin, 243–248. DOI: 10.1007/978-3-642-77353-2_17

Hickey-Vargas, R., Holbik, S., Tormey, D., Frey, F.A., Moreno Roa, H., 2016(a). Basaltic rocks from the Andean Southern Volcanic Zone: Insights from the comparison of along-strike and small-scale geochemical variations and their sources. *Lithos,* 258–259, 115–132. DOI: 10.1016/j.lithos. 2016.04.014

Hickey-Vargas, R., Moreno, H., Lopez-Escobar, L., Frey, F.A., 1989. Geochemical variations in Andean basaltic and silicic lavas from the Villarrica-Lanín volcanic chain (39.5° S): an evaluation of source heterogeneity, fractional crystallization and crustal assimilation. *Contributions to Mineralogy and Petrology,* 103, 361–386. DOI: 10.1007/BF00402922

Hickey-Vargas, R., Sun, M., Holbik, S., 2016(b). Geochemistry of basalts from small eruptive centers near Villarrica stratovolcano, Chile: Evidence for lithospheric mantle components in continental arc magmas. *Geochimica et Cosmochimica Acta,* 185, 358–382. DOI: 10.1016/ j.gca.2016.03.033

Hickey-Vargas, R., Sun, M., López-Escobar, L., Moreno-Roa, H., Reagan, M.K., Morris, J.D., Ryan, J.G., 2002. Multiple subduction components in the mantle wedge: Evidence from eruptive centers in the Central Southern volcanic zone, Chile. *Geology*, 30(3), 199-202. DOI: 10.1130/ 0091-7613(2002)

Higgins, M.D., 2000. Measurement of crystal size distributions. *The American Mineralogist,* 85, 1105–1116. DOI: 10.2138/am-2000-8-901

Higgins, M.D., 2002. Closure in crystal size distributions (CSD), verification of CSD calculations, and the significance of CSD fans. *The American Mineralogist,* 87, 171–175.

Higgins, M.D., 2006. Quantitative Textural Measurements in Igneous and Metamorphic Petrology. Cambridge University Press.

Hildreth, W., 2004. Volcanological perspectives on Long Valley, Mammoth Mountain, and Mono Craters: Several contiguous but discrete systems *Journal of Volcanology and Geothermal Research,* 136, 169–198. DOI: 10.1016/j.jvolgeores.2004.05.019

Hildreth, W., Moorbath, S., 1988. Crustal contributions to arc magmatism in the Andes of Central Chile. *Contributions to Mineralogy and Petrology,* 98, 455–489. DOI: 10.1007/ BF00372365

Ho, C.-H., 1990. Bayesian analysis of volcanic eruptions. *Journal of Volcanology and Geothermal Research,* 43, 91–98. DOI: 10.1016/0377-0273(90)90046-I

Horwell, C.J., Baxter, P.J., 2006. The respiratory health hazards of volcanic ash: A review for volcanic risk mitigation. *Bulletin of Volcanology,* 69, 1–24. DOI: 10.1007/s00445-006-0052-y

Hulton, N.R.J., Purves, R.S., McCulloch, R.D., Sugden, D.E., Bentley, M.J., 2002. The Last Glacial Maximum and deglaciation in southern South America. *Quaternary Science Reviews,* 21, 233–241. DOI: 10.1016/S0277-3791(01)00103-2

Instituto Nacional de Estatísticas, (INE), 2017. Censo 2017 - Regiones, Provincias y Comunas. http://ine-chile.maps.arcgis.com/apps/webappviewer/index.html?id=c2155cac57d04032bf6ca5f151cddd6d (accessed 25/06/20).

Irvine, T.N., Baragar, W.R.A., 1971. A guide to the chemical classification of the common volcanic rocks. *Canadian Journal of Earth Sciences,* 8(5), 523-548. DOI: 10.1139/e71-055

Jenkins, S., Komorowski, J.C., Baxter, P.J., Spence, R., Picquout, A., Lavigne, F., Surono, 2013. The Merapi 2010 eruption: An interdisciplinary impact assessment methodology for studying pyroclastic density current dynamics. *Journal of Volcanology and Geothermal Research,* 261, 316–329. DOI: 10.1016/j.jvolgeores.2013.02.012

Johnson, J.B., Palma, J.L., 2015. Lahar infrasound associated with Villarrica's March 3, 2015 eruption. *Geophysical Research Letters,* 6324–6331. DOI: 10.1002/2015GL065024

Johnson, J.B., Watson, L.M., Palma, J.L., Dunham, E.M., Anderson, J.F., 2018. Forecasting the Eruption of an Open-Vent Volcano Using Resonant Infrasound Tones. *Geophysical Research Letters,* 45, 2213–2220. DOI: 10.1002/2017GL076506

Jones, R., Manville, V., Andrade, D., 2015. Probabilistic analysis of rain-triggered lahar initiation at Tungurahua volcano. *Bulletin of Volcanology,* 77. DOI: 10.1007/s00445-015-0946-7

Kirkbride, M.P., Dugmore, A.J., 2003. Glaciological response to distal tephra fallout from the 1947 eruption of Hekla, south Iceland. *Journal of Glaciology,* 49, 420–428. DOI: 10.3189/ 172756503781830575

Klein, F.W., 1982. Patterns of historical eruptions at Hawaiian volcanoes. *Journal of Volcanology and Geothermal Research,* 12, 1–35.

Komorowski, J.C., Jenkins, S., Baxter, P.J., Picquout, A., Lavigne, F., Charbonnier, S., Gertisser, R., Preece, K., Cholik, N., Budi-Santoso, A., Surono, 2013. Paroxysmal dome explosion during the Merapi 2010 eruption: Processes and facies relationships of associated high-energy pyroclastic density currents. *Journal of Volcanology and Geothermal Research,* 261, 260–294. DOI: 10.1016/j.jvolgeores.2013.01.007

Kratzmann, D.J., Carey, S., Scasso, R., Naranjo, J.A., 2009. Compositional variations and magma mixing in the 1991 eruptions of Hudson volcano, Chile. *Bulletin of Volcanology,* 71, 419–439. DOI: 10.1007/s00445-008-0234-x

La Frenierre, J., Mark, B.G., 2017. Detecting Patterns of Climate Change at Volcán Chimborazo, Ecuador, by Integrating Instrumental Data, Public Observations, and Glacier Change Analysis. *Annals of the American Association of Geographers,* 107, 979–997. DOI: 10.1080/ 24694452.2016.1270185

Lara, 2004. Overview of Villarrica Volcano, in: Lara, L., Clavero, J. (Eds.), Villarrica Volcano (39.5°S), Southern Andes, Chile. Servicio Nacional de Geología y Minería, 5–12.

Lara, L., Moreno, H., 2004. Carta geológica de Chile: Geología del área de Liquiñe-Neltume, Regiones de La Araucanía y de Los Ríos. Escala: 1:100 000.

Lara, L.E., Lavenu, A., Cembrano, J., Rodríguez, C., 2006. Structural controls of volcanism in transversal chains: Re-sheared faults and neotectonics in the Cordón Caulle-Puyehue area (40.5°S), Southern Andes. *Journal of Volcanology and Geothermal Research,* 158, 70–86. DOI: 10.1016/j.jvolgeores.2006.04.017

Lara, L.E., Naranjo, J.A., Moreno, H., 2004. Lanín volcano (39.5°S), Southern Andes: geology and morphostructural evolution. *Revista Geológica de Chile,* 31, 1–14. DOI: 10.4067/ S0716-02082004000200004

Latutrie, B., Harris, A., Médard, E., Gurioli, L., 2017. Eruption and emplacement dynamics of a thick trachytic lava flow of the Sancy volcano (France). *Bulletin of Volcanology,* 79, 1–21. DOI: 10.1007/s00445-016-1084-6

Le Maitre, R.W., Streckeisen, A., Zanettin, B., Le Bas, M.J., Bonin, B., Bateman, P., 2002. Igneous Rocks; A Classification and Glossary of Terms, 2nd Edition. Cambridge University Press.

Lehr, J., Eckel, F., Thorwart, M., Rabbel, W., 2019. Low-Frequency Seismicity at Villarrica Volcano: Source Location and Seismic Velocities. *Journal of Geophysical Research: Solid Earth,* 124, 11505–11530. DOI: 10.1029/2018JB017023

Lentz, R.C.F., McSween, H.Y., 2000. Crystallization of the basaltic shergottites: Insights from crystal size distribution (CSD) analysis of pyroxenes. *Meteoritics and Planetary Science,* 35, 919–927. DOI: 10.1111/j.1945-5100.2000.tb01481.x

Lev, E., Spiegelman, M., Wysocki, R.J., Karson, J.A., 2012. Investigating lava flow rheology using video analysis and numerical flow models. *Journal of Volcanology and Geothermal Research,* 247–248, 62–73. https://doi.org/10.1016/j.jvolgeores.2012.08.002

Lohmar, S., 2008. Petrología de las ignimbritas Licán y Pucón (volcán Villarrica) y Curacautín (volcán Llaima) en Los Andes del Sur de Chile. *Thesis*, Universidad de Chile

Lohmar, S., Parada, M., Gutiérrez, F., Robin, C., Gerbe, M. C., 2012. Mineralogical and numerical approaches to establish the pre-eruptive conditions of the mafic Licán Ignimbrite, Villarrica Volcano (Chilean Southern Andes). *Journal of Volcanology and Geothermal Research,* 235, 55–69. DOI: 10.1016/j.jvolgeores.2012.05.006.

Lohmar, S., Robin, C., Gourgaud, A., Clavero, J., Parada, M.Á., Moreno, H., Ersoy, O., López-Escobar, L., Naranjo, J.A., 2007. Evidence of magma-water interaction during the 13,800 years BP

explosive cycle of the Licán Ignimbrite, Villarrica volcano (southern Chile). *Revista Geológica de Chile,* 34, 233–247. DOI: 10.4067/S0716-02082007000200004

López-Escobar, L., Cembrano, J., Moreno, H., 1995. Geochemistry and tectonics of the Chilean southern Andes basaltic Quaternary volcanism (37-46°S). *Revista Geológica de Chile,* 22, 219–234. DOI: 10.5027/andgeoV22n2-a06

Lorenz, V., 1986. On the growth of maars and diatremes and its relevance to the formation of tuff rings. *Bulletin of Volcanology,* 265–274. DOI: 10.1007/BF01081755

Lowe, D.R., Williams, S.N., Leigh, H., Connort, C.B., Gemmell, J.B., Stoiber, R.E., 1986. Lahars initiated by the 13 November 1985 eruption of Nevado del Ruiz, Colombia. *Nature,* 324, 51–53. DOI: 10.1038/324051a0

Lowell, T. V, Heusser, C.J., Andersen, B.G., Moreno, P.I., Hauser, A., Heusser, L.E., Schluchter, C., Marchant, D.R., Denton, G.H., 1995. Interhemispheric correlation of Late Pleistocene glacial events. *Science,* 269, 1541–1549. DOI: 10.4172/2324-9307.1000133

Lu, Z., Rykhus, R., Masterlark, T., Dean, K.G., 2004. Mapping recent lava flows at Westdahl Volcano, Alaska, using radar and optical satellite imagery. *Remote Sensing of Environment*, 91, 345–353. DOI: 10.1016/j.rse.2004.03.015

Macdonald, G.A., 1953. Pahoehoe, aa, and block lava. *American Journal of Science,* 251, 169–191. DOI: 10.2475/ajs.251.3.169

Macdonald, G.A., 1962. The 1959 and 1960 eruptions of Kilauea volcano, Hawaii, and the construction of walls to restrict the spread of the lava flows. *Bulletin of Volcanology,* 24, 249–294. DOI: 10.1007/BF02599351

Magee, C., Stevenson, C.T.E., Ebmeier, S.K., Keir, D., Hammond, J.O.S., Gottsmann, J.H., Whaler, K.A., Schofield, N., Jackson, C.A.L., Petronis, M.S., O'Driscoll, B., Morgan, J., Cruden, A., Vollgger, S.A., Dering, G., Micklethwaite, S., Jackson, M.D., 2018. Magma plumbing systems: A geophysical perspective. *Journal of Petrology,* 59, 1217–1251. DOI: 10.1093/petrology/egy064

Magill, C., Wilson, T., Okada, T., 2013. Observations of tephra fall impacts from the 2011 Shinmoedake eruption, Japan. *Earth Planets Space*. 65, 677–698. DOI: 10.5047/eps.2013.05.010

Magnall, N., James, M.R., Tuffen, H., Vye-Brown, C., 2017. Emplacing a cooling-limited rhyolite lava flow: Similarities with basaltic lava flows. *Frontiers in Earth Science*, 5(44). DOI: 10.3389/feart.2017.00044

Major, J.J., Newhall, C.G., 1989. Snow and ice perturbation during historical volcanic eruptions and the formation of lahars and floods - A global review. *Bulletin of Volcanology,* 52, 1–27. DOI: 10.1007/BF00641384

Marsh, B.D., 1988. Crystal size distribution (CSD) in rocks and the kinetics and dynamics of crystallization I. Theory. *Contributions to Mineralogy and Petrology,* 99, 277–291.

Marsh, B.D., 1989. Magma chambers. *Annual Reviews of Earth and Planetary Sciences,* 17, 439–474. DOI: 10.1146/annurev.earth.17.1.439

Marsh, B.D., 1998. On the Interpretation of Crystal Size Distributions in Magmatic Systems. *Journal of Petrology,* 39, 553–599. DOI: 10.1093/petroj/39.4.553

Matthews, J.A., Briffa, K.R., 2005. The "Little Ice Age": Re-evaluation of an evolving concept. *Geografiska Annaler (Physical Geography),* 87, 17–36. DOI: 10.1111/j.0435-3676.2005.00242.x

McBirney, A.R., Serva, L., Guerra, M., Connor, C.B., 2003. Volcanic and seismic hazards at a proposed nuclear power site in central Java. *Journal of Volcanology and Geothermal Research,* 126, 11–30. DOI: 10.1016/S0377-0273(03)00114-8

McGarvie, D, Pavez, A., Cortés, J.A., Faggetter, L., Burgess, R., McGarvie, D, 2014. Glaciovolcanism at Volcán Quetrupillán, Chile. Abstract, GSA Annual Meeting.

McGarvie, D., 2009. Rhyolitic volcano-ice interactions in Iceland. *Journal of Volcanology and Geothermal Research,* 185, 367–389. DOI: 10.1016/j.jvolgeores.2008.11.019

McGarvie, D.W., Macdonald, R., Pinkerton, H., Smith, R.L., 1990. Petrogenetic evolution of the torfajökull volcanic complex, Iceland II. The role of magma mixing. *Journal of Petrology,* 31, 461–481. DOI: 10.1093/petrology/31.2.461

McGee, L.E., Brahm, R., Rowe, M.C., Handley, H.K., Morgado, E., Lara, L.E., Turner, M.B., Vinet, N., Parada, M.Á., Valdivia, P., 2017. A geochemical approach to distinguishing competing tectono-magmatic processes preserved in small eruptive centres. *Contributions to Mineralogy and Petrology,* 172, 1–26. DOI: 10.1007/s00410-017-1360-2

McGetchin, T.R., Settle, M., Chouet, B.A., 1974. Cinder cone growth modelled after Northeast Crater, Mount Etna, Sicily. *Journal of Geophysical Research,* 79, 3257–3272. DOI: 10.1029 /jb079i023p03257

Mee, K., Gilbert, J.S., McGarvie, D.W., Naranjo, J.A., Pringle, M.S., 2009. Palaeoenvironment reconstruction, volcanic evolution and geochronology of the Cerro Blanco subcomplex, Nevados de Chillán volcanic complex, central Chile. *Bulletin of Volcanology,* DOI: 10.1007/ s00445-009-0277-7

Melnik, O.E., Blundy, J.D., Rust, A.C., Muir, D.D., 2011. Subvolcanic plumbing systems imaged through crystal size distributions. *Geology,* 39, 403–406. DOI: 10.1130/G31691.1

Mendoza-Rosas, A.T., De la Cruz-Reyna, S., 2008. A statistical method linking geological and historical eruption time series for volcanic hazard estimations: Applications to active polygenetic volcanoes. *Journal of Volcanology and Geothermal Research,* 176, 277–290. DOI: 10.1016/j.jvolgeores.2008.04.005

Mercer, J.H., 1965. Glacier variations in southern Patagonia. *Geographical Review,* 55, 290–413. DOI: 10.2307/213136

Meyer, P.L., 1970. Introductory Probability and Statistical Applications, 2nd Edition, Addison-Wesley Publishing Company.

Miller, T.P., McGimsey, R.G., Richter, D.H., Riehle, J.R., Nye, C.J., Yount, M.E., Dumoulin, J.A., 1998. Catalog of the Historically Active Volcanoes of Alaska. *Department of the Interior, U.S. Geological Survey*

Mock, A., Jerram, D.A., 2005. Crystal size distributions (CSD) in three dimensions: Insights from the 3D reconstruction of a highly porphyritic rhyolite. *Journal of Petrology,* 46, 1525–1541. DOI: 10.1093/petrology/egi024

Möller, R., Möller, M., Kukla, P.A., Schneider, C., 2016. Impact of supraglacial deposits of tephra from Grímsvötn volcano, Iceland, on glacier ablation. *Journal of Glaciology,* 62, 933–943. DOI: 10.1017/jog.2016.82

Moore, J.G., Sisson, T.., 1981. Deposits and effects of the May 18 pyroclastic surge, in: Lipman, P.W., Mullineaux, D.R. (Eds.), The 1980 Eruption of Mount St Helens, Washington. USGS, 421–438.

Moreno, H., 2000. Mapa de peligros del volcán Villarrica, Regiones de la Araucanía y de Los Lagos. Escala 1:75000.

Moreno, H., Lara, L., 2008. Carta geológica de Chile: Geología del área Pucón-Curarrehue, Regiones de La Araucanía y de Los Ríos. Escala: 1:100 000.

Moreno, H., López-Escobar, L., Cembrano, J., 1994. The Villarrica-Quetrupillán-Lanín volcanic chain: A review and probable significance in the Southern Andes, 39.4°S, Chile, in: Congreso Geológico Chileno. 339–341.

Moreno, P.I., Lowell, T. V., Jacobson, G.L., Denton, G.H., 1999. Abrupt vegetation and climate changes during the Last Glacial Maximum and last termination in the Chilean Lake District: A case study from Canal de la Puntilla (41°S). *Geografiska Annaler (Physical Geography),* 81, 285–311. DOI: 10.1111/j.0435-3676.1999.00059.x

Morgado, E., Parada, M.A., Contreras, C., Castruccio, A., Gutiérrez, F., McGee, L.E., 2015. Contrasting records from mantle to surface of Holocene lavas of two nearby arc volcanic complexes: Caburgua-Huelemolle Small Eruptive Centers and Villarrica Volcano, Southern Chile. *Journal of Volcanology and Geothermal Research,* 306, 1–16. DOI: 10.1016/j.jvolgeores. 2015.09.023

Morgan, D.J., Jerram, D.A., 2006. On estimating crystal shape for crystal size distribution analysis. *Journal of Volcanology and Geothermal Research,* 154, 1–7. DOI: 10.1016/ j.jvolgeores.2005.09.016

Morueta-Holme, N., Engemann, K., Sandoval-Acuña, P., Jonas, J.D., Segnitz, R.M., Svenning, J.C., 2015. Strong upslope shifts in Chimborazo's vegetation over two centuries since Humboldt. *Proceedings of the National Academy of Sciences of the United States of America*, 112(41), 12741–12745. DOI: 10.1073/pnas.1509938112

Moussallam, Y., Bani, P., Curtis, A., Barnie, T., Moussallam, M., Peters, N., Schipper, C.I., Aiuppa, A., Giudice, G., Amigo, Á., Velasquez, G., Cardona, C., 2016. Sustaining persistent lava lakes: Observations from high-resolution gas measurements at Villarrica volcano, Chile. *Earth and Planetary Science Letters,* 454, 237–247. DOI: 10.1016/j.epsl.2016.09.012

Murphy, M. D., 1996. Magmatic evolution at Volcán Sollipulli, southern Andes of Chile. *Thesis*, University of Bristol.

Nakada, S., Zaennudin, A., Yoshimoto, M., Maeno, F., Suzuki, Y., Hokanishi, N., Sasaki, H., Iguchi, M., Ohkura, T., Gunawan, H., Triastuty, H., 2019. Growth process of the lava dome/flow complex at Sinabung Volcano during 2013–2016. *Journal of Volcanology and Geothermal Research,* 382, 120–136. DOI: 10.1016/j.jvolgeores.2017.06.012

Naranjo, J.A., Moreno, H., 2004. Laharic debris-flows from Villarrica Volcano. Villarrica Volcano (39.5°S), South. Andes, Chile 28–38.

Naranjo, J.A., Sparks, R.S.J., Stasiuk, M. V., Moreno, H., Ablay, G.J., 1992. Morphological, structural and textural variations in the 1988–1990 andesite lava of Lonquimay Volcano, Chile. *Geological Magazine,* 129, 657–678. DOI: 10.1017/S0016756800008426

Naranjo, J.A., Stern, C.R., 1998. Holocene explosive activity of Hudson Volcano, southern Andes. *Bulletin of Volcanology,* 59, 291–306. DOI: 10.1007/s004450050193

Naranjo, J.L., Sigurdsson, H., Carey, S.N., Fritz, W., 1986. Eruption of the Nevado del Ruiz volcano, Colombia, on 13 November 1985: tephra fall and lahars. *Science*, 233, 961–963. DOI: 10.1126/science.233.4767.961

Nelson, S.T., Montana, A., 1992. Sieve-textured plagioclase in volcanic rocks produced by rapid decompression. *The American Mineralogist,* 77, 1242–1249.

Newhall, C.G., Costa, F., Ratdomopurbo, A., Venezky, D.Y., Widiwijayanti, C., Win, N.T.Z., Tan, K., Fajiculay, E., 2017. WOVOdat – An online, growing library of worldwide volcanic unrest, *Journal*

of Volcanology and Geothermal Research, 345, 184–199. https://doi.org/10.1016/j.jvolgeores.2017.08.003

Nield, J.M., Chiverrell, R.C., Darby, S.E., Leyland, J., Vircavs, L.H., Jacobs, B., 2013. Complex spatial feedbacks of tephra redistribution, ice melt and surface roughness modulate ablation on tephra covered glaciers. *Earth Surface Processes and Landforms,* 38, 95–102. DOI: 10.1002/esp.3352

Nimis, P., 1999a. Clinopyroxene geobarometry of magmatic rocks. Part 2. Structural geobarometers for basic to acid, tholeiitic and mildly alkaline magmatic systems. *Contributions to Mineralogy and Petrology,* 135, 62–74. DOI: 10.1007/s004100050498

Nimis, P., 1999b. CpxBar Excel version. Available from http://dmp.unipd.it/Nimis/researche.html

Olive, V., Ellam, R.M., Wilson, L., 2001. A protocol for the determination of the rare earth elements at micomole level in rocks by ICP-MS: results on geological reference materials USGS PCC-1 and DTS-1. *Geostandards Newsletter*, 25, 219-228. DOI: 10.1111/j.1751-908x.2001. tb00597.x

Palma, J.L., Blake, S., Calder, E.S., 2011. Constraints on the rates of degassing and convection in basaltic open-vent volcanoes. *Geochemistry, Geophysics and Geosystems,* 12. DOI: 10.1029/2011GC003715

Palma, J.L., Calder, E.S., Basualto, D., Blake, S., Rothery, D.A., 2008. Correlations between SO_2 flux, seismicity, and outgassing activity at the open vent of Villarrica volcano, Chile. *Journal of Geophysical Research: Solid Earth,* 113, 1–23. DOI: 10.1029/2008JB005577

Pansino, S., Taisne, B., 2019. How Magmatic Storage Regions Attract and Repel Propagating Dikes. *Journal of Geophysical Research: Solid Earth,* 124. DOI: 10.1029/2018JB016311

Papike, J.J., Cameron, K.L., Baldwin, K., 1974. Amphiboles and pyroxenes: Characterization of other than quadrilateral components and estimates of ferric iron from microprobe data. *Geological Society of America,* 6, 1053–1054.

Pardo-Casas, F., Molnar, P., 1987. Relative motion of the Nazca (Farallon) and South American plates since Late Cretaceous time. *Tectonics,* 6, 233–248.

Pavez, A., 1997. Geología e historia evolutiva del Complejo Volcánico Quetrupillán, Andes del Sur, 39.5° L.S., in: VIII Congreso Geológico Chileno. 1443–1447.

Pearce, J.A., 1983. Role of the sub-continental lithosphere in magma genesis at active continental margins, in: Hawkesworth, C.J., Norry, M.J. (Eds.), Continental Basalts and Mantle Xenoliths. Shive Publications, 230–249.

Petit-Breuilh, M.E., 2004. La historia eruptiva de los volcanes Hispanoamericanos (Siglos XVI al XX). Cabildo Insular de Lanzarote.

Pike, R.J., Clow, G.D., 1981. Revised classification of terrestrial volcanoes and catalog of topographic dimensions, with new results of edifice volume. *USGS report* 81-1038.

Piochi, M., Mastrolorenzo, G., Pappalardo, L., 2005. Magma ascent and eruptive processes from textural and compositional features of Monte Nuovo pyroclastic products, Campi Flegrei, Italy. *Bulletin of Volcanology,* 67, 663–678. DOI: 10.1007/s00445-005-0410-1

Pioli, L., Scalisi, L., Costantini, L., Di Muro, A., Bonadonna, C., Clavero, J., 2015. Explosive style, magma degassing and evolution in the Chaimilla eruption, Villarrica volcano, Southern Andes. *Bulletin of Volcanology,* DOI: 10.1007/s00445-015-0976-1

Plank, S., Nolde, M., Richter, R., Fischer, C., Martinis, S., Riedlinger, T., Schoepfer, E., Klein, D., 2018. Monitoring of the 2015 Villarrica Volcano Eruption by Means of DLR's Experimental TET-1 Satellite. *Remote Sensing,* 10, 1–17. DOI: 10.3390/rs10091379

Preece, K., Barclay, J., Gertisser, R., Herd, R.A., 2013. Textural and micro-petrological variations in the eruptive products of the 2006 dome-forming eruption of Merapi volcano, Indonesia: Implications for sub-surface processes. *Journal of Volcanology and Geothermal Research,* DOI: 10.1016/j.jvolgeores.2013.02.006

Putirka, K.D., 2008. Thermometers and Barometers for Volcanic Systems. *Reviews in Mineralogy and Geochemistry,* 69, 61–120. DOI: 10.2138/rmg.2008.69.3

Rawson, H., Naranjo, J.A., Smith, V.C., Fontijn, K., Pyle, D.M., Mather, T.A., Moreno, H., 2015. The frequency and magnitude of post-glacial explosive eruptions at Volcán Mocho-Choshuenco, southern Chile. *Journal of Volcanology and Geothermal Research,* 299, 103–129. DOI: 10.1016/j.jvolgeores.2015.04.003

Richardson, J.P., Waite, G.P., Palma, J.L., 2014. Varying seismic-acoustic properties of the fluctuating lava lake at Villarrica Volcano, Chile. *Journal of Geophysical Research: Solid Earth,* 119, 5560–5573. DOI: 10.1002/2014JB011002.

Rickwood, P.C., 1989. Boundary lines within petrologic diagrams which use oxides of major and minor elements. *Lithos*, 22, 247-263. DOI: 10.1016/0024-4937(89)90028-5

Rivera, A., Zamora, R., Uribe, J., Wendt, A., Oberreuter, J., Cisternas, S., Gimeno, F., Clavero, J., 2015. Recent changes in total ice volume on Volcán Villarrica, Southern Chile. *Natural Hazards,* 75, 33–55. DOI: 10.1007/s11069-014-1306-1

Robinson, J.A.C., Wood, B.J., 1998. The depth of the spinel to garnet transition at the peridotite solidus. *Earth and Planetary Science Letters*, 164, 277-284. DOI: 10.1016/S0012-821X(98)00213-1

Robock, A., 2000. Volcanic eruptions and climate. *Reviews of Geophysics,* 38, 191–219. DOI: 10.1029/1998RG000054

Rollinson, H.R., 1993. Using geochemical data: evaluation, presentation, interpretation. Longman Scientific and Technical.

Roman, A., Jaupart, C., 2014. The impact of a volcanic edifice on intrusive and eruptive activity. *Earth and Planetary Science Letters*, 408, 1–8. DOI: 10.1016/j.epsl.2014.09.016

Romero, J.E., Morgavi, D., Arzilli, F., Daga, R., Caselli, A., Reckziegel, F., Viramonte, J., Díaz-Alvarado, J., Polacci, M., Burton, M., Perugini, D., 2016. Eruption dynamics of the 22-23 April 2015 Calbuco Volcano (Southern Chile): Analyses of tephra fall deposits. *Journal of Volcanology and Geothermal Research,* 317, 15–29. DOI: 10.1016/j.jvolgeores.2016.02.027

Romero, J.E., Vera, F., Polacci, M., Morgavi, D., Arzilli, F., Alam, M.A., Bustillos, J.E., Guevara, A., Johnson, J.B., Palma, J.L., Burton, M., Cuenca, E., Keller, W., 2018. Tephra from the 3 March 2015 sustained column related to explosive lava fountain activity at Volcán Villarrica (Chile). *Frontiers in Earth Science,* 6, 1–14. DOI: 10.3389/feart.2018.00098

Rosenau, M., Melnick, D., Echtler, H., 2006. Kinematic constraints on intra-arc shear and strain partitioning in the southern Andes between 38°S and 42°S latitude. *Tectonics,* 25. DOI: 10.1029/2005TC001943

Scasso, R., Corbella, H., Tiberi, P., 1994. Sedimentological analysis of the tephra from the 12-15 August 1991 eruption of Hudson volcano. *Bulletin of Volcanology,* 56, 121–132.

Schindelin, J., Arganda-Carreras, I., Frise, E., Kaynig, V., Longair, M., Pietzsch, T., Preibisch, S., Rueden, C., Saalfeld, S., Schmid, B., Tinevez, J.Y., White, D.J., Hartenstein, V., Eliceiri, K., Tomancak, P., Cardona, A., 2012. Fiji: An open-source platform for biological-image analysis. *Nature Methods,* 9, 676–682. DOI: 10.1038/nmeth.2019

Schneider, C.A., Rasband, W.S., Eliceiri, K.W., 2012. NIH Image to ImageJ: 25 years of image analysis. *Nature Methods,* 9, 671–675. DOI: 10.1038/nmeth.2089

Schonwalder-Angel, D., Cortés, J.A., Calder, E.S., 2018. The interplay of magmatism and tectonics: An example based on the satellite scoria cones at Llaima volcano, Chile. *Journal of Volcanology and Geothermal Research,* 367, 31–45. DOI: 10.1016/j.jvolgeores.2018.10.020

SERNAGEOMIN, 2013. Mapa Preliminar de Peligros del Volcán Quetrupillán. http://sitiohistorico.sernageomin.cl/pdf/rnvv/Quetrupillan.pdf (accessed 06/06/16).

SERNAGEOMIN, 2019. Complejo Volcánico Quetrupillán. https://www.sernageomin.cl/complejo-volcanico-quetrupillan/ (accessed 13/08/19).

Siebert, L., Cottrell, E., Venzke, E., Andrews, B., 2015. Earth's Volcanoes and Their Eruptions: An Overview, in: Sigurdsson, H., Houghton, B., McNutt, S.R., Rymer, H., Stix, J. (Eds), The Encyclopedia of Volcanoes, 2nd Edition, Elsevier Inc. 239–255. DOI: 10.1016/B978-0-12-385938-9.00012-2

Simmons, I.C., McGarvie, D., Cortés, J.A., Calder, E.S., Pavez, A., 2020a. Holocene volcanism at the Quetrupillán Volcanic Complex (39°30' S, 71°43' W), southern Chile. *Volcanica*, 3, 115–137. DOI: 10.30909/vol.03.01.115137

Simmons, I.C., Cortés, J.A., McGarvie, D., Calder, E.S., 2020b. Tectonic constraints on a magmatic plumbing system: The Quetrupillán Volcanic Complex (39°30' S, 71°43' W), Southern Andes, Chile. *Journal of Volcanology and Geothermal Research*, vol. 407. DOI: 10.1016/j. jvolgeores.2020.107101

Sparks, R.S.J., Barclay, J., Calder, E.S., Herd, R.A., Komorowski, J.C., Luckett, R., Norton, G.E., Ritchie, L.J., Voight, B., Woods, A., 2002. Generation of a debris avalanche and violent pyroclastic density current on 26 December (Boxing Day) 1997 at Soufrière Hills Volcano, Montserrat, in: Druitt, T.H., Kokelaar, B.P. (Eds.), The Eruption of Soufrière Hills Volcano, Montserrat, from 1995 to 1999. Geological Society, London, 409–434.

Sparks, R.S.J., Pinkerton, H., Hulme, G., 1976. Classification and formation of lava levees on Mount Etna, Sicily. *Geology,* 4, 269–271. DOI: 10.1130/0091-7613(1976)

Sparks, R.S.J., Wilson, L., Hulme, G., 1978. Theoretical modeling of the generation, movement and emplacement of pyroclastic flows by column collapse. *Journal of Geophysical Research,* 83, 1727-1739.

Spence, R.J.S., Kelman, I., Baxter, P.J., Zuccaro, G., Petrazzuoli, S., 2005. Residential building and occupant vulnerability to tephra fall. *Natural Hazards and Earth System Sciences,* 5, 477–494. DOI: 10.5194/nhess-5-477-2005

Stern, C.R., 1991. Role of subduction erosion in the generation of Andean magmas. *Geology,* 19, 78–81. DOI: 10.1130/0091-7613(1991)

Stern, C.R., 2004. Active Andean volcanism: Its geologic and tectonic setting. *Revista Geológica de Chile,* 31, 161–206. DOI: 10.4067/S0716-02082004000200001

Stern, C.R., Moreno, H., Lopéz-Escobar, L., Clavero, J.E., Lara, L.E., Naranjo, J.A., Parada, M.A., Skewes, M.A., 2007. Chilean Volcanoes, in: Moreno, T., Gibbons, W. (Eds.), The Geology of Chile. Geological Society of London Special Publication, 147–178. DOI: 10.1144/GOCH.5

Sumner, J.M., 1998. Formation of clastogenic lava flows during fissure eruption and scoria cone collapse: The 1986 eruption of Izu-Oshima Volcano, eastern Japan. *Bulletin of Volcanology,* 60, 195–212. DOI: 10.1007/s004450050227

Sun, M., 2001. Geochemical variation among small eruptive centers in the central SVZ of the Andes: an evaluation of subduction, mantle and crustal influences. *Thesis*, Florida International University. DOI: 10.25148/etd.FI15071601

Sun, S.S., McDonough, W.F., 1989. Chemical and isotopic systematics of oceanic basalts: Implications for mantle composition and processes. *Geological Society Special Publications,* 42, 313–345. DOI: 10.1144/GSL.SP.1989.042.01.19

Taddeucci, J., Alatorre-Ibargüengoitia, M.A., Cruz-Vázquez, O., Del Bello, E., Scarlato, P., Ricci, T., 2017. In-flight dynamics of volcanic ballistic projectiles. *Reviews of Geophysics,* 55, 675–718. DOI: 10.1002/2017RG000564

Tanguy, J.C., Ribière, C., Scarth, A., Tjetjep, W.S., 1998. Victims from volcanic eruptions: a revised database. *Bulletin of Volcanology,* 60, 137–144. DOI: 10.1007/s004450050222

Taylor, G.A.M., 1983. The 1951 eruption of Mount Lamington, Papua. *Bureau of Mineral Resources, Geology and Geophysics, Australia*, 129 p.

Thouret, J.C., Ramírez, J.C., Gibert-Malengreau, B., Vargas, C.A., Naranjo, J.L., Vandemeulebrouck, J., Valla, F., Funk, M., 2007. Volcano-glacier interactions on composite cones and lahar generation: Nevado del Ruiz, Colombia, case study. *Annals of Glaciology,* 45, 115–127. DOI: 10.3189/172756407782282589

Tibaldi, A., 1995. Morphology of pyroclastic cones and tectonics. *Journal of Geophysical Research,* 100, 24521–24534. DOI: 10.1029/95JB02250

Tierz, P., Loughlin, S.C., Calder, E.S., 2019. VOLCANS: an objective, structured and reproducible method for identifying sets of analogue volcanoes. *Bulletin of Volcanology,* 81. DOI: 10.1007/s00445-019-1336-3

Toloza, V., 2015. Tefroestratigrafía postglacial del Complejo Volcánico Quetrupillán 39° 30’ S, 71° 43’ O. Regiones de la Araucanía y de Los Ríos, Chile. *Thesis*, Universidad de Concepción.

Tuffen, H., James, M.R., Castro, J.M., Schipper, C.I., 2013. Exceptional mobility of an advancing rhyolitic obsidian flow at Cordon Caulle volcano in Chile. *Nature Communications*. 4. DOI: 10.1038/ncomms3709

Turner, S., George, R., Jerram, D.A., Carpenter, N., Hawkesworth, C., 2003. Case studies of plagioclase growth and residence times in island arc lavas from Tonga and the Lesser Antilles, and a model to reconcile discordant age information. *Earth and Planetary Science Letters,* 214, 279–294. DOI: 10.1016/S0012-821X(03)00376-5

Valdivia Muñoz, P.A., 2016. Estudio Petrológico Y Geoquímico Del Volcán Huililco, IX Región, Chile. *Thesis*, Universidad de Chile.

Valentine, G.A., Connor, C.B., 2015. Basaltic Volcanic Fields, in: Sigurdsson, H., Houghton, B., McNutt, S.R., Rymer, H., Stix, J. (Eds), The Encyclopedia of Volcanoes, 2nd Edition, Elsevier Inc. DOI: 10.1016/B978-0-12-385938-9.00023-7

Valentine, G.A., Gregg, T.K.P., 2008. Continental basaltic volcanoes - Processes and problems. *Journal of Volcanology and Geothermal Research,* DOI: 10.1016/j.jvolgeores.2008.01.050

Valentine, G.A., Shufelt, N.L., Hintz, A.R.L., 2011. Models of maar volcanoes, Lunar Crater (Nevada, USA). *Bulletin of Volcanology,* 73, 753–765. DOI: 10.1007/s00445-011-0451-6

Vera Rivadeneira, F.E., 2018. Origen, transporte y emplazamiento de lahares y avalanchas mixtas generadas en la erupción del 03 de marzo de 2015 en el Volcán Villarrica, regiones de La Araucanía y Los Ríos, Chile. *Thesis*, Universidad de Concepción.

Wehrmann, H., Dzierma, Y., 2011. Applicability of statistical eruption analysis to the geological record of Villarrica and Lanín volcanoes, Southern Volcanic Zone, Chile. *Journal of Volcanology and Geothermal Research,* 200, 99–115. DOI: 10.1016/j.jvolgeores.2010.11.009

Wehrmann, H., Hoernle, K., Jacques, G., Garbe-Schönberg, D., Schumann, K., Mahlke, J., Lara, L. E., 2014. Volatile (sulphur and chlorine), major, and trace element geochemistry of mafic to intermediate tephras from the Chilean Southern Volcanic Zone (33–43°S). *International Journal of Earth Sciences*, 103(7), 1945–1962. DOI: 10.1007/s00531-014-1006-9

Weidmann, C., Spagnotto, S., Giménez, M., Martínez, P., Álvarez, O., Sánchez, M., Lince Klinger, F., 2013. Crustal structure and tectonic setting of the south central Andes from gravimetric analysis. *Geofísica Internacional*, 52, 197–208. DOI: 10.1016/S0016-7169(13)71472-7

Whitty, R.C.W., Ilyinskaya, E., Mason, E., Wieser, P.E., Liu, E.J., Schmidt, A., Roberts, T., Pfeffer, M.A., Brooks, B., Mather, T.A., Edmonds, M., Elias, T., Schneider, D.J., Oppenheimer, C., Dybwad, A., Nadeau, P.A., Kern, C., 2020. Spatial and Temporal Variations in SO_2 and $PM_{2.5}$ Levels Around Kīlauea Volcano, Hawai'i during 2007–2018. *Frontiers in Earth Science,* 8(36). DOI: 10.3389/feart.2020.00036

Wickman, F.E., 1966. Repose-period patterns of volcanoes. *Arkiv för Mineralogi och Geologi,* 4, 291–367.

Wilson, S.A., 1997. The collection, preparation and testing of USGS reference material BCR-2 (Columbia River Basalt). *US Geological Survey Report.*

Wilson, T.M., Stewart, C., Sword-Daniels, V., Leonard, G.S., Johnston, D.M., Cole, J.W., Wardman, J., Wilson, G., Barnard, S.T., 2012. Volcanic ash impacts on critical infrastructure. *Physics and Chemistry of the Earth,* 45–46, 5–23. DOI: 10.1016/j.pce.2011.06.006

Witter, J.B., Kress, V.C., Delmelle, P., Stix, J., 2004. Volatile degassing, petrology, and magma dynamics of the Villarrica Lava Lake, Southern Chile. *Journal of Volcanology and Geothermal Research,* 134, 303–337. DOI: 10.1016/j.jvolgeores.2004.03.002

Wohletz, K.H., Sheridan, M.F., 1983. Hydrovolcanic explosions II. Evolution of basaltic tuff rings and tuff cones. *American Journal of Science,* 283, 385–413. DOI: 10.2475/ajs.283.5.385

Published manuscripts

Evening light

RESEARCH ARTICLE

VOLCANICA

Holocene volcanism at the Quetrupillán Volcanic Complex (39°30' S, 71°43' W), southern Chile

Isla C. Simmons*[α], Dave McGarvie[β], Joaquín A. Cortés[α, γ], Eliza S. Calder[α], Andrés Pavez[δ]

[α] School of GeoSciences, University of Edinburgh, Edinburgh, UK
[β] Lancaster Environment Centre, Lancaster University, Lancaster, UK
[γ] Department of Geography, Edge Hill University, Ormskirk, UK
[δ] GEO-3, Chile

Abstract

This paper provides the first detailed description of Holocene volcanism at the Quetrupillán Volcanic Complex. This volcanic complex consists of a truncated and eroded stratocone plus sixteen well-preserved satellite vents on its lower flanks. Intense scouring of the stratocone's flanks (presumably by ice) has removed much evidence of its Holocene eruptions, and thus the Holocene construction of the stratocone (i.e. number and volume of eruptions) cannot be determined. The sixteen satellite vents are the products of an uncertain number of eruptions, with trachyte comprising ~97% of the lava erupted. Geochemical analysis of tephra layers from three logged sections in nearby valleys provides evidence of three explosive eruptions from Quetrupillán. In these sections, no evidence of pyroclastic density current deposits was identified, which may suggest that explosive volcanic hazards from Quetrupillán are less than indicated on current hazard maps.

Keywords: `Holocene; Volcanism; Chile; Trachyte; Glacier-volcano interactions`

1 Introduction

The Quetrupillán Volcanic Complex (Complejo Volcánico Quetrupillán), henceforth shortened to Quetrupillán, lies in the Southern Volcanic Zone of the Chilean Andes, with the stratocone summit (elevation 2360 m) located at 39°30' S, 71°43' W (Figure 1). Unlike its prominent neighbouring volcanoes, Villarrica and Lanín, Quetrupillán is somewhat hidden from view, and this may explain why there is uncertainty over whether there have been any eruptions from Quetrupillán since the surrounding valleys were first settled by the Spanish in the mid-16th century. For example, Quetrupillán cannot be seen from the main settlements of either Villarrica or Pucón as it is hidden behind Volcán Villarrica. The last eruption from Quetrupillán is suspected to have occurred in 1872 CE [Petit-Breuilh Sepúlveda 2004], but we consider the evidence for this weak, as it lacks corroboration from multiple independent sources.

Past work on Quetrupillán has been sporadic, and a detailed geological map of the volcanic complex has not been published. Consequently, the volcanic stratigraphy is unknown. Only reconnaissance-level mapping has been carried out and results were presented at conferences [Pavez 1997], but not in peer-reviewed journals. Likewise, a study of volcano-ice interactions during the late Pleistocene began in 2012 but has only appeared in conference presentations [e.g. McGarvie 2014]. A study of tephra layers in the nearby Trancura Valley that have been attributed to explosive eruptions at Quetrupillán was the subject of a dissertation [Toloza 2015]. Most recently, Brahm et al. [2018] conducted a study that analysed a limited subset of Holocene trachytic lavas.

The volcanic complex of Quetrupillán consists of a truncated (headless) stratocone, and numerous satellite vents around the lower flanks of the stratocone, particularly on the southern flank (Figure 2). Two areas of distal volcanism are speculated to be satellite vents of Quetrupillán: Huililco, a small basaltic andesite scoria cone ~12 km to the northeast, and Llizan, a cluster of vegetated scoria cones ~14 km to the SSW (Figure 1; Brahm et al. [2018]; Pavez [1997]; Sun [2001]; Valdivia Muñoz [2016]). Given that their relationship to Quetrupillán is currently both uncertain and unproven, we do not consider these further in this paper.

The aims of this study are to: (1) map Holocene volcanism at Quetrupillán, so as to understand the pattern of eruptive activity; (2) analyse lavas and pyroclastics, so as to understand the range of compositions erupted; (3) log pyroclastic deposits in nearby valleys in order to establish the wider distribution and effects of explosive eruptions; and (4) synthesise the information obtained in (1–3) and use this to evaluate hazards from future eruptions of Quetrupillán.

*Corresponding author: isla.simmons@ed.ac.uk

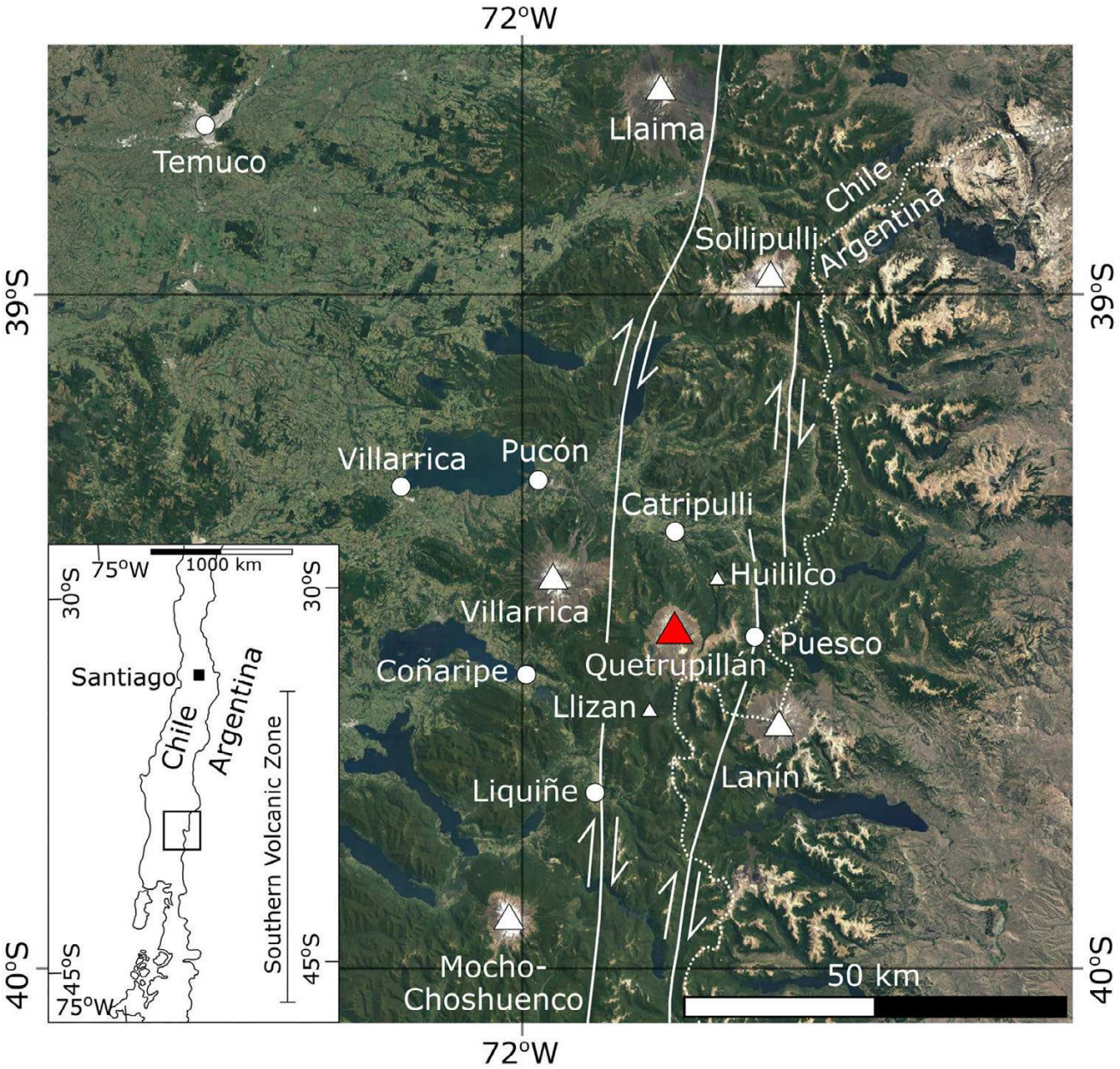

Figure 1: Satellite image of the area surrounding Quetrupillán showing the trace of the Liquiñe-Ofqui Fault Zone faults (solid lines), as mapped by Hernandez-Moreno et al. [2014]. Volcanoes (triangles; Quetrupillán highlighted in red) and settlements (circles; notable towns or those mentioned in this paper) are indicated. Satellite image from Google Earth (downloaded 03/02/2020). Dotted line: international border between Chile and Argentina. The inset shows the location of the region within Chile, and the location of the Southern Volcanic Zone.

2 Regional setting

Along the western edge of South America, the oceanic Nazca Plate is subducting below the continental South American Plate with oblique convergence [Cembrano and Lara 2009; Stern 2004], resulting in the NNE-trending margin-parallel volcanic arc of the Andes. The Southern Volcanic Zone (SVZ) lies between 33°S and 46°S [López-Escobar et al. 1995], where magmatism is controlled primarily by the dehydration of the subducted Nazca Plate and resultant partial melting of the mantle wedge [Cembrano and Lara 2009; Stern 2004; Tatsumi 2005].

The main structural feature of the SVZ is the Liquiñe-Ofqui Fault Zone (LOFZ), a ~1000 km long NNE-trending intra-arc fault system [Cembrano et al. 1996; Hernandez-Moreno et al. 2014] which has been interpreted to act as an active dextral transpressive strike-slip structure for at least the last 6 Ma [Cembrano and Lara 2009]. Quetrupillán sits within the LOFZ (Figure 1), though there is debate on the precise location of the actual LOFZ faults. For example,

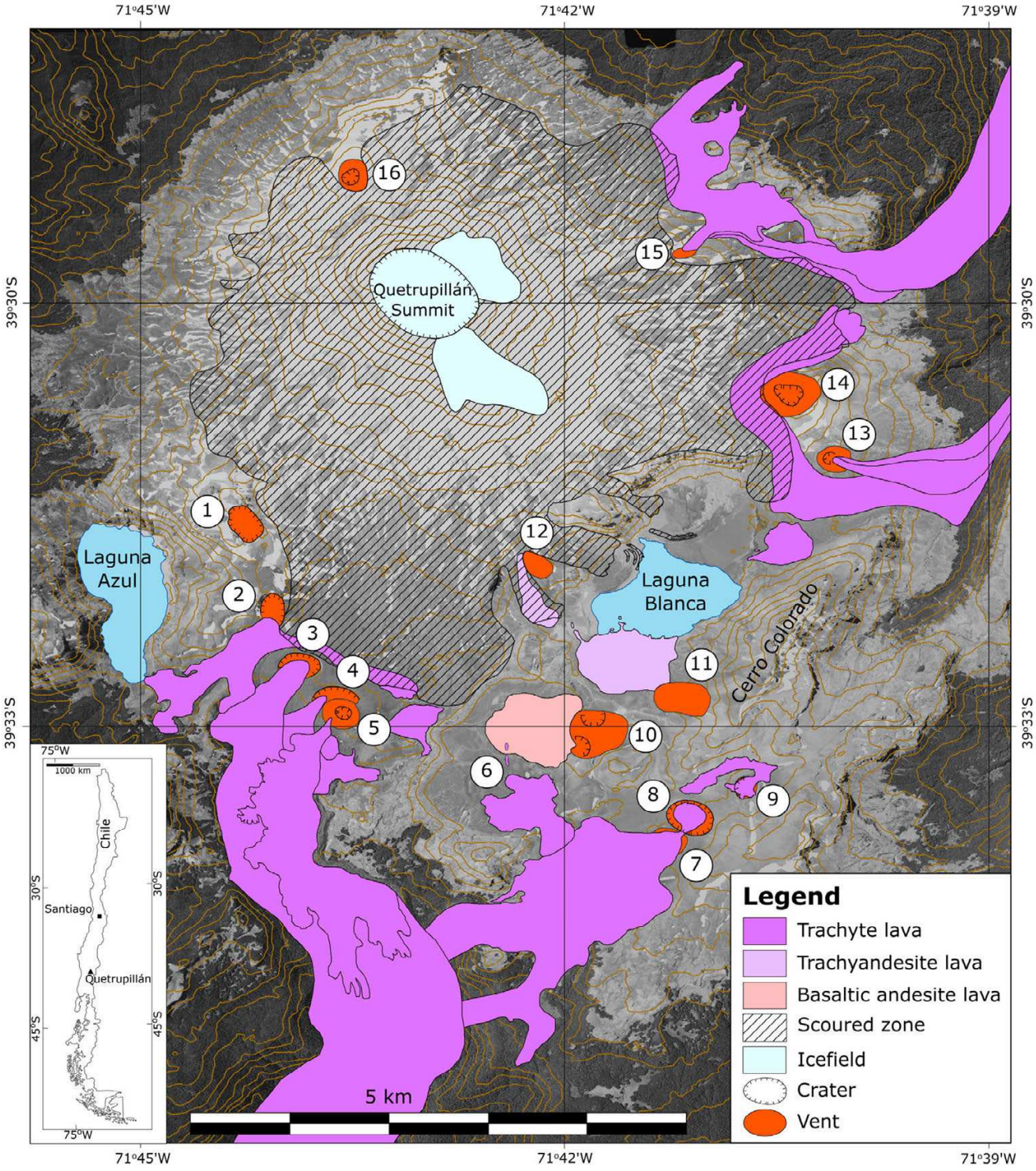

Figure 2: Map of the Holocene geology of Quetrupillán from the satellite flank vents. Satellite vents are labelled with the numbers that they are referred to in the text. The glacially scoured zone is indicated by the area of hatching. The aerial photo background image is from the Servicio Aerofotogramétrico and 50 m interval contours were created from a digital elevation model downloaded from earthexplorer.usgs.gov (downloaded 21/10/2016). The inset shows the location of Quetrupillán in Chile.

Moreno Roa and Lara [2008] map the LOFZ as passing immediately to the west of Quetrupillán, along the Palguin Valley, while Rosenau et al. [2006] map one fault terminating immediately south of Quetrupillán and another along the Trancura Valley to the east. Hernandez-Moreno et al. [2014] map a splay of the LOFZ on either side of Quetrupillán, along the Trancura Valley to the east, and across the eastern flank of

Villarrica to the west. Irrespective of the precise location of LOFZ faults in the area, it is evident that faulting associated with the LOFZ has had a major influence on both the location and triggering of eruptions at Quetrupillán [McGarvie 2014].

Quetrupillán sits within the NW–SE orientated Villarrica-Quetrupillán-Lanín volcanic chain (Figure 1 and Figure 3), a chain of three active volcanoes, that lies oblique to the main volcanic arc of the Andes [Cembrano and Lara 2009; Hickey-Vargas et al. 1989]. Villarrica (39°25' S, 71°56' W), the westernmost volcano, is one of the most active volcanoes in South America [Petit-Breuilh Sepúlveda 2004]. It is an ice-capped, basaltic andesite stratocone with persistent open-vent degassing from the lava lake in its summit crater [Witter et al. 2004]. The easternmost volcano is the basalt-to-dacite stratocone of Lanín (39°38' S, 71°30' W), which has not had any recorded historic eruptions [Lara et al. 2004] and which has a small summit ice cap. Quetrupillán lies between Villarrica and Lanín, and its truncated stratocone contrasts strongly with the conical stratocones of Villarrica and Lanín (Figure 3).

Quetrupillán has been constructed on a basement of Cretaceous and Miocene plutonic units and Triassic to Miocene volcano-sedimentary sequences of the Panguipulli, Curarrehue and Trapatrapa Formations [Moreno Roa et al. 1994]. It has been suggested that Quetrupillán overlies the eroded remnants of the unstudied and undated (Pleistocene?) stratovolcanoes of Quinquilil (also known as "Colmillo del Diablo") and Cordillera El Mocho [Pavez 1997].

3 Methods

Two field seasons were conducted at Quetrupillán, in February 2017 and January 2018. Observations of deposits were made, samples were collected from lava flows and pyroclastic sequences, and field mapping was supplemented with satellite images. In total, 70 samples were collected from lava flows on the flanks of Quetrupillán, and 48 pyroclastic deposits were sampled in the Palguin and Trancura valleys, to the northwest and east of Quetrupillán, respectively.

All further analyses were undertaken at the University of Edinburgh. Polished thin sections of 36 samples of Holocene lavas were cut, and these were analysed under a petrological microscope. Twenty-one thin sections were studied using the scanning electron microscope (SEM) and semi-quantitative analyses were performed using the energy dispersive spectrometer (EDS) included in the instrument [https://www.ed.ac.uk/geosciences/facilities/sem/specification]. Thirteen thin sections were further analysed with the electron microprobe (EMPA) [https://www.ed.ac.uk/geosciences/facilities/electron/instrumentspec].

Fifty-seven samples of Holocene lavas and pyroclastic deposits were selected for X-ray fluorescence (XRF) analysis [https://www.ed.ac.uk/geosciences/facilities/xrayfluorescence/xrf] to determine abundances of major and trace elements. Samples were crushed and then ground to powder using agate grinding jars. Trace element concentrations were measured from pressed powder pellets. Major element concentrations were measured from fused glass discs. To create the discs, powders were heated at 1100 °C for 20 min and the loss on ignition (LOI) of volatiles was recorded (tephra samples were first heated overnight at 450 °C to burn off any organic material). Powders were then mixed with a borate flux and remelted at 1100 °C, before casting on a hotplate.

4 Holocene Volcanism at Quetrupillán

4.1 Introduction

As a volcanic stratigraphy corroborated by absolute age dating has not been established for Quetrupillán, care needs to be taken when assigning volcanic features to a particular epoch. In southern Chile the last glacial period is known as the Llanquihue (29,400–14,550 ^{14}C yr BP; Glasser et al. [2008]), with the last glacial maximum (LGM) occurring 23,000–19,000 cal yr ago, when ice covered the crest of the Andes for ~1800 km [Hulton et al. 2002]. At Quetrupillán, the ice would have been at least 500 m thick, and possibly as thick as 1300 m [Hulton et al. 2002]. Deglaciation started ~17,500–17,150 cal yr ago with abrupt and stepped warming resulting in a dramatic reduction of the ice mass covering the Andes in this part of Chile [Hulton et al. 2002; Moreno et al. 1999]. Glacial retreat was rapid, and within ~2000 years glaciers in this region had receded to within 10 km of their current termini [Lowell et al. 1995].

Given the above, any lava at Quetrupillán that clearly shows the combined evidence of ice confinement and of ice/meltwater-induced cooling fracture systems (characteristic of intermediate-silicic glaciovolcanic eruptions, e.g. McGarvie [2009]) is assumed to have erupted when ice covered the area, and is assigned a Pleistocene age [McGarvie 2014]. In contrast, any lava that demonstrates the typical subaerial characteristics of (unconfined) spreading across the landscape, plus preservation of 'delicate' features (e.g. loose, blocky carapaces), is assigned a Holocene age. This simple two-fold classification scheme has been used at other Chilean volcanoes such as Nevados de Chillán [Dixon et al. 1999], and the nearby volcanoes of Villarrica and Lanín [Lara et al. 2004; Moreno Roa et al. 1994].

One issue with this simple two-fold classification is that local ice masses increased during the Little Ice Age (~14th–19th century; Matthews and Briffa [2005]), and thus Holocene eruptions during this period would have encountered ice and acquired the characteristics

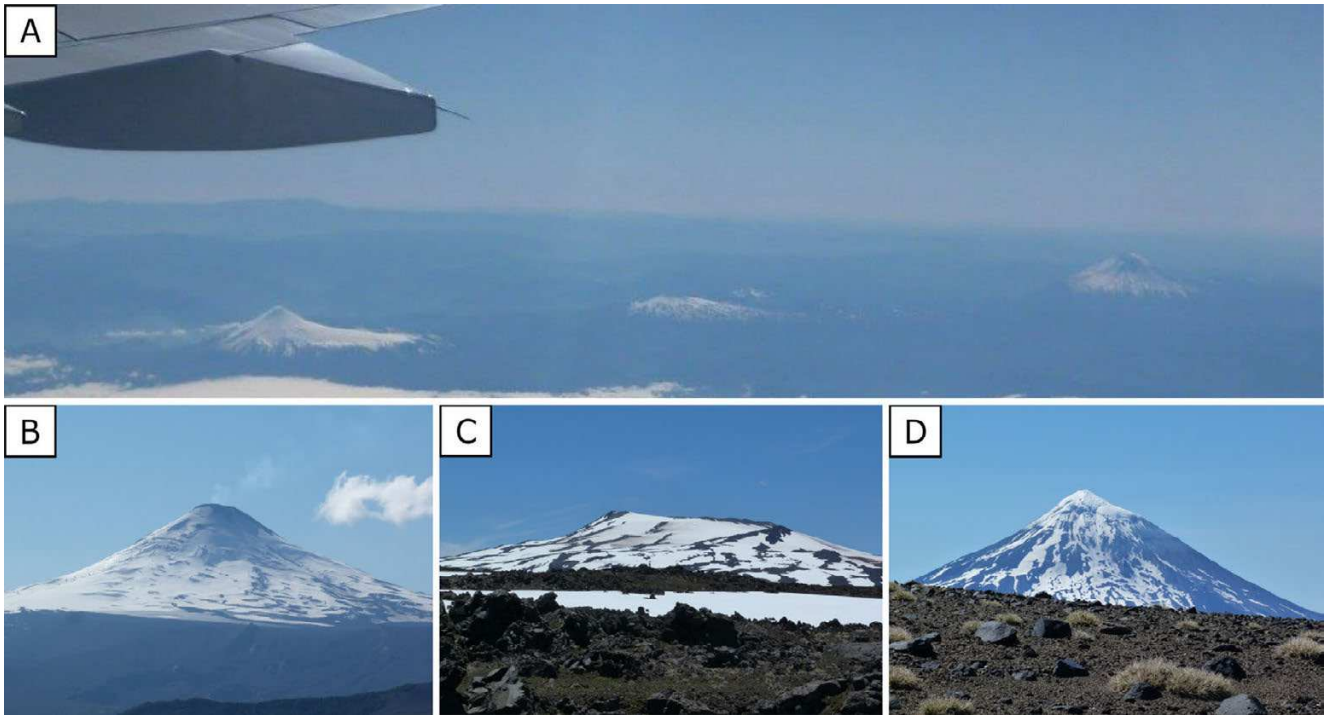

Figure 3: [A] The Villarrica-Quetrupillán-Lanín volcanic chain (looking northeast) with Villarrica [B] to the left, Quetrupillán [C] in the middle and Lanín [D] to the right. The difference in morphology between the conical volcanoes of Villarrica and Lanín and the truncated stratocone of Quetrupillán is clearly visible. The distance between the summits of Villarrica and Lanín is ~45 km.

of glaciovolcanic eruptions. A consequence of this is that lavas may have been assigned a Pleistocene age when in fact they are Holocene, leading to an under-reporting of Holocene erupted volumes. No study that we are aware of has addressed this issue at a Chilean volcano.

At Quetrupillán, we assign a Holocene age to lavas and pyroclastic edifices that have clear and well-preserved subaerial features. An interglacial age is ruled out on the grounds that substantial erosion by the thick ice of the Llanquihue glaciation [Denton et al. 1999; Hulton et al. 2002] would have removed loose material such as scoria and blocky lava carapaces.

4.2 Holocene glacier-volcano interactions

Currently, icefields of unknown thickness occur on the upper parts of the stratocone (Figure 2), with the main ice mass occupying the oval ~1.3 × 1 km summit crater and having an ice surface that dips gently to the south-east. The summit crater has walls of variable height, and at two low points ice has flowed out to form a small (~0.8 × 0.4 km) icefield to the northeast and another to the southeast (~1.4 × 0.7 km).

Surrounding the stratocone and extending some 2–5 km from the summit is a zone that we call the scoured zone (Figure 2), within which all exposed lavas surfaces are smooth and etched with parallel linear scratches and gouges (Figure 4A), and covered by an impersistent blanket of diamict (Figure 4B and 4C). Etching directions can be determined both on a micro scale from scratches on smooth lava surfaces (Figure 4A), and on a macro scale from satellite imagery in which irregular linear channels are eroded into the lava and diamict deposits (Figure 5A). All micro and macro direction indicators are oriented radially to the stratocone summit.

The diamict blanket is a poorly sorted and unconsolidated deposit consisting of sub-rounded to sub-angular lava boulders of varying size, with a smaller sand-silt sized fraction (Figure 4B). The circumference of the scoured zone is often marked by curved ridges of boulders that form distinct topographic highs (Figure 5B). These are typically ~2 metres high but occasionally reach up to 4 metres in height. Our interpretation of these features is that the scoured zone is the product of glacial processes, with the scratches and gouges being glacial striations produced during ice advance, and the diamict representing glacial till deposition during ice retreat. The ridges of boulders around the circumference are terminal moraines that represent the farthest extent of ice advance.

We rule out the Llanquihue glaciation as being the cause of this scoured zone. During the Llanquihue glaciation, thick (>500 m) ice extended for many tens of km on either side of the Andean chain [Hulton et al. 2002], whereas this scoured zone is a local feature, extending 2–5 km from the summit of Quetrupil-

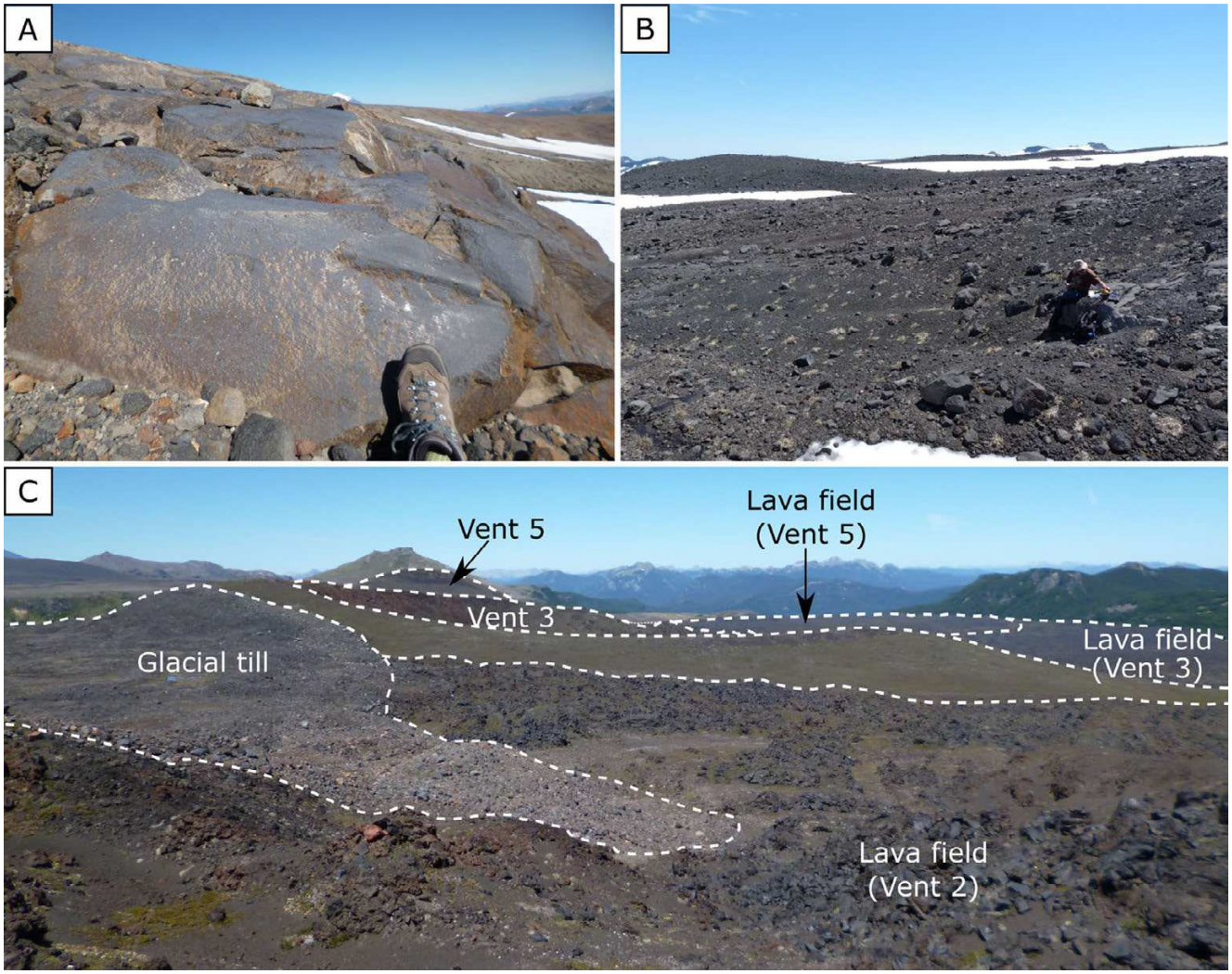

Figure 4: [A] A scoured Holocene lava from the upper flanks. Striations are faintly visible above the boot, striking in a downhill (240°) direction (looking southeast). [B] Diamict, composed of lava boulders of varying size and fine-grained silt, covers most of the upper flanks of Quetrupillán within the scoured zone, obscuring all underlying lava fields (looking west). [C] Glacial till covers the lava field of Vent 2 and the tuff ring of Vent 3 (looking southeast). The field of view is ~200 m wide.

lán. Also, well-preserved subaerial lavas of nominally Holocene age (see above) exposed below the terminus of the scoured zone can be traced upslope into the scoured zone, where they have been scraped and/or covered in diamict. We conclude that as what are clearly Holocene lavas have been eroded within the scoured zone, it must be a Holocene feature.

An important implication of the Holocene glacial erosion of the stratocone is that crucial evidence related to the growth and construction of the stratocone has been removed, such as the locations, numbers, and volumes of stratocone eruptions. Consequently, the total volume of well-preserved Holocene lava (~225 × 10^6 m^3; see Subsection *4.4.1*) that lies outside of the scoured zone is therefore a minimum estimate.

No Holocene lavas with well-preserved blocky carapaces were found within the scoured zone. This means the most recent lava erupted from the stratocone has been eroded, and thus must be older than the latest ice advance and retreat. In their study of Nevados de Chillán, Dixon et al. [1999] suggest that young small-scale moraines on Nevados de Chillán may have been formed during late Holocene re-advances such as the Little Ice Age (LIA), which ended at the end of the 19th century [Matthews and Briffa 2005]. From radiocarbon dates, dendrochronological data, and pollen analyses, glacial advances throughout South America are known to have occurred from the 15th to late 19th centuries [Clapperton and Sugden 1988]. Patagonian glaciers reached their maximum limits at various stages throughout the 17th, 18th, and 19th centuries [Mercer 1965], and glaciers in the Andes began to recede within the last two decades of the 19th century [Clapperton 1983].

Given evidence of local ice advances across the An-

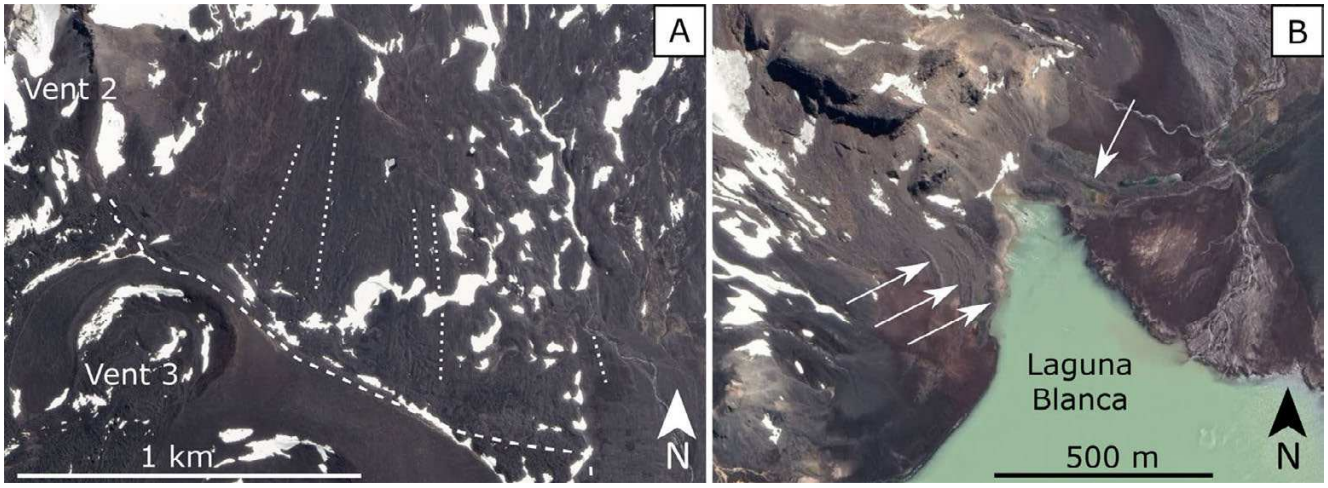

Figure 5: [A] Linear channels are visible in the diamict in satellite images, oriented radially from the summit. The dotted lines highlight some that are visible to the north of Vent 3. The dashed line represents the edge of the moraine. Satellite image from Google Earth (downloaded 09/10/2019). [B] Distinctive curving ridges of glacial deposits are visible in satellite images at the edge of the scoured zone on the shores of Laguna Blanca, highlighted by arrows. Satellite image from Google Earth (downloaded 07/10/2019).

des during the LIA, it is highly likely that glacial advances at Quetrupillán also occurred, with the last one being towards the end of the 19th century. Scouring of the stratocone by ice is likely to have occurred during each period of glacial advance and retreat throughout the LIA. The presence of a clear terminal moraine at the outer limit of the scoured zone, coupled with a lack of terminal moraines within the scoured zone, implies that the most recent glacial advance at Quetrupillán (in the late 19th century) was also the largest and most extensive. As the terminal moraine overlies the youngest erupted lavas on the lower flanks of the stratocone (Figure 4C), this implies that there have been no effusive eruptions within the scoured zone since the major 19th century glacial advance.

The scoured zone of Quetrupillán (2360 m) is unusual, as scrutiny of satellite images suggests that there is no equivalent scoured zone at the nearby volcanoes of either Villarrica or Lanín. Villarrica (2847 m) currently has a much greater ice mass occupying its upper flanks than Quetrupillán, which would have been larger still during the LIA. Although Lanín (3747 m) currently has only a small summit ice cap, its summit lies at a much higher elevation than Quetrupillán, and so during the LIA it is likely that the summit ice mass would have increased and spread substantially.

Temperature fluctuations in the LIA will have resulted in similar and multiple episodes of ice accumulation (in summit regions) followed by ice advance (to lower elevations) at the ice-capped volcanoes of the Villarrica-Quetrupillán-Lanín chain. However, while Quetrupillán was extensively scoured by these LIA ice advances, the same process has not obviously occurred at either Villarrica or Lanín, even though their higher elevations would have led to accumulation of larger ice masses, with the potential to form extensive scoured zones on their stratocone flanks.

The process(es) that formed the scoured zone at Quetrupillán is (are) not known, and require further investigation. It is possible that the location and/or specific glacier-volcano architecture of Quetrupillán resulted in it having a higher sensitivity to LIA conditions, and resulted in the more extensive ice advances and retreats which produced Quetrupillan's well-defined scoured zone, a feature that both Villarrica and Lanín apparently lack.

4.3 Geochemistry and mineralogy

Holocene lavas and eruptive products range in composition from basaltic andesite to trachyte (from 55 wt. % SiO_2 to 66 wt. % SiO_2; Figure 6A; Table 1), with most satellite vents having erupted trachytic magma (64–66 wt. % SiO_2; 7–8 wt. % Na_2O+K_2O). Note that the "T" field on the Total Alkali Silica plot (Figure 6A) includes both trachytes and trachydacites, but following the criteria in Le Maitre et al. [2002] for distinguishing between them, the Quetrupillán rocks in the "T" field are all trachytes. The sampled Holocene lavas erupted from the summit crater also vary in composition from basaltic andesite to trachyte (56–64 wt. % SiO_2).

Trachyte lavas contain phenocrysts and glomerocrysts of pyroxene (augite and enstatite, with minor pigeonite in some samples; Figure 6B), plagioclase (oligoclase to bytownite; Figure 6C), and magnetite and/or ilmenite within glassy groundmass that contains microlites of the same minerals (Figure 7). The trachyandesite and basaltic andesite samples contain phenocrysts and glomerocrysts of pyroxene (augite and enstatite; Figure 6B), plagioclase (andesine to bytownite;

Table 1 – XRF results of samples. Some trace elements were not determined (n.d.) or below detection limit (b.d.l.). Samples were collected from Quetrupillán (Quet), the Trancura Valley (Tran) or the Palguin Valley (Pal).

Location	Vent	Sample type	Sample	Major elements											
				SiO_2	TiO_2	Al_2O_3	Fe_2O_3T	MnO	MgO	CaO	Na_2O	K_2O	P_2O_5	LOI	Total
Quet	1	Lava	Q61	63.92	1.07	15.25	5.42	0.13	1.18	3.18	4.68	2.96	0.33	0.19	98.31
Quet	2	Lava	Q3	64.96	1.11	15.36	5.54	0.13	1.21	3.11	4.85	3.05	0.33	0.20	99.84
Quet	2	Lava	Q53	64.97	1.10	15.63	5.45	0.12	1.18	3.09	4.83	2.96	0.32	0.19	99.84
Quet	3	Lava	Q7	65.03	1.12	15.35	5.56	0.13	1.18	3.12	4.75	3.05	0.32	0.34	99.94
Quet	4	Lava	Q10	64.89	1.11	15.50	5.59	0.13	1.23	3.25	4.77	2.94	0.32	0.03	99.77
Quet	4?	Lava	Q54	64.92	1.08	15.37	5.43	0.13	1.19	3.16	4.90	3.03	0.33	−0.03	99.50
Quet	5	Lava	Q12	64.74	1.15	15.48	5.72	0.13	1.23	3.26	4.83	2.99	0.34	0.11	99.98
Quet	5	Lava	Q56	64.78	1.11	15.36	5.57	0.13	1.20	3.21	4.72	2.96	0.33	0.19	99.55
Quet	6	Lava	Q48	64.24	1.11	15.37	5.59	0.13	1.25	3.30	4.82	2.95	0.35	0.03	99.13
Quet	6	Enclave	Q46	61.56	0.72	16.07	5.97	0.12	3.77	5.49	4.03	2.17	0.17	0.20	100.27
Quet	7	Lava	Q41	64.38	1.10	15.43	5.56	0.13	1.24	3.28	4.74	2.95	0.35	0.03	99.19
Quet	7	Lava	Q43	64.91	1.11	15.46	5.56	0.13	1.18	3.16	4.81	2.97	0.33	0.11	99.71
Quet	8	Lava	Q40	64.49	1.11	15.42	5.52	0.13	1.23	3.25	4.76	2.97	0.35	0.15	99.37
Quet	9	Lava	Q39	65.13	1.08	15.34	5.40	0.12	1.16	3.06	4.82	3.07	0.33	0.03	99.54
Quet	10	Lava	Q50	54.84	1.04	16.23	8.80	0.14	6.50	7.67	3.22	1.48	0.28	−0.21	100.00
Quet	11	Lava	Q8	58.66	1.36	16.17	8.16	0.13	2.89	5.88	3.92	2.34	0.36	−0.02	99.84
Quet	12	Lava	Q17	57.64	1.19	16.51	7.85	0.13	3.63	6.05	3.82	2.20	0.34	0.28	99.63
Quet	13	Lava	Q31	64.52	1.09	15.43	5.59	0.12	1.21	3.15	4.75	3.02	0.29	0.46	99.64
Quet	13	Lava	Q34	64.89	1.08	15.53	5.57	0.13	1.19	3.16	4.82	3.05	0.32	0.22	99.95
Quet	14	Lava	Q29	63.06	1.12	15.46	5.85	0.12	1.35	3.29	4.36	2.77	0.30	1.93	99.63
Quet	14	Lava	Q36	64.05	1.08	15.16	6.61	0.23	1.16	3.06	4.74	3.05	0.31	0.35	99.80
Quet	14	Lava	Q65	64.59	1.05	15.01	5.40	0.12	1.13	2.85	4.66	3.02	0.22	0.41	98.45
Quet	15	Lava	Q69	65.02	1.08	15.22	5.36	0.13	1.14	2.96	4.79	3.07	0.32	0.19	99.28
Quet	Summit	Lava	Q16	55.32	1.07	16.85	8.42	0.14	5.50	7.62	3.17	1.45	0.29	0.08	99.91
Quet	Summit	Lava	Q20	61.06	1.18	16.07	6.77	0.11	2.26	4.62	4.23	2.75	0.35	0.11	99.52
Quet	Summit	Lava	Q23	57.20	1.00	16.65	7.84	0.13	5.14	6.97	3.32	1.80	0.26	0.02	100.34
Quet	Summit	Lava	Q60	58.25	1.17	16.08	7.64	0.13	3.49	5.96	3.80	2.31	0.35	−0.14	99.04
Quet	Summit	Lava	Q62	63.56	1.24	14.97	6.39	0.13	1.39	3.48	4.51	3.16	0.43	−0.06	99.19
Quet	Summit	Lava	Q63	55.37	1.06	16.03	8.01	0.14	5.12	6.94	3.32	1.74	0.28	−0.04	97.96
Tran		Tephra	T1	64.10	1.08	15.70	5.50	0.12	1.09	3.03	4.70	3.02	0.32	1.22	99.88
Tran		Tephra	T2	53.14	1.27	17.76	10.63	0.17	3.44	7.00	3.06	0.73	0.23	2.43	99.86
Tran		Tephra	T5	64.42	1.13	16.01	5.63	0.13	1.21	3.16	4.47	3.02	0.33	0.40	99.91
Tran		Tephra	T6	50.32	1.24	19.16	9.98	0.17	5.76	8.54	2.57	0.88	0.40	0.60	99.62
Tran		Tephra	T7	52.09	1.34	20.37	10.98	0.19	3.37	6.57	2.47	0.67	0.33	1.37	99.75
Tran		Tephra	T8	53.85	1.20	18.17	9.79	0.15	4.06	8.33	2.86	0.75	0.22	0.22	99.60
Tran		Tephra	T9	53.40	1.31	18.75	10.84	0.17	3.65	6.97	2.69	0.73	0.23	1.09	99.83
Tran		Tephra	T10	64.31	1.14	15.84	5.72	0.13	1.53	3.20	4.50	2.86	0.31	0.31	99.86
Tran		Tephra	T12	53.38	1.37	19.58	10.20	0.18	2.72	5.44	2.72	1.20	0.28	2.64	99.71
Tran		Tephra	T13	59.30	1.51	17.46	7.97	0.13	1.56	3.60	3.80	2.63	0.45	1.38	99.79
Tran		Tephra	T14	53.39	1.42	19.46	10.38	0.15	2.74	4.79	2.35	1.18	0.29	3.54	99.71
Tran		Tephra	T15	52.46	1.19	18.20	10.43	0.17	4.74	7.82	2.54	0.68	0.20	1.26	99.69
Tran		Tephra	T16	52.62	1.34	20.32	10.40	0.21	2.72	4.74	2.82	1.08	0.26	3.46	99.96
Pal		Tephra	P13	61.76	0.71	18.75	4.33	0.13	0.80	2.57	4.19	1.67	0.17	4.76	99.85
Pal		Tephra	P17	49.91	0.97	19.77	9.70	0.13	4.81	8.28	2.29	0.44	0.29	3.07	99.66
Pal		Tephra	P21	50.51	0.94	19.43	8.84	0.14	5.88	9.68	2.43	0.54	0.16	1.07	99.63
Pal		Tephra	P23	51.95	1.06	20.86	8.04	0.17	3.16	5.21	2.93	0.82	0.20	5.60	99.98
Pal		Tephra	P24	43.79	1.86	22.32	13.68	0.15	2.66	5.31	1.89	0.27	0.35	7.58	99.85

Continued on next page.

Table 1: [cont.] – XRF results of samples.

Location	Sample	Detection limit	Trace elements																
		Ba	Th	U	Pb	Nb	Sr	Zr	Y	La	Ce	Nd	Zn	Cu	Ni	Cr	V	Sc	Rb
		3.7	0.4	0.4	0.4	0.1	0.3	0.3	0.2	1.6	2.1	1.4	0.7	0.7	1.0	1.2	2.2	1.0	0.2
Quet	Q61	751.6	n.d	n.d	n.d	14.2	313.3	327.0	43.3	31.4	74.1	41.4	73.2	31.4	2.5	2.6	63.7	15.5	78.6
Quet	Q3	737.8	10.1	2.8	22.7	14.1	284.3	352.2	44.4	32.5	79.2	38.8	71.2	14.5	b.d.l.	4.0	63.7	16.6	77.8
Quet	Q53	710.4	10.3	3.4	21.5	13.3	294.3	337.6	44.5	33.6	81.2	40.9	68.6	13.8	b.d.l.	2.8	63.3	16.0	75.8
Quet	Q7	733.8	10.2	2.7	22.3	13.6	285.5	345.4	43.9	31.7	79.3	38.5	70.3	14.2	b.d.l.	3.0	63.4	17.1	77.1
Quet	Q10	701.8	10.3	3.2	21.8	12.9	292.9	328.0	43.2	32.4	81.2	39.5	70.1	15.3	b.d.l.	3.2	64.8	17.0	74.1
Quet	Q54	754.0	n.d	n.d	n.d	14.5	307.3	331.0	43.6	31.6	74.9	42.2	72.9	15.1	0.5	2.4	64.2	16.2	79.3
Quet	Q12	730.0	10.0	2.6	22.3	13.5	299.6	339.5	43.8	32.3	79.7	38.1	72.5	15.2	b.d.l.	3.5	66.3	17.2	75.4
Quet	Q56	696.4	10.3	3.1	21.8	13.0	296.4	332.7	44.4	34.9	82.7	39.6	69.4	15.2	b.d.l.	3.3	63.0	17.5	n.d
Quet	Q48	744.4	n.d	n.d	n.d	14.2	320.0	322.0	43.4	31.8	74.8	42.5	75.5	15.9	0.2	1.7	70.4	18.1	76.9
Quet	Q46	580.9	n.d	n.d	n.d	8.0	467.5	222.1	28.9	21.1	46.0	24.5	51.5	29.2	30.9	88.1	103.5	15.7	54.5
Quet	Q41	741.0	n.d	n.d	n.d	14.1	320.3	323.9	43.5	30.0	75.0	40.9	71.7	16.5	0.8	1.4	67.6	17.3	77.8
Quet	Q43	697.6	10.3	3.3	21.2	13.2	294.1	337.9	44.4	31.0	81.7	39.7	68.1	13.7	b.d.l.	2.7	62.6	17.8	76.2
Quet	Q40	739.2	n.d	n.d	n.d	14.4	317.0	325.1	43.6	30.9	74.8	40.9	72.2	15.1	0.1	b.d.l.	65.6	16.5	77.8
Quet	Q39	755.3	n.d	n.d	n.d	14.6	299.9	334.7	44.0	30.8	75.4	41.3	70.5	14.1	b.d.l.	b.d.l.	60.6	15.9	80.6
Quet	Q50	402.5	n.d	n.d	n.d	7.4	442.4	177.3	27.8	17.1	41.4	22.6	74.4	56.7	78.3	179.8	210.5	27.3	37.4
Quet	Q8	583.2	8.5	1.6	19.2	10.9	371.8	270.6	36.9	22.5	64.5	32.2	76.1	59.9	18.6	28.2	228.8	24.3	60.3
Quet	Q17	545.1	8.0	2.2	18.6	10.5	389.0	258.1	34.2	23.3	61.1	30.6	73.0	65.5	35.0	78.6	186.1	24.9	56.9
Quet	Q31	731.6	10.4	2.6	23.3	13.6	287.3	346.1	42.3	31.6	77.6	36.3	68.7	18.0	0.4	2.7	70.3	16.4	78.2
Quet	Q34	737.7	10.0	3.2	22.5	13.4	286.2	347.7	43.4	31.4	78.3	38.3	68.3	18.7	b.d.l.	3.5	67.3	16.8	78.4
Quet	Q29	691.8	9.4	2.4	28.9	12.7	288.2	326.0	39.0	29.2	72.4	35.3	72.3	23.1	1.9	9.6	86.0	18.4	70.7
Quet	Q36	736.3	10.1	2.9	21.4	13.7	280.2	349.0	43.5	31.9	78.6	38.3	66.9	13.4	b.d.l.	3.4	67.4	16.0	78.8
Quet	Q65	752.2	n.d	n.d	n.d	14.3	289.6	335.4	40.4	28.3	70.0	36.9	70.8	19.5	0.5	3.2	64.9	15.5	80.4
Quet	Q69	756.7	n.d	n.d	n.d	14.8	294.7	336.6	43.8	31.5	75.5	40.1	70.0	15.0	b.d.l.	2.8	56.9	16.5	80.6
Quet	Q16	403.1	3.8	2.4	10.0	7.1	471.2	166.6	25.8	14.7	45.1	23.7	70.5	51.8	62.5	152.2	191.8	24.8	34.7
Quet	Q20	648.9	9.3	2.8	20.9	12.0	324.6	314.5	39.3	27.5	70.7	35.8	68.6	39.8	12.8	21.2	156.6	19.3	71.4
Quet	Q23	440.9	6.7	2.6	12.9	8.0	410.2	202.4	28.5	19.1	53.0	24.7	64.2	46.5	49.5	141.2	170.9	23.3	45.3
Quet	Q60	581.1	n.d	n.d	n.d	11.3	402.8	260.8	35.6	24.3	57.1	33.4	69.9	46.3	27.8	59.9	172.6	22.4	62.3
Quet	Q62	748.9	n.d	n.d	n.d	15.3	290.9	352.4	47.1	32.1	79.1	44.4	75.9	21.0	1.3	3.1	95.7	18.9	84.7
Quet	Q63	467.7	n.d	n.d	n.d	8.5	416.7	204.1	30.4	19.6	45.2	24.6	68.7	44.1	66.2	154.9	192.8	24.7	45.3
Tran	T1	728.1	10.8	2.8	22.5	13.9	271.1	359.4	44.8	32.5	81.1	40.3	69.9	16.7	b.d.l.	3.8	69.3	16.8	77.1
Tran	T2	237.6	2.4	b.d.l.	9.8	2.9	362.6	115.4	27.5	6.3	24.8	17.4	99.0	108.1	15.2	39.2	332.9	37.8	17.7
Tran	T5	721.8	10.7	3.8	22.7	13.5	274.5	355.3	44.9	34.0	83.9	41.9	68.5	18.3	1.4	2.0	78.1	16.6	73.9
Tran	T6	304.9	2.5	1.6	8.1	7.1	496.4	134.5	23.7	15.2	44.9	22.7	76.9	70.0	65.1	177.7	265.0	36.5	18.2
Tran	T7	262.6	2.2	1.2	9.3	3.6	326.0	109.4	25.8	10.0	34.2	19.8	96.5	97.2	24.6	68.0	297.3	38.2	13.9
Tran	T8	247.7	2.1	1.9	8.2	2.4	413.1	101.9	25.9	6.0	24.6	17.1	97.0	105.7	29.9	53.3	312.7	34.8	17.3
Tran	T9	301.2	1.0	1.6	9.4	2.6	353.6	115.4	28.8	8.7	26.1	17.5	111.0	120.7	28.0	43.9	334.7	37.7	17.2
Tran	T10	695.0	9.8	3.6	22.8	12.8	304.2	329.6	42.4	32.9	75.3	39.0	72.8	12.6	3.4	10.1	70.8	18.4	68.8
Tran	T12	447.4	7.5	2.6	15.8	7.0	410.2	185.4	43.5	27.7	55.0	37.1	92.4	114.3	16.4	55.3	259.3	36.5	25.7
Tran	T13	640.6	12.3	3.4	28.0	14.8	259.2	387.1	47.2	37.6	85.9	46.3	76.0	33.7	4.0	3.7	154.3	24.6	62.8
Tran	T14	423.7	7.6	2.2	19.7	7.3	286.5	212.8	37.1	21.9	57.5	31.6	94.5	82.0	22.6	67.0	283.4	36.6	25.8
Tran	T15	223.5	0.7	1.5	8.6	2.4	345.7	106.9	26.2	6.5	25.7	17.1	94.6	93.7	41.0	94.6	312.7	40.8	15.3
Tran	T16	346.2	5.8	1.6	15.4	6.2	310.3	182.2	40.5	20.8	54.5	33.6	92.4	127.9	27.2	81.2	234.5	37.3	23.2
Pal	P13	735.0	6.1	2.3	18.9	7.0	372.0	244.8	46.1	21.4	60.2	34.0	89.5	10.3	5.3	5.3	44.1	19.1	40.7
Pal	P17	206.6	b.d.l.	1.3	7.7	2.3	410.4	51.8	21.0	3.3	22.3	13.8	66.1	94.2	53.4	150.7	281.1	50.2	9.8
Pal	P21	226.8	3.0	1.9	9.5	1.7	586.2	22.3	18.1	2.8	21.6	13.6	70.1	117.3	81.3	188.3	291.7	41.2	10.9
Pal	P23	354.1	5.1	2.0	17.4	5.0	381.5	116.1	36.8	15.5	46.7	27.6	77.8	101.4	38.4	82.7	201.7	37.8	18.9
Pal	P24	209.6	3.0	1.4	12.2	3.4	411.9	87.3	34.5	8.5	38.0	26.7	63.9	146.8	35.3	68.5	467.8	64.6	5.3

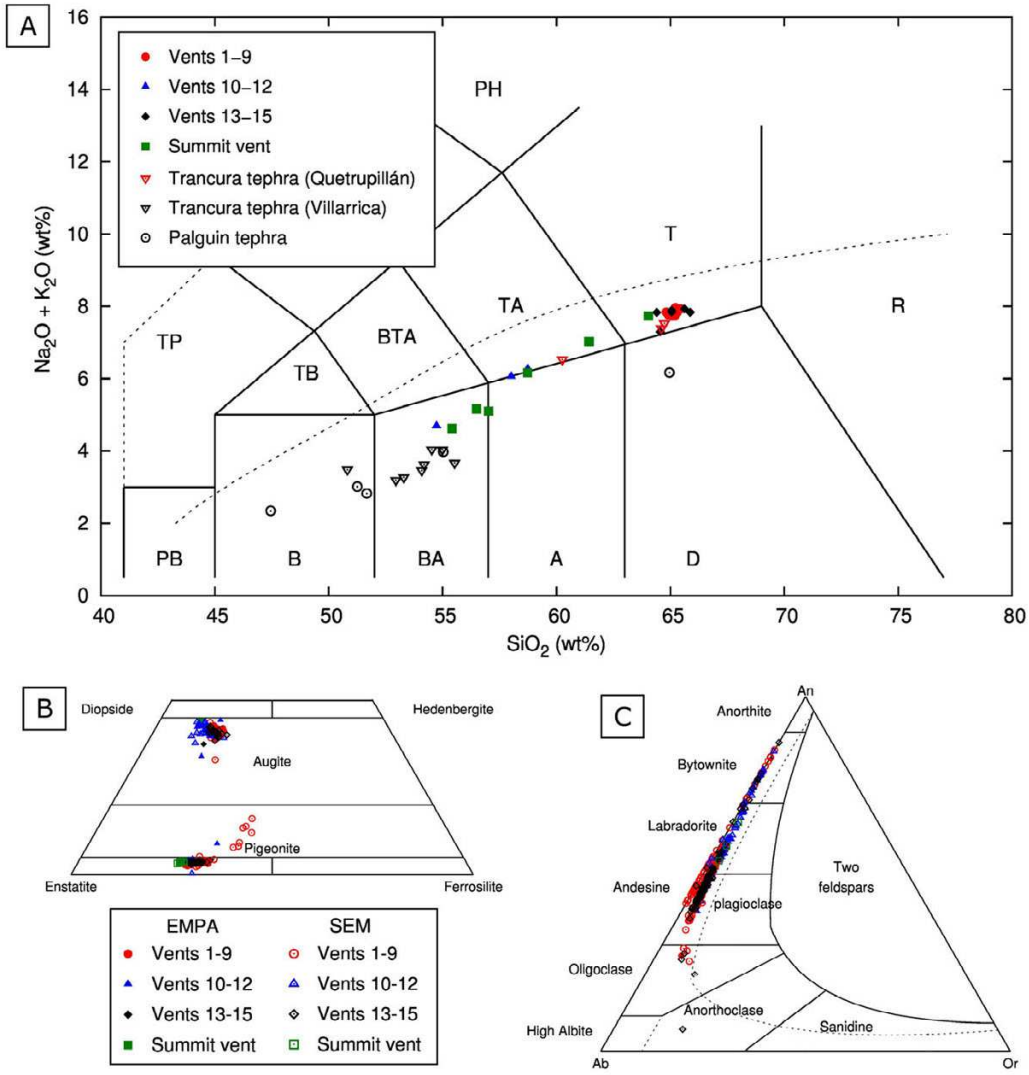

Figure 6: Geochemical diagrams of lavas from Quetrupillán. [A] Total alkali silica plot (including tephra deposits in the Trancura and Palguin Valleys). [B] Pyroxene compositions. [C] Feldspar compositions. Samples are grouped according to their source vent: red circles – Vents 1–9; blue triangles – Vents 10–12; black diamonds – Vents 13–15; green squares – summit vent; inverted red triangle – Quetrupillán Trancura tephra; inverted black triangle – Villarrica Trancura tephra; open black circle – Palguin tephra. In diagrams [B] and [C] filled symbols represent data collected by EMPA and open symbols represent data from the SEM.

Figure 6C), olivine with resorbed rims, and magnetite (Figure 7). Groundmass glass and melt inclusions have compositions that range from basalt to high-silica trachyte and rhyolite. Lavas contain two populations of plagioclase phenocrysts, a pristine euhedral population and a population with resorbed rims, sieve-textured interior, and composition that varies from rim to core.

Tephra deposits preserved in valleys surrounding Quetrupillán were analysed by XRF in order to determine their provenance (Table 1). Trace element abundances were compared with the characteristic elemental abundances from Quetrupillán, Villarrica, and Lanín (Figure 8; this work and other sources, see Supplementary Material for references). Tephra produced by Quetrupillán has compositions of trachyte and trachyandesite (Figure 6A).

4.4 Satellite vents and lavas

The most obvious and best-preserved products of Holocene volcanism at Quetrupillán are the sixteen exposed vents and their associated lavas that lie around the lower flanks of the stratocone (labelled in Figure 2). Twelve of these sixteen vents lie in a volcanic field that is located 3–7 km south of the stratocone summit. In this southern volcanic field, the volumetrically dominant erupted composition is trachyte (Table 2), with just one eruption of basaltic andesite and two eruptions of trachyandesite. The three vents on the eastern flanks of Quetrupillán (Vents 13, 14, and 15) have erupted

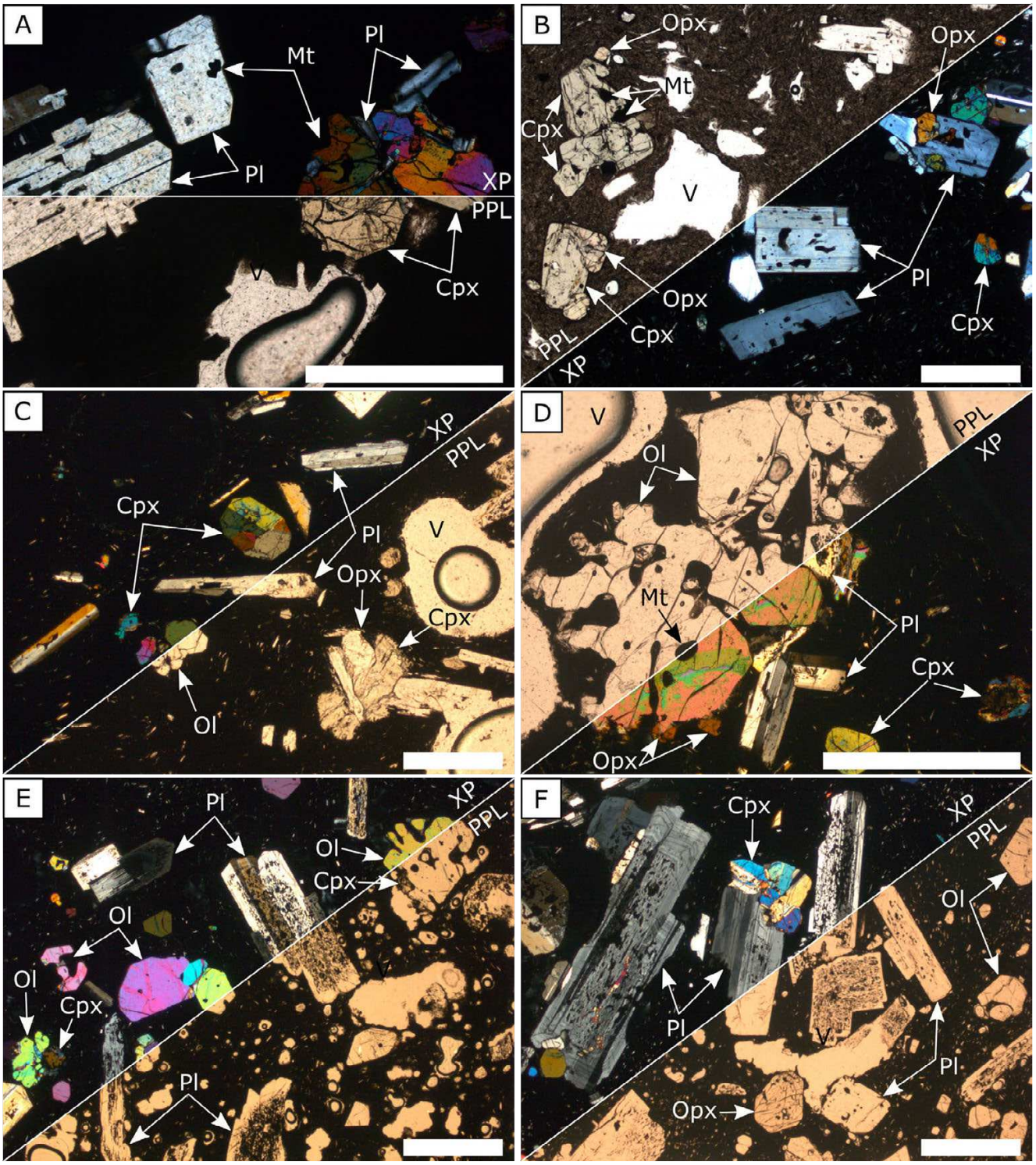

Figure 7: Thin section images of lavas from satellite vents at Quetrupillán, of trachyte ([A] and [B]), trachyandesite ([C] and [D]) and basaltic andesite ([E] and [F]) composition. Pl – plagioclase, Cpx – clinopyroxene, Opx – orthopyroxene, Ol – olivine, Mt – magnetite, V – vesicle. Scale bar in each image is 1 mm. Images show thin sections under plane polarised light (PPL) and under crossed polars (XP).

trachyte and have produced two sizeable scoria cones, along with a number of trachytic lavas that have flowed east until they met a ~250 m high (fault) scarp and were channelled northwards along the Huililco Valley, against the lower edge of the scarp. Vent 16 is evident on aerial imagery but was not visited during fieldwork and so its composition is unknown.

Most of the vents that lie within the southern volcanic field lie along two lineaments. Vents 1 to 5 (labelled in Figure 2) lie along a 2.7 km long lineament

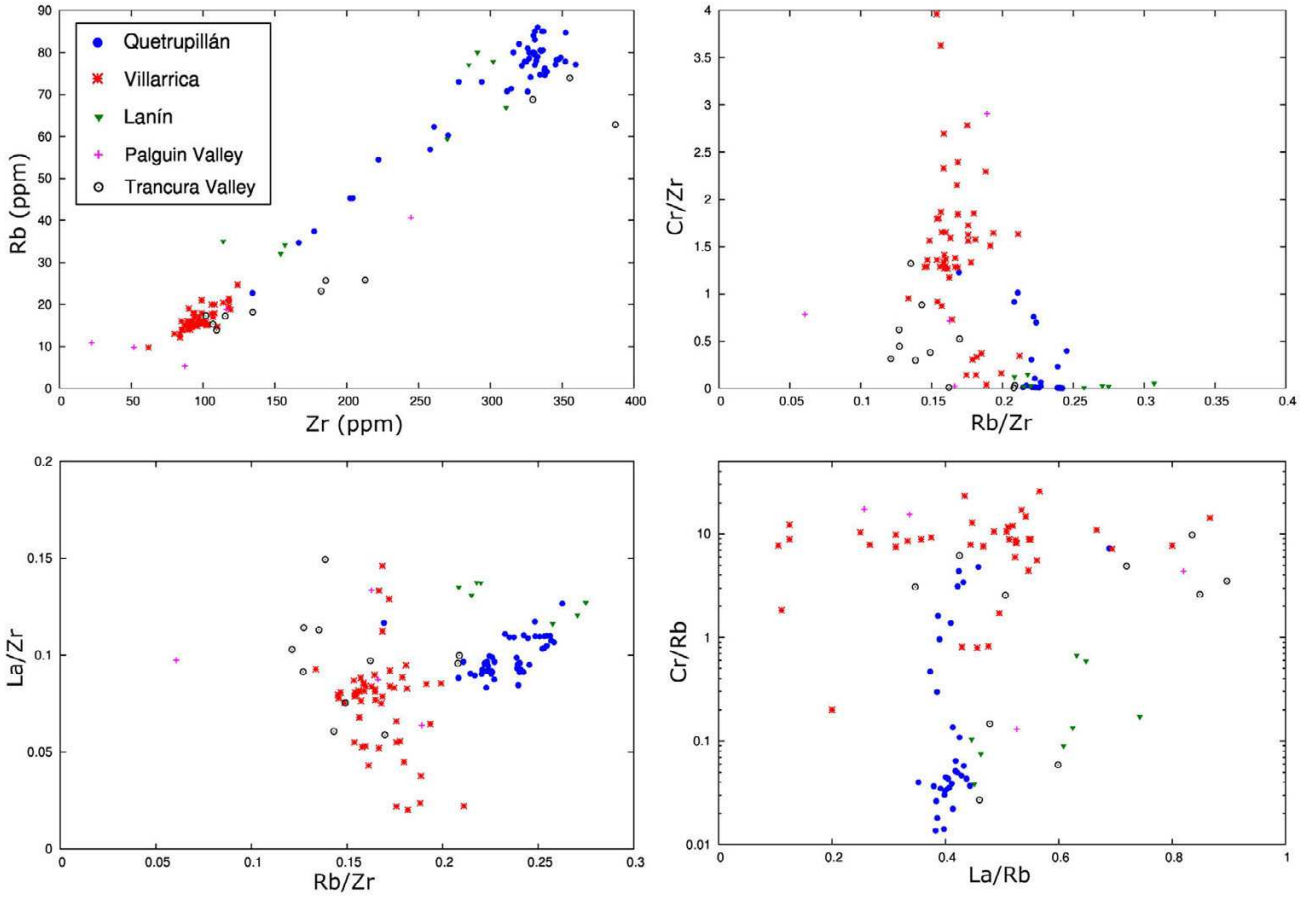

Figure 8: Trace element abundances of tephra samples from the Palguin Valley (pink crosses) and Trancura Valley (open black circles), compared with Quetrupillán (blue circles), Villarrica (red stars) and Lanín (green triangles). Data for Quetrupillán, Villarrica and Lanín is from this work and work by other authors. See Supplementary Material for full references.

orientated at 157°. This is roughly parallel to the Pleistocene trachyte fissure that lies to the west of Laguna Azul [McGarvie 2014], and is approximately perpendicular to the alignment of Vents 7, 8, and 9 (048°). Field evidence indicates that each of the vents within this volcanic field were only active for the duration of the related eruption.

As Holocene volcanism at Quetrupillán has not been the subject of a detailed study, we provide a description of the volcanic features, with a focus on the trachyte lavas.

4.4.1 *Trachyte lavas*

Of the sixteen flank vents at Quetrupillán, thirteen have effused lavas, which range in volume from ~0.9×10^6 m^3 to over 61×10^6 m^3 (Table 2). Of these, ten vents have produced trachyte lavas (over 200×10^6 m^3 in total), while two have produced trachyandesite lavas (4.1×10^6 m^3) and one has produced basaltic andesite lava (3.4×10^6 m^3).

Trachyte lavas on Quetrupillán commonly contain patches of oxidised, red spatter fragments, which increase in abundance towards their source vents (Figure 9A). As such, they are interpreted as clastogenic lava flows, formed when accumulated spatter is sufficiently molten to coalesce and remobilise into a lava flow [Andronico et al. 2008; Sumner 1998]. The trachyte lavas form blocky lava fields, with surfaces, flanks and termini consisting of black, glassy blocks that range in size from <30 cm to 1.5 m (Figure 9B). The blocks have a combination of rough, vesicular, irregular surfaces, and smooth, planar surfaces bounded by straight, sharp edges (Figure 9C and 9D), characteristic of typical blocky lava flows [Cigolini et al. 1984; Macdonald 1953].

Many trachyte lava fields have ogives (arcuate ridges orthogonal to flow direction) on their surface, caused by folding and wrinkling of the lava flow crust during emplacement [Fink 1980; Magnall et al. 2017]. This is most clearly observed in aerial images of the lava field from Vent 5, where well-developed ogives are 40–80 m in wavelength and up to 15 m in amplitude (Figure 10A). Several of the lava fields have rubbly levees along their margins (Figure 10B), forming the edges of what was, during emplacement, the active flow chan-

Table 2 – Composition, areas, and volumes of lava fields produced by satellite vents on the flanks of Quetrupillán.

Vent	Location	Composition	Area (km^2)	Thickness (m)	Volume ($\times 10^6$ m^3)	Notes
1	39°31'40" S, 71°44'09" W	Trachyte	NA	NA	NA	No lava field
2	39°32'12" S, 71°44'01" W	Trachyte	1.07	10	10.7	Includes assumed area below moraine
3	39°32'35" S, 71°43'51" W	Trachyte	6.16	10	61.6	Includes assumed area under Vent 5 field. May extend further south in the forested valley towards the cones of Llizan.
4	39°32'49" S, 71°43'36" W	Trachyte	0.13	10	1.3	Only includes exposed area. It will extend below the fields of Vents 3 and 5.
5	39°32'54" S, 71°43'31" W	Trachyte	2.30	25	57.5	
6	39°33'24" S, 71°42'19" W	Trachyte	0.50	10	5	
7	39°33'49" S, 71°41'17" W	Trachyte	3.06	10	30.6	May extend below Vent 3 field
8	39°33'37" S, 71°41'06" W	Trachyte	NA	NA	NA	No lava field
9	39°33'24" S, 71°40'43" W	Trachyte	0.23	5	1.2	
10	39°33'01" S, 71°41'45" W	Basaltic andesite	0.67	5	3.4	
11	39°32'48" S, 71°41'12" W	Trachyandesite	0.63	5	3.2	
12	39°31'50" S, 71°42'13" W	Trachyandesite	0.18	5	0.9	
13	39°31'06" S, 71°40'09" W	Trachyte	0.88	10	8.8	Not including any of the flow in the forested Huililco Valley
14	39°30'38" S, 71°40'25" W	Trachyte	1.98	10	19.8	Not including any of the flow in the forested Huililco Valley
15	39°29'40" S, 71°41'08" W	Trachyte	2.09	10	20.9	Not including any of the flow in the forested Huililco Valley
16	39°29'05" S, 71°43'30" W	NA	NA	NA	NA	No lava field, vent not visited

nel [Sparks et al. 1976]. The lava field of Vent 5 is the thickest of all Holocene lava flows, with steep flow margins up to 25 m high defined by well-developed levees (Figure 10A). Numerous breakout lobes have also formed along the margins of this lava field (Figure 10A and 10C).

Five channelized lava flows are visible in aerial images of the large (~30 × 10^6 m^3) trachyte lava field from Vent 7, highlighted by ogives on their surfaces and bounded by marginal shear zones (Figure 11A; Tuffen et al. [2013]). During emplacement, separate channels were active at different times as the lava flowed downslope. In contrast, the emplacement of lava from Vent 6 across relatively flat topography may account for the fact that no features of channelisation are visible. Instead, the lava field has expanded laterally across the plain.

4.4.2 *Trachyte Vents*

Seven of the satellite vents have constructed scoria cones (Figure 11B), of which four are trachytic, and of which all but one have produced lava fields. These are interpreted to have been created by conventional Strombolian activity, with magma fragmentation producing tephra, scoria, and bombs which followed bal-

Figure 9: Trachytic blocky lavas. [A] Trachyte lava from Vent 13 that contains red oxidised patches. [B] The steep flow front of the lava field from Vent 7 (looking west), composed of polyhedral blocks of black, glassy trachyte. [C] The lava field from Vent 2 (looking east). Polyhedral blocks have a combination of smooth, planar surfaces with straight sharp edges (yellow arrows) and rough, vesicular, irregular surfaces (red arrows). [D] A lava block from the lava field of Vent 13, showing the contrasting smooth and spinose edges to the polyhedral lava fragments.

listic trajectories to be deposited surrounding the vent [McGetchin et al. 1974; Valentine and Connor 2015]. The scoria cones range in height from 25 m to 120 m and have average basal diameters of ~290 m to 650 m, though all are asymmetric in shape due to a combination of prevailing wind direction, underlying palaeoslope, and conduit orientation [Tibaldi 1995].

There is evidence at some satellite vents that water has been involved in the eruptive activity. Two trachyte vents (1 and 2) have excavated craters through pre-existing volcanic deposits (Figure 11C). Both craters have similar dimensions of ~270 × 400 m, with their long axes aligned with the strike of the associated fissure. A small amount of pyroclastic material has accumulated on the eastern rim of Vent 1, and no lava has been produced. There is an absence of pyroclastic deposits on the crater rim of Vent 2, but lava flows have effused from the vent and flowed southwest and southeast (Figure 1). We interpret that explosive phreatic eruptions formed these craters when rising magma encountered groundwater within the bedrock. Once the groundwater supply had been exhausted (i.e. the water: lava ratio had been greatly reduced), pyroclastic material was erupted at Vent 1 and effusion of lava occurred at Vent 2.

Three trachyte vents (3, 4, and 8) have produced shallow craters with diameters of ~400 m, surrounded by low-rimmed mounds of tephra with gently sloping sides (Figure 12A). The interior walls of the craters are composed of vesicular, welded spatter while unconsolidated tephra (vesicular bombs, lapilli, and ash) drape the outer rims. We interpret these as tuff rings, formed during phreatomagmatic eruptions when interaction between magma and sufficient external water caused explosive fragmentation [Lorenz 1986; Wohletz and Sheridan 1983]. As the influence of groundwa-

Figure 10: [A] Satellite image of the lava field from Vent 5 highlighting ogives in the flow interior (dotted lines), spidery breakout lobes (solid arrows) and levees along the flow margins (dashed arrows). The dashed line outlines the scoria cone built around Vent 5. Satellite image from Google Earth (downloaded 03/12/2018). [B] Rubbly levees along the edge of a lava field from Vent 11 (looking south from Vent 12). The lava channel is 20 m wide. [C] A breakout lobe from the lava field of Vent 5 (looking south).

ter waned, lava flows effused from Vents 3 and 4 and breached the tuff rings. Spines of lava aligned with the flow direction are interpreted as remnants of the breached tuff ring ramparts that have been transported in the lava flow (Figure 12B). As only three of the satellite vents of Quetrupillán have produced tuff rings, this suggests that the presence of water was both transient and local, given that neighbouring vents active during the same fissure eruption do not show any features indicating magma-water interactions.

The vigour of explosive phases of Holocene eruptions is reflected in the extent and character of tephra blankets that occur generally to the east (i.e. downwind) of vents. For example, a particularly vigorous explosive phase is inferred to have occurred from Vent 11, as a tephra blanket which consists of agglutinated trachyandesite spatter ~10 m thick at a distance of 1 km from the vent (Figure 12C) covers the ridge of Cerro Colorado, southeast of Laguna Blanca (see Figure 2 for location of named places).

4.4.3 *Eruption stratigraphy of the satellite eruptions*

Stratigraphic relationships can determine the relative ages of some of the lava fields from the satellite vents on the flanks of Quetrupillán (Table 3; Figure 2). However, many of the lava fields are geographically isolated and so it is not possible to determine their relative stratigraphy. It was not possible to use tephrostratigraphy to assist with this, as tephra deposits are poorly preserved on the exposed, unvegetated flanks of Quetrupillán and are only locally preserved. In addition, thick snow covers the area during winter months, so any tephra deposited on the snow would be removed or modified

Figure 11: [A] Satellite image of the lava field from Vent 7. Five channelized lava flows are highlighted with dotted lines. Satellite image from Google Earth (downloaded 03/12/2018). [B] The scoria cone of Vent 14 (looking north). The cone has a basal diameter of 650 m. [C] The Pre-Holocene lavas and pyroclastics exposed in the excavated crater of Vent 2 (looking north). The crater width is 240 m.

during melting in spring. For this reason, the stratigraphy presented in Table 3 must be considered as tentative as well as incomplete.

In the southern volcanic field the most recent eruption occurred from a fissure to the east of Laguna Azul, with activity from Vents 1 to 5 (termed Eruption A). The lava field of Vent 4 is overlain by the lava field of Vent 3, which is in turn overlain by the lava field of Vent 5, indicating that activity began at Vent 4. The younger Vent 5 has also constructed a scoria cone on the edge of the older tuff ring formed around Vent 4. The lava field of Vent 2 diverges around and overlies the tuff rings of Vents 3 and 4 and so must be younger than they are. This lava has the freshest appearance of all Holocene lavas, and so is interpreted as the youngest lava field of Quetrupillán. Vent 1 did not produce a lava field, and so the relative timing of its activity is unknown.

A second fissure eruption occurred on the southeast flanks of Quetrupillán, with activity from Vents 7 to 9 (Eruption B). The creation of the Vent 8 tuff ring predates the effusion of lava from Vent 7, as lava spills over the tuff ring into the Vent 8 crater. The Vent 7 lava field also spills into the valley containing the Vent 3 lava field, which it underlies, indicating that Eruption B is older than Eruption A.

Vents 6 (Eruption C) and 10 (Eruption D) are located on a plateau of Pre-Holocene lava. The Vent 7 lava field infills the lobate edge of the Vent 6 lava field, indicating that fissure Eruption B is younger than Eruption C. An eroded lobe of lava from Vent 6 overlies the Vent 10 lava field, implying Eruption D pre-dates Eruption C. The Vent 10 basaltic andesite lava field is completely infilled by tephra, with highly weathered lava only occasionally exposed at the edges of the field. This appearance suggests that Eruption D is significantly older than the trachytic Eruptions A, B, and C.

The trachyandesite lava fields of Vents 11 and 12 are geographically isolated, with the lack of contact between them preventing determination of their relative stratigraphy. They have been termed Eruption E and F, respectively (Table 3). On the eastern flanks of Quetrupillán, the Vent 13 lava field (Eruption G) overlies the Vent 14 lava field (Eruption H), indicating that it is younger. The Vent 15 lava field (Eruption I) is geographically isolated, as is the cone of Vent 16 (Eruption J), and so the relative timing of these eruptions cannot be constrained.

4.4.4 *The stratocone*

In Subsection 4.2 we highlighted how the record of Holocene volcanic activity that constructed the stratocone has been removed by repeated ice advances and retreats during the Little Ice Age of the 17th–19th centuries, and evidence suggests that the most recent (19th century) ice advance was also the most extensive. Consequently, a major gap in our understanding of the

Figure 12: [A] Vent 8 has produced a shallow c.400 m wide crater surrounded by a low-rimmed tuff ring. The lava flow of Vent 9 is visible in the foreground, and Volcán Mocho-Choshuenco is in the background (looking southwest). [B] Lava spines aligned with the flow direction of the lava field of Vent 3 (looking south). [C] A ~10 m thick drape of agglutinated spatter on the ridge of Cerro Colorado. Person for scale, highlighted by arrow (looking NNW).

Holocene eruptive activity of Quetrupillán will be the number, composition and volume of effusive eruptions that took place anywhere on the stratocone. This includes lavas effused from the summit crater and from any satellite vents on the upper flanks of the stratocone within the scoured zone.

The remnants of columnar-jointed trachyte lava buttresses that are exposed within the scoured zone provide evidence that effusion of trachyte lavas from the stratocone took place during the last (Llanquihue) glacial period and/or earlier glacial periods. During past glaciations, relatively thick ice covered the stratocone and surrounding area [Hulton et al. 2002; McGarvie 2014], and so construction of at least an embryonic stratocone must have taken place prior to the Holocene. Logically, construction of the stratocone would have continued during the Holocene, and the partial burial of suspected Llanquihue glaciovolcanic lava buttresses by scoured Holocene lavas supports this.

Within the inner walls of the summit crater are beds of spatter and scoria (mostly oxidised), which are assumed to represent the remnants of an unknown number of eruptions from the summit, of unknown age. Due to accessibility difficulties these were not sampled. Consequently, due to the removal of an unknown amount of lava from the stratocone by Holocene glacial erosion up until the end of the 19th century, it is not possible to state anything definitive about the Holocene construction of the stratocone by lava effusions from either the summit crater or from flank vents within the scoured zone.

4.5 Tephra layers in nearby valleys

Tephra layers are exposed in road cuttings in valleys surrounding Quetrupillán. Two road cuttings were

Table 3 – Relative eruption stratigraphy of activity from the satellite vents.

Eruption	Vents	Stratigraphic evidence	Notes
A	1, 2, 3, 4, 5	Lavas overlie lava from Vent 7 so are younger than Eruption B	This eruptive activity pre-dates the most recent ice advance as the moraine partly covers the lava field of Vent 2 and the tuff rings of Vents 3 and 4 (Figure 4C)
B	7, 8, 9	Lava from Vent 7 underlies lava from Vent 3 so is older than Eruption A. Lava from Vent 7 abuts against the Vent 6 lava field suggesting it is younger than Eruption C	
C	6	The edge of the Vent 6 lava field has an irregular shape which is infilled by the lava field from Vent 7	
D	10	An eroded lobe of lava from Vent 6 overlies the lava field of Vent 10	Lava field is completely infilled by tephra with only small patches of lava exposed
E	11	None – isolated lava field	
F	12	None – isolated lava field	
G	13	Overlies the lava field of Vent 14	
H	14	Underlies the lava field of Vent 13	
I	15	None – isolated lava field	
J	16	None – isolated scoria cone, no lava field	

logged in the Trancura valley near Puesco, to the east of Quetrupillán (Figure 13). An outcrop of Cretaceous granite basement rock is exposed at the base of section T1, presumably cleared of all overlying material during the last glacial period, indicating that the overlying pyroclastic sequence has all been deposited during the Holocene. Eleven tephra layers were identified within this section (Figure 13) of which, according to analysis of trace element abundances (Figure 8), three were produced by Quetrupillán. Villarrica is the source of the remaining eight tephra layers.

Quetrupillán has produced the uppermost two tephra layers in the sequence (Figure 13). The top tephra layer is a 30 cm thick horizon of gritty, grey ash, with abundant modern organic material due to the presence of root matter from the overlying vegetation. It has a trachytic composition (Figure 6A). Below this is a 1 m thick tephra layer which consists of pale, poorly sorted subangular pumice that ranges from 2–40 mm and is interspersed with sparse obsidian lithics. This tephra layer, described elsewhere along the Trancura Valley, is an airfall deposit that has been named the Puesco Pumice by previous studies and dated at 1650 ± 70 yr BP [Toloza 2015] and 1850–1987 cal BP [Fontijn et al. 2016]. Our XRF analysis shows that the Puesco Pumice is trachytic (Figure 9A), and has a similar composition to the Holocene trachyte lava fields on the flanks of Quetrupillán.

The third tephra layer produced by Quetrupillán is in the lower half of the sequence. It is a 15 cm thick horizon of moderately sorted, orange-brown pumice ranging from 1–15 mm with an ashy matrix. This pumice is a trachyandesite (Figure 6A).

At the two locations in the Trancura Valley that were logged and sampled for this paper, all three of the Quetrupillán tephra layers had the characteristics of airfall deposits. There was no clear evidence of characteristics representing the lateral movement of clasts that characterise pyroclastic density current deposits.

A pyroclastic sequence in the Palguin Valley to the northwest of Quetrupillán was also studied. Analysis of trace element abundances (Figure 8) suggests that none of the sampled tephra layers were produced by Quetrupillán.

5 Discussion

5.1 The pattern of Holocene volcanism

The clearest expressions of Holocene volcanism at Quetrupillán are the satellite vents and their lavas. Compositionally, these are trachytes, trachyandesites, and basaltic andesites, with trachytes being volumetrically dominant (Table 2; Figure 6A). Limited analyses

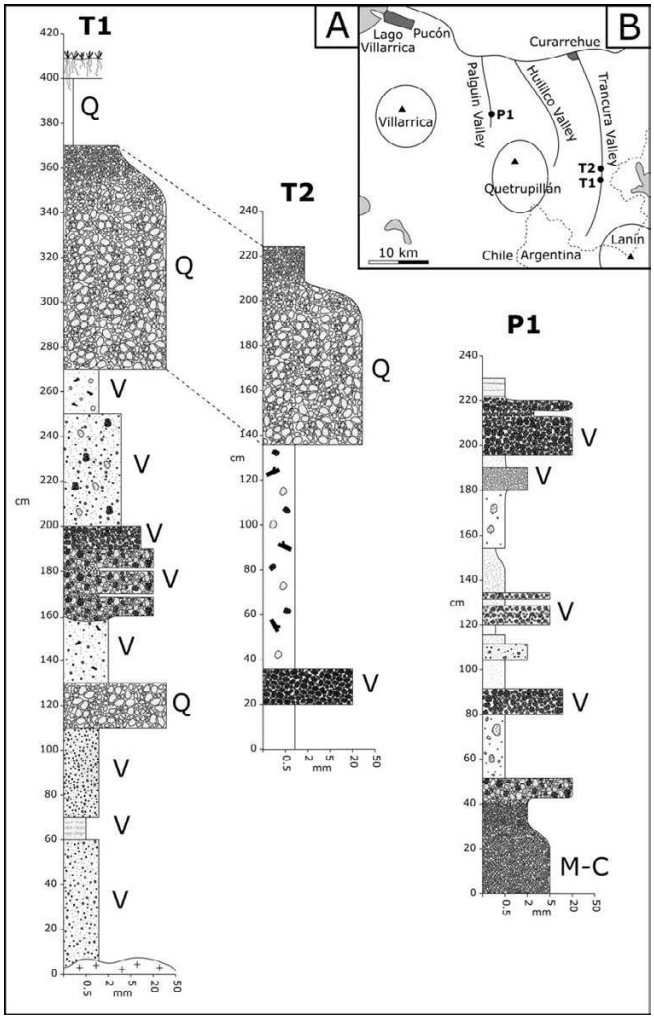

Figure 13: [A] Logs of three pyroclastic sequences studied and sampled in the Trancura Valley (T1 and T2) and the Palguin Valley (P1), with labels identifying tephra layers from Quetrupillán (Q), Villarrica (V) and Mocho-Choshuenco (M-C). [B] Schematic map showing the location of the logged sections in relation to Quetrupillán. T1: 39.52365°S, 71.55047°W; T2: 39.51823°S, 71.54813°W; P1: 39.42695°S, 71.76594°W

of lavas from the eroded stratocone indicate eruption of the same compositional range from the summit region. Consequently, there is no spatial-compositional pattern at Quetrupillán, as seen at some volcanic complexes, as all three magma types have been erupted both at the stratocone and from the satellite vents. In contrast, at Nevados de Chillán, the Cerro Blanco subcomplex erupts basaltic andesite and the Las Termas subcomplex erupts dacite to rhyolite [Dixon et al. 1999; Mee et al. 2009]. This suggests that the plumbing system beneath Quetrupillán is in a less-ordered state.

There is a noticeable "non-eruptive" arc of ~8 km in length around the western and northern margins of the scoured zone, in which there is only one vent (Vent 16; Figure 2), that appears to have produced only a small scoria cone. Elsewhere, gaps between vents are from a few hundred metres up to 2 km, with a concentration of twelve of the sixteen satellite vents in a ~6 km long sector to the south of the stratocone, that we have termed the southern volcanic field. This pattern may be related to a tendency for crustal rupturing to be focused in a zone south of the stratocone, associated with fault splays from the nearby Liquiñe-Ofqui Fault Zone [e.g. Cembrano and Lara 2009; Schonwalder-Angel et al. 2018]. It is notable that Vents 1–5 lie on a distinct fissure, as do Vents 7–9. Further evidence of crustal rupturing in this zone comes from two NNE-striking Pleistocene subglacial trachyte fissure eruptions that flank Laguna Azul [McGarvie 2014].

It is not possible to determine how many eruptions have occurred from the summit of the stratocone, as glacial scouring has removed evidence of Holocene lava stratigraphy. However, as presented in Subsection 4.4.4, within the scoured zone are numerous eroded Holocene lava fields that have flowed around suspected Llanquihue-age lava buttresses, and have partly buried them. From this, we suggest that the stratocone grew during the Holocene as a result of substantial pre-LIA lava effusions that resurfaced its upper flanks. However, the lack of pristine lavas within the scoured zone implies there have been no lava effusions on the upper flanks of the stratocone since the end of the LIA in the late 19th century.

To evaluate the number of Holocene eruptions from the satellite vents, we consider two contrasting scenarios; a simple scenario (i.e. fewest eruptions), and a complex scenario (i.e. the maximum reasonable number of eruptions). In the most complex scenario, each identified vent represents a separate eruptive episode. This would imply that sixteen eruptions have occurred on the lower flanks of Quetrupillán. An argument against this is that the orientation and physical nature of Vents 1–5 indicate that they lie along a fissure, and so would have all been active during the same eruptive episode.

The simple scenario involves just three eruptions: one trachyte eruption, one trachyandesite eruption, and one basaltic andesite eruption. If all the trachyte vents were produced during just one eruption, then this eruption occurred along an arc of ~14 km in length, from Vent 1 in the west to Vent 15 in the northeast (possibly longer if Vent 16 is trachyte; Figure 2). This single trachyte eruption would define an arc that may be related either to a previous ring fracture (caldera fault), or to a more recent crustal weakness that could be activated during a future caldera-forming eruption.

We currently favour an intermediate scenario, whereby the sixteen vents represent ~10 different eruptive episodes, as presented in Table 3. Vents 1–5 and Vents 7–9 represent fissure eruptions, with several vents active during a single eruptive episode, as discussed in Subsection 4.4.3. The remaining vents are likely to represent individual eruptions.

5.2 Hazard implications

This study provides additional information on the potential hazards from effusive and explosive eruptions that complements the existing "Mapa Preliminar De Peligros Del Volcán Quetrupillán" (Preliminary Hazard Map of Quetrupillán Volcano) published by the Servicio Nacional de Geología y Minería [SERNAGEOMIN 2013]. Our study contributes no new information on lahar hazards as we did not find any conclusive evidence of preserved lahar deposits.

5.2.1 *Effusive eruptions*

Holocene lavas (largely trachytes) from the stratocone and satellite vents have flowed down valleys and travelled a maximum of ~15 km from their source vents. Lavas are channelled to the north along the Huililco Valley towards Catripulli, a lava pathway of ~17 km from Quetrupillán's summit, or to the south, where it is a ~30 km lava pathway from the summit to Liquiñe (see Figure 1 for named settlements). To the west there is a potential lava pathway of ~22 km from the summit towards Coñaripe, but there are no known Holocene lavas that have travelled in this direction.

Provided future eruptions occur in the vicinity of known Holocene vents, there is little possibility of lavas causing damage to any larger settlements. Given the distances involved and the expected relatively low velocities of trachytic lavas, and assuming good communication, there should be ample time for evacuation of remote properties located in the higher valleys surrounding Quetrupillán.

5.2.2 *Explosive eruptions*

During this study, three pyroclastic sequences were logged and sampled to evaluate explosive eruptive activity from Quetrupillán (Figure 13). One section was to the northwest, in the Palguin Valley, and two sections were to the east, in the Trancura Valley. The prevailing wind is towards the east, so it was anticipated that the Trancura section would provide the most comprehensive record of explosive volcanism from Quetrupillán. The Palguin section was chosen as it was likely to contain tephra only from the largest of Quetrupillán's explosive eruptions, as it is orthogonal to the expected west-to-east dispersal axis of Quetrupillán eruptive plumes [SERNAGEOMIN 2013].

Trace element analyses of tephra layers in the Palguin Valley indicate that none of the sampled tephra layers have been produced by Quetrupillán (Figure 8). Instead, one dacite layer comes from Mocho-Choshuenco [Rawson et al. 2015], and the rest are from Villarrica, which lies 15 km to the west (upwind). The absence of any tephra from Quetrupillán suggests that there have been no very large explosive eruptions from Quetrupillán in the Holocene.

In the Trancura Valley, trace element analyses identified three tephra layers from explosive eruptions at Quetrupillán (Figure 8), of which two are trachytic and one is trachyandesite (Figure 6A). This section is notable as it covers the entire Holocene, with the lowermost tephra sitting directly on the plutonic basement (Figure 13).

According to information provided by Servicio Nacional de Geología y Minería [SERNAGEOMIN 2019], which appears to be based on the undergraduate dissertation study by Toloza [2015], nine explosive eruptions from Quetrupillán are preserved in the Trancura Valley. Our findings disagree with this, as we only assign three units to Quetrupillán, and consequently the hazard from explosive eruptions affecting areas to the east (e.g. the Trancura Valley) is a factor of three less than currently stated by SERNAGEOMIN.

It should be noted that Toloza [2015] does not provide any geochemical evidence to support the claim that there are nine Holocene explosive eruptions from Quetrupillán preserved in the Trancura Valley. Their underlying assumption is that the vast majority of tephra layers in the Trancura Valley must have come from Quetrupillán. However, only by geochemically analysing each unit can the provenance of each tephra layer be established.

Toloza [2015] and the official hazard map [SERNAGEOMIN 2013] also suggest that there is a substantial pyroclastic density current (PDC) hazard from Quetrupillán in the Trancura Valley. Our observations suggest that all three Quetrupillán tephra layers are airfall deposits. We found no evidence of sedimentary structures reflecting lateral transport, characteristic of PDC deposits, nor did any of these three layers show the very poor sorting that characterises PDCs. However, it is notable that Fontijn et al. [2014] and Rawson et al. [2015], who carried out detailed logging and sampling of tephra layers from numerous sites in this region of Chile, both comment on the variability in preservation of tephra even over short distances (i.e. 10s of metres). So whilst we found no evidence of PDC deposition at our two sites, this may exist elsewhere.

In this context, it is important to note that the eroded remnants of the Colmillo del Diablo volcano lie to the east of Quetrupillán, as does the 200–380 m high near-vertical fault scarp along the eastern edge of the Huililco Valley. These form a major topographic barrier that would hinder, if not block, the passage of PDCs moving eastwards from Quetrupillán and into the Trancura Valley. However, should PDCs be channelled northwards down the Huililco Valley by this topographic barrier then they may reach the isolated settlements located there.

In summary, our work suggests that the hazard from explosive eruptions at Quetrupillán is less than the current hazard map indicates [SERNAGEOMIN 2013], given that our geochemical analyses identified only three, rather than nine, units produced by explosive eruptions that have reached the Trancura Valley. We

also found no unequivocal evidence of PDC activity at our studied sites in the Trancura Valley. This implies either that no substantial PDCs have been produced during the Holocene, or that the topographic barrier to the east of Quetrupillán has prevented them from reaching the Trancura Valley. However, we wish to emphasise that our studied sections may have occurred away from PDC pathways, and therefore a future target for hazard evaluation would be a detailed study along the length of the Trancura Valley to establish the past pathways of PDCs, should they exist.

6 Conclusions

This paper provides the first detailed account of Holocene volcanism at Quetrupillán. Holocene eruptions have occurred both at the stratocone and from satellite vents on its flanks. The number and type of eruptions from the summit is unknown due to removal of lavas by ice during LIA glacial advances, resulting in the prominent scoured zone. However, glaciovolcanic buttresses on the flanks of the stratocone that are partly buried by scoured summit lavas indicate that some construction has taken place. We suggest that effusive activity from the stratocone summit has been higher during the Holocene than its scoured appearance implies.

We identified sixteen satellite vents on the flanks of Quetrupillán, which we consider to represent ten Holocene eruptive episodes. Satellite vents have produced tuff rings, scoria cones and phreatic craters, as well as extensive lava fields. Some eruptions have occurred on fissures, suggesting that fault splays related to the LOFZ continue to influence the locations of eruptions at Quetrupillán. The volumetrically dominant composition erupted from the satellite vents is trachyte, with minor trachyandesite and basaltic andesite. Limited sampling of stratocone lavas indicates that all three compositions have also erupted from the summit. Thus, unlike some Chilean volcanic complexes, there is no relationship between eruption location and magma composition at Quetrupillán.

Geochemical evidence from tephra layers in the nearby Trancura Valley (downwind of Quetrupillán) indicates that three sizeable explosive eruptions have occurred from Quetrupillán during the Holocene. This is much fewer than the nine eruptions stated by previous workers, however their study provided no geochemical evidence to identify which volcano had produced the deposits. They also state that all deposits were produced by PDC activity, while our examination of tephra layers in road cuttings did not reveal any unequivocal evidence of the lateral transport structures that are characteristic of PDCs. We consider it important to note that there is a substantial topographic barrier that would either hinder or block passage of PDCs from Quetrupillán to the Trancura Valley. We would suggest that a detailed study of multiple road cuttings is undertaken to resolve the issue of PDC activity.

Acknowledgements

The work in this paper forms part of a NERC-funded PhD studentship by Isla Simmons (Grant number NE/L002558/1). Joaquín Cortés received funding from Edge Hill University (RIF grant 1CORTE18) and Santander Universities supported Dave McGarvie. Huge thanks to John Simmons, Franco Vera Rivadeneira, Jack McGarvie and Jonathan Moles for being wonderful field assistants, and to Christa Bönninghoff, Cristian Silva and Claudia Guzmán Roa for help with logistics in the field. We thank Nic Odling, Nicola Cayzer, John Craven, Chris Hayward and Mike Hall at the University of Edinburgh for help with analysis. And finally, thank you the two reviewers for their comments and suggestions which have improved this manuscript, and to Nick Varley and Jamie Farquharson for editorial handling.

Author contributions

Isla Simmons, Joaquín Cortés and Dave McGarvie conducted fieldwork at Quetrupillán, based on initial reconnaissance mapping by Andrés Pavez. Isla Simmons performed subsequent analyses at the University of Edinburgh. Isla Simmons and Dave McGarvie wrote the manuscript, with assistance from Joaquín Cortés. Eliza Calder, Joaquín Cortés and Dave McGarvie assisted with project supervision.

Data availability

The Supplementary Material spreadsheet includes XRF analyses (collected during this study, and data used in this study collected by other authors), mineral analyses and sample locations.

References

Andronico, D., A. Cristaldi, and S. Scollo (2008). "The 4–5 September 2007 lava fountain at South-East Crater of Mt Etna, Italy". *Journal of Volcanology and Geothermal Research* 173.3-4, pp. 325–328. doi: 10.1016/j.jvolgeores.2008.02.004.

Brahm, R., M. A. Parada, E. Morgado, C. Contreras, and L. E. McGee (2018). "Origin of Holocene trachyte lavas of the Quetrupillán volcanic complex, Chile: Examples of residual melts in a rejuvenated crystalline mush reservoir". *Journal of Volcanology and*

Geothermal Research 357, pp. 163–176. DOI: 10.1016/j.jvolgeores.2018.04.020.

Cembrano, J., F. Hervé, and A. Lavenu (1996). "The Liquiñe Ofqui fault zone: a long-lived intra-arc fault system in southern Chile". *Tectonophysics* 259.1-3, pp. 55–66. DOI: 10.1016/0040-1951(95)00066-6.

Cembrano, J. and L. Lara (2009). "The link between volcanism and tectonics in the southern volcanic zone of the Chilean Andes: A review". *Tectonophysics* 471.1-2, pp. 96–113. DOI: 10.1016/j.tecto.2009.02.038.

Cigolini, C., A. Borgia, and L. Casertano (1984). "Intracrater activity, aa-block lava, viscosity and flow dynamics: Arenal Volcano, Costa Rica". *Journal of Volcanology and Geothermal Research* 20.1-2, pp. 155–176. DOI: 10.1016/0377-0273(84)90072-6.

Clapperton, C. (1983). "The glaciation of the Andes". *Quaternary Science Reviews* 2.2-3, pp. 83–155. DOI: 10.1016/0277-3791(83)90005-7.

Clapperton, C. and D. Sugden (1988). "Holocene glacier fluctuations in South America and Antarctica". *Quaternary Science Reviews* 7.2, pp. 185–198. DOI: 10.1016/0277-3791(88)90005-4.

Denton, G., C. J. Heusser, T. Lowel, P. Moreno, B. Andersen, L. E. Heusser, C. Schluhter, and D. Marchant (1999). "Interhemispheric Linkage of Paleoclimate During the Last Glaciation". *Geografiska Annaler, Series A: Physical Geography* 81.2, pp. 107–153. DOI: 10.1111/j.0435-3676.1999.00055.x.

Dixon, H. J., M. D. Murphy, S. J. Sparks, R. Chávez, J. A. Naranjo, P. N. Dunkley, S. R. Young, J. S. Gilbert, and M. R. Pringle (1999). "The geology of Nevados de Chillán volcano, Chile". *Revista geológica de Chile* 26.2. DOI: 10.4067/s0716-02081999000200006.

Fink, J. (1980). "Surface folding and viscosity of rhyolite flows". *Geology* 8.5, p. 250. DOI: 10.1130/0091-7613(1980)8<250:sfavor>2.0.co;2.

Fontijn, K., S. M. Lachowycz, H. Rawson, D. M. Pyle, T. A. Mather, J. A. Naranjo, and H. Moreno Roa (2014). "Late Quaternary tephrostratigraphy of southern Chile and Argentina". *Quaternary Science Reviews* 89, pp. 70–84. DOI: 10.1016/j.quascirev.2014.02.007.

Fontijn, K., H. Rawson, M. V. Daele, J. Moernaut, A. M. Abarzúa, K. Heirman, S. Bertrand, D. M. Pyle, T. A. Mather, M. D. Batist, J.-A. Naranjo, and H. Moreno Roa (2016). "Synchronisation of sedimentary records using tephra: A postglacial tephrochronological model for the Chilean Lake District". *Quaternary Science Reviews* 137, pp. 234–254. DOI: 10.1016/j.quascirev.2016.02.015.

Glasser, N. F., K. N. Jansson, S. Harrison, and J. Kleman (2008). "The glacial geomorphology and Pleistocene history of South America between 38°S and 56°S". *Quaternary Science Reviews* 27.3-4, pp. 365–390. DOI: 10.1016/j.quascirev.2007.11.011.

Hernandez-Moreno, C., F. Speranza, and A. Di Chiara (2014). "Understanding kinematics of intra-arc transcurrent deformation: Paleomagnetic evidence from the Liquiñe-Ofqui fault zone (Chile, 38-41°S)". *Tectonics* 33.10, pp. 1964–1988. DOI: 10.1002/2014tc003622.

Hickey-Vargas, R., H. Moreno Roa, L. Lopez Escobar, and F. A. Frey (1989). "Geochemical variations in Andean basaltic and silicic lavas from the Villarrica-Lanin volcanic chain (39.5°S): an evaluation of source heterogeneity, fractional crystallization and crustal assimilation". *Contributions to Mineralogy and Petrology* 103.3, pp. 361–386. DOI: 10.1007/bf00402922.

Hulton, N., R. Purves, R. McCulloch, D. Sugden, and M. Bentley (2002). "The Last Glacial Maximum and deglaciation in southern South America". *Quaternary Science Reviews* 21.1-3, pp. 233–241. DOI: 10.1016/s0277-3791(01)00103-2.

Lara, L. E., J. A. Naranjo, and H. Moreno Roa (2004). "Lanín volcano (39.5°S), Southern Andes: geology and morphostructural evolution". *Revista geológica de Chile* 31.2. DOI: 10.4067/s0716-02082004000200004.

Le Maitre, R., A. Streckeisen, B. Zanettin, M. Le Bas, B. Bonin, and P. Bateman (2002). "Igneous rocks: A classification and glossary of terms; Recommendations of the International Union of Geological Sciences". *Subcommission on the Systematics of Igneous rocks*. Cambridge University Press. DOI: 10.1017/cbo9780511535581.

López-Escobar, L., J. Cembrano, and H. Moreno Roa (1995). "Geochemistry and tectonics of the Chilean Southern Andes basaltic Quaternary volcanism (37-46°S)". *Revista Geológica de Chile* 22.2, pp. 219–234. DOI: http://dx.doi.org/10.5027/andgeoV22n2-a06.

Lorenz, V. (1986). "On the growth of maars and diatremes and its relevance to the formation of tuff rings". *Bulletin of Volcanology* 48.5, pp. 265–274. DOI: 10.1007/bf01081755.

Lowell, T. V., C. J. Heusser, B. G. Andersen, P. I. Moreno, A. Hauser, L. E. Heusser, C. Schluchter, D. R. Marchant, and G. H. Denton (1995). "Interhemispheric Correlation of Late Pleistocene Glacial Events". *Science* 269.5230, pp. 1541–1549. DOI: 10.1126/science.269.5230.1541.

Macdonald, G. A. (1953). "Pahoehoe, aa, and block lava". *American Journal of Science* 251.3, pp. 169–191. DOI: 10.2475/ajs.251.3.169.

Magnall, N., M. R. James, H. Tuffen, and C. Vye-Brown (2017). "Emplacing a Cooling-Limited Rhyolite Lava Flow: Similarities with Basaltic Lava Flows". *Frontiers in Earth Science* 5. DOI: 10.3389/feart.2017.00044.

Matthews, J. A. and K. R. Briffa (2005). "The 'little ice age': re-evaluation of an evolving concept". *Geografiska Annaler: Series A, Physical Geography* 87.1, pp. 17–36. DOI: 10.1111/j.0435-3676.2005.00242.x.

McGarvie, D. (2009). "Rhyolitic volcano–ice interactions in Iceland". *Journal of Volcanology and Geothermal Research* 185.4, pp. 367–389. DOI: 10.1016/j.jvolgeores.2008.11.019.

– (2014). "Glaciovolcanism at Volcán Quetrupillán, Chile". *2014 GSA Annual Meeting in Vancouver, British Columbia*.

McGetchin, T. R., M. Settle, and B. A. Chouet (1974). "Cinder cone growth modeled after Northeast Crater, Mount Etna, Sicily". *Journal of Geophysical Research* 79.23, pp. 3257–3272. doi: 10.1029/jb079i023p03257.

Mee, K., J. S. Gilbert, D. W. McGarvie, J. A. Naranjo, and M. S. Pringle (2009). "Palaeoenvironment reconstruction, volcanic evolution and geochronology of the Cerro Blanco subcomplex, Nevados de Chillán volcanic complex, central Chile". *Bulletin of Volcanology* 71.8, pp. 933–952. doi: 10.1007/s00445-009-0277-7.

Mercer, J. H. (1965). "Glacier Variations in Southern Patagonia". *Geographical Review* 55.3, p. 390. doi: 10.2307/213136.

Moreno Roa, H., L. López-Escobar, and J. Cembrano (1994). "The Villarrica-Quetrupillan-Lanin volcanic chain: a review and probable significance in the Southern Andes, Chile". *Congreso Geologico Chileno*. 7, pp. 339–341.

Moreno Roa, H. and L. Lara (2008). *Geología del área Pucón-Curarrehue: regiones de La Araucanía y de Los Ríos: Regiones de la Araucanía y de los Ríos*. [Map scale 1:100000.]

Moreno, P., T. Lowell, G. J. Jr, and G. Denton (1999). "Abrupt Vegetation and Climate Changes During the Last Glacial Maximumand Last Termination in The Chilean Lake District: A Case Study from Canal De La Puntilla (41oS)". *Geografiska Annaler, Series A: Physical Geography* 81.2, pp. 285–311. doi: 10.1111/j.0435-3676.1999.00059.x.

Pavez, A. (1997). "Geología e historia evolutiva del Complejo Volcánico Quetrupillán, Andes del Sur, 39, 5° S". *VIII Congreso Geológico Chileno*. Vol. 2, pp. 1443–1447. [In Spanish].

Petit-Breuilh Sepúlveda, M. E. (2004). *La historia eruptiva de los volcanes hispanoamericanos (siglos XVI al XX)*. Cabildo Insular de Lanzarote. [In Spanish].

Rawson, H., J. A. Naranjo, V. C. Smith, K. Fontijn, D. M. Pyle, T. A. Mather, and H. Moreno Roa (2015). "The frequency and magnitude of post-glacial explosive eruptions at Volcán Mocho-Choshuenco, southern Chile". *Journal of Volcanology and Geothermal Research* 299, pp. 103–129. doi: 10.1016/j.jvolgeores.2015.04.003.

Rosenau, M., D. Melnick, and H. Echtler (2006). "Kinematic constraints on intra-arc shear and strain partitioning in the southern Andes between 38°S and 42°S latitude". *Tectonics* 25.4. doi: 10.1029/2005tc001943.

Schonwalder-Angel, D., J. A. Cortés, and E. S. Calder (2018). "The interplay of magmatism and tectonics: An example based on the satellite scoria cones at Llaima volcano, Chile". *Journal of Volcanology and Geothermal Research* 367, pp. 31–45. doi: 10.1016/j.jvolgeores.2018.10.020.

Servicio Nacional de Geología y Minería (2013). *Mapa Preliminar de Peligros del Volcán Quetrupillán*. url: http://sitiohistorico.sernageomin.cl/pdf/rnvv/Quetrupillan.pdf.

– (2019). *Complejo Volcánico Quetrupillán*. url: https://www.sernageomin.cl/complejo-volcanico-quetrupillan/.

Sparks, R., H. Pinkerton, and G. Hulme (1976). "Classification and formation of lava levees on Mount Etna, Sicily". *Geology* 4.5, p. 269. doi: 10.1130/0091-7613(1976)4<269:cafoll>2.0.co;2.

Stern, C. R. (2004). "Active Andean volcanism: its geologic and tectonic setting". *Revista geológica de Chile* 31.2. doi: 10.4067/s0716-02082004000200001.

Sumner, J. M. (1998). "Formation of clastogenic lava flows during fissure eruption and scoria cone collapse: the 1986 eruption of Izu-Oshima Volcano, eastern Japan". *Bulletin of Volcanology* 60.3, pp. 195–212. doi: 10.1007/s004450050227.

Sun, M. (2001). "Geochemical variation among small eruptive centers in the central SVZ of the Andes : an evaluation of subduction, mantle and crustal influences". PhD thesis. Florida International University. doi: 10.25148/etd.fi15071601.

Tatsumi, Y. (2005). "The subduction factory: How it operates in the evolving Earth". *GSA Today* 15.7, p. 4. doi: 10.1130/1052-5173(2005)015[4:tsfhio]2.0.co;2.

Tibaldi, A. (1995). "Morphology of pyroclastic cones and tectonics". *Journal of Geophysical Research: Solid Earth* 100.B12, pp. 24521–24535. doi: 10.1029/95jb02250.

Toloza, V. (2015). "Tefroestratigrafía postglacial del Complejo Volcánico Quetrupillán 39° 30'S, 71° 43'O. Regiones de La Araucanía y de Los Ríos, Chile." Universidad de Concepción.

Tuffen, H., M. R. James, J. M. Castro, and C. I. Schipper (2013). "Exceptional mobility of an advancing rhyolitic obsidian flow at Cordón Caulle volcano in Chile". *Nature Communications* 4.1. doi: 10.1038/ncomms3709.

Valdivia Muñoz, P. A. (2016). "Estudio petrológico y geoquímico del volcán Huililco, IX Región, Chile". Universidad de Chile.

Valentine, G. A. and C. B. Connor (2015). "Basaltic Volcanic Fields". *The Encyclopedia of Volcanoes*. Elsevier, pp. 423–439. doi: 10.1016/b978-0-12-385938-9.00023-7.

Witter, J. B., V. C. Kress, P. Delmelle, and J. Stix (2004). "Volatile degassing, petrology, and magma dynamics of the Villarrica Lava Lake, Southern Chile". *Journal of Volcanology and Geothermal Research* 134.4, pp. 303–337. doi: 10.1016/j.jvolgeores.2004.03.002.

Wohletz, K. H. and M. F. Sheridan (1983). "Hydrovolcanic explosions; II, Evolution of basaltic tuff rings and tuff cones". *American Journal of Science* 283.5, pp. 385–413. doi: 10.2475/ajs.283.5.385.

Journal of Volcanology and Geothermal Research 407 (2020) 107101

Contents lists available at ScienceDirect

Journal of Volcanology and Geothermal Research

journal homepage: www.elsevier.com/locate/jvolgeores

Invited Research Article

Tectonic constraints on a magmatic plumbing system: The Quetrupillán Volcanic Complex (39°30′ S, 71°43′ W), Southern Andes, Chile

Isla C. Simmons [a,*], Joaquín A. Cortés [a,b], Dave McGarvie [c], Eliza S. Calder [a]

[a] School of GeoSciences, Grant Institute, University of Edinburgh, King's Buildings, Edinburgh EH9 3FE, UK
[b] Department of Geography, Edge Hill University, St Helens Road, Ormskirk L39 4QP, UK
[c] Lancaster Environment Centre, Library Avenue, Lancaster University, Lancaster LA1 4YQ, UK

ARTICLE INFO

Article history:
Received 15 June 2020
Received in revised form 6 October 2020
Accepted 24 October 2020
Available online 27 October 2020

Keywords:
Quetrupillán Volcanic Complex
Magmatic plumbing system geometry
Volcano tectonics
Magma mixing
Trachytic melts

ABSTRACT

The Quetrupillán Volcanic Complex is a composite system, active since the Pleistocene. We combine petrological and geochemical data from its erupted products with structural and geometrical constraints applied to the overall system and region. We conclude that a basaltic source melt is hindered on its ascent through the crust due to a compressional tectonic regime, influenced further by the structural control imposed by the Liquiñe-Ofqui Fault Zone. The stalled melt evolves by fractional crystallisation within the crust and undergoes a degree of crustal contamination, resulting in a network of trachytic melt pockets within a transcrustal magmatic system. Eruptions sourced from these pockets have generated numerous lava flows with trachytic compositions, which have occurred from the summit and flanks of Quetrupillán during the Holocene. Occasionally, some of the basaltic source melt has reached shallow levels within the plumbing system with minor interaction with the trachytic melt, resulting in the eruption of lavas with basalt, basaltic andesite and trachyandesite compositions. We propose a conceptual model for the magmatic system of Quetrupillán, in which the Liquiñe-Ofqui Fault Zone plays an important role in exerting a structural control on the crust on which Quetrupillán resides, influencing magma residence times and pathways to the surface.

1. Introduction

Petrological and geochemical studies allow us to unravel the evolution of magmatic systems, by determining the processes that magmas underwent before eruption at the surface. The textures of volcanic rocks record their magmatic history (Hersum and Marsh, 2007) and this can provide us with a first-order understanding of the magmatic plumbing system beneath a volcano. Current thinking about volcanic plumbing systems has moved away from the idea of magma chambers as spherical or oblate bodies of liquid magma below volcanoes (Daly, 1911; Marsh, 1989; Gudmundsson, 2012) to transcrustal magmatic systems composed of transient, interconnected lenses of magma within a crystal mush (Cashman et al., 2017; Magee et al., 2018). Partial melting in the mantle supplies basaltic melt and thermal energy to the base of these transcrustal magmatic systems, then the local and regional crustal tectonics influence whether this basaltic magma is able to reach the surface to erupt or whether it would stall within the crust and evolve into more differentiated products (López-Escobar et al., 1995; Cembrano and Lara, 2009). We explore the application of this concept at the Quetrupillán Volcanic Complex (39°30′ S, 71°43′ W) in the Southern Andes of Chile (Stern et al., 2007) and propose a conceptual model for its plumbing system.

2. Geological background

2.1. Regional geological setting

Subduction of the Nazca Plate below the South American Plate has resulted in the volcanic arc of the Andes along the western edge of South America (Stern, 2004; Stern et al., 2007). The rate and angle of convergence between these plates has varied through time, with alternating periods of rapid and slow convergence, at dextral-oblique or orthogonal angles (Pardo-Casas and Molnar, 1987). Slow convergence from the Late Cretaceous to Early Eocene was followed by a period of rapid convergence during the Late Eocene, before a return to slow convergence (3.5 ± 2.5 cm/yr) during the Oligocene (Pardo-Casas and Molnar, 1987). The current period of fast convergence has been active since 26 Ma (just before the start of the Miocene) with rates of up to 11 cm/yr. Convergence changed from orthogonal to dextral-oblique at 20 Ma (Pardo-Casas and Molnar, 1987; Cembrano et al., 2000).

* Corresponding author.
E-mail addresses: isla.simmons@ed.ac.uk (I.C. Simmons), joaquin.cortes@edgehill.ac.uk (J.A. Cortés), d.mcgarvie@lancaster.ac.uk (D. McGarvie), eliza.calder@ed.ac.uk (E.S. Calder).

https://doi.org/10.1016/j.jvolgeores.2020.107101
0377-0273/

The Southern Volcanic Zone (SVZ) of the Andes lies between 33° S and 46° S (Fig. 1; López-Escobar et al., 1995), coinciding with the subduction of the Juan Fernandez Ridge into the Peru-Chile trench at the northern end and with the subduction of the Chile Rise at the southern end (Stern, 2004; Stern et al., 2007). Beneath the SVZ, the crustal thickness decreases steadily from ~50 km at 33° S to 35 km at 46° S, with a corresponding decrease in elevation of the main cordillera, from 5000 m to less than 2000 m (Stern, 2004; Cembrano and Lara, 2009), and the angle of the subducted Nazca Plate increases from ~20° at the northern end to >25° at the southern end (Stern, 2004).

The dominant tectonic feature of the SVZ is the Liquiñe-Ofqui Fault Zone (LOFZ; Fig. 1), a ~1000 km long NNE-trending intra-arc fault system that dominates the tectonics of the region from 38° S to 47° S (Cembrano et al., 1996; Hernandez-Moreno et al., 2014). Transpression caused by the oblique convergence of the Nazca and South American Plates generated the LOFZ (Hervé, 1994; Cembrano et al., 2000), which has acted as a dextral transpressive strike-slip structure for at least the last 6 Ma (Cembrano and Lara, 2009).

Most Holocene volcanoes are located to the west of the LOFZ (e.g. Llaima, Villarrica, Mocho-Choshuenco and Calbuco). Between ~38.5° S and ~41.5° S the LOFZ splits into two parallel branches (Fig. 1; Cembrano and Lara, 2009), and a few volcanoes are located to the east of the eastern branch (e.g. Lanín and Tronador). Quetrupillán is unusual among the volcanoes of the SVZ as it is one of only two stratovolcanoes that lie between the two main branches of the LOFZ (the other being Sollipulli), though several stratovolcanoes appear to lie above or very close to the main trace of the LOFZ (e.g. Lonquimay and Yate; Fig. 1; Cembrano and Lara, 2009).

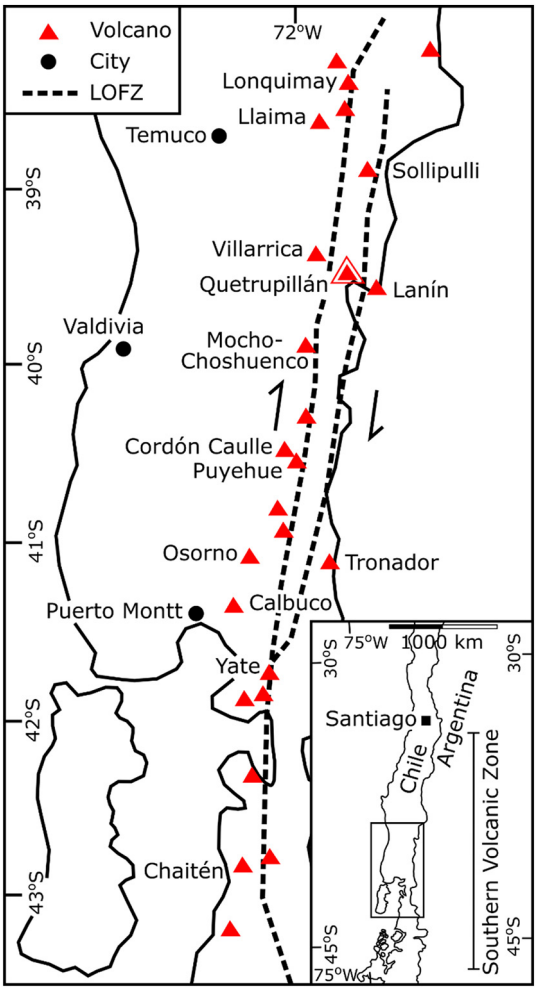

Fig. 1. The LOFZ (dashed line) between 38° S and 43.5° S, modified from Cembrano and Lara (2009). The northern terminus of the LOFZ is at 38° S, but it continues for a further ~400 km to the south of this map. Holocene stratovolcanoes are denoted by red triangles and major cities by black circles. Quetrupillán (highlighted) sits between the two main parallel branches of the LOFZ. The inset shows the location of this map and the Southern Volcanic Zone within Chile. (For interpretation of the references to colour in this figure legend, the reader is referred to the web version of this article.)

Primary melts in the SVZ are generated by dehydration of the subducted Nazca Plate and consequent partial melting of the lithospheric mantle wedge (Stern, 2004; Cembrano and Lara, 2009). Along-arc variations in the isotopic compositions of SVZ volcanic rocks indicate varying degrees of contribution from different processes in the production of these arc magmas (Cembrano and Lara, 2009). The signature of SVZ magmas can be altered by crustal assimilation (Hildreth and Moorbath, 1988), interaction with the continental lithosphere (Hickey-Vargas et al., 2002) and contamination of the magma source region due to subduction erosion (Stern, 1991). The relative contribution of the different processes will depend on a number of factors such as the composition and rheology of the continental crust, the crustal thickness, local and regional tectonic regimes (which will control magma ascent pathways), and the rate of subduction erosion (Cembrano and Lara, 2009).

Tholeiitic, high Al-basalts and basaltic andesites are the dominant products erupted from both stratovolcanoes and minor eruptive centres in the central and southern SVZ (south of 37° S; Hickey-Vargas et al., 1989; López-Escobar et al., 1995; Stern, 2004; Stern et al., 2007), while andesites, dacites and rhyolites are uncommon (Lara et al., 2006). The basalts of the central SVZ typically have lower than expected concentrations of MgO, Ni and Cr than basalts derived from primary mantle melts, which has been suggested to be due to deep fractional crystallisation (López-Escobar et al., 1995).

Regional tectonics control the alignment of volcanic chains in the SVZ, and the composition of erupted products. NE-striking alignments usually consist of basaltic and basaltic andesite stratovolcanoes and minor eruptive centres, while stratovolcanoes of a range of compositions are found in NW-striking alignments (López-Escobar et al., 1995; Cembrano and Lara, 2009). In general, NW-trending domains are more compressive, undergoing shortening and strike-slip deformation, resulting in longer magma residence time within the crust, allowing greater differentiation of eruptive products (López-Escobar et al., 1995; Cembrano and Lara, 2009).

2.2. The Quetrupillán Volcanic Complex

The Quetrupillán Volcanic Complex (Complejo Volcánico Quetrupillán), henceforth shortened to Quetrupillán, lies in the SVZ, at 39°30′ S, 71°43′ W. During the Holocene, activity at Quetrupillán has occurred from the summit of the stratocone and from at least sixteen vents around the flanks of the volcano (Fig. 2), of which twelve form a volcanic field on the southern flank. The presence of icefields during the Holocene has resulted in extensive scouring of the stratocone, removing volcanic products erupted from the summit and covering the upper flanks with glacial till (Simmons et al., 2020).

The sixteen flank vents display a range of features: some have constructed scoria cones, some have excavated craters, some have built tuff rings, and some have neither excavated a crater nor constructed any feature around the vent. Most vents have also effused lava flows, ranging in size from less than 1×10^6 m^3 to over 60×10^6 m^3, though three vents have not produced any associated lava flow (Simmons et al., 2020). The variation in vent features and morphology implies that a variety of eruption styles occurred around the flanks of Quetrupillán during the Holocene. Scoria cones were built by conventional Strombolian activity, with scoria and volcanic bombs formed by magma fragmentation following ballistic trajectories (Valentine and Gregg, 2008; Valentine and Connor, 2015). Excavated craters formed when rising magma encountered groundwater and resulted in explosive phreatic eruptions, with tuff rings constructed around some craters when sufficient water enabled phreatomagmatic eruptions (Wohletz and Sheridan, 1983; Lorenz, 1986).

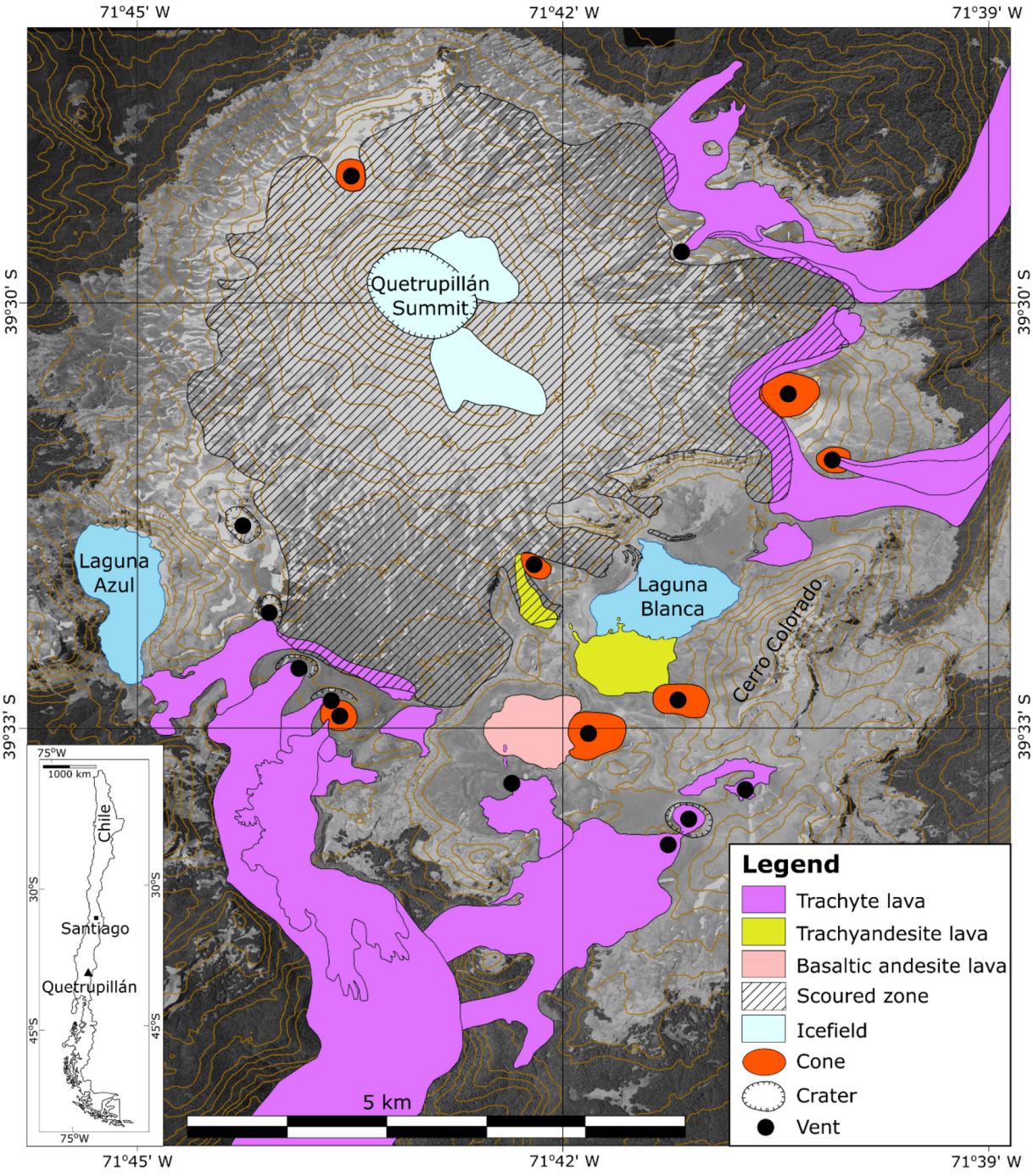

Fig. 2. Map of the Holocene geology of Quetrupillán from the satellite flank vents (modified from Simmons et al., 2020). The glacially scoured zone (indicated by the hatched area) prevents mapping of Holocene products erupted from the summit region. The aerial photo background image is from the Servicio Aerofotogramétrico (SAF), Chile, and 50 m interval contours were obtained from a digital elevation model downloaded from earthexplorer.usgs.gov (downloaded 21/10/2016). The inset shows the location of Quetrupillán in Chile.

No detailed geological map of Quetrupillán has been published, and although uneroded Holocene vents and lavas are obvious in the field, no detailed field-based study has been published on either the pre-Holocene volcanic formations or on the structural evolution of the volcanic complex. Reconnaissance-level mapping led to the suggestion that an 8 km diameter caldera may exist (Pavez, 1997), but this has never been confirmed by detailed field observations and evidence has not been evaluated in peer-reviewed literature. No conclusive evidence confirming the presence of a caldera at Quetrupillán was found during this study.

Most (~96.7%) lava erupted from flank vents during the Holocene is trachytic in composition, with only minor trachyandesite and basaltic andesite lavas erupted (Simmons et al., 2020). The flank lava flows are predominantly composed of blocky lavas consisting of angular blocks of black, glassy trachyte lava. Where sampled, the composition of cone material is the same as the composition of any corresponding lava flow.

3. Methods

3.1. Sampling

Two field seasons were conducted at Quetrupillán, in February 2017 and January 2018, to map Holocene eruptive products and features, and

to collect samples from lava deposits and pyroclastic sequences (see supplementary material for sample locations). Samples were collected from each Holocene lava flow produced by vents on the lower flanks of the volcano, and a selection of Holocene lavas erupted from the summit of the stratocone was also sampled. Pleistocene lavas were sampled by one of the authors (McGarvie) during prior field trips.

3.2. Geochemical analysis

Whole rock compositions of 66 Holocene and Pleistocene lavas and pyroclastic samples were analysed using a Panalytical PW2404 wavelength-dispersive sequential X-ray fluorescence (XRF) instrument, hosted at the University of Edinburgh (www.ed.ac.uk/geosciences/facilities/xrayfluorescence/xrf). Powdered samples were prepared as fused glass discs for major element analyses and pressed powder pellets for trace element analyses. Powders were heated at 1100 °C for 20 min and the loss on ignition (LOI) of volatiles was recorded, tephra samples having first been heated overnight at 450 °C to burn off any organic matter.

Rare earth element concentrations were measured in 14 selected samples (a sample from all, except two, flank vents) by inductively-coupled plasma mass spectrometry (ICP-MS). The analytical procedure is detailed in Olive et al. (2001), whereby dissolution of 0.1 g of sample powder was achieved by three-acid digestion (HF, HNO_3, HCl), followed by $HClO_4$ digestion to avoid the formation of insoluble fluorite and to ensure dissolution of spinel phases. Analyses were performed on the Agilent 7500ce ICP-MS instrument at the Scottish Universities Environmental Research Centre (SUERC; www.gla.ac.uk/research/az/suerc/researchthemes/isotopegeoscience/icp-ms-oes/), using the USGS BCR2 standard (Wilson, 1997) as a quality check.

Polished thin sections of 36 samples of lavas were cut, and these were studied under a petrological microscope. A subset of eighteen thin sections were analysed using the CAMECA SX100 electron microprobe at the University of Edinburgh (www.ed.ac.uk/geosciences/facilities/electron/instrumentspec) to determine mineral chemistry and glass compositions. Mineral phases were analysed using the following beam conditions: pyroxene with 2 μm beam diameter, 4 nA beam current and 15 kV accelerating voltage; plagioclase and olivine with initial conditions of 2 μm beam diameter, 4 nA beam current and 15 kV accelerating voltage, followed by 2 μm beam diameter, 100 nA beam current and 15 kV accelerating voltage; groundmass glass and melt inclusions were analysed with initial conditions of 5 μm beam diameter, 1 nA beam current and 15 kV accelerating voltage followed by 5 μm beam diameter, 80 nA beam current and 15 kV accelerating voltage. If measured, Na was analysed first to minimise its diffusion.

3.3. Geothermobarometry

Results from electron microprobe analysis (EMPA) of melt inclusions within clinopyroxene phenocryst hosts were used to estimate pressures and temperatures of crystallisation of Quetrupillán magmas. As the composition of the melt inclusion may continue to evolve due to post-entrapment fractionation, a correction for this was applied. Several post-entrapment corrections have been devised for the composition of melt inclusions hosted in olivine (e.g. Putirka, 2008; Danyushevsky and Plechov, 2011), based on the partition coefficient $K_D\,(Fe2+/Mg)^{ol\text{-}liq} = 0.3$ (Roeder and Emslie, 1970). This procedure involves adding the composition of the host olivine to the composition of the melt inclusion in 0.01% increments, until equilibrium is achieved. We adopted this approach to correct the composition of melt inclusions hosted in clinopyroxene, but with the following corrections: the partition coefficient is assumed to be $K_D\,(Fe2+/Mg)^{cpx\text{-}liq} = 0.23$ (Sisson and Grove, 1993); the speciation of iron in the clinopyroxene is calculated based on the charge balance in the mineral chemistry, following Papike et al. (1974) and Cameron and Papike (1981); the speciation of iron in the melt is calculated assuming the NNO buffer typical of arc products (Toplis and Carroll, 1995) and the calibration of Cortés et al. (2006).

Pressures were calculated using the clinopyroxene geobarometer of Nimis (1999a), computed using the CpxBar Excel spreadsheet (Nimis, 1999b), and temperatures were calculated from the clinopyroxene-liquid geothermometers presented as Eqs. 33 and 34 in Putirka (2008). Temperatures were calculated from Eq. 33, unless the concentrations of Al_2O_3 and Na_2O in the clinopyroxene host were such that the jadeite component yields negative values, in which case temperatures were calculated from Eq. 34. Both geothermometers (Eqs. 33 and 34) estimate temperatures with uncertainties of ±45 °C (Putirka, 2008) and estimated pressures have uncertainties of ±2 kbar (Nimis, 1999a). As the geothermometer requires an input of pressure and the geobarometer requires an input of temperature, these equations were solved iteratively until convergence of the results.

3.4. Structural analysis

The geometry of features and structures on Quetrupillán was measured from satellite imagery, downloaded from Google Earth and imported into Fiji (Schindelin et al., 2012). Visible features that were used in analysis include fissures, dykes, possible fault scarps, and orientation of asymmetric cones, as well as lineaments defined by topography and geomorphology. Many of these features were identified only from satellite imagery based on their aerial appearance, and so lack robust field evidence to support their identification. Holocene fissures were mapped in the field during this study, while Pleistocene fissures were mapped during previous fieldwork (McGarvie et al., 2014). Fault scarps were not examined in the field, and so field observations of features to confirm the identification of faults (e.g. slickensides, brecciation along fault planes etc.) are unavailable, as are data such as fault offsets and the direction of fault motion. The identification of possible faults is therefore an assumption. The orientation of each lineament was measured and converted from a mathematical angle to a geological strike (from North at 000°) using the Fiji plugin *Strike_Results.ijm* (Cortés, 2019). Lineament orientations were imported into Stereonet

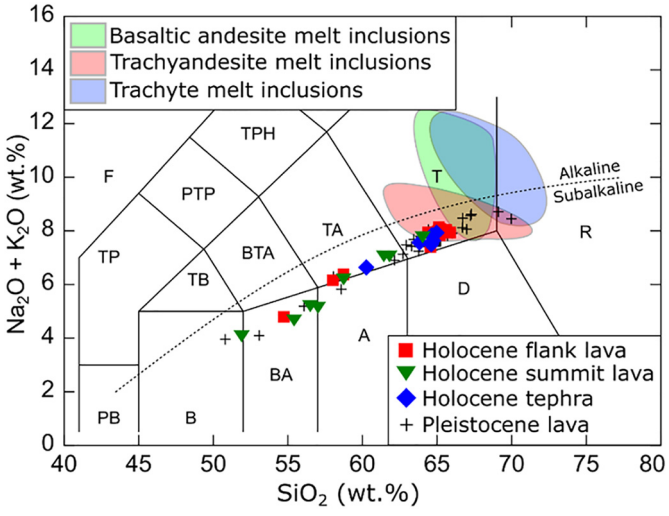

Fig. 3. Total alkali silica (TAS) plot with whole rock compositions of Holocene flank lavas (red squares), Holocene summit lavas (green triangles), Holocene tephra deposits (blue diamonds) and Pleistocene lavas (black crosses). Coloured regions indicate the composition of melt inclusions hosted in clinopyroxene crystals in lavas of different composition (green – basaltic andesite; red – trachyandesite; blue – trachyte). Classification is according to Le Maitre et al. (2002) and the dashed line represents the alkaline-subalkaline boundary proposed by Irvine and Baragar (1971). (For interpretation of the references to colour in this figure legend, the reader is referred to the web version of this article.)

(Allmendinger et al., 2013; Cardozo and Allmendinger, 2013) to generate rose diagrams.

4. Results

4.1. Geochemistry, petrography and mineral chemistry

Holocene lavas erupted from the summit of the stratocone range in composition from basalt to trachyte (52–64 wt% SiO_2, 3.0–4.5 wt% Na_2O, 1.0–3.2 wt% K_2O), while Holocene lavas erupted from the flank vents range in composition from basaltic andesite to trachyte (55–65 wt% SiO_2, 3.2–5.0 wt% Na_2O, 1.5–3.1 wt% K_2O; Fig. 3; Table 1 and in supplementary material). This is a narrower compositional range than the whole rock compositions of the sampled Pleistocene lavas, which span from basalt to rhyolite (50–69 wt% SiO_2, 2.9–5.6 wt % Na_2O, 0.9–3.6 wt% K_2O; Fig. 3; see supplementary material). Most Holocene lavas are trachytic (62–65 wt% SiO_2, 4.4–5.0 wt% Na_2O, 2.7–3.2 wt% K_2O). Twelve of the flank vents produced trachytic products, representing ~96.7% of the volume of Holocene lava erupted from flank vents (Simmons et al., 2020). Note that the "T" field on the Total Alkali Silica plot (Fig. 3) includes both trachytes and trachydacites, but following the criteria in Le Maitre et al. (2002) for distinguishing between them, the Quetrupillán rocks in the "T" field are all trachytes.

Trachyte lavas are porphyritic (Fig. 4A and B), containing 5–15% phenocrysts and glomerocrysts (normalised to vesicle-free). Plagioclase is the most abundant mineral phase, representing 50–70% of the phenocrysts, and has compositions from Andesine to Labradorite (An_{36-61}; Fig. 5A; Table 2). One population of plagioclases have partially resorbed cores, surrounded by a zone of more calcic composition, before a return to the original composition at the phenocryst rim (Fig. 6A and B).

Ortho- and clinopyroxene phenocrysts comprise 15–40% of the phenocryst population in trachyte lavas (Augite; Mg# 67–77, and Enstatite; Mg# 61–73; Fig. 5B). Trachyte lavas also contain Titanomagnetite and Ilmenite, which form a minor constituent of the phenocryst assemblage (2–10%; Fig. 5D).

Trachyte lavas have glassy groundmass with a composition of trachyte to rhyolite (63–72 wt% SiO_2, 4.0–6.9 wt% Na_2O, 1.8–5.7 wt% K_2O), containing microlites of the same mineral phases plus Pigeonite, and minor Apatite as an accessory phase. Melt inclusions within ortho- and clinopyroxene hosts have similar compositions (66–72 wt% SiO_2, 4.0–8.6 wt% Na_2O, 3.0–5.9 wt% K_2O) though some have anomalously high alkali contents (up to 12 wt% $Na_2O + K_2O$; Fig. 3).

Table 1
Whole rock geochemical analyses of representative samples from Quetrupillán. Major element analyses are in wt% and trace element analyses are in ppm. Some trace elements were not determined (n.d.) or below detection limit (b.d.l.). Samples marked * were analysed by ICP-MS for La, Ce, Pr, Nd, Sm, Eu, Gd, Tb, Dy, Ho, Er, Tm, Yb, Lu, Hf, Pb, Th and U. All other analyses were done by XRF. Results of all samples analysed during this study are available in the supplementary material.

Sample	Q3*	Q8*	Q50*	Q62	Q60	Q63	Q67	Q26
Comp.	Trachyte	Trachyandesite	Basaltic andesite	Trachyte	Trachyandesite	Basaltic andesite	Basalt	Trachyte
Source /type	Flank	Flank	Flank	Summit	Summit	Summit	Summit	Tephra
SiO_2	64.96	58.66	54.84	63.56	58.25	55.37	51.93	64.34
TiO_2	1.11	1.36	1.04	1.24	1.17	1.06	1.06	1.14
Al_2O_3	15.36	16.17	16.23	14.97	16.08	16.03	17.87	15.51
$Fe_2O_3^T$	5.54	8.16	8.80	6.39	7.64	8.01	8.97	5.71
MnO	0.13	0.13	0.14	0.13	0.13	0.14	0.15	0.13
MgO	1.21	2.89	6.50	1.39	3.49	5.12	6.37	1.26
CaO	3.11	5.88	7.67	3.48	5.96	6.94	9.33	3.33
Na_2O	4.85	3.92	3.22	4.51	3.80	3.32	3.02	4.74
K_2O	3.05	2.34	1.48	3.16	2.31	1.74	1.01	2.95
P_2O_5	0.33	0.36	0.28	0.43	0.35	0.28	0.31	0.35
LOI	0.20	−0.02	−0.21	−0.06	−0.14	−0.04	−0.21	0.30
Total	99.84	99.84	100.00	99.19	99.04	97.96	99.80	99.77
Sc	16.6	24.3	27.3	18.9	22.4	24.7	28.1	17.4
V	63.7	228.8	210.5	95.7	172.6	192.8	214.4	70.4
Cr	4.0	28.2	179.8	3.1	59.9	154.9	164.9	4.3
Ni	b.d.l.	18.6	78.3	1.3	27.8	66.2	66.4	b.d.l.
Cu	14.5	59.9	56.7	21.0	46.3	44.1	63.2	15.5
Zn	71.2	76.1	74.4	75.9	69.9	68.7	65.7	75.4
Rb	77.8	60.3	36.2	82.1	60.4	43.9	22.0	74.7
Sr	284.3	371.8	429.4	276.9	389.5	403.5	568.1	301.7
Y	44.4	36.9	27.5	47.7	35.7	30.2	22.9	43.9
Zr	352.2	270.6	174.3	378.9	271.8	205.6	124.1	334.6
Nb	14.1	10.9	7.4	15.2	11.2	8.5	6.8	13.2
Ba	737.8	583.2	383.0	713.1	553.2	445.1	334.8	729.7
La	33.82	25.46	18.16	35.9	25.6	19.4	14.3	32.3
Ce	75.53	56.85	40.52	83.8	60.4	47.8	39.4	79.7
Pr	9.32	7.16	5.21	n.d.	n.d.	n.d.	n.d.	n.d.
Nd	37.31	29.12	21.59	42.0	32.3	24.5	20.3	39.2
Sm	7.73	6.20	4.70	n.d.	n.d.	n.d.	n.d.	n.d.
Eu	1.78	1.47	1.25	n.d.	n.d.	n.d.	n.d.	n.d.
Gd	7.43	5.95	4.51	n.d.	n.d.	n.d.	n.d.	n.d.
Tb	1.13	0.91	0.70	n.d.	n.d.	n.d.	n.d.	n.d.
Dy	6.84	5.44	4.16	n.d.	n.d.	n.d.	n.d.	n.d.
Ho	1.39	1.10	0.84	n.d.	n.d.	n.d.	n.d.	n.d.
Er	4.23	3.31	2.51	n.d.	n.d.	n.d.	n.d.	n.d.
Tm	0.69	0.52	0.39	n.d.	n.d.	n.d.	n.d.	n.d.
Yb	4.29	3.28	2.46	n.d.	n.d.	n.d.	n.d.	n.d.
Lu	0.67	0.51	0.37	n.d.	n.d.	n.d.	n.d.	n.d.
Hf	7.89	5.77	3.76	n.d.	n.d.	n.d.	n.d.	n.d.
Pb	24.74	17.54	11.19	n.d.	n.d.	n.d.	n.d.	21.3
Th	9.88	7.13	4.31	n.d.	n.d.	n.d.	n.d.	9.7
U	2.71	1.99	1.22	n.d.	n.d.	n.d.	n.d.	2.7

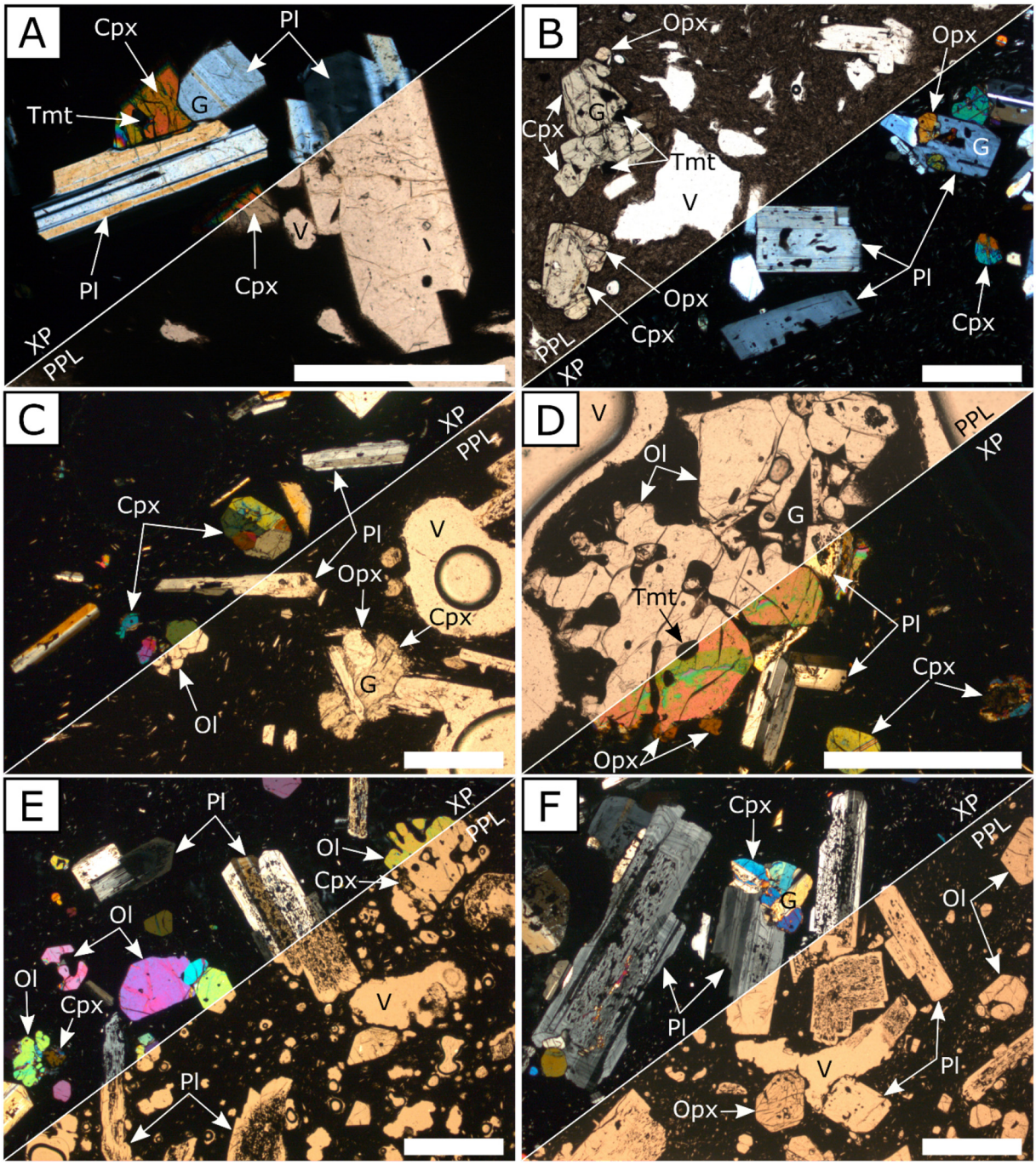

Fig. 4. Thin section images of lavas from flank vents at Quetrupillán, of trachyte (A and B), trachyandesite (C and D) and basaltic andesite (E and F) composition. Pl – plagioclase, Cpx – clinopyroxene, Opx – orthopyroxene, Ol – olivine, Tmt – titanomagnetite, V – vesicle, G – glomerocryst. Scale bar in each image is 1 mm. Images show thin sections under plane polarised light (PPL) and under crossed polars (XP). Modified from Simmons et al. (2020).

Two Holocene flank vents produced trachyandesite lava flows, representing ~1.8% of the volume of Holocene lava erupted from flank vents (Simmons et al., 2020). Trachyandesite lavas are also porphyritic (Fig. 4C and D) and have a higher abundance of phenocrysts and glomerocrysts than trachyte lavas (~30%). Plagioclase is the dominant mineral phase (~60%), with compositions varying from Labradorite to Bytownite (An_{51-84}; Fig. 5A). There are two distinct plagioclase populations, one of pristine phenocrysts and one showing sieve textures (Fig. 6C and D). Ortho- and clinopyroxene phenocrysts (~23%) occur as Augite to Diopside (Mg# 67–82) and rare Enstatite (Mg# ~68; Fig. 5B). Trachyandesite lavas also contain ~15% olivine (Fo_{57-70}; Fig. 5C), often with resorbed rims, and ~2% Titanomagnetite (Fig. 5D). The groundmass of trachyandesite lavas is fully crystalline, composed of the same mineral phases, though plagioclase groundmass crystals are more sodic with a composition of Andesine (An_{39-42}; Fig. 5A). Melt inclusions in clinopyroxene hosts have trachytic to rhyolitic glass compositions (62–70 wt% SiO_2, 4.4–6.0 wt% Na_2O, 2.2–5.4 wt% K_2O; Fig. 3).

Only one Holocene flank vent produced a basaltic andesite lava flow, accounting for ~1.5% of the volume of Holocene lava erupted from flank vents (Simmons et al., 2020). The basaltic andesite lava is porphyritic, with ~37% phenocrysts (Fig. 4E and F). Plagioclase is still the most

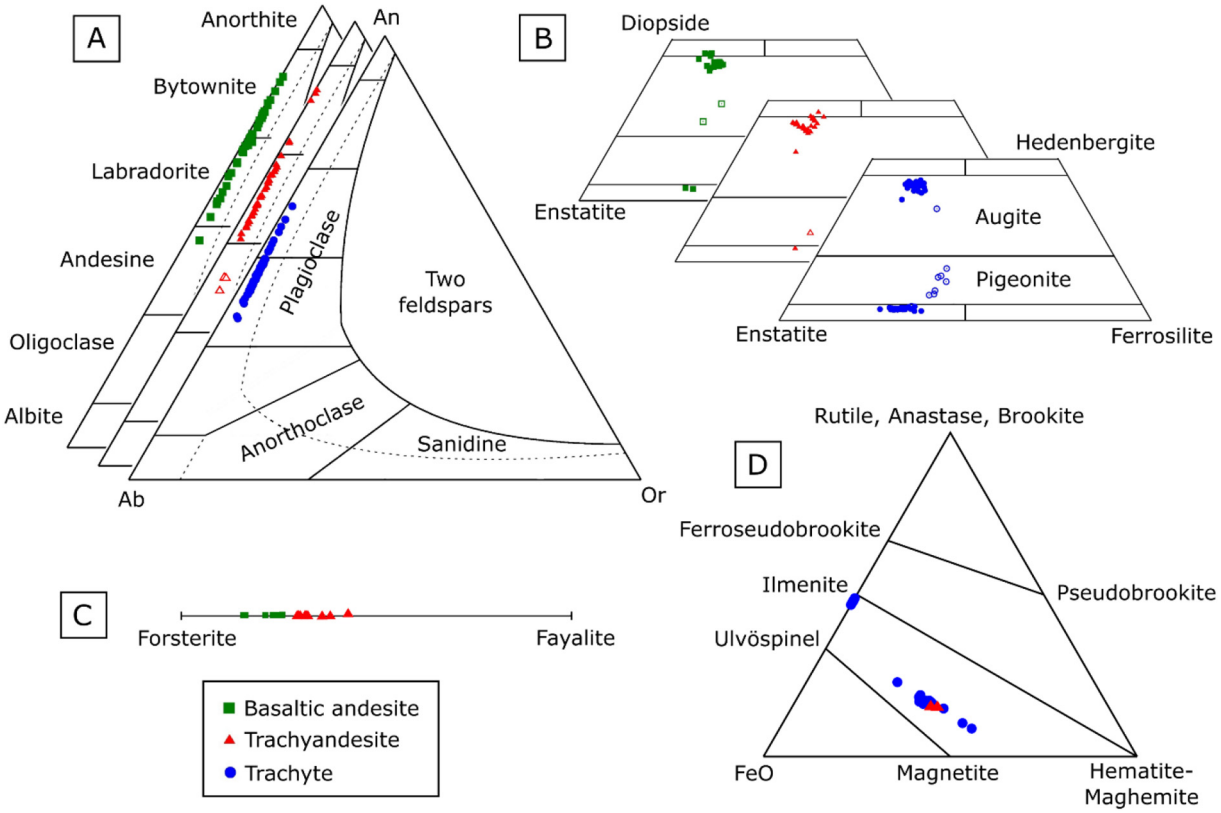

Fig. 5. Mineral chemistry of plagioclase (A), pyroxene (B), olivine (C) and oxide (D) phenocrysts are arranged by whole rock composition: basaltic andesite – green squares, trachyandesite – red triangles, trachyte – blue circles. Open symbols represent groundmass microlites. (For interpretation of the references to colour in this figure legend, the reader is referred to the web version of this article.)

abundant mineral phase, comprising ~40% of the phenocrysts, with compositions ranging from Andesine to Bytownite ($An_{47–84}$; Fig. 5A). Phenocrysts are up to 2 mm, and most have highly sieve-textured interiors though some have pristine textures (Fig. 6E and F). The secondary phenocryst phase in basaltic andesite lava is olivine ($Fo_{74–84}$; Fig. 5C) which accounts for ~35% of the phenocrysts. Some olivines have resorbed rims while others display pristine crystal morphologies (Fig. 4E). Ortho- and clinopyroxene phenocrysts comprise ~23% of phenocrysts in the basaltic andesite lava and consist of Augite to Diopside (Mg# 69–81) and rare Enstatite (Mg# 69–72; Fig. 5B). There is also minor (~2%) Cr-spinel as an accessory phase. Melt inclusions in clinopyroxene hosts have compositions of trachyte (64–69 wt% SiO_2, 3.8–6.5 wt% Na_2O, 2.2–6.4 wt% K_2O; Fig. 3).

The rare earth elements (REE) diagram (Fig. 7A), normalised to chondrite (Sun and McDonough, 1989), discriminates between the three different lava compositions. Trachyte lavas have the greatest values of rock/chondrite for each element, while the basaltic andesite lava has the lowest values. Lavas of all three composition have a gentle slope (La/Yb ~7–9) and display a small negative Eu anomaly. The spider diagram (Fig. 7B; Pearce, 1983), normalised to normal mid ocean ridge basalt (N-MORB) according to Sun and McDonough (1989), also distinguishes between the three lava compositions. All lavas have a small negative Nb anomaly and are enriched in high field strength elements (HFSE) compared to N-MORB. Trace element ratio plots (Fig. 7C-F) also distinguish between samples of different whole rock composition. Plotting Rb against Cr (Fig. 7F) shows a steepening curve from basaltic andesite to trachyandesite to trachyte.

4.2. Geothermobarometry

Seventeen pairs of melt inclusions within clinopyroxene hosts were used to estimate temperatures and pressures of crystallisation in trachyte, trachyandesite and basaltic andesite magmas (Fig. 8; see supplementary material). Calculated temperatures range from 913 to 1020 ± 45 °C for trachyte lavas, 997–1001 ± 45 °C for trachyandesite lava and 941–1022 ± 45 °C for basaltic andesite lavas. Pressures range from 1.2–6.9 ± 2 kbar for trachyte lavas, 3.2–4.0 ± 2 kbar for trachyandesite lava and 3.5–6.1 ± 2 kbar for basaltic andesite lavas. Assuming a crustal density of 2800 kg/m^3 (Weidmann et al., 2013), these pressures correspond to depths of ~4–25 km for trachyte lavas, ~12–15 km for trachyandesite lava and ~13–22 km for basaltic andesite lava, with most calculated depths between 7 and 19 km (Fig. 8). It should be noted that no independent determination of crystallisation pressures and temperatures was achieved, as these two variables were solved iteratively.

Unlike the clinopyroxene-liquid geothermometer of Putirka (2008), which depends upon the composition of the melt in equilibrium with the clinopyroxene, the geobarometer of Nimis (1999a) depends upon the clinopyroxene composition and the nature of the magma (subalkaline in the case of Quetrupillán; Fig. 3), to estimate pressures of crystallisation. As the equilibrium melt is not necessary for estimation of pressure, the geobarometer was also used to estimate the pressures of crystallisation for 40 clinopyroxene phenocrysts in trachyte lavas that do not contain melt inclusions (i.e. do not have a proxy of the equilibrium melt), in order to increase the dataset. EMPA analyses were made in the core of clinopyroxene phenocrysts, and a temperature of 968 °C was used for all pressure calculations, as this is the average of temperatures calculated iteratively from clinopyroxene-melt pairs. This generated pressure estimates of 2.3–4.8 ± 2 kbar, corresponding to depths of ~8–18 km (Fig. 8), within the range of pressures estimated from clinopyroxene-melt pairs.

4.3. Structural analysis

Forty-four lineaments (e.g. fissures, dykes, possible fault scarps) were identified and measured from satellite imagery of Quetrupillán,

Table 2
Mineral analyses of representative minerals from samples of Quetrupillán lavas. Analyses were made by EMPA and are in wt%. Cations per formula unit (c.f.u.) were recalculated based on the number of oxygen (N.O.). Some elements were below detection limit (b.d.l.). Results of all mineral analyses are available in the supplementary material. Speciation of iron was estimated following Papike et al. (1974).

Mineral	Augite	Augite	Augite	Augite	Augite	Augite	Enstatite	Enstatite	Enstatite	Pigeonite
Analysis	Core	Core	Core	Core	Core	Core	Core	Core	Core	Microlite
Lava composition	Basaltic andesite	Basaltic andesite	Trachy-andesite	Trachy-andesite	Trachyte	Trachyte	Trachy-andesite	Trachyte	Trachyte	Trachyte
Sample	Q50	Q50	Q8	Q8	Q3	Q3	Q8	Q3	Q3	Q7
SiO_2	51.90	52.38	50.44	51.87	51.81	51.44	53.58	52.38	52.94	52.42
TiO_2	0.71	0.58	0.72	0.72	0.83	0.66	0.40	0.32	0.46	0.67
Al_2O_3	2.03	1.51	1.93	2.01	2.02	1.60	0.94	0.58	1.18	1.45
FeO^T	9.64	9.79	9.34	9.34	10.57	11.49	18.54	19.47	20.90	22.94
MnO	0.26	0.30	0.30	0.29	0.48	0.57	0.45	0.72	0.79	n.d.
MgO	14.17	13.77	15.50	13.70	14.73	13.70	22.60	23.73	21.00	18.62
NiO	0.02	0.03	b.d.l.	0.02	b.d.l.	b.d.l.	0.04	b.d.l.	b.d.l.	b.d.l.
CaO	20.38	20.38	20.07	20.35	20.17	18.89	1.97	1.80	2.06	3.91
Na_2O	0.32	0.32	0.32	0.30	0.37	0.32	0.03	0.03	0.04	n.d.
Total	99.42	99.05	98.61	98.59	100.98	98.67	98.55	99.03	99.37	100.01
N.O.	6	6	6	6	6	6	6	6	6	6
Si	1.9460	1.9711	1.9108	1.9578	1.9235	1.9563	1.9946	1.9581	1.9808	1.9714
Ti	0.0200	0.0164	0.0205	0.0204	0.0232	0.0189	0.0112	0.0090	0.0129	0.0190
Al	0.0897	0.0670	0.0862	0.0894	0.0884	0.0717	0.0412	0.0256	0.0520	0.0643
Fe^{3+}	0.0016	0.0000	0.0741	0.0000	0.0449	0.0015	0.0000	0.0424	0.0000	0.0000
Fe^{2+}	0.3007	0.3081	0.2218	0.2948	0.2833	0.3640	0.5772	0.5663	0.6540	0.7215
Mn	0.0083	0.0096	0.0096	0.0093	0.0151	0.0184	0.0142	0.0228	0.0250	0.0000
Mg	0.7921	0.7725	0.8754	0.7709	0.8153	0.7768	1.2543	1.3225	1.1714	1.0439
Ni	0.0006	0.0009	0.0000	0.0006	0.0000	0.0000	0.0012	0.0000	0.0000	0.0000
Ca	0.8186	0.8216	0.8145	0.8229	0.8022	0.7697	0.0786	0.0721	0.0826	0.1575
Na	0.0233	0.0233	0.0235	0.0220	0.0266	0.0236	0.0022	0.0022	0.0029	0.0000
Cation sum	4.00	3.99	4.04	3.99	4.02	4.00	3.97	4.02	3.98	3.98
Mg#	72	71	79	72	73	67	68	69	63	59

Mineral	Plagioclase (sieve)	Plagioclase (sieve)	Plagioclase (pristine)	Plagioclase (sieve)	Plagioclase (microlite)	Plagioclase (pristine)	Plagioclase (pristine)	Plagioclase (pristine)
Analysis	Core	Core	Core	Core	Microlite	Core	Middle	Rim
Lava composition	Basaltic andesite	Basaltic andesite	Trachy-andesite	Trachy-andesite	Trachy-andesite	Trachyte	Trachyte	Trachyte
Sample	Q50	Q50	Q8	Q8	Q8	Q3	Q3	Q3
SiO_2	49.42	53.90	52.12	47.43	56.56	57.95	56.91	58.02
TiO_2	0.04	0.06	0.05	0.03	0.13	0.06	0.06	0.06
Al_2O_3	31.44	28.16	29.99	32.99	25.22	26.38	27.00	26.66
$Fe_2O_3^T$	0.67	0.65	0.73	0.71	1.16	0.53	0.54	0.50
SrO	0.13	0.13	0.14	0.12	0.16	0.12	0.13	0.14
MnO	b.d.l.	0.01	b.d.l.	b.d.l.	0.01	b.d.l.	0.01	b.d.l.
MgO	0.10	0.11	0.09	0.06	0.13	0.04	0.04	0.05
CaO	15.18	11.65	13.56	17.32	8.94	8.88	9.71	9.22
Na_2O	2.71	4.56	3.64	2.05	6.41	6.28	5.52	5.98
K_2O	0.13	0.26	0.20	0.07	0.61	0.41	0.35	0.37
Total	99.81	99.50	100.51	100.79	99.32	100.66	100.26	100.98
N.O.	8	8	8	8	8	8	8	8
Si	2.2691	2.4566	2.3645	2.1737	2.5805	2.5891	2.5547	2.5824
Ti	0.0014	0.0021	0.0017	0.0010	0.0045	0.0020	0.0020	0.0020
Al	1.7012	1.5125	1.6034	1.7818	1.3560	1.3890	1.4284	1.3984
Fe^{3+}	0.0231	0.0223	0.0249	0.0245	0.0397	0.0178	0.0182	0.0167
Sr	0.0035	0.0034	0.0037	0.0032	0.0042	0.0031	0.0034	0.0036
Mn	0.0000	0.0004	0.0000	0.0000	0.0004	0.0000	0.0004	0.0000
Mg	0.0068	0.0075	0.0061	0.0041	0.0088	0.0027	0.0027	0.0033
Ca	0.7467	0.5688	0.6591	0.8504	0.4370	0.4250	0.4670	0.4396
Na	0.2412	0.4029	0.3201	0.1821	0.5670	0.5440	0.4804	0.5160
K	0.0076	0.0151	0.0116	0.0041	0.0355	0.0234	0.0200	0.0210
Cation sum	5.00	4.99	5.00	5.03	5.04	5.00	4.98	4.98
%An	75	58	67	82	42	43	48	45

Mineral	Olivine	Olivine	Olivine	Olivine
Analysis	Core	Core	Core	Core
Lava composition	Basaltic andesite	Basaltic andesite	Trachy-andesite	Trachy-andesite
Sample	Q50	Q50	Q8	Q8
SiO_2	39.83	38.33	35.63	36.97
Al_2O_3	0.06	0.03	0.02	0.03
FeO	15.15	22.70	33.51	27.00
MnO	0.21	0.38	0.54	0.45
MgO	44.86	38.97	30.39	35.61

Table 2 (*continued*)

Mineral	Olivine	Olivine	Olivine	Olivine
Analysis	Core	Core	Core	Core
Lava composition	Basaltic andesite	Basaltic andesite	Trachy-andesite	Trachy-andesite
Sample	Q50	Q50	Q8	Q8
NiO	0.23	0.10	0.05	0.09
CaO	0.19	0.18	0.21	0.18
P_2O_5	0.04	0.05	0.05	b.d.l.
Total	100.58	100.74	100.40	100.34
N.O.	4	4	4	4
Si	0.9960	0.9924	0.9798	0.9837
Al	0.0018	0.0009	0.0006	0.0009
Fe^{2+}	0.3168	0.4915	0.7707	0.6008
Mn	0.0044	0.0083	0.0126	0.0101
Mg	1.6723	1.5042	1.2459	1.4125
Ni	0.0046	0.0021	0.0011	0.0019
Ca	0.0051	0.0050	0.0062	0.0051
P	0.0008	0.0011	0.0012	0.0000
Cation sum	3.00	3.01	3.02	3.02
%Fo	84	75	61	70

Mineral	Cr-spinel	Cr-spinel	Ilmenite	Ilmenite	Magnetite	Magnetite
Analysis	Core	Core	Core	Core	Core	Core
Lava composition	Basaltic andesite	Basaltic andesite	Trachyte	Trachyte	Trachyte	Trachyte
Sample	Q50	Q50	Q12	Q69	Q53	Q61
TiO_2	0.76	6.24	49.21	47.76	17.55	17.24
Al_2O_3	22.65	10.22	0.36	0.46	2.89	2.77
Cr_2O_3	30.05	21.63	b.d.l.	b.d.l.	b.d.l.	b.d.l.
FeO^T	37.14	55.49	46.28	46.85	75.79	76.04
MnO	b.d.l.	b.d.l.	b.d.l.	0.77	0.60	0.72
MgO	9.88	6.69	3.23	3.97	2.58	3.20
Total	100.48	100.27	99.08	99.81	99.41	99.97
N.O.	8	8	3	3	4	4
Ti	0.0373	0.3430	0.9396	0.9102	0.5321	0.5198
Al	1.7417	0.8801	0.0108	0.0137	0.1373	0.1308
Cr	1.5501	1.2495	0.0000	0.0000	0.0000	0.0000
Fe^{2+}	2.0266	3.3909	0.9823	0.9925	2.5544	2.5486
Mn	0.0000	0.0000	0.0000	0.0165	0.0205	0.0244
Mg	0.9611	0.7288	0.1222	0.1499	0.1550	0.1912
Cation sum	6.32	6.59	2.05	2.08	3.40	3.41

and their orientations were plotted in rose diagrams (Fig. 9). When considering the whole area around Quetrupillán, lineaments have a primary preferential orientation of NW-SE and a secondary orientation of NNE-SSW (Fig. 9B). No lineaments are oriented W-E, and almost none are oriented N-S. Most observed lineaments are oriented tangentially to the summit, rather than radially to it. However, as the scoured zone is covered with glacial till, there may be radially-oriented lineaments around the stratocone summit that have not been observed.

To enable comparison of lineaments across different zones of Quetrupillán, the volcano was divided into quadrants, centred on the southern rim of the summit crater (due to the asymmetric shape of the main edifice this is more central than the middle of the crater; Fig. 9A) and aligned N-S as this is the approximate orientation of the LOFZ. This division results in clear differences in lineament orientation across different flanks of the volcano (Fig. 9C). In the northeast and southwest quadrants, lineaments are mainly oriented NW-SE, while in the southeast quadrant, lineaments are mostly perpendicular to this orientation, aligned NE-SW. In the northwest quadrant, lineaments mainly follow two preferred orientations at NW-SE and NNE-SSW. Differences in lineament orientation across flanks are also observed when the flanks are divided into North, South, East and West (Fig. 9D). Lineaments in the western and southern quadrants are mainly oriented NW-SE. In the eastern quadrant lineaments have two perpendicular orientations at NE-SW and NW-SE. Lineaments in the northern quadrant show no preferential orientation.

5. Discussion

5.1. Petrology and geochemistry

Clinopyroxene phenocrysts in basaltic andesite and trachyandesite lavas, erupted from the flanks and summit of Quetrupillán, contain melt inclusions of trachytic composition (Fig. 3). They also show an overlap in ranges of pressures and temperatures of crystallisation calculated by geothermobarometry (Fig. 8). The composition of these melt inclusions, and the pressure and temperature results, strongly suggest that these clinopyroxene phenocrysts crystallised in a trachytic melt and they are xenocrysts in the basaltic andesite and trachyandesite lavas.

The basaltic andesite and trachyandesite lavas also contain uncommon phenocrysts of orthopyroxene which exist alongside the abundant phenocrysts of olivine (Figs. 4 and 5). As olivine and orthopyroxene should not co-exist in equilibrium within a melt (e.g. Carmichael et al., 1970), the presence of these phases strongly suggests that magma mixing has resulted in hybrid compositions. The high Forsterite content of olivines in the basaltic andesite lava ($Fo_{74–84}$) indicates that they have crystallised from a relatively primitive basaltic melt. In contrast, the orthopyroxene phenocrysts have crystallised in a more evolved melt. Like the clinopyroxenes with trachytic melt inclusions, the orthopyroxene phenocrysts are likely to be xenocrysts in the basaltic andesite and trachyandesite lavas. Olivine phenocrysts in the trachyandesite lavas have lower Forsterite contents ($Fo_{57–70}$), which suggests that olivine

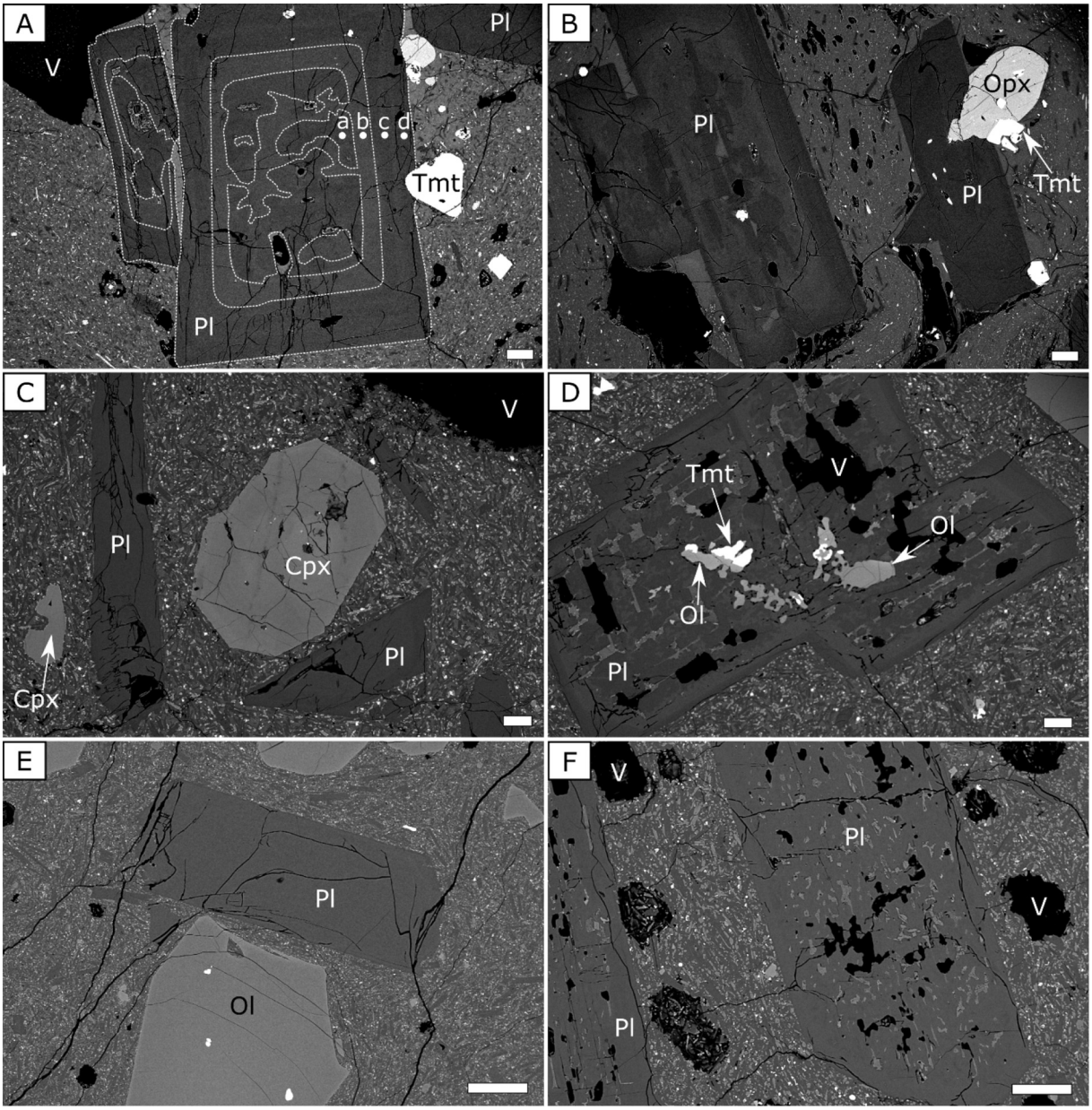

Fig. 6. BSE images of different populations of plagioclase phenocrysts. A) A plagioclase phenocryst in trachyte lava with a partially resorbed core (a – An_{47}), surrounded by a more calcic zone (b – An_{54}), before a return to the original composition for the rim (c – An_{46}; d – An_{46}); B) plagioclase phenocrysts in trachyte lava, with partially resorbed core (left) and pristine texture (right); C) pristine plagioclase phenocrysts in trachyandesite lava; D) sieve-textured plagioclase phenocryst in trachyandesite lava; E) pristine plagioclase phenocryst in basaltic andesite; F) sieve-textured plagioclase phenocrysts in basaltic andesite. Pl – plagioclase, Cpx – clinopyroxene, Opx – orthopyroxene, Ol – olivine, Tmt – titanomagnetite, V – vesicle. Scale bar in each image is 100 μm.

continued to crystallise in the hybrid trachyandesite melt after the mixing event.

In contrast to the basaltic andesite and trachyandesite lavas, the mineral assemblage in the Holocene trachytes appears to be in equilibrium with the whole rock composition. The trachyte lavas contain two pyroxene populations (opx and cpx) and plagioclase with compositions of Andesine to Labradorite ($An_{36–61}$), within trachytic to rhyolitic glass (Figs. 3 and 5). This strongly suggests that the phenocryst assemblage in the trachyte lavas crystallised from the melt represented by the whole rock composition. However, variations in the composition of melt inclusions, groundmass glass and the plagioclase phase suggest a range of melt compositions from which the trachyte lavas have been derived. Within individual samples, melt inclusions in ortho- and clinopyroxenes have similar compositions to groundmass glasses, suggesting that trachyte lavas crystallised in equilibrium with the melt in which they formed. This crystallisation is calculated to have occurred over a wide range of pressures (Fig. 8), suggesting that crystallisation of clinopyroxene phenocrysts happened across a range of depths (~7–19 km) below the volcano.

5.2. Textural implications

Sieve-textured plagioclases are uncommon in Quetrupillán's trachyte lavas, but abundant in trachyandesite and basaltic andesite lavas, where many plagioclase phenocrysts have well defined sieve textures (Figs. 4 and 6). The mineral chemistries of plagioclase phenocrysts appear to be in chemical equilibrium with their whole rock composition ($An_{47–84}$ in the basaltic andesite, $An_{51–84}$ in the trachyandesite and $An_{36–61}$ in the trachyte), suggesting that the sieve textures are not the result of magma mixing leading to chemical disequilibrium. If sieve texture is not the

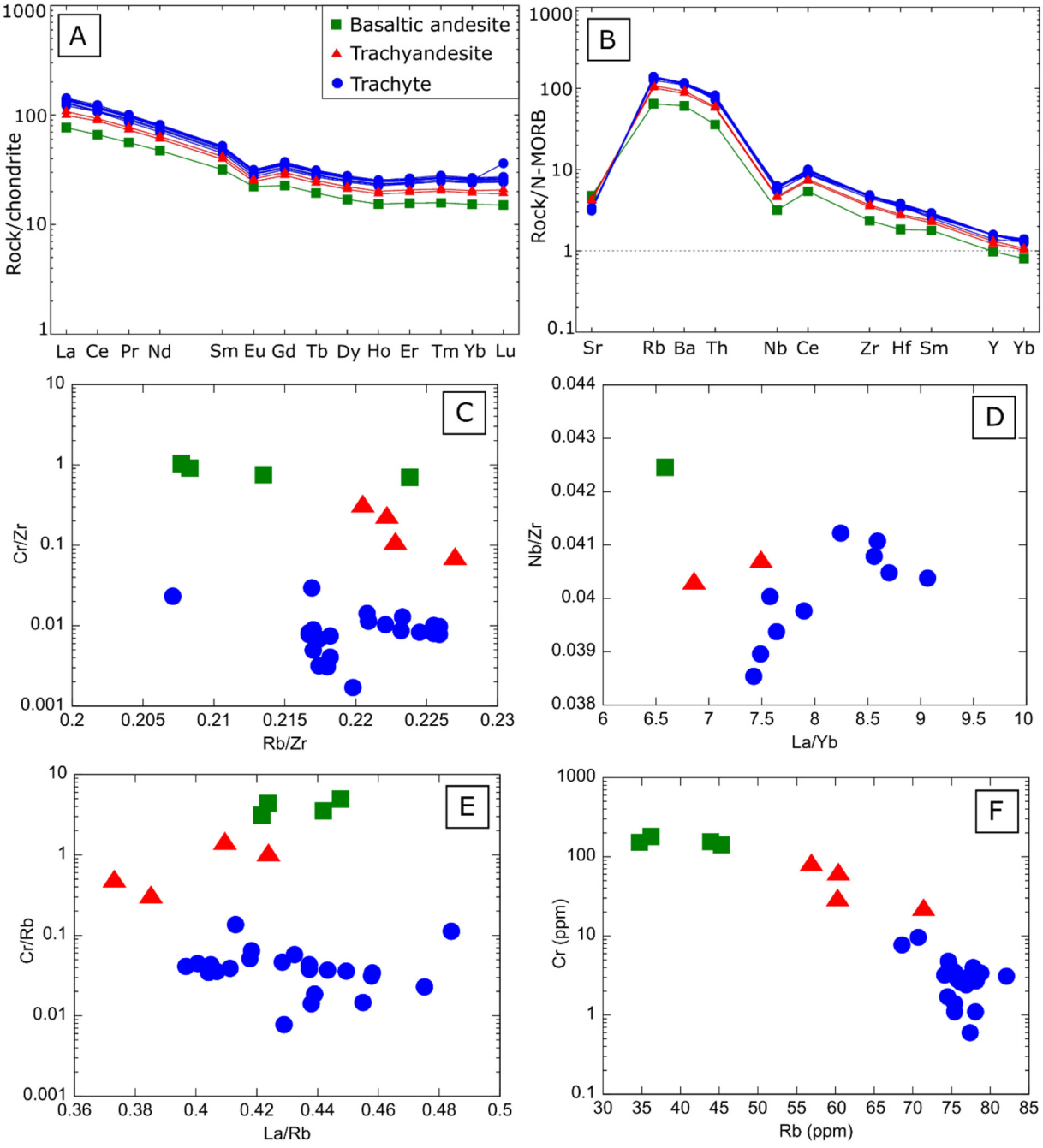

Fig. 7. Rare earth and trace element plots. A) REE diagram, normalised to chondrite (Sun and McDonough, 1989); B) spider diagram (Pearce, 1983), normalised using N-MORB (Sun and McDonough, 1989), with large ion lithophile elements (LILE) to the left and high field strength elements (HFSE) to the right; C) Rb/Zr vs Cr/Zr; D) La/Yb vs Nb/Zr; E) La/Rb vs Cr/Rb and F) Rb vs Cr. Sample symbols are according to whole rock composition: basaltic andesite – green squares, trachyandesite – red triangles, trachyte – blue circles. (For interpretation of the references to colour in this figure legend, the reader is referred to the web version of this article.)

consequence of chemical disequilibrium, it can be produced by increasing temperature or decreasing pressure (Nelson and Montana, 1992). As we have estimated a wide range of pressures for the magmatic system, we favour rapid decompression during magma ascent. Along these lines, the occurrence of zoned plagioclases could be interpreted as crystal growth happening in a heterogeneous melt or in a melt of changing compositions, or as a result of mixing events (e.g. Ginibre et al., 2002).

5.3. REE and trace elements

The REE profiles of trachyte, trachyandesite and basaltic andesite lavas (Fig. 7A) all have a gentle slope and display a small negative Eu anomaly, suggesting fractionation of plagioclase in the mantle source (Rollinson, 1993), which is the dominant mineral phase in all Quetrupillán lavas. The relatively flat REE profile (La/Yb ~7–9; Fig. 7D) suggests there has been little or no fractionation of garnet, following the extraction of the parental melt from the mantle source, as this would lead to a steeper REE profile (Rollinson, 1993). The absence of garnet fractionation in the generation of Quetrupillán melts suggests that the primary melts have been generated within the lithospheric mantle.

The spider diagram (Fig. 7B) of Holocene lava samples from Quetrupillán shows enrichment of HFSEs compared to an uncontaminated melt derived from a N-MORB source. In comparison, the HFSEs

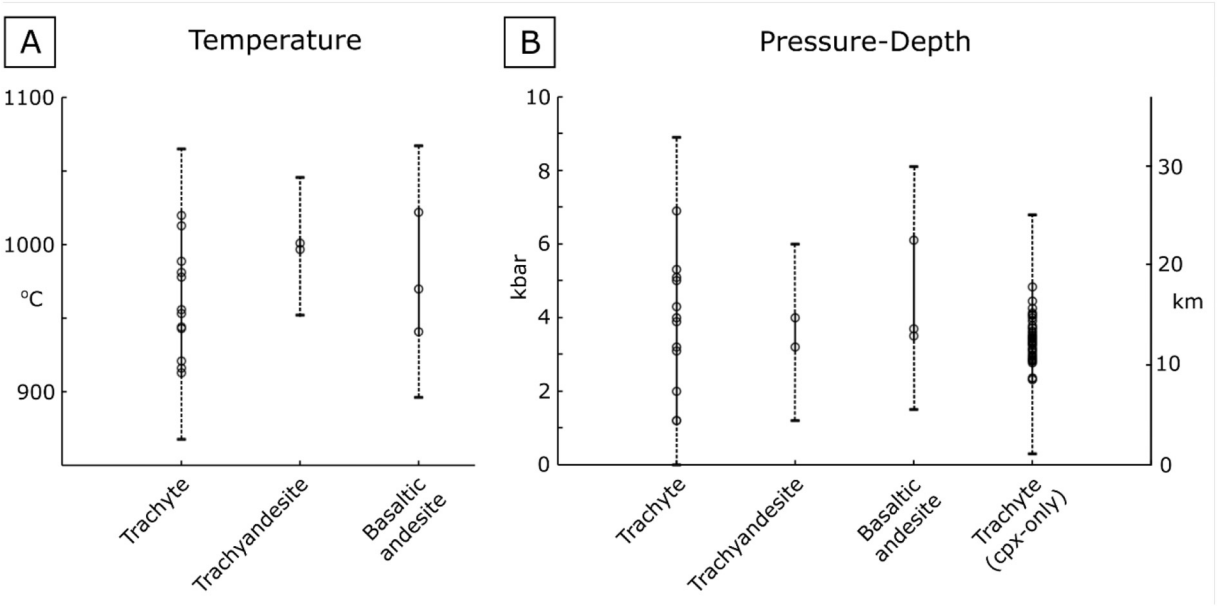

Fig. 8. Estimated temperatures (A) and pressures (B) from clinopyroxene-melt pairs in trachyte, trachyandesite and basaltic andesite lavas. Depths (B) are calculated assuming a crustal density of 2800 kg/m^3 (Weidmann et al., 2013). The "Trachyte (cpx-only)" datapoints (in B) are pressures and depths estimated using clinopyroxenes in trachyte lavas that did not contain melt inclusions, assuming a temperature of 968 °C. Solid lines connect estimated values (circles) and dashed lines represent the uncertainties of 45 °C (Putirka, 2008) and 2 kbar (Nimis, 1999a).

in lavas erupted from Villarrica (Fig. 10) do not show this enrichment compared to N-MORB (except in Ce) as values of rock/N-MORB plot at around 1. Data from Lanín and Sollipulli show a similar pattern (Fig. 10; see supplementary material for data and references), but with variable levels of enrichment, spanning the range observed at Quetrupillán and Villarrica. Evolved products from Lanín and Sollipulli have HSFE ratios similar to those of Quetrupillán, while basalts from Lanín and Sollipulli have HFSE ratios similar to those of Villarrica.

This strongly suggests a common mantle source for these volcanoes (N-MORB), that undergoes variable amounts of contamination. Villarrica represents little or no enrichment, while at Quetrupillán, enrichment is higher. At Lanín and Sollipulli, enriched products are similar to Quetrupillán lavas, while non-enriched products are similar to Villarrica lavas. We propose that this enrichment is likely from crustal assimilation, and that Villarrica and Quetrupillán represent end members of the extent of enrichment.

Figs. 7C to 7E show different combinations of compatible-incompatible (Cr/Zr, Cr/Rb) and incompatible-incompatible (La/Yb, Rb/Zr) ratios to test for a common source and provide insights on the fractionation process. The relatively small variation in incompatible-incompatible ratios clearly supports a common single source for these magmas, while the observed decreasing trend in compatible-incompatible ratios (e.g. Cr/Rb) supports a fractionation model as the main process for magma evolution. The trend in the plot of Rb vs Cr (Fig. 7F) with a slight enrichment in Rb, compared with the expected evolution of Rb in a fractionation-only model, is compatible with the contamination hypothesis and longer crustal residence time during fractionation. As Cr-spinel occurs in basaltic andesite lavas, the early fractionation of this phase might have played an important role in Cr behaviour. Additionally, although chromium is incompatible in olivine (crystallising in a basalt or a basaltic andesite) it is compatible in clinopyroxene (Rollinson, 1993), suggesting a process with the initial fractionation of olivine in the basaltic andesite, followed by the fractionation of olivine + clinopyroxene.

5.4. Quetrupillán magma generation

In this region of the SVZ, basaltic melt is produced by dehydration of the subducted slab and the partial melting of a mantle source (Hildreth and Moorbath, 1988; Stern et al., 2007; Hickey-Vargas et al., 2016a). Deep fractionation of this melt will provide the source of magmas erupted in the region (Stern, 2004; Cembrano and Lara, 2009). Basalts are significant constituents of erupted products from Villarrica and Lanín (Fig. 11; Clavero and Moreno, 2004; Lara et al., 2004), and are minor products erupted by Quetrupillán (Fig. 3). Basalts have also been erupted by eight minor eruptive centres (MECs) that are located 12–35 km north of Quetrupillán, including Huililco, Caburgua and San Jorge (McGee et al., 2017). The abundance of basalt produced by surrounding volcanoes suggests that the composition of the original source melt at Quetrupillán is likely to be basaltic.

Previous authors (Pavez, 1997; Brahm et al., 2018) have suggested that the basaltic to basaltic andesite MEC of Huililco, which lies 12 km northeast of Quetrupillán's summit, represents the parental melt of Quetrupillán. As a result, Huililco basalt has been used in modelling calculations to determine the generation of Quetrupillán magmas (Brahm et al., 2018). During fieldwork, we identified a Holocene basaltic lava flow on the flanks of Quetrupillán, assumed to have erupted from the summit region. This provides a parental melt composition that is definitely present in the magmatic plumbing system below Quetrupillán, rather than a composition erupted from Huililco, a different volcano, 12 km away from Quetrupillán's main edifice.

This Holocene basalt is porphyritic, with phenocrysts of plagioclase, olivine, clinopyroxene and an oxide phase in a highly crystalline groundmass of the same minerals. We modelled mixing of this basalt sample from Quetrupillán (Q67; Table 1) with a representative trachyte sample from Quetrupillán (Q3; Table 1) using the online tool Olive 2.1.1 (Cortés, 2016). Modelled major element concentrations match the major element concentrations of erupted Holocene basaltic andesite and trachyandesite lava samples (Fig. 12).

Mixing 77% basalt and 23% trachyte (sample Q67 and Q3 respectively; Table 1) produces a basaltic andesite very similar to the basaltic andesite erupted from the flanks of Quetrupillán, and mixing 71% basalt with 29% trachyte produces a composition similar to basaltic andesite erupted from the summit of Quetrupillán. The two trachyandesite flank lava compositions are reproduced when mixing 56% and 48% basalt with 44% and 52% trachyte, respectively.

The modelled compositions generated when mixing Quetrupillán basalt and trachyte lavas are a close fit in the concentration of CaO,

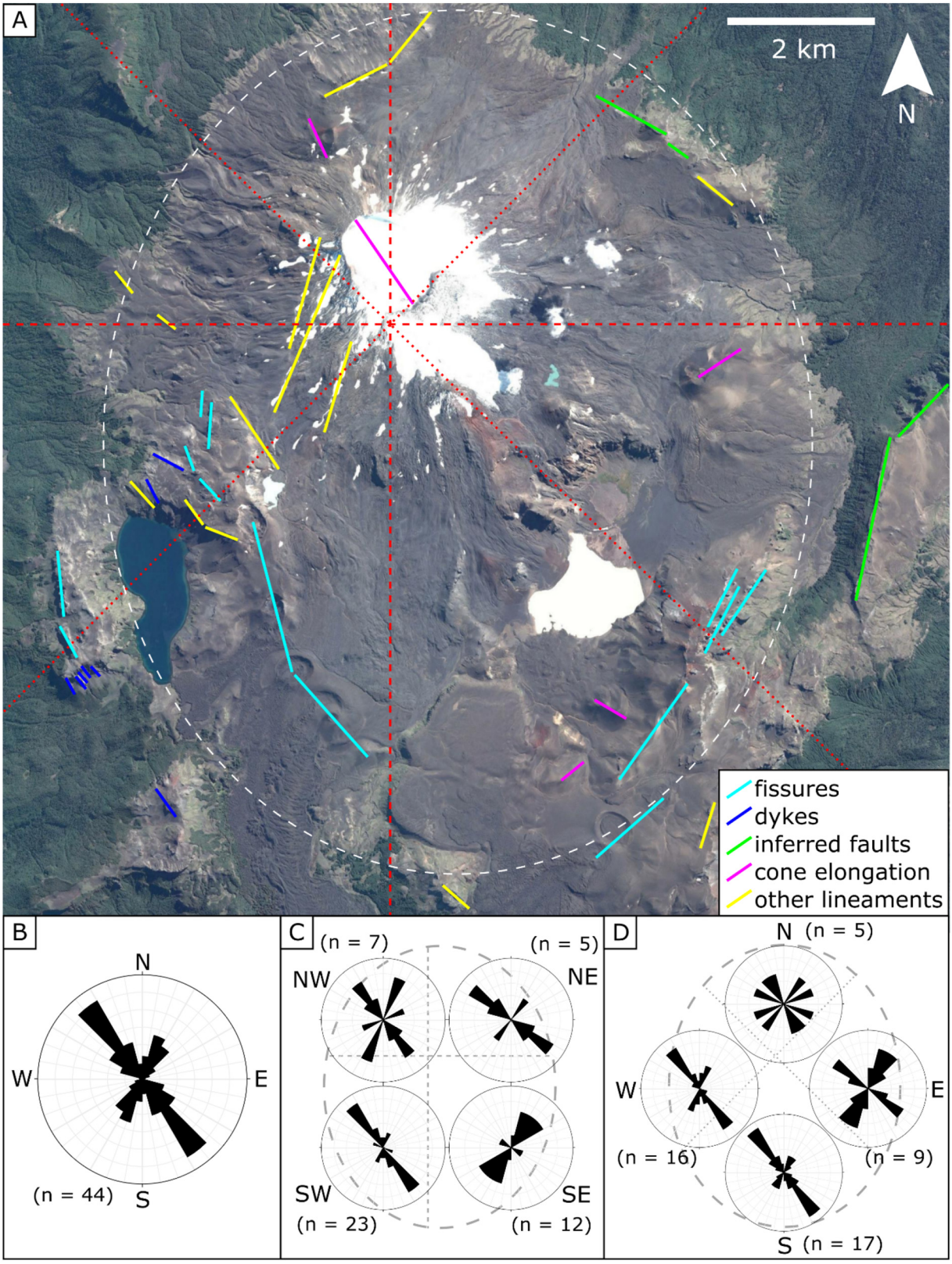

Fig. 9. A) Identified structural lineaments on the flanks of Quetrupillán (light blue – Holocene and possible Pleistocene fissures; dark blue – dykes; green – inferred faults; pink – cone elongation; yellow – other lineaments defined by topography and geomorphology) with the flanks divided into segments (red dotted lines divide N-E-S-W quadrants; red dashed lines divide NW-NE-SE-SW quadrants; white dashed oval represents the volcano outline used in C and D); B) rose diagram of all 44 lineaments; C) rose diagrams of flanks divided into NW-NE-SE-SW quadrants; D) rose diagrams of flanks divided into N-E-S-W quadrants. Google Earth image downloaded 24/02/2020. (For interpretation of the references to colour in this figure legend, the reader is referred to the web version of this article.)

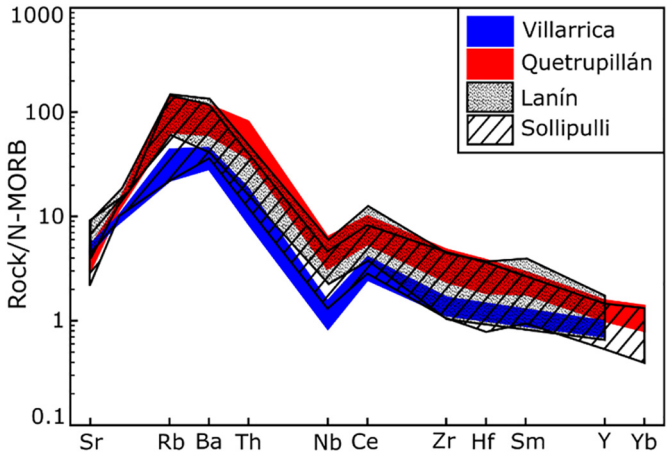

Fig. 10. Spider diagram of lavas from Quetrupillán (red field; this study, Holocene samples only), Villarrica (blue field), Lanín (dotted field) and Sollipulli (hatched field). See supplementary material for data and references for Villarrica, Lanín and Sollipulli. (For interpretation of the references to colour in this figure legend, the reader is referred to the web version of this article.)

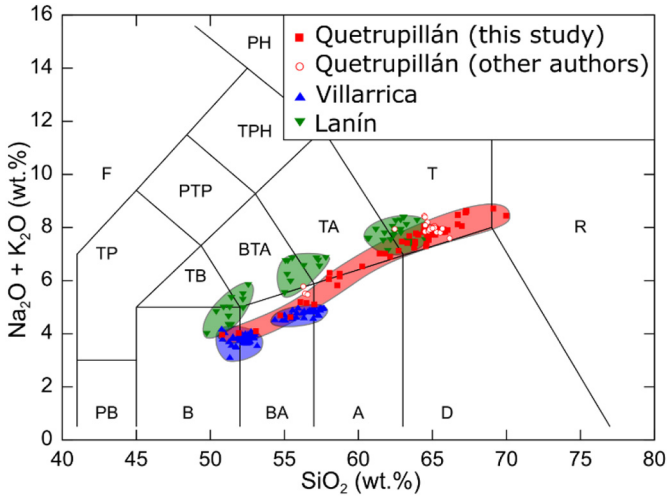

Fig. 11. TAS plot of whole rock analyses of samples from Villarrica (blue triangles), Quetrupillán (red squares – this study; red open circles – other authors) and Lanín (green inverted triangles). Data and data sources are listed in the supplementary material. (For interpretation of the references to colour in this figure legend, the reader is referred to the web version of this article.)

Na_2O, K_2O and MgO when compared to the basaltic andesite and trachyandesite lavas erupted from the flanks and summit of Quetrupillán. The modelled compositions underestimate the concentration of $Fe_2O_3^T$ in the basaltic andesite and trachyandesite samples and overestimate the concentration of Al_2O_3. Neither TiO_2 nor P_2O_5 are well modelled, due to their low concentrations in all Quetrupillán samples. TiO_2 is present in Ilmenite and Titanomagnetite, and P_2O_5 is present in Apatite, all accessory phases in Quetrupillán lavas that have not been considered in the presented modelling.

The basalt lava that erupted at Quetrupillán may have been altered from its original, parental composition, resulting in the observed variations between the modelled and erupted basaltic andesites and trachyandesites. By altering the composition of the basalt input in the modelled mixing, a closer fit to the basaltic andesite and trachyandesite samples can be achieved (Fig. 12B). The concentration of $Fe_2O_3^T$ was increased from 8.97 wt% to 9.8 wt%, and the concentration of Al_2O_3 was decreased from 17.87 wt% to 17.1 wt%. Although the modelled compositions have a close fit for Na_2O and K_2O, Na_2O is overestimated for basaltic andesite samples and K_2O is underestimated for trachyandesite samples. To improve the fit of the modelled compositions, the concentration of Na_2O in the basaltic input was decreased from 3.02 wt% to 2.7 wt%, and the concentration of K_2O was increased from 1.01 wt% to 1.25 wt%, resulting in modelled compositions closer to those present in the basaltic andesite and trachyandesite samples of Quetrupillán.

The mixing of basalt and trachyte to produce the basaltic andesite and trachyandesite magmas is also supported by plotting major and trace element concentrations on an abacus diagram (Fig. 13). The basaltic andesite and trachyandesite lavas from flank vents plot as near-vertical lines, indicating that they are very likely to be hybrid magmas formed by mixing the selected trachyte and basalt end member magmas (McGarvie et al., 1990). Mixing of ~80% basalt with ~20% trachyte can produce the basaltic andesite lava and mixing of ~35–45% basalt with ~55–65% trachyte can produce the trachyandesite lavas, consistent with the proportions found using just major elements (Fig. 12). The mixing relationship is not perfect, as the basaltic andesite sample (Q50) is offset from a vertical line for Sr and Nb and the trachyandesite samples (Q8 and Q17) are slightly offset for SiO_2, CaO, Nd, and La. It should be noted that this diagram only produces near-vertical mixing lines when both end member magmas and the hybrids produced by mixing them occur in the same eruption. This does not occur at Quetrupillán, as magma mixing takes place at depth, and only the hybrid magma is erupted.

Consequently, the precise composition of the two end member magmas is not known, although the abundance and restricted compositional range of Holocene trachyte lavas provides a good approximation of the likely trachyte end member. The strong similarity in the range of compositions that have been erupted during both the Pleistocene and Holocene (Fig. 3) suggests a continuity in the generation of magmas produced beneath Quetrupillán through time.

The basalt sample used as the basaltic end member for mixing with trachyte has total mineral proportions (converted to weight percent) of 28% olivine, 20% clinopyroxene, 32% plagioclase and 20% oxide. Modelling batch fractionation of these mineral proportions (assuming the oxide phase is all Magnetite) from the basaltic andesite sample can reproduce the REE concentrations observed in the trachyandesite and trachyte samples from Quetrupillán (Fig. 14). The trachyte REE profile is reproduced when $F = 0.7$ and the trachyandesite REE profile is reproduced when $F = 0.4$, though in both cases the concentrations of La and Ce are underestimated by the model. As fractionating the mineral assemblage equivalent to the basalt from the basaltic andesite is able to reproduce the trachyte, mixing of the trachyte with the basalt should therefore also produce the basaltic andesite.

5.5. Tectonic constraints

Our proposed model for the tectonic setting at Quetrupillán (Fig. 15) is based on Quetrupillán's location in relation to the geometry of the LOFZ in the area. Dextral strike-slip movement along the branches of the LOFZ would result in the central block undergoing rotation, leading to zones of compression and tension within the block. The dextral-oblique convergence between the Nazca and South American Plates has resulted in a maximum compression axis (σ_1) that is subhorizontal and NE-trending in the SVZ, while the minimum compression axis (σ_3) is subhorizontal and NW-trending (Cembrano and Lara, 2009).

Assuming Quetrupillán is located in the southwest compressive quadrant, then the theoretical N-S strike-slip fault in the model matches the ~N-S aligned fault scarp that runs along the Huililco Valley. If so, Volcán Huililco (a basaltic scoria cone) would be located in the southeast extensional quadrant, as it is on the other side of the Huililco Valley fault scarp. The theoretical W-E strike-slip fault on our model could be matched with the strike-slip fault running ~NW-SE along the Rio Pucón Valley, north of Quetrupillán, defined by Rosenau et al. (2006).

Tectonically, Quetrupillán has a unique position among the Holocene volcanoes of the SVZ as it is located between the two main

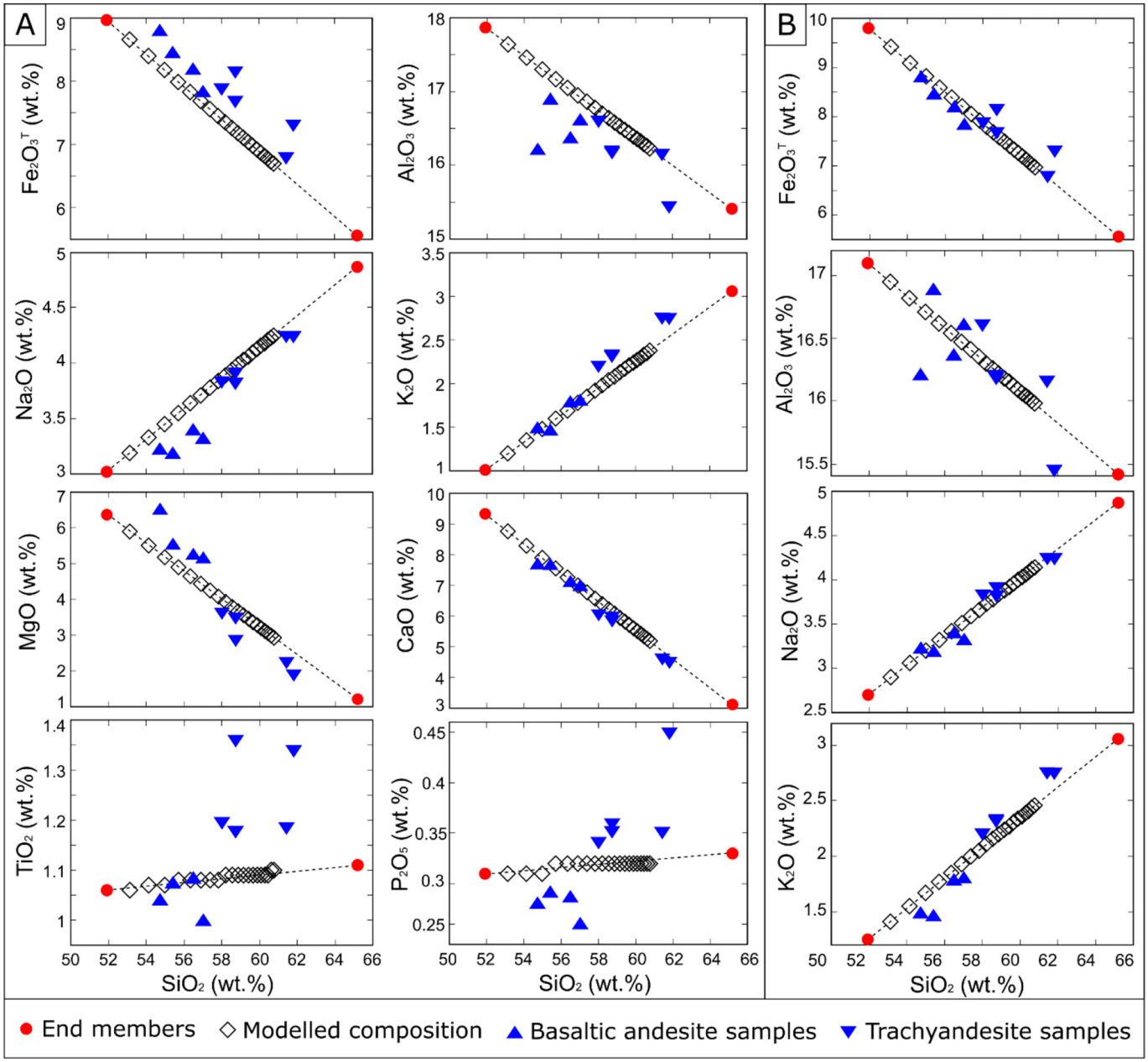

Fig. 12. A) Harker diagrams showing modelled major element compositions (black diamonds) when mixing a basalt lava sample from Quetrupillán (Q67) with a trachyte lava sample (Q3; red circles). Basaltic andesite samples (blue triangles) and trachyandesite samples (inverted blue triangles) from Quetrupillán are also plotted. B) Harker diagrams showing the same modelling, but with altered Fe_2O_3 (9.8 wt%), Al_2O_3 (17.1 wt%), Na_2O (2.7 wt%) and K_2O (1.25 wt%) in the basalt input. (For interpretation of the references to colour in this figure legend, the reader is referred to the web version of this article.)

branches of the LOFZ (Fig. 1). According to Cembrano and Lara (2009), Quetrupillán and Sollipulli are the only stratovolcanoes that lie between the two branches of the LOFZ. Sollipulli, which lies 60 km north of Quetrupillán, is the closest analogue volcano to Quetrupillán in terms of being a volcanic complex in the same tectonic position, sitting between the branches of the LOFZ. However, we know of no study that links the tectonic and magmatic interplay at Sollipulli, and so we are unable to compare whether similar structural controls have influenced its magmatism. Although its overall volcano-tectonic setting will be different from Quetrupillán, it seems likely that similar tectonic stresses have also influenced magmatism at Sollipulli. Erupted products from Sollipulli show a range of enrichment (Fig. 10), suggesting they have undergone different degrees of contamination and evolution, controlled by the tectonic stresses at the volcano.

Observed lineaments around the flanks of Quetrupillán are predominantly oriented tangentially to the main edifice, with very few oriented radially to it (Fig. 9). The load imposed by a volcanic edifice on the crust will cause stress perturbations that are expected to result in dykes and fissures with trajectories that are radial to the edifice summit, while beyond the influence of the volcanic edifice any lineaments are expected to be oriented to the regional stress regime (Roman and Jaupart, 2014).

At Volcán Llaima, 90 km north of Quetrupillán, the influence of the tectonic regime is superimposed on the influence of the volcanic edifice, resulting in two sets of dykes, one oriented radial to the summit and one oriented to the stress regime generated by the relative location of the LOFZ (Schonwalder-Angel et al., 2018). At Quetrupillán, the absence of radially oriented lineaments strongly suggests that the regional stress regime generated by the LOFZ overwhelms the local stress

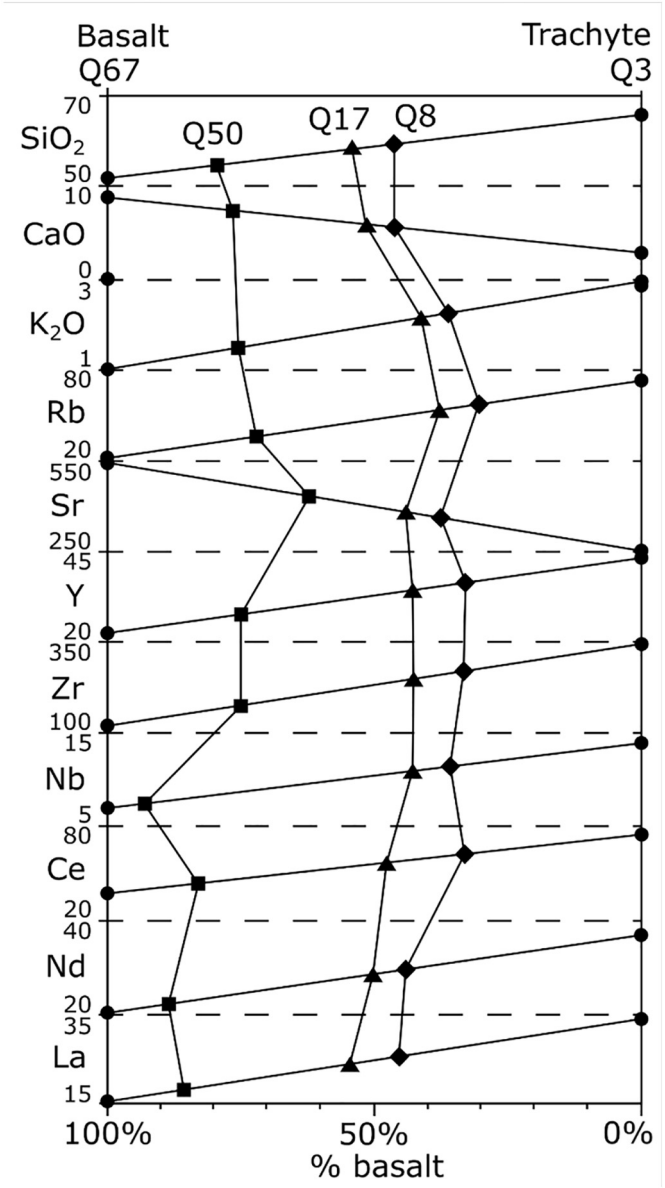

Fig. 13. Abacus diagram illustrating mixing between a trachyte end member magma (Q3) and a basalt end member (Q67). The x-axis shows the proportion of the basalt end member magma, and the y-axis gives major element (oxide wt%) and trace element (ppm) concentrations. On this diagram, hybrid compositions produced by mixing together the two selected end member magmas will produce straight vertical lines (McGarvie et al., 1990). The compositions of the basaltic andesite (Q50 – squares) and trachyandesite (Q8 – diamonds; Q17 – triangles) flank vent lavas are plotted.

perturbations caused by the volcanic edifice. And unlike at Llaima (Schonwalder-Angel et al., 2018), there is no relation between the composition of products from vents on the flanks of Quetrupillán, and the location of the vents (Fig. 2). This implies that although the orientation of lineaments is influenced by the tectonic regime, the variation in composition of volcanic products is not, suggesting that such variation is a consequence of a more localised process.

The secondary set of lineaments at Quetrupillán corresponds to the orientation of the LOFZ (NNE), while the primary set of lineaments seems to be a conjugate set to them (Fig. 89). The dominant structures at other volcanoes located on or near the LOFZ show similar orientations to this, such as at Yate and Michinmahuida (Watt et al., 2009). This suggests that the stress field of the LOFZ may have a similar influence on the magmatic plumbing systems of other volcanoes within the SVZ.

5.6. Conceptual model

It is generally accepted that magmatic plumbing systems form stable transcrustal structures (Cashman et al., 2017; Magee et al., 2018). We adapt this conceptual model for the magmatic plumbing system of Quetrupillán, in which pockets of trachytic melt are contained within a region of crystal mush (Fig. 16). Partial melting in the lithospheric mantle feeds basaltic melt into the base of the crust (Hildreth and Moorbath, 1988; Hickey-Vargas et al., 2016b; Magee et al., 2018), which stalls on its ascent through the crust due to the local compressional tectonic regime in which Quetrupillán is located (Fig. 15). In accordance with this model, these pockets of stalled melt evolve through fractional crystallisation (Hickey-Vargas et al., 1989; Brahm et al., 2018), and as liquid magma crystallises, the proportion of crystals suspended in the melt increases until they have formed a network of crystals containing interstitial melt, at which point they become crystal mush (Hildreth, 2004; Glazner et al., 2016). Crystallisation will result in an increased silica content in the remaining melt. It is proposed that a degree of crustal contamination will result in increased alkali and LILE concentrations, as well as enrichment in some of the HFSEs (Fig. 7), producing the trachytic magmatic system present below Quetrupillán. The production of trachytes is regionally unusual (Stern, 2004), and is speculated to occur at Quetrupillán due to its unique tectonic setting.

Partial melting in the mantle generates the basaltic melt that is injected into the base of the crust at all the magmatic plumbing systems in the SVZ (Hildreth and Moorbath, 1988). The local tectonic regime at each volcano will control how fast this basalt ascends through the crust, determining whether it will evolve to more differentiated compositions (Cembrano and Lara, 2009). At Volcán Villarrica, there is a continual flux of magma through the system. As one of the most active volcanoes in South America (Lara, 2004; Petit-Breuilh, 2004), the basaltic input is rapidly fluxed through the magmatic plumbing system and so does not evolve beyond basaltic andesite. This suggests that the stress conditions to the west of the LOFZ promote magma ascent, while within the LOFZ magma ascent is hindered. If an equivalent rate of basaltic injection is occurring beneath Quetrupillán as beneath Villarrica, then the tectonic setting at Quetrupillán is preventing it from fluxing through the system so rapidly. Instead, the melt stalls below Quetrupillán, where it evolves into the trachytic plumbing system.

Most basaltic magma that is injected into the base of the magmatic plumbing system will stall within the plumbing system, either in a melt pocket or in the crystal mush, where it will evolve and/or mix with the established trachytic resident melts. While most injected basalt transported by deeply sourced feeder dykes will encounter melt pockets and mingle with the existing magma, some will reach the surface with only minimal interaction with the resident melts (Pansino and Taisne, 2019). The degree of interaction will control the extent of mixing, determining whether the resultant hybrid magma is basaltic andesite ($>$ ~60% basalt mixed with $<$ ~40% trachyte) or trachyandesite ($<$ ~60% basalt mixed with $>$ ~40% trachyte). The varying degrees of interaction may reflect whether ascending basalt intersects the thicker centre of a trachyte pocket (labelled "b" in Fig. 16) or the thinner margin (labelled "c" in Fig. 16), or whether ascending basalt intersects multiple stacked pockets. The eruption of basaltic lavas suggests that some rising basaltic magma had no interaction with trachytic melt pockets during its ascent (labelled "d" in Fig. 16), retaining its basaltic composition when reaching the surface.

In trachyte lavas, the variations in the compositions of melt inclusions, groundmass glass and plagioclase suggest variations in the composition of the melts from which the trachyte lavas have been sourced. Each trachytic melt pocket in the magmatic system will evolve with a slightly different composition, and extraction of melt from different pockets will result in the slight differences observed in trachytic erupted products. This implies slight variations in the composition of the trachyte end members that mixed with ascending basalt to produce the hybrid basaltic andesite and trachyandesite

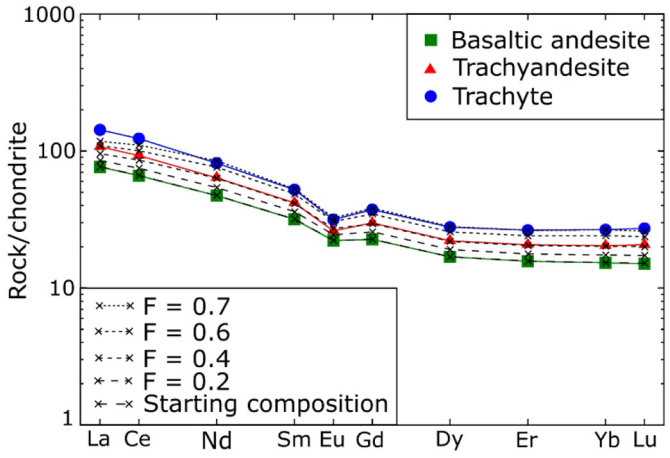

Fig. 14. REE profiles of modelled compositions (black crosses) generated by batch fractionation of 28% olivine, 20% clinopyroxene, 32% plagioclase and 20% Magnetite from a basaltic andesite (green squares) lava from Quetrupillán. Different degrees of fractionation (F) are denoted by different styles of dashed lines. REE profiles of trachyte (blue circles) and trachyandesite (red triangles) lavas from Quetrupillán are also included. (For interpretation of the references to colour in this figure legend, the reader is referred to the web version of this article.)

lavas, explaining the range in melt inclusion compositions found in clinopyroxene xenocrysts.

The Holocene basalt erupted from the summit region and used in the modelled magma mixing is a good approximation for the composition of the source basalt that was input into the base of the system. The similarity in the range of erupted products through the Pleistocene and Holocene (Fig. 3) suggests that there has been no significant change in magma production through time, implying that Quetrupillán's magmatic plumbing system is a stable feature that was established by the Pleistocene.

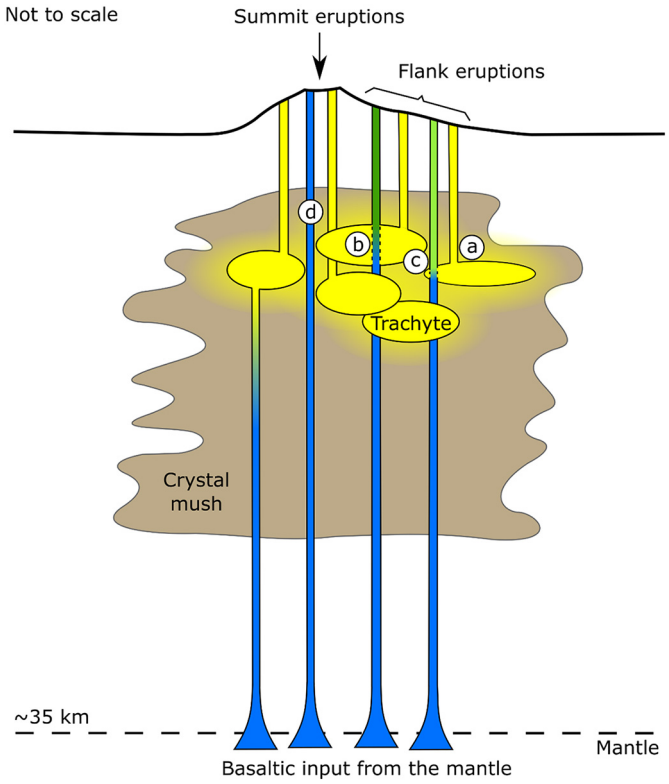

Fig. 16. A conceptual model for the magmatic plumbing system below Quetrupillán, in which pockets of trachytic melt are contained within a region of crystal mush. Extraction of melt from these pockets produces trachytic eruptions (a). Basaltic melt is injected into the system at the base of the crust, and if it ascends close to the surface with minimal interaction with the resident trachyte melts and mush, then trachyandesite (b), basaltic andesite (c) and basalt (d) melts will be produced and erupted, depending on the degree of interaction and mixing.

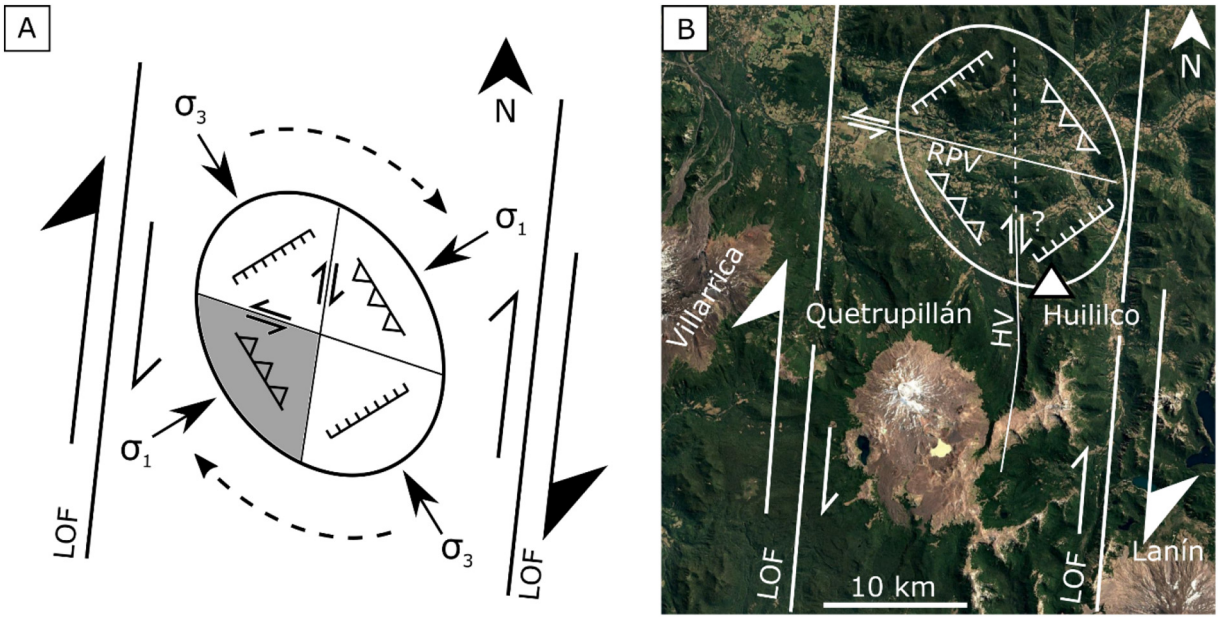

Fig. 15. A) The proposed tectonic model for Quetrupillán, based on the ellipse of deformation from Rosenau et al. (2006). The grey region shows where we propose Quetrupillán is located, on a rotating block between the two NNE-trending dextral strike-slip Liquiñe-Ofqui faults (LOF). B) The proposed tectonic model superimposed over aerial imagery of the Villarrica-Lanín volcanic chain. A fault is suspected along the Huililco Valley (HV) due to the N-trending scarp to the east of Quetrupillán. Consistent with this model, a sinstral strike-slip fault is inferred in the Rio Pucón Valley (RPV) to the north of Quetrupillán, and is outlined by Rosenau et al. (2006). Volcán Huililco is denoted in the figure by a triangle. Satellite image from Google Earth (downloaded 26/05/2020).

6. Conclusions

The plumbing system of Quetrupillán has developed as a transcrustal magmatic system composed of pockets of trachytic melt within a crystal mush, generated by fractional crystallisation and crustal contamination of the basaltic melt injected into the system. Quetrupillán's location within the LOFZ results in compressive tectonic stresses that hinder magma ascent and so promote stalling and evolution of melt within the crust. The tectonic stresses imposed by the LOFZ have a greater influence than the stresses imposed by the load of the volcanic edifice, resulting in lineaments that are tangential to the main edifice, rather than radial to it. Dyke formation enables evolved, trachytic melts to be extracted from the pockets of the magmatic plumbing system and ascend to the surface, forming the numerous trachytic eruptions that have occurred from Quetrupillán's summit and flanks during the Holocene. In some cases, basaltic melt is transported through the system with only minimal interaction with the settled trachytic plumbing system. Varying degrees of mixing between basalt and trachyte produce the basalt, basaltic andesite and trachyandesite products that have been erupted from Quetrupillán.

Data availability

The Supplementary Material contains XRF analyses (collected during this study, and data used in this study collected by other authors), mineral analyses, sample locations and geothermobarometry data.

CRediT authorship contribution statement

Isla Simmons: Investigation, Writing – original draft, Writing – review and editing. **Joaquín Cortés:** Investigation, Writing – original draft, Writing – review and editing, Supervision. **Dave McGarvie:** Investigation, Writing – review and editing, Supervision. **Eliza Calder:** Supervision.

Declaration of Competing Interest

The authors declare that they have no competing interests.

Acknowledgements

The work in this paper forms part of a NERC-funded PhD studentship by Isla Simmons (Grant number NE/L002558/1). Joaquín Cortés received funding from Edge Hill University (RIF grant 1CORTE18) and Santander Universities supported Dave McGarvie. Huge thanks to John Simmons, Franco Vera Rivadeneira, Jack McGarvie and Jonathan Moles for being fantastic field assistants, and to Christa Bönninghoff, Cristian Silva and Claudia Guzmán Roa for help with logistics in the field. We thank Nic Odling, Mike Hall, Nicola Cayzer, Chris Hayward and John Craven at the University of Edinburgh and Valerie Olive at SUERC for analytical support. Sebastian Watt and an anonymous reviewer are acknowledged for comments that greatly improved this manuscript. Diana Roman is acknowledged for editorial handling.

Appendix A. Supplementary data

Supplementary data to this article can be found online at https://doi.org/10.1016/j.jvolgeores.2020.107101.

References

Lara, 2004. Overview of Villarrica Volcano. In: Lara, L., Clavero, J. (Eds.), Villarrica Volcano (39.5ºS). Servicio Nacional de Geología y Minería, Southern Andes, Chile, pp. 5–12.

Allmendinger, R.W., Cardozo, N.C., Fisher, D., 2013. Structural Geology Algorithms: Vectors & Tensors. Cambridge University Press.

Brahm, R., Parada, M.A., Morgado, E., Contreras, C., McGee, L.E., 2018. Origin of Holocene trachyte lavas of the Quetrupillán volcanic complex, Chile: examples of residual melts in a rejuvenated crystalline mush reservoir. J. Volcanol. Geotherm. Res. 357, 163–176. https://doi.org/10.1016/j.jvolgeores.2018.04.020.

Cameron, M., Papike, J.J., 1981. Structural and chemical variations in pyroxenes. Am. Mineral. 66, 1–50.

Cardozo, N.C., Allmendinger, R.W., 2013. Spherical projections with OSXStereonet. Comput. Geosci. 51, 193–205. https://doi.org/10.1016/j.cageo.2012.07.021.

Carmichael, I.S.E., Nicholls, J., Smith, A.L., 1970. Silica activity in Igneous Rocks. Am. Mineral. 55, 246–263.

Cashman, K.V., Sparks, R.S.J., Blundy, J.D., 2017. Vertically extensive and unstable magmatic systems: a unified view of igneous processes. Science (80-.), 355 https://doi.org/10.1126/science.aag3055.

Cembrano, J., Lara, L., 2009. The link between volcanism and tectonics in the southern volcanic zone of the Chilean Andes: a review. Tectonophysics 471, 96–113. https://doi.org/10.1016/j.tecto.2009.02.038.

Cembrano, J., Hervé, F., Lavenu, A., 1996. The Liquiñe Ofqui fault zone: a long-lived intra-arc fault system in southern Chile. Tectonophysics 259, 55–66. https://doi.org/10.1016/0040-1951(95)00066-6.

Cembrano, J., Schermer, E., Lavenu, A., Sanhueza, A., 2000. Contrasting nature of deformation along an intra-arc shear zone, the Liquine-Ofqui fault zone, southern Chilean Andes. Tectonophysics 319, 129–149. https://doi.org/10.1016/S0040-1951(99)00321-2.

Clavero, J., Moreno, H., 2004. Evolution of Villarrica Volcano. In: Lara, L., Clavero, J. (Eds.), Villarrica Volcano (39.5ºS). Servicio Nacional de Geología y Minería, Southern Andes, Chile, pp. 17–27.

Cortés, J.A., 2016. Olive. https://vhub.org/resources/olive.

Cortés, J.A., 2019. Strike converter 1.0 for ImageJ. https://vhub.org/resources/4540.

Cortés, J.A., Wilson, M., Condliffe, E., Francalanci, L., 2006. The occurrence of forsterite and highly oxidizing conditions in basaltic lavas from Stromboli volcano, Italy. J. Petrol. 47, 1345–1373. https://doi.org/10.1093/petrology/egl012.

Daly, R.A., 1911. The Nature of Volcanic Action. Proc. Am. Acad. Arts Sci. 47, 47–122.

Danyushevsky, L.V., Plechov, P., 2011. Petrolog3: Integrated software for modeling crystallization processes. Geochem. Geophys. Geosyst. 12. https://doi.org/10.1029/2011GC003516.

Ginibre, C., Wörner, G., Kronz, A., 2002. Minor- and trace-element zoning in plagioclase: Implications for magma chamber processes at Parinacota volcano, northern Chile. Contrib. Mineral. Petrol. 143, 300–315. https://doi.org/10.1007/s00410-002-0351-z.

Glazner, A., Bartley, J., Coleman, D., 2016. We Need a New Definition for "Magma". Eos (Washington. DC). 97, 1–7. https://doi.org/10.1029/2016eo059741.

Gudmundsson, A., 2012. Magma chambers: Formation, local stresses, excess pressures, and compartments. J. Volcanol. Geotherm. Res. 237–238, 19–41. https://doi.org/10.1016/j.jvolgeores.2012.05.015.

Hernandez-Moreno, C., Speranza, F., Di Chiara, A., 2014. Understanding kinematics of intra-arc transcurrent deformation: Paleomagnetic evidence from the Liquiñe-Ofqui fault zone (Chile, 38–41°S). Tectonics 33, 1964–1988. https://doi.org/10.1002/2014TC003622.

Hersum, T.G., Marsh, B.D., 2007. Igneous textures: on the kinetics behind the words. Elements 3, 247–252. https://doi.org/10.2113/gselements.3.4.247.

Hervé, F., 1994. The Southern Andes between 39° and 44°S latitude: The geological signature of a transpressive tectonic regime related to a magmatic arc. In: Reutter, K.J., Scheuber, E., Wigger, P.J. (Eds.), Tectonics of the Southern Central Andes. Springer, Berlin, pp. 243–248 https://doi.org/10.1007/978-3-642-77353-2_17.

Hickey-Vargas, R., Moreno, H., Lopez-Escobar, L., Frey, F.A., 1989. Geochemical variations in Andean basaltic and silicic lavas from the Villarrica-Lanín volcanic chain (39.5° S): an evaluation of source heterogeneity, fractional crystallization and crustal assimilation. Contrib. Mineral Petrol. 103, 361–386. https://doi.org/10.1007/BF00402922.

Hickey-Vargas, R., Sun, M., López-Escobar, L., Moreno-Roa, H., Reagan, M.K., Morris, J.D., Ryan, J.G., 2002. Multiple subduction components in the mantle wedge: evidence from eruptive centers in the Central Southern volcanic zone, Chile. Geology 30, 199–202. https://doi.org/10.1130/0091-7613(2002)030<0199:MSCITM>2.0.CO;2.

Hickey-Vargas, R., Holbik, S., Tormey, D., Frey, F.A., Moreno Roa, H., 2016a. Basaltic rocks from the Andean Southern Volcanic Zone: Insights from the comparison of along-strike and small-scale geochemical variations and their sources. Lithos 258–259, 115–132. https://doi.org/10.1016/j.lithos.2016.04.014.

Hickey-Vargas, R., Sun, M., Holbik, S., 2016b. Geochemistry of basalts from small eruptive centers near Villarrica stratovolcano, Chile: Evidence for lithospheric mantle components in continental arc magmas. Geochim. Cosmochim. Acta 185, 358–382. https://doi.org/10.1016/j.gca.2016.03.033.

Hildreth, W., 2004. Volcanological perspectives on Long Valley, Mammoth Mountain, and Mono Craters: several contiguous but discrete systems. J. Volcanol. Geotherm. Res. 136, 169–198. https://doi.org/10.1016/j.jvolgeores.2004.05.019.

Hildreth, W., Moorbath, S., 1988. Crustal contributions to arc magmatism in the Andes of Central Chile. Contrib. Mineral. Petrol. 98, 455–489. https://doi.org/10.1007/BF00372365.

Irvine, T.N., Baragar, W.R.A., 1971. A guide to the chemical classification of the common volcanic rocks. Can. J. Earth Sci. 8, 523–548.

Lara, L.E., Naranjo, J.A., Moreno, H., 2004. Lanín volcano (39.5°S), Southern Andes: geology and morphostructural evolution. Rev. Geológica Chile 31, 1–14. https://doi.org/10.4067/S0716-02082004000200004.

Lara, L.E., Lavenu, A., Cembrano, J., Rodríguez, C., 2006. Structural controls of volcanism in transversal chains: Resheared faults and neotectonics in the Cordón Caulle-Puyehue area (40.5°S), Southern Andes. J. Volcanol. Geotherm. Res. 158, 70–86. https://doi.org/10.1016/j.jvolgeores.2006.04.017.

Le Maitre, R.W., Streckeisen, A., Zanettin, B., Le Bas, M.J., Bonin, B., Bateman, P., 2002. Igneous Rocks; a Classification and Glossary of Terms. 2nd ed. Cambridge University Press.
López-Escobar, L., Cembrano, J., Moreno, H., 1995. Geochemistry and tectonics of the Chilean southern Andes basaltic Quaternary volcanism (37-46°S). Rev. Geológica Chile 22, 219–234. https://doi.org/10.5027/andgeoV22n2-a06.
Lorenz, V., 1986. On the growth of maars and diatremes and its relevance to the formation of tuff rings. Bull. Volcanol. 265–274. https://doi.org/10.1007/BF01081755.
Magee, C., Stevenson, C.T.E., Ebmeier, S.K., Keir, D., Hammond, J.O.S., Gottsmann, J.H., Whaler, K.A., Schofield, N., Jackson, C.A.L., Petronis, M.S., O'Driscoll, B., Morgan, J., Cruden, A., Vollgger, S.A., Dering, G., Micklethwaite, S., Jackson, M.D., 2018. Magma plumbing systems: a geophysical perspective. J. Petrol. 59, 1217–1251. https://doi.org/10.1093/petrology/egy064.
Marsh, B.D., 1989. Magma chamber. Annu. Rev. Earth Planet. Sci. Vol. 17, 439–474. https://doi.org/10.1146/annurev.earth.17.1.439.
McGarvie, Dave, Pavez, A., Cortés, J.A., Faggetter, L., Burgess, R., McGarvie, Dan, 2014. Glaciovolcanism at Volcán Quetrupillán, Chile. GSA Annual Meeting.
McGarvie, D.W., Macdonald, R., Pinkerton, H., Smith, R.L., 1990. Petrogenetic evolution of the torfajökull volcanic complex, Iceland II. The role of magma mixing. J. Petrol. 31, 461–481. https://doi.org/10.1093/petrology/31.2.461.
McGee, L.E., Brahm, R., Rowe, M.C., Handley, H.K., Morgado, E., Lara, L.E., Turner, M.B., Vinet, N., Parada, M.Á., Valdivia, P., 2017. A geochemical approach to distinguishing competing tectono-magmatic processes preserved in small eruptive centres. Contrib. Mineral. Petrol. 172, 1–26. https://doi.org/10.1007/s00410-017-1360-2.
Nelson, S.T., Montana, A., 1992. Sieve-textured plagioclase in volcanic rocks produced by rapid decompression. Am. Mineral. 77, 1242–1249.
Nimis, P., 1999a. Clinopyroxene geobarometry of magmatic rocks. Part 2. Structural geobarometers for basic to acid, tholeiitic and mildly alkaline magmatic systems. Contrib. Mineral Petrol. 135, 62–74. https://doi.org/10.1007/s004100050498.
Nimis, P., 1999b. CpxBar Excel version.
Olive, V., Ellam, R.M., Wilson, L., 2001. A protocol for the determination of the rare earth elements at picomole level in rocks by ICP-MS: results on geological reference materials USGS PCC-1 and DTS-1. Geostand. Newslett. 25, 219–228. https://doi.org/10.1111/j.1751-908x.2001.tb00597.x.
Pansino, S., Taisne, B., 2019. How Magmatic Storage Regions Attract and Repel Propagating Dikes. J. Geophys. Res. Solid Earth 124. https://doi.org/10.1029/2018JB016311.
Papike, J.J., Cameron, K.L., Baldwin, K., 1974. Amphiboles and pyroxenes: Characterization of other than quadrilateral components and estimates of ferric iron from microprobe data. Geol. Soc. Am. Abstr. with Programs 6, 1053–1054.
Pardo-Casas, F., Molnar, P., 1987. Relative motion of the Nazca (Farallon) and South American plates since Late Cretaceous time. Tectonics 6, 233–248.
Pavez, A., 1997. Geología e historia evolutiva del Complejo Volcánico Quetrupillán, Andes del Sur, 39.5° L.S. VIII Congreso Geológico Chileno, pp. 1443–1447.
Pearce, J.A., 1983. Role of the sub-continental lithosphere in magma genesis at active continental margins. In: Hawkesworth, C.J., Norry, M.J. (Eds.), Continental Basalts and Mantle Xenoliths. Shive Publications, Nantwich, Cheshire, pp. 230–249.
Petit-Breuilh, M.E., 2004. La historia eruptiva de los volcanes Hispanoamericanos (Siglos XVI al XX) (Cabildo Insular de Lanzarote).
Putirka, K.D., 2008. Thermometers and Barometers for Volcanic Systems. Rev. Mineral. Geochemistry 69, 61–120. https://doi.org/10.2138/rmg.2008.69.3.
Roeder, P.L., Emslie, R.F., 1970. Olivine-liquid equilibrium. Contrib. Mineral. Petrol. 29, 275–289.
Rollinson, H., 1993. Using geochemical data: evaluation, presentation, interpretation. Routledge.
Roman, A., Jaupart, C., 2014. The impact of a volcanic edifice on intrusive and eruptive activity. Earth Planet. Sci. Lett. 408, 1–8. https://doi.org/10.1016/j.epsl.2014.09.016.
Rosenau, M., Melnick, D., Echtler, H., 2006. Kinematic constraints on intra-arc shear and strain partitioning in the southern Andes between 38°S and 42°S latitude. Tectonics 25. https://doi.org/10.1029/2005TC001943.
Schindelin, J., Arganda-Carreras, I., Frise, E., Kaynig, V., Longair, M., Pietzsch, T., Preibisch, S., Rueden, C., Saalfeld, S., Schmid, B., Tinevez, J.Y., White, D.J., Hartenstein, V., Eliceiri, K., Tomancak, P., Cardona, A., 2012. Fiji: an open-source platform for biological-image analysis. Nat. Methods 9, 676–682. https://doi.org/10.1038/nmeth.2019.
Schonwalder-Angel, D., Cortés, J.A., Calder, E.S., 2018. The interplay of magmatism and tectonics: an example based on the satellite scoria cones at Llaima volcano, Chile. J. Volcanol. Geotherm. Res. 367, 31–45. https://doi.org/10.1016/j.jvolgeores.2018.10.020.
Simmons, I.C., McGarvie, D., Cortés, J.A., Calder, E.S., Pavez, A., 2020. Holocene volcanism at the Quetrupillán Volcanic complex (39°30' S, 71°43' W), southern Chile. Volcanica 3, 115–137.
Sisson, T., Grove, T.L., 1993. Temperatures and H2O contents of low-MgO high-alumina basalts. Contrib Mineral. Petrol. 113, 167–184.
Stern, C.R., 1991. Role of subduction erosion in the generation of Andean magmas. Geology 19, 78–81. https://doi.org/10.1130/0091-7613(1991)019<0078:ROSEIT>2.3.CO;2.
Stern, C.R., 2004. Active Andean volcanism: its geologic and tectonic setting. Rev. Geológica Chile 31, 161–206. https://doi.org/10.4067/S0716-02082004000200001.
Stern, C.R., Moreno, H., Lopéz-Escobar, L., Clavero, J.E., Lara, L.E., Naranjo, J.A., Parada, M.A., Skewes, M.A., 2007. Chilean Volcanoes. In: Moreno, T., Gibbons, W. (Eds.), The Geology of Chile. Geological Society of London Special Publication, pp. 147–178 https://doi.org/10.1144/GOCH.5.
Sun, S.S., McDonough, W.F., 1989. Chemical and isotopic systematics of oceanic basalts: Implications for mantle composition and processes. Geol. Soc. Spec. Publ. 42, 313–345. https://doi.org/10.1144/GSL.SP.1989.042.01.19.
Toplis, M.J., Carroll, M.R., 1995. An experimental study of the influence of oxygen fugacity on fe-ti oxide stability, phase relations, and mineral-melt equilibria in ferro-basaltic systems. J. Petrol. 36, 1137–1170. https://doi.org/10.1093/petrology/36.5.1137.
Valentine, G.A., Connor, C.B., 2015. Basaltic Volcanic Fields. The Encyclopedia of Volcanoes, Second ed. Elsevier Inc https://doi.org/10.1016/B978-0-12-385938-9.00023-7.
Valentine, G.A., Gregg, T.K.P., 2008. Continental basaltic volcanoes - Processes and problems. J. Volcanol. Geotherm. Res. https://doi.org/10.1016/j.jvolgeores.2008.01.050.
Watt, S.F.L., Pyle, D.M., Naranjo, J.A., Mather, T.A., 2009. Landslide and tsunami hazard at Yate volcano, Chile as an example of edifice destruction on strike-slip fault zones. Bull. Volcanol. 71, 559–574. https://doi.org/10.1007/s00445-008-0242-x.
Weidmann, C., Spagnotto, S., Giménez, M., Martínez, P., Álvarez, O., Sánchez, M., Lince Klinger, F., 2013. Crustal structure and tectonic setting of the south Central Andes from gravimetric analysis. Geofis. Int. 52, 197–208. https://doi.org/10.1016/S0016-7169(13)71472-7.
Wilson, S.A., 1997. The Collection, Preparation and Testing of USGS Reference Material BCR-2 (Columbia River Basalt).
Wohletz, K.H., Sheridan, M.F., 1983. Hydrovolcanic explosions II. Evolution of basaltic tuff rings and tuff cones. Am. J. Sci. 283, 385–413. https://doi.org/10.2475/ajs.283.5.385.

Sunset, Laguna Azul